



HAL
open science

Cellular mechanisms of cancer collective invasion and response to treatments

Diane-Laure Pagès

► **To cite this version:**

Diane-Laure Pagès. Cellular mechanisms of cancer collective invasion and response to treatments. Cancer. Université Paris-Saclay, 2022. English. NNT : 2022UPASL031 . tel-04131768

HAL Id: tel-04131768

<https://theses.hal.science/tel-04131768>

Submitted on 17 Jun 2023

HAL is a multi-disciplinary open access archive for the deposit and dissemination of scientific research documents, whether they are published or not. The documents may come from teaching and research institutions in France or abroad, or from public or private research centers.

L'archive ouverte pluridisciplinaire **HAL**, est destinée au dépôt et à la diffusion de documents scientifiques de niveau recherche, publiés ou non, émanant des établissements d'enseignement et de recherche français ou étrangers, des laboratoires publics ou privés.

Cellular mechanisms of cancer collective invasion and response to treatments

*Mécanismes cellulaires de l'invasion collective des cancers
et de leur réponse aux traitements*

Thèse de doctorat de l'université Paris-Saclay

École doctorale n° 582, cancérologie : biologie - médecine - santé (CBMS)
Spécialité de doctorat : Aspects moléculaires et cellulaires de la biologie
Graduate School : Sciences de la vie et santé. Référent : Faculté de médecine

Thèse préparée dans l'unité de recherche **U1279 – Dynamique des cellules tumorales** (Université Paris-Saclay, Inserm, Institut Gustave Roussy),
sous la direction de **Fanny JAULIN**, Directrice de recherche

Thèse soutenue à Paris-Saclay, le 16 mai 2022, par

Diane-Laure PAGÈS

Composition du Jury

Matthieu PIEL Directeur de recherche, Institut Curie (Paris)	Président
Benoît LADOUX Directeur de recherche, Institut Jacques Monod (Paris)	Rapporteur & Examineur
Michael SIXT Professeur, Institute of Science and Technology (Austria)	Rapporteur & Examineur
Nicolas DAVID Chargé de recherche, École Polytechnique (Orsay)	Examineur
Sandrine ETIENNE-MANNEVILLE Directrice de recherche, Institut Pasteur (Paris)	Examinatrice
Fanny JAULIN Directrice de recherche, Institut Gustave Roussy (Villejuif)	Directrice de thèse

*"No pessimist ever discovered the secret of the stars
or sailed an uncharted land,
or opened a new doorway for the human spirit."*

HELEN KELLER

Remerciements

Avant toutes choses un immense merci, Fanny, de m'avoir accueillie dans ton laboratoire et pour la confiance que tu m'as faite en me remettant ce si beau projet. Merci pour ton accompagnement patient et exigeant, aussi bien scientifique qu'humain, pour ta motivation inépuisable et pour ton enthousiasme communicatif. J'ai eu beaucoup de chance d'apprendre et travailler avec toi et je suis très heureuse que l'aventure continue.

I would like to thank the members of my jury for taking the time to evaluate this PhD work. I was honoured to share and discuss it with you. It was also a great opportunity to meet some of you and I am grateful to those who have been supporting me for some years now.

Je voudrais aussi remercier mes collaborateurs sans qui ce travail n'aurait jamais été possible et qui ont en ont fait une excitante aventure collective, de giggling à jiggling. Merci Matthieu, Mathieu, Jean, Raphaël, Ananyo, Li, Emilie, Aurore et évidemment Emmanuel, pour ces discussions interminables et si riches, pour votre disponibilité, votre créativité et votre enthousiasme à toute épreuve. Ce fut un réel plaisir de travailler ensemble et vous m'avez beaucoup appris. Merci aussi Grégoire et Marceline d'avoir fait partie de cette histoire, vos stages, quoique bien trop courts, ont été mémorables et j'espère que nous aurons l'occasion de nous revoir bientôt. Merci enfin aux médecins du comité digestif de Gustave Roussy de nous permettre de travailler si proche de la clinique.

Et bien sûr je ne saurai assez remercier la fantastique équipe Jaulin : Joël, Jérôme, Charlotte, Rui, Jean-Baptiste, Emmanuel, Émilie, Sabrina, Alice, Clémence, Nicolas, Aurore, Max, Eva, Neegar et Jacques, ainsi que les équipes Montagnac et Khaled, pour cette vie de laboratoire si riche, autant culinairement que scientifiquement, et qui a tant compté durant ma thèse. Merci pour vos conseils, pour votre relecture attentive de ce manuscrit, pour vos encouragements, pour votre humour et pour ces rires, et pour le cœur que vous mettez à ce que vous faites.

Un remerciement spécial à Mélanie pour ta gestion attentionnée de nos souris à l'animalerie, Tudor et Corinne pour votre soutien en imagerie, Allan et Marc pour votre accompagnement patient dans les méandres du code, et Alexandra, Widad, Amélie, Fatoumata et André qui faites que notre laboratoire tourne tous les jours. Merci à tous pour votre aide précieuse au quotidien.

Enfin, à mes très chères famille et belle-famille et à mes si bons amis, et par-dessus tout à Baptiste, mon mari : merci pour vos regards qui me poussent à donner le meilleur de moi-même, pour tous ces moments passés ensemble, pour l'énergie que vous m'avez donnée durant cette thèse en y croyant et en m'y encourageant jusque dans ces derniers mois de rédaction. Car oui, comme vous le dites si bien, un chercheur qui cherche c'est bien, mais un chercheur qui trouve c'est mieux !

Pour terminer, je pense en particulier à Clémence, Laure, mes grands-parents, les patients de Gustave Roussy et leurs médecins, qui faites preuve de tant courage dans le combat contre le cancer.

Synthèse

La dissémination du cancer, c'est-à-dire la formation de métastases dans des organes distants, est aujourd'hui responsable de la majorité des décès liés au cancer. Malgré les avancées importantes de ces dernières décennies, des thérapies efficaces peinent à être identifiées pour chaque patient. A la source de ces difficultés se trouvent des processus cellulaires complexes dont le décryptage est donc d'importance capitale.

La migration cellulaire joue un rôle clé dans la dissémination tumorale ainsi que dans de nombreux processus physiologiques. Trois modes de migration cellulaire principaux sont connus aujourd'hui. Les cellules uniques sont capables de migrer de manière protrusive en exerçant des forces de traction sur leur substrat grâce à des adhésions focales : c'est le mode « mésenchymateux ». Lorsqu'elles se déplacent de manière indépendante de la formation de ces adhésions focales, elles reposent sur leur contractilité et déformation : il s'agit du mode propulsif « amiboïde ». Les cellules peuvent aussi se déplacer en groupe, et adoptent alors généralement une hiérarchie entre cellules meneuses – qui utilisent un mode d'adhésion-traction – et les suiveuses qui assurent la cohésion du groupe et la transmission de forces. Le cytosquelette d'actomyosine est acteur principal de ces processus.

Ce travail de thèse caractérise un nouveau mode de migration collective identifié chez des intermédiaires tumoraux de patients atteints de cancer colorectal métastatique. Grâce à l'utilisation de micro-canaux et de microscopie, nous avons montré que dans différents types de cancer, ces cellules tumorales sont capables de migrer collectivement sans former d'adhésions focales avec leur substrat. Comme les cellules uniques amiboïdes (lymphocytes, amibes), leur mode de migration repose plutôt sur la contractilité des cellules et la polarisation d'un cortex supracellulaire d'actomyosine. L'inhibition de la contractilité empêche ce mode de migration. Réciproquement, des outils d'optogénétique nous ont permis de mettre en évidence que l'activation de RhoA au cortex d'un côté des clusters dictait la direction de migration. Nous l'avons donc appelée « migration collective amiboïde ». Ce mode de migration est indépendant des flux rétrogrades de myosine ou de cellules observés dans les modes de migration conventionnels. Nous montrons que cette migration est permise par des mouvements aléatoires de myosine et de cellules en particulier au contact avec le substrat, et est orientée par la polarisation du cortex.

La migration collective amiboïde présente un intérêt particulier en cancérologie car elle permettrait aux cellules cancéreuses de se déplacer collectivement dans des environnements n'exposant pas de matrice extracellulaire, tels que les canaux lymphatiques, ou pour lesquels elles n'expriment pas les récepteurs spécifiques. Ce mode de migration peut être induit par un environnement non-adhérent ou par les propriétés cellulaires. En particulier, les TSIPs sont des intermédiaires tumoraux qui présentent spontanément ce mode de migration à cause de leur polarité épithéliale inversée qui empêche le contact entre les molécules permettant l'adhésion à l'environnement (intégrines) et la matrice extracellulaire.

Cette thèse présente en outre une autre caractéristique des TSIPs liée à leur inversion de polarité. Nous avons en effet étudié *in vitro* sur des organoïdes la sensibilité des TSIPs à trois traitements chimiothérapeutiques utilisés classiquement contre le cancer colorectal. Cela a mis en évidence une moindre sensibilité aux chimiothérapies des TSIPs à polarité inversée, en comparaison avec leur équivalent à polarité normale. Une hypothèse expliquant ce phénomène est leur moindre pouvoir de prolifération, observé dans les organoïdes comme dans les groupes de cellules récoltés directement

chez les patients. Cette moindre sensibilité aux traitements anti-cancéreux pourrait ainsi aussi participer au mauvais pronostic des patients présentant des TSIPs.

Table of contents

REMERCIEMENTS	5
SYNTHESE	7
TABLE OF CONTENTS	9
GLOSSARY	13
CHAPTER I. INTRODUCTION	15
1. Cell migration is a key feature of physiological and metastatic processes	17
1.1. Cell migration in physiological processes.....	19
1.1.1. Epithelial cell migration and epithelial-to-mesenchymal transition in embryogenesis	19
1.1.1.1. Structure of epithelia and movements during early steps of gastrulation.....	19
1.1.1.2. Epithelial-to-mesenchymal transition drives single cell dissemination	21
1.1.1.3. Migration of cell clusters.....	24
1.1.1.4. Cell migration to shape functional networks	26
1.1.2. Adult physiological processes.....	27
1.1.2.1. Wound healing: migration of immune cells, fibroblasts, and epithelium.....	27
1.1.2.2. Epithelial migration in mammary duct morphogenesis and gut renewal	28
1.2. Deregulation of cell migration promotes cancer spread.....	29
1.2.1. Colorectal carcinoma, a tumour derived from epithelial tissue.....	30
1.2.2. Prominent role of cell invasion in the metastatic cascade.....	33
1.2.2.1. Cell invasion is a hallmark of cancer.....	33
1.2.2.2. Cancer cells dissemination routes	33
1.2.2.3. Tumour cell invasion and the mechanical properties of the microenvironment	36
1.2.3. Modes of carcinoma cell migration and experimental tools	38
1.2.3.1. EMT promotes cancer cell dissemination as single cells	38
1.2.3.2. Collective dissemination of cancer and discovery of TSIPs in CRC	38
1.2.3.3. Experimental models to study cancer cell migration.....	41
2. Mechanistic basis of cell migration	46
2.1. Front-back polarisation of cells during directed migration.....	46
2.1.1. Asymmetric external cues induce cell polarisation.....	46
2.1.1.1. Chemotaxis.....	47
2.1.1.2. Durotaxis	48
2.1.2. Polarised morphology of migrating cells	49
2.1.2.1. Cells can extend different types of front protrusions	49
2.1.2.2. Polarisation of the nucleus-centrosome axis during migration.....	50
2.1.3. Polarised regulation of actomyosin dynamics during cell migration.....	50
2.1.3.1. Actin filaments architecture in cell polarisation and front protrusions	51
2.1.3.2. Actomyosin contractility contributes to cell polarisation.....	54
2.1.3.3. Small Rho GTPases regulate actin and myosin polarised dynamics	56
2.2. Force generation.....	58
2.2.1. Adhesion-traction in single cells: mesenchymal mode of migration	58
2.2.1.1. General description of mesenchymal migration.....	58
2.2.1.2. Focal adhesion formation and force transmission.....	60
2.2.2. Adhesion-traction in collective cell migration.....	63

2.2.2.1.	Definition and subtypes of collective cell migration.....	63
2.2.2.2.	Force generation through front-rear organisation of the cell cohort.....	64
2.2.3.	Propulsion-friction in amoeboid single cells.....	71
2.2.3.1.	Amoeboid migration is associated with low attachment and high deformability	71
2.2.3.2.	Mechanisms of force generation in amoeboid migration	72
3.	Plasticity of cell migration	75
3.1.	Single cell migration plasticity.....	76
3.1.1.	Regulation of actomyosin dynamics and cell migration mode by small Rho GTPases.....	77
3.1.2.	Low adhesiveness and high confinement promote fast amoeboid migration.....	78
3.1.3.	Regulation of cell speed by substrate stiffness.....	79
3.1.4.	Low proteolytic activity promotes amoeboid migration.....	80
3.2.	Transitions between collective and single cell migration	80
3.2.1.	Modulation of cell-cell and cell-ECM adhesion	80
3.2.1.1.	Impairing cell-ECM adhesion promotes amoeboid detachment.....	80
3.2.1.2.	Cell-cell junction modulation affects collective behaviour.....	81
3.2.1.3.	EMT drives cell-cell adhesion loosening and single cell detachment.....	81
3.2.1.4.	Increased actomyosin dynamics promote single cell migration	82
3.2.2.	Cell density and confined environments	82
3.2.2.1.	Jamming-unjamming transition (JUT): from a solid-like to a glass-like behaviour.....	82
3.2.2.2.	Collective-to-amoeboid transition under confinement.....	83
3.3.	Transitions between collective cell migration modes	83
3.3.1.	Crowding affects collective shape and velocity	84
3.3.2.	Regulation by substrate stiffness.....	84
3.3.3.	A collective amoeboid mode of migration	84
CHAPTER II. PHD PROJECT	87	
CHAPTER III. MATERIAL AND METHODS	91	
1. Statistics, reproducibility and data presentation	93	
2. Biological material and cell culture	93	
3. Microchannels, drug incubation and cluster loading	95	
4. TFM setup preparation.....	95	
5. Plasmids, virus production and infection	96	
6. Imaging, microscope acquisition and optogenetic experiments	97	
7. Immunofluorescence in microchannels.....	97	
8. Immunofluorescence, antibodies, histology and immunohistochemistry	98	
9. Image analysis	99	
10. Organoid polarity reversion and drug testing.....	101	
CHAPTER IV. POLARISED CONTRACTILE JIGGLING DRIVES THE COLLECTIVE AMOEBOID MIGRATION OF CELL CLUSTERS	103	
1. Cell clusters migrate in confined non-adhesive environments	105	
2. Focal adhesions and traction forces are not required for cluster migration	110	

3. Cluster amoeboid migration relies on RhoA activation and polarised actomyosin contractility	117
4. Collective amoeboid migration arises from polarised jiggling	123
5. Conclusions on collective amoeboid migration	130
CHAPTER V. APICO-BASAL POLARITY ORIENTATION INFLUENCES RESPONSE TO CHEMOTHERAPIES	135
1. Apical-out organoids respond less to chemotherapies than apical-in organoids.....	137
1.1.1. Biological models to study TSIP phenotype.....	137
1.1.2. Drug tests on apical-in and apical-out cell clusters	137
2. A lower proliferation rate is observed in apical-out clusters.....	140
CHAPTER VI. DISCUSSION	143
1. TSIPs display lower sensibility to chemotherapies in their apical-out topology	145
1.1. Outlooks on <i>in vitro</i> observations.....	145
1.1.1. Experimental setup: collagen-embedded cell clusters from PDXs and automated protocols	145
1.1.2. Hypotheses for apical-out cell clusters lower response to chemotherapies.....	145
1.2. Perspectives for patient care.....	146
2. Deciphering the basic principles of Collective Amoeboid Migration	147
2.1. Technological innovations	147
2.1.1. The choice of biological material.....	147
2.1.2. Experimental design: microchannels.....	148
2.1.3. Increasing robustness and speed in image analysis	150
2.2. Deciphering CAM through the angle of collective cell migration.....	150
2.2.1. A supracellular mode of cell migration	151
2.2.2. Gradient of intercellular tension and force transmission.....	151
2.2.3. ERK-mediated activation of contraction and jiggling.....	151
2.2.4. Cell-cell junctions composition and distribution: jammed-unjammed states and polarity establishment.....	152
2.2.5. Cluster front-rear organisation during CAM.....	152
2.3. How the knowledge of amoeboid migration can improve CAM understanding.....	153
2.3.1. CAM, as single cell amoeboid migration, relies on actomyosin contractility.....	153
2.3.2. Actomyosin and RhoA/Rac1 polarisation.....	154
2.3.3. Force transmission to the substrate	155
2.3.4. Complementary mechanisms inspired by the knowledge of single cell amoeboid migration	156
2.4. Polarised jiggling.....	157
3. Outlooks on Collective Amoeboid Migration.....	158
3.1. Investigating polarity establishment in CAM	158
3.1.1. Increased actomyosin contractility inducing spontaneous polarisation.....	158
3.1.2. Induction of polarisation by supracellular cluster organisation or at a single cell level	159
3.2. CAM integrates the cell migration plasticity landscape.....	159
3.2.1. Observations of switches in cluster phenotypes	160
3.2.2. Transitions between mesenchymal and amoeboid collective modes, and single cell and collective amoeboid modes	160
3.3. <i>In vivo</i> relevance of CAM.....	161

3.3.1. CAM in physiological contexts	161
3.3.2. <i>In vivo</i> environments deprived of ECM would favour CAM	161
3.3.3. CAM in dense ECM-rich environments	162
4. Targeting cell migration in tumour dissemination	163
CONCLUSION	165
ANNEXES	167
Annex 1. Pagès, Dornier et al., bioRxiv, 2020	169
Annex 2. Supplementary text on « Polarised Jiggling » model.....	193
Annex 3. Canet-Jourdan et al., under revision.....	205
LIST OF FIGURES	253
REFERENCES.....	257

Glossary

2D	Two-dimensional	E	
3D	Three-dimensional	E-cadherin	Epithelial cadherin
5-FU	5-fluorouracil	E-cad	
A		ECM	Extracellular matrix
ABP	Actin-binding protein	EGF	Epidermal growth factor
ActA	Actin assembly-inducing protein	EGFR	Epidermal growth factor receptor
ADF	Actin depolymerising factor	EMT	Epithelial-to-mesenchymal transition
ADP	Adenosine diphosphate	ERM	Ezrin, radixin, moesin
AJ	Adherens junction	F	
A/B	Apico-basal	FA	Focal adhesion
Arp2/3	Actin-related protein 2/3	F-actin	Filamentous actin
ATP	Adenosine triphosphate	FAK	Focal adhesion kinase
B		FBS	Foetal bovine serum
Bleb	Blebbistatin	FGF	Fibroblast growth factor
BRAF	v-raf murine sarcoma viral oncogene homolog B1	FRET	Förster resonance energy transfer
BVI	Blood vessel invasion	G	
C		G-actin	Globular actin
CAF	Cancer-associated fibroblast	GAP	GTPase-activating protein
CAM	Collective amoeboid migration	GDP	Guanine diphosphate
cAMP	cyclic AMP	GEF	Guanine nucleotide exchange factor
CAMT	Collective mesenchymal-to-amoeboid transition	GEMM	Genetically engineered mouse model
CAT	Collective-to-amoeboid transition	GPCR	G-protein-coupled receptor
Cdc42	Cell division control protein 42 homolog	GTP	Guanine triphosphate
CHD	Congenital heart defects	GTPase	Hydrolase of GTP
CIL	Contact inhibition of locomotion	H-K	
CIMP	CpG island methylator phenotype	HA	Hyaluronic acid
CNCCs	Cranial neural crest cells	HeLa	Henrietta Lacks
CRC	Colorectal cancer	HEK	Human embryonic kidney
CTC	Circulating tumour cell	HER2	Human epidermal growth factor receptor 2
CXCL12 / SDF1	Chemokine (C-X-C motif) ligand 12 / Stromal cell-derived factor 1	HUVEC	Human umbilical vein endothelial cells
CXCR4	Chemokine (C-X-C motif) receptor 4	I	
CXCR7	Chemokine (C-X-C motif) receptor 7	ITG	Integrin
D		JAK	Janus kinase
DPBS	Dulbecco's phosphate buffer saline	JAM	Junctional adhesion molecules
DNA	Desoxyribonucleic acid	JUT	Jamming-to-Unjamming transition
		KO	Knockout

KRAS	Kirsten rat sarcoma virus	PLL	Posterior lateral line
L		PLLP	Posterior lateral line primordium
LE	Luminal epithelial	PNI	Perineural invasion
LOX	Lysyl oxidase	Pp1	Protein phosphatase 1
LVD	Lymphovascular dissemination	PSC	Pancreatic stellate cell
LVI	Lymphatic vessel invasion	PTEN	Phosphatase and tensin homologue
M		R	
MAT	Mesenchymal-to-amoeoid transition	Rac1	Ras-related C3 botulinum toxin substrate 1
MCF10A	Michigan cancer foundation-7 breast epithelial cells	RhoA	Ras homolog family member A
MDCK	Madin-Darby canine kidney cells	ROCK	Rho-associated coiled-coil kinase
ME	Myoepithelial	RNA	Ribonucleic acid
MET	Mesenchymal-to-epithelial transition	RTK	Receptor tyrosine kinase
MHC	Myosin heavy chain	S	
MLC	Myosin light chain	SCC	Squamous cell carcinoma
MLCK	Myosin light chain kinase	SHG	Second harmonic generation
MLCP	Myosin light chain phosphatase	siRNA	Small interference RNA
MMP	Matrix metalloprotease	STAT	Signal transducer and activator of transcription
MTOC	Microtubule-organising centre	T	
MUC	Mucinous carcinoma	TFM	Traction force microscopy
N		TGF β	Transforming growth factor β
N-cadherin,	Neural cadherin	THG	Third harmonic generation
N-cad		TJ	Tight junction
NMII	Non-muscle myosin II	Tpm	Tropomyosin
NMDAR	N-methyl-d-aspartate receptor	TSIP	Tumour sphere with inverted polarity
P		U-Z	
PAA	Polyacrylamide	UPD	Unpaired
PBS	Phosphate-buffered saline	VEGF-A	Vascular endothelial growth factor
PBSCM	PBS + 0.1mM CaCl ₂ + 1mM MgCl ₂	WASP	Wiskott–Aldrich syndrome protein
PC	Peritoneal carcinomatosis	WAVE	WASP family Verprolin homolog
PDAC	Pancreatic ductal adenocarcinoma	WT	Wild type
PDGF	Platelet-derived growth factor	ZO-1	Zonula occludens-1
PDMS	Polydimethylsiloxane		
PDX	Patient-derived xenograft		
PDXO	Patient-derived xenograft organoids		
PI3K	Phosphoinositide 3-kinase		
PIP ₃	Phosphatidylinositol (3,4,5)-trisphosphate		
PIV	Particle image velocimetry		

Chapter I. Introduction

Despite decades of scientific research, medical progress, health politics and economical costs, cancer remains a major cause of death worldwide. Its metastatic spread is responsible for most of it, making this disease very difficult to contain and cure. Our lab, housed by the leading European cancer centre Gustave Roussy Institute, investigates the cellular mechanisms underlying tumour cell dissemination.

Physiological processes such as cell proliferation, are known to be deregulated in cancer cells. Similarly, tumour metastatic spread is fostered by enhanced cell migration. Indeed, motility is an essential feature of living organisms, from the random agitation of the smallest bacterium to the organised collective behaviours of animal herds. This essential process is highly complex and regulated at every scale, from the molecule to the tissue. It ensures organism development and homeostasis; however, its deregulation is implicated in several important diseases, including cancer. This makes it a challenging and highly interesting topic for a wide community of scientists, from theoretical physicists to biologists and up to clinicians.

My PhD project takes place in this context, as we discovered new tumour intermediates responsible for colorectal cancer metastasis in patients: I then mainly investigated their peculiar mode of collective invasion. Therefore, this introduction presents the key current knowledge we have on cell migration, either as single cells or in group, and that inspired us to decipher this new mode of collective motility. The first part depicts how cell migration regulates physiological processes from embryogenesis to adulthood, and how it is deregulated in cancer, with a specific interest in colorectal cancer. In a second part, the mechanistic aspects of cell polarisation and force generation driving single cell and collective modes of migration are detailed, mainly considering actin-related processes. The last part emphasises cell plasticity during migration, essentially in the context of cancer.

1. CELL MIGRATION IS A KEY FEATURE OF PHYSIOLOGICAL AND METASTATIC PROCESSES

In physiological processes and in cancer dissemination, cells adopt different modes of migration, either isolated or in groups (**Figure 1**). In particular, epithelial cells can retain their initial properties and migrate in a collective fashion, or switch to single cell dissemination through a process known as epithelial-to-mesenchymal transition (EMT). They are of particular interest as they compose the initial and motile outer cell layer of embryos, shape the numerous interfaces between our body and outer media, and can derive into carcinoma, the most common type of cancer.

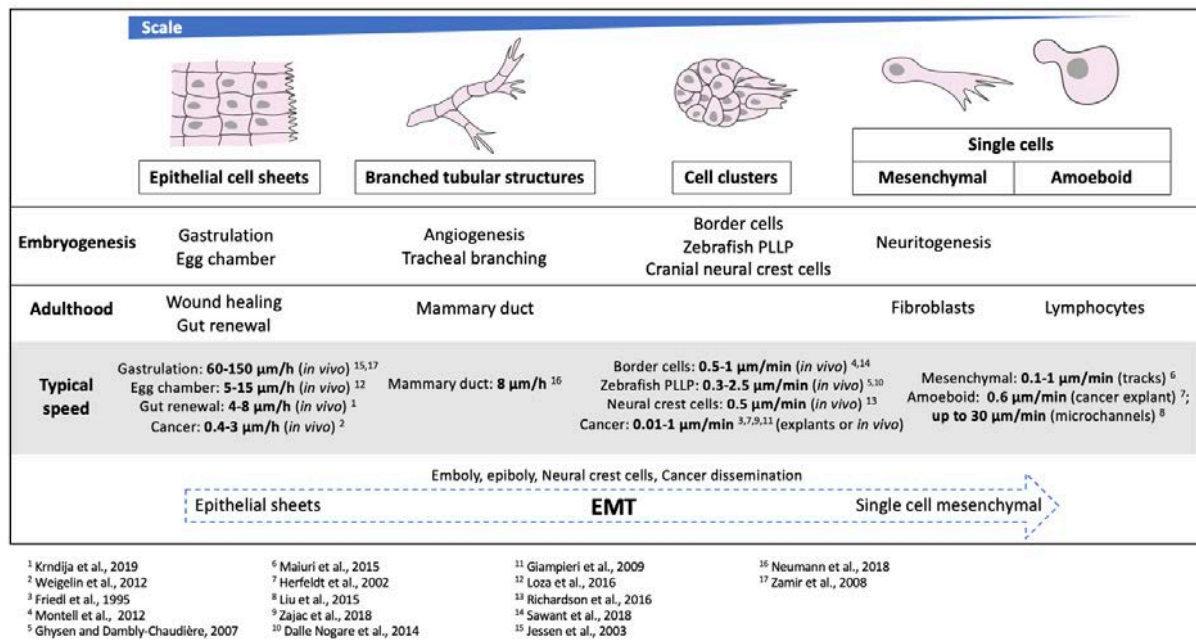


Figure 1. Cell migration in physiology and cancer across scales and typical associated speed. Epithelial-to-mesenchymal transition (EMT) is known to trigger a switch from collective to single cell motility in embryogenesis and in cancer.

Cell migration modes known to date, or “invasion” modes when occurring in 3D environments, can be classified as follows (**Figure 2**) (Friedl and Alexander, 2011). Single cells can migrate in a mesenchymal fashion, relying on traction forces mediated by strong and specific attachment to the environment. On the contrary, the single cell amoeboid mode of migration is propulsion based, with low adhesion but high cell contractility and deformation.

Cells invasion in groups is called collective migration, and can occur either as detached clusters, or through formation of long strands attached to the tumour core, that can keep the luminal architecture of the epithelial tissue of origin. To perform collective migration, cells exert adhesion-mediated traction forces, remodel the surrounding environment, and keep cohesiveness thanks to cell-cell junctions. Multicellular streaming is an intermediate phenotype where single cells reach a certain level of coordination without relying on cell-cell attachment.

Importantly, such a classification provides the big picture, but cells display multiple shades of behaviours between these ones. Also, we will not consider here as an active migration mechanism the “expansive growth”, where tumour cells invade the surroundings because of the proliferation pressure.

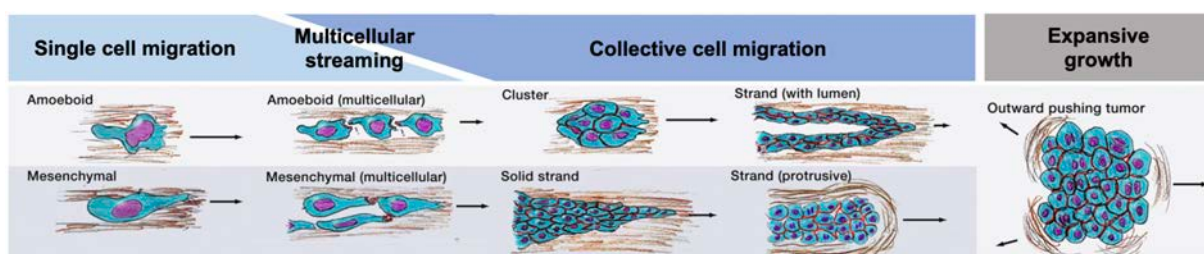


Figure 2. Main modes of cancer cell migration.

Single cells can migrate in a mesenchymal fashion (traction forces, specific attachment to the environment) or an amoeboid fashion (propulsion, low adhesion, high contractility, deformation). Collective migration occurs as detached clusters or long strands attached to the tumour core, keeping the epithelial luminal architecture of the tissue of origin or not: it involves cell-cell junctions, adhesion-mediated traction forces, matrix remodelling. Multicellular streaming is an intermediate phenotype

1. Cell migration is a key feature of physiological and metastatic processes

where single cells gain a certain coordination without relying on cell-cell attachment. "Expansive growth" is excluded as an active migration mechanism. Modified from (Friedl and Alexander, 2011).

Before focusing on cancer features, I must introduce cell migration in physiological contexts. Indeed, this field provides great knowledge to understand cell migration in general, and key models that allow for *in vitro* and *in vivo* investigations.

1.1. Cell migration in physiological processes

After the first observations of cells by Robert Hooke in 1665, Antoni van Leeuwenhoek, a Dutch microscopist and father of microbiology, observed for the first time small moving organisms in water and mouth samples. He reported his discoveries on the behaviour of these "animalcules", that would be renamed bacteria later, in letters to the Royal Society from 1675 to 1683.

Since then, cell migration has been recognised as essential in a myriad of biological processes, from embryonic development to adult homeostasis and disease, with conserved and differentiating features.

1.1.1. Epithelial cell migration and epithelial-to-mesenchymal transition in embryogenesis

During embryogenesis, cells undergo highly coordinated and regulated migratory behaviours, from the migration of whole epithelial sheets composed of thousands of cells during gastrulation, to individual cell migration of neural crest cells.

1.1.1.1. STRUCTURE OF EPITHELIA AND MOVEMENTS DURING EARLY STEPS OF GASTRULATION

Gastrulation is the process by which from one initial epithelial layer in the blastula, cells move to shape the germ layers (mesoderm, ectoderm, and endoderm), provide the embryo with clear polarities (anteroposterior, dorsoventral and left-right), and get positioned for further specification of the organs. The endoderm will give rise to the epithelial layer of digestive organs, the mesoderm to muscles, skeleton and vasculature, and the ectoderm to epidermis and nervous system. Thus, the first steps of gastrulation involve complex collective movements of epithelial cell sheets.

Early steps of gastrulation involve large movements of epithelial cell sheets

During gastrulation, the formation of the primitive streak, or blastopore, is driven by large-scale flows of epithelial cell sheets, highly organised and characterised by maintenance of epithelial cell-cell junctions and apico-basal polarity. It is thought to involve differential and oriented cell division, cell-cell intercalation and chemotaxis, i.e., cell migration towards a gradient of a soluble molecular cue (Chuai et al., 2012). The active migratory mechanism, chemotaxis, has not been confirmed yet *in vivo* given that any alteration in chemotactic response perturbs mesoderm differentiation and movement at the same time. Cells of the outer epithelial layer of the embryo, i.e. epiblastic cells, could also be transported by migration of the underlying cell layer, the hypoblast. Indeed, epiblastic cells and the hypoblast are coupled by ECM that displays similar movements as the cell layers (Chuai et al., 2012; Zamir et al., 2008)

Structure and function of the epithelium

Epithelial tissues, from embryonic development to adulthood, compose the interface between our body and outer media, such as air (lungs, skin) or the gut lumen (gut, colon, rectum). They are endowed with a certain number of characteristics including tissue cohesion and homeostasis, regulation of permeability (in and out), signalling and mechanosensation. In addition, cells composing glandular epithelia have secretory properties, and will deliver these substances either in the bloodstream (endocrine glands, secreting mainly hormones) or in ducts or at inner/outer body surfaces (exocrine glands).

The cells composing these tissues display 3 types of shapes: squamous, cuboidal, and columnar, either organised in a simple layer, like in the blastula, or stratified. They are polarised, with a side facing the lumen or the outer medium, called “apical”, and the opposite “basal” side facing the basal lamina. The lateral sides of cells, facing the tissues, share similar adhesive complexes as the basal side, these adhesive complexes being absent from the apical side. For their similar features, the lateral and basal sides are thus often grouped under the term “basolateral” sides.

This apico-basal polarity is established and maintained by the following three main molecular complexes: Par, Crumbs and Scribble (Thiery et al., 2009). In addition, apico-basal orientation is dependent on the small GTPase Rac1 (O’Brien et al., 2001) and determined by differential localisation of phosphoinositides: PI(3,4)P2 determines the apical membrane identity, while PI(3,4,5)P3 is preferentially located at the basolateral pole (Román-Fernández et al., 2018).

The apical and basolateral poles play different roles, respectively regulating exchanges with the outer medium and ensuring a barrier function, which is reflected by their different molecular composition. Microvilli are characteristic of the apical side, while the basolateral pole is characterised by cell-cell and cell-ECM adhesions. Each of these basolateral molecular complexes has a specific localisation, role and is connected to specific cytoskeleton components (Kawauchi, 2012) (**Figure 3**).

Epithelial cells can harbour the following cell-cell junctions, from the closest to the furthest to the apical side: tight junctions (TJs), adherens junctions (AJs), desmosomes and gap junctions (GJs).

Tight junctions are located at the most apical part of cell lateral membranes and mainly ensure the barrier function and sealing of the epithelium by closing the gap between cells and separating the apical and basolateral domains. They are composed of transmembrane claudins, occludins and junctional adhesion molecules (JAM) that bind to intracellular zonula occludens-1 proteins (ZO-1).

Adherens junctions are composed of extracellular proteins of the cadherin family, whose activity is calcium-dependent, bound to β -catenin and p120-catenin. A-catenin and other proteins (vinculin, EPLIN) link the adherens junction to actin filaments of the cytoskeleton (F-actin). Also, nectin and afadin initiate adherens junction formation through recruitment of cadherin-catenin complex.

Desmosomes' transmembrane proteins are desmocollins and desmogleins, which are non-classic cadherins, providing strong intercellular connexions. They are linked to the intermediate filaments through complexes including plakoglobin, desmoplakin and plakophilin.

Last, *gap junctions* consist of homo- or hetero-hexamers of connexin proteins, forming intercellular channels. They regulate the diffusion of small molecules and electric signals.

At the contact with the basal lamina, epithelial cells attach to the extracellular matrix (ECM) thanks to focal adhesions and hemidesmosomes, mainly.

Hemidesmosomes are similar to desmosomes, except that they are heterophilic, being attached to the extracellular matrix (fibronectin, laminin, collagen, vitronectin) instead of another cell.

Integrins heterodimers are a main component of *focal adhesions* (FAs). This family can form at least 24 combinations of α and β chains, with different affinities to ECM components. They are connected to actin filaments through a complex scaffold that matures over time, composed of signalling proteins such as talin, vinculin, zyxin, focal adhesion kinase (FAK), Src, paxillin and p130^{cas}. Focal adhesions also activate downstream signalling regulating cell migration, morphological changes, survival and proliferation (Kawauchi, 2012).

1. Cell migration is a key feature of physiological and metastatic processes

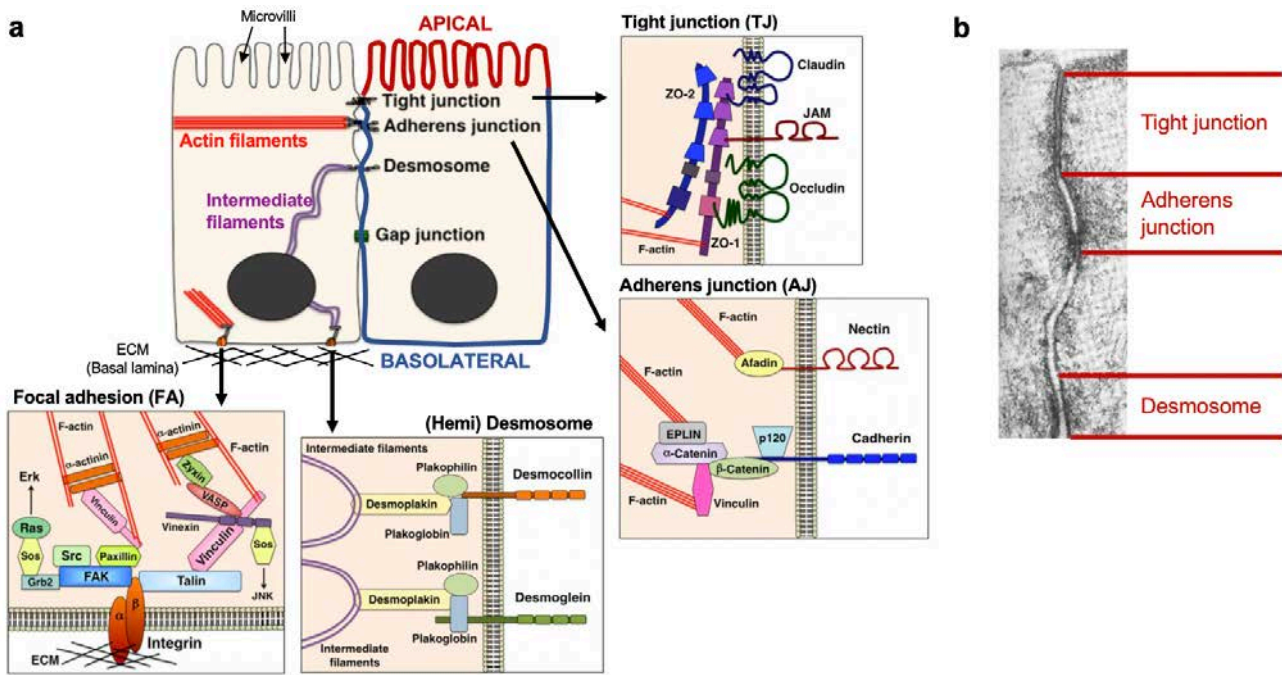


Figure 3. Epithelial architecture.

a, Epithelial cells display apico-basal polarisation and different types of cell-cell and cell-ECM adhesions. Tight junctions, adherens junctions, desmosomes/hemidesmosomes and focal adhesions are enlarged, displaying the main proteins of these complexes and their connection with cytoskeleton. Modified from (Kawauchi, 2012). **b**, Transmission electronic micrograph of epithelial junctions: tight junctions (creating a barrier at the most apical part), adherens junctions and desmosomes. Adapted from (Golovkine et al., 2018).

1.1.1.2. EPITHELIAL-TO-MESENCHYMAL TRANSITION DRIVES SINGLE CELL DISSEMINATION

After the formation of the primitive streak, movements of epithelial cell sheets are coordinated through four major morphogenetic movements: emboly (1), epiboly (2), convergence and extension, the last two being often considered together (3) (Solnica-Krezel and Sepich, 2012).

They also involve partial or complete individual cell detachment from the epithelial cell sheets. These cells would display single cell migration and reach specific sites to give birth to different lineages. It occurs through a process called epithelial-to-mesenchymal transition (EMT). Animal models have been of great help to study these cell movements *in vivo*, the main being: zebrafish embryo, *Drosophila melanogaster* (or *Drosophila*) fly embryo, and *Xenopus laevis* frog embryo.

During *emboly*, future mesoderm and endoderm cells (hypoblastic cells) internalise under the ectoderm through the primitive streak. Highly dense hypoblastic cells move collectively inward, with dynamic rearrangements of cell-cell junctions and neighbours (**Figure 4**). They also undergo either full or partial EMT, switching from their cohesive epithelial state to a mesenchymal one, more individual and protrusive, promoting individual crawling on the ectoderm internal layer (**Figure 5**). In zebrafish, ectodermal cell crawling is random, allowing for their dispersal (Pézeron et al., 2008). Internalising mesodermal cells are also assumed to be pushed by myosin II-dependent apical constriction, well characterised in *Drosophila*. Cells are then guided by a molecular cue, called chemokine, such as platelet-derived growth factors (PDGFs) (Montero and Heisenberg, 2004). Then, *epiboly*, the spreading and thinning of tissues, and *convergence and extension*, leading to dorsoventral narrowing and anteroposterior elongation, are driven by polarised migration of individual cells, cell intercalation, cell divisions and shape changes (Solnica-Krezel and Sepich, 2012).

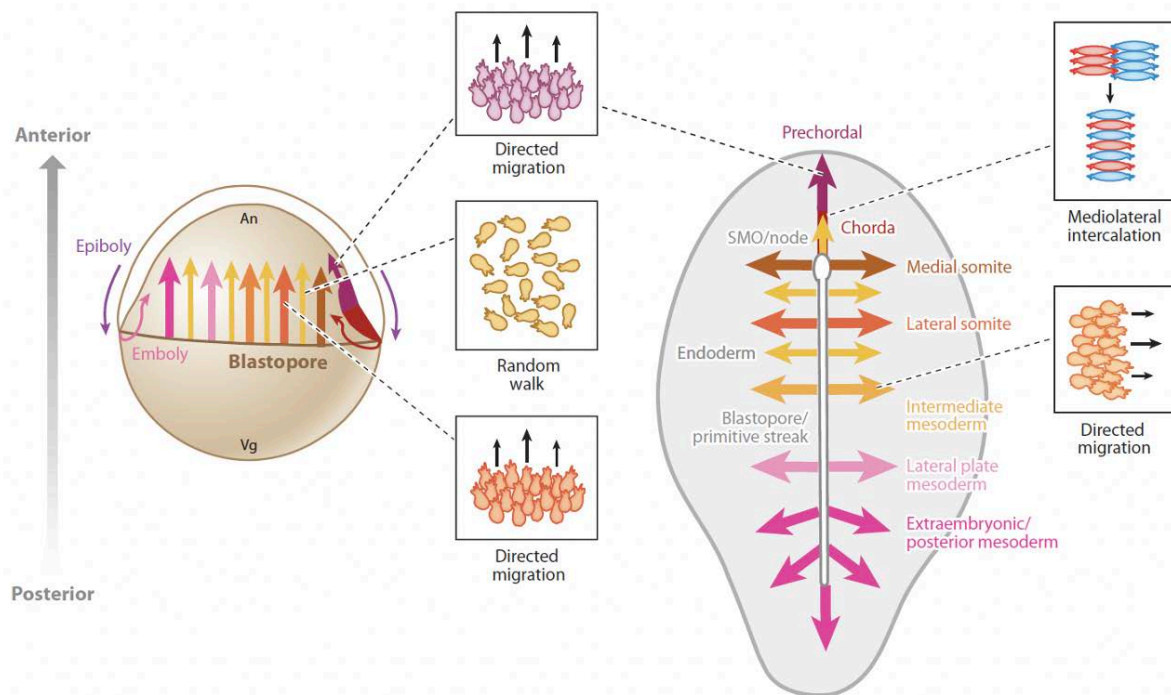


Figure 4. Early gastrulation movements: emboly and epiboly, and specific associated cell behaviours. Zebrafish gastrulation (left) is taken as a representative example. Right: amniote embryo. Emboly, or internalisation: collective migration of highly dense mesodermal cells under the ectoderm through the primitive streak, with dynamic rearrangements of cell-cell junctions and neighbours and EMT (full or partial) allowing individual directed or random crawling on the ectoderm internal layer. Epiboly (spreading and thinning of tissues) is driven by polarised cell intercalation, cell divisions, shape changes, migration of individual cells. Polarisation of the embryo: SMO: Spemann-Mangold organiser. An: animal. / Vg: vegetal. From (Solnica-Krezel and Sepich, 2012).

After gastrulation, a major event is neural crest cells (NCC) migration. Neural crest cells of different subtypes (cranial, cardiac, vagal, sacral, and trunk) undergo EMT and delaminate from the closing neural tube (**Figure 5**). They migrate through the embryo, either individually or in loose groups. Guidance in the embryo can be provided by molecular cues (e.g. cardiac NCC of *Xenopus laevis*, (Shellard et al., 2018)). Once they reached specific places, neural crest cells give rise to multiple organs and tissues: ganglia, pigment cells, head skeleton, and others. Overall, this process requires NCC to initially undergo a proper EMT to eventually form the right organs in the right places.

Phenotypical and molecular changes during EMT lead to single cell invasion

The four steps of gastrulation presented above, as well as neurulation, involve partial or full individual cell detachment from the epithelial cell sheets, followed by single cell migration (**Figure 5**). Indeed, epithelia can undergo epithelial-to-mesenchymal transition (EMT) to give rise to mesenchymal cell types by losing the apico-basal polarisation and gaining invasive properties (Thiery et al., 2009). Reverse EMT, called MET for mesenchymal-to-epithelial transition, may happen later to allow for epithelial specification of mesenchymal cells once they reached their final location.

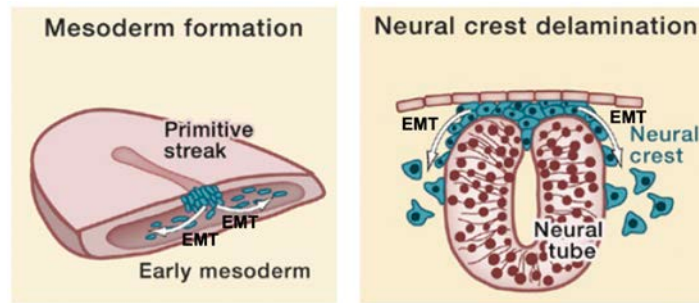


Figure 5. Epithelial-to-mesenchymal transition (EMT) drives single cell motility in development. Left: during embryology, mesoderm formation occurs through EMT of mesodermal cells, internalising through the primitive streak and crawling on the ectoderm internal layer. Right: during neurulation, neural crest cells undergo EMT and delaminate from the neural tube to later differentiate in various cell types in the right places. Adapted from (Thierry et al., 2009).

The identification of EMT occurred through observation of the associated deep changes in cell shape, adhesion, polarity, and migratory properties, leading to dissociation of the cohesive and organised epithelial sheet into single cells of mesenchymal phenotype (**Figure 6**). Indeed, in 1982, the first *in vitro* observations of an ECM-dependent EMT were reported by Greenburg and Hay as follows: once embedded in collagen gels, adult and embryonic epithelial cells from the anterior lens transformed into elongated invasive cells, confirmed to be mesenchymal by a structural analysis (Greenburg and Hay, 1982). A few years later, Stoker and Perryman revealed that secreted molecules can also drive EMT: Madin-Darby canine kidney cells (MDCK) dissociated and acquired an invasive mesenchymal phenotype in a few hours when incubated with the supernatant of a fibroblast culture (Stoker and Perryman, 1985). Similarly, under foetal bovine serum (FBS) addition, Boyer and colleagues identified altered morphology, invasion, cell-cell junctions, and cytoskeleton composition of rat bladder cells (NBT-II cell line), initially forming an epithelial sheet (Boyer et al., 1989).

EMT is coordinated by molecular changes (**Figure 6**). This process is mainly driven by Snail, Zeb1/2 and Twist genes: their role was first uncovered in *Drosophila* gastrulation by Simpson in 1983 (Simpson, 1983), and they were later recognised as coding for transcription factors. They lead to downregulation of E-cadherin (Cano et al., 2000) and other components of cell-cell junctions, and upregulation of less adhesive cadherins (N-cadherin, type II cadherins), extracellular matrix components (fibronectin, collagen), other classes of intermediate filaments (vimentin) and matrix metalloproteinases (MMPs). In addition, Snail, Zeb1 and TGF β prevent the activity of polarity complexes through repression of transcription, localisation regulation or direct inhibition.

Therefore, cell-cell junctions loosen and cell-ECM adhesions, mainly through integrins, are rather reinforced. This favours single cell detachment and motility through traction forces on the substrate: cells lose the apico-basal polarity for the benefit of a rear-front polarity and an elongated invasive phenotype (Lamouille et al., 2014). This new rear-front polarity is correlated with a reorganisation of the cytoplasmic components as well. The nucleus-centrosome axis orientation is reverted: while in epithelia, the centrosome and Golgi apparatus are positioned between the nucleus and the apical pole, they switch to the basal side, facing the newly-formed protrusion, during EMT (Burute et al., 2017; Nelson, 2003). Actin filaments, previously organised as a belt surrounding the cells, form stress fibres and front protrusions.

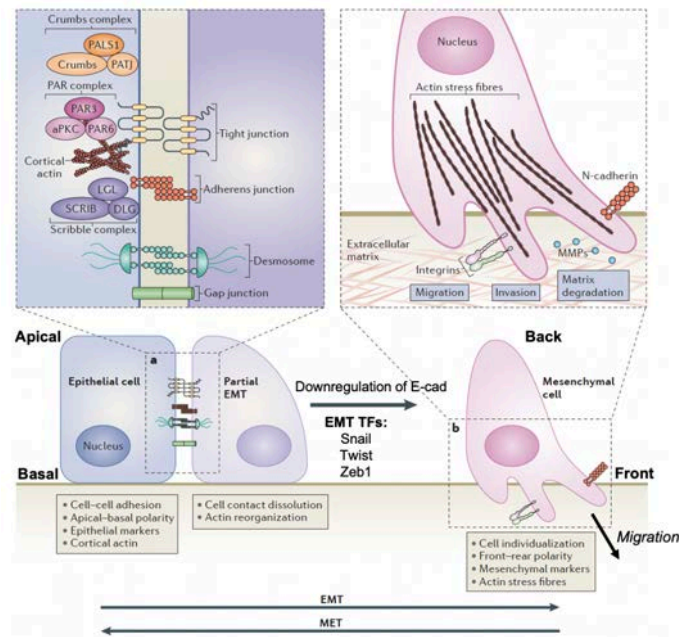


Figure 6. Molecular and structural changes associated with EMT, driven by EMT transcription factors (TFs).

EMT, complete or partial, is associated with loss of epithelial polarity (Crumbs, PAR and Scribble complexes) and epithelial cell-cell junctions (TJs, AJs, Desmosomes, gap junctions), leading to loose N-cadherin junctions or full individualisation. Single mesenchymal cells gain motility by forming protrusions, focal adhesions (integrins) and actin stress fibres, leading to front-back polarisation. They remodel extracellular matrix through enhanced production of matrix metalloproteases (MMPs). Cells can undergo reverse EMT (MET) after reaching their final location. Modified from (Lamouille et al., 2014).

1.1.1.3. MIGRATION OF CELL CLUSTERS

During embryogenesis, cells are also found migrating as groups fulfilling specific roles: some would be guided to new sites for further specification (cranial neural crest cells), transport non-migrating cells to the *Drosophila* oocyte (border cells) or seed cells during their course to create fish lateral line (lateral line primordium of zebrafish). These cell clusters display different structures and regulation of their migration, which will be described for the examples stated above. They also provide important *in vivo* models for the study of collective cell migration.

Collective mesenchymal migration of cranial neural crest cells

The movement of cranial neural crest cells (CNCCs) has been better described to date than other types of NCCs, in particular in *Xenopus laevis*: after undergoing EMT, they display collective migration with loose cell-cell junctions and guided by chemotaxis to stromal cell-derived factor 1 (SDF1) (Shellard et al., 2018). Indeed, the neighbouring cranial placodes generate a gradient of SDF1, guiding neural crest cells migration: SDF1 reduces myosin activity at the front, allowing for formation of protrusions at the leading edge, while actomyosin contractility at the rear generates a treadmilling of cells towards the front (**Figure 7a**). Recent work *in vivo* has provided insights on another guidance cue: self-generated stiffness gradient. Indeed, the neural crest cells induce a local gradient of stiffness through N-cadherin interactions with the adjacent placodal tissue, that will polarise Rac and actomyosin activity to guide migration (Shellard and Mayor, 2021a). Contact inhibition of locomotion (CIL), i.e. the ability of a cell to change its trajectory upon contact with another cell, is also thought to regulate this process.

Border cells migration in *Drosophila*: bringing polar cells to the oocyte

The migration of border cells is specific to *Drosophila melanogaster*. Border cells are germline cells that play an important role in oogenesis, especially in formation of the eggshell and polarisation of the future embryo. The group is composed of 2 polar cells surrounded by 4-8 follicle cells. From stage 9 of oogenesis, they delaminate from the anterior pole of the egg chamber and migrate to the oocyte, positioned at the rear of the egg chamber (**Figure 7b**) (Montell, 2003). The two polar cells are not able to migrate on their own, but they are able to define their surrounding cells as migratory through release of a cytokine, UPD (unpaired), activating JAK-STAT (Janus kinase–signal transducer and activator of transcription) pathway in neighbouring cells. They migrate in a collective fashion, at around 0.5 $\mu\text{m}/\text{min}$ through the nurse cells that fill the egg chamber. Their migration is regulated by actomyosin dynamics: they keep their apico-basal polarity, maintain cell-cell junctions, and form actin-rich protrusions that are stabilised to the front thanks to various guidance cues (Montell et al., 2012).

Migration of posterior lateral line primordium to seed proneuromasts

Fish and amphibians' sensory system is called lateral-line and consists in several sense organs, the neuromasts, distributed over the body during embryonic development. The formation of the posterior part of the lateral line system (PLL) in zebrafish, *Danio rerio*, became a great model to investigate collective cell migration. The PLL forms by migration of the PLL primordium (PLL) along the embryonic body (**Figure 7c**). After delamination of the initial placode just posterior to the otic vesicle, the primordium (~100 cells) migrates to the tail at 150 $\mu\text{m}/\text{h}$ on average, while depositing five groups of 20 cells, the proneuromasts that will differentiate into functional neuromasts (Ghysen and Dambly-Chaudière, 2007). PLLP migration is guided by a trail of chemokine (C-X-C motif) ligand 12 (CXCL12, also named SDF1), and differential expression of its receptors (David et al., 2002). Chemokine (C-X-C motif) receptor 7 (CXCR7) in trailing cells degrades quickly CXCL12, generating a local gradient of the chemokine and inducing directed migration by specific activation of chemokine (C-X-C motif) receptor 4 (CXCR4) at the front (Dalle Nogare et al., 2014). Proneuromast deposition is then allowed and polarised by Wnt and FGF signalling.

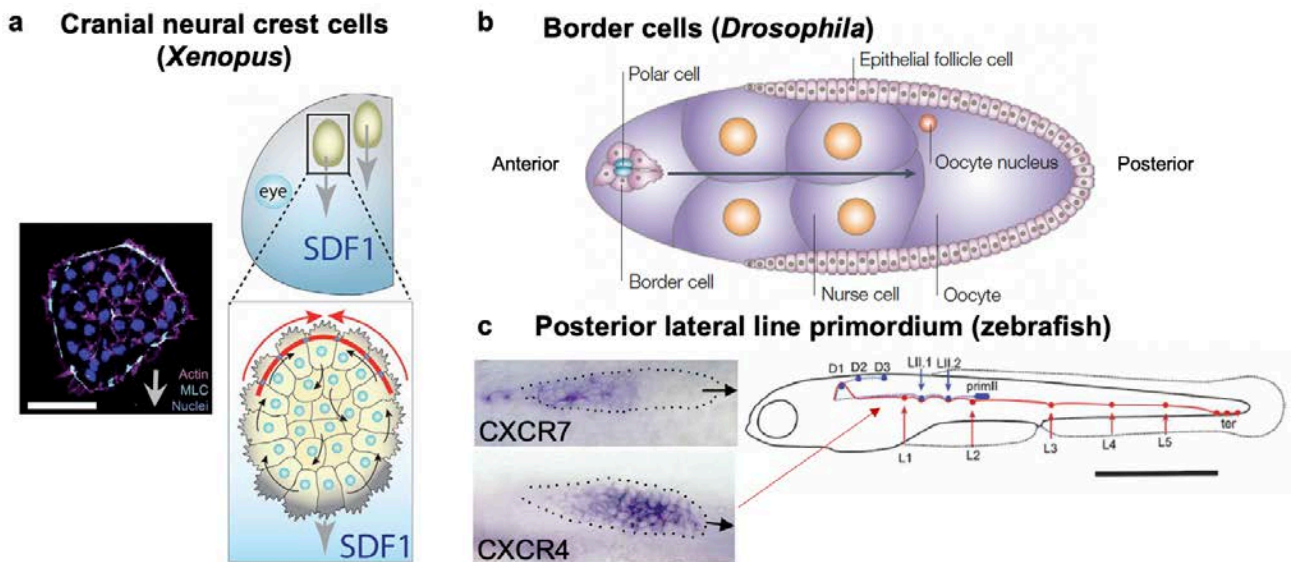


Figure 7. *In vivo* migration of cell clusters.

a, Cranial neural crest cells migration in *Xenopus* to a gradient of SDF1. Left: Immunofluorescence of a neural crest explant (without SDF1). Right: model of CNCC migration: a gradient of SDF1 induces asymmetric actomyosin contractility (red), driving cell intercalation at the rear and treadmilling (black arrows). Grey arrows: direction of migration. Adapted from (Shellard et al., 2018). **b**, Border cells migration in *Drosophila*. Grey arrow: migration path. Adapted from (Montell, 2003). **c**, Migration of the

posterior lateral line primordium (PLLp) in zebrafish. Left: expression of *cxc7* at the trailing edge and *cxc4* mostly in the anterior part. Black arrows: direction of migration. Right: in red, PLLp path and deposition of successive proneuromasts (L1 to L5). In blue, path of the second primordium (primII), that split to deposit the dorsal line as well (D1 to D3). Adapted from (Ghysen and Dambly-Chaudière, 2007).

1.1.1.4. CELL MIGRATION TO SHAPE FUNCTIONAL NETWORKS

Later in embryogenesis, once cells differentiated from neural crest cells, directed cell migration drives the shaping of cell networks to ensure specific functions, through neuritogenesis and angiogenesis. These processes continue even after birth and during adulthood.

During neuritogenesis, neuronal cells' bodies have found their stationary position, while their neurites extend throughout the body to form the mature nervous system. At their tip, growth cones invasion is characterised by the formation of wide branched actin-mediated and adhesive structures called lamellipodia, similar to those found in single cell mesenchymal migration (Kurosaka and Kashina, 2008).

The formation of the vascular system, a branched tubular network, is called angiogenesis (**Figure 8a**). It is promoted by gradients of chemokines, such as vascular endothelial growth factor (VEGF-A). These gradients drive angiogenic sprouting through specification of migratory and protrusive tip cells, forming membrane extensions called filopodia, and enhancement of the proliferation of the following stalk cells (Gerhardt et al., 2003).

Tracheal branching morphogenesis of *Drosophila* is a representative model to decipher the mechanisms underlying morphogenesis of these branched tubular networks, that also shapes our lungs and kidney. The respiratory system develops by sequential sprouting of three levels of branches, consisting in a single epithelial layer, wrapped into a tube. Primary branches form by budding from the tracheal placodes, or tracheal sacs, that invaginated from the ectoderm (Ghabrial et al., 2003): a small number of cells migrates out of the sac, and the monolayered tubular structure is then shaped by cell elongation and intercalation. Secondary and terminal branches are thinner, formed by the folding of only one cell or its protrusion. At each stage, all branches migrate towards dynamic gradients of concentration of a homolog of fibroblast growth factor (FGF), secreted by the neighbouring epidermal and mesodermal cells (**Figure 8b**). FGF activates the spouting of secondary branches and negative feedback loops, through *sprouty* expression, to restrict branching to the areas of highest FGF levels.

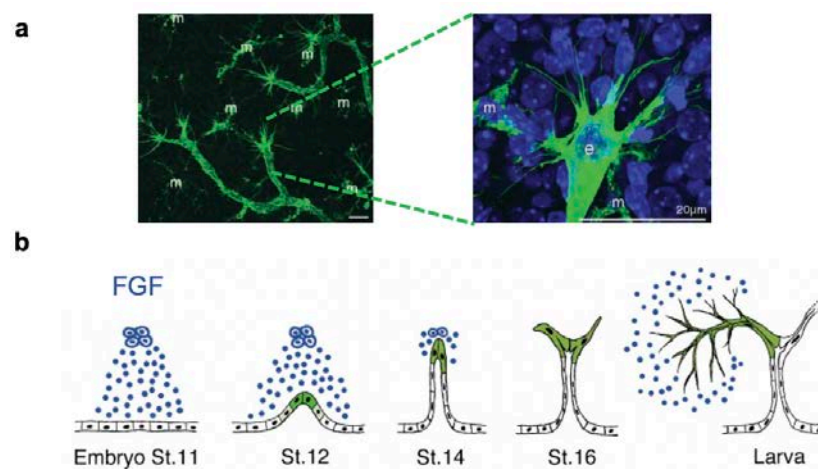


Figure 8. Formation of branched tubular networks.

a, Angiogenesis in mouse retina. Endothelial cells are stained by isolectin (green). Tip cells display filopodia. Left: scale bar, 20 μ m. Right: high magnification on a representative tip cell. e: endothelium;

m: macrophages. Adapted from (Gerhardt et al., 2003). **b**, Tracheal branching morphogenesis in *Drosophila*, driven by a gradient of FGF. Embryonic stages (St.) are indicated at the bottom. Adapted from (Ghabrial et al., 2003).

1.1.2. Adult physiological processes

In adults, the proportion of migrating cells decreases as epithelia stall and cells are positioned for good. However, in addition to angiogenesis – described above in embryogenesis – some migratory patterns remain as single cells and groups, to ensure homeostasis or in response to wounds. The most motile cells are leukocytes, that patrol very fast in the body. During wound healing, fibroblasts regenerate the collagen-rich matrix and collective migration is re-activated in epithelial cells to close the breach. Epithelial cell migration is also continuously displayed in gut to ensure its renewal and is activated during puberty to form the mammary duct.

1.1.2.1. WOUND HEALING: MIGRATION OF IMMUNE CELLS, FIBROBLASTS, AND EPITHELIUM

Wound healing is a multiple-phases process that provides an interesting framework to present single cell amoeboid migration of immune cells, adhesive migration of fibroblasts and collective migration of epithelial cells in adulthood. The skin is composed of a stratified epithelial tissue, the epidermis, forming a barrier from the outside world, and anchored on the connective tissue, connected to the rest of the body and whose extracellular matrix is mainly composed of fibrous proteins (collagen, elastin, fibronectin, laminin) and proteoglycans (Alberts et al., 2002). When the skin is damaged, the wound healing process is activated to allow for rapid protection and efficient repair. It is composed of several steps: formation of a fibrin clot to plug the defect (1), inflammation (2), regeneration of the collagen-rich matrix (3), reepithelialisation and differentiation of keratinocytes (4) (**Figure 9**) (Martin, 1997).

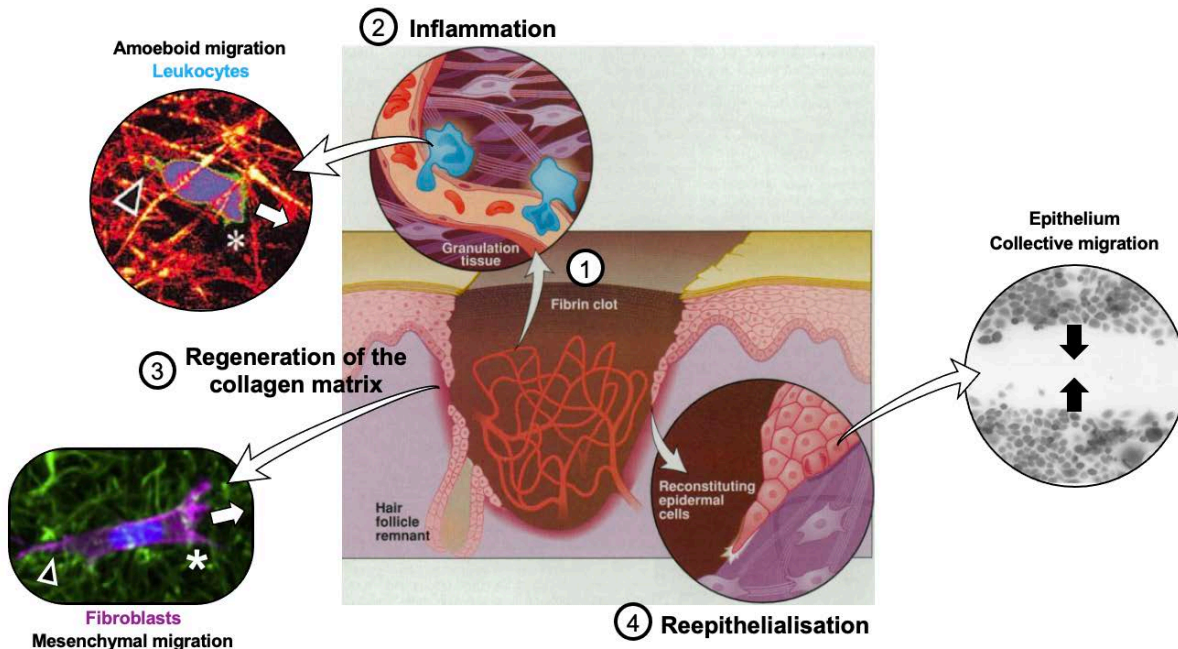


Figure 9. Cell migration involved in wound healing.

Cartoon modified from (Martin, 1997). (1) The wound is rapidly plugged by a fibrin clot. (2) Immune cells (leukocytes), patrolling in the stroma and blood vessels, are then gathered by chemotaxis to clean the wound: image of a T lymphocyte (leukocyte) in a collagen matrix from (Friedl et al., 2001). (3) Fibroblasts reshape the collagen scaffold of the connective tissue: human foreskin fibroblast in a collagen matrix (magenta: LifeAct staining actin) from (Doyle et al., 2021). Star: leading edge, black arrowhead: uropod, white arrow: direction of migration. (4) Keratinocytes migrate collectively to bridge

the wound: representative wound healing assay from (Boyer et al., 1989) with carcinoma cells, black arrows: direction of migration.

After clot formation (1), during inflammation (2), chemotaxis plays a key role in guiding neutrophils and macrophages from circulating blood to the wound, through growth factors released by degranulating platelets and products of bacterial degradation. Leukocytes are among the fastest cells in the human body, performing at up to 20-30 $\mu\text{m}/\text{min}$ on average (Lam and Huttenlocher, 2013). When patrolling in tissues, they display a characteristic “amoeboid” mode of migration (Friedl et al., 2001): they show very low adhesion and are almost insensitive to integrin inhibition to migrate in 3D matrices. They also extend a protrusive front and have a great capacity to deform in order to squeeze through very small spaces. Since they migrate towards gradients of chemokines, they are a good model to study chemotaxis. Once activated, leukocytes enter in a second phase of their migration: they start expressing more integrins, which allow for optimal migration and haptotaxis, i.e., migration towards a gradient of matrix-bound molecules. When endothelial cells, that cover the surface of blood vessels, start expressing selectins, they trap immune cells through light and fast adhesions. $\beta 2$ integrins then allow for formation of stronger adhesions and diapedesis, i.e., leukocytes crawling between endothelial cells to leave blood vessels. Neutrophils and macrophages clean the wound and secrete growth factors including transforming growth factor β (TGF β), and pro-inflammatory cytokines to amplify the preliminary signal and activate keratinocytes and fibroblasts for efficient repair.

Early in the response to injury, fibroblasts proliferate and migrate to the wound to deposit a new collagen-rich matrix (3), allowing for contraction of the wound, thus helping keratinocytes close it. They adapt the integrins composing their adhesions to the substrate to migrate on top of fibrin, fibronectin and vitronectin instead of collagen-I. In a few days, the fibrin clot will be fully replaced by the collagen-rich matrix produced by fibroblasts. Representative of “mesenchymal migration”, fibroblasts migration has been extensively studied, mainly on 2D substrates, because of their easy culture and manipulation: this mode of migration occurs through formation of a wide lamellipodium at the front and traction on integrin-mediated focal adhesions on the substrate.

Reepithelialisation (4) is first mediated by collective epithelial migration of keratinocytes on the basal lamina before a proliferative burst happens to replace cells that died during the injury. To crawl forward, keratinocytes activate several machineries and undergo partial EMT at the front (Thiery et al., 2009). They adapt their adhesion to the underlying matrix by dissolving hemidesmosomes and producing new integrins. Actin and myosin are activated, allowing formation of lamellipodia at the front of the wound, contraction of actomyosin filaments on adhesions, and formation of an actin cable on the edge for “purse-string” closure. The fibrin clot is dissolved by proteases secreted by wound-edge keratinocytes, mainly plasmin and matrix metalloproteinases (MMPs). When their migratory activity stops, cells differentiate to reform the stratified epithelium.

1.1.2.2. EPITHELIAL MIGRATION IN MAMMARY DUCT MORPHOGENESIS AND GUT RENEWAL

Although generally immobile during adulthood in healthy conditions, epithelial cells have been observed to display migration to ensure gut renewal and formation of the mammary duct.

Indeed, it has been recently reported that gut renewal is mediated not only by mitotic pressure from the crypts, but also by active migration of cells from the stem cell niche in the crypt, to the apex of the villi (van der Flier and Clevers, 2009; Krndija et al., 2019). Colonic epithelial cells in the upper part of the villi do not divide. Instead, they display actin-driven collective migration to the tip, with minimal rearrangements of cell-cell contacts and polarised protrusive activity, extending below the front rows and called “cryptic lamellipodia” (**Figure 10**).

1. Cell migration is a key feature of physiological and metastatic processes

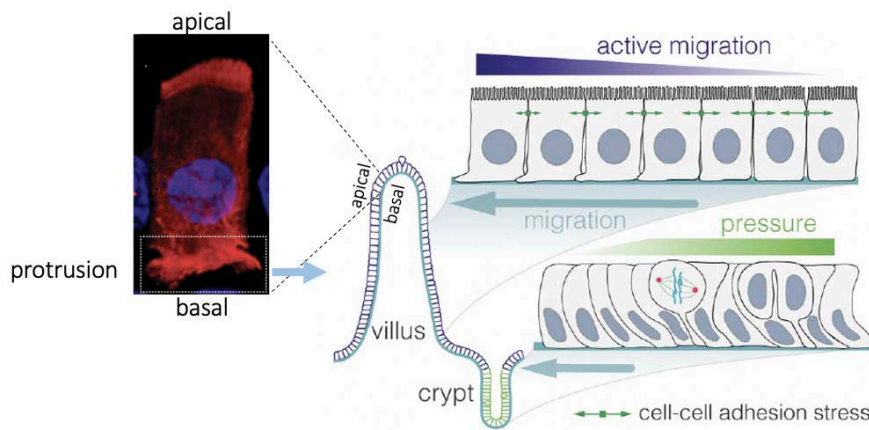


Figure 10. Gut renewal is mediated by active migration from the crypt to the tip of the villus. Enterocytes (left) display cryptic actin-rich protrusions at the basal side. Modified from (Krdnja et al., 2019).

During puberty mainly, the morphogenesis of the mammary duct also involves epithelial cell migration. Quiescent mammary ducts formed during embryonic development are composed of an inner layer of luminal epithelial (LE) cells and an outer layer of myoepithelial (ME) cells. During puberty, terminal end buds (TEBs) form at the end of each primary duct: they are hyperproliferative multilayered areas with low polarity and weak intercellular adhesions (Ewald et al., 2008). Ducts elongate thanks to dynamic rearrangements within TEBs (**Figure 11**), where cells migrate with a protrusive activity and tension gradient, and intercalate radially in the outer layer of LE, in contact with ME (Ewald et al., 2012; Neumann et al., 2018). Together with a tensile stress provided by ME cells, this results in an elongated bilayered duct, with ME cells surrounding LE cells and regulating bifurcations. The authors propose that this “morphogenetically active epithelial state” found in TEBs could underlie neoplasia as well (Ewald et al., 2008).

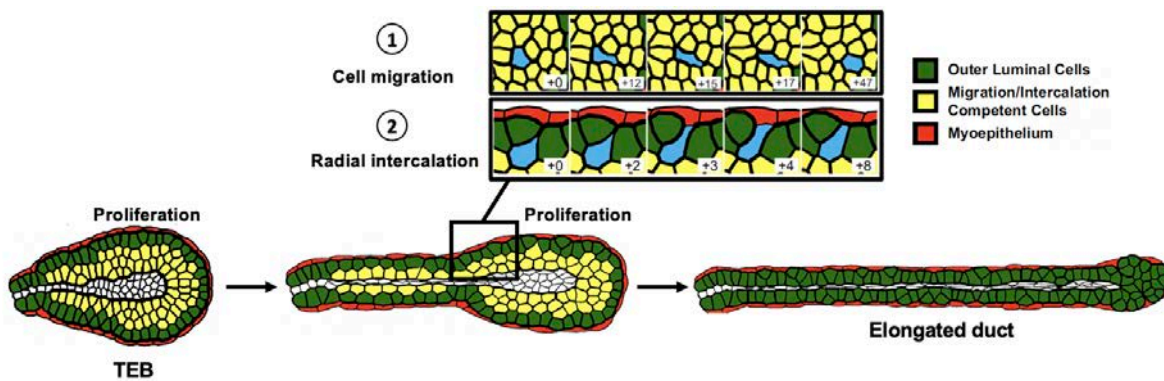


Figure 11. Elongation of mammary ducts through proliferation, migration, and radial intercalation. Modified from (Neumann et al., 2018).

1.2. Deregulation of cell migration promotes cancer spread

Not surprisingly, given its importance described above in embryonic development, defects in cell migration during morphogenesis can lead to severe birth defects and human diseases. Defects in neural crest cells migration may cause diverse types of congenital diseases, depending on the cell lineage. Heart defects are associated with abnormal cardiac neural crest cells migration, including heart septation defects, one of the most frequent congenital heart defects (CHD), and DiGeorge syndrome which is a common cause of CHD associated with other disorders (Epstein and Parmacek, 2005). Deregulated migration of vagal neural crest

cells can lead to Hirschsprung's disease, or HSCR, which is one of the most common gut motility disorders, affecting 1:5000 births, caused by the absence of enteric neurons in regions of the gut (Heanue and Pachnis, 2007).

A major example of deregulation of cell migration during adult life is certainly cancer spread, where cell migration hijacking leads to a metastatic disease (Friedl and Gilmour, 2009). Indeed, with 19 million people diagnosed per year, and considering a 2% annual growth rate, cancer remains the 2nd cause of mortality worldwide, responsible for 10 million deaths in 2020 despite decades of medical and scientific research (Bray et al., 2018; Sung et al., 2021). The fight against cancer is still challenged by its numerous and heterogeneous subtypes, the development of resistance to treatments, and its metastasis spread.

1.2.1. Colorectal carcinoma, a tumour derived from epithelial tissue

Carcinomas are tumours derived from epithelial tissues, and represent the main type of solid tumours (e.g. colon, lung, breast cancers) (SEER Training Modules). They are called "adenocarcinoma" when they affect glandular structures. While the following sections describe mechanisms that are common to most cancers, in particular carcinomas, a main focus of our team is CRC, as being the second cause of cancer-related death worldwide with almost one million deaths in 2020 (Sung et al., 2021). Risk factors include dietary habits, obesity, lack of physical exercise and smoking, while family history accounts for 10-20% of CRC patients (Dekker et al., 2019).

Histological description

Colorectal carcinomas develop from a polyp, which is a neoplastic precursor lesion formed in an aberrant crypt located in the colon or rectum. Different subtypes of CRC can emerge depending on the "cell-of-origin", i.e. the cell type from which the tumour originates (whether it is a stem cell from the niche or a differentiated cell from higher in the villus for example) (Barker et al., 2009; Schwitalla et al., 2013).

Most CRC patients display adenocarcinomas, derived from epithelial cells of the colon mucosa and recapitulating histologically its glandular structure if they are well differentiated.

When the tumour histology displays more than 50% of mucus, the tumour is then considered as mucinous (MUC). MUC carcinomas are the second most common (10-15% of patients), and they are more metastatic, especially to the peritoneum (Nagtegaal and Hugen, 2015). Thus, they focus an important part of our research, and in particular of my PhD.

Other subtypes, less frequent, include signet ring cell, neuroendocrine, adenosquamous, medullary, serrated and micropapillary carcinomas, for which representative histologies are presented in **Figure 12**. Mucinous, serrated and micropapillary subtypes originate from the serrated pathway presented above.

1. Cell migration is a key feature of physiological and metastatic processes

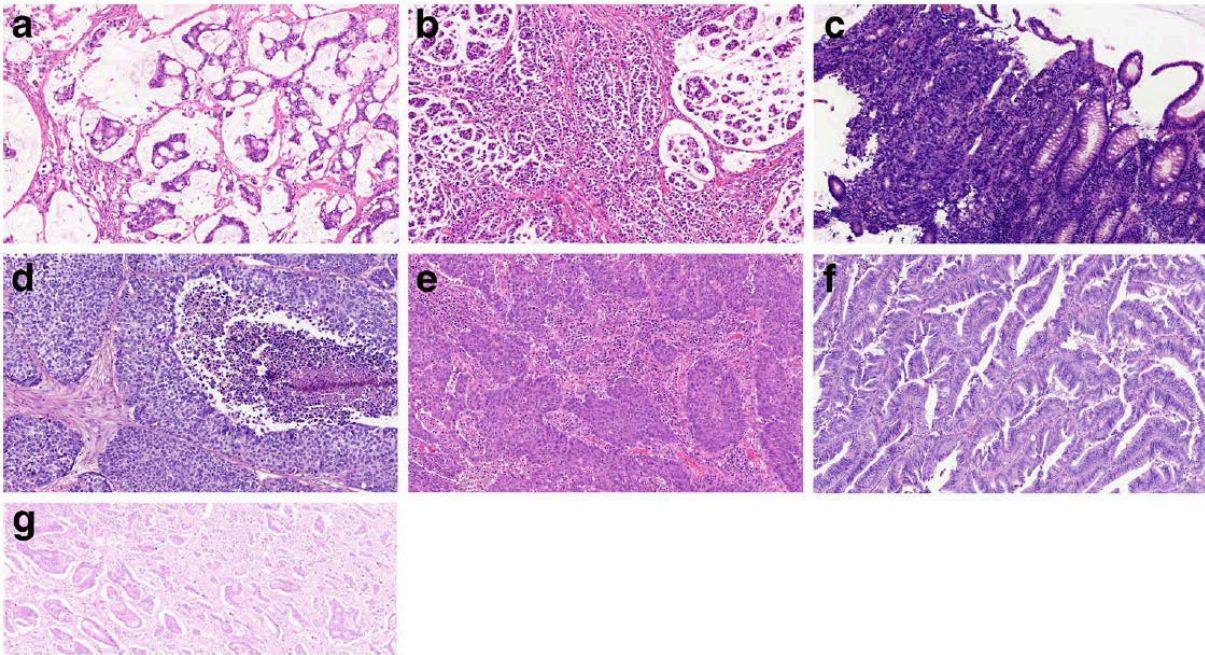


Figure 12. Histological subtypes of colorectal cancer
Mucinous **a**, signet ring cell **b**, neuroendocrine **c**, adenosquamous **d**, medullary **e**, serrated **f** and micropapillary **g** carcinomas. From (Nagtegaal and Hugen, 2015).

Oncogenic pathways

Two main oncogenic pathways have been described in CRC, depending on the activated oncogenes or inactivated tumour suppressor genes (TSG) (Brenner et al., 2014):

- the *adenoma-carcinoma sequence* is the most frequent, based on successive genetic alterations leading to cell transformation. Adenomatous polyposis gene (*APC*) loss of function occurs early and activates Wnt- β -catenin pathway related to stemness. This is followed by *KRAS* gain of function (in 40% of patients) and downregulation of TGF β pathway and *TP53* inactivation. Thus, abnormal cell proliferation is sustained through MAPK and PI3K pathways. Cancers developing from this oncogenic pathway are often accompanied by chromosomal instability (CIN) where cells display aneuploidy or aberrant chromosomal structure (overall, >2/3 of CRC display CIN).
- the *serrated pathway* occurs in 15-30% of CRCs, is associated with advanced disease. It displays serrated polyps as early neoplastic lesions. This sequence is characterised by early activation of MAPK pathway, through *BRAF* or *KRAS* mutations. Microsatellite instability (MSI, or dMMR) is also often observed, inducing hypermutability because of mismatch repair (MMR) machinery loss of function. Conversely, tumours that are not MSI are called microsatellite stable (MSS) or pMMR. In addition, tumours from the serrated pathway often display a CpG island methylator phenotype (CIMP), where hypermethylation of gene promoters can lead to silencing of tumour suppressor genes.

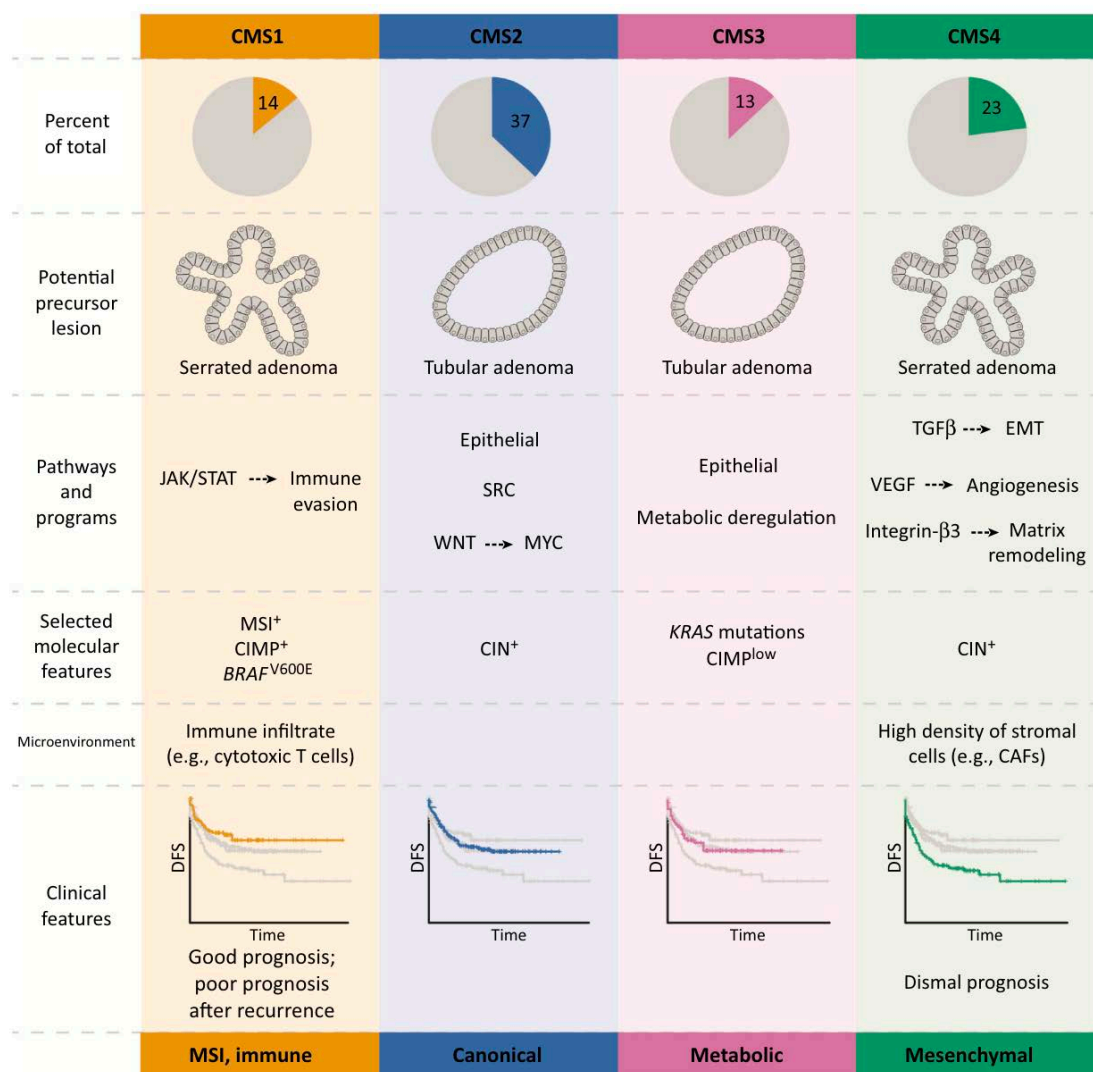
Consensus molecular subtypes

This heterogeneity of colorectal cancer subtypes makes CRC difficult to stratify. In order to globalise different classifications of CRC, a meta-analysis based on six gene expression-based studies has been performed Guinney and colleagues to propose a classification of CRC (Fessler and Medema, 2016; Guinney et al., 2015). It relies on their molecular features, and identified four main patterns of genetic alterations

that are biologically interpretable, called consensus molecular features (CMS). CMS1 to CMS4 are characterised as follows:

- CMS1 (14% of patients): MSI and immune signature for CIMP tumours, enriched in BRAF mutations, presence of immune infiltrate (associated to MSI status). They are associated with the best prognosis.
- CMS2 (37%): epithelial signature, upregulation of WNT and MYC downstream targets
- CMS3 (13%): metabolic signature, related to KRAS mutations
- CMS4 (23%): mesenchymal signature, upregulation of genes involved in EMT, TGF β signalling and matrix remodelling, high density of tumour microenvironment. They are associated with the worst prognosis.

The 13% remaining display either mixed or partial molecular phenotypes.



Trends in Cancer

Figure 13. Consensus molecular subtypes in colorectal cancer.
From (Fessler and Medema, 2016)

Therefore, mucinous carcinoma, derived from serrated lesions, concentrated most of our research, for they are highly invasive.

1.2.2. Prominent role of cell invasion in the metastatic cascade

1.2.2.1. CELL INVASION IS A HALLMARK OF CANCER

Cancer rises with the development of several abnormal cell and tissue behaviours, leading to more than a hundred cancer types. In a matter of simplification, Hanahan and Weinberg proposed an interesting summary of these key features allowing tumour development, that they call “hallmarks of cancer” (**Figure 14**):

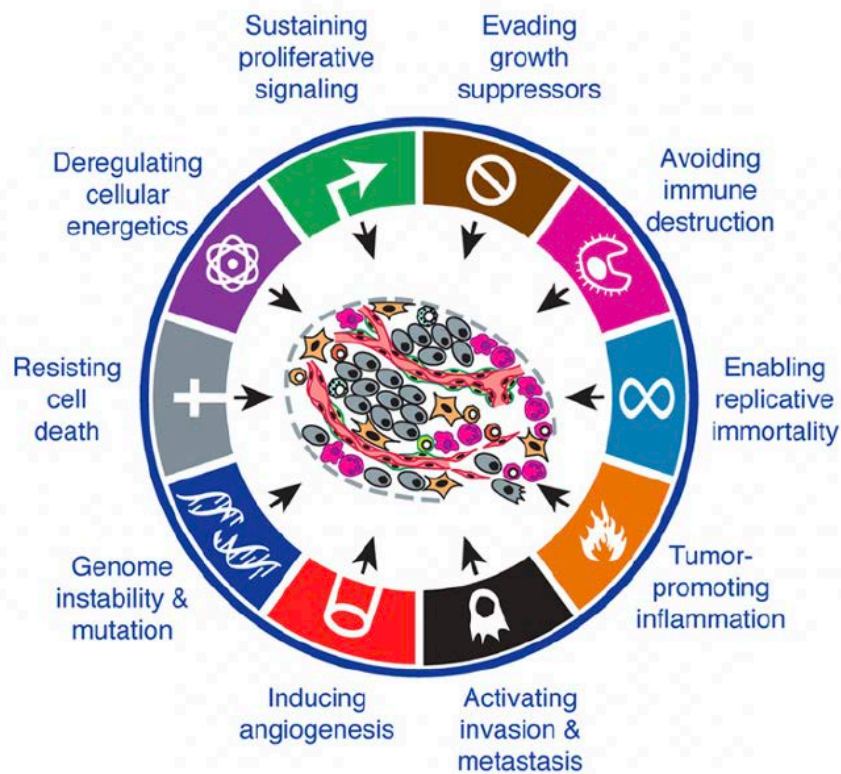


Figure 14. Hallmarks of cancer: 10 key features promoting tumour development. From (Hanahan and Weinberg, 2011).

These tumour-promoting characteristics are enabled by the development of genomic instability and tumour-promoting inflammation (Hanahan and Weinberg, 2000, 2011).

Thus, activation of cell invasion and metastasis stand out as a hallmark of cancer development and presents today an important clinical challenge as they cause at least two thirds of deaths from cancer today (Dillekås et al., 2019). Indeed, contrary to *in situ* carcinoma, a cytoreductive surgery cannot be envisioned in metastatic cancer, which participates in such a lethality.

1.2.2.2. CANCER CELLS DISSEMINATION ROUTES

Invasive tumour cells escape the primary tumour by invading the adjacent tissues to join the main dissemination routes (peritoneum/pleura, blood/lymph vasculatures, nerves). The cells that survived reach distant tissues where they quit the dissemination route and migrate to the metastatic site. Here, they would eventually proliferate and form a secondary tumour called metastasis.

Hematogenous and lymphatic routes: the most common dissemination routes

Among all routes, the most well-known are blood and lymphatic vasculatures, and a lot of research has been especially concentrated on blood-borne metastasis. As early as 1952, Zeidman and Buss were able to show on rats and rabbits, that tumour cells are able to use the blood circulation as a route to colonise distant organs, with some cells passing through lungs without even attaching, therefore reaching further sites (Zeidman and Buss, 1952).

Since then, multiple studies have highlighted the prognostic interest of assessing for blood vessel invasion (BVI) and lymphatic vessel invasion (LVI), respectively the presence of tumour cells inside blood and lymph vessels, called emboli (Minsky and Mies, 1989). LVI was demonstrated to be related with poor survival of patients and high metastatic burden in several types of cancer, including prostate cancer and CRC (Barresi et al., 2012; Herman et al., 2000; Lim et al., 2010; Matsumoto et al., 2007). Zhang and colleagues mapped the metastatic routes of tumour cells after LVI, and were able to show that circulation through lymph vessels allows for formation of metastases from the primary tumour, as well as from other metastases (Zhang et al., 2020). Lymphatic dissemination is now thought to mediate up to 80% of metastasis in solid tumours (Alitalo and Detmar, 2012), and tumour invasion to lymph nodes is widely accepted as an indicator of patient's prognosis: it is included in the TNM scoring of all solid tumours (N), together with the size and invasiveness of the primary tumour (T) and metastasis (M). Lymph nodes are consequently also often removed by surgery.

The invasion of tumour cells in hematogenous and lymphatic circulations is promoted by the formation of new vessels in tumours, respectively angiogenesis and lymphangiogenesis. This process relies on collective migration of endothelial cells, activated by tumour-secreted VEGF (Stacker et al., 2014). Tumour cells enter vessels by a process called intravasation, they are transported by the lymphatic or blood flow in the vasculature – that can undergo profound modifications and enlargement – and the surviving cells would exit the circulation (extravasation) to seed a distant organ (Figure 15). There, if they do not undergo apoptosis, they either get into a dormancy state or proliferate to form a metastasis.

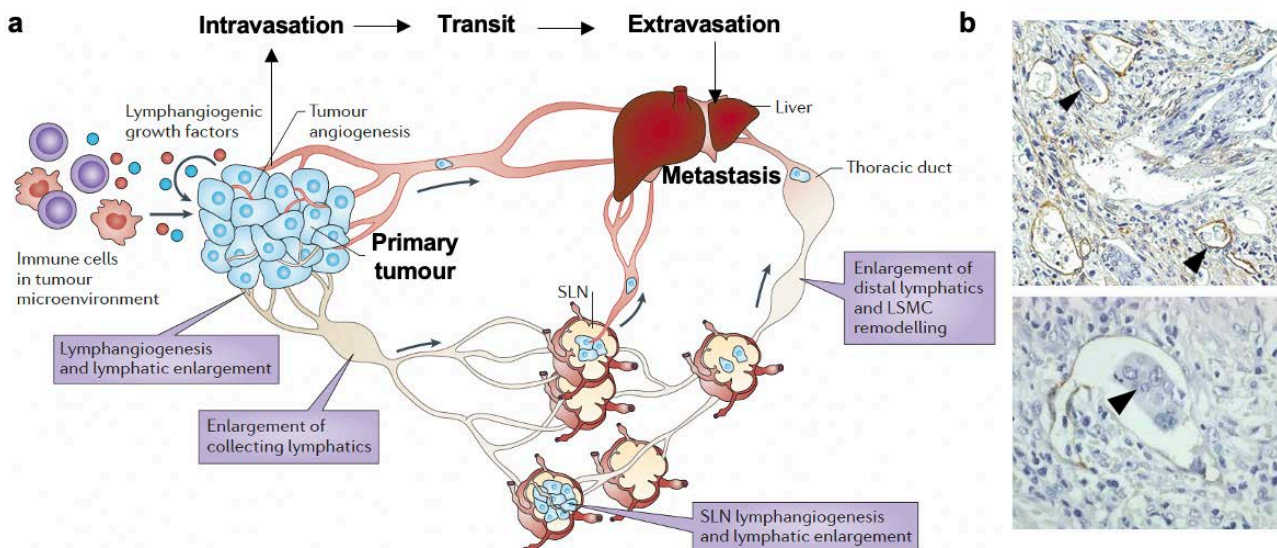


Figure 15. Tumour cells can spread through hematogenous and lymphatic circulation.

a, Steps of cancer cell spread, from the primary tumour to a distant organ (here, liver), and corresponding remodelling of lymphatics. Modified from (Stacker et al., 2014). **b**, Immunohistology lymphatic emboli (single cells and cell cluster). Top: From (Matsumoto et al., 2007). Bottom: Adapted from (Barresi et al., 2012). Black arrows: tumour cells, single cells, or clusters, in lymphatics.

Perineural invasion

Perineural invasion (PNI), i.e., cancer cells invasion of nerves close to the tumour, is also very common in certain types of cancers – particularly pancreatic cancer – and provides alternative routes for their dissemination (Bapat et al., 2011). PNI is also correlated with a worse survival rate for patients (Amit et al., 2016). Cells would use nerves as tracks to reach distant organs. Recent observations also suggested a molecular interplay between cancer cells and nerves, explaining the high attractivity of pancreatic cancer cells to nerves. In addition, synapses promote breast-to-brain metastases through activation of N-methyl-d-aspartate receptors (NMDARs) in breast cancer cells that capture the glutamate released in synapses (Zeng et al., 2019).

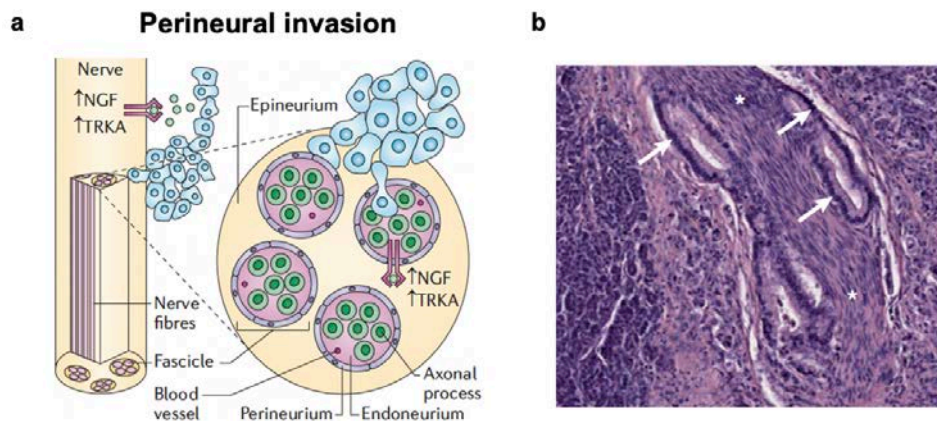


Figure 16. Perineural invasion of pancreatic cancer cells.

a, Invasion of tumour cells in nerves, promoted, as well as survival, by overexpression of NGF ligand and TRKA, its receptor, in tumour cells and nerves. **b**, Pancreatic ductal adenocarcinoma tissue sample stained with haematoxylin and eosin (H and E). The nerve (white asterisks) is invaded by tumour cells (white arrows). Modified from (Bapat et al., 2011).

Transcoelomic spread: using membranes and cavities lining organs

Tumour cells can also use the membranes and cavities lining organs, such as the pleura and peritoneum: this is called transcoelomic spread. They are major sites of metastasis of tumours from neighbouring organs and constitute efficient routes for tumour cells to spread to distant sites. Transcoelomic spread along peritoneum, the double membrane holding all abdominal organs together, is the most common route for some abdominal cancers, including ovarian cancer (Tan et al., 2006), and the presence of metastasis on the peritoneum, peritoneal carcinomatosis (PC), is correlated with a poor prognosis for patients (Aoyagi et al., 2014). Once they reached the peritoneum, cancer cells are subject either to passive drift by gravity, fluid transport and diaphragm movements, or active migration along this track (Cortés-Guiral et al., 2021). The pleura plays a similar role in the metastatic spread of organs from the upper part. These membranes are also connected with blood vessels and lymphatic circulation (through the diaphragmatic stomata, for peritoneum), which allows tumour cells to pass from one to the other dissemination route.

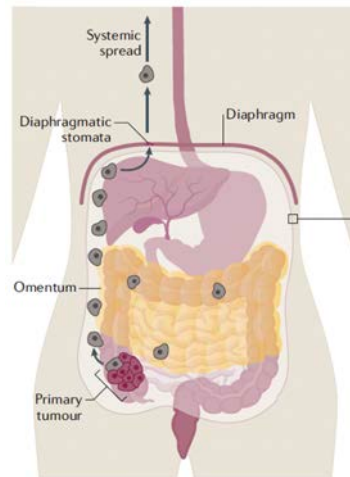


Figure 17. Transcoelomic spread through peritoneum.

Tumour cells escape the primary tumour (located in colon here) and reach the peritoneum. They then move along the peritoneum, can seed other organs in contact, and can even reach the lymphatic circulation through the stomata, leading to systemic spread. From (Cortés-Guiral et al., 2021)

1.2.2.3. TUMOUR CELL INVASION AND THE MECHANICAL PROPERTIES OF THE MICROENVIRONMENT

During their dissemination, tumour cells would thus cross a variety of environments, with different molecular and mechanical (topology, stiffness) properties, that influence at a cellular scale their migratory behaviour and speed.

The environment topology can be captured thanks to histological images of fixed specimens, and to second and third harmonic generation (SHG and THG) microscopy in dynamic intravital imaging. SHG and THG microscopy detect non-centrosymmetric structures and water-lipid/water-protein interfaces respectively (Sahai, 2007; Weigelin et al., 2016).

The dissemination routes presented above often provide paths of least resistance and tracks, promoting fast invasion. Indeed, in complex environments such as the dense collagen network close to the primary tumour, the role of matrix proteolysis and/or cell deformation plays an important role, whereas on pre-existing tracks, cancer cells will move faster (Sahai, 2007). Intravital imaging highlighted that between myofibers or nerves, cancer cells (B16F10 melanoma) formed linear collective strands that invaded much faster (up to 70 $\mu\text{m}/\text{d}$) than broad and poorly organised collectives among crowded fat tissue (10 to 15 $\mu\text{m}/\text{d}$) (Weigelin et al., 2012). Blood vessels also provide tracks along which tumour cells can easily migrate (Gritsenko et al., 2012). The main paths of least resistance are presented in blue in Figure 18 (Friedl and Alexander, 2011; Weigelin et al., 2012).

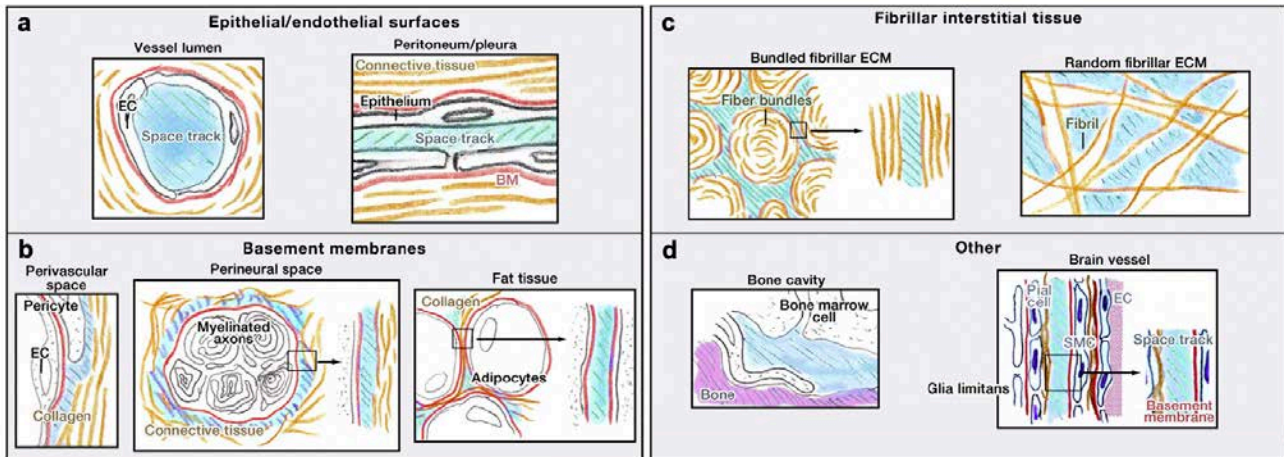


Figure 18. The environment provides paths of least resistance favouring cancer cell invasion.
a, Cancer cells find space in cavities formed between epithelial or endothelial (vessels) surfaces.
b, Spaces can also be found close to basement membranes, around vessels, nerves or in fat tissue.
c, Fibrillar interstitial tissue can provide tracks along bundled fibres, and cells can make their path between fibres organised randomly. **d,** Other paths of least resistance: bone cavities and brain vessels.
 From (Friedl and Alexander, 2011).

Of note, the development of a neoplasia is also accompanied by significant changes in the tumour microenvironment, promoting tumour growth and invasion: it affects the molecular and mechanical properties of the ECM, and involves other neighbouring cell types such as tumour-associated macrophages and CAFs.

Cancer cells are sensitive to molecular changes in the microenvironment in particular to gradients that allow for haptotaxis or chemotaxis. Indeed, proteoglycans and matricellular proteins, like osteopontin and thrombospondin-1, can be deposited close to the front of invading tumours: they would provide guidance to tumour cells that sense gradients of substrate-bound molecules (haptotaxis) (Gritsenko et al., 2012). They may also lead to matrix remodelling, changes in its mechanical properties, cell adhesion and activation of tumour cells receptors.

Imaging breast cancer cells highlighted the interplay between macrophages and tumour cells: macrophages, often located close to blood vessels, produce EGF that would attract tumour cells and promote their intravasation (chemotaxis) (Sahai, 2007).

In addition, important mechanical changes are observed during tumorigenesis – stiffness increase and generation of tracks – and have been shown to promote tumour cell invasion.

Stiffness of the underlying matrix is induced by matrix secretion and assembly from CAFs and tumour cells (van Helvert and Friedl, 2016). It has been associated with increased metastases and poor patient outcome. Indeed, it promotes squamous cell carcinoma (SCC) collective cell migration through increased sensitivity to epidermal growth factor (EGF) (Grasset et al., 2018). Pancreatic ductal adenocarcinoma (PDAC) is also characterised by a strong increase in stiffness, called fibrosis, thought to promote tumour progression: pancreatic stellate cells (PSCs, myofibroblast-like cells), activated by cytokines produced by cancer cells, change matrix rigidity. This may alter integrin signalling in cancer cells (Lachowski et al., 2017). In addition, a positive feed-back loop involving PSCs, which are sensitive to matrix stiffness, sustains fibrosis. Migration of epithelial ovarian cancer cells is also favoured by a matrix stiffness increase, through cell spreading, focal adhesion formation, myosin light chain phosphorylation and traction forces (McKenzie et al., 2018). Moreover, cancer cells are sensitive to gradients of rigidity, called durotaxis, through regulation of actin branching and especially in areas of lower rigidity (DuChes et al., 2019).

In addition, close to the primary tumour, CAFs can remodel and align bundled ECM fibers, forming tracks that considerably promote single cell and collective migration (Gaggioli et al., 2007).

1.2.3. Modes of carcinoma cell migration and experimental tools

Following intrinsic and extrinsic parameters, and similarly to non-transformed cells presented above, cancer cells can adopt various modes of migration (Figure 1). Indeed, carcinoma dissemination was long thought to be mediated by single cell migration, following an EMT transition reminiscent of embryonic processes. However, growing evidence suggest that cancer cells can also disseminate and migrate as groups of cells, keeping epithelial characteristics. Therefore, to decipher the underlying mechanisms of cancer cell migration in its different modes, various *in vivo* and *in vitro* experimental models have been developed and will be presented at the end of this section.

1.2.3.1. EMT PROMOTES CANCER CELL DISSEMINATION AS SINGLE CELLS

Correlative data from mice models (GEMMs) and CRC patients highlighted a potential role of EMT in diverse types of cancers. Indeed, a CRC mouse model in which Snail was overexpressed developed a higher metastatic burden (Fan et al., 2012). Likewise, the deletion of ZEB1 in a pancreatic cancer mouse model led to lower metastasis (Krebs et al., 2017). In addition, in CRC patients, the consensus molecular subtype associated with a mesenchymal signature (CMS 4) is characterised by a lower survival (Guinney et al., 2015).

Tumour cells can hijack this developmental process in particular at the tumour invasive front, thus driving tumour cell dissemination (Thiery et al., 2009): in colon cancer, the invasive front releases motile single cells and displays EMT and Wnt deregulation. In addition, PDGF can induce EMT in CRC through β -catenin nuclear translocation, and VEGF, which promotes angiogenesis, activates EMT as well in pancreatic and breast tumour cells through expression of *Snail* and *Twist*. EMT can happen in response to TGF β , where Smad proteins bind Snail and act as corepressors of E-cadherin. Snail translocation to the nucleus and translation are also stimulated by breast cancer-associated proteins like LIV1 and Y-box binding protein 1 (YB-1).

Once they reached the secondary metastatic site, tumour cells can undergo the inverse process, mesenchymal-to-epithelial transition (MET), to re-differentiate in an epithelial tissue. Such differentiation-dedifferentiation processes, and their relationship with cancer cell stemness, have been reviewed recently by Wang and Unternaehrer (Wang and Unternaehrer, 2019).

However, conclusions on the specific role of EMT in cancer must be tempered by the fact that data obtained above are mostly correlative (and not causative) and that transcription factors display pleiotropic effects. In addition, in CRC, the mesenchymal signature associated with CMS4 subtype has been questioned in several publications. Indeed, the stroma seems to be responsible for most, if not all, of the mesenchymal signature in explants of patients whose cancer is classified CMS4 (Calon et al., 2015; Isella et al., 2015). Also, mouse models for different types of cancer, breast and pancreas, revealed that EMT is not required for metastasis (Fischer et al., 2015; Zheng et al., 2015). However, these papers confirmed that EMT contributes to chemoresistance. EMT pathway could also promote tumorigenicity as it is involved in the regulation of stemness and thought to confer resistance to cell death.

1.2.3.2. COLLECTIVE DISSEMINATION OF CANCER AND DISCOVERY OF TSIPs IN CRC

There are still lots of questions on how tumour cell dissemination truly happens in patients and what the main intermediates are, single cells or collectives. Yet, many studies suggest today that cancer

dissemination is also, if not mainly, mediated by the escape of tumour cells as groups, and their subsequent collective migration.

First observations of collective cancer cell migration

Historically, tumour cell dissemination has been mainly studied and described in experimental model systems as a single cell process and the discovery of the role of EMT in tumour progression reinforced this vision. Yet, in 1995, Friedl and his lab observed *ex vivo* on collagen gels that tumour cells from melanoma, oral squamous cell carcinomas, ductal breast carcinomas and rhabdomyosarcoma are also able to escape and migrate as groups of 15 to 100 cells, in a collective fashion, and that a same tumour can display both single cell and collective migration (Friedl et al., 1995; Hegerfeldt et al., 2002). In fact, collective and single cell modes of migration can alternate *in vivo*, under the regulation of TGF β signalling such as in rat mammary carcinoma (Giampieri et al., 2009) or the composition of the microenvironment (Clark and Vignjevic, 2015). This will be discussed in more details as cell plasticity in part 3.

Evidence of collective epithelial dissemination in patients and discovery of TSIPs in CRC

Already in the 70's, researchers and clinicians related the presence of tumour cell emboli, or clumps, with the extent of metastases (Liotta et al., 1976). Since then, Ruiter and colleagues reported the presence of tumour cell groups in the lymphatic system, through a histopathological review of various types of carcinomas (**Figure 21a**) (Ruiter et al., 2001). Groups of tumour cells were identified during dissemination in breast cancer, proven to cause the metastatic burden and correlated with patients' prognosis (Aceto et al., 2014; Cheung et al., 2016). Kojima and colleagues were even able to show that claudin-6 overexpression in endometrial cancer, strengthening cell-cell junctions, promotes invasion (Kojima et al., 2021).

In 2016, Cheung and Ewald reviewed evidences of collective dissemination of cancer (Cheung and Ewald, 2016). They recalled several studies showing that collective dissemination would be more efficient than single cells at seeding metastases when artificially induced in mice and correlated with patient poor prognosis. This collective process could occur while retaining epithelial properties, and consequently without undergoing EMT. They came up with the following conclusion: "metastases could arise from a less efficient process of seeding by abundant single cells or from a more efficient process of seeding by rare clusters". Both are certainly concomitant.

In addition, considering that our knowledge on cancer dissemination mainly relies on *in vitro* experiments or mouse models, our lab investigated how colorectal cancer could disseminate to the peritoneum in patients, by collecting more than 50 patients' peritoneal effusions and analysing their content (Zajac et al., 2018). The main tumour intermediates were found to be tumour spheres that surprisingly kept the epithelial structure of the primary tumour and were negative for EMT markers (**Figure 19a,b**). In addition, they displayed a peculiar topology, keeping their apical pole outwards towards the ECM, hence their name: TSIPs, for tumour spheres with inverted polarity. This inverted topology was found as well in the primary tumour, in metastases and in *in vitro* collagen matrices (**Figure 19c**). TSIPs were found in the different histological subtypes (mucinous (MUC), micropapillary and cribriform) of CRC developed from the CpG island methylator phenotype (CIMP), and their presence is associated with a poor patient prognosis. The number of TSIPs in patients' peritoneal effusions is correlated with the presence and level of peritoneal carcinomatosis (**Figure 19d**). Their ability to initiate metastasis has been confirmed in mice, where intraperitoneal injection of TSIPs leads to formation of peritoneal metastasis in forty days (**Figure 19e**): they metastasise only as groups and not when dissociated into single cells. In addition, TSIPs invade within peritoneal explants while keeping their "apical-out" topology. Of note, TSIPs are also released in the peritoneal cavity of patients with other cancers than CRC: breast, ovarian, pancreatic, and stomach cancers

(unpublished data from J. Raingeaud). Thus, they could be metastatic intermediates in various cancer types, independently from the organ of origin, suggesting common features of these cancers.

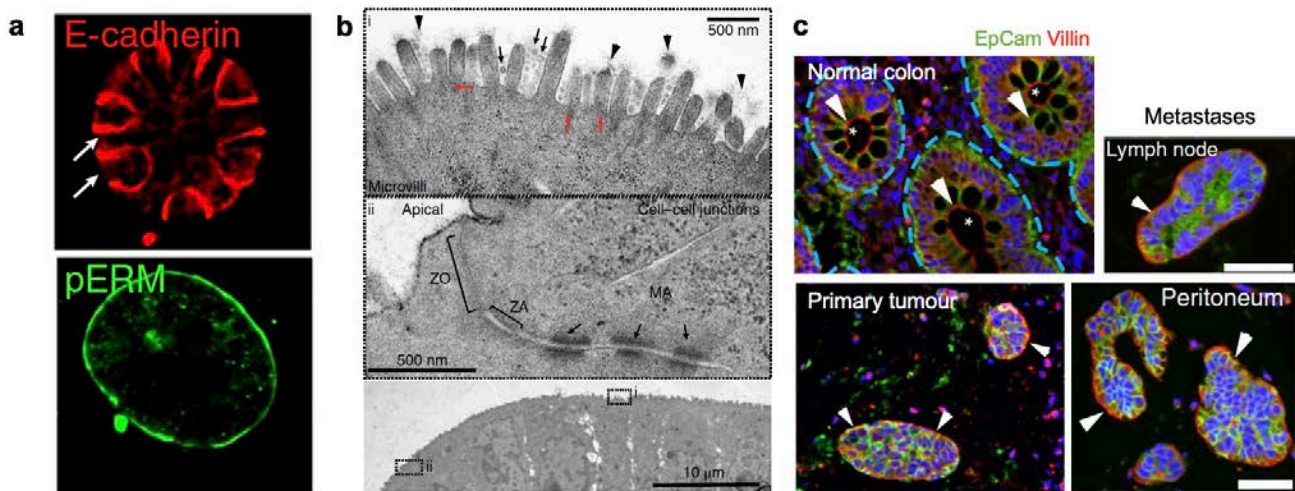


Figure 19. Tumour spheres with inverted polarity (TSIPs) are the main intermediates of CRC dissemination in patients.

a, Immunofluorescence of TSIPs from patients, fixed in suspension and stained for the epithelial marker E-cadherin and apical marker phospho-ERM (pERM). **b**, Electron microscopic micrograph of the surface of a TSIP displaying microvilli. **c**, Normal epithelial structure (normal colon) compared to TSIPs present in the primary tumour of a MUC CRC. Apical marker: villin, epithelial cell-cell junctions: EpCam. Arrowhead: apical pole; white asterisk: lumen. Adapted from (Zajac et al., 2018).

Formation of collective tumour intermediates by budding

The evasion of tumour cells in groups may happen through a process described by anatomopathologists as “budding”. Bronsert and colleagues highlighted it by reconstituting 3D stacks of immunohistochemical patients’ specimens, and showing the presence of those cell buds, with 9 to 22% being disconnected from the tumour core, and virtually no single cells (Bronsert et al., 2014). Our lab also reported that TSIPs form by collective apical budding from the serrated precursor lesions, following downregulation of canonical and non-canonical TGF β signalling (**Figure 20**). This is consistent with the fact that TGF β downregulation blocks single cell but not collective dissemination (Giampieri et al., 2009).

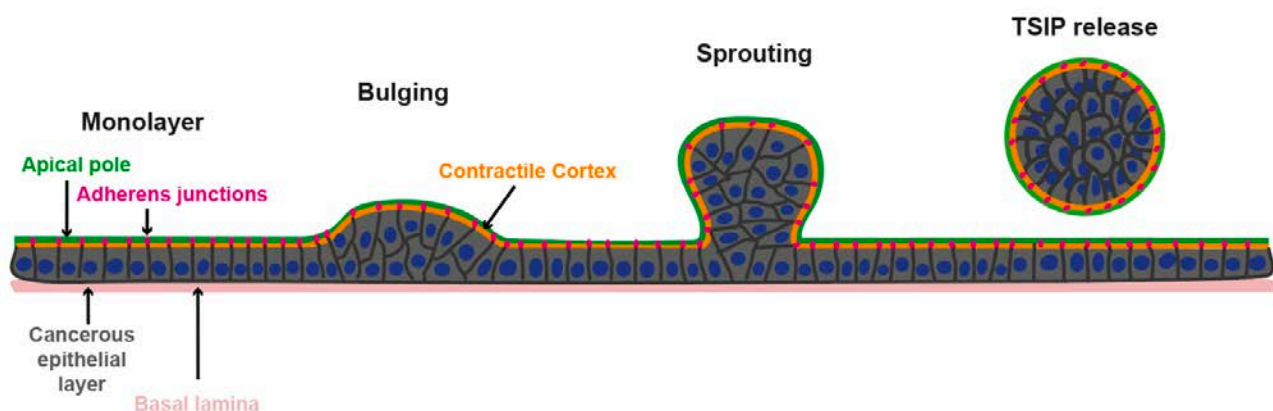


Figure 20. Schematic representation of TSIPs forming by collective apical budding.

Collective apical budding arises in CIMP cancers from serrated precursors: from the apical cell layer, bulging and sprouting eventually result in TSIP release at the apical pole. Modified from work of Jean-Baptiste Lopez (PhD student, «Digestive Cancer Dissemination» team, U1279), version 2021.

Advantages of collective cell dissemination

Collective dissemination can present several advantages for cancer propagation and resistance. The seeding by tumour cells clusters composed of different cell types, would lead to polyclonal metastases, hence increasing their ability to resist to some therapies (**Figure 21b**) (Cheung and Ewald, 2016). Interestingly, deep-sequencing analysis of human tumours and reconstitution of their history, as well as following tumour clones in mice, confirmed the hypothesis of a polyclonal seeding by tumour cell clusters for some prostate cancer patients (Gundem et al., 2015). Moreover, cell clusters were observed *in vivo* and *in vitro* to better survive and form colonies than isolated cells (Cheung and Ewald, 2016).

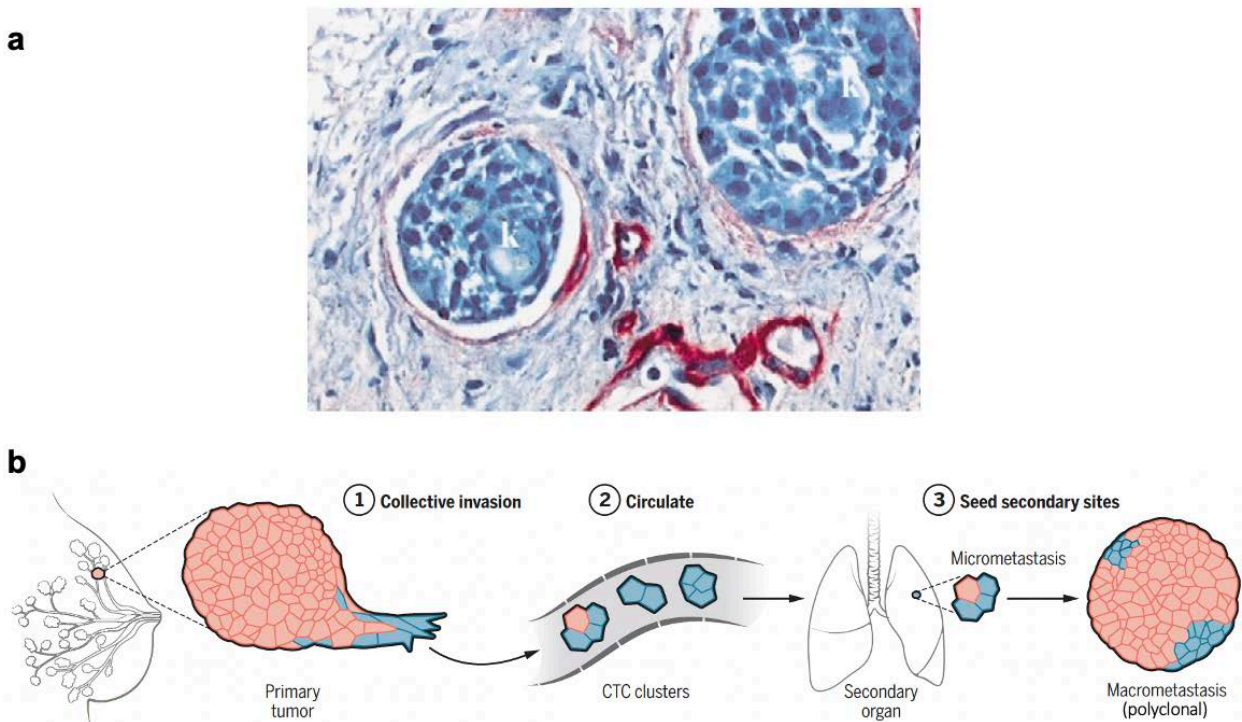


Figure 21. Collective dissemination in cancer.

a, Histopathology of oropharynx squamous-cell carcinoma emboli. From (Ruiter et al., 2001).

b, Model of collective cancer spread: example of breast cancer spread, where different cell types are required for dissemination (blue) and macrometastasis formation (red). Adapted from (Cheung and Ewald, 2016).

1.2.3.3. EXPERIMENTAL MODELS TO STUDY CANCER CELL MIGRATION

Biological material

Organoids from patient-derived xenografts

In our lab, to reproduce and study TSIP phenotype and dissemination, we form tumour organoids from three patient-derived xenografts (PDX) CRC MUC models of the CReMEC tumour collection: LRB-009C (TSIP) and IGR-014P (PDX#3) (Julien et al., 2012; Zajac et al., 2018). In suspension, their apical side always faces the external liquid medium: this topology is called “apical-out”. Once embedded in collagen gels, TSIPs keep their apical-out topology, with their apical pole outside, facing the collagen fibres, and retaining their basolateral compartment inside the cluster. Meanwhile, PDX#3 switches to an “apical-in” phenotype, which looks like a normal epithelial topology with formation of a lumen, hence letting the protrusive

basolateral pole outside, facing the collagen (**Figure 22**). Indeed, normal epithelial cells are sensitive to the extracellular matrix and adopt an “apical-in” protrusive phenotype once embedded in collagen, through Rac1 activation, laminin assembly and integrin signalling (O’Brien et al., 2001).

Therefore, these organoids embedded in 3D collagen matrices recapitulate the normal phenotype and the phenotype found in MUC CRC patients. It makes them of high interest to study TSIP dissemination and response to treatments.

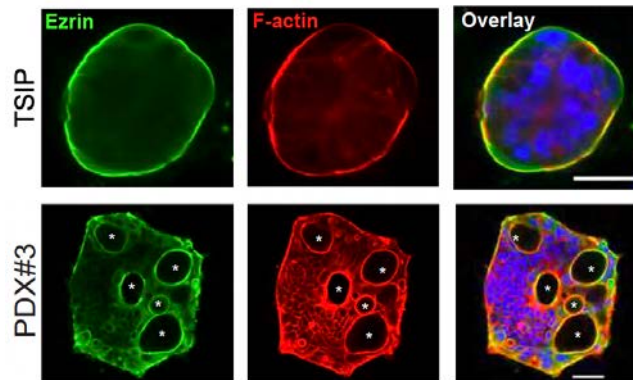


Figure 22. PDX models used to study TSIP polarity reversion.

Organoids are embedded in collagen-I 3D matrices (2 mg/ml). TSIP is apical-out whereas PDX#3 displays an apical-in topology. Images are obtained with a spinning-disk microscope. Blue: nuclei. White asterisk: lumen. Scale bar: 50 μ m. Adapted from (Canet-Jourdan et al., under revision).

Animal models allow in vivo study of cell migration

The embryonic context also provides powerful *in vivo* tools to study cell migration, and in particular collective cell migration. Indeed, they present several important advantages: the transparency of the organisms, the possibility of genetic manipulations and a limited number of cells and cell types at this stage (Boutillon et al., 2018). In order to capture and manipulate more specifically cancer dissemination *in vivo*, genetically engineered mouse models (GEMMs) were produced, with mutations fostering the development of specific tumours.

These models allow the study in a proper microenvironment; however, they are time consuming and expensive. In addition, as stated above, they require the use of complex imaging tools to have a significant spatial resolution.

Patient samples

To investigate patient samples, end-point studies can also be conducted on tissue samples resected by biopsy or surgery, at the primary or secondary sites, fixed and analysed by histology or immunohistochemistry. RNA analyses with laser-microdissection can be combined to reconstitute gene expression patterns (Zhang et al., 2020).

Experimental methods

Given the various forms that cancer cell invasion can adopt, as single cells or collectives, with various types of interaction with the substrate (adhesion strength, stiffness sensitivity...), several assays have been developed to reproduce it and study the underlying mechanisms (**Figure 23**). The strengths and limitations of each experimental design are highlighted here.

1. Cell migration is a key feature of physiological and metastatic processes


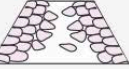

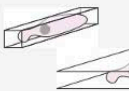





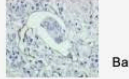
Assay	Dim.	Cells migration type	Handling	Imaging	Physio	References
 Migration on 2D substrates	2D	Single cell adherent (fibroblasts...) or Dictie				Consalvo et al., 2019; Binamé et al., 2016; Maiuri et al., 2012; Gupton and Waterman-Storer, 2006
 Wound healing assay	2D	Collective Epithelial cells (MDCK, ...)				Boyer et al., 1989; Justus et al., 2014; Etienne-Manneville & Hall, 2003
 Transwell	2.5D	<u>Chemotaxis</u> Single cells				
 Synthetic microchannels	2.5D	Single cells Leucocytes				<i>Agarose pads</i> : Nelson et al., 1975; Repo et al., 1978 <i>Microchannels</i> : Liu et al., 2015; Pagès et al., 2020; Bergert et al., 2015; Reversat et al., 2020; Stroka et al., 2014
 3D invasion assay	3D					
 Single cells in 3D scaffold (collagen, polymer,...)	3D	Leucocytes				Lomakin et al., 2020; Wolf et al., 2003b; Sanz-Moreno et al., 2008
 Organoids in 3D scaffold	3D	Tumour organoids				Kleinman and Martin, 2005; Niggemann et al., 2004; Zajac et al., 2018 Mammary organoids: Ewald et al., 2008; Ewald et al., 2012; Neumann et al., 2018
 Embryonic models	3D	Collective migration of border cells (<i>Drosophila</i>), posterior lateral line primordium (zebrafish), neural crest cells (<i>Xenopus</i>)				<i>Chick embryo</i> : Chuai et al., 2012; Zamir et al., 2008 <i>Drosophila</i> : Simpson, 1983; Montell et al., 2012 <i>Xenopus</i> : Shellard et al., 2018 Zebrafish: Dalle Nogare et al., 2014
 Intravital imaging	3D					Beerling et al., 2011; Weigel et al., 2012
 Histology <small>Barresi et al., 2012</small>	3D	Patient and mice specimens				Barresi et al., 2012; Herman et al., 2000; Lim et al., 2010; Matsumoto et al., 2007; Zhang et al., 2020 (laser-capture microdissection)

Figure 23. Techniques for studying cancer cell motility.

Modified from (Sahai, 2005) and (Wolf and Friedl, 2011). For each assay, dimensionality of the confinement (Dim.) is specified, as well as the main migration types studied thanks to the specific design. The subsequent imaging, handling, and physiological resemblance (Physio) are noted from easy to difficult (green to red). When applicable, representative examples provided in this manuscript are listed in “references”.

2D assays for an easy study of single cell and collective cell migration

The simplest assays have been developed on 2D surfaces, in culture dishes or on glass. These surfaces can be coated with various extracellular matrix components (laminin, fibronectin, collagen...) to mimic physiological context. In addition, polyacrylamide (PAA) substrates of different composition are often used to tune the stiffness or create gradients of rigidity.

On 2D substrates, collective migration can be evaluated through the well-known “wound healing assay”, where a wound is made in an epithelial layer and time to close it is then monitored in various conditions (Justus et al., 2014). A similar type of collective migration assays, based on microfabrication, has been developed to avoid other contributions such as cell damage and permeabilisation during the scratch (Poujade et al., 2007).

These assays on 2D flat surfaces are quite artificial, compared to *in vivo* environments that are essentially 3D, and they can only account for adherent cell migration. However, they allow the easiest manipulation and imaging, and are very useful for quantification of forces and stresses exerted by cells during collective or single cell migration (Roure et al., 2005).

Transwell assay introduces chemotaxis

In this assay, cells are plated on a filter, on top of a lower chamber containing a chemoattractant. The number of cells that responded to the chemotactic cue and have crossed the filter is then easily quantified. However, imaging at a high resolution is very difficult.

Introducing cell confinement with microchannels

Cell confinement can be introduced to better mimic *in vivo* conditions, while keeping a limited number of degrees of freedom to allow for easy imaging and quantification. They are often called 2.5D assays. It also allows the study of cells displaying low attachment. Indeed, the migration of immune cells in response to chemotaxis has been extensively studied in assays under agarose pads, a method developed early in the 70's (Nelson et al., 1975; Repo et al., 1978).

Microchannels of custom width, usually made of polydimethylsiloxane (PDMS), can provide better control of cell confinement, on 2 or 4 sides of cells, while allowing surface coating with either adhesive extracellular matrix components or passivating polymers such as polyethylene glycol (PEG) or poloxamers (Pluronic). Their tubular structure also recapitulates *in vivo* tracks encountered between muscle fibres, nerves or in capillaries (Wolf and Friedl, 2011). These microchannels can be textured to introduce topographical cues. Today, they are mostly used to study single cell migration and provide satisfying results as being more relevant than 2D surfaces, better controlled than 3D matrices, and allowing easy quantification and imaging. They can also be combined with microfluidics to perform chemotactic gradients.

However, they do not allow to easily change the surrounding culture medium and drugs. Also, one remaining issue is the nature of the PDMS polymer, which absorbs small hydrophobic molecules, thereby preventing a precise monitoring of drug concentration (van Meer et al., 2017). This can be overcome using certain coatings.

3D matrices to recapitulate in vivo complex fibrillar structure in a dish

The *in vitro* experimental designs that reproduce most the *in vivo* conditions for cancer cell migration are probably 3D matrices of fibrillar collagen-I, usually extracted from rat tail, or Matrigel, a basement membrane secreted by mouse sarcoma and composed essentially of collagen-IV and laminin (Kleinman and Martin, 2005; Niggemann et al., 2004). They can be mixed at different ratios. In collagen gels, the size of pores and fibres can be tuned through different polymerisation conditions (temperature, pH). This allows the study of single cell and collective invasion, i.e. 3D migration, in complex environments, either for adherent or non-adherent cells.

The transwell assay presented above can be improved by coating with ECM components. It can also be combined with "3D invasion assays", where cells are directly plated on top of 3D matrices: the number of cells that invaded and the distance they crossed is then quantified. Last, in absence of a chemotactic gradient, cells can also be directly embedded in the 3D matrices and monitored over time.

These 3D gels also allow more accurate study of collective behaviour. Cells can be cultured in groups as "organoids" to recapitulate the 3D organisation of the organ (e.g. the study of mammary duct morphogenesis (Ewald et al., 2008), TSIP study (Zajac et al., 2018)), intratumoral heterogeneity, and 3D interactions between cells. They can be embedded in these matrices and monitored with live imaging, allowing the study of the specific behaviours of the edge and core of the structures.

1. Cell migration is a key feature of physiological and metastatic processes

However, given the thickness of samples, resolution at the cell level requires more sophisticated imaging tools, such as confocal or spinning-disk microscopes. In addition, as cells can move in any direction in 3D, the quantification of the characteristics of their migration (total distance, persistence), is difficult to perform.

Also, the variability between the lots of commercial components and the complexity of understanding cell-ECM interactions in such meshes led some labs to use synthetic polymers and hydrogels to provide a better controlled 3D structure, allowing a precise tuning of stiffness, pore size, adhesion, and matrix degradability.

In vivo imaging in mice

From GEMMs or orthotopic grafts, whole body imaging with fluorescence or bioluminescence is often used to monitor tumour invasiveness, with poor resolution but low invasiveness (Sahai, 2007). Higher spatial and time resolution can be obtained by invasive intravital imaging, usually through windows installed dorsally or at the fat pad position for breast cancer, and limited to a few hundreds of microns in depth (Beerling et al., 2011; Weigelin et al., 2012). Such imaging techniques can be combined with second-harmonic generation microscopy for the observation of fibrillar structures, and 2-photon microscopy for precise spatial resolution and high penetration.

2. MECHANISTIC BASIS OF CELL MIGRATION

The mechanisms underlying cell migration have become a large area of investigation for cell biologists, molecular biologists, and biophysicists, to understand how motion is generated in cells and what are its properties. This research enlightened two fundamental aspects of cell migration: cell polarisation and force generation. Whereas polarisation mechanisms are quite consistent among cell types and modes of migration, force generation can occur in multiple ways depending on the mode of migration, single cell or collective, traction-based (pulling force at the front) or propulsion-based (often relying on contractility at the rear).

These two main features will be decrypted here with a special interest on actin dynamics and cancer alterations. Indeed, except in some rare cases among eukaryotes like sperm cells, actin microfilaments play an essential role in cell migration through regulation of cell polarisation, force sensing and force generation, thanks to their dynamics and their numerous partners. Nevertheless, there is much to uncover on the contribution of the other members of the cytoskeleton (microtubules and intermediate filaments) to cell migration, as they have also been shown to participate and crosstalk to regulate cell polarisation and migration (Coles and Bradke, 2015; Dogterom and Koenderink, 2019; Seetharaman and Etienne-Manneville, 2020).

2.1. Front-back polarisation of cells during directed migration

To allow for any motion, single cells or groups must be polarised, i.e. present a front-back asymmetry that will induce a preferential direction. In addition, to allow for directed migration, the spontaneous random walk of cells must be persistently biased, which can be promoted by asymmetric external cues. These external cues often induce internal cell polarisation, which will be the focus of the first part of this section. Polarised cells then generally adopt an asymmetric morphology by extending protrusions at their leading edge. This is allowed and sustained by the polarisation of the cytoskeleton – essentially actin microfilaments – under the regulation of small Rho GTPases.

2.1.1. Asymmetric external cues induce cell polarisation

Cells can migrate towards various types of polarised external cues, that can be summarised as the following (**Figure 24**): diffusible molecules (chemotaxis), substrate-bound molecules (haptotaxis), higher substrate stiffness (durotaxis), geometrical features (topotaxis), lower hydraulic pressure (barotaxis) and in electric fields (galvanotaxis) (Lennon-Duménil and Moreau, 2021; SenGupta et al., 2021).

2. Mechanistic basis of cell migration

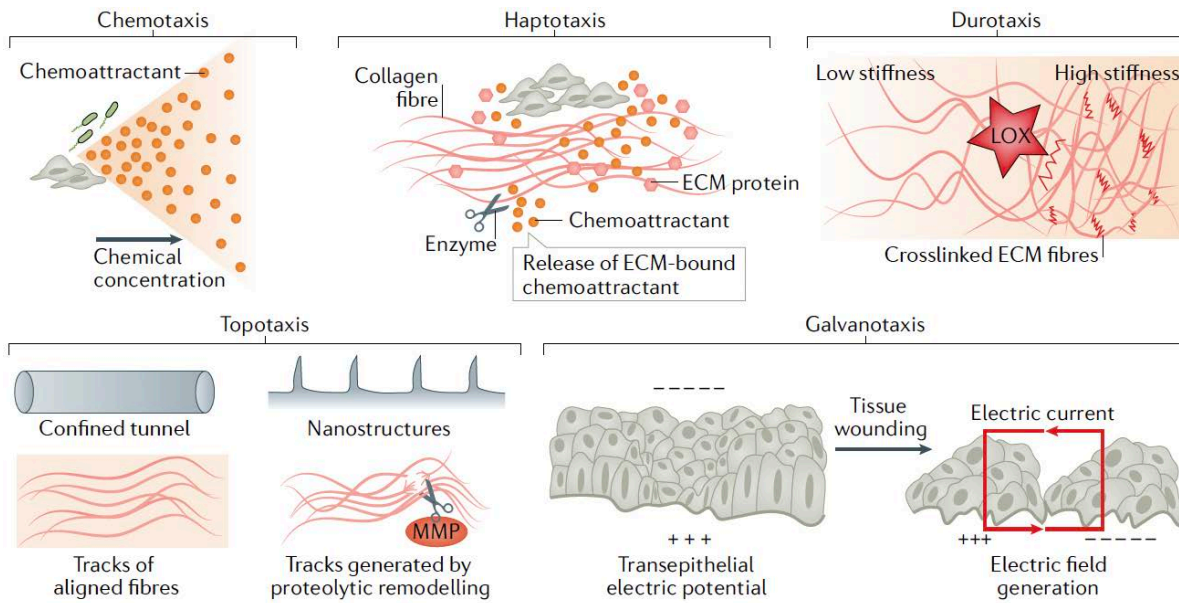


Figure 24. Guidance of cell migration by external cues.

Guidance can be provided by diffusible molecules (chemotaxis), substrate-bound molecules (haptotaxis), higher substrate stiffness (durotaxis), geometrical features (topotaxis), and in electric fields (galvanotaxis). From (SenGupta et al., 2021).

Chemotaxis and durotaxis are the most unravelled today and provide representative examples to illustrate the effect of external cues on downstream signalling.

2.1.1.1. CHEMOTAXIS

During embryogenesis, cell migration is often guided by chemotactic cues, such as growth factors released by surrounding tissues. For example, *Drosophila* border cells migrate towards the oocyte that secretes higher concentration of PVF1 (platelet-derived growth factor (PDGF) and vascular endothelial growth factor (VEGF)-related factor 1), Spitz and Keren (Montell et al., 2012). It requires expression of their associated receptors, respectively PVR (PDGF- and VEGF-receptor related) and EGFR (epidermal growth factor receptor). Similarly, to drive immune response, leucocytes sense the environmental chemotactic cues – released by injured epithelia for example – thanks to heterotrimeric G-protein-coupled receptors (GPCRs) (Lam and Huttenlocher, 2013). Cells migrating in a mesenchymal adhesive way, like fibroblasts, are also sensitive to chemoattractants: fibroblasts express receptors of the tyrosine kinase class (RTKs), activated by PDGF, FGF and EGF, allowing them to migrate towards a wound (Bear and Haugh, 2014).

Thus, cells migrating in an adhesive mesenchymal fashion, a non-adhesive amoeboid fashion (leukocytes), and in groups (border cells) can all follow chemotactic cues leading to directed migration. The social amoeba *Dictyostelium discoideum*, or Dictie, allowed great advances in the understanding of chemotaxis (Consalvo et al., 2019). In this system, isolated cells stochastically extend protrusions in any direction. However, under the release of cyclic AMP (cAMP) by neighbouring cells, the 30% of protrusions (pseudopods) are biased in the direction of the highest cAMP concentration, thereby generating directed migration and cell clustering (Andrew and Insall, 2007).

Through sensing by GPCRs or RTKs, chemoattractants activate downstream pathways that amplify the signal and regulate actin and myosin behaviour.

In Dictie cells, they activate small GTPases Ras and Rac via phosphoinositide 3-kinase (PI3K) signalling. This induces actin polymerisation and maintenance of the pseudopod on the side close to the highest

concentration of activated receptors. Meanwhile, contractile activity is enhanced at the opposite side to generate forward movement of Dicty cells (Consalvo et al., 2019).

Similarly, PI3K signalling downstream of GPCR activation promotes actin polymerisation at the leading edge of neutrophils and fibroblasts via formation of PIP₃ (phosphatidylinositol (3,4,5)-trisphosphate) at the membrane and activation of small GTPases (Bear and Haugh, 2014; Lam and Huttenlocher, 2013). The roles small GTPases in cell migration will be detailed later. In addition, PI3K-PTEN loop enhances the chemotactic signal, allowing for migration in very shallow gradients: PI3K generates PIP₃ phosphoinositides at the front while phosphatase and tensin homologue (PTEN) removes them at the back (Montell et al., 2012).

In *Drosophila* border cells collective migration as well as *Xenopus* neural crest cells migration, chemotaxis directly regulates actomyosin contractility, thus creating an internal polarisation of the cluster and directed migration (Combedazou et al., 2017; Shellard et al., 2018). E-cadherin then mediates a positive feedback loop that sustains and amplifies Rac relocalisation and activity at the front of border cells clusters (Cai et al., 2014).

2.1.1.2. DUROTAXIS

Cells are able to sense the mechanical properties of their environment, including stiffness which is often key in initiating migration and impacts cell behaviour. Embryonic development is a good example of cell response to substrate rigidity: in *Xenopus* neural crest cells migration, increased stiffness of the underlying mesoderm triggers EMT and cell migration through integrin/vinculin/talin mechanosensing (Barriga et al., 2018). The study of stiffness-dependent cell migration has usually been studied on 2D substrates, mainly on polyacrylamide gels whose stiffness can be easily modulated without changing ligands concentrations. Microchannels of different rigidity allowed to show that it also occurs in 3D environments (Pathak and Kumar, 2012).

In addition to being sensitive to ECM stiffness, cells can also respond to gradients of rigidity, i.e., durotaxis. Fibroblasts were the first to be observed as moving towards increasing stiffness (Lo et al., 2000), and later, many other cell types as well, including smooth muscle cells, immune cells, cancer cells and others. The general mechanism can be summarised as follows: nascent focal adhesions mature on stiff regions, allowing the cells to grip harder, inducing better force transmission on the stiff part of the substrate. On top of it, positive feedback loops involving Arp2/3 and Rac1 lead to increased protrusive activity on the stiffest side. Myosin activity is also affected by mechanosensation: on stiff regions, myosin IIA is dephosphorylated, leading to its relocalisation at stress fibres and relocalisation of myosin IIB at the softer side to contract the rear of the cell (Shellard and Mayor, 2021b).

Of note, cell migrating collectively are able to sense more subtle gradients than single cells because of the higher range they capture along the length of the group: for example, MCF10A breast epithelial cells are sensitive to durotaxis at the collective scale only, via more efficient force transmission to the substrate on the stiffer side and force transmission by cell-cell junctions (Sunyer et al., 2016). Durotaxis can also be combined with chemotaxis to drive collective cell migration *in vivo*, as reported recently for *Xenopus* neural crest cells migration (Shellard and Mayor, 2021a).

The formation of focal adhesions seems to be a prerequisite in the ability of cells to respond to a gradient of stiffness. Durotaxis has not been investigated yet in non-adhesive amoeboid cells, probably because of experimental difficulties as this mode of migration requires confinement. However, in non-adhesive conditions, cells are sensitive to other external parameters such as confinement. This has been exemplified by experiments involving microchannels of different cross-sections: when in contact with a more narrow section, cells would reverse direction or migrate towards this region of higher confinement (Bodor et al., 2020; Mak et al., 2011).

2.1.2. Polarised morphology of migrating cells

Migrating cells have generally a highly asymmetric morphology that reflects and sustains their overall molecular polarisation. They often form membrane extensions, called protrusions, at the front. These protrusions can display various shapes, from thin filopodia to large pseudopodia (Bodor et al., 2020). Their main role is the generation of forward translation, but they are endowed with a certain number of other skills as well, including sensing of the environment. Their rear, called the uropod, is generally more contractile to allow for body retraction. The observation that a cell forms oriented protrusions is also a key element in assessing for active migration: for example, small protrusions at a single cell level came as one of the first evidence of active epithelial cell migration towards the tip of the villus during gut renewal (Krndija et al., 2019).

In collective migration, cells at the leading edge generally display similar features and protrusive activity as the front of isolated cells. When detached as cell clusters of a limited number of cells, a full front-back polarisation often occurs at a supracellular level. Otherwise, in some cases, polarisation can be observed at a single cell level.

Of note, cell morphology during migration is often described as related to the type of front protrusions, but cell shape encompasses the whole body, and overall, often follows the dimensionality and porosity of the surrounding environment (1D tracks, 2D surfaces, 3D meshwork).

2.1.2.1. CELLS CAN EXTEND DIFFERENT TYPES OF FRONT PROTRUSIONS

The most widely studied type of protrusions, and most impressive also, are *lamellipodia* whose best ambassadors are certainly keratocytes (cornea fibroblasts). Lamellipodia are the widest protrusions, quite specific to 2D migration, sheet-like and thin (200 nm high). They allow for random spatial exploration and extend by being pushed forward by actin branching close to the border. Similar branched actin-mediated broad membrane extensions (1 to 5 μm) are observed in 3D environments and called *pseudopodia*. However, they do not form specific adhesions with the substrate (Fritz-Laylin et al., 2017a).

In addition, *filopodia* can extend further at the edge of lamellipodia, or other front protrusions, to stabilise them by anchoring to the substrate (Stevenson et al., 2012). They are spike-like thin extensions (200 nm in diameter, 30 μm long) formed of parallel actin bundles. They drive directed migration and have also a sensory role related to the number of receptors they cluster.

Very contractile cells often form *blebs* through hydrostatic pressure, where the actin cortex that surrounds the cell, or its attachment to the membrane, is weakened. They grow as spherical membrane extension (up to 5 μm diameter) devoid of actin, then the cortex reassembles, and the bleb retracts. *Lobopodia* are also thought to form under cytoplasmic pressure, but with a different shape: they correspond to large cylindrical membrane extensions, and anchor on the ECM to generate traction forces while the nucleus is pushed forward (Yamada and Sixt, 2019).

Small invasive cell feet, containing branched and bundled actin, are used for matrix remodelling. They are called *invadopodia* in cancer cells, and *podosomes* in other cell types: hematopoietic cells, endothelial cells and Src-transformed fibroblasts (Stevenson et al., 2012).

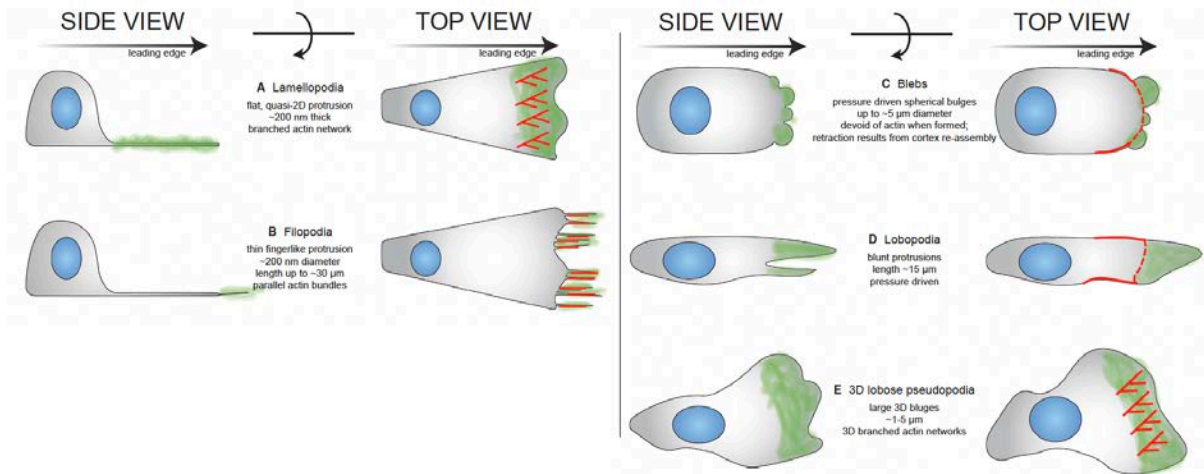


Figure 25. Types of protrusions in migrating cells and corresponding actin network (red). Modified from (Bodor et al., 2020).

Nevertheless, such a classification is certainly not exhaustive. For example, not mentioned above, neutrophils have also been observed forming thin lamellipodium-like pseudopods in 3D matrices (Fritz-Laylin et al., 2017b).

Other classifications have also been proposed, sometimes more general, for example by defining lamellipodia as any dynamic actin-containing structures that disappears upon deletion of small GTPase Rac and its downstream effectors (Rottner and Schaks, 2019).

Also, external and internal parameters play an important role in determining cell shape and front protrusions: ECM topology, but also its adhesiveness, stiffness, cell contractility, matrix remodelling and others. Therefore, as the modulation of these parameters also induce cells to switch between one morphology and another, intermediate phenotypes certainly happen.

2.1.2.2. POLARISATION OF THE NUCLEUS-CENTROSOME AXIS DURING MIGRATION

In addition to the formation of front protrusions, other cell components are highly polarised during cell migration. I will not describe every of them, only mention that the nucleus and microtubule-organising centre (MTOC) positioning can vary from one mode of migration to the other but is highly conserved in each of them. In single cell mesenchymal migration, the centrosome generally faces the protrusion, before the nucleus: this allows for targeting of vesicles at the front of the cell, containing proteases or membrane components (Yamada and Sixt, 2019). This polarisation has also been observed at the leading edge during collective migration of astrocytes, in a scratch-induced migration assay (Etienne-Manneville and Hall, 2003). It is the inverse in amoeboid single cell migration, where cells deform more and need no proteolytic activity. In this case, the nucleus, positioned before the MTOC, may act at the front as a ruler to determine in which path the cell will be able to pass through (Lomakin et al., 2020; Venturini et al., 2020).

2.1.3. Polarised regulation of actomyosin dynamics during cell migration

Actin microfilaments modulate cell structure and contractility (especially in muscle cells), and tissue architecture through cell-cell and cell-ECM adhesions. During migration, under the control of small Rho GTPases, they also play a key role in cell polarisation: actin polymerisation at the front leads to formation of most protrusions, while the retraction of the cell rear is allowed by enhanced contractility through actin coupling with myosin fibres. In addition, the polarisation of actin and myosin can generate persistent intracellular retrograde flows that contribute to sustained cell polarisation, and to force generation.

2.1.3.1. ACTIN FILAMENTS ARCHITECTURE IN CELL POLARISATION AND FRONT PROTRUSIONS

Polymerisation of actin filaments: a polarised ATP-dependent process

Actin filaments are intrinsically polarised. Indeed, they are characterised by different attachment and dissociation constants of G-actin (globular actin) monomers on both sides, favouring a faster attachment at the barbed end than at the opposite end, the pointed end, making them highly polarised and dynamic structures. This polymerisation process, called actin treadmilling, relies on ATP hydrolysis cycles (**Figure 26**): G-actin monomers bound to ATP are added at the + end of F-actin (filamentous actin), and dissociate at the pointed end as hydrolysed ADP-actin monomers, that will be phosphorylated in the cytoplasm into ATP-actin (Rottner and Schaks, 2019).

These microfilaments are helicoidal, double-stranded, and, with a thickness of 7-9 nm, the thinnest of the three main components of the cytoskeleton (Coles and Bradke, 2015). Actin is also the most abundant protein in the cytoplasm, composing up to 15% of the protein mass.

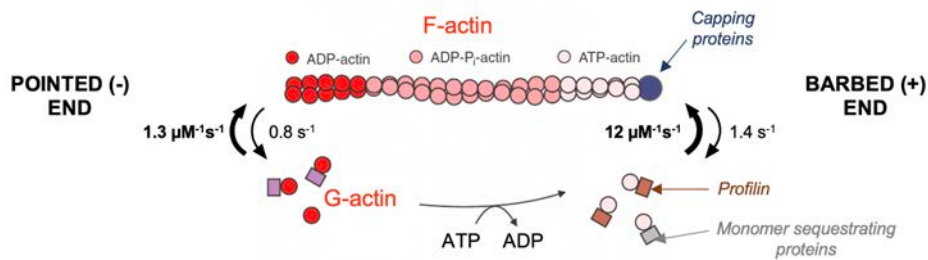


Figure 26. Polymerisation of actin filaments through ATP hydrolysis cycles and with different attachment constants at both ends (bold arrows).

A few actin binding partners are also introduced: capping proteins that promote or block polymerisation at the barbed end, profilin that enhances G-actin binding to F-actin, and monomer-sequestering proteins that prevent polymerisation of monomers. Modified from (Coles and Bradke, 2015). Association constants from (Lodish et al., 2008).

Actin structures are modulated by specific actin-binding proteins during cell migration

The architecture of actin filaments varies with the roles it plays in the cell and the different structures are adapted to undergo different kinds of forces (**Figure 27**) (Fletcher and Mullins, 2010).

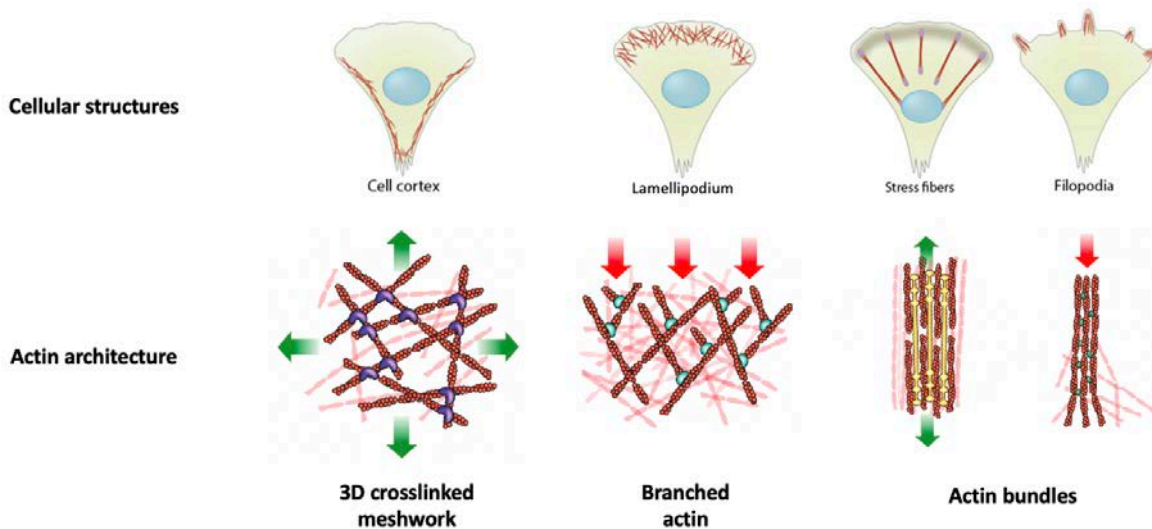


Figure 27. Cellular structures (top) and corresponding actin architecture (bottom). Red arrows: compression forces; green arrows: tension forces. Modified from (Fletcher and Mullins, 2010; MBInfo).

Actin is regulated by actin-binding proteins (ABP) to form these structures (Alberts et al., 2010), and *in vitro* reconstituted systems have been of great help to decipher the interplay between actin and its binding partners, allowing a maximum simplification of cellular systems (Fletcher and Mullins, 2010).

Both filopodia and stress fibres are composed of *bundled actin cables*. The first resist to pressure to push the membrane forward, while the latter are attached to focal adhesions exerting high tensions. Here, linear actin elongation is mainly mediated by nucleating proteins called formins (including mDia family): they act in dimer, each subunit binding two actin monomers, and accumulate at the tip of filopodia. In addition, bundling proteins foster filament assembly and generate stiff actin elongated networks: this allows for example filopodia and invadopodia to push efficiently the plasma membrane for elongation.

Branched actin polymerises in lamellipodia and pseudopodia and faces compression forces while pushing the front membrane. The Arp2/3 complex is the key molecule to initiate actin branches: it binds to the elongated mother filament, and triggers assembly of monomers to form a new branch characterised by a 70° angle between filaments (Rottner and Schaks, 2019). This complex is composed of the actin-related proteins Arp2 and Arp3, that resemble actin, and five smaller subunits (ArpC1-5). It is frequently activated by Wiskott–Aldrich syndrome protein (WASP, N-WASP) in podosomes and invadopodia, and WAVE (WASP family Verprolin homolog) regulatory complex in lamellipodia. WASP and WAVE are themselves activated at the cell membrane. Actin branches are then stabilised by cortactin. This dynamic and efficient cellular machinery can be hijacked during bacterial infection, and the bacteria *Listeria monocytogenes* is a well-known example: it presents actin assembly-inducing protein (ActA) at the rear that activates Arp2/3 complex and branched-actin polymerisation. This creates actin tails, called “comet tails”, allowing fast movement in and through cells (Merz and Higgs, 2003).

There is also an interplay between Arp2/3 and actin elongators (such as formins), but to date, it remains unclear (Ridley et al., 2003). In addition, capping proteins (capping protein CP, tropomodulin at the pointed end) regulate polymerisation at the barbed or pointed ends; severing proteins (ADF (actin depolymerising factor)/cofilin family members) fragment filaments by twisting them, and monomer-sequestering proteins (thymosin) prevent monomer binding to filaments. Four main toxins are well-known to prevent actin from fulfilling its missions and have comparable roles as ABP can have: cytochalasin D and latrunculin A, respectively a mycotoxin and a sponge toxin, prevent actin polymerisation while jasplakinolide, another sponge toxin, stabilising F-actin and makes amorphous actin webs. Phalloidin, a mycotoxin, stabilises F-actin as well and prevents its depolymerisation, and is mainly used as a staining for filamentous actin in fixed specimens.

During directed cell migration, actin fibres constantly polymerise at the leading edge, therefore treadmill rearward in the cell reference frame at around 0.25-1.5 µm/min: these *retrograde flows* reinforce cell polarisation, coupling cell speed with migration persistence (Maiuri et al., 2015). They also contribute importantly to force generation, which will be detailed in the next section (Case and Waterman, 2015).

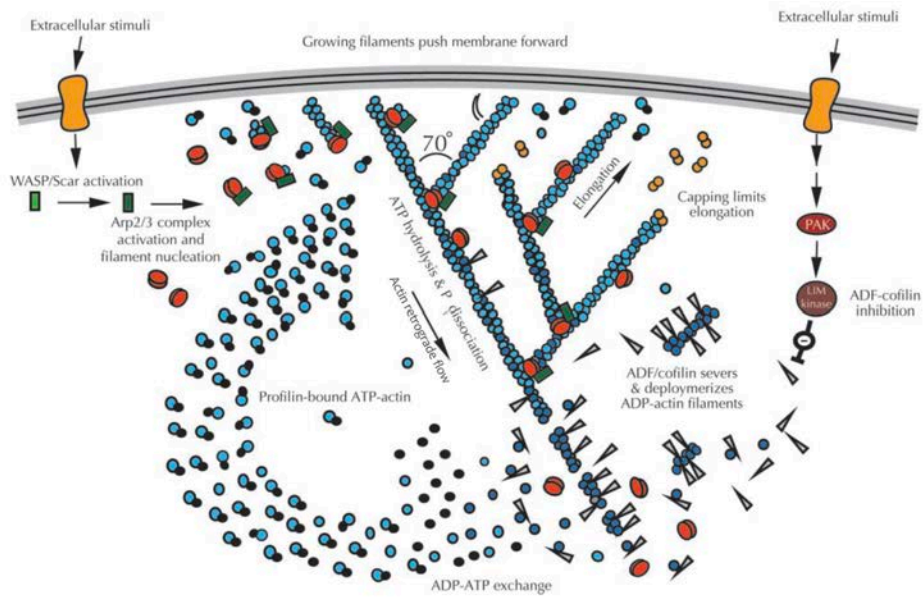


Figure 28. Branched actin nucleation and actin polymerisation at the leading edge drive lamellipodia extension. This process is regulated by multiple complementary actin-binding proteins and under the control of external stimuli. Adapted from (Miller, 2002).

Actin filaments also compose the cell cortex, which is a dense and elastic meshwork surrounding cells. Its stiffness can be modulated, leading to different cell migratory behaviours, and is mainly regulated by non-muscle myosin IIa and IIb, as well as spectrin and filamins that cross-link filaments. Several proteins link actin filaments to the cell plasma membrane: dystrophin, and ERM proteins (Ezrin, Radixin, Moesin), characteristic of the apical side of epithelial cells. In addition, in cell sheets and clusters, actin contributes to maintenance of cell-cell junctions and force transmission.

Deregulation of actin dynamics promotes cancer invasiveness

Actin-associated proteins are often upregulated in cancer, hence favouring microfilaments activity and cell migration. Indeed, when interfering with key actin players like actin-related proteins complex (Arp2/3) and cofilin, tumour metastasis is reduced in melanoma and breast cancer mouse models (Kurusu et al., 2005; Wang et al., 2006).

Arp2/3 complex and associated proteins are upregulated in a high number of cancer types including lung, breast (via overexpression of human epidermal growth factor receptor 2, HER2), gliomas, gastric and CRC, and often correlate with reduced survival (Molinie and Gautreau, 2018). Likewise, Stevenson and colleagues wrote a first review about the regulation of actin-bundling proteins in cancer (Stevenson et al., 2012).

Such deregulations can be caused by fundamental oncogenic mutations. In particular, KRAS (Kirsten rat sarcoma virus gene) and BRAF (v-raf murine sarcoma viral oncogene homolog B1 gene) activating mutations are found respectively in 35% and 12-18% of colon carcinomas, and BRAF in 70% of malignant melanomas. They can affect tumour cell motility through activation of small GTPases (RhoA, Cdc42) that regulate actin polymerisation and actomyosin contractility in cell migration (**Figure 29**) (Makrodouli et al., 2011).

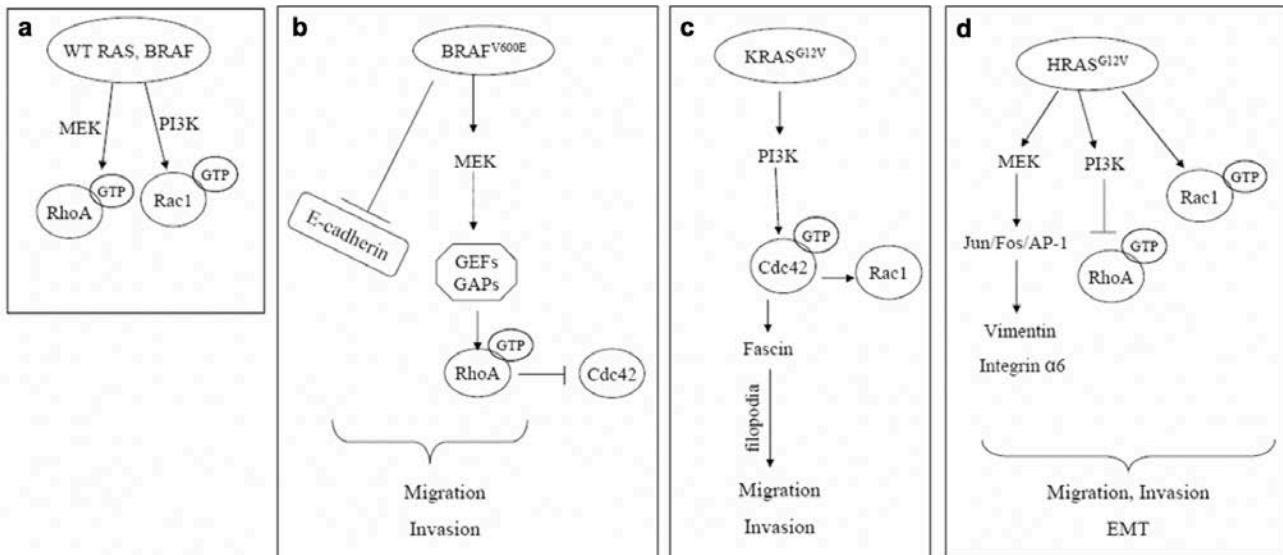


Figure 29. Putative pathways leading to upregulation of cell motility depending on the RAS (KRAS, HRAS) and BRAF activating mutations in colon cancer progression.

From their experimental results and literature, the authors propose four different pathways accounting for the invasiveness gained in transformed cells, through activation of small Rho GTPases and PI3K and MEK pathways. From (Makrodouli et al., 2011).

2.1.3.2. ACTOMYOSIN CONTRACTILITY CONTRIBUTES TO CELL POLARISATION

Another prominent group of proteins that interact with actin are motor proteins of the myosin family. Their two identical heavy chains (MHC) compose the tail while the head domain is formed by various combinations of light chains (MLC), including essential and regulatory chains (ELC and RLC). Myosin motors allow for transport of cargo along actin filaments: heads are in contact with the filaments, while their tail binds the cargo. Their motor activity then relies on ATP hydrolysis cycles to provide the energy needed to change conformation and move along actin cables.

Myosins are differentially expressed among cell types and the different subtypes of myosin family play different roles. Myosin II molecules are the most prominent of them, and they are essential in most cell migration modes. They are activated by phosphorylation of their light chain (MLC) on two preferential sites: serine 19 (Ser19) and threonine 18 (Thr18) (**Figure 30a**). This phosphorylation is performed by MLC kinase (MLCK) or Rho kinase (ROCK). MLCK is regulated by the concentration of intracellular calcium and its own phosphorylation. ROCK, activated by binding Rho-GTP, also phosphorylates MLC phosphatase (MLCP), thereby preventing its inhibitory activity on myosin (Ridley et al., 2003).

Myosin II molecules can assemble in filaments, creating bipolar structures that bind actin on both sides (**Figure 30b**) (Vicente-Manzanares et al., 2009). Their ATP-dependent motor activity then causes translation of filaments on one another, hence contracting or relaxing cells (**Figure 30c**). For muscle contraction, their speed along filaments can then reach up to 15 $\mu\text{m/s}$.

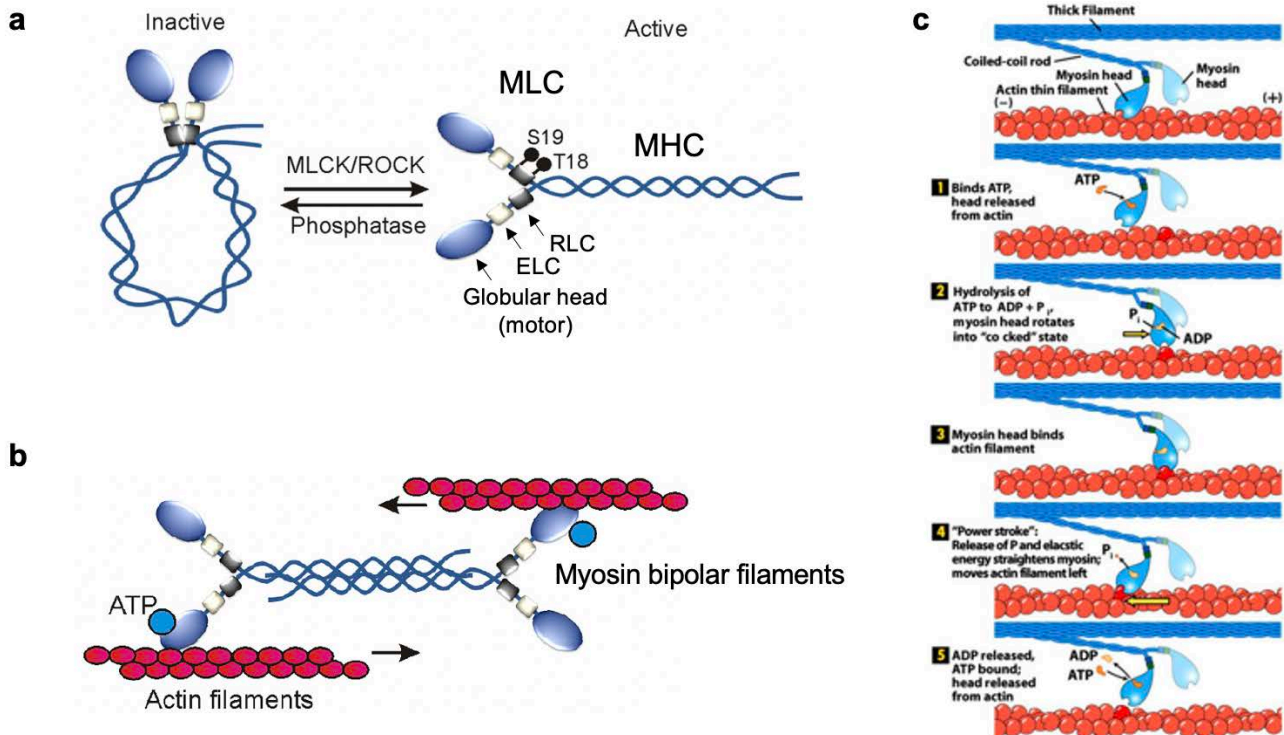


Figure 30. Myosin II drives cell contractility. **a**, Activation of myosin II by phosphorylation on Ser19 (S19) and Thr18 (T18) sites. Modified from (Betapudi, 2014). **b**, Myosin bipolar filaments bind 2 actin cables and drive contraction or relaxation. Adapted from (Betapudi, 2014). **c**, An ATP-dependent cycle drives the activity of filaments of myosin II motors on actin filaments. From (Lodish et al., 2008).

Myosin II plays a key role in the regulation and maintenance of cell polarity, as well as in force generation which will be detailed in the next section. Indeed, its activity is generally enhanced at the rear of cells, helping *retraction* and detaching when it is bound to the substrate through focal adhesions. Cell retraction also contributes to cell polarity by inducing recycling of focal adhesion components for protrusive activity at the front (Ridley et al., 2003).

In very contractile cells that can perform amoeboid migration, cortex contraction by myosin activity drives *bleb formation* through pressure increase. In addition, it drives cell polarisation through generation of *retrograde flows of the actomyosin cortex*, in crosstalk with actin polymerisation (**Figure 31**). Indeed, as there is still poor knowledge on the microscopic organisation of the cortex and its underlying biochemical processes, the cortex is often described in the active gel theory as a continuous gel, where active, ATP-dependent mechanisms generate internal stresses. This modelling allowed for a better understanding of the effects of internal fluctuations and stresses on the establishment of spontaneous flows: as contractility increases, myosin flows can appear fast following any small fluctuation from dynamic cortical instability, towards the higher concentration of myosin (Hawkins et al., 2011; Salbreux et al., 2012). These flows generate physical transport of actin and myosin and reinforce the initial instability, driving the stabilisation of the bleb. They can only be sustained if active polymerisation of actin is maintained at the front as well. These hypotheses have been confirmed *in vitro*, for example in 3D migration of breast cancer cells or experiments with artificial increase of cell contractility (Hawkins et al., 2011; Ruprecht et al., 2015).

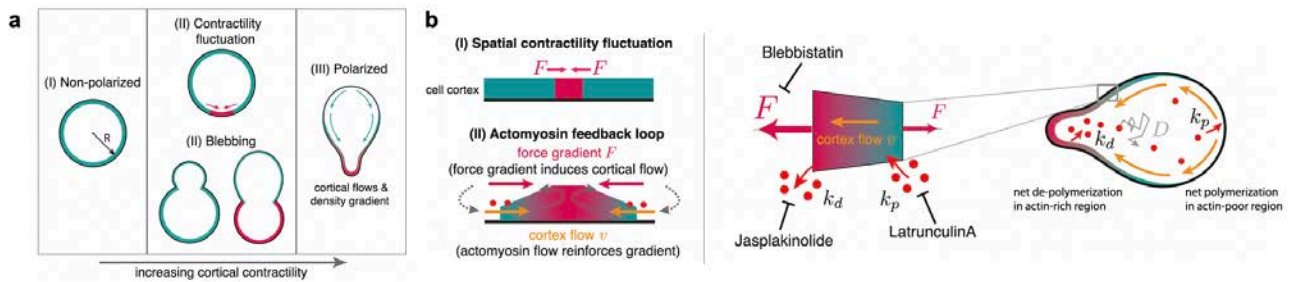


Figure 31. Myosin contractility promotes blebbing and generation of polarised flows.

a, Summary scheme of appearance of blebbing and cortical myosin flows upon contractility increase, thus polarising single cells. **b**, Illustration of the feedback loop between cortical density gradients and rearward cortical flows. This process also relies on actin dynamics: polarisation is lost upon inhibition of actin polymerisation at the front (latrunculin A) or actin depolymerisation at the back (jaspilakinolide). From (Ruprecht et al., 2015).

Given the prominent role of myosin in cell migration, interference with actomyosin contractility is often performed in cell biology. Among myosin inhibitors, blebbistatin and Y27632 are the most widely used. Blebbistatin inhibits myosin ATPase activity by binding the nucleotide binding pocket and actin binding cleft of myosin: this blocks myosin in a conformation detached from actin. Y27632 inhibits ROCK1 and ROCK2, hence preventing myosin phosphorylation and activation.

2.1.3.3. SMALL RHO GTPASES REGULATE ACTIN AND MYOSIN POLARISED DYNAMICS

Polarisation of actin activity and its partners is mainly regulated through asymmetrical distribution of Rho family of small guanosine triphosphate-binding proteins (small GTPases), that act downstream reception of extracellular signals.

Twenty mammalian small Rho GTPases have been described to date (Etienne-Manneville and Hall, 2002). They are mainly activated at the plasma membrane, regulating actin-related processes. They are active when bound to GTP, which is achieved by guanine nucleotide exchange factors (GEFs), and they are inactivated by GTPase activating proteins (GAPs) (**Figure 32**). Their targets include protein kinases, lipid-modifying enzymes, and Arp2/3 activators.

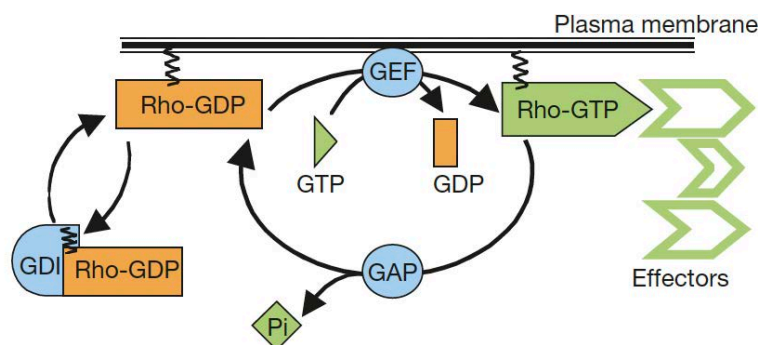


Figure 32. Activation and inactivation of small Rho GTPases by GEFs and GAPs.

From (Etienne-Manneville and Hall, 2002).

The main small Rho GTPases subfamilies regulating actin in migration are: Rac (Rac1, Rac2, Rac3, RhoG), Cdc42 (Cdc42, RhoW, RhoJ) and Rho (RhoA, RhoB, RhoC) (Crosas-Molist et al., 2022; Ridley et al., 2003).

Rac1 and Cdc42 are rather activated at the front of cells, where Rac1 activates WAVE proteins and Cdc42 binds WASP proteins (**Figure 33a**). Thus, both stimulate Arp2/3-mediated extension of the lamellipodium. Cdc42 also plays an important role in filopodia formation through formin activation.

RhoA is mainly present at the rear of cells, activating myosin activity (Bear and Haugh, 2014). Therefore, RhoA-mediated actomyosin contractility allows retraction of the cell body and detachment from the substrate, to move forward (Mattila and Lappalainen, 2008). At the front of the cell, RhoA also promotes formin-mediated actin elongation in filopodia and bleb formation through enhanced contractility (Crosas-Molist et al., 2022).

RhoA and Rac1 appear to be mutually antagonistic, with Rac1 activity at the front inhibiting RhoA, while RhoA is active at the rear and prevents Rac1-mediated formation of protrusions (**Figure 33b**) (Evers et al., 2000). Through a complex GEF and GAP interplay, their polarisation dictates cell migration, and loss of polarisation by inhibition or global activation leads to loss of migration (Etienne-Manneville and Hall, 2002).

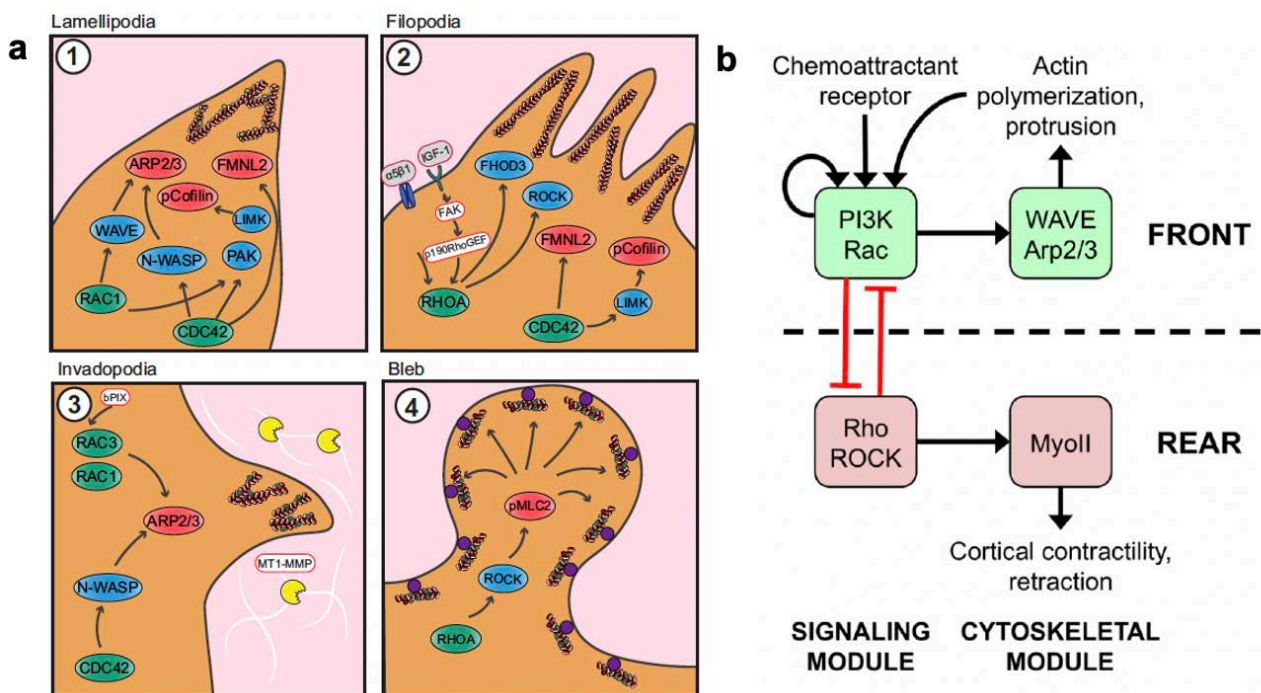


Figure 33. Small Rho GTPases drive cell polarisation and protrusion formation through subtle regulation of actin dynamics.

a, Small Rho GTPases Rac1, Cdc42 and RhoA drive specific actin dynamics (elongation, branched actin polymerisation or actomyosin contractility), resulting in different types of protrusions at the front of cells. From (Crosas-Molist et al., 2022). **b**, Polarisation of actin dynamics is regulated by asymmetric and co-repressive distribution of small Rho GTPases Rac and Rho. From (Bear and Haugh, 2014).

In addition, positive and negative feedback loops regulate their activity (Ridley et al., 2003). WAVE and WASP proteins bind to GAPs and GEFs, and can be activated by other stimuli than Rac and Cdc42 (Ridley et al., 2003). Positive feedback loops sustaining Cdc42 polarised activity can involve either integrins or kinase PAK1, a downstream effector of Cdc42 that mediates its activation downstream of GPCRs, at the front. PI3Ks also exert a positive feedback loop on Rac: Rac recruits PI3Ks at the membrane, which in turn activates some GEFs upstream of Rac. Also, integrin activation leads to Rac stimulation, which induces clustering of integrins at the leading edge. When PIP₃ is also recruited at the front and activates integrins, it activates Rac at the front in response.

2.2. Force generation

As cell migration occurs at low Reynolds number where viscous forces dominate, they do not benefit from inertia and need to generate a constant active force for movement. This has been well described by Taylor and Purcell, and today we still build our physical understanding of cell migration on these principles (Purcell, 1977).

These active forces need anchorage of the cell on the substrate, either through specific or non-specific attachment. Then, if the force is generated at the front, generally related to focal adhesion formation, it can be called traction, while propulsion refers to a force provided by the back, often through actomyosin contractility.

The study of cell migration was initially extensively performed on 2D substrates. The use of 3D environments uncovered a much wider spectrum of migration modes, spanning from the various cell shapes described above and the complex interactions with their surrounding ECM (Yamada and Sixt, 2019). The generation of migration forces often relies on actomyosin retrograde flows, and their distribution is affected by cell polarisation.

Single cell modes of migration are usually classified into two main categories: focal-adhesion-dependent and traction-based, termed mesenchymal, and focal-adhesion-independent and propulsion-based, termed amoeboid. Like single cells migrating in a mesenchymal fashion, collective migration described to date relies on strong adhesion on the substrate and traction forces (**Figure 34**). Nevertheless, this classification characterises two extreme behaviours on the spectrum, between which a variety of shades can occur.

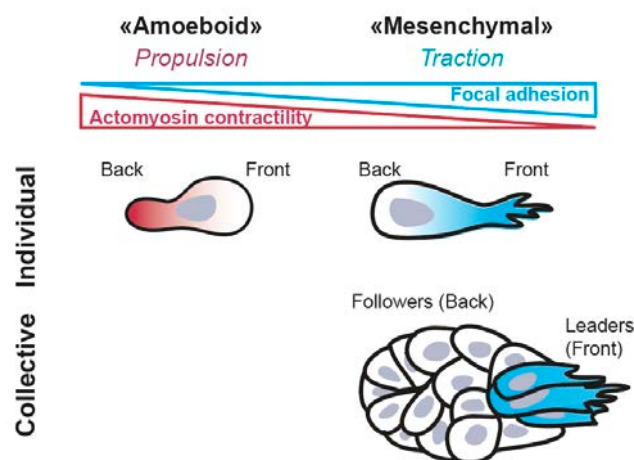


Figure 34. Scheme of the migration modes known to date

Single cells can display either a propulsion-based amoeboid migration or a mesenchymal traction-based one. Cell clusters rely on traction on the substrate like single mesenchymal cells.

2.2.1. Adhesion-traction in single cells: mesenchymal mode of migration

2.2.1.1. GENERAL DESCRIPTION OF MESENCHYMAL MIGRATION

Cell motility was first observed as a focal-adhesion and traction-based mechanism and named “mesenchymal” after the migration on 2D surfaces of fibroblasts, which are mesenchymal cells from the connective tissue synthesising extracellular matrix (**Figure 35**). Its first methodical characterisation is assessed in 1980 when Abercrombie summarised the first discoveries that had been made on cell

migration, on fibroblasts, immune cells and in development (Abercrombie, 1980). This mode of migration is shared by multiple cell types, including cancer cells (Binamé et al., 2016). It occurs at 0.1-1 $\mu\text{m}/\text{min}$ on average (Maiuri et al., 2012).

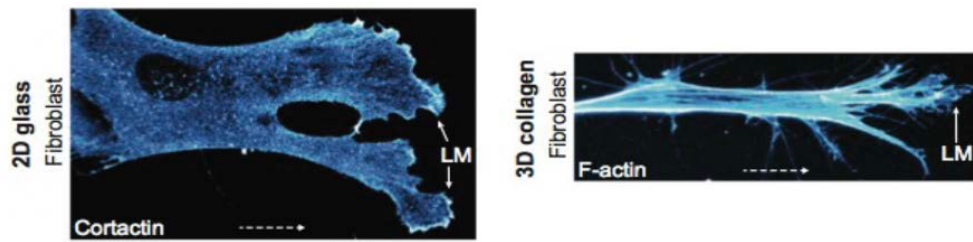


Figure 35. Front of migrating fibroblasts in 2D and 3D environments, stained for cortactin and F-actin. LM: lamellipodia. From (Lodish et al., 2008).

The mesenchymal mode of migration can be described as the succession of four main steps (Figure 36) (Mattila and Lappalainen, 2008):

- 1) Cells extend protrusions at the front: lamellipodia, allowing for random space exploration or filopodia, driving directed migration.
- 2) Focal adhesions form at the tip of protrusions.
- 3) The membrane anchors via formation of focal adhesions on the substrate, allowing cell traction to the front.
- 4) Retraction fibres at the rear of the cell, mediated by myosin activity, allow for detachment of the cell body and forward movement.

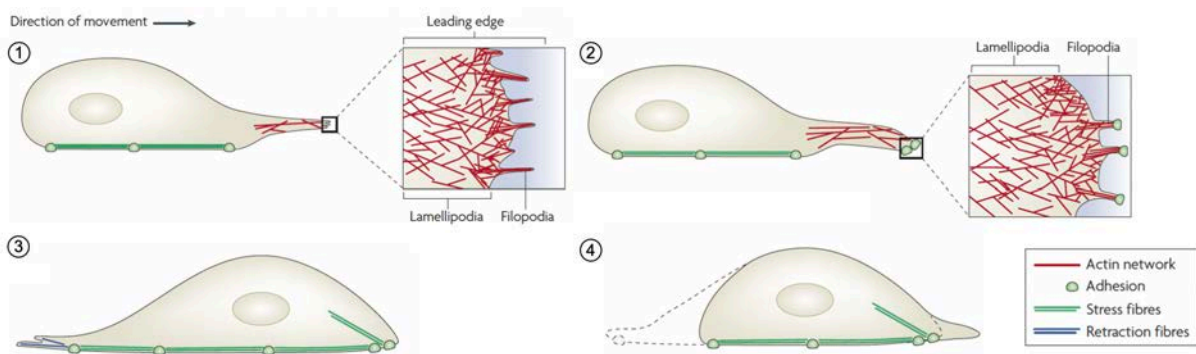


Figure 36. Steps of single cell mesenchymal migration.

- (1) Extension of membrane protrusions at the front. (2) Focal adhesion formation. (3) Membrane anchoring on the substrate. (4) Retraction of the rear. Adapted from (Mattila and Lappalainen, 2008).

In order to move forward in complex environments, cells also produce proteases that cleave fibrillar structures like collagen webs. This creates space and matrix tracks that guide cell migration. In addition, this cleavage forms active epitopes stimulating cell adhesion and migration. The main families known to date are matrix metalloproteinases (MMPs) and cathepsins (Kawauchi, 2012). This is also allowed by the presence of the MTOC before the nucleus, allowing delivery of proteases at the front of the cell. In addition, Welf and colleagues discovered recently that cells can also create space thanks to branched actin-mediated blebs. These blebs exert constant worrying on the ECM, that creates breakage and internalisation via macropinocytosis to create space, in a PI3K-dependent fashion (Welf et al., 2020).

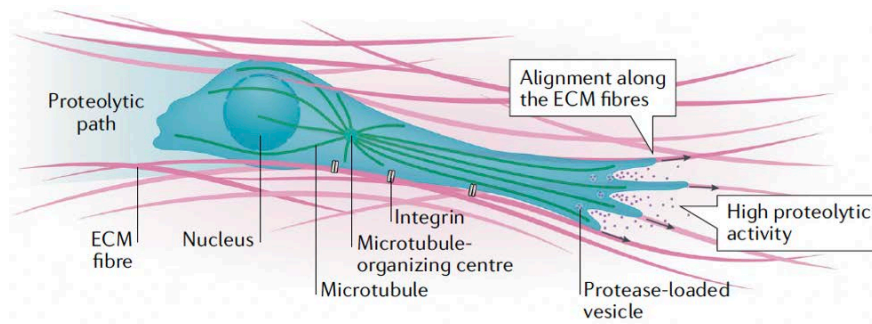


Figure 37. Scheme depicting cell mesenchymal mode of migration. Front protrusions extend at the leading edge, and polarisation of the centrosome before the nucleus allows delivery of proteases at the front of the cell to remodel ECM. From (Yamada and Sixt, 2019).

2.2.1.2. FOCAL ADHESION FORMATION AND FORCE TRANSMISSION

In this mode of migration, formation of long-lived focal adhesions drives force transmission from actin to the substrate. Focal adhesions are molecular complexes composed of transmembrane proteins, bound to the extracellular matrix and to cytoplasmic proteins that drive downstream signalling pathways. The main family of these transmembrane proteins is integrins (ITG).

Role of integrins in focal adhesion formation

Integrins are composed of two subunits, α (18 types) and β (8 types), that are known to make 24 combinations with different affinity to ECM proteins (**Figure 38**) (Kawauchi, 2012). The binding of a ligand to integrins changes their conformation and activates the clustering of other focal adhesion components, like Rac, Cdc42, PI3K, Ras, FAK, Src, paxillin or talin that contributes to further clustering of integrins and formation of adhesions. Therefore, downstream signalling is also enhanced, in particular small Rho GTPases activity, leading to regulation of cytoskeleton dynamics and cell polarisation. In addition, interactions of the intracellular domain with cytoplasmic components, via talin for example, can modulate integrin affinity at the extracellular domain (Rap1 GTPase, Raf-1 kinase, PKC) or modify the signalling potential (posttranslational modifications) (Ridley et al., 2003).

Integrin subunits		Major Ligands	Integrin subunits		Major Ligands
$\alpha 1$	$\beta 1$	Collagen, Laminin	$\alpha 11$	$\beta 1$	Collagen
$\alpha 2$	$\beta 1$	Collagen, Laminin, Tenascin,	$\alpha 1b$	$\beta 3$	Fibronectin, Vitronectin, Fibrinogen
$\alpha 3$	$\beta 1$	Laminin, Collagen	αv	$\beta 1$	Vitronectin, Fibronectin
$\alpha 4$	$\beta 1$	Fibronectin, VCAM-1	$\beta 3$	$\beta 3$	Vitronectin, Fibronectin, Fibrinogen
	$\beta 7$	MAdCAM-1, Fibronectin	$\beta 5$	$\beta 5$	Vitronectin
$\alpha 5$	$\beta 1$	Fibronectin	$\beta 6$	$\beta 6$	Fibronectin, Tenascin
$\alpha 6$	$\beta 1$	Laminin		$\beta 8$	Vitronectin
	$\beta 4$	Laminin	αL	$\beta 2$	ICAM-1, -2, -3
$\alpha 7$	$\beta 1$	Laminin	αM	$\beta 2$	Fibrinogen, iC3b
$\alpha 8$	$\beta 1$	Fibronectin, Tenascin	αX	$\beta 2$	Fibrinogen, iC3b
$\alpha 9$	$\beta 1$	Tenascin	αD	$\beta 2$	ICAM-3, VCAM-1
$\alpha 10$	$\beta 1$	Collagen	αE	$\beta 7$	E-cadherin

Figure 38. Integrin α and β dimers can form 24 combinations with different specificities to ECM components. From (Kawauchi, 2012).

Integrin expression is often deregulated in neoplastic cells, either up or down, endowing them with more metastatic potential (Hood and Cheresch, 2002). For example, melanoma cells display more integrins $\alpha\beta 3$ at the invasive front and $\alpha 6\beta 4$ laminin-binding integrins are overexpressed in several carcinomas such as

invasive thyroid carcinoma and in migratory regions of papillomas. The affinity of integrins for their ligands can also be increased in neoplasms to lead to a more migratory phenotype. All in all, integrin expression and properties appear to be adapted in cancer cells to confer them more invasiveness (Mizejewski, 1999).

Focal adhesion maturation and traction force generation by molecular clutch

From their initiation, focal adhesions (FAs) will evolve to form mature adhesions of increasing size and resisting increasing tension: nascent adhesions, focal complex, focal adhesion and fibrillar adhesion (**Figure 39**). The latter do not promote cell migration but allow ECM remodelling (Gardel et al., 2010). During FA maturation, the composition of the molecular complex evolves: tensin and paxillin are present early, in nascent adhesions, while vinculin, zyxin and α -actinin are recruited upon FA maturation (Webb et al., 2002).

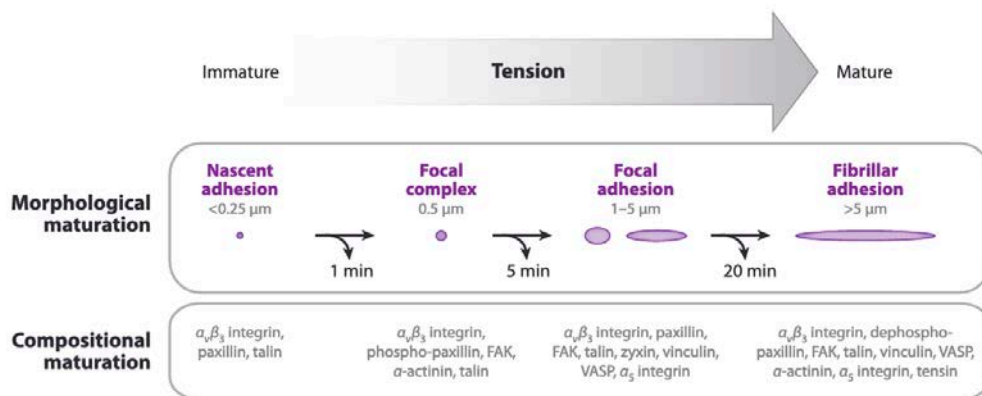


Figure 39. The maturation of focal adhesions allows cells to undergo increasing tension forces. From nascent adhesions to fibrillar adhesions, the composition of the molecular complex evolves. From (Gardel et al., 2010).

At the focal adhesion site, tension is also increased by actin polymerisation, with FA allowing for its force transmission to the substrate.

Indeed, there is an interplay between focal adhesion formation and actin filaments elongation, that has been dissected in *in vitro* systems with purified proteins (Ciobanasu et al., 2014): integrin attachment to ECM promotes actin filaments polymerisation (**Figure 40a**) and stabilisation of actin-based protrusions (Romero et al., 2020). Actin filaments are then bound to the focal adhesion complex by proteins like vinculin: it allows for a coupling between elongation-induced actin retrograde movements and the substrate through the focal adhesion acting as a “molecular clutch”, resulting in traction force generation and migration (**Figure 40b**) (Case and Waterman, 2015). It also slows actin retrograde flows by dissipation. The amplitude of the force transmitted to adhesions depends on the interaction between myosin II and actin filaments that are attached to the adhesion (Ridley et al., 2003).

In addition, between focal adhesions, actin fibres form bundles of mixed polarity, called stress fibres. They connect the cytoskeleton to the ECM and exert tension on FAs in a myosin-dependent manner, through crosslinking of actin fibres and myosin II motor by α -actinin and Ena/VASP (Stevenson et al., 2012).

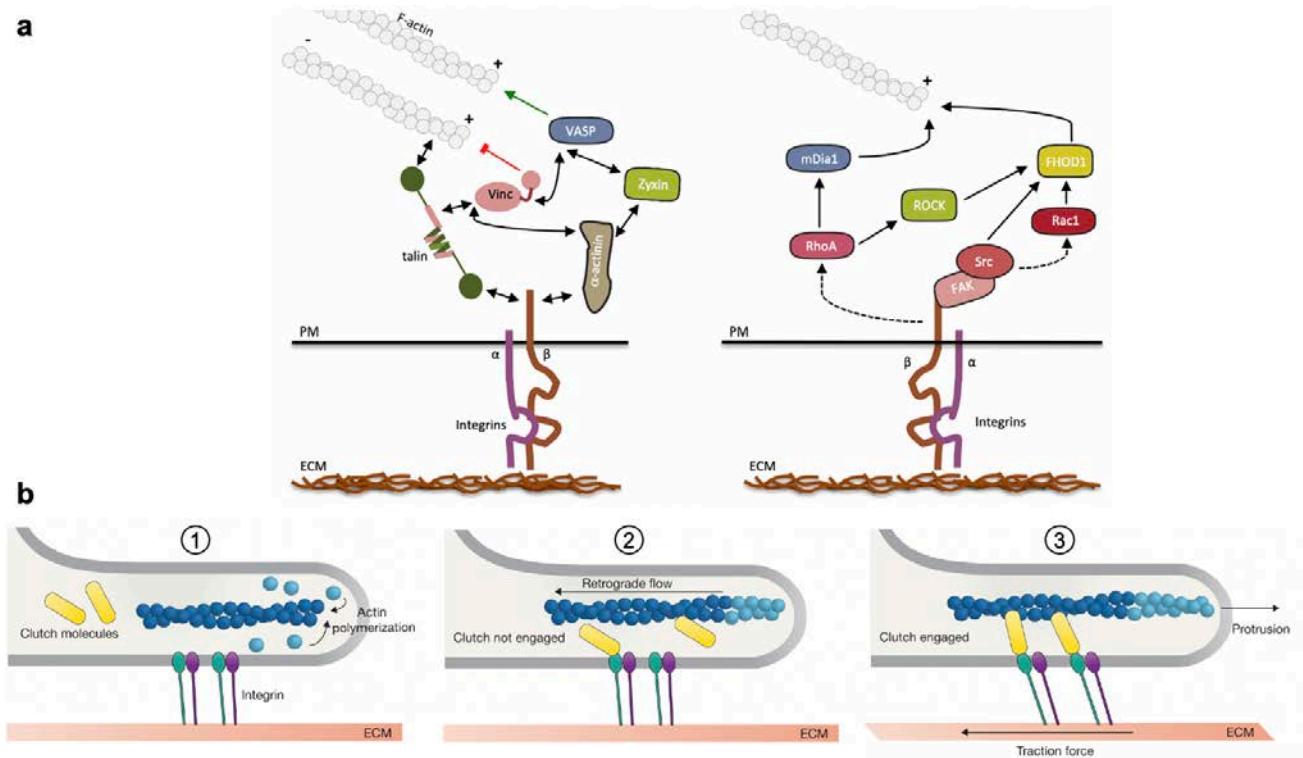


Figure 40. Actin filament elongation and force transmission.

a, Linear elongation of actin filaments is promoted at focal adhesion sites, through VASP (left) or mDiaA and FHOD1 formins (right). PM: plasma membrane. + and – indicate barbed end and pointed end of actin filaments respectively. From (Romero et al., 2020). **b**, Molecular clutch hypothesis. (1) Incorporation of new actin monomers (light blue) to F-actin filaments (dark blue) at the edge of the lamellipodium. (2) When the molecular clutch is not yet engaged, actin polymerisation drives fast retrograde flow and no membrane extension. (3) Once the molecular clutch is engaged, polymerisation forces are transmitted to the substrate, resulting in traction forces, membrane extension, and slowing retrograde flow. From (Case and Waterman, 2015).

Focal adhesion turnover and forward movement

To allow for retraction of the cell body and forward movement, focal adhesions are disassembled at the cell rear. This detachment is mainly mediated by myosin II, and is modulated by FAK, Src, ERK and intracellular calcium. It also results in recycling of FA components.

The balance between FA attachment and disassembly in cell migration leads to a bell curve on 2D substrates, describing the relationship between cell speed and cell-substrate attachment (or ECM ligand concentration) (**Figure 41**) (Gupton and Waterman-Storer, 2006). Indeed, cells need enough attachment to produce efficient traction forces, but too much anchoring to the substrate prevents body retraction, sticks the cells and stops migration. Nevertheless, as precise studies of cell migration in 3D environments are only at their early stage, it remains to be determined whether the same mechanisms are at play in 3D conditions (Yamada and Sixt, 2019).

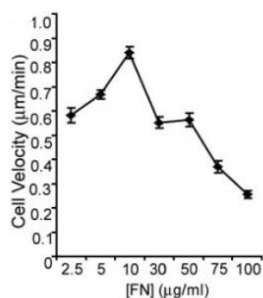


Figure 41. The velocity of PtK1 epithelial cells (from rat kangaroo kidney) displays an optimum velocity at intermediate concentration of fibronectin (FN)
FN concentration is correlated with adhesion strength. From (Gupton and Waterman-Storer, 2006).

2.2.2. Adhesion-traction in collective cell migration

Collective cell migration occurs when cells maintain cell-cell adhesions over time and migrate in a coordinated fashion. This mode of migration is thus even more complex than single cell migration: in 2011, it was even proposed as one of the ten prominent lingering mysteries of cell biology and keeps lots of secrets from us until today (Travis, 2011).

As presented in the first part, collective migration is particularly important in embryonic development and in cancer dissemination, and it is the subject of more and more investigations. It shares common features with single cells migrating in a mesenchymal fashion, including traction force generation and adhesion to the substrate (Friedl et al., 2012). In addition, the organisation of the cell cohort plays an important role in polarisation, force generation and force transmission, and can differ depending on cell types.

2.2.2.1. DEFINITION AND SUBTYPES OF COLLECTIVE CELL MIGRATION

Definition of collective cell migration features

Collective cell migration describes the migration of a group of cells, moving as a whole in a directed fashion while maintaining cell-cell adhesions (Friedl et al., 2012). Shellard and Mayor provided recently a nice comprehensive definition of collective migration and related modes of migration (Shellard and Mayor, 2019). They distinguish collective migration, cooperative migration, coordinated migration and supracellular migration:

Cells move *cooperatively* when their interactions influence their behaviours. Contact inhibition of locomotion (CIL) is a well-known example of how short contacts can drive cell reorientation, and cell dispersion. Davis and colleagues described this process for *Drosophila* haemocytes, dispersing during development through CIL (Davis et al., 2015): when two cells get in contact, an intercellular actin clutch engages and stress fibres form, parallel between the two cells, with coordinated actin flows. Then, the lamellipodia recoil and clutch disengages, for cell separation in opposite directions.

They are *coordinated* when they move in the same direction. This happens in multicellular streaming, where cells migrate towards an external cue, which can be chemotactic and drives polarisation of each individual cell. All cells then migrate in the same direction but with no necessary dependence on cell-cell contacts. However, multicellular streaming does not exclude cell-cell paracrine signalling, as highlighted in Dicty migration (Kriebel et al., 2003). A such mode of migration has been observed in cancer as well, for example *in vivo* in a breast carcinoma mouse model displaying no cell-cell junctions during coordinated cell

migration (Roussos et al., 2011). The authors report that this mode of migration, which resembles more single cell migration, is 10-100 faster than collective cell migration.

Collective cell migration then occurs when at least two cells migrate in a coordinated and cooperative fashion. This intercellular coupling is generally mediated by cell-cell adhesions, strong in epithelial sheets and looser in mesenchymal sheets. Interestingly, multicellular streaming and CIL also fuel collective migration of neural crest cells from *Xenopus* or chick embryos (Theveneau and Mayor, 2012). In addition, when cell cohorts display features comparable to that of a single big cell, this is called *supracellular* migration. In this case, the movement is better explained at a scale larger than that of the single cell: for example in *Xenopus* CNCC migration, the entire cluster is polarised with protrusive activity at the front, contractility at the rear, and supracellular organisation of the contractile actomyosin cortex (Shellard and Mayor, 2019).

Morphology of collective cell migration

Like single cells that display various shapes during migration, there is a broad repertoire of morphologies characterising collective cell migration *in vivo* (Friedl and Alexander, 2011; Friedl et al., 2012).

Cell sheets are observed during wound healing, where the leading edge is wide and protrusive, and pulls the rest of the monolayer.

In cancer invasion, cells can sprout collectively from the primary tumour in the form of elongated strands of only one or two cells in diameter, or as broad cohorts, with a thickness of several cells, where cells in the middle would not even be in contact with the extracellular matrix. Such invasive structures sometimes keep very a differentiated luminal architecture, as described on histopathologies of several invasive carcinomas (Christiansen and Rajasekaran, 2006).

Cells can also migrate as smaller groups of tens of cells, as exemplified by *Drosophila* border cell migration and observed when cancer cells detach from the primary tumour (Bronsert et al., 2014; Friedl et al., 1995).

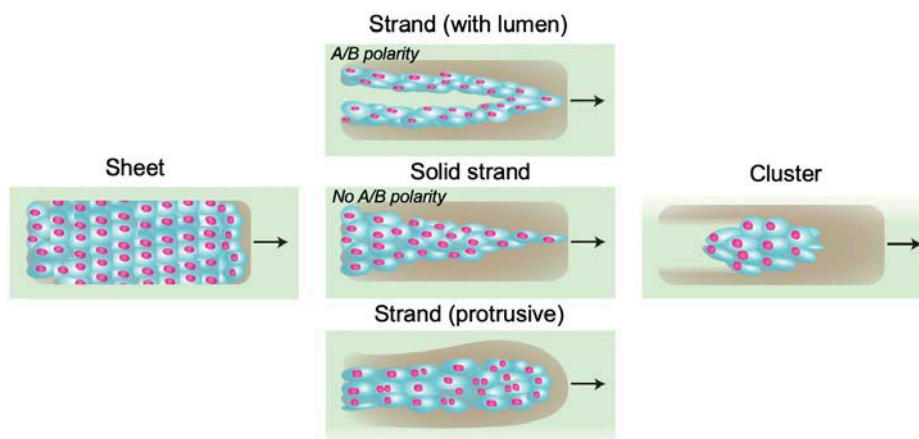


Figure 42. Morphology of collective cell migration.

Cells can invade as wide sheets, strands or detached cell clusters. Modified from (Friedl and Alexander, 2011; Friedl et al., 2012).

2.2.2.2. FORCE GENERATION THROUGH FRONT-REAR ORGANISATION OF THE CELL COHORT

Collective cell migration shares important similarities with single cell mesenchymal migration (Figure 43). Indeed, cell groups often display an elongated branched actin-mediated protrusive morphology at the leading edge, and higher contractility at the rear. As a consequence, the organisation of cell groups is often described at the cluster scale with classification of the cohort between two different groups of cells: the "leaders" and the "followers", endowed with different roles promoting force transmission and directionality

(Mayor and Etienne-Manneville, 2016). This description is particularly relevant for cell groups organised in a “supracellular” fashion and does not fit every type of collective migration.

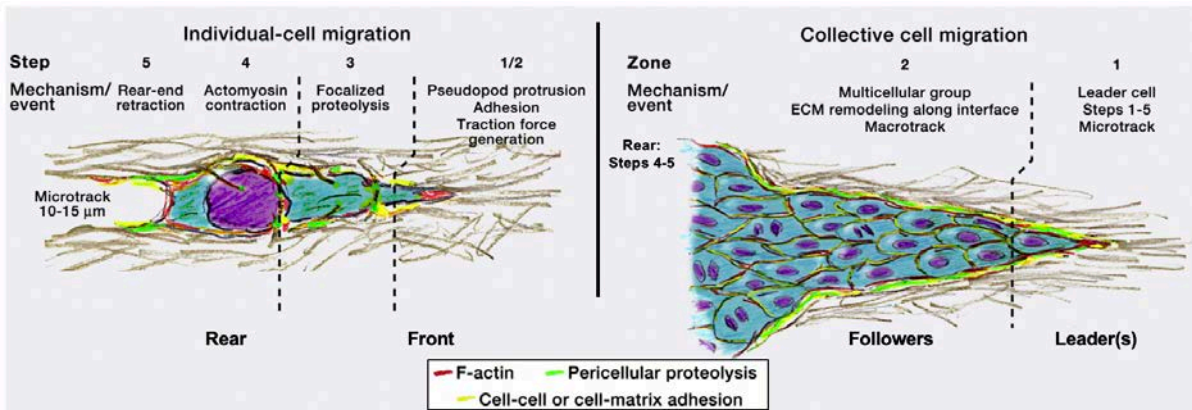


Figure 43. Common features between collective cell migration and single cell mesenchymal migration. Both display a protrusive leading edge, proteolysis and track formation, rear contractility (for “finite” cell groups). Groups can be divided into 2 zones with distinct roles: 1 for leaders, and 2 for followers. Modified from (Friedl and Alexander, 2011).

Like single cell mesenchymal migration, cell cohorts then move forward thanks to traction forces exerted on the substrate by protrusive tip cells. Measurements of these forces in monolayers highlighted even higher traction forces at the leading edge of epithelial sheets than at the front of single cells, which could be enabled by collectiveness (Roure et al., 2005).

Force transmission is then ensured by the regulation of cell-cell junctions and actomyosin dynamics. They also exert proteolytic activity, at a higher level than single cells given the size of the groups.

Leaders, followers, steering cells: characteristics and specification

Conventional definition of leader cells and followers and specification of each type

Leaders and followers can be first distinguished following their localisation and morphology: the leader are protrusive cells at the front of the cohorts, while the followers retain a more standard shape in the bulk (Friedl et al., 1995; Krndija et al., 2019).

The specific skills of leader cells are very similar to the leading edge of single cells: they form filopodia and/or lamellipodia, pull on the ECM through focal adhesion, retract their body thanks to actomyosin contractility, and create a path by remodelling the ECM (Khalil and Friedl, 2010). They can also display higher levels of $\beta 1$ integrin expression, as observed in primary melanoma explants invading in 3D collagen gels (Hegerfeldt et al., 2002). This can be mediated by Rac1 signalling, and concomitant with upregulation of PI3K (Yamaguchi et al., 2015). It results in upregulation of actin polymerisation at the front, as reported in border cell migration, hence providing a strong directionality (Wang et al., 2010).

These invasive features can be gained by undergoing a “partial-EMT” (Friedl et al., 2012). However, EMT-independent processes also happen: for example, the expression of podoplanin, a small mucin-like protein, is upregulated at the front of invasive carcinoma and promotes collective cell migration without induction of EMT in leader cells, through downregulation of RhoA promoting filopodia formation (Wicki et al., 2006).

Followers are bound to each other and to leader cells through cell-cell junctions. They follow the tracks created by leaders and produce proteases to create a path as well. In cell clusters behaving in a supracellular manner, they are bound to leader cells through an actomyosin cable, that can fully surround

clusters, providing force transmission between cells in addition to cell-cell junctions. In *Drosophila* border cell clusters, the actin cable can also prevent non-leader cells from forming protrusions, discriminating a unique directional cue for efficient directed migration (Mishra et al., 2019; Wang et al., 2020).

“Leader” and “follower” specifications differ between cell types and configurations. Genomic profiling of leader versus follower cells in lung cancer explants revealed distinct fates as they displayed different RNA profiles (Konen et al., 2017). Specific genetic profiles have also been described for breast cancer cells, with leader cells only expressing p53 and K14 (keratin 14) (Cheung et al., 2013).

On the contrary, they are not cell-specific when leader identity is induced by a chemotactic gradient such as VEGF-mediated leader induction in mouse retina angiogenesis (Gerhardt et al., 2003). Leader and followers can even exchange positions during migration in some systems. Indeed, observed in cancer cell migration, leaders and followers can be energetically regulated by glucose uptake, leading to leader and follower exchanges during the course of their migration (Zhang et al., 2019). This is in accordance with a higher energetic demand of leaders, polymerising actin and forming stress fibres in an ATP-dependent manner. Similarly, while leaders and followers are predetermined in trunk neural crest cells, no persistent leaders are present among cranial neural crest cells of chick and *Xenopus* (Richardson et al., 2016).

Front, back and steering cells: towards a more relevant classification

Some biological models of detached cell cohorts questioned the definition of “leaders” and “followers” as presented above, in particular zebrafish posterior lateral line primordium (PLL), for which cells at the rear play an important role in directionality by generating a chemotactic gradient (section 1.1.1.3.) (Dalle Nogare et al., 2014).

This led Theveneau and Linker to propose another interesting terminology, with “front cells” and “rear cells” defined on their localisation only, and “steering cells” determining directionality of the group, whatever their position (**Figure 44**) (Theveneau and Linker, 2017). Indeed, even if the cells that give directionality are often located at the front of the group, it may not always be the case in principle, as exemplified by zebrafish PLLP.

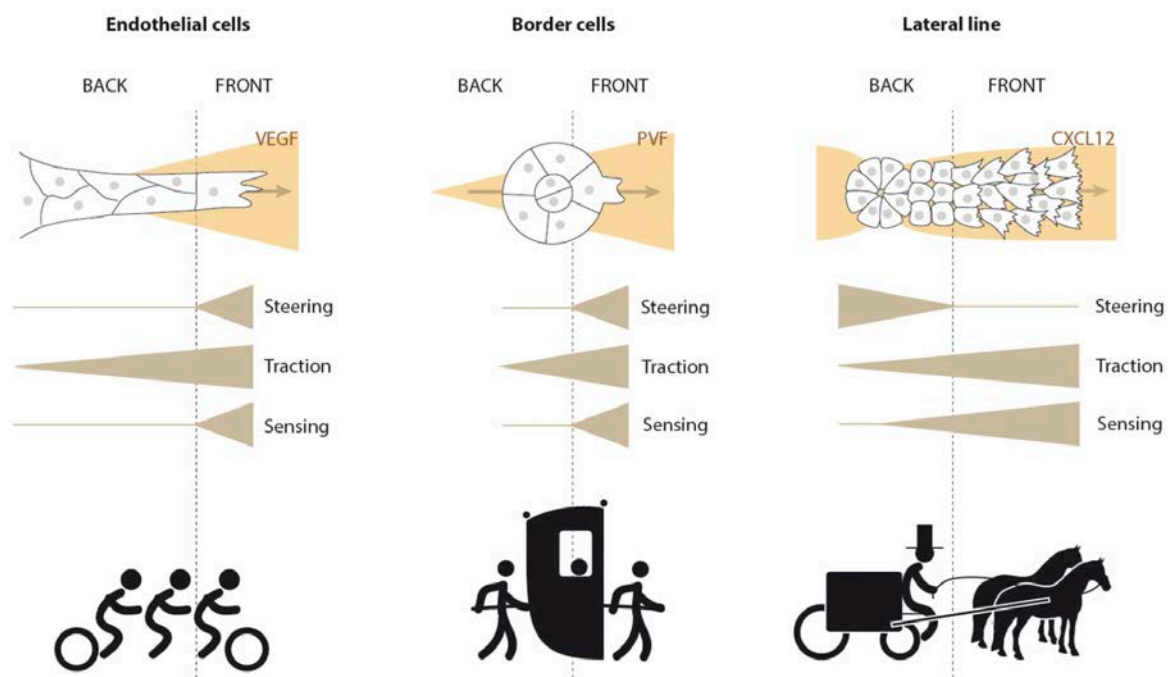


Figure 44. Position of steering cells during collective cell migration in three representative models. From (Theveneau and Linker, 2017).

Other modes of migration further question the leader-follower model, highlighting the diversity of organisation in cell cohorts. For example, when lacking a free front edge because of a confined space for example, collective migration sometimes does not display leader cells with a specific morphology. Polarisation can then be acquired continuously in the cell sheet at the single cell level: each cell displays protrusions in the follicle cells sheet that makes *Drosophila* egg chamber rotate (**Figure 45**) and in MDCK cells migrating as “trains” in circular micropatterns (Jain et al., 2020; Uechi and Kuranaga, 2018). These actin-based “cryptic” protrusions have been observed only quite recently in epithelial cell sheets, probably because they extend below the front rows, and suggest an active participation of the bulk cells in driving collective epithelial migration and long-range signal transmission (Jain et al., 2021).

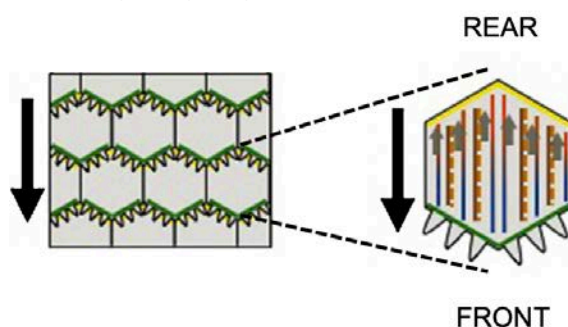


Figure 45. Polarisation at the single cell level during epithelial collective migration of *Drosophila* follicle cells.

The magnified view (right) of a single cell also displays the retrograde myosin flows (grey arrow). Adapted from (Uechi and Kuranaga, 2018). Black arrows: direction of migration.

Self-generated directional cues reinforce collective cell migration

In addition to being responsive to external gradients, the cellular group can generate by itself directional cues thanks to the front-rear organisation of the cell cohort. This specific feature of cell cohorts initiates and/or sustains collective migration over time.

First, like single cells, front-rear polarisation generally provides an intrinsic directional and sustained cue, with actin polymerisation at the front and rear contractility, combined with similar feedback loops as in single cells. In addition, some systems like endothelial cells, can generate single cell polarisation in the whole cell sheet upon leader orientation, thanks to asymmetric cell-cell junctions: at their rear, leader cells extend what the authors call “cadherin fingers”, that are engulfed by a contractility-low lamellipodium-like area at the front of follower cells, and will be reproduced by the following cell rows, driving an internal directional cue (Hayer et al., 2016).

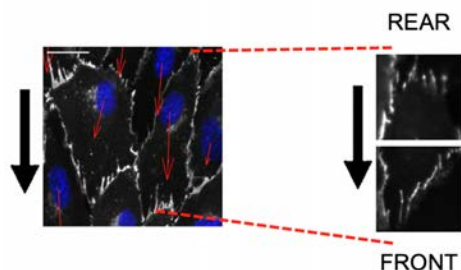


Figure 46. Cadherin fingers in a migrating HUVEC endothelial cell sheet.

Red arrows: individual cell migration. Blue: nuclei (Hoechst); white: E-cadherin junctions (CDH5). Black arrows: direction of migration. Magnification (right) shows a cell expressing cell-cell junction (CDH5) staining and surrounded by cells that do not express the fluorescent probe: this highlights the protrusions formed at the rear of the cell and invaginations at the front. Adapted from (Hayer et al., 2016).

Cell-cell junctions could also translate a mechanical asymmetry into a guidance cue through a gradient of cellular tension. This is supposed to be at the origin of the mesendoderm prechordal plate migration, for which no extracellular cue has been identified to date. Indeed, tension exerted specifically on one side of single *Xenopus* mesendoderm cells through cadherins was able to induce cell polarisation (Weber et al., 2012). This mechanism, called “cohesotaxis” by the authors, if extended to cell cohorts, could be at play in collective migration of the axial mesendoderm prechordal plate, the gradient of tension rising from the asymmetry between a free edge and attachment to the mesoderm on the opposite side (Dumortier et al., 2012; Theveneau and David, 2014). This would explain the polarisation at the single cell level of prechordal plate cells and the loss of directionality in isolated cells, observed in zebrafish embryos (Dumortier et al., 2012).

In addition, large cell groups can generate by themselves external cues. The zebrafish posterior lateral line primordium (PLL) provides an interesting example of self-generated chemotaxis: the homogeneous concentration of the surrounding chemokine CXCL12 is converted into a gradient by CXCR7 receptor-mediated degradation at the rear of the group (**Figure 47a**) (Dalle Nogare et al., 2014).

Recently, neural crest cells were found to be able to generate a local gradient of stiffness *in vivo* through N-cadherin interactions with the underlying placodes (**Figure 47b**) (Shellard and Mayor, 2021a). This stiffness gradient promotes directionality through cell cluster durotaxis.

Cells can also induce asymmetrical matrix organisation, such as cancer cell from squamous carcinoma (A431 cell line) with no apparent canonical polarity, generating collagen gradients (denser at the rear). The viscoelastic relaxation of collagen networks then leads to migration (Clark et al., 2020). This is also an interesting example of rear cells endowed with a steering role.

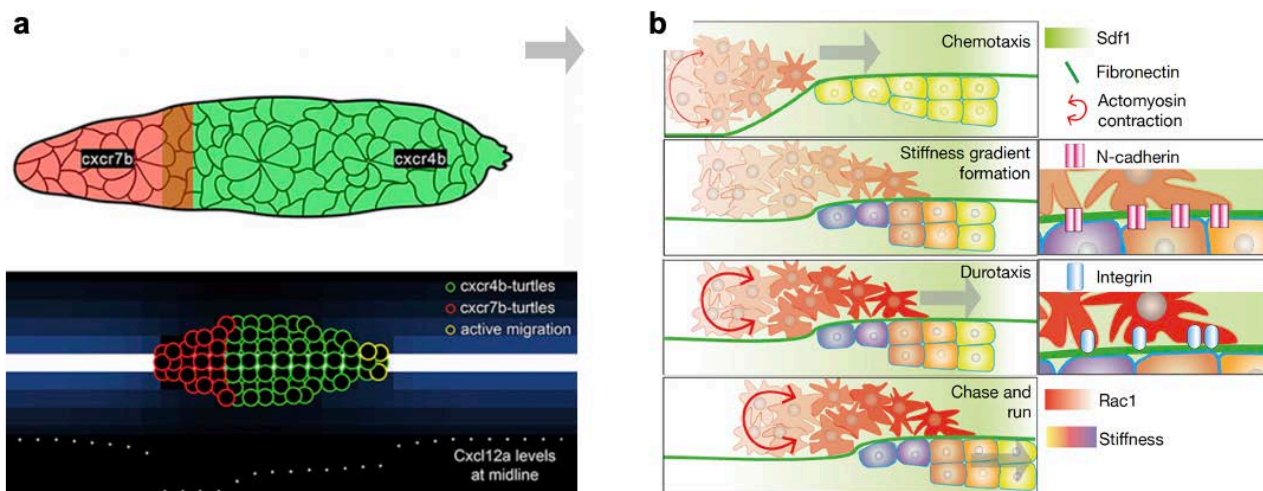


Figure 47. Self-generation of directional cues during collective cell migration.

a, Top: expression domains of *Cxcr7b* and *Cxcr4b*. Bottom: computational modelling of self-generated gradient of CXCL12A inducing cell migration. Grey arrow: direction of migration. Adapted from (Dalle Nogare et al., 2014). **b**, Model of self-generated stiffness gradient by neural crest cells (red) on placodes (purple to yellow = stiff to soft). From (Shellard and Mayor, 2021a).

Interestingly, these self-generated directional cues are a specificity of collective migration, and in certain circumstances, it favours collective migration compared to single cell migration. Indeed, Clark and colleagues pointed out that single cells can produce asymmetric network deformation as well in collagen gels, but they are only short range and lead to lower migration persistence (Clark et al., 2020). The long scale sensitivity to durotaxis has also been mentioned in section 2.1.1.2. with the work of Sunyer and

colleagues, who proved that breast cancer cells could only sense durotaxis at the collective scale, because it requires intercellular force transmission to capture shallow gradients along the length of the cluster (Sunyer et al., 2016).

Cell flows sustaining collective cell migration

Another specificity of collective cell migration is the appearance of cell flows. They might not happen when leader cells are specified and not exchangeable, but as soon as cells can change position, internal forces and external cues can drive persistent cell flows.

Cell treadmilling has been observed to foster neural crest cells collective migrating on adhesive substrates (Shellard et al., 2018). A such cell flow had already been observed during mammalian hair follicles polarisation, during primitive streak development and invagination of the ventral furrow of *Drosophila* (Shellard and Mayor, 2019). Neural crest cells are organised supracellularly and actomyosin contractility at the rear induces cell invagination inside the cluster hence generating a treadmilling of cells. This drives forward movement of the inner cells and of the cohort (Figure 48). Indeed, more contractile cells will spontaneously get invaginated inside cell clusters, as was pointed out by Maître and colleagues in embryos with a mix of more and less contractile cells (Maître et al., 2016).

Rotational movements resulting from collective motility have been often observed as well during morphogenetic processes (**Figure 48**). *Drosophila* egg chamber rotates under collective migration of follicle cells (Uechi and Kuranaga, 2018) and breast cancer cells are known to rotate before cyst formation, while assembling laminin (Wang et al., 2013). Dictie prespore and prestalk cells also rotate due to a competition between chemotaxis and cell-cell junction engagement (Fujimori et al., 2019). Upon KRAS activation, a well-known oncogene, MDCK cells rotate as clusters or cysts (Hirata et al., 2018).

The rise of coordinated movements in epithelial monolayers has been deciphered recently by the Ladoux lab, investigating spontaneous collective rotational motion of epithelial cells (MDCK) on closed micropatterns of different shapes (Jain et al., 2020). They highlighted the role of polarisation at the single cell level and intercellular junction-mediated signal transmission: cryptic lamellipodia at the leading edge of cells drive Rac1-mediated polarisation of the whole monolayer, thanks to establishment of adherens junctions and force dipoles at the single cell level. Individual cell polarisation is then sufficient to maintain this coordinated motion and cell-cell junctions become dispensable.

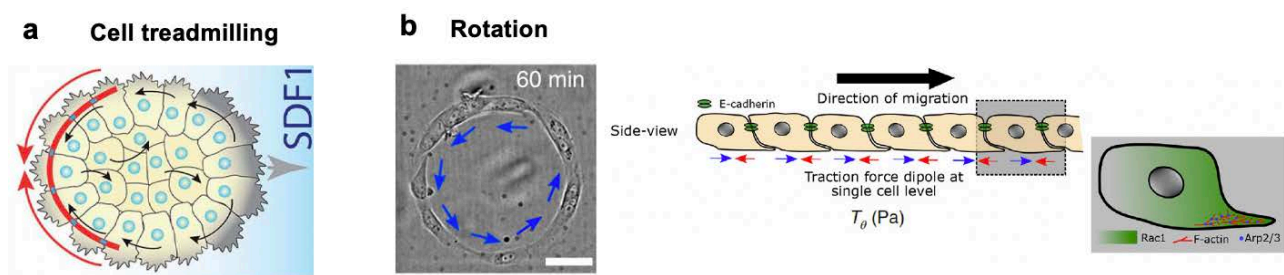


Figure 48. Cell flows sustaining collective cell migration.

a, Cranial neural crest cells migrate collectively in an SDF1 gradient, while high contractile activity at the rear induces cell treadmilling. From (Shellard et al., 2018). **b**, MDCK cells constrained on circular micropatterns display a collective rotational motion. Coordinated motion rises from single cell polarisation with actin-based lamellipodia, and adherens junctions establishment. From (Jain et al., 2020, 2021).

Role of cell-cell adhesions and actomyosin contractility in collective migration

Cell-cell junctions and actomyosin contractility play an important role to ensure cohesiveness, coordination, and force transmission in cell cohorts. In cell sheets, the high traction forces exerted mainly by leader cells induce increasing tension in the following cell rows, as observed in gut epithelial cells and border cells migration (Krndija et al., 2019; Trepap et al., 2009). This is often called the “tug-of-war” mechanism (**Figure 49**). There, E-cadherin cell-cell junctions maintain cohesiveness and allow for mechanical coupling and force transmission to followers, up to a long-range scale as exemplified above in MDCK trains (Jain et al., 2020). Epithelial cell-cell junctions can also be retained in invasive carcinoma (Friedl and Gilmour, 2009; Friedl and Mayor, 2017), and their expression at the front of tumours promotes endometrial cancer collective invasion (Kojima et al., 2021). Unique types of cell-cell contacts can provide an additional directional cue, such as cadherin fingers of endothelial cells (Hayer et al., 2016).

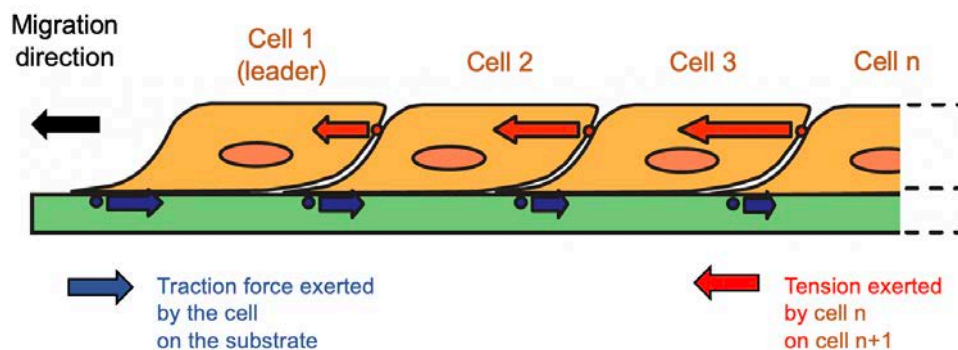


Figure 49. Tug-of-war model.

Cells at the front exert high traction forces on the substrate, that are transmitted through tension forces to the followers. Modified from (Trepap et al., 2009)

In addition, in supracellular types of migration, an actomyosin belt may surround cell clusters, such as in *Xenopus* neural crest cell clusters or *Drosophila* border cells. Actomyosin contractility is fundamental in collective cell migration to transmit forces at a supracellular scale, and allows for sensing gradients of stiffness (Sunyer et al., 2016). In *Xenopus* neural crest cells, this cortex is polarised following SDF1 chemotactic gradient and participates actively in the guidance of cell migration through generation of cell flows. Interestingly, artificial activation of contractility at the rear of these groups or relaxation at the front is enough to induce collective migration even in absence of a chemical gradient (Shellard et al., 2018). In border cells, the actomyosin cortex has been shown to prevent the formation of other “leader” cells, to protect directionality (Mishra et al., 2019; Wang et al., 2020).

There is an interplay between cell-cell junctions and actomyosin contractility. Indeed, Kriegman and colleagues observed that the clustering of *Xenopus* cardiac progenitor cells lead to the appearance of spontaneous contraction waves (Kriegman et al., 2020), highlighting that the formation of cell-cell contacts leads to strong molecular and supracellular changes. This interplay also preserves cohesion of the cell clusters. In *Drosophila* border cell migration, cell-cell contacts are maintained by E-cadherin adherens junctions, under the control of Rap1 (Montell et al., 2012; Sawant et al., 2018). They ensure polarisation and directionality during chemotaxis (Cai et al., 2014). In addition, protein phosphatase 1 (Pp1) controls the level of cadherin and catenin at cell-cell junctions and actomyosin contractility at the periphery, leading to low levels of actomyosin contractility at cell-cell contacts: loss of Pp1 leads to cluster dissociation (Chen et al., 2020). Similarly, collective cell migration of cancer cells needs suppression of actomyosin at cell-cell contacts, which is allowed by DDR1, Par3 and Par6 (Hidalgo-Carcedo et al., 2011).

2.2.3. Propulsion-friction in amoeboid single cells

In contrast with single cell mesenchymal migration and collective migration that rely on strong and specific adhesion to the substrate, amoebas gave their name to the second main mode of single cell migration, called “amoeboid”. This mode of migration is focal-adhesion independent, is associated with rapid and wide deformations of cell shapes and relies on friction forces rather than traction forces (Paluch et al., 2016).

Amoeboid mode of migration is displayed by immune cells, which display low adhesion, high deformability, and are very fast. It was first highlighted by looking at them *in vitro* (Repo et al., 1978) and then observed *in vivo* after diaporesis (Lam and Huttenlocher, 2013). In 1990, the Condeelis lab was able to associate this mode of migration with cancer invasion (Condeelis, 1990), and it was confirmed *in vivo* in melanoma (Xue et al., 2006).

An unequivocal evidence that focal adhesion-independent cell migration can happen has been provided by Lämmermann and colleagues who studied dendritic cell migration in mice after integrin or talin knockout (Lämmermann et al., 2008). This focal adhesion-independent mode of migration was eventually found surprisingly even faster than the mesenchymal focal adhesion-mediated mode of migration, with average speeds around 1-10 $\mu\text{m}/\text{min}$ (Liu et al., 2015).

Interestingly, on an evolutionary perspective and based on phylogenetic studies, it is likely that actin-based adhesion-independent mode of migration, in its pseudopodal form, have preceded focal adhesion-dependent migration (Fritz-Laylin et al., 2017a).

2.2.3.1. AMOEBOID MIGRATION IS ASSOCIATED WITH LOW ATTACHMENT AND HIGH DEFORMABILITY

As they do not form focal adhesion on their substrate, cells migrating in an amoeboid fashion do not spread. They rather display a rounded phenotype, with “dewetted” low contact angles with the substrate (**Figure 50**). The protrusions they form (blebs, pseudopodia) are produced by contractility of their cortex, cytoplasmic pressure, or actin branching, but do not attach through specific adhesion. In addition, cells migrating in an amoeboid fashion often lack matrix proteolysis (Wolf et al., 2003a). Instead, they are highly deformable and can squeeze rapidly through pores.

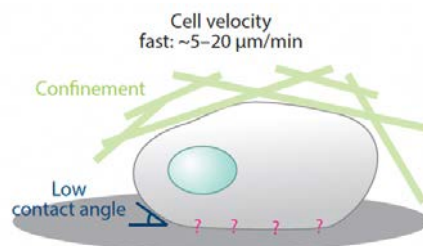


Figure 50. Main characteristics of amoeboid mode of migration

Single cells migrating in an amoeboid mode display low contact angles, cell deformation, fast velocity and non-specific interactions with the substrate. From (Paluch et al., 2016).

The fastness of amoeboid mode of migration is thought to be allowed by the independence from focal adhesions, that take time to form and disassemble. Instead, cell-substrate interactions are very transient. This also implies the need for a 3D confinement to counteract cell detachment and Brownian motion, hence the development of confining microchannels, often made of PDMS or PAA, to study this mode of migration (Bergert et al., 2015; Lämmermann et al., 2008). However, although amoeboid migration has been shown to need a 3D confinement, Dicty seems to be able to move on 2D substrates without specific adhesion molecules: the underlying mechanism is thought to rely on van der Waals interactions but remains to be uncovered (Loomis et al., 2012; McCann et al., 2014; Reversat et al., 2020; Tozluoğlu et al., 2013).

Nevertheless, this is discussed as a β integrin homologue has also been identified recently that could mediate Dicty attachment to the substrate (Cornillon et al., 2006).

Of note, although it has not been proven yet, amoeboid migration, because of its independence from focal adhesion formation, leads probably to a lower energy cost, and this is consistent with faster migration (Bodor et al., 2020).

A such mode of migration is of high interest when cells cross a high diversity of media, as it does not rely on specific cell-substrate interactions nor specific proteolysis, and it is likely that cells would use a combination of focal adhesion-dependent and friction-based mechanisms when moving *in vivo* (Bodor et al., 2020).

The amoeboid motility is a highly contractile-dependent mode of migration. In addition to inducing retrograde flows and membrane protrusions, myosin is required to squeeze the cell and propel the nucleus through narrow spaces (Lämmermann et al., 2008; Lomakin et al., 2020). High levels of contractility can be an inherent capacity of cells, or promoted by extracellular cues such as pro-inflammatory cytokines, that are often present in cancer microenvironment (Sanz-Moreno et al., 2011). In cancer spread, contractility increase by overexpression of EGFR (ErbB1 in melanoma) promotes single cell fast amoeboid migration of cancer cells as well (Xue et al., 2006).

2.2.3.2. MECHANISMS OF FORCE GENERATION IN AMOEBOID MIGRATION

Forces exerted by mesenchymal cells and amoeboid cells have been quantified thanks to traction force microscopy (TFM), where movements of beads embedded in a soft polymer layer (PDMS or PAA usually) are measured under cells. This led to the conclusion that adherent cells exert strong traction forces and large stresses in the order of kPa, while amoeboid cells rather exert small extensile stresses (in the order of Pa) on the substrate, and traction forces are non-measurable (Bergert et al., 2015; Yip et al., 2015). This is related to the fact that amoeboid cells rather exert weak friction forces on their environment. In fact, the forces exerted by an amoeboid cell to move forward are ideally just enough to counteract the viscous force or ECM resistance (Yamada and Sixt, 2019).

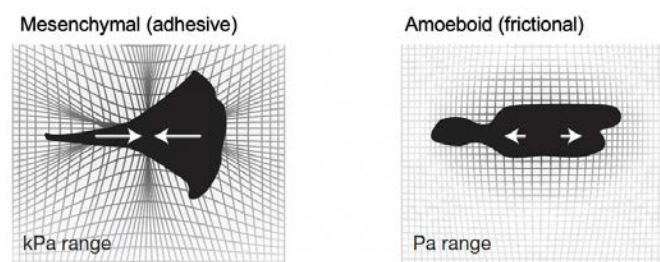


Figure 51. Schematic comparison of stresses exerted by cells during mesenchymal versus amoeboid cell migration.

Mesenchymal cells exert large stresses and contractile deformations, while amoeboid cells exert small stresses and weak extensile deformations. Adapted from (Bergert et al., 2015).

Actomyosin flow-mediated friction forces

The mechanism that has been most investigated and is consistent with a body of experimental evidence, is actomyosin flow-mediated friction forces. Depending on the level of contractility of cells, amoeboid cells can either display a fast bleb-based mode of migration with spontaneous appearance of actomyosin retrograde flows (called A2), or a slowest mode of migration, less contractile, with need for an external polarising cue (A1) (Liu et al., 2015).

Intracellular actomyosin flows would induce friction forces, whose importance in amoeboid migration was highlighted by Bergert and colleagues, as they reported increased cell speed upon higher friction coefficient of the substrate (Bergert et al., 2015). Interestingly, contrary to mesenchymal migration, friction forces can increase without slowing cell migration, and increasing friction rather leads to a plateau for cell speed. However, the molecular coupling of actin retrograde flows to the environment is still unclear. It is thought to occur through transmembrane molecules, exerting non-specific interactions with the substrate and friction forces (Bodor et al., 2020; Reversat et al., 2020). Other interactions that are thought to mediate friction generation could be electrostatic interactions between cellular charged and uncharged residues of glycocalyx and the ECM (Friedl and Bröcker, 2000).

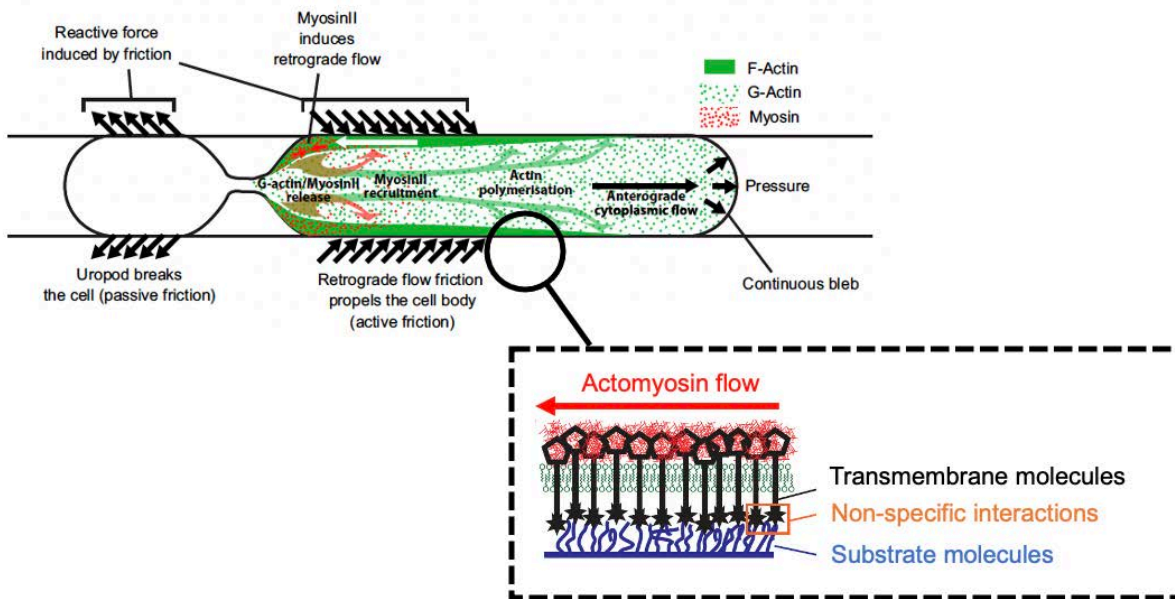


Figure 52. Actomyosin retrograde flow-mediated amoeboid migration.

Top: increased contractility drives appearance of spontaneous actomyosin retrograde flows in A2 mode of migration, sustained by actin polymerisation. From (Liu et al., 2015). Bottom: intracellular actomyosin retrograde flows are thought to induce friction forces through transmembrane molecules and non-specific interactions (Bodor et al., 2020).

Cell deformation and topological features result in migration with no transmembrane coupling

In complex environments such as fibrillar networks encountered *in vivo*, actin retrograde flows can also induce forward movement without any transmembrane coupling to the substrate. This can occur with the help of the environmental topography, as highlighted by leukocytes migrating in wavy channels (**Figure 53a**) (Reversat et al., 2020). When the topographical features are smaller than the typical scale of actin flows, the actin retrograde flow would induce shear forces, and thus asymmetrical pressure on the surroundings leading to forward movement. This mechanism does not occur in smooth channels.

The topography of a confined environment can also be exploited by the blebbing activity of cells to generate non-adhesive migration with no special need for actomyosin retrograde flows. This hypothesis was proposed by Tozluoglu and colleagues, who created a computational model that takes into account various parameters in cell migration: substrate topography, cell contractility, adhesion to the substrate, polarisation, formation of blebs or protrusions (Tozluoğlu et al., 2013). There, they highlight and confirm experimentally on melanoma cells (A375 cell line) that in the case of a textured topology and under an external biased cue, cells can exert traction forces due to asymmetrical bleb formation and “inter-

digitation”, leading to forward movement even in the absence of cell attachment ($\beta 1$ integrin inhibition) (**Figure 53b**).

Another theoretical hypothesis is that travelling waves of cytoskeleton-induced cell deformation could exert pressure on a textured ECM (Yamada and Sixt, 2019). In this mode of migration, cells would not need any adhesive interaction with the substrate either.

These mechanisms relying on substrate topography are consistent with the high deformability and low proteolytic activity of amoeboid cells.

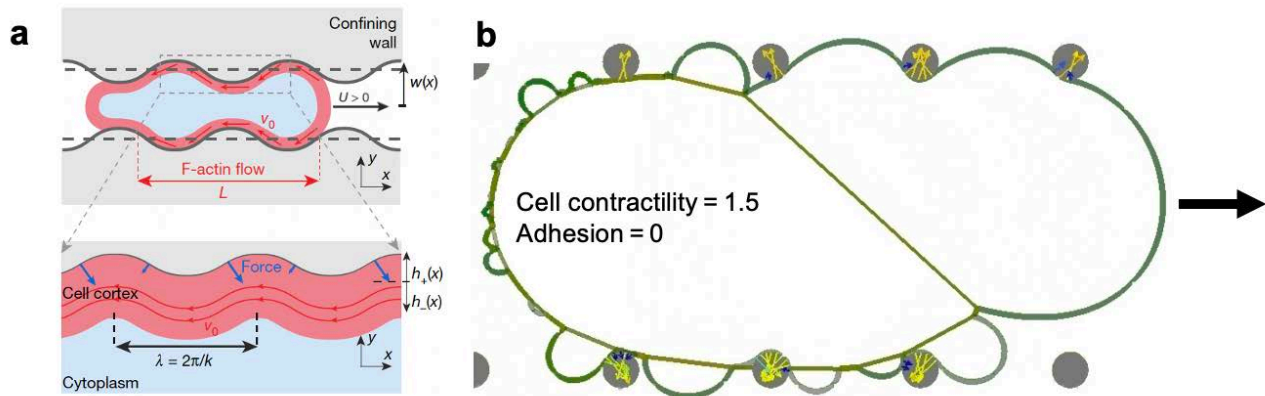


Figure 53. Amoeboid cells can use the environmental topology.

a, Physical model of amoeboid migration in a textured environment (a wavy channel here) thanks to actin retrograde flows, modelled as a viscous fluid. h : thickness of the viscous layer of cortical actin; L : typical length of actin retrograde flow (red); v_0 : speed of retrograde flow. From (Reversat et al., 2020). **b**, Numerical simulation of cell migration in a complex geometry, with no cell-ECM adhesion and high contractility. Blebs can intercalate between pillars and generate sufficient traction force for the cell to move. Black arrow: direction of migration. Adapted from (Tozluoğlu et al., 2013).

Water permeation

Last, one group, to our knowledge, reported that water permeation could drive migration of cells confined in microchannels, with either an asymmetric osmotic pressure or asymmetric repartition of Na^+/H^+ pumps and aquaporins (Stroka et al., 2014).

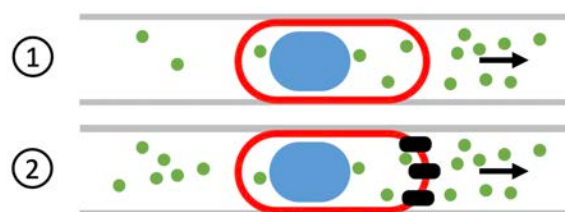


Figure 54. Osmotic engine model.

Cell migration in a focal adhesion-independent fashion, through (1) asymmetric osmotic pressure or (2) asymmetric distribution of ion channels (black rectangles). Black arrow: direction of migration.

3. PLASTICITY OF CELL MIGRATION

Several key parameters have been presented in the previous part as characteristic of each of the main modes of cell migration. A useful summary of cell migration specification is proposed below, for three single cell patterns of migration and two collective ones (Friedl and Wolf, 2010): depending on external or internal parameters – including ECM architecture, proteolysis, cell adhesion and actin dynamics – cells will preferentially adopt one or the other modes of migration (**Figure 55**).

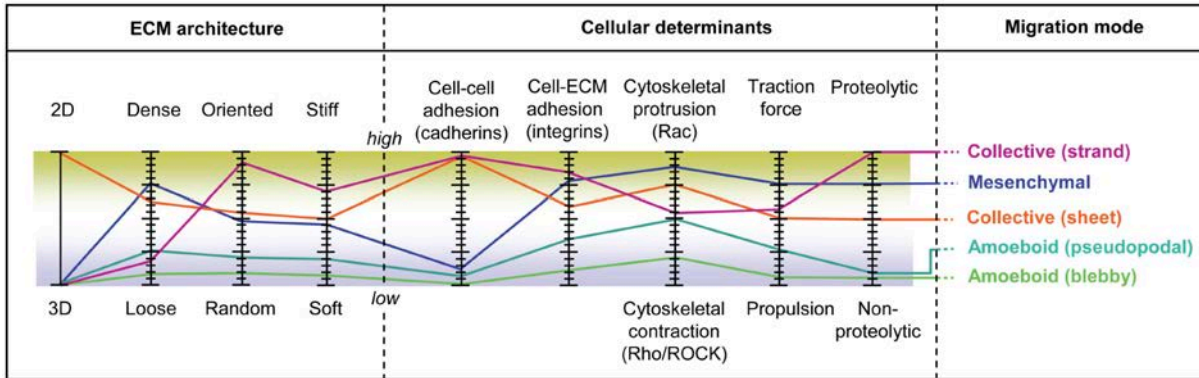


Figure 55. Extracellular and intracellular parameters drive determination of the mode of migration. From (Friedl and Wolf, 2010).

Each of these parameters can vary continuously, whereas the modes of migration schematise certain discrete configurations. Thus, migration classification presented above needs to be qualified. In addition, under the influence of the microenvironment or cell-cell interactions, cells are able to switch their mode of migration, either from an adherent to a non-adherent mode, or from single cell to collective (and *vice versa*) (**Figure 56**). This ability of cells to adapt to their environment is called “cell plasticity”. Plasticity of cancer cells can allow them to migrate almost anywhere during dissemination and resulted in low efficiency of cancer therapeutics targeting adhesion receptors and proteases (Friedl and Wolf, 2003). In addition, as in embryogenesis, their intrinsic properties can vary importantly during cancer progression, leading to a change in cell migration features (Friedl and Alexander, 2011).

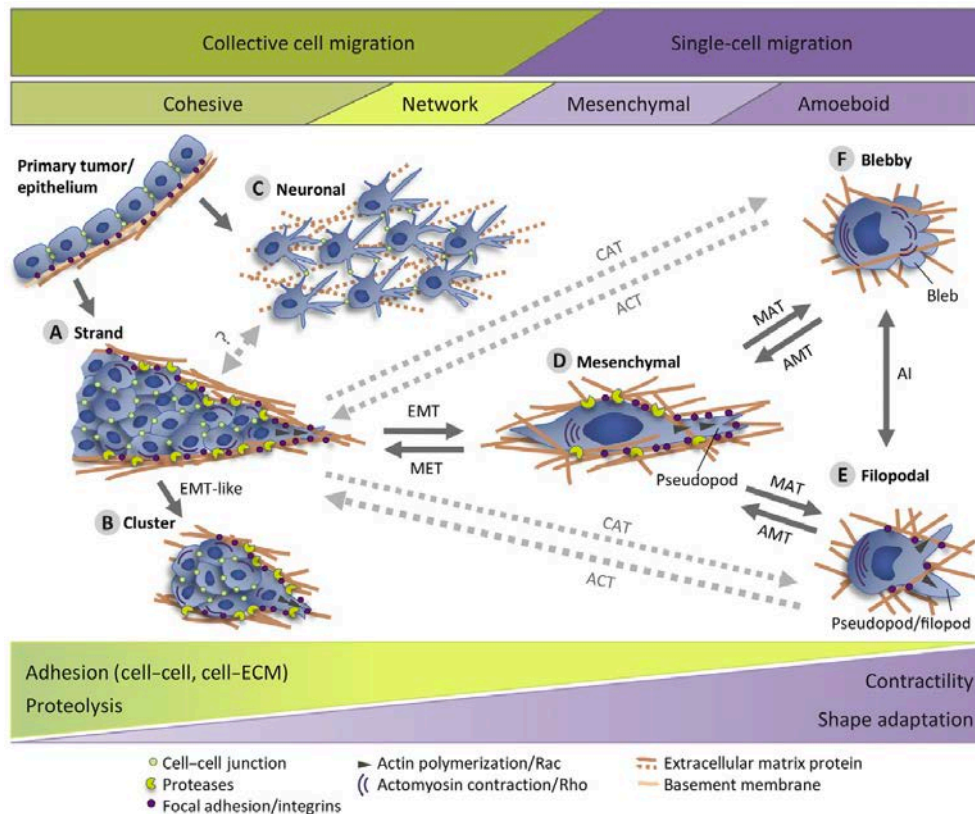


Figure 56. Cell migration plasticity.

Following the modulation of intrinsic and extrinsic determinants, cells are able to switch from one mode of migration to the other. CAT: collective-to-amoeoid transition; ACT: amoeoid-to-collective transition; EMT: epithelial-to-mesenchymal transition; MET: mesenchymal-to-epithelial transition; MAT: mesenchymal-to-amoeoid transition; AMT: amoeoid-to-mesenchymal transition. AI: amoeoid interconversion. From (te Boekhorst and Friedl, 2016).

3.1. Single cell migration plasticity

The most well-known transitions observed in cell migration are from the mesenchymal single cell mode of migration to the amoeoid one, known as mesenchymal-to-amoeoid transition (MAT) and conversely, amoeoid-to-mesenchymal transition (AMT). The main regulator of this transition is actomyosin activity (either protrusive or contractile), which can be tuned directly, through cell-ECM attachment or cell confinement. Substrate stiffness, ECM molecular composition or proteolysis activity can also trigger this transition. Of note, amoeoid migration can only be observed if a minimal confinement is maintained.

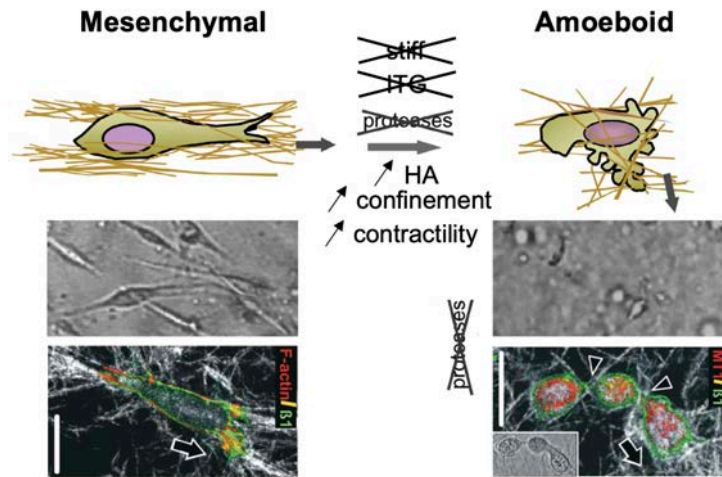


Figure 57. Mesenchymal-to-amoeboid transition (MAT).

MAT can occur after variation of one of the following parameters: cell-ECM adhesion, actomyosin dynamics, cell confinement, substrate stiffness, ECM molecular composition or proteolysis activity. Bottom: representative example of MAT after inhibition of proteolysis. Mesenchymal: integrins ($\beta 1$) cluster around collagen fibres. Amoeboid: Loss of integrins and MMP (MT1) clustering around collagen fibres. Arrowheads: constriction rings. Arrows: direction of movement. Modified from (Friedl and Wolf, 2010; Wolf et al., 2003b).

3.1.1. Regulation of actomyosin dynamics and cell migration mode by small Rho GTPases

As the main regulators of actomyosin contractility and actin polymerisation, Rho and Rac small Rho GTPases are key players in the amoeboid and mesenchymal single cell migration. Their tight balance induces preferentially either one or the other mode of migration in the same cells, and intrinsic changes affecting Rho or Rac can induce MAT, and the reverse. For example, in melanoma cells (A375M2), a systematic siRNA screen of Rac GEFs and GAPs, revealed that DOCK3 (GEF) expression drives mesenchymal migration and prevents amoeboid migration on thick collagen layers. ARHGAP22 (GAP) has the opposite effect and promotes amoeboid migration (**Figure 58**) (Sanz-Moreno et al., 2008). Interestingly, the authors reported that the level of cell plasticity, i.e., their ability to switch from one to the other mode of migration, varies among melanoma cell lines.

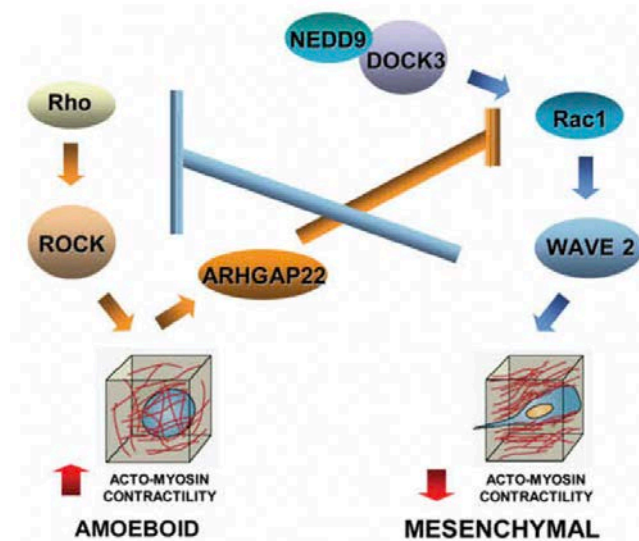


Figure 58. Switch between amoeboid and mesenchymal modes of migration upon small Rho GTPase Rac regulation.
From (Sanz-Moreno et al., 2008).

3.1.2. Low adhesiveness and high confinement promote fast amoeboid migration

In mesenchymal single cell motility, focal adhesions allow for traction force generation and activate downstream signalling pathways promoting actin polymerisation and cell polarity. Preventing their formation leads to cell rounding and acquisition of an amoeboid motility. Indeed, while maintaining confinement, the decrease of substrate adhesiveness led to increased amoeboid phenotype of normal human dermal fibroblast cells (NHDF) and other cell types (Liu et al., 2015). The authors suggest that this change occurs through an increase in cell contractility which promotes amoeboid migration, as mentioned above. Indeed, they propose that focal adhesions and cortical contractility compete in the recruitment of actomyosin machinery. Therefore, the disassembly of focal adhesions would release actin and myosin, relocalising to a contractile flowing cortex and promote amoeboid migration.

The increase in cell confinement also promotes increased cell contractility and fast single cell migration. Liu and colleagues were able to show that artificial confinement and low adhesion induce fast A2 single cell amoeboid migration in a number of cell lines, including some that display a slowest adherent mesenchymal migration under smaller confinement (**Figure 59**) (Liu et al., 2015). Indeed, high confinement increases cell contractility, promoting rearward flows of actin.

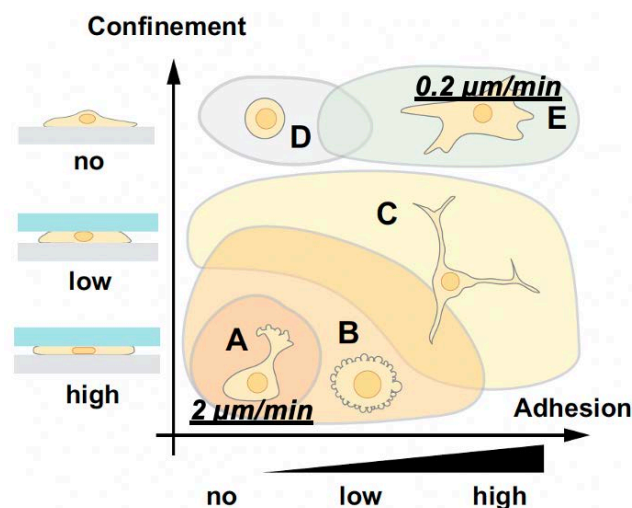


Figure 59. Mesenchymal to amoeboid transition under confinement and low adhesion.
Adapted from (Liu et al., 2015).

When maintaining a certain level of adhesion to the substrate, increasing the confinement can promote fast migration of single cells with no necessary switch to an amoeboid type. Indeed, single cells of breast adenocarcinoma (MDA-MB-231) migrating in a mesenchymal fashion would migrate faster under high confinement, thanks to fewer but larger adhesions generating greater strains on the surrounding collagen (Mosier et al., 2019a). Cell morphology also changed following the degree of confinement, with more elongation under lower confinement.

These confining conditions are especially relevant in the context of cancer as when tumour cells escape from the primary tumour, they cross environments in which they are physically constrained, such as collagen meshwork, small capillaries or between muscle fibres (Friedl and Alexander, 2011; Paul et al., 2017;

Weigel et al., 2012; Zhang et al., 2020). They can serve as tracks but would often impose a significant confinement as well.

3.1.3. Regulation of cell speed by substrate stiffness

During cancer progression, CAFs and cancer cells also often deregulate ECM composition and topography, which leads to key characteristics of cancer progression: fibrosis (increased density via higher deposition of collagen and other ECM components), higher crosslinking (lysyl oxidase), MMPs overexpression and linearisation of fibres (Lu et al., 2011). This remodelling and increased matrix deposition result in increased stiffness of the tumour microenvironment. Conversely, the changes in ECM properties promote cell migration and tumour invasion. Breast density is even a prognostic indicator for patients and is correlated with high levels of collagen and proteoglycan and increased cell invasion. ECM changes are also thought to promote cell survival via integrin signalling.

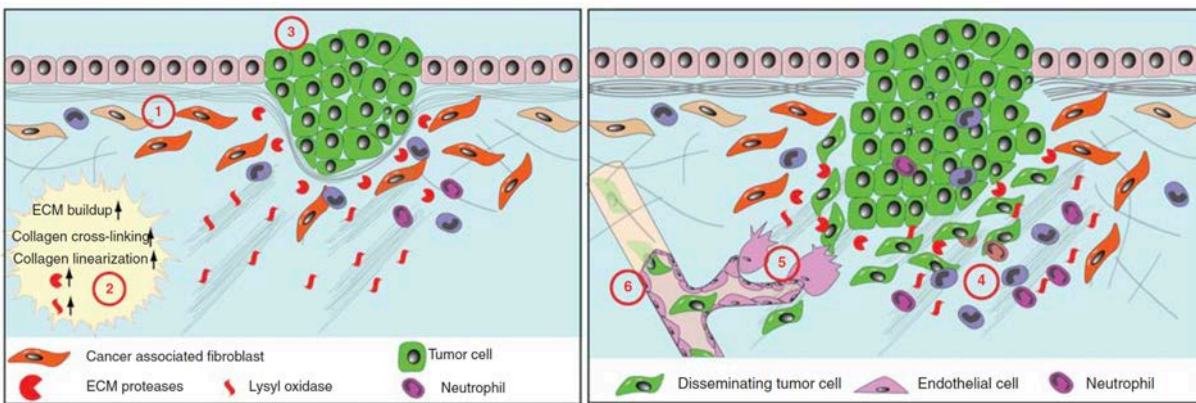


Figure 60. Deregulation of extracellular matrix in cancer progression. (1) Activation of CAFs. (2) CAFs increase ECM production and remodeling. (3) ECM deregulation can promote cell transformation and hyperplasia. (4) Immune cells are recruited and promote cancer progression. (5) ECM deregulation promotes angiogenesis. (6) The leaky vasculature promotes tumour dissemination. Adapted from (Lu et al., 2011).

To decouple the effects of confinement and stiffness in a 3D environment, Pathak and Kumar used microchannels of various size and rigidity (Pathak and Kumar, 2012). Under high confinement, a stiffness increase led to faster single cell migration, while under low confinement – which is close to migration on a 2D substrate, they observed that the relationship between stiffness and speed is biphasic. This behaviour is proposed to be related to two other key elements in cell migration: cell contractility and polarisation, which are promoted by a higher confinement, and cell adhesion to the substrate, which was shown previously to be correlated with cell speed in a biphasic manner.

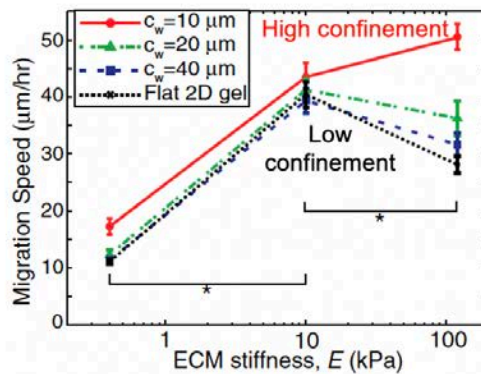


Figure 61. Changes in substrate stiffness drive different patterns of single cell migration. Under high confinement, a stiffness increase leads to faster single cell migration (red). Under low confinement, the relationship between stiffness and speed is biphasic (black). Adapted from (Pathak and Kumar, 2012).

3.1.4. Low proteolytic activity promotes amoeboid migration

The overproduction of matrix and stiffness increase observed around tumours comes together with the adaptation of cancer cells to this new environment, with upregulation of proteases expression (MMPs), allowing for tumour invasion (Lu et al., 2011). Proteases are indeed necessary for single cells migrating in a mesenchymal fashion to perform proteolytic degradation and migrate in complex networks. However, their inhibition in cancer cells does not lead to complete loss of migration properties: indeed, cells are able to switch to an amoeboid-like mode of migration, propulsive, and protease-independent, while losing clustered integrins (Wolf et al., 2003b).

Of note, single melanoma cells migrating in a round amoeboid fashion have also been reported to produce high levels of MMPs (Orgaz et al., 2014). Conversely, MMP-9 would promote their amoeboid migration by regulating actomyosin contractility through CD44 receptor.

ECM molecular composition impacts cell migration mode

In addition to the mechanical properties of ECM mentioned above (stiffness and confinement), cells can adopt different modes of migration depending on the molecular composition of the ECM they are in contact with. This has been particularly highlighted by a study of glioblastoma cancer cells (U87) invasion into matrices that better resemble the *in vivo* conditions of their dissemination in brain: the addition of hyaluronic acid (HA) to collagen-based 3D matrices induced a switch from mesenchymal to amoeboid single cell migration, in a ROCK-dependent manner and with half lower velocity (Cui et al., 2020).

3.2. Transitions between collective and single cell migration

The switch between collective and single cell migration modes is mainly observed upon modulation of cell-cell junctions. They can be affected by various parameters, including cell confinement and density, or actomyosin dynamics. In addition, the levels of cell adhesion to the ECM also affect the transition from a collective mode of migration to a single cell one. Transition from a collective to a single cell mesenchymal mode of migration often occurs under EMT. Otherwise, cell detachment from cohorts in an amoeboid fashion is called collective-to-amoeboid transition (CAT).

3.2.1. Modulation of cell-cell and cell-ECM adhesion

In tissues or groups, cells usually express different types of complementary cell-cell adhesion systems that ensure the coordination of collective migration, but also regulate the ability of cells to adopt a collective or single cell mode of migration. Their expression pattern and composition may vary in time and space, leading to the activation of subsequent intracellular signalling pathways and cytoskeleton remodelling. Cell-cell junctions are also modulated by adjacent cell-ECM receptors (Friedl and Mayor, 2017).

3.2.1.1. IMPAIRING CELL-ECM ADHESION PROMOTES AMOEBOID DETACHMENT

The impairment of formation of focal adhesions during collective invasion, by artificially suppressing $\beta 1$ integrin activity in collagen matrices for example, leads to a transition from collective invasion to amoeboid single cell dissemination, or collective-to-amoeboid transition (CAT) (Hegerfeldt et al., 2002). This comes together with the loss of polarity and cluster disruption of melanoma explants.

3.2.1.2. CELL-CELL JUNCTION MODULATION AFFECTS COLLECTIVE BEHAVIOUR

When two cells meet, cell-cell junction establishment can be only transient: contact inhibition of locomotion occurs when no persistent cell-cell junctions are formed, only a transient contact that leads to cell detachment and modification of cell direction (Davis et al., 2015). On the contrary, new cell-cell contacts can lead to formation of stable intercellular junctions and dramatic changes in cell motility and behaviour. For example, when motile myoblasts meet, they would engage intercellular adhesion molecules (cadherins, NCAM, VCAM-1, etc.), that disable individual migration and rather improve force transmission and collective contractility, for further formation of myofibers (Charrasse et al., 2006). This is allowed by reduced contractility during cell-cell contact formation.

Conversely, loss of cell-cell junctions in breast cancer epithelial cell sheets by E-cadherin downregulation results in single cell detachment and motility (Iliina et al., 2020). Their deregulation by inhibition of α -catenin or modulation of extracellular calcium, sometimes only prevents initiation of coordination. A hypothesis is that coordination is allowed by intercellular tension and Rho recruitment at cell-cell junctions, leading to formation of lamellipodia on follower cells (Jain et al., 2021). However, interestingly, in their system, once cells get polarised thanks to cell-cell junctions, their directionality is maintained even after downregulation of cell-cell junctions.

3.2.1.3. EMT DRIVES CELL-CELL ADHESION LOOSENING AND SINGLE CELL DETACHMENT

As in embryonic development, cancer cells can undergo epithelial-to-mesenchymal transition, which is a major example of how cell-cell junction remodelling impacts cell migration: cell-cell junction reprogramming, from E-cadherin to N-cadherin, leads to weaker cell-cell adhesions or even full individualisation, thus favouring cell dissemination (Thiery et al., 2009). The fact that EMT can be only partially achieved, or only in a subset of cells, suggests a wide panel of combinations of cell-cell junction levels and subsequent collective coordination and migratory behaviours.

TGF β pathway is known to drive epithelial-to-mesenchymal transition in cancer cells, hence promoting single cell invasion (Lamouille et al., 2014). It also promotes a switch from collective cell migration to single cell motility, showed in breast cancer to involve a transcriptional program mediated by Smad4, EGFR, Nedd9, M-RIP, FARP and RhoC (Giampieri et al., 2009). By blocking TGF β signalling *in vivo*, the authors pointed out that this TGF β -mediated activation of single cell motility is required to perform blood-borne metastasis, but not for collective invasion.

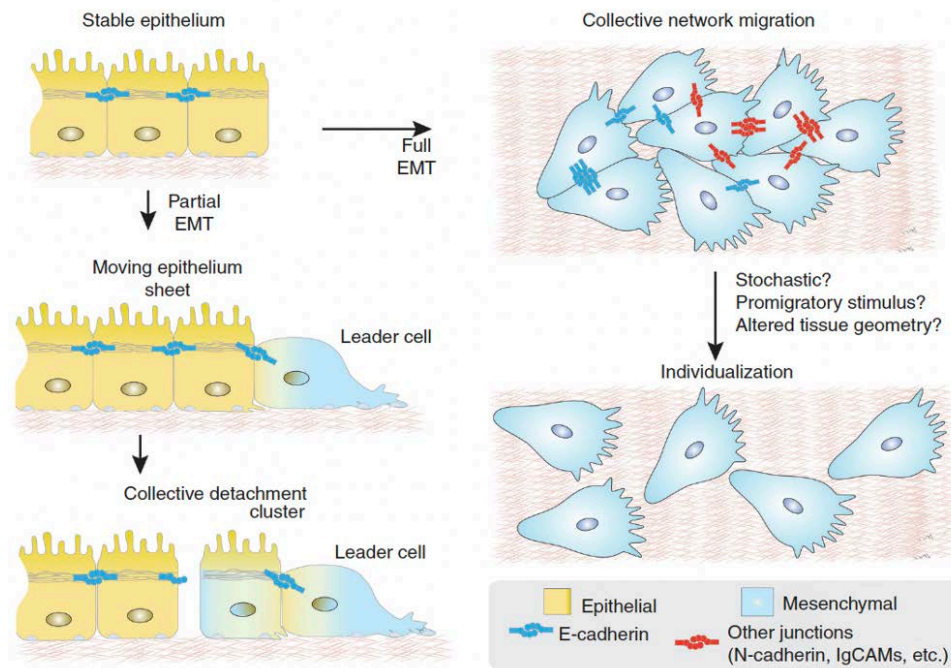


Figure 62. Cell-cell adhesion modulation during migration through partial or full EMT. From (Friedl and Mayor, 2017).

3.2.1.4. INCREASED ACTOMYOSIN DYNAMICS PROMOTE SINGLE CELL MIGRATION

The metastatic process is often fostered by alterations directly affecting actin and ABP regulation. They modulate collective or single cell motility. For example, downregulation of tropomyosin Tpm2.1 in breast epithelial cells (MCF10A) leads to increased Rho/ROCK activity. Therefore, it promotes single cell amoeboid invasion but decreases collective migration (Shin et al., 2017).

3.2.2. Cell density and confined environments

The formation of cell-cell junctions can also be affected by cell density, which can be increased by cell proliferation and physical confinement. The response of cell sheet dynamics to variations of these parameters can be modelled by jamming-unjamming transitions, where cells behave either as a fluid, with low cell-cell attachment and coordination but high velocity, or a jammed immobile solid, with high coordination and cell-cell attachment. Increased confinement can also directly induce collective-to-amoeboid transition.

3.2.2.1. JAMMING-UNJAMMING TRANSITION (JUT): FROM A SOLID-LIKE TO A GLASS-LIKE BEHAVIOUR

Cell jamming has been proposed approximately ten years ago to explain cell migration in monolayers, while unifying the different parameters previously presented as independent but that certainly play hand in hand: cell crowding, forces (underwent and transmitted), adhesions (cell-cell and cell-substrate), actin dynamics, shape, proliferation (Sadati et al., 2013). There, cell motion in tissues is explained through physical laws related to amorphous solid and liquid states of materials. At low density, cells behave in liquid-like dynamics characterised by high motility and cell rearrangements, whereas when cell density increases, they reach a solid-like “jammed” state, with slow motion but full coordination via increased cell-cell adhesions. The transition between both behaviours is called “jamming-to-unjamming transition” (JUT). Conversely, alignment of cell polarisation/interactions with cell velocity facilitates collective motion and solidification (Giavazzi et al., 2018).

The “unjammed” state of epithelial sheets has been proposed to drive cancer progression: discovered in breast epithelium (MCF10A cell line) and confirmed in various carcinoma cell lines, the small GTPase RAB5A drives collective motion through EGFR internalisation, activation of ERK1/2 pathway and WAVE activation, leading to JUT (Malinverno et al., 2017; Palamidessi et al., 2019). Interestingly, the core of intestinal carcinoma explants display dynamic and correlated migration patterns, driven by the actin cytoskeleton: given the relationship between migration speed and correlation length in these regions, cells are certainly near a jamming transition (Staneva et al., 2019).

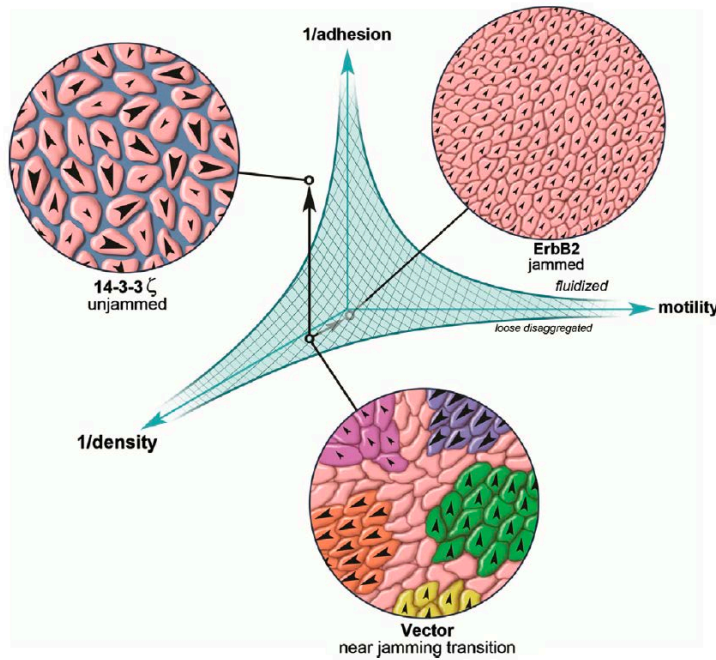


Figure 63. Jamming and unjamming in epithelial monolayers. Motility is presented as a function of cell density and cell adhesion. From (Sadati et al., 2013).

3.2.2.2. COLLECTIVE-TO-AMOEBOID TRANSITION UNDER CONFINEMENT

Increased 3D confinement in complex matrices induces a transition from a collective mode of migration to a single cell amoeboid mode of migration. This has been for example reported when increasing the proportion of agarose into a collagen network, providing a denser matrix because of agarose filling collagen pores, hence promoting CAT in glioblastoma spheroids (Ulrich et al., 2010). Single cells detached and migrating in an amoeboid fashion can then squeeze between the small pores of the matrix.

3.3. Transitions between collective cell migration modes

Transitions among collective cell migration modes have been underinvestigated. This is mainly due to the fact that the main modes of collective migration described to date share common patterns, with cell-cell junctions and exerting traction forces like single cell mesenchymal migration. However, the discovery of TSIPs uncovered a potentially new mode of collective cell migration, that could be equivalent to single cell amoeboid motility as occurring with low attachment.

3.3.1. Crowding affects collective shape and velocity

Cell density varies following *in vivo* events and has been shown recently as a key actor of collective cell migration. It can alter the shape of collective cell migration: an increased cell density, often observed in cancer progression, transforms *in vitro* broad collectives of breast epithelial cells (MCF10A) to narrow streams (Loza et al., 2016). The authors also observed the effects of lowering cell density, mimicking what happens at the front of wounds: it leads to large collectives with a leader-follower organisation. These observations were then confirmed in an *in vivo* epithelium of *Drosophila* egg chamber. A complementary physical modelling allowed them to link this behaviour to force-sensitive contractility, and show that together with cell density, the contractile state of cells also influences the mode of collective cell migration. In addition to shape modulation, cell density can impact the velocity and coordination of groups as well: Hayer and colleagues noticed an optimum cell density (700 cells/mm²) at which human umbilical vein endothelial cell (HUVEC) sheets reach a highly coordinated movement (Hayer et al., 2016).

3.3.2. Regulation by substrate stiffness

A nice study of Beaune and colleagues investigated the role of stiffness on collective cell migration plasticity on 2D PAA substrates and highlighted the impact of substrate rigidity on cohesiveness, adhesion, shape, and velocity of cell groups (Beaune et al., 2018). On a very stiff surface, aggregates of murine sarcoma cells spread with no motility. When decreasing rigidity, cellular aggregates migrated like “giant keratocytes”, thanks to the dewetting of the rear while a cell monolayer still spread at the front and behaved like a lamellipodium. At lower rigidity, cell aggregates displayed a “penguin-like” motion, with higher dewetting around the cluster and loss of part of the lamellipodium. The loss of rigidity on the softest gels was accompanied with a certain loss of cell-substrate and cell-cell attachment: aggregates moved as less cohesive “running spheroids”. All in all, a decrease in stiffness lead to lower attachment and slower migration, but a certain dewetting is necessary to allow for polarisation and collective migration.

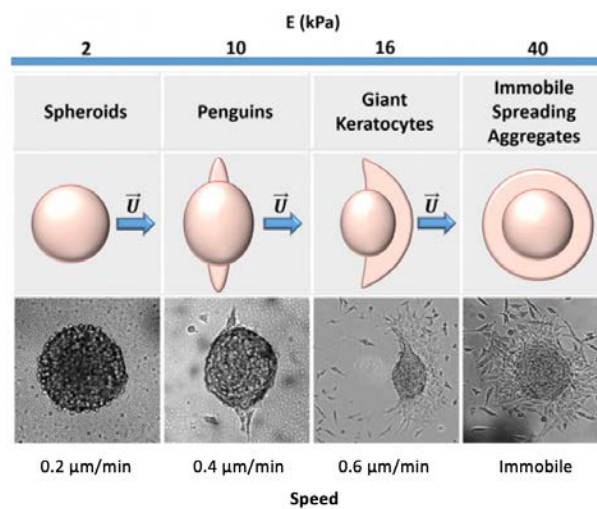


Figure 64. Changes in substrate stiffness drive different modes of collective cell migration. Adapted from (Beaune et al., 2018).

3.3.3. A collective amoeboid mode of migration

TSIPs discovery in cancer patients led to the idea of a new mode of collective cell migration, theoretically similar to amoeboid single cell invasion. Indeed, they are invasive tumour intermediates, and invade within peritoneal explants while keeping their “apical-out” topology. Therefore, integrins are expected to stay segregated inside clusters (**Figure 65a**), which would prevent TSIPs from exerting traction forces on the

substrate through focal adhesions, like what has been described to date in conventional collective migration. Confirming this hypothesis, inhibition of focal adhesion pathways did not prevent collective invasion of TSIPs through collagen gels (**Figure 65 b, c**). However, myosin inhibition leads to a significant loss of collective invasion, suggesting a role for actomyosin contractility in this mode of invasion, which may be mediated by the surrounding actin belt (**Figure 65a,d**).

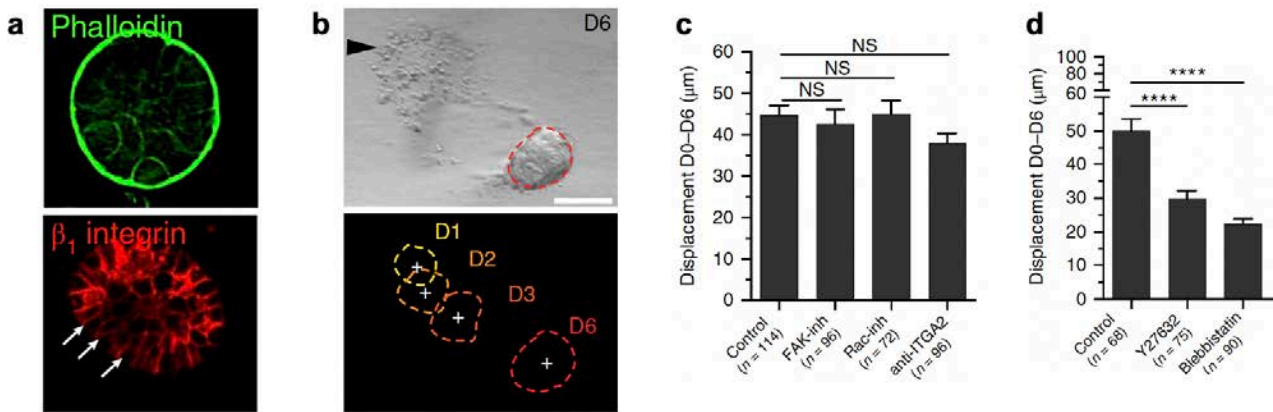


Figure 65. TSIPs can invade in collagen matrices in an integrin-independent but contractility-dependent fashion.

Adapted from (Zajac et al., 2018). (A) Immunofluorescence of TSIPs in suspension: actin cortex (phalloidin) and basolateral integrins (β_1 integrin). (B) Invasion of a TSIP in a collagen matrix for 6 days. (C) Inhibition of focal adhesion components does not prevent TSIP migration. (D) Inhibition of actomyosin contractility decreases by half TSIP migration.

These results suggest that TSIPs could display a collective mode of migration relying on actomyosin contractility, rather than focal adhesion-based traction forces. Thus, it could share similar features with the amoeboid single cell mode of migration, which had not been reported for collectives to date, providing cancer cells with additional skills (**Figure 66**).

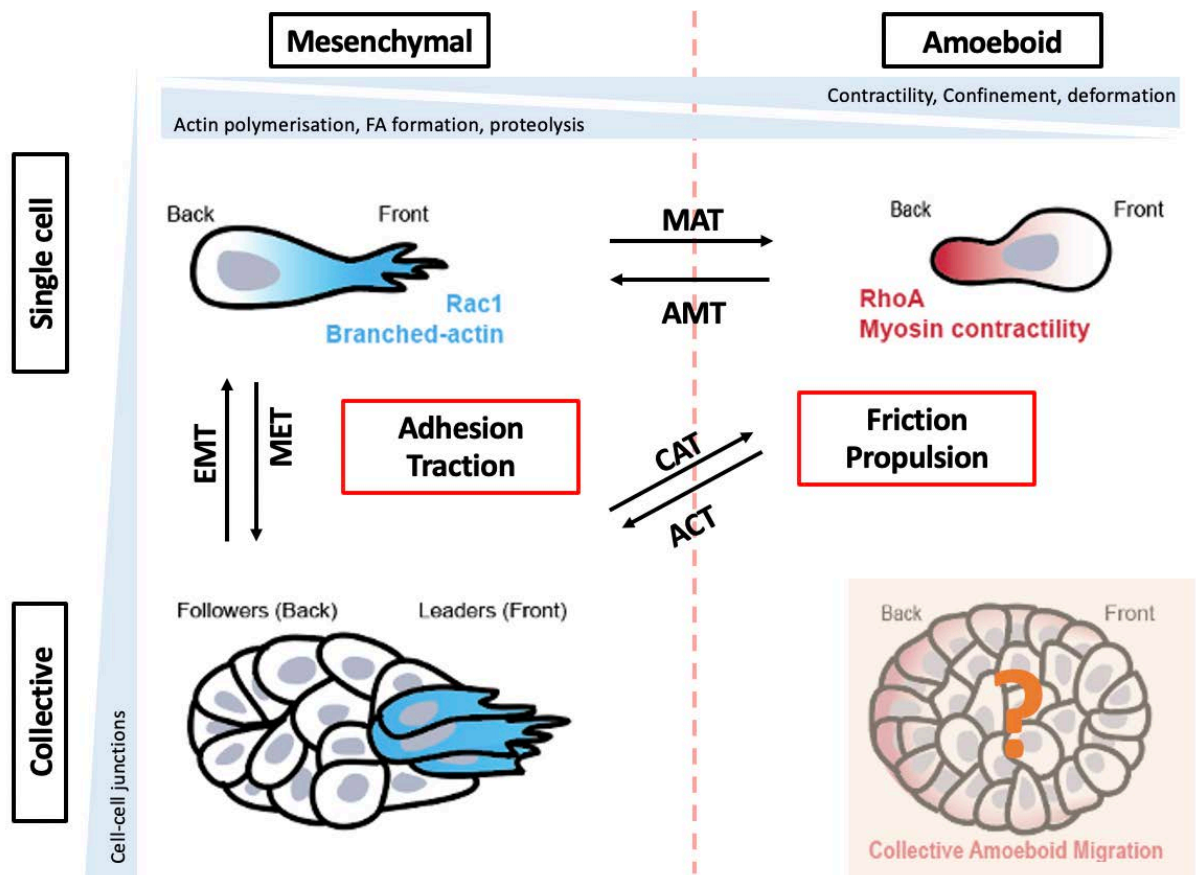


Figure 66. Main known cell migration modes and determinants of their plasticity.

Does a collective amoeboid migration mode exist, as suggested by TSIPs migration features?

In the first part, I presented how cell migration plays an important role in embryonic morphogenesis and physiological processes, as well as in the metastatic cascade. The second part detailed the various modes of migration that cells, and in particular cancer cells, can display either as single cells or in groups during their dissemination, and their underlying mechanisms. This last part underlined the high plasticity of cells to switch from one migration to another, following mutational changes or external cues.

This highlights the ability of some cells to migrate almost anywhere in the human body, through various mechanisms that are certainly not all known to date, which complexifies our fight against cancer dissemination and the therapeutic targeting of cell migration. More investigations need to be done to understand what mechanisms could foster cancer spread in patients, and growing evidence indicate that collective migration could play an important role while it still keeps important secrets.

Chapter II. PhD project

Despite tremendous efforts in understanding the systemic, cellular, and molecular aspects of cancer, we still face today its outstanding capacity to disseminate throughout the organism and with high plasticity, making it almost impossible to contain.

Growing evidence highlight the importance of collective dissemination in cancer spread, including a study of our group unravelling TSIPs as collective tumour intermediates. However, collective cell motility *in vivo* has been poorly described, and especially in patients, and little is known about whether cells could adapt collectively to various environments as single cells do.

Our lab recently discovered that certain groups of tumour cells were able to perform collectively an unknown mode of cell invasion in 3D matrices, independent from focal adhesion formation and relying on contractility of the cluster (Zajac et al., 2018). This suggests that cancer cells could enable an amoeboid-like mode of migration, collectively, which has never been reported until now.

To investigate the mechanism underlying such a mode of migration, Dr Fanny Jaulin developed collaborations with other expert research teams: Matthieu Piel's laboratory, who builds important knowledge on single cell migration by extensive use of microchannels, and Raphaël Voituriez' laboratory, who performs biophysical modelling of various biological processes, especially cell migration. This interdisciplinary project on cancer dissemination, bridging fresh patient's samples, cell biology, microfluidics, and biophysical modelling, perfectly matched my interests and background, and I jumped without hesitation in the meanders of this mysterious mode of collective cell migration. We later welcomed a new team on this project: Mathieu Coppey's team, with expertise in optogenetics, that would allow precise manipulation of cell clusters contractility.

Thus, my PhD mainly aimed at deciphering this new mode of collective cell migration. We addressed this topic through the following questions:

1. Does a focal adhesion-independent collective mode of migration exist? If so, is it specific to apical-out TSIPs? (See sections **1.** and **2.**)
2. Are cell clusters polarised to allow for migration? (See section **3.**)
3. What is the force generation-mechanism underlying this non-adhesive mode of migration? (See section **4.**)

The first part of my PhD was dedicated to optimizing the experimental setting. Indeed, the preliminary experiments had been made in the lab in 3D collagen matrices, and with clusters formed from PDXs, both providing physiological results but being complicated to control and handle. I investigated the most relevant and convenient one that would allow us to observe focal adhesion-independent collective migration, and the subsequent imaging tools and automated image analysis. The microchannels, developed with the help of Matthieu Piel's lab and with which the lab had previously conducted preliminary tests, appeared to be the most efficient tool once adapted to the dimensions of large groups of cells. To verify whether this motion was focal adhesion-independent, we performed control of focal-adhesion formation and traction forces generation in such environments. Then, to investigate which cells would be able to migrate in this fashion, I took advantage of our close collaboration with Gustave Roussy hospital and gathered several patient samples directly from the clinic.

In a second part that aimed at investigating the polarisation of the cohort, we took advantage of the knowledge acquired on single cell amoeboid migration. We focused on cluster shape and actomyosin features thanks to the establishment of different cell lines expressing fluorescent probes. We also used optogenetic tools – originally developed for single cell study – to interfere with molecular processes at a cellular level in the cluster.

The last part aimed at understanding how a cluster would generate propulsive forces for migration in this non-adhesive environment. I investigated cell flows and individual movements inside the cluster, and we performed particle image velocimetry (PIV) to monitor actomyosin dynamics on the long and short timescales. Biophysical modelling would help us imagine new possibilities to understand clusters mode of migration.

In addition, I had the chance to take part in another study from the lab, from Canet-Jourdan and colleagues, whose aim was to investigate the clinical issues and molecular processes underlying the polarity reversion of TSIPs. This was a great opportunity for me to tackle more clinical aspects in the study of our CRC organoids, and I investigated the effect of polarity reversal on the response of TSIPs to chemotherapies. The expertise of our team on chemotherapy testing on organoids allowed us to combine their protocols to our classical approach for polarity reversion to perform this study.

All in all, this project was about characterising different aspects of cancer dissemination, in particular in CRC: 1/ invasion and 2/ response to chemotherapies. This also fostered the development of new protocols and tools to study organoids migration and drug response.

Chapter III. Material and methods

ANTOINE DE MAXIMY

1. STATISTICS, REPRODUCIBILITY AND DATA PRESENTATION

Data are presented using SuperPlots (Lord et al., 2020). Briefly, violin plots display the whole population of clusters, median (dashed grey line) and quartiles (dotted grey lines). Except for **Figure 68** (see corresponding legend), dots of the same colour represent the mean of the matched control and experimental conditions performed in each individual experiment (red control dot goes with the red experimental condition dots). The black line is the mean of all experiments for each condition.

Normality or lognormality of all data distribution was tested using the Kolmogorov-Smirnov, d'Agostino-Pearson or Shapiro-Wilk test in Prism 9 (GraphPad). When distributions are best fitted by a lognormal distribution, statistical tests were performed on log-transformed data. Significance for datasets displaying normal distributions were calculated in Prism with unpaired (unless otherwise specified) two-tailed Student's t test or one-way analysis of variance (ANOVA) and Dunnett's multiple comparison test when comparing more than two conditions. Significance for non-normally distributed datasets were calculated in Prism using a Mann-Whitney test or a Welch's t test for different SD, or a Kruskal-Wallis test and Dunn's multiple comparison test when comparing more than two conditions. P values of statistical significance are represented as ****P <0.0001, ***P <0.001, **P <0.01, *P <0.05, ns, not significant. n numbers of clusters/cells analysed are indicated in the figure legends. The number of independent experiments (biological and technical replicates) is either represented on Superplots as the number of dots, either indicated in the figure legend. Experiments were performed independently for each cell line.

2. BIOLOGICAL MATERIAL AND CELL CULTURE

Human primary specimens. The human study protocols followed all relevant ethical regulations in accordance with the declaration of Helsinki principles. The study was approved by the ethics committee of Gustave Roussy hospital and written informed consent was obtained from all patients.

Recovery of peritoneal effusions from patients. Tumour cell clusters from colorectal cancer (CRC, with a 50% mucinous contingent) and pseudomyxoma patients are harvested by collecting serous fluid after addition and reabsorption of 500 ml of saline solution immediately after laparotomy. Ascites from esogastric, pancreatic, ovarian and uterus cancer patients are collected at day hospital. The processing of peritoneal effusions is adapted from the protocol described in (Zajac et al., 2018). Briefly, fresh specimens are centrifuged twice at 400g for 5min and tumour cells are isolated via a Ficoll-Paque PLUS (GE HealthCare, 17144002) centrifugation, following the manufacturer's protocol. Cell clusters are then purified from single cells through several pulse centrifugations at 400g.

The non-seminomatous germ cell tumour specimen was isolated from biopsy. Tumoroids are kept in Matrigel for 6 weeks in colon organoid medium³⁹. They are then gently resuspended with Tryple 1X and kept in suspension in an ultra-low adhesion 6-well plate (Corning, CLS3471-24EA) overnight before use in the microchannels.

Healthy colon. The normal colon tissue was collected from colectomy tissue at least 10cm away from the tumour margin. Tissues are minced and digested with 2mg/ml collagenase type I-A for 1h at 37°C. Following digestion, mechanical force by pipetting is applied to facilitate crypt release in solution. Crypts are pelleted (300g, 5min, 4°C), resuspended in 400µl of growth factor reduced (GFR) Matrigel (Corning), and seeded in a 6-well culture plate. Matrigel is incubated for 20min at 37°C then overlaid with 3ml of IntestiCult (STEMCELL Technologies). Medium is refreshed every two days. Healthy colon organoids are

split every 10 days using Gentle Cell Dissociation Reagent (GDCR, STEMCELL Technologies) according to manufacturer's protocol.

Tumoroids generated from Patient-Derived Xenografts (PDX). Two human colorectal tumours (TSIP corresponding to LRB-0009C, PDX#2 corresponding to IGR-0012P, PDX#3 corresponding to IGR-0014P) from the CReMEC tumour collection (Julien et al., 2012) were maintained in immunocompromised NSG mice (males or females). Animal experiments are compliant with French legislation and EU Directive 2010/63. The project received a favourable evaluation from Animal Care and Use Committee n°26 and granted French government authorization under number 517-2015042114005883 and 8867-2017020914112908. Mice were obtained from Charles River and Gustave Roussy in-house facility, housed and bred at the Gustave Roussy animal core facility (accreditation D94-076-11) and euthanised following endpoints validated by the Ethical Committee and the French government (Ministère de l'Enseignement Supérieur, de la Recherche et de l'Innovation).

Tumoroids (TSIPs) formation from PDXs was adapted from the protocol described in (Zajac et al., 2018). Tumours between 1000-1500 mm³ are minced and incubated in 5 to 10ml of DMEM medium containing GlutaMAX (Gibco, 31966-021) supplemented with 2 mg/ml collagenase-VIII (Sigma, C2139) for 1h15 at 37°C under agitation. Tumour fragments are resuspended in 50ml of DMEM and filtered through 100µm cell strainers (EASYstrainer, 542000). Filtered tumour cells and clusters are pelleted at 800g for 10min. Pellets are further washed 4 times by adding 10ml of DMEM medium and pulse-centrifuged at 800g and 400g to collect clusters only. Clusters are kept in suspension in ultra-low adhesion 6-well plates (Corning, CLS3471-24EA) with DMEM medium supplemented with 10% foetal bovine serum (FBS, Gibco, 10270-106) (hereafter referred to as "full DMEM"). They form tumoroids after 3 days of culture.

Prostate cancer PDX (MR191) and ovarian cancer PDX (MR0097) are gifts from Dr C. Robert's lab. Tumour fragments were digested to form clusters after 2 and 7 days of culture in 6-well ultra-low attachment plates in prostate culture medium (Drost et al., 2016) and full DMEM respectively.

All media are supplemented with 1% penicillin and streptomycin (P/S, Gibco, 15140-122).

Cell lines. Triple-negative breast cancer SUM52PE cells (gift from Dr F. André's lab) and LS513 cells (CRC, ATCC, CRL-2134) are cultured in RPMI (RPMI 1640 1X, Gibco, 61870-010) medium supplemented with 10% FBS. HT29 (ATCC HTB-38, CRC) cells from human colon adenocarcinoma are grown in full DMEM. Mucous secreting HT29-MTX (clone E12, ECACC 12040401, CRC) cells, derived from HT29 cell line, are grown in full DMEM supplemented by 1% non-essential amino acids (NEAA, Gibco, 11140050). HT29 and HT29-MTX cell lines are used for mechanistic studies because they are the fastest cell lines and can be easily infected to express tagged-proteins or trackers. Cell lines are dissociated with 0.05% trypsin-EDTA for passaging. For cluster production, 1.5 million cells are plated in a Petri dish (non culture coated) with 10ml of culture medium for 3-5 days.

Circulating Tumour Cell lines (CTC44, CTC45) from human colorectal cancer (gift from Julie Pannequin's lab) and cultivated as previously described (Grillet et al., 2017). In brief, they are maintained in suspension as clusters in advanced DMEM-F12 (Gibco, 12634-010) supplemented with 1% GlutaMax (Invitrogen, 35050-061), 1% N2 supplement (Invitrogen, 17502-048), 20ng/ml of human EGF and 10ng/ml of human FGF-2. They are split once a week, by pelleting at 300g for 5min and incubated with Accumax for 45min at 37°C. 5ml of PBS containing 2% FBS is then added to inactivate Accumax. Clusters are filtered through a 40µm strainer, pelleted and resuspended in M12 medium.

All cell lines and clusters are cultured in a humidified incubator at 37°C under a 5% CO₂ atmosphere.

3. MICROCHANNELS, DRUG INCUBATION AND CLUSTER LOADING

Design of the channels. We designed microchannels with the following dimensions to match the dimensions of cell clusters from patients and PDXs: height $h=30\mu\text{m}$, width $w=60\mu\text{m}$, length $l=7\text{mm}$. The loading chamber's height is $h=180\mu\text{m}$, in order not to stress cells too much before entering the channels. Each chip contains 3 independent series of 30 microchannels and is dimensioned to fit in a 25mm-diameter well. Epoxy molds are made from an original mold fabricated on a silicon wafer by standard photolithography with an SU8 photoresist (Microchem), following the manufacturer's instructions.

Microchannels preparation and drug incubation. Chips are made of a polydimethylsiloxane mixture (PDMS, RTV615, Neyco) 10:1 w:w ratio with crosslinker, which is the most often used in the field of single cell amoeboid migration (Liu et al., 2015). The mixture is poured on the epoxy mold and polymerised at room temperature for at least 48h. Loading ports are made with a 1mm hole puncher. Chips are sterilized with 70% ethanol for a few minutes, dried and activated for 1 min in a plasma chamber (Diener, Zepto V2, 30W) together with a glass substrate (12-well-glass-bottom plate (CellVis, P12-1.5H-N) or 25-mm glass coverslip for optogenetic experiments). The 12-well-glass-bottom plate is previously plasma-activated alone for 5 min. PDMS chips are stuck to the activated glass and heated at 95°C for 30s for maximum binding. They are then cooled at room temperature for a few seconds before coating for at least 30 min with an anti-adhesive reagent (0.1mg/ml pLL-g-PEG (pLL(20)-g[3.5]-PEG(2) from SuSoS) or pLL-g-PEG + 1% Pluronic F-127) or $20\mu\text{g/ml}$ rat-tail collagen-I (Corning, 354236). For Fig. 2A, collagen-I is labelled with Alexa647 (coupling of the collagen was done in-house, using Invitrogen labelling kit #A20006). For the experiments on friction, bovine serum albumin (BSA) was added at the indicated concentrations in the PEG+F127 mixture for coating the channels. This was previously shown to increase friction¹⁸. Chips are washed once in full DMEM and then submerged with medium for 1h to overnight.

For drug treatments (Y27632 (Sigma, Y0503-5MG, $25\mu\text{M}$), Blebbistatin (Calbiochem, 203391, $50\mu\text{M}$), cyclic RGD (Cilengitide, Selleckchem, $10\mu\text{M}$), SB273005 (Selleckchem, $10\mu\text{M}$), PF562271 (TargetMol, 250nM), Saracatinib (MedChem Express, 100nM), SU6656 (Sigma, $10\mu\text{M}$), EIPA (Sigma, 20- $50\mu\text{M}$)) or DMSO, chips are incubated with medium and drugs 1-5h prior to cluster loading.

Cluster loading. Clusters are filtered on a $70\mu\text{m}$ strainer (EASYStrainer, 542070), pelleted by a 400g pulse centrifugation and resuspended at 250 clusters/ μl in full DMEM. Clusters are loaded using a $25\mu\text{l}$ syringe (Hamilton, 702SNR 22/51mm/pst3). All media are supplemented with 1% penicillin and streptomycin.

Flushing of the channels. After 1 day of migration in PEG- or col-I-coated microchannels, HT29-MTX clusters are flushed very gently with a syringe filled with water, at $2.8\mu\text{l/min}$. The whole chips are imaged before and after flushing at 4X magnification on an Olympus inverted X83 microscope with a Hamamatsu camera. Clusters before and after flushing are then counted to quantify the effect of flushing, as a proxy for adhesiveness of the microchannels.

Single cell experiments. Microchannels have the following dimensions: width $w=20\mu\text{m}$, height $h=3$ or $5\mu\text{m}$. They are stuck to a 12-well-plate or to a μ -Dish (Ibidi, 81151) following the experimental procedure described above, and are coated with pLL-PEG. Single cells in suspension are then pushed inside the channels using a $25\mu\text{l}$ Hamilton syringe (Hamilton, 702SNR 22/51mm/pst3).

4. TFM SETUP PREPARATION

Protocol adapted from (Bergert et al., 2015).

Soft PDMS substrate preparation. A 100 μm -soft PDMS layer (between 3kPa and 20kPa, (Bergert et al., 2015; Kenry et al., 2015)) is made of polydimethylsiloxane mixture (PDMS, CY 52-276, A+B) 1:1 w:w ratio of A to B, spin-coated (spin acceleration 250 rpm/s, 500 rpm during 10s, then 750 rpm during 40s) on a FluoroDish (WPI, 35mm, FD35-100), and let to polymerize overnight at 80°C.

Soft PDMS substrate functionalisation. Substrates are silanized using a 1:10 v:v solution of 3-aminopropyltriethoxysilane (Sigma, A3648) diluted in 100% lab grade ethanol. Substrates are incubated for 10 minutes in the silane solution, rinsed with 100% ethanol 3 times and dried at 80°C for 10 minutes. A 2:1000 v:v solution of fluorescent beads (FluoSpheres™ carboxylate-modified microspheres, 0.1 μm or 0.2 μm) in Millipore water is sonicated during 5 min and filtered using a 0.45 μm filter. Activated substrates are then incubated in the fluorescent beads solution for 10 minutes, washed 3 times with Millipore water, and dried at 80°C for 10 minutes. Samples can be stored at room temperature under dark conditions for up to 2-3 weeks. FluoroDish are then coated overnight with an adhesive (rat tail collagen-I 200 $\mu\text{g}/\text{ml}$ in PBS) or antiadhesive reagent (0.1mg/ml pLL(20)-g[3.5]-PEG(2) diluted in HEPES buffer) solution under biofilm.

Cluster loading. Clusters are filtered on a 70 μm strainer (EASYStrainer, 542070), pelleted by a 400g pulse centrifugation and deposited on the 2D PDMS substrate. Clusters on PEG substrate are overlaid with an agarose pad to prevent them from floating. They are then incubated overnight with culture medium in this configuration before imaging.

SDS treatment and imaging. Timelapse imaging was done using a Spinning Disk confocal microscope Andor on DMI8, powered by Metamorph software. A first image of the sample is taken, then Sodium dodecylsulphate (SDS, Sigma, L3771) is added with a syringe either directly on top of the clusters on col-I-coated Fluorodish, or through the agarose pad on top of clusters on pLL-PEG-coated substrates. Sample is imaged every 1 min until the cell cluster is completely dissociated.

5. PLASMIDS, VIRUS PRODUCTION AND INFECTION

Plasmids. TIAM-CRY2-mCherry was constructed as detailed previously (Kennedy et al., 2010). The ARHGEF11 domain was amplified and cloned into CRY2PHR-mCherry. pCIBN(deltaNLS)-pmGFP (Addgene plasmid # 26867; <http://n2t.net/addgene:26867>; RRID:Addgene_26867) (Kennedy et al., 2010) and pCRY2PHR-mCherryN1 (Addgene plasmid # 26866; <http://n2t.net/addgene:26866>; RRID:Addgene_26866) (Kennedy et al., 2010) are a gift from Chandra Tucker. The H2B-RFP plasmid is a gift from the Hall lab. pLV-Ftractin-mRuby3-p2A-mTurquoise-MLC-IRES-Blast is a gift from T. Meyer (Hayer et al., 2016) (Addgene plasmid # 85146; <http://n2t.net/addgene:85146>; RRID:Addgene_85146), mCherry-Paxillin is a gift from the Vignjevic lab and pLentiblast-Paxillin-mTurquoise is a gift from J. Debnath (Kenific et al., 2016) (Addgene plasmid #74206; <http://n2t.net/addgene:74206>; RRID:Addgene_74206).

Virus production and infection. Ectopic expression of fluorescent probes is achieved using lentiviruses. Lentiviruses are obtained by co-transfection of the plasmid of interest with the packaging vectors pMD2G (Addgene plasmid #12259; <http://n2t.net/addgene:12259>; RRID:Addgene_12259) and pCMVdR8,74 (Addgene plasmid #8455; <http://n2t.net/addgene:8455>; RRID:Addgene_8455) into HEK293T cells with the transfection reagent JetPrime (Polyplus, 114-15). Lentiviruses-containing supernatants are collected on days 2 and 3 following transfection, concentrated by ultracentrifugation (24000g, 2h) and stored at -80 °C.

Infection is performed as described previously (Zajac et al., 2018). Briefly, HT29-MTX (1x10⁶ cells) are exposed to lentiviruses in 500 μl full DMEM containing 16 $\mu\text{g}/\text{ml}$ protamine overnight before being sorted by FACS to establish stable cell lines. Cell lines were then used for experiments as specified in the figures and legends. optoRhoA HT29-MTX cells express ARHGEF11-CRY2PHR-mCherry and CIBN-GFP, optoRac

HT29-MTX cells express TIAM-CRY2PHR-mCherry and CIBN-GFP, and control cells express CRY2PHR-mCherryN1 and CIBN-eGFP-CaaX.

6. IMAGING, MICROSCOPE ACQUISITION AND OPTOGENETIC EXPERIMENTS

Time-lapse imaging. Timelapse bright-field imaging is done using an Olympus inverted X83 microscope with a Hamamatsu camera or a Spinning Disk CSU-W1 (Yokogawa) with a Prime 95B sCMOC camera. The latter is also used for live fluorescence imaging.

Imaging of Integrin alpha V (ITGAV) internalisation. Before injection in the microchannels, clusters are incubated in DMSO for control condition or with 10 μ M cyclic RGD (cilengitide, cRGD) for 30min. Transferrin (Alexa488-Transferrin, Invitrogen, T13342, 5 μ g/ml) is also added for all conditions to reveal the endosomal fraction. Clusters are then injected in PEG-coated microchannels in full media containing Transferrin and cRGD or DMSO and incubated overnight. ITGAV and Transferrin are then imaged using a Spinning Disk CSU-W1 microscope (Yokogawa) with a Prime 95B sCMOC camera.

Interference reflexion microscopy (IRM). IRM is performed on an SP8 Leica confocal microscope with the beamsplitter RT 15/85 and a laser at 638nm.

Optogenetics. Clusters are incubated in the chips for at least 1 hour before imaging. Experiments are performed at 37°C in 5% CO₂ in a heating chamber (Pecan, Meyer Instruments, Houston, TX) placed on an inverted microscope model No. IX71 equipped with a 60 \times objective with NA 1.45 (Olympus, Melville, NY) and a camera ORCA-Flash4 (Hamamatsu, Japan). The microscope is controlled with the software Metamorph (Molecular Devices, Eugene, OR). Differential interference contrast (DIC) imaging is performed with a far-red filter in the illumination path to avoid CRY2 activation. Optogenetic stimulations are performed every 2-2.5 or 5min with a DMD in epi-mode (DLP Light Crafter, Texas Instruments) illuminated with a SPECTRA Light Engine (Lumencor, Beaverton, OR USA) at 440 \pm 10 nm. Total Internal Reflection Fluorescence (TIRF) images are acquired using an azimuthal TIRF module (iLas2; Roper Scientific, Tucson, AZ). An automated tracking algorithm is designed in MATLAB with a feedback-loop routine to ensure that the optogenetic activation is maintained in the specific area of interest.

7. IMMUNOFLUORESCENCE IN MICROCHANNELS

Chip design. To prevent cell clusters to be flushed out from non-adhesive PEG-coated microchannels during media exchanges, specific chips are designed with large channels surrounding the ones in which cell clusters are confined (**Figure 76**). Very gentle pressure must be applied to avoid pushing medium in the orthogonal confining channels. At this point, media are injected by hand with a Hamilton syringe. The flow could be better controlled with the use of pumps.

Cluster loading and monitoring migration. Microchannels and cell clusters are prepared as described above and concentrated to 4000-5000 cell clusters / 10 μ l in culture medium. After cell cluster filtration, 10 μ l of the suspension are injected through one of the central access holes at the concentration while the opposite central access hole is blocked (for example by a tip filled up to the filter). Medium is gently pushed or aspirated in the wide channels to remove excess clusters. Imaging can be performed over a few hours to monitor cell cluster migration, while reconstituting the whole field of view for better identification of cell clusters afterwards.

Fixation, permeabilization. After imaging, clusters are fixed as soon as possible. Culture medium is replaced in the well by PBS supplemented with calcium (0.1mM) and magnesium (1mM) (PBSCM), to preserve intercellular junctions (Zajac et al., 2018). Clusters are fixed with 4% PFA diluted in PBSCM by injecting 10 μ l

in each access hole at 2 μ l/s, 3 times. In collagen condition where clusters are attached, this slow injection is not necessary at any step: 30 μ l are injected per hole at once, gently. After fixation, calcium and magnesium are not required anymore. In order to optimise the permeabilization step, two detergents are combined: Triton X-100 and saponin. Triton X-100 contains uncharged hydrophilic head groups (polyoxyethylene), and extract lipids; being non-selective, it may remove proteins as well. Saponin selectively removes membrane cholesterol, which makes 100Å holes; thus, it does not affect nuclear and mitochondrial membranes. Clusters are permeabilised by injection of 10 μ l of the permeabilization solution (PBS, 1% Triton X-100, 0.5M Saponin, 4% BSA, 0.05% Azide, sterilised by filtration through a 0.2 μ m filter) in each access hole at 2 μ l/s, 5 times. Chips are incubated over night at room temperature.

Antibodies and dyes. Primary antibodies are diluted at 1/100 or 1/50 in the permeabilization solution and 10 μ l are injected in each access hole at 2 μ l/s. For thick samples, the duration of incubation is often enlarged up to a few days to allow for complete diffusion and penetration. Temperature can be increased to accelerate diffusion, some performing these steps at up to 37°C. In my hands, 37°C temperature increase did not improve significantly the stainings. Thus, primary antibodies are incubated over night at room temperature. Channels are washed twice with the permeabilization solution (10 μ l in each access hole at 2 μ l/s, 5 times) with 5min incubation for the first washing step and 1h for the second. Secondary antibodies (1/250), DAPI (1/50) and Phalloidin (1/1000) diluted in the permeabilization solution are injected like primary antibodies and incubated over night at room temperature. Channels are washed twice with the permeabilization solution (50 μ l in each access hole at 2 μ l/s) with 5min incubation for the first washing step and 1h for the second. PBS, 0.05% azide is then injected (50 μ l in each access hole at 2 μ l/s) and for conservation of the chip before imaging.

8. IMMUNOFLOUORESCENCE, ANTIBODIES, HISTOLOGY AND IMMUNOHISTOCHEMISTRY

Immunofluorescence. TSIP in Fig. 1b was fixed in 4% PFA after 24h of incubation in collagen-I. Cell clusters in fig. S1F were fixed in PFA 4% for 10min and embedded in a collagen-I gel before immunofluorescence, as described previously (Zajac et al., 2018). Images were acquired with a SpinningDisk CSU-W1 (Yokogawa) with a Zyla sCMOC camera driven by an Olympus X83.

Antibodies and dyes. Primary antibodies: anti-Integrin β 1 (P5D2, DSHB, deposited by Wayner, E.A. (DSHB Hybridoma Product), 1:500); pMLC T18/S18 (anti-phospho Myosin Light Chain T18/S19, Cell Signaling, 3674S, 1:100 or 1:200).

Secondary antibodies: anti-Mouse-FITC (Jackson ImmunoResearch, 711-545-152, 1:500), anti-Rabbit-Alexa Fluor 647 (Jackson ImmunoResearch, 715-605-152, 1:250 or 1:500).

Dyes: Alexa Fluor Phalloidin Rhodamine (Life Technologies, AF12415, 1:1000), Alexa Fluor Phalloidin 488 (Life Technologies, A12379, 1:1000), DAPI.

Histology and immunohistochemistry. CRC (micropapillary histotype) primary tumours obtained after surgical resection are formalin-fixed and paraffin embedded (FFPE) according to routine protocols. 3mm sections of FFPE samples are deparaffinized, unmasked (Ph8) and rehydrated prior to Hematoxylin Eosin Saffron (HES) staining or immunohistochemistry.

Immunohistochemistry. Sections are immunostained with Ezrin (BD Biosciences, 610603, 1:100) or CK20 specific mouse monoclonal antibody (clone Ks20.8, Dako, Glostrup, Denmark). Stainings are performed with Ventana BenchMark XT immunostainer (Ventana Medical Systems, Tucson, AZ) using an UltraView DABv3 kit (Ventana). The chromogene is 3,3'-diaminobenzidine (DAB) in all the stainings.

9. IMAGE ANALYSIS

Naming. “Speed” is computed as the average of the absolute values of every instantaneous displacement. “Velocity” is oriented and describes the final true displacement of objects: it is computed as the displacement vector between two time points or, by extension, as the algebraic displacement along one direction (usually X direction).

Analysis of cluster displacements from bright-field time-lapse sequences. For bright-field movies, displacement of clusters centroid is tracked every hour using the Manual Tracking plugin in Fiji. Clusters that are too small to be confined or dissociating during the experiment are ignored. Speed ($\mu\text{m}/\text{day}$) corresponds to the accumulated distance over 12 to 24h, extrapolated to 24h. *Persistence* is calculated as the ratio of Euclidean distance travelled by the cluster monitored every 1h for 1 day, over its total displacement. *Maximum speed* is calculated as the maximum instantaneous speed. *Maximum consecutive migration duration* is the longest period of continuous migration over 1px ($1.07\mu\text{m}$ or $1.369\mu\text{m}$) per hour. These three last metrics are calculated for clusters migrating more than $25\mu\text{m}$ per day.

Cell segmentation for cell tracking in optogenetic experiments. Movies are analysed using custom-built routines in Fiji ⁴⁶ and MATLAB (The MathWorks, Natick, MA). ARHGEF11-CRY2-mCherry signal is used to segment clusters by applying a gaussian filter and a threshold. Trajectories are then analysed in MATLAB, taking the displacement of the center of each segmented cluster along the microchannel. The beginning of the activation is considered as time 0 and origin of the position for all the trajectories. Trajectories are sometimes flipped to put all the activation on the same side (left side of the cluster).

Analysis of Paxillin foci. Paxillin images are treated with the Subtract background plugin, using a 2-pixels rolling ball. Threshold is then set to highlight and best separate all the foci. The area of each structure is collected using the Analyse Particles Fiji plugin, considering particles of 10-infinite sizes. The proportion of area covered by Paxillin foci is obtained by normalising the sum of Paxillin foci individual areas by the total area of the cluster.

Analysis of αV integrin (ITGAV) internalisation. To determine the endosomal fraction, the Transferrin images are thresholded to best delineate endosomes. The thresholded image is then used to create a mask that is transferred to the ITGAV image. The amount of ITGAV is calculated by summing the “Integrated intensity Value” of each ROI from the Transferrin image. The ITGAV image is then thresholded to determine the total amount of ITGAV. We then calculate the ratio of ITGAV signal contained in the Transferrin mask over the total ITGAV signal.

Analysis of beads displacements in TFM experiments. Time sequence images of fluorescent beads are aligned using the SIFT algorithm in Fiji (Lowe, 2004). Beads displacements between first and last time points are then calculated using the cross-correlation PIV plugin in Fiji (Tseng, 2011; Tseng et al., 2012). The heatmap of beads displacements is coded in MATLAB. *Maximum bead displacement* is computed as the mean of 0.2% highest displacement amplitudes (mean over at least 3 displacement vectors) from the PIV result on the entire image field. *Variation coefficient* is computed as the ratio of standard deviation of bead displacement amplitudes over their mean. It characterises the dispersion of the distribution of bead displacements by the cluster: the higher it is, the more localised beads displacements are. *Orientation of bead displacement vectors* is computed as the average of $\cos(\theta) = (\mathbf{u} \cdot \mathbf{v}) / (|\mathbf{u}| \cdot |\mathbf{v}|)$ where \mathbf{u} is the vector pointing from the cluster centroid (computed using ROI analysis in Fiji) to the coordinates of each bead, \mathbf{v} is the bead displacement vector, and $|\mathbf{u}|$ (resp. $|\mathbf{v}|$) is the amplitude of \mathbf{u} (resp. \mathbf{v}) vector. Traction forces exerted by clusters on the beads lead to a $\cos(\theta) > 0$, whereas $\cos(\theta) < 0$ corresponds to pushing forces. On PEG-coated substrates, small pushing forces can be detected, probably due to the light confinement by the agarose pad.

Analysis of MLC and actin polarisation. Direction of migration for each cluster is determined by tracking its movement for at least 2h prior to fluorescence imaging. Myosin and actin are imaged in a median section of the cluster using a spinning disk fluorescence microscope. For analysing the intensity at the cortex, a 20-pixel Subtract background is performed before using a 15 pixels wide line scan to delineate the cortex and measure myosin intensity signal in each halves of the cluster. The intensity in each half is normalised to the perimeter of the line scan to calculate the rear to front ratio (Raw Integrated Density over Perimeter).

Myosin flow analyses. Myosin flows are analysed from movies of median sections of HT29-MTX clusters stably expressing mTurquoise-Myosin Light Chain (MLC) using a custom-built routine in Fiji (Schindelin et al., 2012) and MATLAB (The MathWorks, Natick, MA). Images are acquired every 1 to 5 min during 20min to 7.4h and the MLC channel is used to map actomyosin flow dynamics in clusters. Background contribution is removed using a custom-built macro in Fiji before Particle Image Velocimetry (PIV) analysis. A bounding rectangle is adjusted to the cluster shape at every time point to obtain the cluster centroid positions. The Stramer Lab (King's College London, UK) PIV package, developed in MATLAB (Yolland et al., 2019), is used to extract maps of myosin flow velocity vectors from the median section of clusters. The size of objects to be tracked is 4 μm (50% wider than the cluster cortex) and the size of the analysis window is the value of the mean displacement of myosin between two consecutive frames (5 to 7 μm).

A MATLAB code was developed to display and exploit the PIV analysis. Mean PIV map of myosin flows of all clusters was obtained in two steps: i) averaging over time the PIV maps of individual clusters, centered around a reference position and ii) averaging the time-averaged PIV maps over the clusters. This leads to a time-average mean PIV map, averaged over the whole population of clusters considered. Myosin flow kinetics are extracted at every time point from observation windows in contact with the channel walls (both clusters sides): these windows are 15 μm wide, and we chose for each cluster at what distance to the ends of the cluster (front and back) they start and finish, to avoid considering the curvature of the clusters that is not in contact with the channel walls (**Figure 81e**). In the cluster reference frame, for each cluster i , the amplitude of the fluctuations of myosin speeds (along x axis only, $fluct_i$) are calculated by subtracting the average velocity of myosin flows at the contact (averaged over space and time, \bar{v}_x) to the instantaneous velocity of myosin of each pixel n ($v_{x,n}(t)$), and taking the absolute value of this quantity. These fluctuations are then averaged over space and over time for each cluster.

$$fluct_i = \frac{1}{ttot} \sum_{t=1}^{ttot} \frac{1}{ntot(t)} \sum_{n=1}^{ntot(t)} abs(v_{x,n}(t) - \bar{v}_x)$$

Analysis of myosin flows in single cells. HT29-MTX single cells are tracked every 21s to 27s during 7min to 37min. For 4 cells expressing mTurquoise-MLC, several myosin particles (4 to 7) are tracked manually as well in the lab reference frame every 21s or 27s using the Manual Tracking plugin in Fiji. Before PIV analysis in the cell reference frame, images are realigned on the first image using the template matching plugin with the option of slices alignment and background contribution is reduced with a custom-built macro in Fiji similar to the clusters'. PIV analysis is then performed in MATLAB with the Stramer Lab (King's College London, UK) PIV package (Yolland et al., 2019).

Analysis of nuclei movements. For H2B-RFP-expressing HT29 clusters, nuclei of a median section are imaged every 15 min to 1h for 8 to 24h, manually tracked every 1h in the lab reference frame and displayed using MTrackJ (Meijering et al., 2012) Fiji plugin. Centroids of clusters are tracked as well with Manual Tracking plugin. A custom-made R code was used for further analysis and graphical representations. Nuclei velocities are extracted at every time point from observation windows in contact with the channel walls (both clusters sides) that are a cell width-wide (12 μm), and start and finish 12 μm away from each end of the clusters (front and back) to avoid considering cells not in contact with the channel walls. In the cluster

reference frame, for each cluster i , the fluctuations of nuclei speeds (along x axis, $fluct_i$) are calculated like the fluctuations of myosin flow speeds (see *Myosin flow analyses*), by subtracting the average velocity of lateral nuclei (averaged over nuclei and time, $\overline{v_x}$) to the instantaneous velocity of each nucleus n ($v_{x,n}(t)$), and taking the absolute value of this quantity. These fluctuations are then averaged over nuclei and over time for each cluster.

Automated segmentation and tracking of cell clusters in microchannels. A manual segmentation of clusters in bright field images is used to train a deep learning model in TensorFlow. This model then allows automated segmentation of clusters on new images, followed by a small post-processing of the masks. The tracking is then performed in R software v3.6.1 (trackParticles, trackdem_0.5.2) with a quality control: link to maximum 4 subsequent frames, cluster present on at least a quarter of total frames, removal of outliers in cluster size. When a cluster is not detected on some frames, the displacement is linearised between the frames where it is detected. The following parameters are then computed for each cluster, and averaged per experimental condition: area, circularity, speed, persistence, number of timepoints.

10. ORGANOID POLARITY REVERSION AND DRUG TESTING

Collagen embedding. Organoids are prepared as described above (see *Tumoroids generated from Patient-Derived Xenografts (PDX)*). After 3 days in suspension, they are filtered on a 70 μ m cell strainer. Collagen-I (Corning, 354236) is neutralized with 1.0 M NaOH and 10x MEM (Life Technologies, 21430-02) according to the ratio: 1.0:0.032:0.1 (vol/vol/vol). The concentration is then adjusted to 2 mg/ml with DMEM 1X. Organoids are placed in this collagen-I mix and evenly distributed in a 48-wells NUNC plate (ThermoFisher, #150687) using the Integra Assist Plus. The gel is allowed to polymerize for 45 min at 37°C. Organoids are then cultured in culture medium supplemented with FBS 10 %.

Polarity reversion. Polarity reversion is obtained by incubating organoids with Y27632 or AIB2 on PDX#1 and PDX#3 respectively. The drugs are diluted in the media as followed: AIB2 (DSHB, AB_528306), Y27632 (Calbiochem, 688000, 25 μ M).

Chemotherapy test. After polarity reversion is achieved, the medium is withdrawn and drugs are added using the Tecan D300e (software: D300e control version3.4.1) as follows: 5-Fluorouracil, Oxaliplatin and Irinotecan at the IC70 determined on CRC organoids. Control conditions are obtained using DMSO.

Viability test. After 2 days, viability is assessed using CellTiter-Glo 3D according to the manufacturer's instructions and bioluminescence is measured with the BioTek Synergy LK (software: Gen5TM version 3.10) in white-bottom 96-well plates.

The ATP bioluminescence signal was averaged over the 3 wells of the same condition in the apical-in or apical-out topology. This provided ATP (Chemo A-in) or ATP (Chemo A-out) values when organoids were treated with a chemotherapeutic agent, and ATP (Ctrl A-in) or ATP(Ctrl A-out) in control condition.

Viability in apical-in and apical-out topologies were then calculated as follows:

$$\text{Viability A - in} = \frac{\text{ATP(Chemo A - in)}}{\text{ATP(Ctrl A - in)}} \quad \text{and} \quad \text{Viability A - out} = \frac{\text{ATP(Chemo A - out)}}{\text{ATP(Ctrl A - out)}}$$

Finally, the ratio between apical-in and apical-out topologies was calculated as:

$$\text{Viability Ratio} = \frac{\text{Viability A - out}}{\text{Viability A - in}}$$

Chapter IV. Polarised contractile jiggling drives the collective amoeboid migration of cell clusters

This first study follows the discovery of TSIPs in mucinous colorectal cancer (MUC CRC) patients, i.e. tumour cell cohorts that efficiently seed metastases and appear to migrate collectively in an unconventional fashion. Here, we aimed at deciphering the mechanisms underlying this focal adhesion-independent collective mode of migration, which is displayed in various types of cancers.

Most of the work I present here has been submitted for publication and a part is also published on bioRxiv (Pagès et al., 2020) (see **Annex 1**).

1. CELL CLUSTERS MIGRATE IN CONFINED NON-ADHESIVE ENVIRONMENTS

To study focal adhesion-independent mode of migration, we were inspired by the systems used for promoting and studying amoeboid migration in single cells (Liu et al., 2015). These systems, such as cell confiners and microchannels, confine cells and maintain contact between cell membrane and the substrate. This is necessary as amoeboid cells would not strongly attach on 2D substrates and be transported by fluid flows. In addition, in single cells, confinement promotes amoeboid migration even in mesenchymal cells, by increasing single cell contractility (Liu et al., 2015). The surface can then be passivated thanks to coatings such as polyethylene glycol (PEG): PEG creates a small liquid film between cells and their substrate, preventing focal adhesion formation.

Therefore, we engineered microchannels devoid of any physiological substrates or chemotactic cues but coated with the anti-adhesive PEG (**Figure 67a**). Their dimensions were adapted to confine TSIPs and cell clusters from our CRC cell lines. We also designed chambers, confining cell clusters between two planes. I then controlled the low adhesiveness provided by PEG coating by comparing a gentle flushing of cell clusters in collagen-coated versus PEG-coated channels (**Figure 67b**).

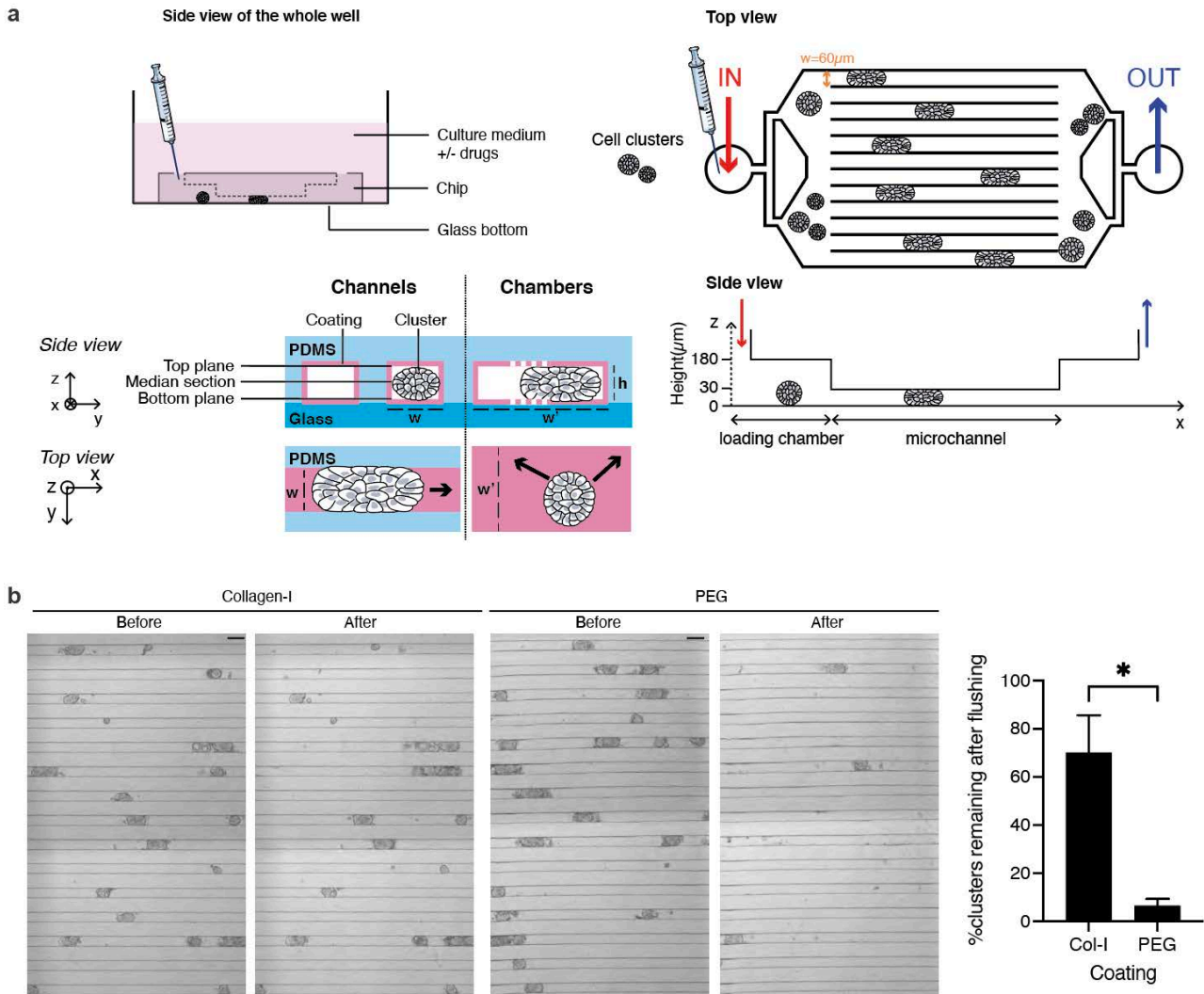


Figure 67. Non-adhesive environments to study collective migration.

a, Design of microchannels and chambers. Top left and right: Schematic representation of experimental setup. Bottom left: Schematic representation, not to scale, of microchannels and chambers (width: $w=60\mu\text{m}$; $w'=500\mu\text{m}$; height: $h=30\mu\text{m}$). **b**, Gentle flushing of cell clusters in collagen-I-(Col-I)- or PEG-coated microchannels. Left: bright field images before and after flushing. Scale bar, $100\mu\text{m}$. Right: quantification of the proportion of cell clusters not removed by the flushing. Mean \pm standard error of the mean (s.e.m). $n=3$ independent microfluidic chips containing both conditions (Student's t-test).

Given that TSIPs migrated around $50\mu\text{m/d}$ in collagen gels (**Figure 65**), time-lapse imaging was performed during 20 to 24 hours. It revealed TSIPs were able to migrate collectively into non-adhesive microchannels (**Figure 68a**).

Wondering whether this ability to migrate in these environments was related to TSIPs intrinsic properties, I observed the behaviour of PDX#3 organoids known to change their apico-basal polarity when embedded in collagen. Interestingly, they were also able to migrate in these non-adhesive microchannels, indicating that this feature is thus not restricted to TSIPs (**Figure 68b**).

This mode of migration was eventually enabled by TSIPs and fresh cell clusters collected from patient peritoneal effusions or formed from patient-derived xenografts (PDXs), and in a variety of digestive and genitourinary cancers, with some reaching speeds of up to 2mm/d (**Figure 68b,c**). It was also recapitulated

by clusters made from cell lines from several types of cancers, including circulating tumour cells (**Figure 68b,c**).

To identify whether this mode of migration was cancer specific, I explored the migration of organoids made from primary specimens of healthy colon tissue from two patients. They also migrated collectively, and fast, in these PEG-coated microchannels (**Figure 68b,c**). Of note, the cancer PDXs and healthy patient samples displayed similar heterogeneity, as represented by the distribution of cluster speeds (**Figure 68d**). Speed distribution of clusters from cell lines was much thinner, confirming with the loss of heterogeneity in these biological models.

Together, these data suggest that this mode of migration could be another general feature of cells that tumours hijack during their collective dissemination.

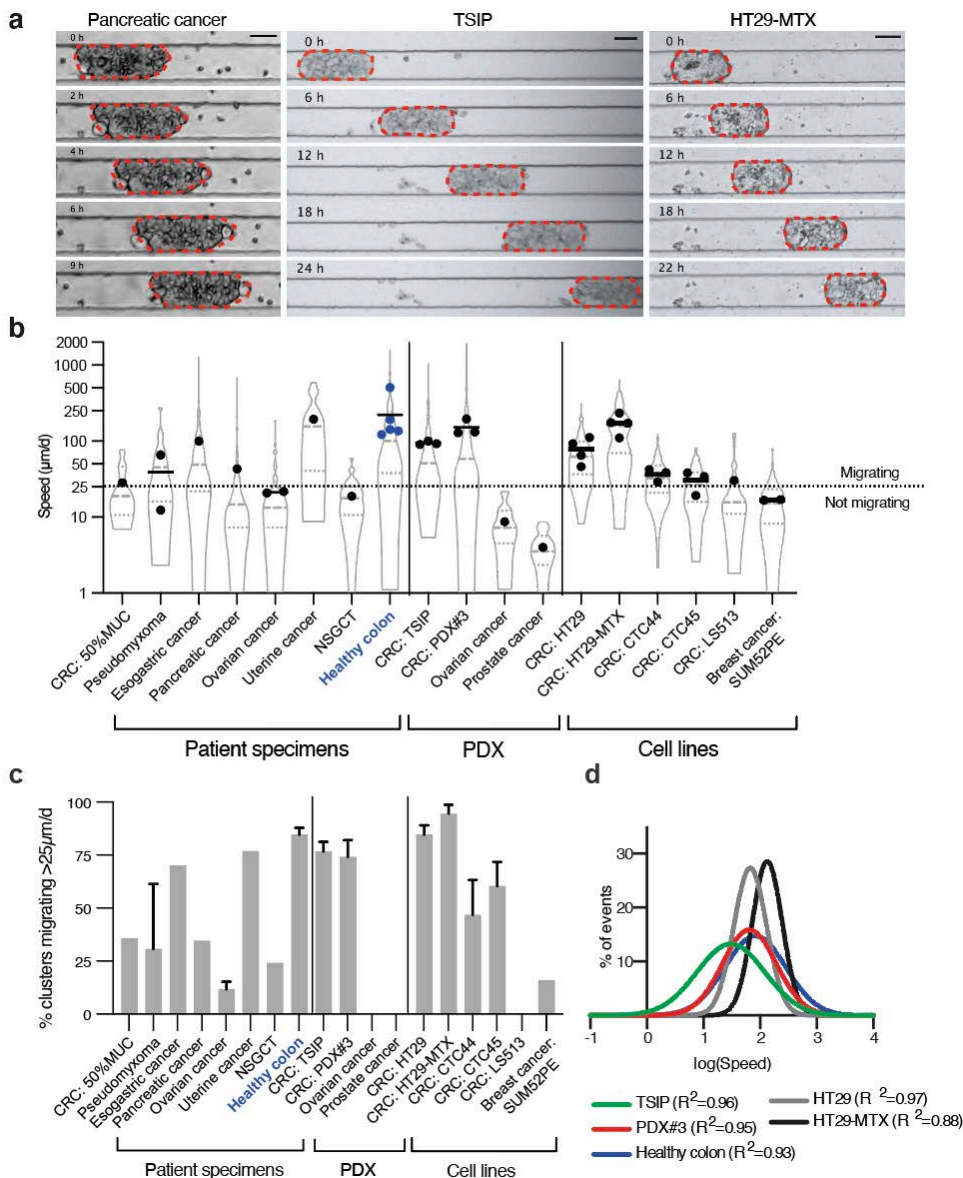


Figure 68. Cell clusters from a variety of transformed and non-transformed cell types migrate collectively in non-adhesive microchannels.

a, Representative time-lapse sequences of the migration pancreatic cancer cell clusters, TSIPs and HT29-MTX cell clusters. Scale bar, 50 μm; **b**, Mean instantaneous migration speed of diverse types of

tumour clusters from patients (CRC: colorectal cancer, NSGCT: nonseminomatous germ cell tumour), Patient-derived Xenografts (PDXs) and cell lines (CTC: circulating tumour cells). Log10-scale. Dots are the mean speed over clusters for each independent experiment; lines are means over experiments. **c**, Proportion of migrating clusters (above 25 $\mu\text{m}/\text{d}$) of each cell type. Error bars are s.e.m. For b,c, n=14 to 153 clusters per cell type. **d**, Gaussian fit of the distribution of cluster migration speeds for different models.

I investigated the impact of small geometrical changes on cell clusters migration to identify an optimal setting. For a similar confinement, clusters migrated at the same speed independently from the shape of the channels, with a square or a rectangular section (**Figure 69a**). When confined between two planes only, in “chambers”, cell clusters migrated as well, in the two dimensions and even faster than in the one-dimensional microchannels (**Figure 69b**).

30x60 μm^2 section microchannels were chosen for further investigations, for they provide more cluster surface and thus more information on a horizontal imaging plane than 40x40 μm^2 . They also allow easier monitoring of the migration than chambers by limiting its dimension to a 1D track.

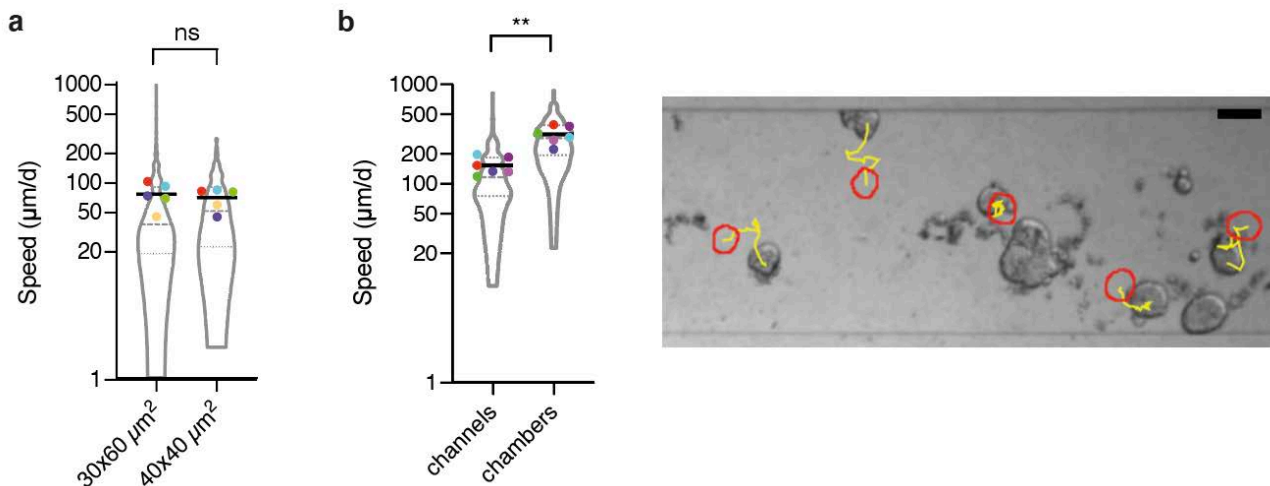


Figure 69. Cell clusters migration in other geometries.

a, TSIP (red), HT29 (green) and PDX#3 (purple, yellow) migration in square section channels (40x40 μm^2). **b**, HT29-MTX cell clusters migration confined between two planes in chambers. Left: mean migration speed. Right: representative displacements of cell clusters in chambers; red: initial position; yellow: track over 13.5h every 30min; scale bar, 100 μm . Superplots are described in the Material & Methods section: briefly, violin plots display the whole population of clusters; dots of the same colour represent the mean of the matched control and experimental conditions performed in each individual experiment; the black line is the mean of all experiments for each condition. Superplots are described in the Material & Methods section.

I also investigated whether cluster size impacted their speed, by quantifying their aspect ratio (length over width). Once confined into microchannels, small HT29-MTX clusters migrate as fast as the up to 3-fold larger ones (**Figure 70a,b**). Conversely, no difference was observed in the average aspect ratio of TSIPs and HT29-MTX, while the first migrate much less than the last (**Figure 68b, Figure 70c**). This indicates that in these conditions, migration speed is not significantly impacted by size of cell clusters.

Given that small and large cluster are confined in microchannels of the same dimensions, their size indicates their level of confinement: the largest are more deformed and confined than the smallest. However, the fact that increased confinement is not correlated with their migration speed seemed in disagreement with what is described for single cells (Liu et al., 2015). I suspected that in clusters, individual cell did not undergo a confinement proportional to the cluster they compose, e.g. because of internal cell

reorganisation. Thus, I quantified confinement at the single cell scale in clusters through measurement of nuclei shape. Nuclei deformation was not correlated with cluster deformation, suggesting that indeed, the level of confinement of the cluster does not affect individual cell confinement (**Figure 70d**). It may rather induce a reorganisation of the cells relative to each other in clusters.

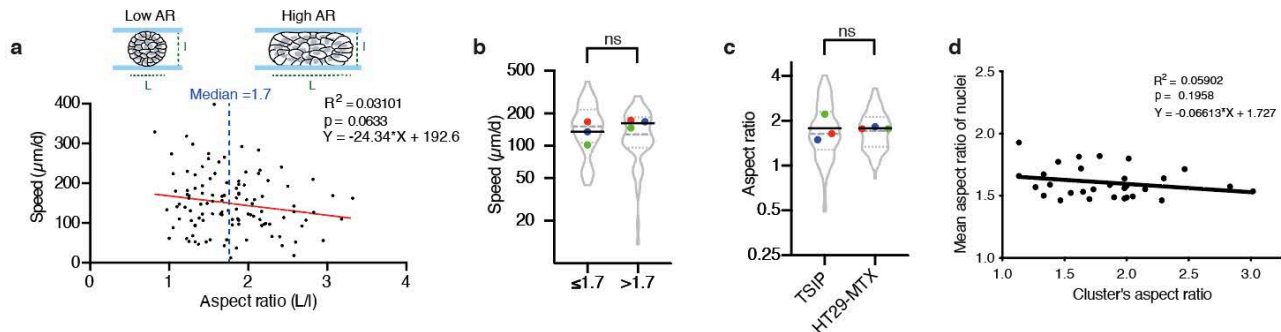


Figure 70. Clusters confinement is not related with migration speed.

a, Speed and aspect ratio (AR) of HT29-MTX clusters migrating one day in PEG-coated microchannels. $n=112$ clusters from 3 independent experiments. Line: linear regression. **b**, Comparison of the speed of HT29-MTX clusters migrating one day in PEG-coated microchannels, depending on their aspect ratio (relative to median $AR=1.7$, illustrated in **a**), log₂-scale. $n=112$ clusters from 3 independent experiments (Mann-Whitney test). **c**, Aspect ratio of TSIP and HT29-MTX cell clusters migrating one day in PEG-coated microchannels, log₂-scale. $n=112$ or 162 clusters from 3 independent experiments (two-tailed Student's *t* test). **d**, Mean aspect ratio of nuclei and HT29-MTX clusters' aspect ratios with linear regression. $n=30$ clusters from 3 independent experiments (26 nuclei per cluster on average) ns, not significant. Superplots are described in the Material & Methods section.

We further analysed the migration characteristics of cell clusters from pancreatic (patient ascites) or colorectal cancer (TSIPs from PDXs and HT29-MTX cell line). They migrated in any direction (left or right), confirming that their migration in our system was not biased by macroscopic gradients or flows of medium (**Figure 71a**).

On average, these clusters migrated consecutively for about 6 hours (up to 19h), with a persistence of 0.66 ± 0.04 and 0.75 ± 0.01 for TSIPs and HT29-MTX respectively (mean \pm SEM) (**Figure 71b-d**). They reached a maximum instantaneous speed of $21.7 \pm 0.7 \mu\text{m/h}$ (TSIPs) and $26.5 \pm 2.5 \mu\text{m/h}$ (HT29-MTX) (**Figure 71e**). Average speeds were $174 \pm 25 \mu\text{m/d}$ for HT29-MTX and $95 \pm 3 \mu\text{m/d}$ for TSIPs (**Figure 71b**). Although quite slow when compared to single cell migration in experimental settings, this speed is in the order of magnitude of collective migration speeds reported in vivo (Krnđija et al., 2019; Weigelin et al., 2012). TSIPs and HT29-MTX were chosen for further mechanistic studies, the latter allowing easier expression of fluorescent probes.

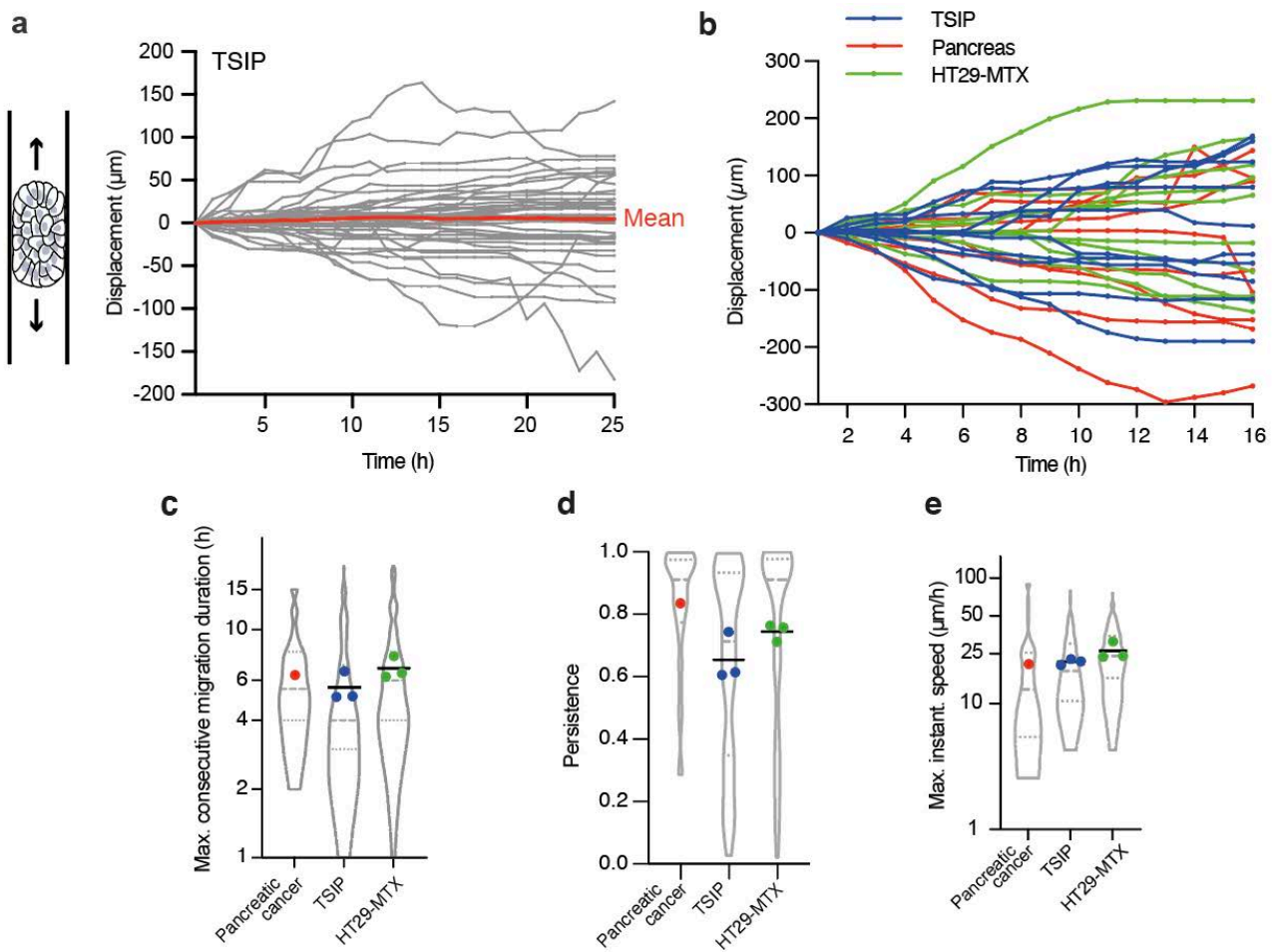


Figure 71. Characteristics of collective migration in PEG-coated microchannels.

a, Isotropic displacements of TSIPs in microchannels illustrate the absence of fluid flow. Bold red line: mean. **b**, Representative tracks of clusters migrating in one direction (positive numbers) or the other (negative numbers). $n=9$ to 10 representative clusters of each cell type. **c,d**, For clusters migrating significantly ($>25 \mu\text{m/d}$), duration of the longest period of consecutive migration (j, log₁₀-scale) and persistence (k). $n=38$ to 107 clusters. **e**, Maximum instantaneous (Max. instant.) speed of clusters, log₁₀-scale. For c-e, clusters migrate one day in PEG-coated microchannels. Superplots are described in the Material & Methods section.

Given the ability of these cancer cells clusters to migrate in PEG-coated channels, we first investigated whether this mode of collective migration occurred independently from the formation of strong attachment to the substrate (such as focal adhesions). Indeed, despite the presence of the non-adhesive PEG coating, cell clusters could either degrade it, deposit extracellular matrix on top of it, or use any other way to migrate in a conventional traction-based mechanism.

2. FOCAL ADHESIONS AND TRACTION FORCES ARE NOT REQUIRED FOR CLUSTER MIGRATION

Looking at cluster morphology, we found that migration in PEG-coated microchannels is associated with a compact rounded morphology that contrasts with the loose and spread shape observed when microchannels are coated with collagen-I (**Figure 72a**).

2. Focal adhesions and traction forces are not required for cluster migration

In single cells, adhesive migration is usually related to a protrusive “wetting” morphology, characterised by high contact angles with the substrate, while non-adhesive amoeboid migration is associated with a “dewetting” round morphology, like water drops on a waterproof surface (Paluch et al., 2016). Measuring the contact angles between the cluster boundaries and the microchannel walls highlighted the “dewetting” morphology of the clusters and the absence of protrusions for HT29, HT29-MTX and TSIPs migrating in PEG-coated microchannels, as opposed to the “wetting” morphology of HT29 in collagen-I(col-I)-coated conditions (**Figure 72a,b**).

Of note, contrary to most single cell and collective migration modes, no polarised morphology could be identified during cluster migration. I evaluated the presence or not of this asymmetry by quantifying the area of the convex ends of cell clusters (**Figure 72c**). The area between the front and back of migrating clusters was similar to the left and right sides of static clusters (**Figure 72d**). In addition, the asymmetry between front and back of migrating clusters (evaluated by the ratio between the smallest and largest convex areas) was similar to the asymmetry of both sides in static clusters (**Figure 72d**).

These results indicate that cell clusters do not display a protrusive activity while migrating in PEG-coated channels.

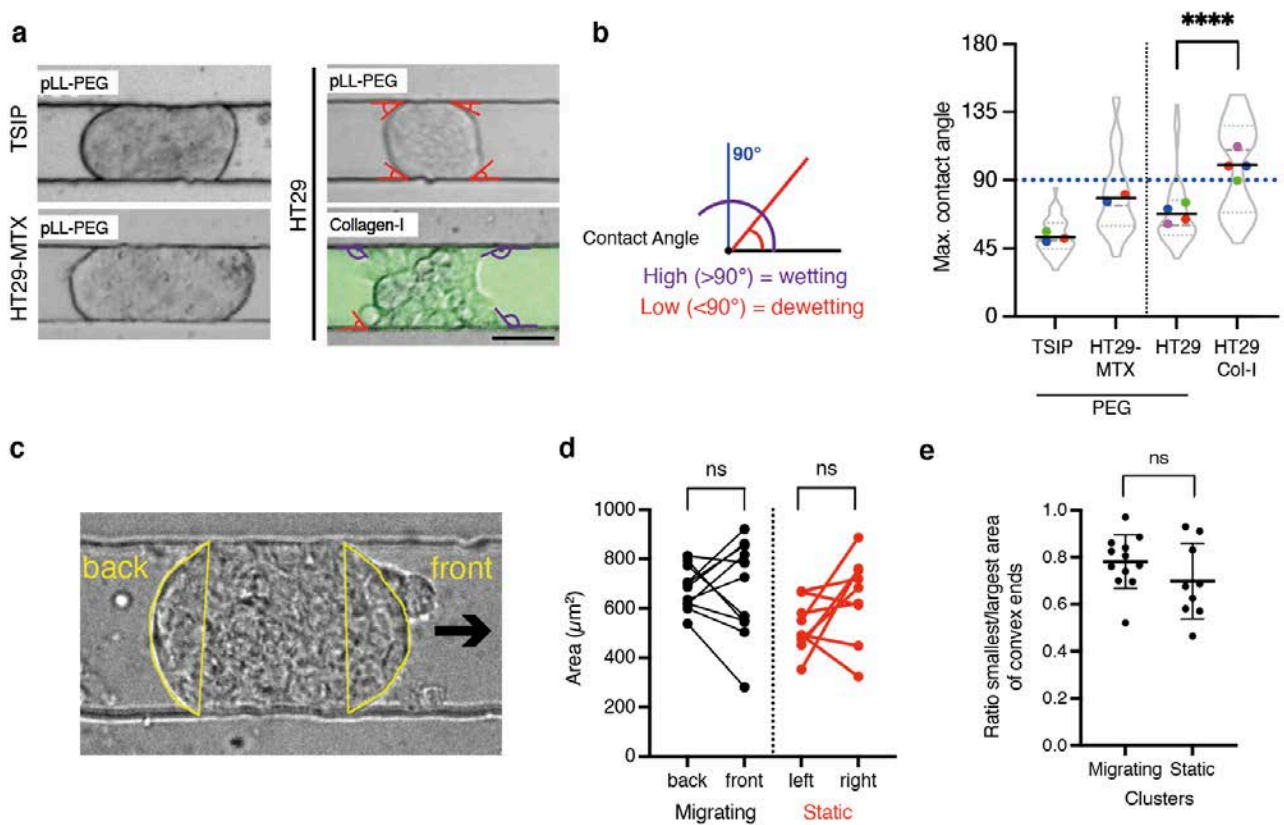


Figure 72. Clusters display no protrusive activity when migrating in PEG-coated microchannels. **a,b**, Representative images (**a**, scale bar: 50 μm) and maximum (Max.) contact angle quantification (**b**) for clusters migrating in PEG- or Cy5-collagen-I(Col-I)-coated microchannels. Wetting or dewetting contact angles are represented on HT29 clusters (**a**) and as a schematic representation (**b**, left). **b**, $n=39$ to 59 clusters (Mann-Whitney t-test). **c-e**, Areas of the convex ends of HT29-MTX clusters (**c**, yellow). ns, not significant, **** $P<0.0001$. Superplots are described in the Material & Methods section.

We then explored more precisely the contribution of focal adhesions to cluster migration in non-adhesive channels, and the subsequent traction forces that cell clusters could exert on their environment.

Concerning TSIPs, as presented in introduction, they are known to segregate their integrins at their basolateral pole, away from the surrounding ECM (**Figure 73a**). Therefore, contrary to normally polarised epithelial clusters such as PDX#3 organoids, they hardly interact with ECM and exert very low traction on collagen fibres when embedded in collagen-I gels (**Figure 73b**). Consequently, it is very unlikely that they would form focal adhesions on PEG-coated surfaces.

Of note, I observed a remaining level of interaction between collagen and TSIPs, highlighted by injecting TSIPs in microchannels filled with polymerised collagen-I (**Figure 73c**). This resulted in fast migration when it occurs on one side only, while clusters stall when there is competition between both sides (**Figure 73c,d**). Therefore, even if focal adhesion pathway did not result in loss of migration in 3D matrices (**Figure 65**), we cannot exclude that a minimal level of interaction has the potential to contribute to their migration in 3D. This will be discussed in **Chapter IV**.

We also expressed fluorescent-tagged paxillin in HT29 and HT29-MTX. While it revealed numerous paxillin foci on the collagen-I-coated surface, they were nearly absent in PEG-coated microchannels (**Figure 73e,f**). In addition, the collagen-I coating reduced HT29-MTX migration speeds from $264.6 \pm 14.95 \mu\text{m/d}$ to $92.76 \pm 15.89 \mu\text{m/d}$, in line with observations made from single cells where focal-adhesion-dependent migration is slower than amoeboid migration (Liu et al., 2015) (**Figure 73g**). Similarly, it decreased significantly the migration of HT29 cell clusters, that also displayed focal adhesions observed by Paxillin foci (not shown). On the contrary, TSIP migration was unchanged, consistent with an absence of focal adhesion formation.

To confirm functionally that focal adhesion pathway was not at play in this mode of migration, we inhibited two of the main regulators of focal adhesions, FAK and Src, using different pharmacological inhibitors (respectively PF271 and SU6656 or Saracatinib). They inhibited focal adhesion formation in collagen-I-coated microchannels (**Figure 73h,i**). These treatments did not slow down the migration of HT29-MTX clusters in non-adhesive microchannels (**Figure 73j,k**).

Together, these data indicate that when migrating in PEG-coated microchannels, cell clusters do not use the conventional focal adhesion pathway.

2. Focal adhesions and traction forces are not required for cluster migration

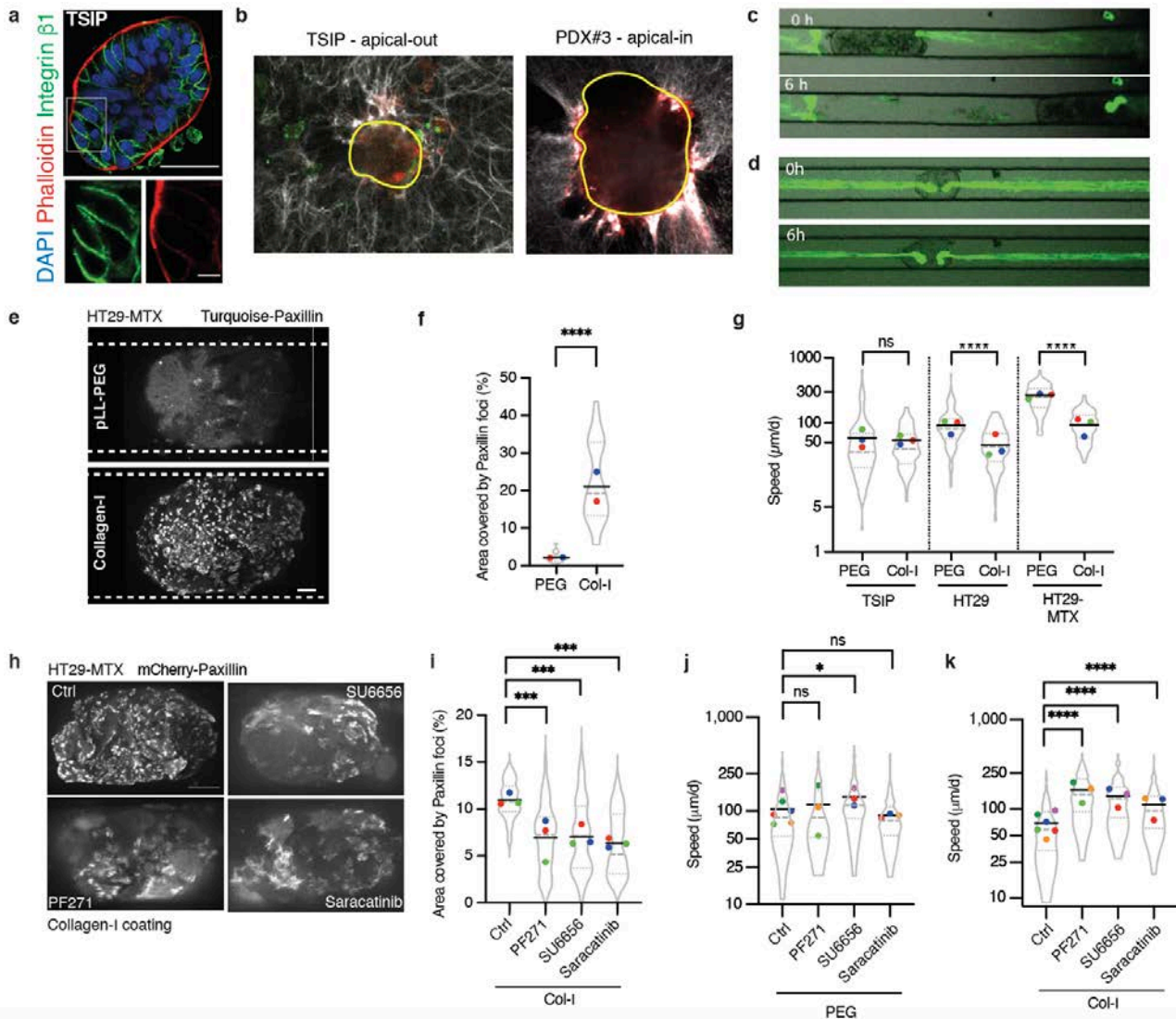


Figure 73. Collective migration in PEG-coated microchannels does not depend on focal adhesion formation.

a, Immunofluorescence of a transverse section of TSIP#1 stained after 24h in collagen-I for integrin $\beta 1$ (green), filamentous actin (Phalloidin, red), and nuclei (DAPI, blue). The boxed region is shown at high magnification. Scale bars, 50 μm (low mag.); 10 μm (high mag.). **b**, Representative of TSIPs (inverted apical-out polarity) and PDX#3 organoids (normal apical-in polarity) embedded in fluorescent collagen-I matrix (white). PDX#3 bundle and pull on collagen fibres (white bundles) much more than TSIPs. Red: $\beta 1$ integrins were stained by immunofluorescence without permeabilization to reveal only the ones present in contact with the substrate. Yellow: shape of the cluster. **c, d**, Representative images of TSIPs in microchannels filled with fluorescent collagen-I gels that are able to grab collagen fibres and migrate (c) or not (d). **e, f**, Representative images of the bottom plane (e, scale bar: 10 μm , bottom plane represented in **Figure 67a**) and quantification of the area covered by Paxillin foci (f, n=19 to 28 clusters, Mann-Whitney t-test) for HT29-MTX clusters stably expressing mTurquoise-Paxillin in PEG- or Col-I-coated microchannels. **g**, Mean instantaneous speed of cell clusters in PEG- or collagen-I-coated microchannels. n=90 to 166 clusters, two-tailed Student's t-test **h, i**, Representative images of the bottom plane (h, scale bar: 20 μm) and quantification of area covered by Paxillin foci (i, n=30 clusters, one-way ANOVA) of HT29-MTX clusters stably expressing mCherry-Paxillin and migrating in Col-I-coated microchannels. **j, k**, Mean instantaneous speed of HT29-MTX clusters treated with PF562271 (PF271), SU6656 or Saracatinib in PEG-coated (j) or col-I-coated (k) microchannels (n=70 to 182 clusters, one-way ANOVA). ns, not significant, *P<0.05, **P<0.01, ***P<0.001, ****P<0.0001. Superplots are described in the Material & Methods section.

In addition, we performed interference reflection microscopy (IRM) and traction force microscopy (TFM) experiments to analyse the interaction between the clusters and the channels more exhaustively, without selecting specific molecular players as above.

In both adhesive and non-adhesive conditions, the confined clusters press against the substrate. IRM allows to identify regions of tight contact, where interference are destructive (black areas), and regions where the plasma membrane stands further away from the coverslip, resulting in constructive interference (grey/white areas) (Cardoso Dos Santos et al., 2016; Verschueren, 1985). In collagen-coated channels, we detected very dark areas due to the presence of focal adhesions. I quantified the variation coefficient of the interface between the cell cluster and the substrate (standard deviation over mean intensity): a high variation coefficient indicated high contrasts, while a low variation coefficient indicates diffuse objects. This revealed that the contact area is much more homogenous on PEG than on collagen-I (**Figure 74a,b**). This is consistent with the presence of strong focal adhesions in collagen-I-coated microchannels, as opposed to a more homogeneous contact in PEG-coated microchannels. Together, these data confirmed that clusters interact differently with PEG and collagen-I coated surfaces.

Traction force microscopy then allowed to compare the forces exerted by cell clusters on adhesive and non-adhesive surfaces (Roca-Cusachs et al., 2017). To perform traction force microscopy experiments, we deposited clusters on collagen- or PEG-coated soft PDMS substrates in which fluorescent beads were embedded (Bergert et al., 2015). As clusters do not adhere on PEG-coated substrates, we added an agarose pad on top to maintain them in close contact (**Figure 74c**). Measuring the orientation of beads displacements revealed that clusters exert no traction forces on PEG-coated PDMS substrates compared to forces exerted on collagen-I coated substrates (**Figure 74d-f**). In addition, bead movements were of higher amplitude on collagen-coated substrates, as opposed to localised pulling forces observed on collagen-I-coated PDMS substrates (**Figure 74g,h**).

Overall, these results indicate that in non-adhesive microchannels, collective migration does not rely on focal adhesion formation, nor close localised contacts with the substrate, nor forces exerted on their environment comparable to conventional traction-based single cell or collective migration.

2. Focal adhesions and traction forces are not required for cluster migration

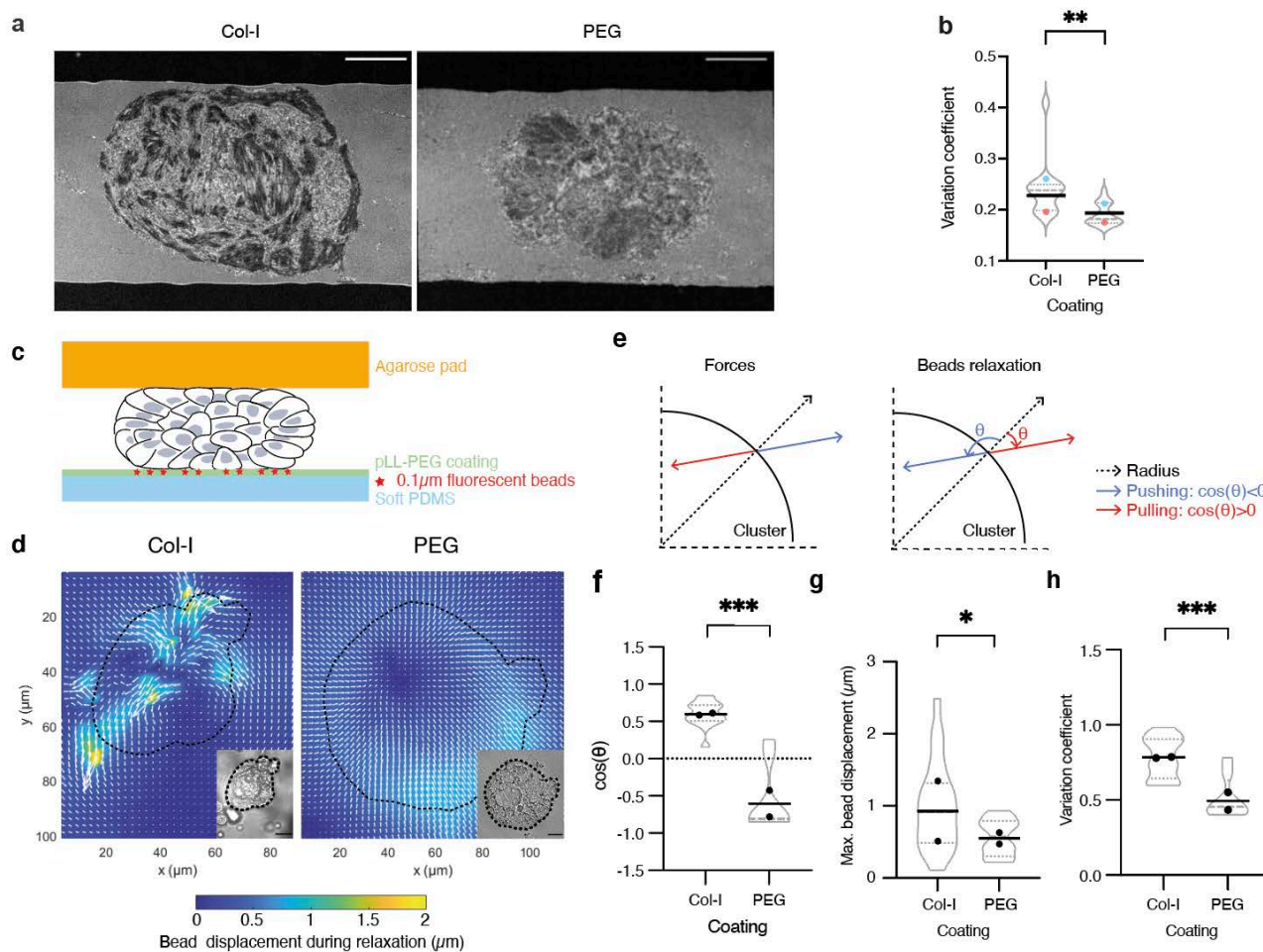


Figure 74. Clusters do not form focal contacts on PEG substrates, nor do they exert traction forces.

a, Interference reflection microscopy of the bottom plane of HT20-MTX cell clusters in collagen-I (Col-I)- or PEG-coated microchannels. Scale bar, 20 μm . **b**, Variation coefficient (=SD/mean, see Methods) of IRM intensity. $n=13$ (Col-I) and 34 (PEG) clusters from 2 (Col-I) and 3 (PEG) experiments. **c**, Schematic representation of the experimental design for traction force microscopy (TFM) on a PEG-coated substrate. The agarose pad is necessary to prevent the clusters from floating, whereas it is not needed on a Col-I-coated substrate. **d**, PIV maps of TFM measurements (beads displacements following SDS-mediated relaxation) on Col-I- or PEG-coated substrates. Scale bars, 20 μm . **e**, Orientation of forces exerted by clusters: schematic representation of the angle θ formed between a radius of the cluster and bead's displacement vector for calculation of $\cos(\theta)$. A positive value is measured when the cluster pulls on the substrate, whereas a negative value is measured when the cluster pushes. **f**, Orientation of forces exerted by clusters: $\cos(\theta)$, θ being the angle formed between a radius of the cluster and bead displacement vector. The value is positive when the cluster is pulling on the substrate, negative when it is pushing. $n=8$ (PEG) to 14 (Col-I) clusters (Welch's t test). **g**, Maximum (Max.) bead displacement (averaged on the 0.2% highest for each cluster) measured by TFM on Col-I- or PEG-coated substrates. **h**, Variation coefficient (= SD/mean, see Methods) of beads displacements for each condition describes the distribution of displacements in each condition: the higher it is, the more localised beads displacements are. For g,h, $n=22$ (Col-I) and 8 (PEG) clusters from 3 and 2 independent experiments respectively. * $P < 0.05$, ** $P < 0.01$, *** $P < 0.001$ (Welch's t tests). Superplots are described in the Material & Methods section.

In absence of traction forces, we investigated the role of friction forces, which are suggested to promote single cell amoeboid migration (Bergert et al., 2015). Increasing non-specific friction forces using BSA speeded-up migration by up to 56%, indicating that friction forces promote this mode of migration (**Figure 75a**).

While integrins are essential components of focal adhesions, they also have alternative functions by transmitting propelling friction forces against the substrate during single cell amoeboid migration (Bergert et al., 2015; Reversat et al., 2020). Inducing integrin internalisation with a cyclic-RGD peptide (cilengitide, cRGD) decreased migration speed in PEG-coated channels by 1.8-fold (**Figure 75b,c**). Similarly, using a small molecule inhibitor (SB273005), inhibiting $\alpha\beta3$ and $\alpha\beta5$ integrins, decreased migration by 3.2-fold. On the contrary, increasing friction forces (BSA coating) partially rescued the migration of clusters treated with cRGD peptides (**Figure 75d,e**) (Bergert et al., 2015).

These results indicate that, unlike traction-based collective migration (Friedl and Gilmour, 2009; Mayor and Etienne-Manneville, 2016; Shellard et al., 2018), clusters rely on friction forces to migrate without focal adhesions in non-adhesive microchannels, and integrins are likely to play a role in exerting these friction forces.

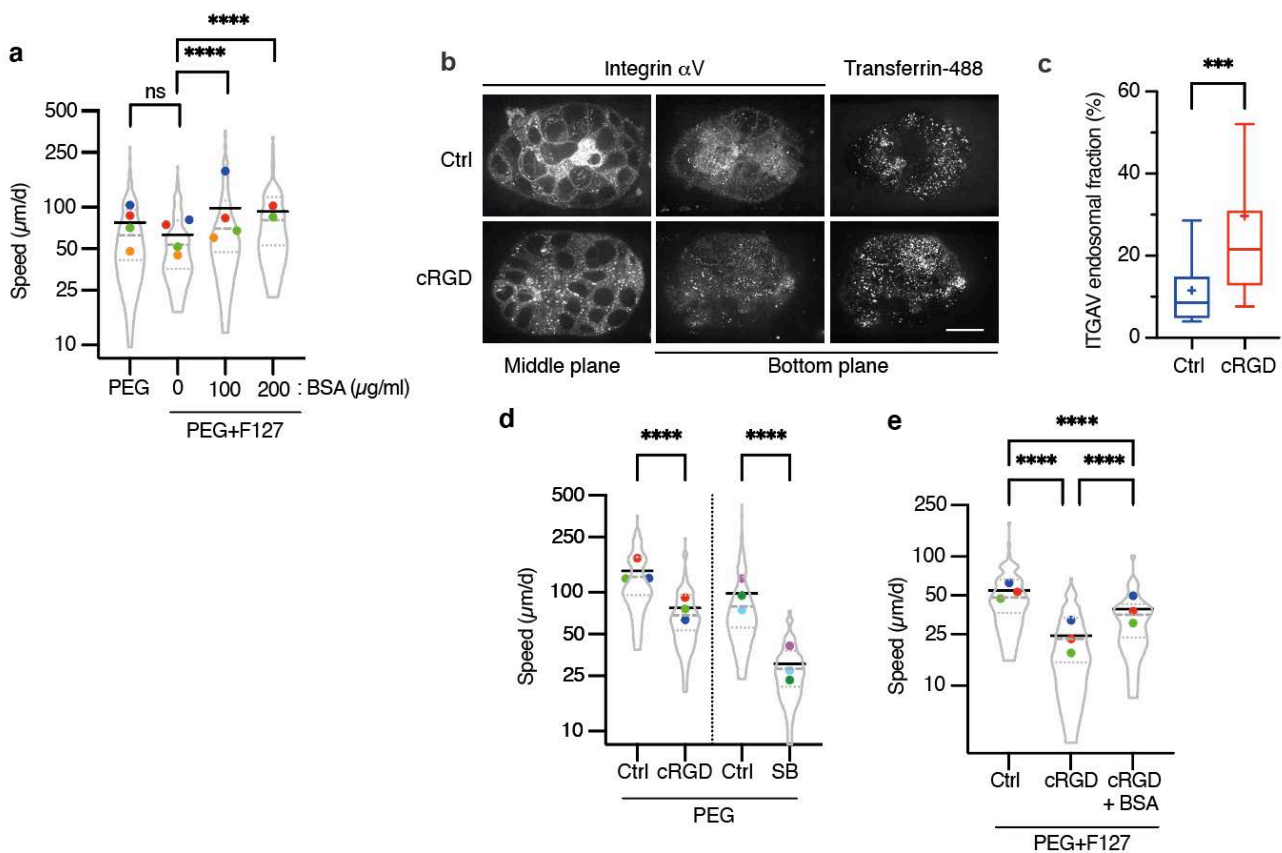


Figure 75. In non-adhesive conditions, cluster migration relies on friction, which could be mediated by integrins.

a, Mean instantaneous speed of HT29-MTX clusters migrating in microchannels coated with PEG+F127 +/-BSA at indicated concentrations. $n=78$ to 151 clusters (one-way ANOVA). **b**, Representative pictures with or without cyclic RGD (cRGD) treatment of the bottom plane (in contact with the PEG-coated glass) and the middle plane of HT29-MTX clusters expressing stably mCherry-ITGAV and stained with Transferrin to label the endosomal compartment. **c**, Fraction of ITGAV signal present in the endosomal compartment, in the bottom plane (in contact with the glass) of clusters treated with or without cRGD. $n=20$ clusters from 3 independent experiments (Mann-Whitney t-test). **d**, Mean instantaneous speed of HT29-MTX clusters treated with cyclic RGD (cRGD) or SB273005 (SB). $n=74$ to 149 clusters (Student's t tests). **e**, Mean instantaneous speed of HT29-MTX clusters treated with DMSO (Ctrl) or cyclic RGD (cRGD) migrating in microchannels coated in PEG+F127 alone or supplemented with 300 $\mu\text{g/ml}$ BSA (cRGD+BSA). $n=67$ to 82 clusters (one-way ANOVA). Scale bar, 20 μm . ns, not significant, * $P < 0.05$, ** $P < 0.01$, *** $P < 0.001$, **** $P < 0.0001$.

3. CLUSTER AMOEBOID MIGRATION RELIES ON RHOA ACTIVATION AND POLARISED ACTOMYOSIN CONTRACTILITY

In suspension, epithelial cell clusters display a robust supracellular actomyosin cortex (**Figure 76a**) (Cai et al., 2014; Hidalgo-Carcedo et al., 2011; Shellard et al., 2018).

To investigate actin and myosin organisation in microchannels, we developed new microchannels designs and protocols to perform immunofluorescence stainings (IF) (**Figure 76b**). These protocols are challenging as clusters do not adhere to microchannels (see Methods): it requires the use of large surrounding channels for gentle medium changes, long incubation times to allow for diffusion of media and antibodies, and strong permeabilization for homogeneous penetration in the thickness of cell clusters.

Immunofluorescence revealed that when confined in PEG-coated microchannels, cell clusters such as PDX#3 organoids et HT29-MTX keep their surrounding actomyosin cortex (**Figure 76b,c**). They also keep their epithelial cell-cell junctions, as showed by E-cadherin staining of adherens junctions, here in HT29-MTX cell clusters (**Figure 76b**).

Highlighting the contractility of this actomyosin cortex, the expression of fluorescent myosin combined with live imaging revealed a blebbing activity at the cortex of HT29-MTX cell clusters (**Figure 76d**).

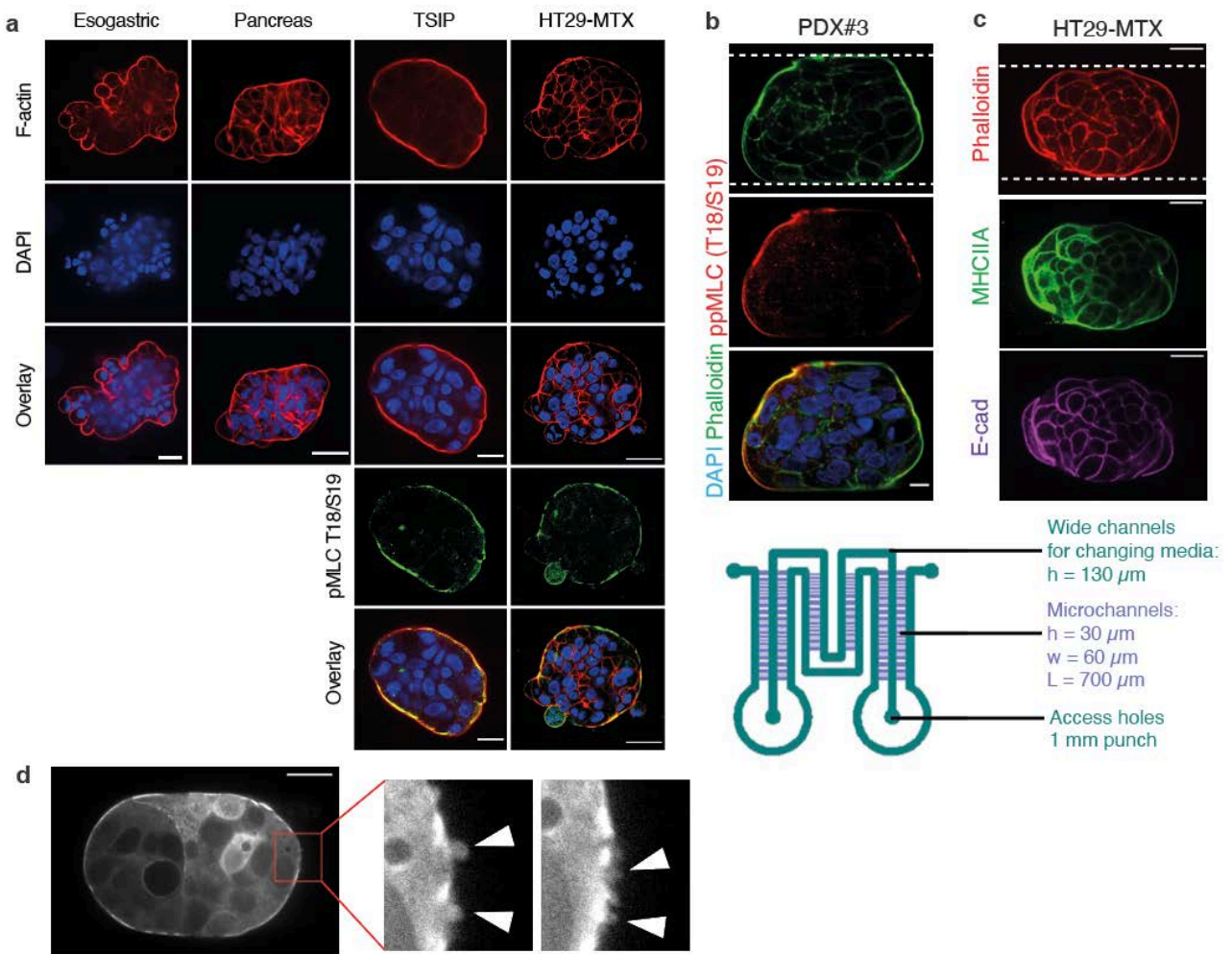


Figure 76. Cell clusters maintain epithelial cell-cell junctions and a supracellular actomyosin cortex when confined in non-adhesive microchannels.

a, Immunofluorescence of a transverse section of different types of clusters fixed in suspension. For display purposes, contrast was adjusted independently for each cluster type. Scale bars, 20 μm . **b,c,** Immunofluorescence of a median section of cell clusters in microchannels and design of immunofluorescence PDMS chips (bottom). Scale bars, 10 μm (b), 20 μm (c). **d,** Representative images of blebbing activity at the cortex in a mTurquoise-Myosin Light Chain (MLC)-expressing HT29-MTX cluster. Scale bar, 20 μm .

Given these observations and that the actomyosin cortex powers single cell focal adhesion-independent amoeboid migration, we reasoned that it could power this collective motion as well (Bergert et al., 2015; Lämmermann et al., 2008; Liu et al., 2015; Paluch et al., 2016). We investigated it by monitoring F-tractin and Turquoise-tagged myosin light chain (MLC) in HT29-MTX. The MLC cortex was evenly distributed in static clusters but displayed a strong polarisation, with a 2-fold enrichment toward the back, during their migration (**Figure 77a,b**). Cluster front/back polarity was even positively correlated with migration speed, suggestive of a pro-migratory function (**Figure 77c**).

The role of actomyosin contractility in cluster migration was confirmed by pharmacological inhibition of Myosin-II (blebbistatin) or ROCK (Y27632) activities. The inhibition of actomyosin contractility significantly reduced migration speeds of both TSIPs and HT29-MTX clusters, by 1.7- and 3-fold respectively (**Figure 77d,e**). This inhibition was accompanied by the abolishment, in part or totally, of the localisation of myosin at the cortex in HT29-MTX clusters, and often induced a change of morphology, with the appearance of protrusions and lumen (**Figure 77f**). This suggests that contractility inhibition, more than preventing this non-adhesive collective motion, could induce a whole phenotypic change like in single cells.

We noticed that after contractility inhibition, there was a remaining level of cluster migration, and hypothesised that a complementary mechanism could be at stake. I investigated the actomyosin-independent “osmotic engine” mechanism proposed by Stroka and colleagues for single cells migration (Stroka et al., 2014). It relies on a polarised distribution of aquaporins and Na^+/H^+ pumps or a differential osmolarity between the cell and the surrounding media. Nevertheless, inhibiting Na^+/H^+ pumps (EIPA) did not alter HT29-MTX clusters migration in non-adhesive microchannels (**Figure 77g**). This suggested that fluid fluxes do not contribute to this focal-adhesion independent collective migration and we focused on the role of actomyosin contractility in the rest of the study.

3. Cluster amoeboid migration relies on RhoA activation and polarised actomyosin contractility

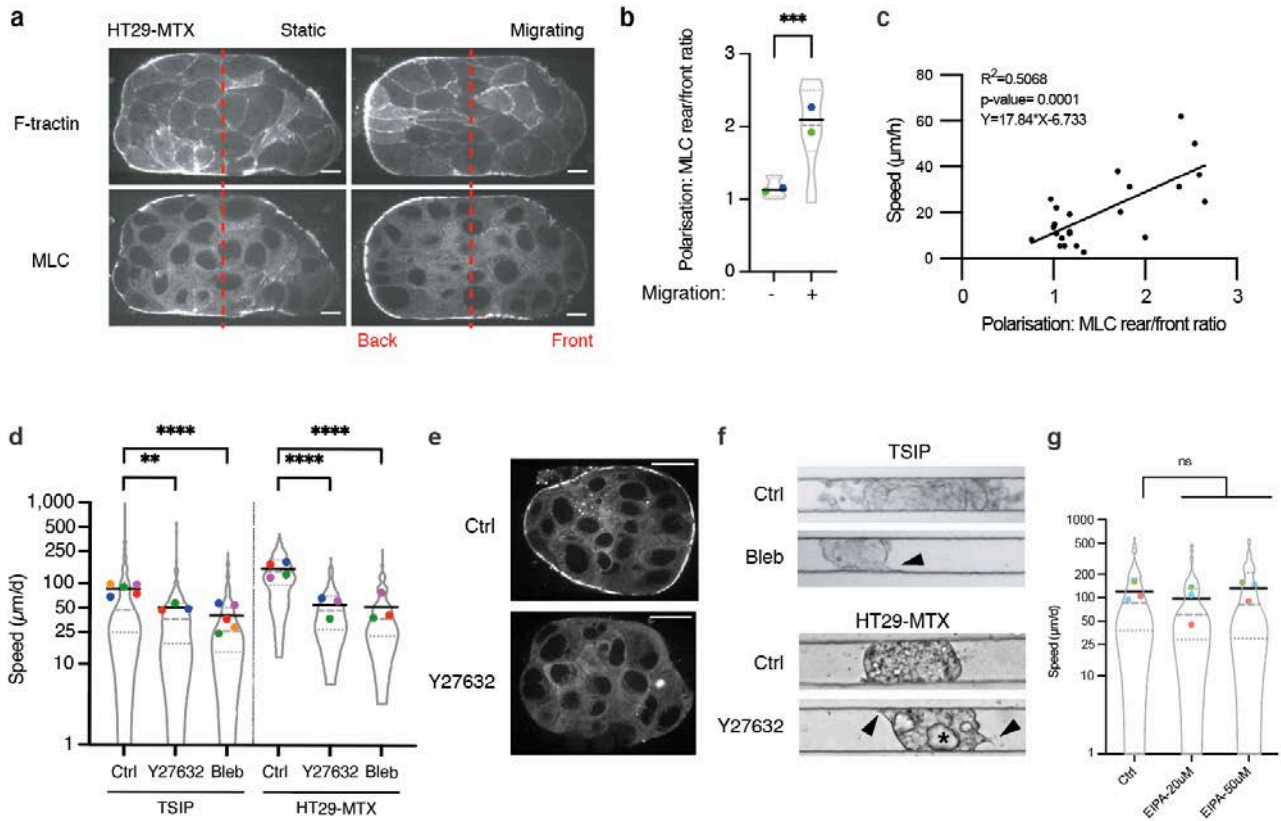


Figure 77. The contractility of the polarised acto-myosin cortex drives focal-adhesion independent collective migration.

a, Median section of HT29-MTX stably expressing F-tractin-mRuby3 (top) and mTurquoise-MLC (bottom), in PEG-coated channels. Red dashed lines separate the front and back of clusters for quantification of ratio in **b**, Scale bar, 10 μm . **b**, Polarisation of clusters as MLC (Myosin Light Chain) ratio between rear and front of the clusters migrating in PEG- or PEG+F127-coated microchannels, as indicated in Methods. $n=12$ to 13 clusters. **c**, Mean instantaneous speed and polarisation of clusters, with linear regression. $n=23$ clusters from 3 independent experiments. **d**, Mean instantaneous speed of clusters treated with Y27632, Blebbistatin (Bleb) or DMSO (Ctrl), log10-scale. $n=106$ to 205 clusters (one-way ANOVA), $**P<0.01$, $***P<0.001$, $****P<0.0001$. **e**, Representative images of myosin cortex in mTurquoise-MLC-expressing HT29-MTX clusters in control condition or after Y27632 treatment. **f**, Representative images of cluster shape after Blebbistatin or Y27632 treatments. Arrowheads: protrusions; star: cavity. **g**, Migration of HT29-MTX clusters in PEG-coated channels under Na^+/H^+ channels inhibition (EIPA). ns, not significant (One-way ANOVA).

RhoA is a well-known regulator of actomyosin contractility. In single cells, it is also a key contributor to cell front-rear polarisation with Rac1, which regulates actin polymerisation at the front of cells and plays an antagonistic role to RhoA (Bear and Haugh, 2014; Crosas-Molist et al., 2022).

Thus, in collaboration with the Coppey lab, we used optogenetics to investigate the roles of RhoA and Rac1 in cluster migration in non-adhesive environments. To this end, we transduced HT29-MTX cells with the optoRhoA and optoRac systems. It enables an acute spatiotemporal recruitment of RhoA activator ARHGEF11 to the membrane (and of Rac1 activator TIAM respectively) using the CRY2/CIBN light gated optogenetic dimerisation system (**Figure 78a**) (Valon et al., 2017). Control cells expressed the same optogenetic dimerization system, except the sequences coding for the GEFs. We then illuminated one side of the clusters, either migrating or non-migrating, and monitored their trajectories for up to 10 hours by using an automated stage and activation routine maintaining a constant illumination region despite the movement of the cluster (**Figure 78b**).

We illuminated the front of migrating optoRhoA clusters to investigate whether increasing RhoA levels was sufficient to drive the direction of their migration. Control clusters essentially pursued their migration in their initial direction. In contrast, 67% of illuminated clusters expressing optoRhoA reverted their direction of migration (**Figure 78c-e**). This indicates that increasing actomyosin activity in a subset of cells dictates the direction of migrating clusters.

Similarly, we recruited Rac1 at the rear of migrating clusters (**Figure 78f,g**). The proportion of cell clusters that changed direction upon Rac1 recruitment at the membrane was much lower than after RhoA activation. Nevertheless, we observed that Rac1 activation was able to dictate direction for some of them immediately after the onset of illumination.

We then explored the role of RhoA and Rac1 in the initiation of cluster migration. Thus, we activated each of them on one side of non-migrating clusters and compared to the control the number of clusters that started migrating and in which direction (**Figure 78h-j**). RhoA activation did not induce cluster migration compared to the control, neither did it bias the direction of migration for the ones that started migrating. On the contrary, Rac1 recruitment biased the initiation of cluster migration towards the side of activation, from 30% to 56%.

These experiments highlighted that the RhoA/Rac1 rear/front balance, well-known in cell migration, is also at play in this mode of migration. More specifically, it revealed a steering role for RhoA in migrating clusters, confirming observations with myosin above. The onset of migration could be biased by increased levels of Rac1 that would define their front. Next experiments will involve myosin monitoring, to observe the impact of RhoA and Rac1 activation on cluster polarisation.

3. Cluster amoeboid migration relies on RhoA activation and polarised actomyosin contractility

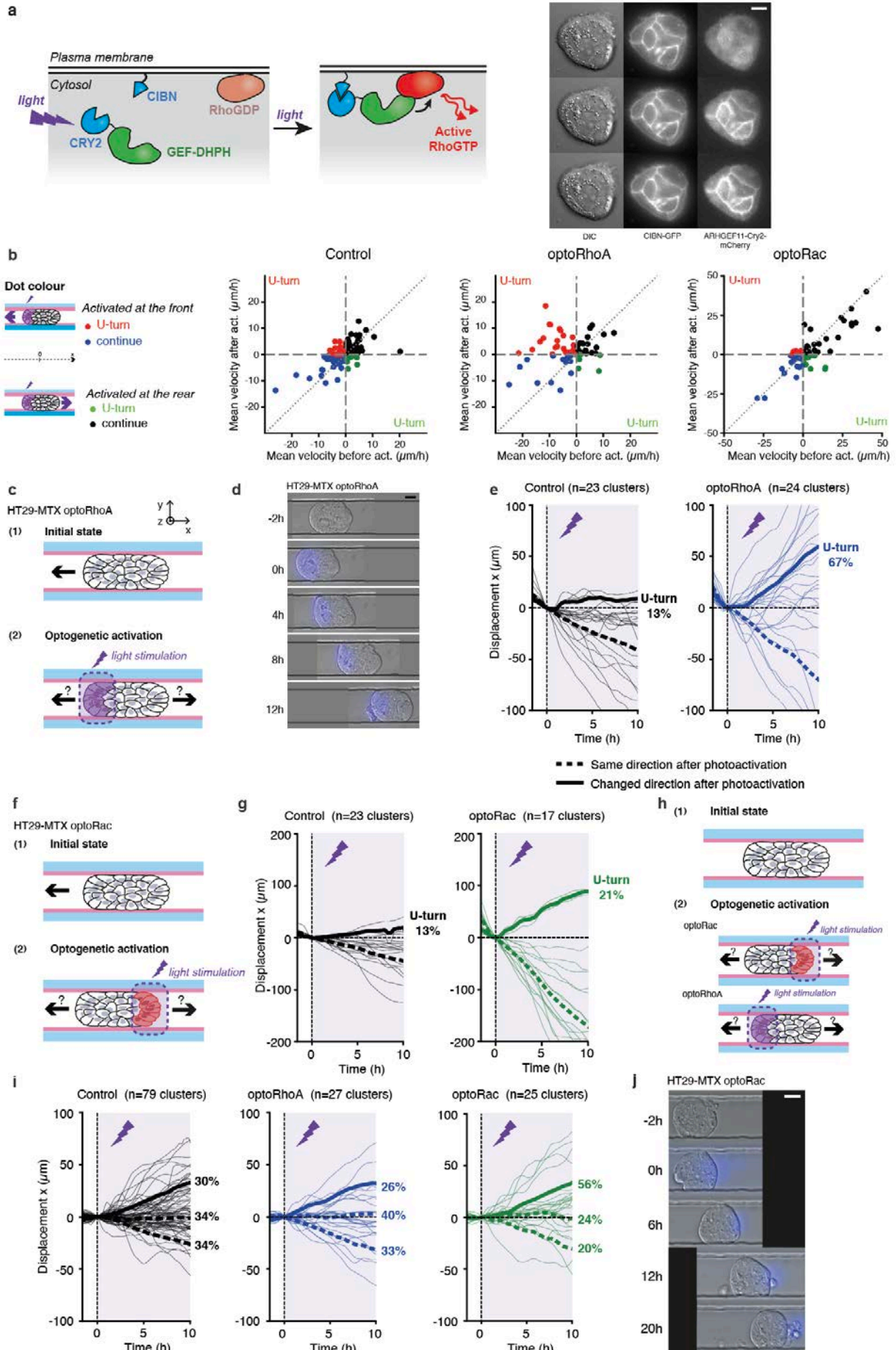


Figure 78. Polarised RhoA and Rac1 activity dictate cluster direction of migration.

a, Schematic of the molecular effect of light activation in optoRhoA cells (left) and global activation of optoRhoA cell line (right). ARHGEF11-Cry2-mCherry and CIBN-GFP are observed in Total Internal Reflection Fluorescence (TIRF). Activation every 30s with 488nm-laser. Scale bar, 10 μ m. **b**, Mean velocity along the x-axis before (average over 1h30) and after (average over 10h) activation (act.) of control, optoRhoA and optoRac clusters. n=119 (control), 62 (optoRhoA) 89 (optoRac) clusters. **c,f,h**, Experimental setups of optogenetic manipulations. **d,j**, Representative time-lapse sequences. Scale bar, 20 μ m. **e,g,i**, Displacement of clusters over time before (-1h30<t<0h) and after (0h<t<10h) optogenetic activation. Bold lines are the mean displacement of clusters going to the right (mean displacement after activation >0). Dotted lines are the mean of clusters going to the left or not moving (mean displacement after activation <0). Purple zone: optogenetic activation. At least 3 independent experiments were performed for each condition and the number of clusters are indicated on the graphs. For e, P=0.0003 (Fisher's exact test on the proportion of turning clusters).

As no external cue is provided in the system, we wondered how polarisation could appear spontaneously in these clusters. We observed that the nuclei of the outer layer of cells, participating in the actomyosin cortex, are more deformed than in internal layers in HT29 and HT29-MTX clusters (**Figure 79a-c**). Migrating clusters displayed even more elongated nuclei in their outer layer (**Figure 79b,c**).

When cells are confined, the stretching of the nuclear envelope can induce increased cortical actomyosin contractility of single cells: this can occur through cPLA2 pathway, triggering the release of arachidonic acid in the cytoplasm which activates actomyosin contractility (**Figure 79d**) (Lomakin et al., 2020). In addition, increased contractility can lead to spontaneous polarisation of single amoeboid cells (**Figure 31**) (Hawkins et al., 2011; Salbreux et al., 2012).

Nevertheless, inhibition of cPLA2 pathway by pyrrophenone and AACOCF3 only induced a slight decrease of cluster migration (**Figure 79e**) and did not impair actomyosin recruitment at the cluster cortex (**Figure 79f**). These results suggest that cPLA2 does not play a major role in inducing clusters polarisation through increased contractility.

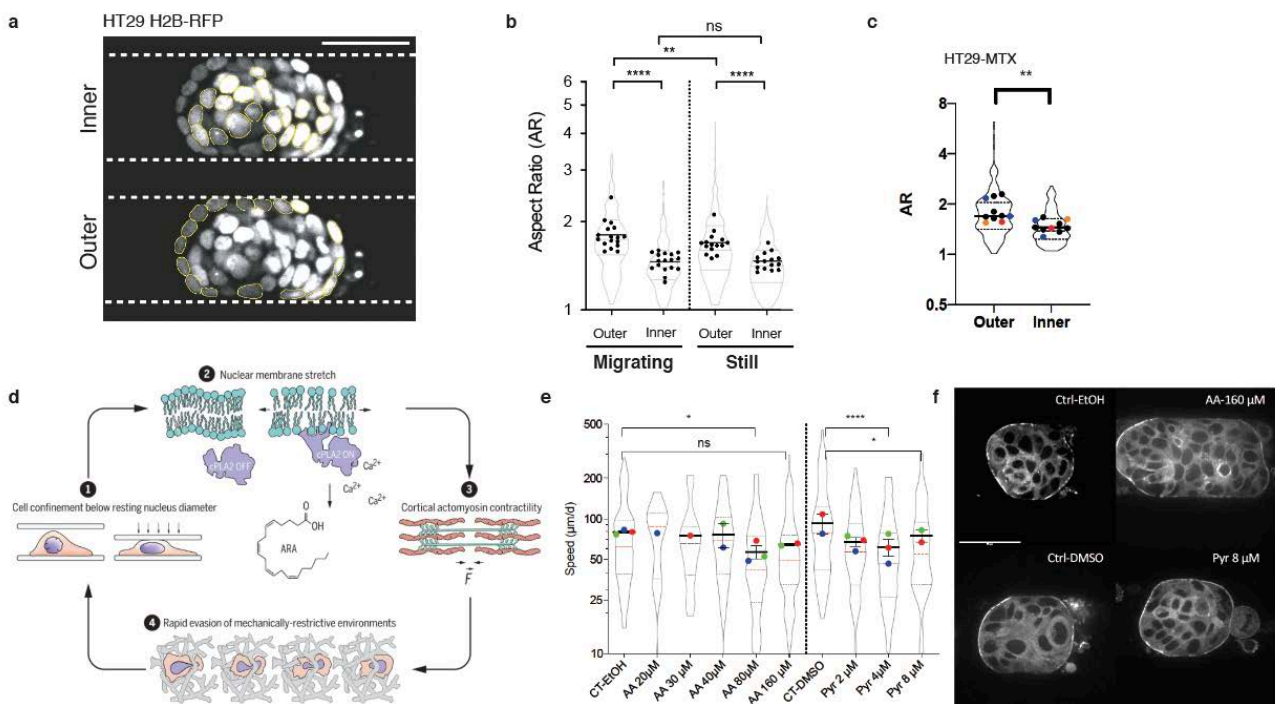


Figure 79. Nuclei of the outer cell layer are more deformed, but this does not lead to cluster increased contractility and polarisation through cPLA2 pathway.

a, Manual segmentation (yellow) of nuclei in the inner and outer cell layers in microchannels. Scale bar, 50 μm . **b,c,** Aspect ratio of nuclei from the inner and outer cell layers in migrating and not migrating HT29 cluster (b) and in HT29-MTX clusters (c) in PEG-coated microchannels. Violin plots represent individual nuclei, dots represent mean aspect ratio (AR) for each cluster. $n \geq 3$ independent experiments. **d,** Scheme of confinement-induced activation of cPLA2 pathway and actomyosin contractility. From (Lomakin et al., 2020). **e,** Speed of HT29-MTX cell clusters migrating in PEG-coated microchannels and incubated with different concentrations of cPLA2 inhibitors: AACOCF3 (AA) and pyrrophenone (Pyr). Solvents: EtOH for AACOCF3, DMSO for pyrrophenone. Error bars are s.e.m. $n=3$ independent experiments. Log-10 scale. **f,** mTurquoise-MLC-expressing HT20-MTX clusters with or without highest concentrations of drugs. Scale bar, 50 μm .

4. COLLECTIVE AMOEBOID MIGRATION ARISES FROM POLARISED JIGGLING

Polarised contractility to the rear is known to support collective and single cell migration by orienting retrograde flows of cells or actin. We hypothesized that in confined environments, these retrograde movements could induce friction forces along the channel walls and propel clusters (**Figure 80a**) (Liu et al., 2015; Ruprecht et al., 2015; Shellard et al., 2018)

I first investigated the participation of cell treadmilling, i.e. retrograde flows of the outer cell layer (**Figure 80a**), described to power the collective migration of neural crest cell clusters or giant keratocytes aggregates (Beaune et al., 2018; Shellard et al., 2018). To this end, I expressed RFP-tagged Histone 2B (H2B) in HT29, HT29-MTX clusters and TSIPs. I then tracked individual cell movements, either manually or automatically, during 8 to 24h migration periods in non-adhesive microchannels.

First, I did not identify significant exchanges between neighbouring cells (**Figure 80b-e**). Individual cells rather translated in the same direction (**Figure 80d,e**). I only noted that a half of HT29 clusters rotated in their reference frame, which could be induced by any asymmetry in the friction against the channels' walls or in actomyosin contraction (**Figure 80c**).

Nevertheless, in the lab reference frame, the average velocity of individual cells, in particular cells in contact with the channel walls, was always anterograde and centred around the speed of the cluster centre of mass (**Figure 80e-g**). I obtained similar data at the bottom of HT29 clusters, indicating that no major 3D flow seems to be at play (not shown). Supporting this idea, cells remained in the same z section over the entire movie.

Thus, the clusters move cohesively as solids in absence of sustained retrograde cellular flows, excluding cell treadmilling as the main migration mechanism (**Figure 80h**).

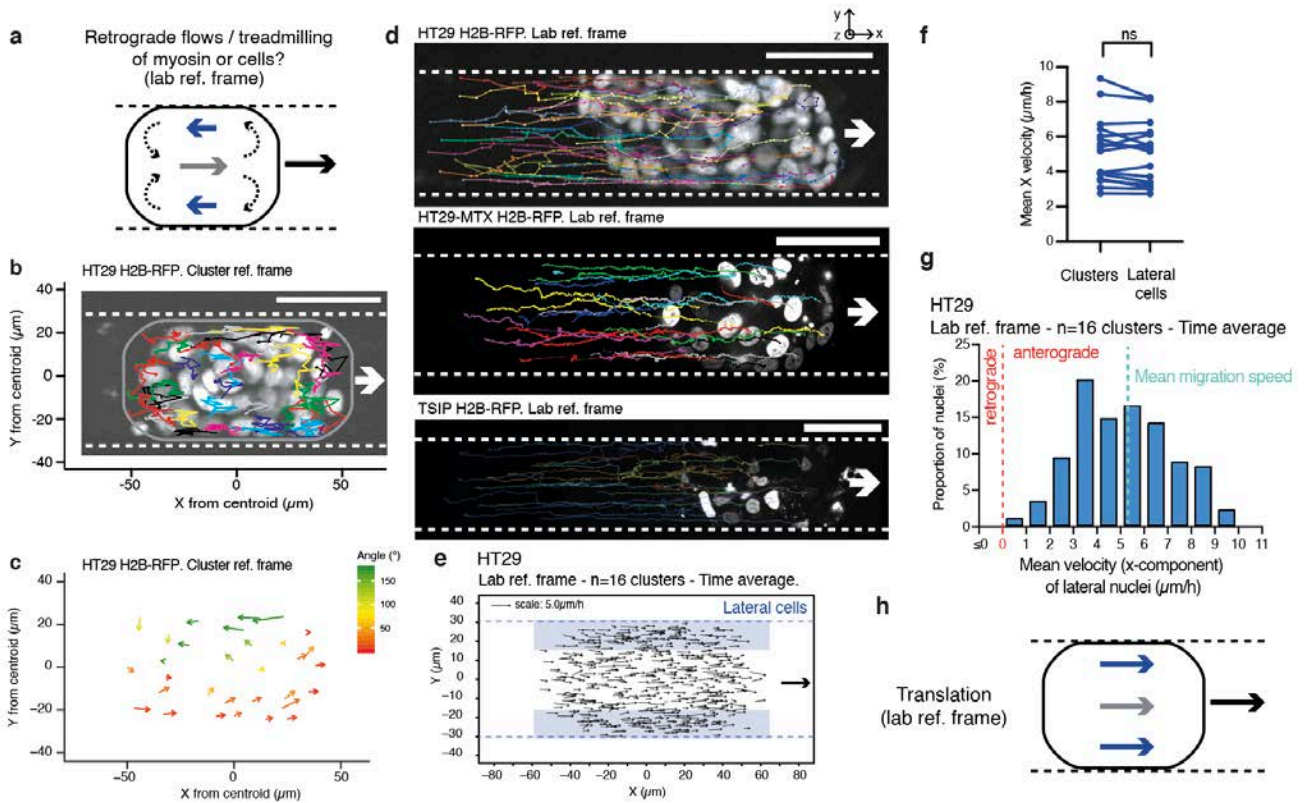


Figure 80. Clusters translate as solids with no persistent cell flows.

a, Schematic representation of cell or myosin treadmilling in a median section of clusters. Velocity arrows of not to scale. **b**, Representative tracks of nuclei in the cluster reference frame. Median section of a Histone 2B(H2B)-RFP-expressing HT29 cluster, migrating to the right in a PEG-coated microchannel over 24h. The picture is the first timepoint. White arrow: direction of migration. **c**, Velocity vectors of nuclei displacements in the cluster reference frame for a representative H2B-RFP-expressing HT29 cluster displaying rotation. Color code: angle to the direction of migration (to the right on x axis). **d**, Representative examples of nuclei tracks in median sections of HT29, HT29-MTX clusters and TSIP stably expressing H2B-RFP, over one day of migration in a PEG-coated microchannel. Scale bars, 50 μm . **e**, Superimposition of the maps of individual nuclei displacements for n=16 clusters (from 3 independent experiments). Nuclei are tracked in median sections of H2B-RFP-expressing HT29 clusters migrating in PEG-coated microchannels for 8 to 24h. Blue boxes highlight the lateral nuclei (of cells in contact with the channels walls) considered for f,g. **f**, Mean velocity in the direction of migration (X axis) of clusters and corresponding nuclei of the outer cell layer, from the map in e. **g**, Frequency distribution of x-component of the mean velocity of every lateral nucleus ($\leq 12 \mu\text{m}$ away from the channel walls; mean cluster speed = $5.3 \mu\text{m/h}$), from the map in e. **h**, Schematic representation of the movements observed for cells in the lab reference frame.

We next evaluated whether propulsive forces could be generated at the subcellular scale by persistent actomyosin retrograde flows using mTurquoise-MLC (Bergert et al., 2015; Liu et al., 2015; Ruprecht et al., 2015).

Above a certain level of confinement, HT29-MTX single cells can display an amoeboid mode of migration, characterised by large front membrane extensions and persistent myosin retrograde flows in the cell and substrate reference frames (**Figure 81a-d**).

We investigated whether HT29-MTX cell clusters could display similar myosin retrograde flows by performing particle image velocimetry (PIV) analyses of MLC. From median planes, we specifically selected the cluster contact areas with the substrate (**Figure 81e**). When averaged over time and multiple clusters,

4. Collective amoeboid migration arises from polarised jiggling

these PIV analyses yielded mostly anterograde flows in the substrate frame of reference (**Figure 81f,g**). This therefore excludes the contribution of persistent actomyosin retrograde flows at the single cell level, coordinated at the cluster scale, as the propulsive mechanism.

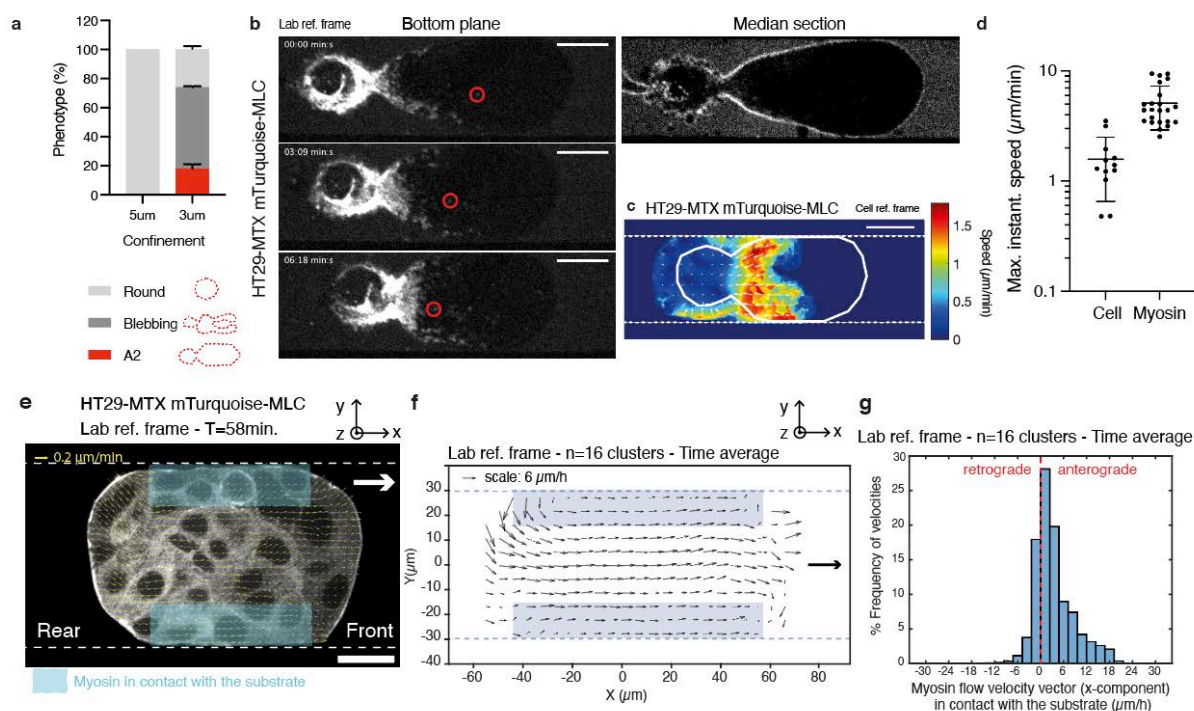


Figure 81. Cell clusters do not display persistent retrograde myosin flows during migration in non-adhesive microchannels.

a, Proportion of phenotypes displayed by single HT29-MTX cells under 3 and 5 μm confinement in PEG-coated microchannels. $n=51$ to 91 cells from 2 independent experiments. **b, c**, Time-lapse sequence (b) and PIV heatmap in the lab reference frame of mean (over 6 min 18 s) myosin flows at the bottom plane (c), color-coded in amplitude, and velocity vectors of an mTurquoise-MLC-expressing HT29-MTX single cell in a 3 μm -high PEG-coated microchannel. In b, a red circle follows a dot of myosin in the lab reference frame. **d**, Maximum migration speed of single cells ($n=12$ cells from 3 independent experiments) and myosin flows in the lab reference frame ($n=23$ myosin particles from 4 cells from 2 independent experiments) during migration in 3 μm -confining PEG-coated channels during 7 min to 37 min. Scale bars, 10 μm . For **e-g**, MLC-mTurquoise-expressing HT29-MTX clusters are observed every 1 to 5 min during 20 to 450 min while migrating in PEG- or PEG+F127-coated microchannels. **e**, Median section showing instantaneous myosin flows superimposed on the raw image and detected by particle image velocimetry (PIV) of a representative HT29-MTX cluster expressing mTurquoise-MLC and migrating in a PEG-coated channel. Timepoint: $T=18$ min. Blue boxes: areas defined for myosin flows analysis in contact with the microchannels over 15 μm thickness of the median plane in e-g. Scale bar: 20 μm . **f**, PIV map of myosin flow velocity vectors of median sections of clusters, averaged over time (20 min to 7.4 h) and clusters ($n=16$ migrating clusters from 5 independent experiments). **g**, Frequency of velocities (x-component) of pooled myosin flow velocity vectors in the contact zone obtained from time-averaged (20 min to 7.4 h) PIV maps of median sections of 16 migrating clusters from 5 independent experiments.

Together, tracking cells and their actomyosin cytoskeleton showed that migrating clusters translate as a whole and do not use any of the known mechanisms of cell migration which are based on sustained retrograde flows, either at the cellular or intracellular levels (Friedl et al., 2012; Liu et al., 2015; Shellard et al., 2018; Yamada and Sixt, 2019) (**Figure 80e, Figure 81f**).

Therefore, we used a higher time resolution, in the order of minutes, to resolve the transient actomyosin dynamics that we could observe on movies. PIV analyses revealed complex myosin flow patterns in the lab reference frame. In contact with the substrate, myosin flow velocities displayed fluctuations in amplitude over time (**Figure 82a**). Stochastic and short-lived retrograde flows indicated the presence of transient propulsive events, that can contribute to cluster migration (**Figure 82b**). They are balanced by anterograde movements, suggestive of resistive friction forces, which leads to the average anterograde myosin flows over time mentioned above (**Figure 81f**). Of note, the average velocity of myosin flows in the cluster reference frame was mostly negative, reminiscent of the retrograde flows induced by myosin cortex polarisation in single cells, but it was not correlated with migration speed (**Figure 82c**).

Since it is still experimentally challenging to measure forces associated with the retrograde/propulsive events, we used the amplitude of myosin flow speed fluctuations as a proxy. To quantify them, myosin flow velocities in the cluster reference frame were centred around zero, i.e. we subtracted their algebraic temporal mean mentioned above.

In migrating clusters, the amplitude of these fluctuations – that we called myosin “jiggling” – was positively correlated with cluster instantaneous speed (or “cluster jiggling”): the more myosin speed fluctuates, the faster the cluster (**Figure 82d**). Interestingly, this correlation was observed as well in non-migrating clusters but as they display low persistence, their instantaneous displacements do not lead to directed motion (**Figure 82c-e**).

These results suggest that myosin speed fluctuations could contribute to instantaneous cluster displacements but are not sufficient to generate directed motion.

Directionality is thus likely to be provided by myosin polarisation. Indeed, in migrating clusters, the more myosin is polarised to the rear, the more persistent the clusters (**Figure 82f,g**). Conversely, non-migrating clusters display low polarisation and persistence.

4. Collective amoeboid migration arises from polarised jigging

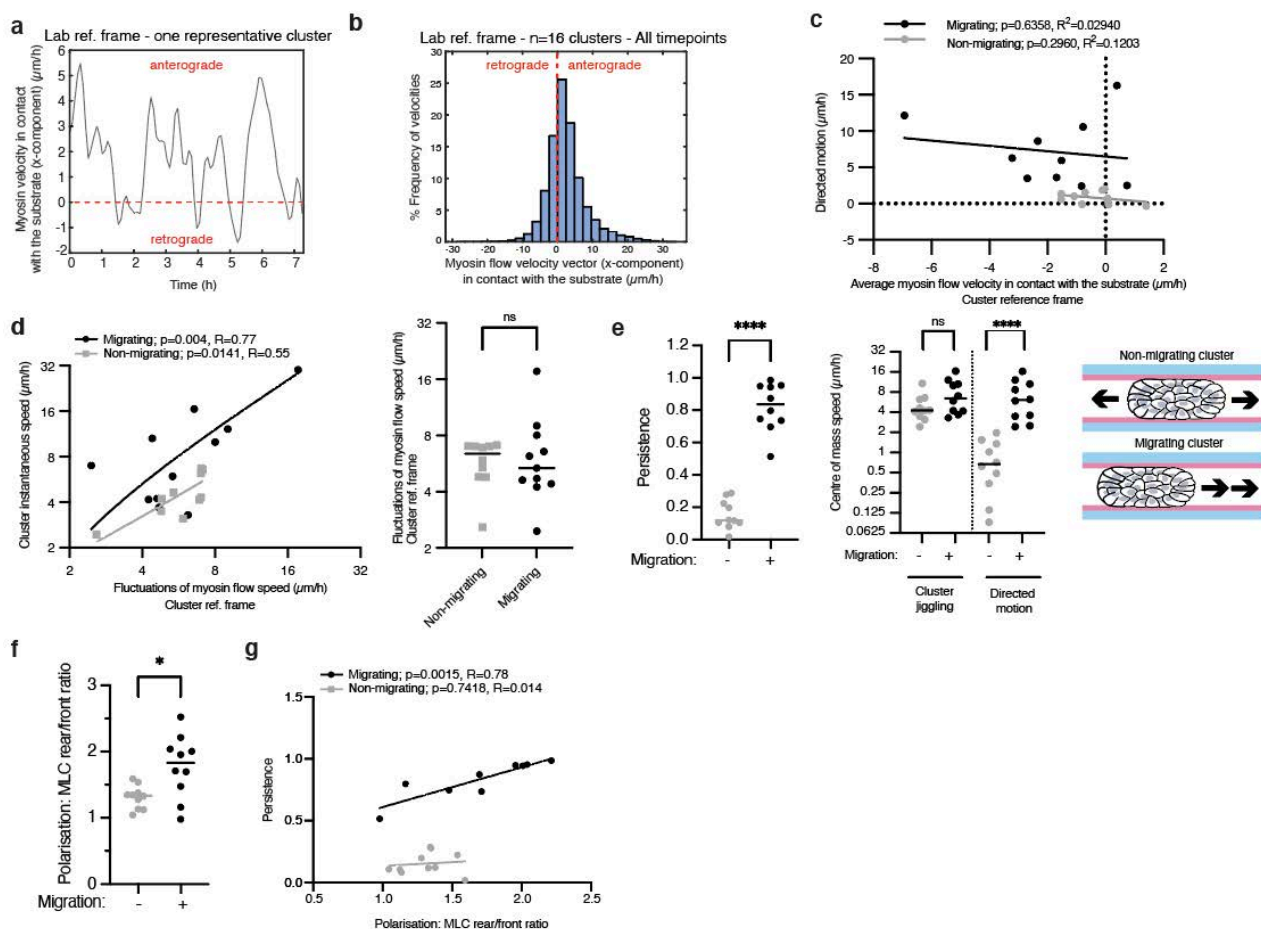


Figure 82. Myosin jigging promotes cluster instantaneous displacement and, with myosin polarisation, directed motion.

a, Kinetics of myosin flow velocity (x-component) averaged spatially at the contact with the channels, for the representative cluster shown in **Figure 81**. **b**, Frequency of velocities (x-component) of myosin flow velocity vectors at the contact obtained by PIV maps of median sections. $n=16$ migrating clusters from 5 independent experiments. **c**, Average myosin flow velocity in the cluster reference frame and average cluster velocity (directed motion), both in x direction. Linear regressions are displayed for migrating and non-migrating clusters. **d**, Left: Correlation between cluster instantaneous speed and the fluctuations of myosin flow speeds in contact with the substrate. Right: Fluctuations of myosin flow speeds in the cluster reference frame for migrating and non-migrating clusters (Mann-Whitney t-test). **e**, Polarisation and persistence of non-migrating and migrating clusters (Mann-Whitney t-test). **f**, MLC polarisation in migrating and non-migrating clusters. **g**, Correlation between persistence and polarisation. For c-g, $n=10$ migrating (black) and non-migrating (grey) mTurquoise-MLC-expressing HT29-MTX clusters in PEG-coated microchannels. ns, not significant, $*P<0.05$, $**** P<0.0001$

As actomyosin contractility can induce cell deformation, we reasoned that these myosin flows could be associated with cell movements in clusters. To probe for cellular “jigging”, I tracked individual nuclei in H2B-RFP-expressing HT29, HT29-MTX clusters and TSIPs. This revealed that over short timescales, nuclei and myosin move in similar directions (**Figure 83a**). In addition, the amplitude of nuclei speed fluctuations was also correlated with cluster migration speed, with more cellular jigging in migrating clusters and in the same order of magnitude as the migration speed (**Figure 83b**). This observation is in accordance with clusters behaving as elastic solids, with fluctuating internal deformations (jigging) quantifiable by myosin flows at the cortex, as described above, or nuclei speeds.

To explore whether this cellular jiggling was maintained over the course of the migration, I then investigated cellular movements at long timescales, in the range of cluster migration. It revealed that this correlation between cellular jiggling and cluster speed is maintained over long timescales in both HT29 and TSIP models (**Figure 83c-f**).

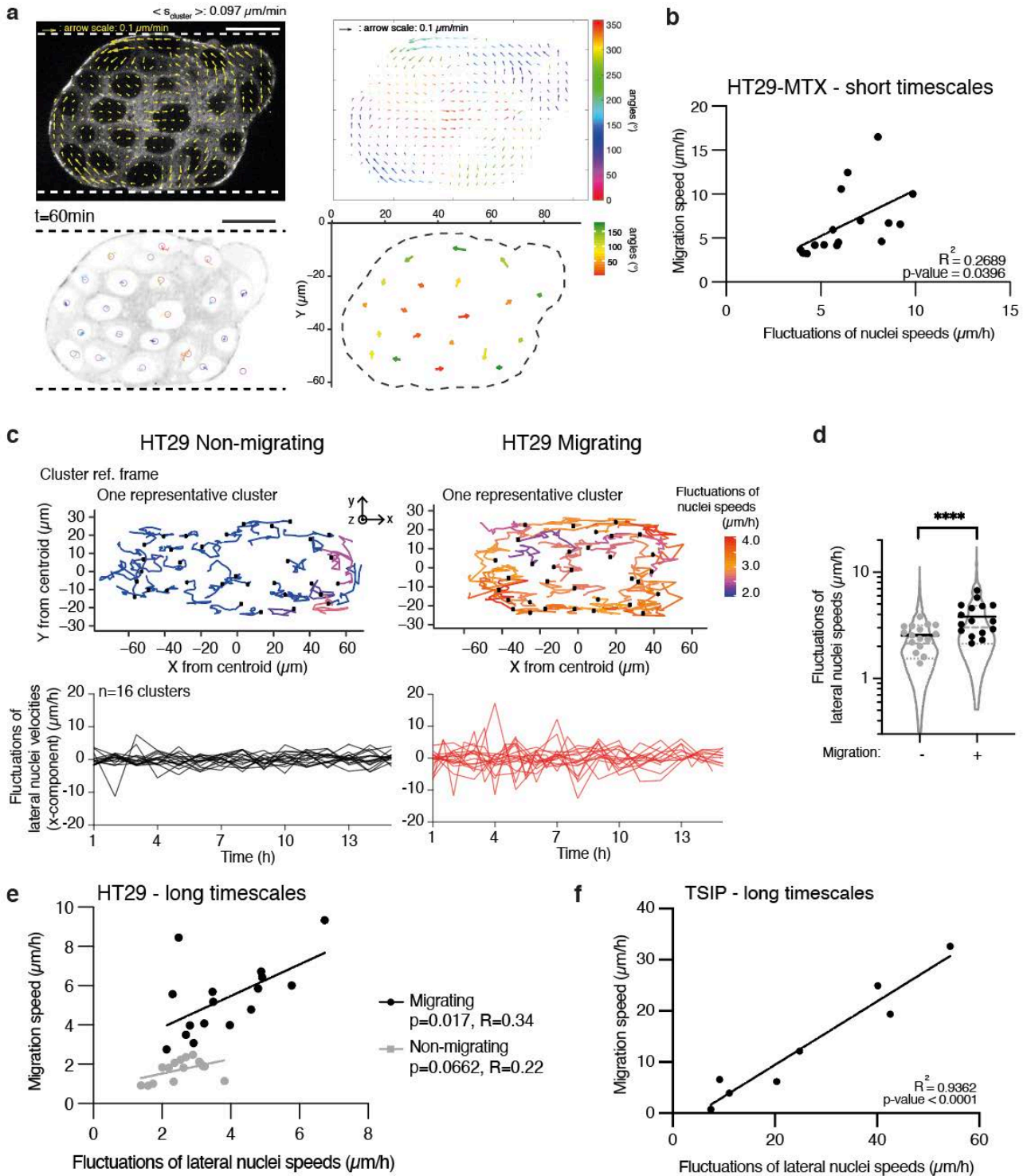


Figure 83. Cellular jiggling promotes cluster migration over long timescales.

a, Top: Time averaged PIV map of myosin flows of an mTurquoise-MLC-expressing HT29-MTX cluster. $\langle v_{\text{cluster}} \rangle$: mean speed of the cluster. Bottom: Nuclei displacements over 1h-automated tracking (left) and time-averaged displacements of individual nuclei (right). Cluster reference frame. The cluster

4. Collective amoeboid migration arises from polarised jiggling

migrates to the right in a PEG-coated microchannel. Scale bar, 20 μ m. Color code: angle to the direction of migration. **b**, Correlation between migration speed and the fluctuations of lateral nuclei speeds. For **c-e**, H2B-RFP-expressing HT29 clusters are followed every 30min to 1h during 8h to 24h in PEG-coated microchannels. **c**, Top: tracks of nuclei displacements in the cluster ref. frame, in median sections of representative migrating and non-migrating clusters, followed every 1h over 1day in PEG-coated microchannels. The track of each nucleus is color coded for its average fluctuations. For the migrating cluster, corresponding tracks in the lab reference frame are represented in **Figure 80**. Bottom: average fluctuations of lateral nuclei speeds over time, for H2B-RFP-expressing HT29 clusters migrating (red) or not (black) in PEG-coated microchannels. **d**, Fluctuations of nuclei speeds averaged among lateral nuclei, for migrating and non-migrating clusters. $n=16$ clusters each (Student's t-test). Log-10 scale. **e**, Migration speed of clusters as a function of mean fluctuations of lateral nuclei speeds., with linear regressions $n=16$ migrating (black dots) and $n=16$ non-migrating (grey dots) clusters. **f**, Migration speed and fluctuations of lateral nuclei speeds in TSIPs with linear regression. $n=8$ clusters.

Altogether, these experimental results point to a propulsion mechanism based on random fluctuating deformations focused by polarised actomyosin contractility as the main driver of collective amoeboid migration.

Inspired by earlier analytic descriptions of synthetic crawling or swimming machines (Baule et al., 2008; Najafi and Golestanian, 2004; Purcell, 1977), we propose a minimal physical model for collective amoeboid migration that describes the cluster as an actively polarised jiggling elastic solid, migrating in spite of any persistent cellular or myosin flow (**Annex 2**). This mechanism stems from the observed polarisation of the clusters (**Figure 77**), their migration speed being correlated with the amplitude of both myosin and nuclei flow fluctuations (**Figure 82**, **Figure 83**).

The cluster is endowed with an active fluctuating contractile stress, whose magnitude ζ follows the local myosin concentration and therefore displays a front-back gradient $\nabla\zeta$, which in turn causes a gradient of fluctuating deformations (**Figure 84a**). This is the key ingredient that drives the cluster out of equilibrium and is eventually responsible for self-propulsion (**Figure 84b,c**). Data presented in **Figure 75** suggest that clusters interact with the substrate via passive friction forces, which are generically non-linear and assumed to be strain (i.e. deformation) dependent. We provide in **Annex 2** a proof of principle calculation showing that these minimal ingredients are sufficient to induce cluster self-propulsion, with velocity $v \sim \nabla\zeta$ (**Figure 84a-c**).

As a consequence, this biophysical modelling highlights the following key elements.

Only the fluctuating part of the contractile stress contributes to migration: the time-averaged part makes only the effective elastic moduli of the cluster inhomogeneous, not leading to motion. This is in accordance with our experimental observations, showing that this time-averaged part is not correlated with migration speed, and it was indeed removed from myosin/nuclei speed in our calculation of their fluctuations (**Figure 82c**).

Cluster velocity increases with the gradient of fluctuating contractile stress and can follow a linear relationship (**Figure 84c**): this is indeed what we observed, with positive correlation between myosin polarisation and cluster speed (**Figure 77**). In addition, in this model, a uniform enhancement of contractile stress fluctuations induces a proportional increase of cluster velocity: this is indeed what we reported **Figure 82** and **Figure 83**, where fluctuations of myosin and nuclei speeds are positively correlated with migration speed.

Last, of note, in this model, myosin/nuclei jiggling are necessary, but not sufficient, and myosin polarisation is critical for transforming cluster jiggling into directed motion. This is in accordance with our experimental observations: at low timescales with high temporal resolution, myosin/cellular jiggling are found to induce cluster instantaneous displacements, but only polarised clusters are able to transform this random "noise" into persistent motion (**Figure 82**).

Thus, in this general migration mechanism that we named “polarised jiggling”, self-propulsion arises from a front-back asymmetry of friction forces with the substrate, which is induced by fluctuating deformations within the cluster under a polarised myosin cortex.

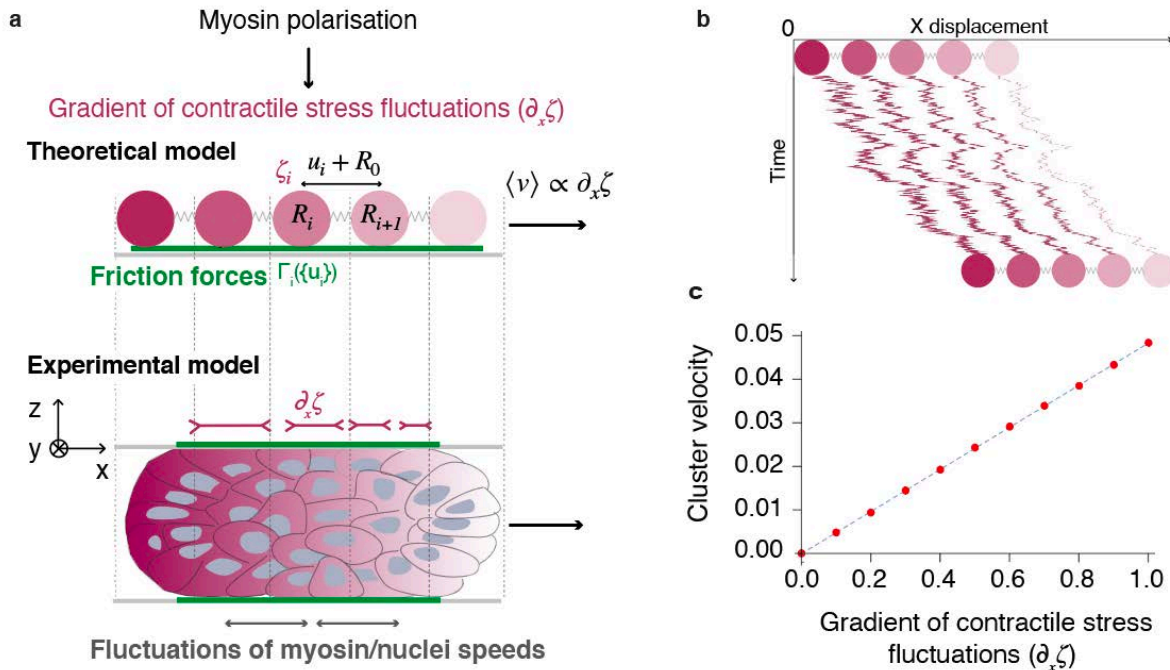


Figure 84. Model of collective amoeboid migration, driven by polarised jiggling.

a, Top: Discrete, one-dimensional model of the cell cluster obtained by averaging over the cluster along z -direction and discretizing along x -direction. The cluster is modelled as a series of beads, with average separation R_0 , connected by elastic elements modelled by gray springs. The active fluctuation of contractile stress on each bead is ζ_i which decreases from left to right and is represented by a colour gradient. The friction experienced by each bead is Γ_i which depends on the local strain u expressed as $u = R_{i+1} - R_i - R_0$. Bottom: schematic of the model of the cell cluster: fluctuations of cell displacements, friction forces Γ with the microchannels (green plain line), gradient of contractile stress fluctuations $\partial_x \zeta$ and cluster speed v . **b**, A representative trajectory of a five-bead model with the strength of contractile fluctuations decreasing from left to right. This was obtained from a stochastic simulation of the model depicted in **a** with mobility $M_i = \Gamma_{i-1} = M_0 + M_1 u_i$ and an elastic potential $\sum_i k u_i^2 / 2$. The distance is measured in units of R_0 and time in units of $1/M_0 k \equiv \Gamma_0/k$. **c**, Average velocity of the cluster and $\partial_x \zeta$ for $M_1/M_0 = -0.1$. The time-step in the numerical evaluation was 0.01 and each run consisted of 5×10^7 time-steps. Each point was additionally averaged over 10 independent runs.

5. CONCLUSIONS ON COLLECTIVE AMOEBOID MIGRATION

Identified from patient explants, we report an undescribed mode of migration that we named “collective amoeboid” because of several key features shared with amoeboid single cell motility: like a giant super cell, clusters mobilise their polarised supracellular actomyosin cortex to generate propulsive friction forces and migrate in absence of focal adhesion-mediated traction (**Figure 85**). Yet, the mechanism producing motility is completely different: neither cell nor actomyosin retrograde flows are coordinated at the cluster scale. This ruled out conventional models of migration such as cell treadmilling described by the Mayor lab (Shellard et al., 2018), or other “toothpaste-like” models comparable to the bleb-based mode of migration of single cells (Bergert et al., 2015; Liu et al., 2015; Yamada and Sixt, 2019). Instead, we identified random fluctuations of myosin flows and cell displacements in migrating clusters. We propose a physical mechanism of polarised jiggling based on a polarised contractile stress that yields directed motion in non-adhesive environments. This mechanism is consistent with the migration of engineered biological robots

made by Kriegman and colleagues (Kriegman et al., 2020). In this system, asymmetric biological aggregates made of non-contractile stem cells and contractile cardiomyocytes are able to generate directed motion without temporal coordination of the contractions. Our study elucidates the physical basis of this type of mechanism and shows it requires only minimal elements: a front-back polarisation, the presence of random contractile forces at the cluster scale, and non-specific friction forces with the environment. We anticipate that this principle underlying the migration of cancer cell clusters, could be extended to understand the movement of other biological systems.

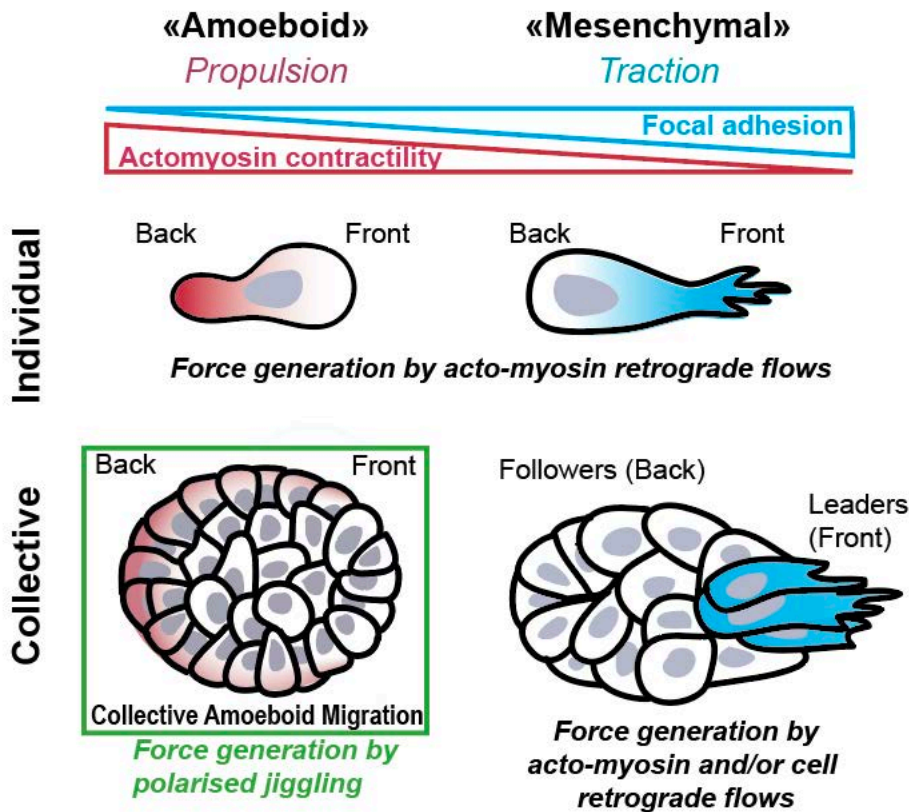


Figure 85. Scheme of cell migration modes.

Schematic representation of the different modes of cell migration based on the ability of the cells to adhere to each other (individual versus collective migration) and to their environment (mesenchymal versus amoeboid). This results in traction- or propulsion-based locomotion. Single cell amoeboid migration and collective adhesion-based migration are driven by sustained acto-myosin or cell retrograde flows whereas collective amoeboid migration is driven by polarised jiggling.

The discovery of collective amoeboid migration opens a wide field in cell migration, and a large number of biological questions – which will be detailed in **Chapter VI** – remain to be answered today. Therefore, the exploration of CAM will require innovative and robust technological and analytical tools to improve robustness and increase the speed of experiments and data processing.

On the technological side, microchannels provided useful environments to allow the study of patient explants as well as clusters from cell lines, and powerful imaging. Results were found robust between the different people and labs who participated in this project.

On the analytical part, progress needs to be made in image analysis and cell cluster tracking to increase robustness and speed.

Indeed, the standard migration experiments that we perform over hours remain captured in bright field, but this does not allow for easy image segmentation. Bright field imaging is the most simple and efficient modality, applicable to any biological material (patients, PDXs, cell lines), avoids cytotoxicity, and gives unbiased visibility on cluster shape and state. However, efficient tools are lacking today to segment automatically bright-field images and allow for complete data extraction (cluster shape, position, size, ...). Therefore, we still track cluster migration manually for hundreds of images. A powerful automated workflow is needed to analyse this amount of data produced with high time-resolution and a large number of conditions per experiment.

Therefore, with the help of bioinformaticians, I am developing a deep learning-based algorithm to allow automated segmentation and analysis of timelapse bright-field imaging. It is based on the Google TensorFlow deep learning package and run on R in batch on GPU (graphics processing units) to allow for fast analysis (**Figure 86a**). The algorithm extracts morphological features as well as cluster position and reports comprehensive results with individual cluster data over time (position, area, circularity, perimeter) and summary data, together with visual feedback on image segmentation to allow for manual data cleaning if necessary (**Figure 86b**).

First analyses were consistent with the results obtained manually, with lower migration in Y27632 (**Figure 86c,d**) and more elongated phenotype in collagen (**Figure 86e**). Some optimisation is still ongoing to improve cluster segmentation in protrusive phenotypes, which are less contrasted, and to allow for manipulation of large amounts of data. In addition to saving time, this would help obtaining robust user-independent results and new data such as monitoring shape over time, which is impossible to obtain with manual tools and of special interest to study cell migration plasticity.

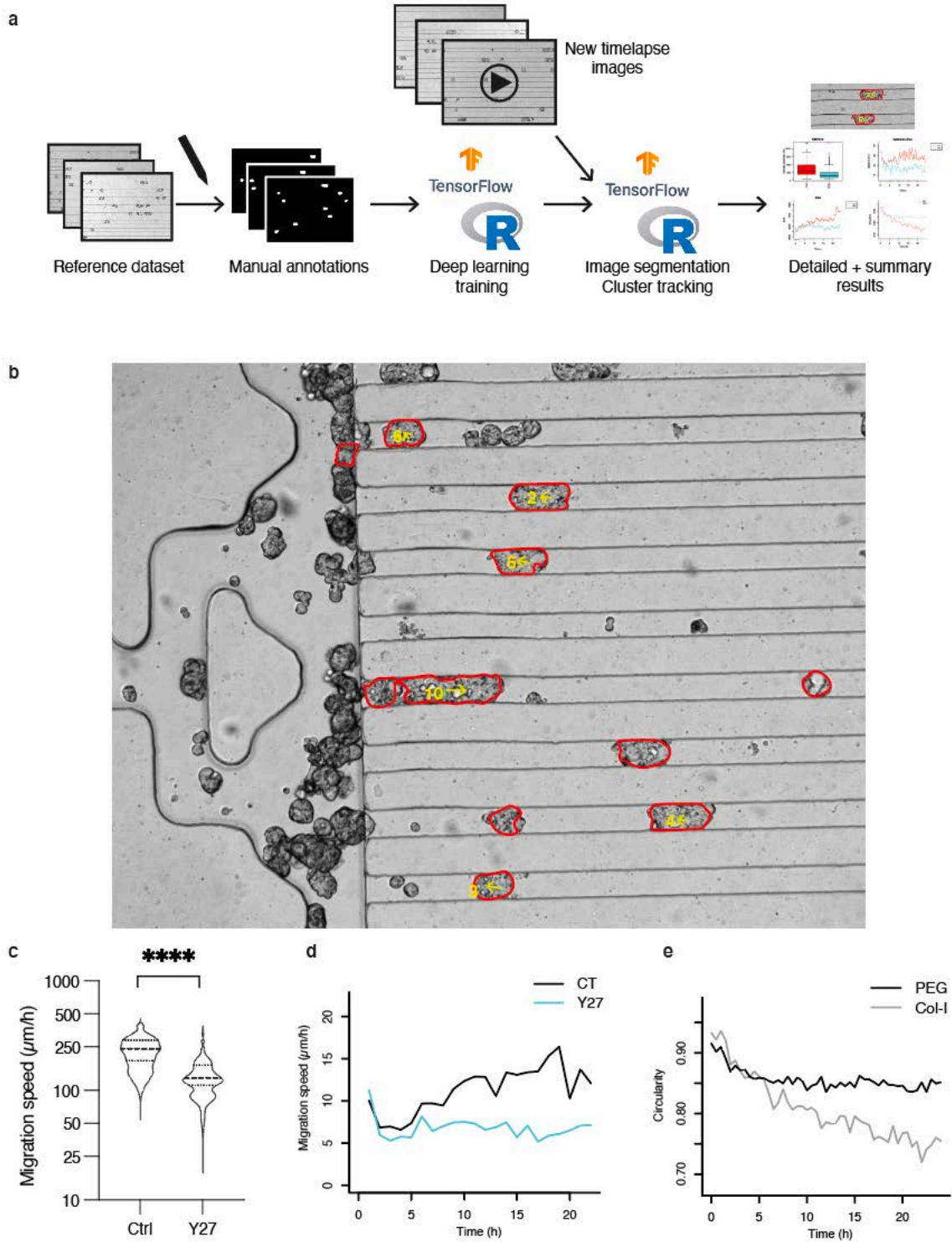


Figure 86. Automated image segmentation and cluster tracking.

a, Workflow for deep-learning-based automated segmentation and tracking. **b**, Representative image of results obtained at one timepoint, HT29-MTX in PEG-coated channels. Red: segmentation, yellow: instantaneous velocity. **c,d**, Mean migration speed (**c**) and corresponding instantaneous speed over time averaged over HT29-MTX clusters (**d**) in control and Y27632 (Y27) conditions after one day of migration in PEG-coated microchannels. $n=53$ (Ctrl) and 145 (Y27) clusters. **e**, Circularity of PDX#3 organoids in PEG- and collagen-I(Col-I)-coated microchannels.

Chapter V. Apico-basal polarity orientation influences response to chemotherapies

In this second part, I will present results from a study of Canet-Jourdan and colleagues, which is currently under revision for publication (see **Annex 3**). There, I investigated the impact of the apico-basal orientation of TSIPs on their response to chemotherapeutic agents.

Indeed, the metastatic dissemination of cancer remains a major issue in patient treatment but the molecular and cellular mechanisms underlying cancer cell invasion remain unclear. Following our discovery of TSIPs in the peritoneal effusions of patients with mucinous colorectal carcinoma (MUC CRC) (Zajac et al., 2018), they used primary explants and organoids from patients harbouring MUC CRC, a highly invasive histological form of digestive cancers, to study the architecture and invasive behaviour of tumour cell intermediates.

They report that these tumours maintain a robust apico-basal polarity as they spread in the peritumoral stroma or organotypic collagen-I gels. They identified two distinct topologies: MUC CRCs either display a conventional “apical-in” polarity or harbour an inverted “apical-out” topology. Transcriptomic analyses combined with interference experiments on organoids showed that TGF β and focal adhesion signalling are the main drivers of polarity orientation. A cohort of primary cancer explants with peritoneal carcinomatosis, confirmed the heterogeneity of MUC CRC patients, showing that the majority of these cancers use a TSIP-based dissemination with persistent apical-out polarity while a subset mainly spread in apical-in polarity.

We investigated the physio-pathological relevance of MUC CRC apico-basal polarity orientation, both *in vitro* and based on clinical data. Several studies already highlighted the predictive potential of tumour organoids submitted *in vitro* to chemotherapies. Therefore, thanks to our PDX models for TSIPs, I studied the impact of the apico-basal orientation on TSIP response to the main chemotherapies used in clinic, here as single agents.

1. APICAL-OUT ORGANOIDs RESPOND LESS TO CHEMOTHERAPIES THAN APICAL-IN ORGANOIDs

1.1.1. Biological models to study TSIP phenotype

As presented in introduction, we use TSIPs and PDX#3 organoids formed from the CRC MUC PDX models of CReMEC tumour collection to reproduce and study TSIP phenotype (Julien et al., 2012; Zajac et al., 2018). In contact with the stroma, which we mimic by embedding the organoids in collagen-I gels, TSIPs keep their round apical-out topology, while PDX#3 switches to an “apical-in” phenotype with formation of a lumen and protrusions (**Figure 22**).

The topology of these organoids depends on their adhesion to the surrounding collagen and to their contractility (Canet-Jourdan et al., under revision). Therefore, incubation of TSIPs with Y27632, that inhibits their contractility, induces a switch to the apical-in phenotype, protrusive with lumen formation. Conversely, incubation of PDX#3 organoids with integrin inhibitors (e.g. A11B2 targeting β 1 integrins), reverses their polarity to apical-out

1.1.2. Drug tests on apical-in and apical-out cell clusters

We compared the survival of TSIPs and PDX#3 organoids embedded in collagen-I gels, in their native or inverted topologies (**Figure 87a**) and after treatment with cytotoxics widely used in CRC chemotherapies: Oxaliplatin, 5-Fluorouracil (5-FU) and Irinotecan (SN-38). We chose the IC70 concentrations calculated on the dose-response curve obtained in our lab from a collection of 25 organoids derived from CRC patients (**Figure 87b**).

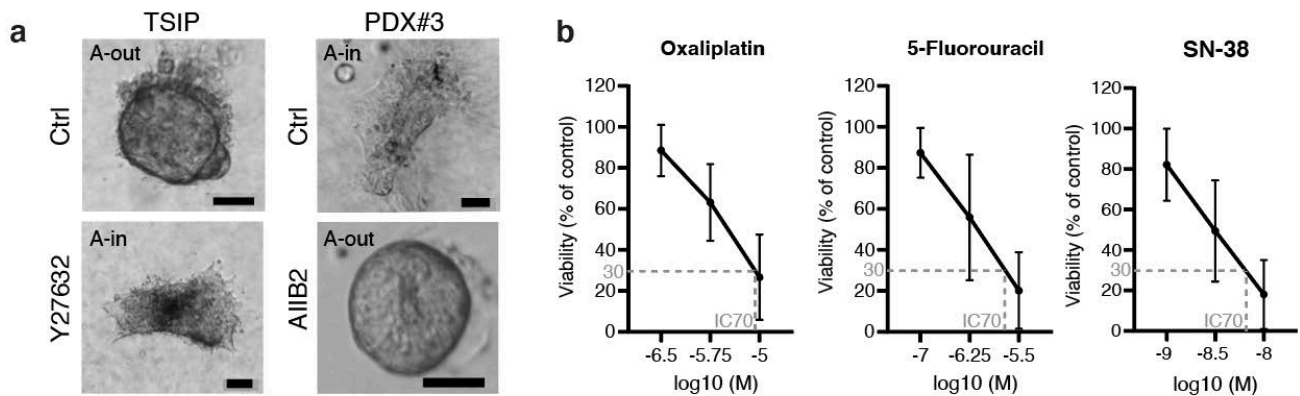


Figure 87. Organoid reversion and determination of drug concentration.

a, Phenotype of TSIPs and PDX#3 assessing their normal polarity and its reversion. Scale bar=50 μ m. **(b)** Determination of the IC70 on dose-response curves for CRC organoids. **b**, Viability of a cohort of 27 patients CRC organoids treated with Oxaliplatin, 5-Fluorouracil and Irinotecan (SN-38), used to determine the IC70.

TSIPs (apical-out) and Y27632-treated PDX#1 clusters (apical-in, **Figure 87a**) were incubated with the drugs for 2-4 days and the number of viable cells was assessed using ATP-bioluminescence (**Figure 88a**). The viability of the organoids in response to the three drug treatments was increased in the apical-out topology, as shown an Apical-out/Apical-in ratio of viable cells over 1 (**Figure 88b,c**).

Using a similar strategy, we added cytotoxic agents to PDX#3 clusters in their native (apical-in) and inverted (apical-out induced by A11B2 function blocking antibody, **Figure 87a**) topologies (**Figure 88d**). Likewise, cell survival to the three drug treatments was enhanced in the apical-out compared with the apical-in topology, suggestive of a higher resistance or lower sensitivity to chemotherapies compared to apical-in topology (**Figure 88e,f**).

1. Apical-out organoids respond less to chemotherapies than apical-in organoids

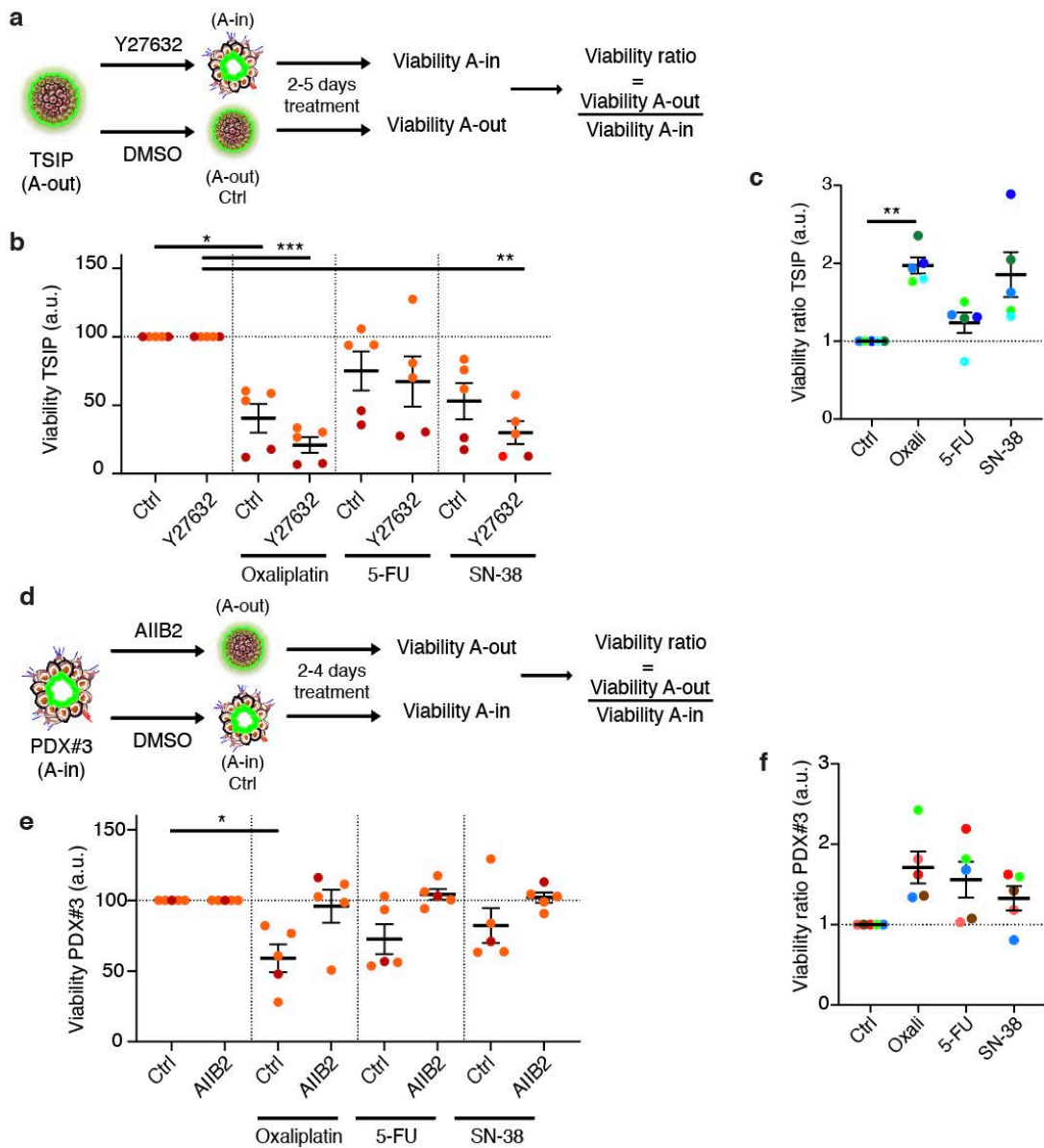


Figure 88. TSIPs and PDX#3 clusters are less sensitive to chemotherapies in their apical-out conformation.

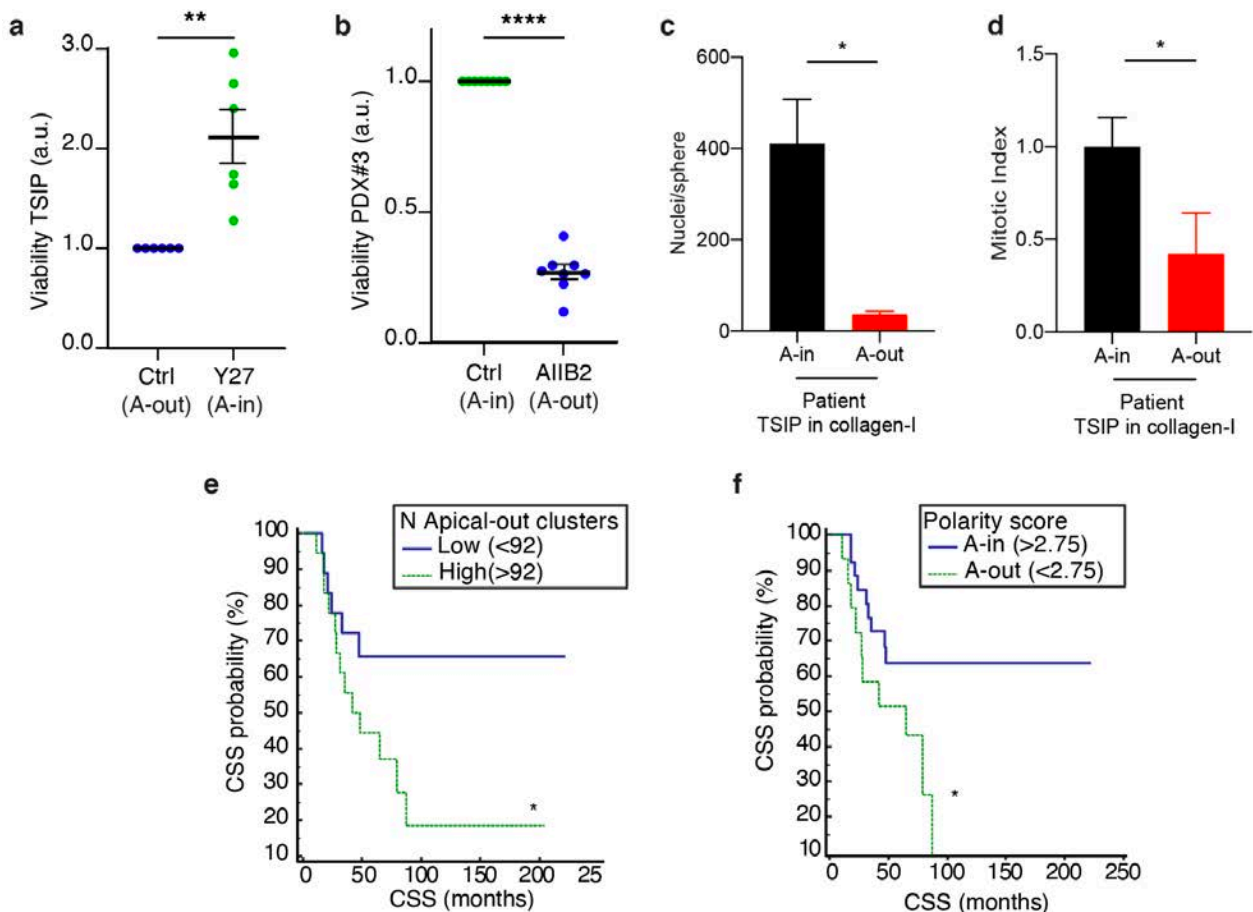
a,d, Schematic representation of the protocol for assessment of polarity-related chemosensitivity for PDX#1 and PDX#3. **b,e**, Viability of TSIPs (b) and PDX#3 (e) organoids in wild-type (Ctrl) or treated with Y27632 (25 μM) or AIB2 (10 μM) respectively, and incubated for 2 days (orange dots) or 4-5 days (red dots) with Oxaliplatin (10 μM), 5-Fluorouracil (5-FU, 1.8 μM) or Irinotecan (SN-38, 6.10⁻³ μM). One-way ANOVA between chemotherapy condition and condition without chemotherapy. When chemotherapy is applied clusters after reversion, the corresponding control is Y27 or AIB2 without chemotherapy. Orange dots: 2 days of incubation with chemotherapies; red dots: 5 days (TSIPs) or 4 days (PDX#3). **c,f**, Viability ratio of TSIPs and PDX#3 organoids in control condition (Ctrl) or after treatment for 2 to 5 days with Oxaliplatin (Oxali, 10 μM), 5-Fluorouracil (5-FU, 1.8 μM) or Irinotecan (SN-38, 6.10⁻³ μM). Green: 4-5 days of incubation with chemotherapies; other colours: 2 days. One-way ANOVA. *** $P < 0.001$, ** $P < 0.01$, * $P < 0.05$. Data are represented as mean \pm s.e.m.

Together these experiments ruled-out off-target effects of AIB2 or Y27632: we obtained the same results whatever the “normal” organoid topology and whatever the drug used for polarity reversion. These functional assays pointed to inverted apico-basal polarity as a protective topology against chemotherapeutics-induced cell death.

2. A LOWER PROLIFERATION RATE IS OBSERVED IN APICAL-OUT CLUSTERS

Independently of the genetic make-up of the tumour, we observed that TSIPs and PDX#3 organoids in the apical-out topology harbour a higher viability (ATP levels) in control condition than their apical-in counterparts (**Figure 89a,b**). As the same number of cell clusters and of comparable size were initially embedded in collagen, this indicates a higher lower proliferation rate for apical-in organoids. This could explain their decreased vulnerability to chemotherapies, targeting cell division. Interestingly, this lower proliferation rate of the apical-out topology was observed in live patients specimens from peritoneal effusions as well: they display a lower mitotic index and contain a lower number of cells per sphere (**Figure 89c,d**).

Canet-Jourdan and colleagues then showed that patients harbouring a CRC with a high number of apical-out clusters collected in 500ml of peritoneal effusion (> 92) had a significantly shorter cancer-specific survival (CSS) than patients having a CRC with a low count of apical-out clusters (≤ 92) ($P = 0.04$; H.R.: 2.5; C.I.: 1-6.3) (**Figure 89e**). Similarly, based on an automated histological analysis of a published cohort of MUC CRC patients (Barresi et al., 2015), the patients having a CRC with a low polarity score (ratio apical-in/apical-out < 2.75) had significantly shorter CSS than those with a high score (≥ 2.75) ($P = 0.02$; H.R.: 3.1; C.I.: 1.1-8.4) (**Figure 89f**). Therefore, the clinical outcome of patients correlates with the polarity orientation of their tumour, the apical-out MUC CRCs being associated with shorter survival.



2. A lower proliferation rate is observed in apical-out clusters

Figure 89. Apical-out spheres display lower proliferation rate and their presence correlates with lower patients survival.

a,b, Viability assessment using ATP-bioluminescence for TSIPs (a) and PDX#3 organoids (b) in control condition or after polarity reversion (Y27632 at 25 μ M or AIB2 at 1 μ g/mL respectively). Mean \pm s.e.m.

c,d, Number of nuclei per sphere (c) and the mitotic index (d), associated with apical-in and apical-out morphologies, counted using DAPI staining, respectively from n=19 spheres and 7792 nuclei and n=10 spheres and 364 nuclei from 3 patients. Data are represented as mean \pm s.e.m in (d). **e,f,** Kaplan-Meier curves displaying cancer-specific survival depending on the number of apical-out clusters (e) and polarity score (f). Log-rank tests for panels (e) and (f) with *P<0.05.

Chapter VI. Discussion

Tumour metastasis is a major concern in cancer care. It accounts for most deaths, and highly complexifies patient treatment. Therefore, understanding the biological bases of the metastatic process is presently an important challenge that carries hope in the future of cancer treatment.

While cancer has long been thought to disseminate through an epithelial-to-mesenchymal transition, we discovered a few years ago that CRC metastasis is often mediated by cell cohorts that disseminate collectively while keeping strong epithelial properties (Zajac et al., 2018). This work was in line with recent studies highlighting collective cancer spread (Aceto et al., 2014; Cheung and Ewald, 2016; Cheung et al., 2016; Gundem et al., 2015; Liotta et al., 1976; Ruitter et al., 2001). The cell cohorts we discovered in patients with colorectal cancer displayed a peculiar topology, keeping their apical pole outwards. We named them TSIPs for Tumour Spheres with Inverted Polarity. The discovery of TSIPs raised new questions on collective invasion mechanisms and cancer cell response to treatments.

1. TSIPs DISPLAY LOWER SENSIBILITY TO CHEMOTHERAPIES IN THEIR APICAL-OUT TOPOLOGY

Studying organoids from two different PDXs revealed that the apical-out topology is associated with TSIPs lower response to the three chemotherapies widely used in colorectal cancer treatment that we tested: irinotecan (SN-38), oxaliplatin and 5-fluorouracil (5-FU).

1.1. Outlooks on *in vitro* observations

1.1.1. Experimental setup: collagen-embedded cell clusters from PDXs and automated protocols

To investigate the impact of the epithelial orientation (apical-in/apical-out) on the response to chemotherapies, the only models we have to date that reproduce patients' TSIPs come from a PDX bank, the CReMEC repository (**Figure 87**) (Julien et al., 2012).

Because of their *in vivo* 3D expansion in mice, patient-derived xenografts (PDXs) display much more patient-like responses compared to cell lines. Indeed, the biological properties of the latter are affected by their culture and expansion on 2D substrates over passages. This results in cell selection and lower heterogeneity of cell lines. Their invasive behaviour in microchannels strikingly highlighted this difference in cell heterogeneity: cell clusters from cell lines displayed much more narrow distributions of their velocities compared to primary patient explants and cell clusters from PDXs, whose distribution were similar (**Figure 68d**). Therefore, expecting high intra- and inter-sample biological variability, I used or developed automated protocols for as much experimental steps as I could to limit the experimental variability: collagen drop deposition, drug testing and ATP bioluminescence measurements. Automation also increased considerably the speed of manipulation, allowing me to perform a higher number of technical replicates. It also ensured user-independent control of the experimental conditions, which was particularly important as a colleague and I performed these experiments in pair.

Also, organoid experiments are usually performed in Matrigel to allow for their proliferation and morphogenesis (Clevers, 2016). Here, to mimic the stroma that these cell clusters would invade during their dissemination, we rather embedded them in collagen.

1.1.2. Hypotheses for apical-out cell clusters lower response to chemotherapies

All in all, the difference between apical-in and apical-out clusters response to chemotherapies was reproducible between several chemotherapies (**Figure 88**). The use of the two PDXs also showed that it

was reproducible whether we treated apical-in and apical-out TSIPs in their natural or inverted topologies, excluding an off-target effect of polarity reversion.

A first hypothesis of this lower response to chemotherapies is a lower proliferation rate in apical-in cell clusters. Indeed, we observed that from a similar initial quantity of clusters, cell viability of control conditions was lower in the apical-out topology than in the apical-in one at the end of the experiment. This could be interpreted as a lower proliferation or higher senescence of the apical-out phenotype. The quantification of the mitotic index and number of cells in patient apical-out and apical-in clusters comforted the hypothesis of a lower proliferation rate in apical-out clusters. Given that chemotherapies target cell cycle, this would thus be a relevant hypothesis to explain the lower response to chemotherapies of apical-out cell clusters.

Another hypothesis could be the accessibility to the treatment. Indeed, treatment accessibility could reasonably be higher in apical-in clusters, that are flatter and thinner compared to the very dense and packed rounded apical-out clusters. In addition, the apical actomyosin belt surrounding apical-out clusters, with tight junctions at the most apical part could form a barrier reducing accessibility to the treatment (**Figure 76a**). In line with this, we observed that fluorescent dyes penetrate far less in apical-out clusters than apical-in..

Also, receptors related to chemotherapeutic agents' in-take our our-take may be reverted, conferring more resistance to apical-out cell clusters. A recent study proved that indeed, when cultured in suspension, CRC organoids presented on their outward apical side the multidrug resistance protein ABCB1, while in collagen gels it faced central lumens (Ashley et al., 2019). Consequently, they observed that when the apical pole faced outwards, CRC organoids were more resistant to various anti-cancer drugs.

1.2. Perspectives for patient care

As exemplified here and in other studies from our lab, *in vitro* drug testing on primary 3D multicellular clusters can be performed easily and automatically to try to anticipate patients responses to treatments (Libanje et al., 2019). The predictive value of such tests has been highlighted in 17 publications since 2018 using patient-derived organoids (PDOs), i.e. tridimensional multicellular clusters made from patient specimens and cultured *in vitro* (Wensink et al., 2021). This robustness also highlights the importance of cell-autonomous properties, as these tests do not involve the tumour microenvironment at this point.

Such diagnostic tests carry a great hope for precision medicine in oncology today. Indeed, most deaths from cancer are related to its metastatic dissemination, which cannot be overcome by cytoreductive surgery. Only treatments can cure patients with metastatic cancer. However, despite the number of therapies that have been developed in the last decades, finding the right therapy for each patient remains a challenge. Precision medicine was an important breakthrough but relying on molecular data only, no more than 7% patients can really benefit from it today (Haslam et al., 2021). This is related to several factors including the presence of actionable mutations, the availability of the treatment at the hospital and tumour response to the treatment. Therefore, *in vitro* functional assays predicting tumour response would bring important insights on efficient therapies, while discarding the ones to which the tumour is resistant. That is why we are currently developing robust PDO-based automated drug tests. They are applicable to chemotherapies and targeted therapies at this point and can be combined with the knowledge of the patient's molecular data. Their predictive value and clinical utility are under evaluation in a clinical trial promoted by Gustave Roussy Institute. We hope that such *in vitro* diagnostic tests, through the functional information they provide to doctors, will significantly improve patient survival.

The results we obtained in our chemotherapy assay on TSIPs provide a first important hypothesis to explain the lower survival of patients with TSIP-producing tumours. We can expect this inverted topology to impact other cellular properties of TSIPs, explaining this worse prognosis. For example, their apical-out topology could make them better escape to the immune surveillance, and to immunotherapies, by retaining active epitopes on the internal basolateral side. This interaction between TSIPs and immune cells can be investigated *in vitro*. Microfluidic devices combined with image analysis pipelines have already shown their relevance to investigate immune cell behaviours in contact with tumour spheroids (Ronteix et al., 2021).

In addition, our group previously showed that TSIPs are potent metastasis initiators in mice and invade efficiently in peritoneum explants and 3D physiological matrices (collagen-I, Matrigel) (Zajac et al., 2018). These results also suggested that mechanistically, their inverted polarity would endow them with peculiar invasive properties, leading us to investigate how they can perform this unknown motion and what molecular pathways are at stake.

2. DECIPHERING THE BASIC PRINCIPLES OF COLLECTIVE AMOEBOID MIGRATION

When investigating the invasive properties of TSIPs, the most striking was their ability to migrate independently from focal adhesion formation (Zajac et al., 2018). This surprising observation already had the potential to be a breakthrough in the field of cell migration. Indeed, despite the diversity of their patterns, all collective modes of migration known to date shared at least this common feature: traction forces generation on the substrate through focal adhesions (Friedl et al., 2012). Therefore, TSIP specific behaviour suggested that collective migration could occur in a totally different way, reminiscent of the duality between mesenchymal and amoeboid single cell migration.

This opened a whole new area of investigations. To address it, scientifically and technologically, we first combined the knowledge gathered on the modes of migration that shared some features with TSIP invasion: migration of epithelial cell collectives and single cell focal adhesion-independent migration (amoeboid mode). This revealed strong common patterns as well as unexpected differences with the basic principles of what we call “collective amoeboid migration” (CAM).

2.1. Technological innovations

First, new developments were required to observe focal adhesion-independent collective migration and analyse it. We developed innovative approaches by combining recent technical advances: microchannels, optogenetics, confocal live imaging, 3D cell clusters. I also used biological material from various origins to ensure the biological relevance of our work while allowing experimental versatility.

2.1.1. The choice of biological material

Bench to bedside, bedside to bench in cell biology. Our lab is ideally located at Gustave Roussy Institute to implement bedside to bench and bench to bedside approaches. It is the analysis of peritoneal effusions from patients that made us discover TSIPs and their role as tumour intermediates. Together with recent studies and previous histological observations, it revealed the importance of collective cell dissemination and invasion in cancer, which was understudied in cell biology compared to single cell dissemination (Aceto et al., 2014; Cheung and Ewald, 2016; Cheung et al., 2016; Gudem et al., 2015; Liotta et al., 1976; Ruiters et al., 2001). Indeed, while there is an important interplay in molecular biology between *in vitro* analyses and patient's data, cell biology experiments are often performed quite far from clinical issues. Since the original experiments from Friedl that revealed collective cancer cell migration, very few would perform their investigations directly on patient explants (Friedl et al., 1995). This is certainly due in part to experimental challenges: biological variability is better controlled by using cell lines, easy to manipulate but often studied

at the single cell level. On the contrary, patient specimens provide a variable amount of material, and strongly depend on patients' practical organisation with the hospital.

All in all, TSIP discovery highlighted how interactions between cell biology research and the clinic must be preserved to uncover cellular processes that are relevant for cancer dissemination in patients.

Primary samples for CAM investigations. Following this key observation, I studied cell clusters that I found in patient ascites to investigate the existence of collective amoeboid migration. It revealed that indeed, this mode of migration can be activated by cell clusters right after their recovery from ascites, suggesting that it may occur before as well in patients, e.g. between the peritoneal interfaces.

Interestingly, I observed that their behaviour was much more heterogenous than cell lines'. This can be seen in the distribution of cell clusters speeds, which is wider in primary samples – cancerous or not – than the speed of cell clusters from cell lines (**Figure 68b,d**). This difference could be expected as the culture of cell lines on 2D substrates do not promote cell heterogeneity and rather tends to select cell subsets. It also confirmed the similarity between patient's samples and organoids from patient-derived xenografts (PDXs). These observations, together with the previous paragraph, suggest that once results have been obtained with cell lines, experimental validation should be sought on primary samples to ensure biological relevance.

Using cell lines to uncover the underlying mechanisms. Indeed, we were pleased to find HT29-MTX cell line (and HT29) as displaying fast migration in microchannels. They have been convenient tools for our investigations compared to primary samples, for the reasons described above. In addition, cell lines allowed the expression of fluorescent probes by lentiviral infection (**Figure 73, Figure 75, Figure 77, Figure 78, Figure 80**). Lentiviral infection and gene expression were indeed much more complicated in organoids from PDXs. A plausible reason is their low survival as single cells that prevents efficient cell sorting or selection after infection. Nevertheless, I was able to confirm on primary samples from PDX most results obtained on CAM: existence of collective amoeboid migration (**Figure 68b,c**), dependence to contractility (**Figure 77d**), overall translation (**Figure 80d**) and cellular jiggling (**Figure 83f**). Yet, the study of myosin polarisation and dynamics have not been possible yet: they require homogeneous expression of the fluorescent probe which is not possible at this point as mentioned above.

Long-term culture of patient-derived organoids and PDX organoids. However, we should soon be able to express fluorescent probes in organoids cultured on the long term from PDXs (PDXOs) and even in patient-derived organoids (PDOs) lines. The PDXO line derived from PDX#3 displays CAM and can be cultured in Matrigel in our lab, which would allow cell infection and sorting together with a steadier cell clusters production. In addition, studies from different groups have proven that organoids are reliable models of patients' tumours biology (Wensink et al., 2021; Zajac et al., 2018). Today, they are often used as developmental models or to study their response to treatments, thus their use for invasion studies as we do comes as a new application (Clevers, 2016; Wensink et al., 2021).

2.1.2. Experimental design: microchannels

Collagen-I gels as the best physiological-like system. Collagen-I gels are conventionally used to mimic *in vivo* 3D conditions in fibrillar networks and to investigate either single cell or collective invasion (Niggemann et al., 2004; Wolf et al., 2009). Their composition can be tuned either to vary their stiffness and pore size (Wolf et al., 2009). Collagen can also be mixed with other extracellular matrix components to represent specific microenvironments, e.g. with hyaluronic acid to represent glioblastoma microenvironment (Cui et al., 2020).

Nevertheless for our migration studies, a 3D collagen-I matrix complexified the study of organoids migration. They could move in any direction, including through the thickness of the gel, which prevented from efficient tracking and fluorescence imaging. They could also display complex interactions with the collagen-rich environment, while we were interested in limiting such interactions to study CAM.

Microchannels to allow better control of environmental conditions and powerful imaging. Therefore, we took inspiration from the experimental setups used to study single cell non-adherent migration (Liu et al., 2015). We designed micro-engineered channels and chambers and adapted their dimensions to confine our cell clusters, which promotes amoeboid migration in single cells (Liu et al., 2015). These devices constrained directionality and regulated cell-substrate interaction with polyethylene glycol (PEG) or collagen-I coatings. Microchannels also allow for powerful imaging, as cells are directly in contact with the glass bottom. They are very versatile and we adapted them to be compatible with changing the surrounding medium for immunofluorescence stainings. In addition, they provide a good reproducibility of experiments, even between users, as they all originate from a parent mould.

Nevertheless, my experiments revealed two challenges:

- *Imaging organoids in their thickness:*

In our experimental setting, the top of clusters is in contact with the PEG-coated PDMS while the bottom is in contact with PEG-coated glass. In order to investigate actomyosin dynamics on both sides, I tried to image the top and bottom of cell clusters. Nevertheless, even over only a 30 μ m-thickness, I obtained poor resolution at the top of the clusters. Indeed, cluster compression and density can induce increased light absorption and light diffraction because of the lipids composing cell membranes. This would affect both excitation and emission. Thus, with the microscopy platform, we identified two possible improvements:

1/ *2-photon microscopy* can improve the imaging thanks to the higher wavelengths used for illumination: this should lead to less absorption and more penetration to allow fluorophore excitation.

2/ *Water immersion-objectives* display a closer refractive index to the immersion medium than oil immersion, and thus should improve the resolution ($n(\text{water})=1.3$, $n(\text{cells})=1.4$, $n(\text{oil})=1.5$, $n(\text{glass})=1.5$).

A slightly better resolution on top of the clusters was obtained by using 2-photon microscopy and/or water immersion-objectives (data not shown). This was true in particular for immunofluorescence stainings, where fluorescence is much brighter than fluorescent protein expression. However, the duration of each single acquisition was not compatible with live imaging.

Light sheet microscopy would probably be a perfect solution as it is not affected by sample thickness and often used to image thick samples. It is unfortunately not compatible with the current microchannel settings. We could envision a new experimental setting to observe CAM under light sheet microscopy, by creating cylindrical microchannels in a gel.

- *Cluster low attachment prevents easy medium changes for immunofluorescence stainings:*

An important strength of PDMS microchannels is that they can be easily adapted to various applications. We set up an immunofluorescence chip and protocol in order to study endogenous protein expression. It would also allow to image those proteins (actin, myosin, others) in patient samples that cannot express fluorescent probes. It required the design of large channels orthogonal to those that contain cell clusters in order to change the culture medium (**Figure 76b**). Despite this design, this was still challenging as the cell clusters do not attach to the channels and can be easily flushed away (**Figure 67b**). The use of pumps with a chosen fluid flow could help gain control on this part. This setting is compatible with following cluster migration before immunofluorescence, the channels being shorter to allow diffusion of molecules in the channel during stainings.

Another challenge is to ensure homogeneous penetration of antibodies: any bias would prevent from analysis myosin (or any other protein) polarisation. Improving the permeabilization solution (use of Triton X-100 and saponin), enlarging the incubation times (over-night) and increasing the temperature of incubation (room temperature), allowed us me to obtain homogeneous stainings (**Figure 76b,c**). Nevertheless, low and anisotropic penetration of antibodies can still be observed in some experiments. This can be due to cluster crowding in channels or bad fluid flow control. Next developments can involve a new design for better fluid flows, or the use of a more porous polymer than PDMS to ensure better medium exchanges.

All in all, microchannels are perfectly suited for long-term imaging of non-adherent cell cluster migration, either in bright field microscopy or in fluorescence. Immunofluorescence needs certain improvements, but first results are promising. Last, organoids have always been more difficult to image in their thickness, hence the need of advanced microscopy techniques to optimise the acquisition.

2.1.3. Increasing robustness and speed in image analysis

Today, the large amount of data generated by live microscopy requires powerful tools to extract quantitative results. More and more tools are developed allowing for a robust quantitative analysis of imaging-based experiments. That is why we used already available algorithms or developed ours to allow for high-throughput and more robust image analysis, in particular in migration experiments, with automated nuclei, myosin tracking and analyses of the tracking parameters (see **Material and methods**).

Besides, we are developing a deep learning-based automated segmentation and tracking of clusters in microchannels from bright-field images (**Figure 86**). Indeed, while traditional image segmentation provides convincing results on fluorescence images, bright field images are much more complicated to analyse with similar techniques because of their low contrasts. Bright field imaging still remains a method of choice in many cases. Some cell clusters – such as TSIPs – are not easily permeable to fluorescent probes nor can they provide a homogeneous fluorescent protein expression. Those probes – and laser illumination – can also have cytotoxic or functional effects on cells, impeding the reliability of the experimental setup. That is why bright field imaging is still often performed in cell biology, even if generally induces manual quantitative analyses.

Deep learning-based approaches certainly made a breakthrough in our field, allowing automated segmentation and tracking in label-free cell systems. They are now more and more accessible through open-access packages and user-friendly softwares (Chamier et al., 2020; Matthews et al., 2022; Stringer et al., 2020). In addition, deep learning training on fluorescence images can now even allow the segmentation of subcellular structures (mitochondria, nuclei, actin filaments) on bright field images, in absence of stainings.

These would be great advances for non-invasive cell microscopy, especially helpful in the study of TSIPs or fresh patient explants.

2.2. Deciphering CAM through the angle of collective cell migration

The first fundamental feature of CAM that I will describe here is its collectiveness. While clusters CAM strikingly differs from traction-based collective migration as being focal adhesion-independent, this collectiveness brings several important hypotheses on the orchestration of this migration based on the current knowledge on collective cell migration.

2.2.1. A supracellular mode of cell migration

When migrating in PEG-coated microchannels, most cell clusters remained cohesive (**Figure 71**). There were a few exceptions: cell clusters from MDCK and glioblastoma (U87) cell lines adhered to the channel walls and released single cells migrating alone (data not shown). They would probably either deposit their own matrix on top of PEG or degrade PEG coating. These adhesive properties could be inherited from their culture as cell lines on 2D substrates.

Phenotypically, all other cell clusters kept a round and cohesive shape when migrating in microchannels. CAM is associated with the maintenance of cell-cell contacts and cells are all migrating in the same direction on average. These are the main characteristics of cooperation and coordination of collective cell migration (Friedl et al., 2012; Shellard and Mayor, 2019).

In collective cell migration, force is known to be transmitted between cells through intercellular junctions, and when existing, through a supracellular actomyosin cable (Friedl and Mayor, 2017; Shellard and Mayor, 2019; Sunyer et al., 2016). Immunofluorescence confirmed that HT29-MTX cell clusters, TSIPs and PDX#3 kept E-cadherin all along intercellular contacts in microchannels (**Figure 76c**). In addition, cell clusters displayed a surrounding actin and myosin contractile cortex, either in suspension or in microchannels, that reconstitutes fast after cell extrusion or mitosis (**Figure 76**). This feature of supracellular migration suggests that coordination and force generation in CAM should be apprehended at the cluster scale. Our observations of myosin polarisation and steering of the contractility at the cluster scale (**Figure 77**, **Figure 78**) and our model of a global gradient of contractile stress (**Figure 84**) comfort this approach.

In the context of collective cell migration, this supracellular organisation of clusters displaying CAM can suggest other important features concerning force transmission in the cluster.

2.2.2. Gradient of intercellular tension and force transmission

An asymmetrical front-rear distribution of intercellular forces has been observed during traction-based collective cell migration of epithelial cell sheets. The expression of Förster resonance energy transfer (FRET)-based tension sensors coupled to cell-cell junctions proteins (E-cadherin, α -catenin, ...) can provide the map of internal forces distribution in this system (Cai et al., 2014; Teo et al., 2020). Upon mechanical force, the distance between the fluorescent proteins increases and FRET decreases. Laser cut at cell-cell contacts and measurements of the recoil can provide similar information more locally (Krndija et al., 2019). In the conventional traction-based mode of migration of cell monolayers, tensions are higher at the back of the cohort, exerting most traction forces to pull the whole (Krndija et al., 2019; Trepast et al., 2009). Given the absence of traction forces on the substrate during CAM, we cannot expect a tug-of-war mechanism by itself, and the 3D structure also has to be taken into account. However, we can expect higher tension in rear cells present at the cortex, undergoing higher contractility. This would be consistent with our hypothesis of a gradient of contractile stress to the rear.

2.2.3. ERK-mediated activation of contraction and jiggling

We suspect the jiggling to be induced by cell contractility. This can be confirmed by monitoring cell and myosin dynamics under contractility inhibition. This can be difficult for myosin as cortex intensity is expected to decrease as well, thus having cell tracking would be helpful.

In addition, a recent paper emphasized a role for ERK-mediated mechanochemical waves in epithelial cell sheet migration. In their system, mechanical stretch induces ERK activation and cell contraction (Hino et al., 2020). This contraction would then activate sequentially ERK and contraction of the neighbours, resulting in ERK activation waves and polarity alignment. During CAM, in addition to overall cluster polarisation, the internal jiggling could emerge from ERK activity as well. This can be monitored through

KTR reporter localisation in the nucleus or cytoplasm: ERK activation leads to KTR phosphorylation in the nucleus and export to the cytoplasm.

2.2.4. Cell-cell junctions composition and distribution: jammed-unjammed states and polarity establishment

I have not assessed at this point the composition and distribution of intercellular junctions, except by reporting the presence of E-cadherin. Their composition can strongly affect the behaviour of cell cohorts (Friedl and Mayor, 2017). Therefore, differences can be expected between migrating and non-migrating clusters, and between cell types, e.g. assessing the presence of strong epithelial junctions versus looser N-cadherin junctions (Shellard et al., 2018).

The level of intercellular junctions can also regulate coordination and lead to jamming-unjamming transitions, thus impacting cluster velocity (Sadati et al., 2013). In CAM, the jammed or unjammed state could be directly related to the amplitude of the cellular jiggling, as in a constrained jammed state, we would expect lower fluctuating movements.

Besides, adherens junctions have been described to maintain integrity and polarity of the actomyosin cortex, as observed in border cells (Chen et al., 2020). This interplay could be assessed by partial or total inhibition of E-cadherin. This should be done carefully while monitoring cluster cohesion.

2.2.5. Cluster front-rear organisation during CAM

The presence of a polarised actomyosin cortex could induce cell invagination at the rear and treadmill-like in neural crest cells migration (Maître et al., 2016; Shellard et al., 2018). Nevertheless, this has not been observed during CAM, neither in the lab nor in the cluster reference frame (**Figure 80**).

Cells rather translated as a whole. The very few neighbour exchanges occurred mainly when dying cells were extruded or during mitosis, as they underwent major changes in shape and contractility. This absence of significant exchanges at the front is also consistent with a low energetic mode of migration, that does not imply focal adhesion formation and traction (Zhang et al., 2019).

Therefore, with cells staying roughly at the same place in the cluster reference frame over time, this raises the question of a front/rear hierarchy like in conventional traction-based collective cell migration (Mayor and Etienne-Manneville, 2016). Given the presence of a supracellular polarisation, different hypotheses on cluster organisation can emerge:

1/ *Specific front and back cell specification*, i.e. a specific molecular determination of front and rear cells. A certain level of cell sorting could be at stake before the initiation of migration: for example, clusters would only migrate once the most contractile cells are segregated at the rear, and the less contractile at the front. A reorganisation of this kind would rely on the remodelling of cell-cell junctions and the differences in contractility between neighbours.

This hypothesis can be investigated by the use of photoconvertible probes, such as Dendra, coupled with widespread proteins (e.g. histones), a technique used in (Konen et al., 2017). Indeed, after monitoring the direction of migration, cells of one side (front for example) could be photoconverted. Flushing the channels and dissociating the clusters would allow subsequent cell sorting and genomic profiling. The same should be performed for the opposite side for comparison.

2/ *A few steering cells*, either at the front or at the back, could induce the overall polarisation by dictating the orientation of the actomyosin cortex, similar to the regulation of leader formations in border cells (Mishra et al., 2019; Wang et al., 2020).

Following a molecular hypothesis, optogenetic tools can be used for specific activation of this pathway in a subset of cells, at the front or at the rear (even more locally than what we propose in **Figure 78**). This should be followed by the monitoring of cluster migration and myosin polarisation. The experiments presented in **Figure 78** already indicate that activation of RhoA or Rac in several cells can induce migration or directionality and can be interesting candidates. The levels of endogenous expression of this protein should also be monitored before the onset of polarisation/migration to establish the sequence of events. 2-photon-mediated laser ablation can also be performed to identify whether some specific cells are required, whether they can be replaced.

Cell clusters being able to switch direction during migration in channels, this hypothesis may be more reasonable than the previous one. In any case, following cell rearrangements during cluster changes of direction should give interesting clues. In particular, chambers (**Figure 67a**) would certainly provide more information as they allow degrees of liberty and more direction changes.

3/ A *front-rear polarisation* could emerge from (small) environmental inhomogeneities (Dumortier et al., 2012)

This question is much more complicated to address in our microchannels setting, where the molecular and mechanical conditions are supposed to be homogeneous. An interesting way to address it would be to adapt the system to chemotactic cues and rigidity gradients, for example, to investigate CAM response in such environments. A durotactic response would be of high interest as the current known mechanism exclusively relies on focal adhesion strength, which is impossible in this system. It would thus also bring completely new knowledge in this field.

Of note, when investigating the front-back organisation of the cell cohort, the question of which cells are endowed with *steering and powering* skills has to be addressed (Theveneau and Linker, 2017). These functions can be either split to one end of the cluster, or shared. It is a complicated question to separate both roles, as interfering with either of them can impact the other, particularly if both are related to actomyosin contractility.

In our model of “polarised jiggling”, we could expect that the cells that induce polarisation are “steering”. Our optogenetics results suggest that at least both ends have this potential. Thus, the onset of polarisation has to be better identified, it will be discussed in a following section.

Our model proposes that the power is provided by the cellular and myosin jiggling, at the contact with the substrate. I would thus suggest that the outer layer of cells is “powering”. This model of a polarised jiggling would be strengthened by the observation of another gradient than the gradient of myosin concentration: in the amplitude of the myosin/cell speed fluctuations, in cell density, ... I did not observe it, nevertheless, if such a gradient was eventually observed, the cells with the highest quantity of it could be considered more specifically as “powering”. In our model, we expect them to be at the rear, propulsing the cell cohort.

2.3. How the knowledge of amoeboid migration can improve CAM understanding

The focal adhesion-independence and myosin polarisation observed in CAM are strikingly similar with single cell amoeboid migration features (Liu et al., 2015; Paluch et al., 2016; Ruprecht et al., 2015). In addition, cells displaying amoeboid migration are highly contractile: during CAM, it seems that the outer layer of cells that displays the myosin cortex is also contractile, given their blebbing activity (Charras and Paluch, 2008).

2.3.1. CAM, as single cell amoeboid migration, relies on actomyosin contractility

Actomyosin contractility plays a key role in single cell amoeboid migration. Blebbistatin and Y27632 compounds are most often used to interfere with actomyosin contractility, either directly or indirectly respectively. Inhibiting myosin activity stops or decreases significantly single cell amoeboid migration in

different cell types, with variations in the level of inhibition (Huang et al., 2018; Jacobelli et al., 2009; Lämmermann et al., 2008; Liu et al., 2015; Sadok et al., 2015; Sahai and Marshall, 2003). Similarly, its inhibition decreases CAM for HT29-MTX clusters and TSIPs, by 3-fold and 1.7-fold respectively (**Figure 77d**).

It can be noticed that it does not fully abolish CAM and that the effect is more important for HT29-MTX clusters than for TSIPs. Of note, the distribution of TSIPs velocities after Y27632 or Blebbistatin incubation is, as in control, still wider than that of HT29-MTX. This can result from the higher heterogeneity existing in clusters from PDXs compared to cell lines as described above. This partial inhibition is also consistent with the variability of the level of inhibition of amoeboid migration in single cells, varying between a full inhibition and a 2-fold and 3-fold decrease in the papers cited above, and between cell types.

It could result from a partial inhibition of myosin activity: Liu and colleagues showed that for single cells, 20% of myosin phosphorylation remains after inhibition by Y27632 at 30 μ M (Liu et al., 2015). Such a quantification could be performed by western blot for cell clusters incubated with these drugs.

Nevertheless, it has to be considered that our experimental setting itself can also affect drug concentration in contact with cell clusters: PDMS is known to absorb most drugs and makes it very challenging to ensure that their concentration in microchannels is as expected (Liu et al., 2015; van Meer et al., 2017; Shirure and George, 2017).

It can also suggest the existence of a complementary mechanism for collective amoeboid migration, that I will discuss in a following section.

2.3.2. Actomyosin and RhoA/Rac1 polarisation

The presence of a polarised actomyosin cortex is also an important characteristic of single cell amoeboid migration (Liu et al., 2015; Poincloux et al., 2011), present at the cluster level in CAM (**Figure 77**). In addition, during CAM, its level of polarisation is correlated with migration speed.

We used optogenetics to manipulate RhoA, which is an important regulator of myosin activity, mainly active at the rear during single cell migration (Bear and Haugh, 2014). RhoA activation on migrating clusters dictated their direction, indicating its steering role at the rear of the cluster (**Figure 78**).

Its activation on one side of non-migrating clusters did not induce migration towards the opposite side. This suggests that either this activation was experimentally not sufficient to induce cluster polarisation towards RhoA activation in non-migrating clusters, or that the powering mechanism (jiggling) is still missing and does not depend on RhoA (or not exclusively).

Of note, we observed that Rac1 light activation led to the onset of migration towards the side of activation. This can emerge from either cluster polarisation (which would indicate a steering role in front cells) or increased myosin/cellular jiggling (indicative of a powering role). However, the model would rather predict increased jiggling at the rear than at the front: this suggests that the first hypothesis of Rac1 inducing polarisation might be more plausible. In agreement with this steering role, Rac1 activation also dictated the direction in some clusters, but much fewer than RhoA (**Figure 78**).

These results suggest that a RhoA/Rac1 overall polarisation at a supracellular scale in cell clusters leads to CAM, which is reminiscent of single cell polarisation (Bear and Haugh, 2014). The higher impact of Rac1 activity than RhoA in the onset of migration may be related to the fact that non-migrating clusters already display an intense actomyosin cortex (**Figure 77**). Thus, polarisation would rather emerge from decreased levels of myosin at the front rather than higher levels at the back. These results are consistent with a RhoA/Rac1 antagonism (Evers et al., 2000). They are also similar to those observed in neural crest cells migration with activation or relaxation of myosin contractility through RhoA (Shellard et al., 2018).

The roles of RhoA and Rac1 in CAM by triggering myosin relocalisation should be confirmed by monitoring myosin polarisation at the cortex while activating RhoA or Rac1. In addition, this hypothesis of an onset of polarisation following decreased contractility at the front can be investigated by a more direct RhoA inhibition. An optogenetic tool could be used that targets RhoA to mitochondria and thus inhibits contractility (Valon et al., 2017). Otherwise, Rac1 could induce polarisation through other pathways, such as inducing actin polymerisation. I observed that actin polymerisation inhibition at a cluster level indeed induces lower migration (CK666 inhibitor, not shown), however it can affect cell-cell junctions as well which would impact CAM. Branched actin distribution in the cluster can rather be investigated by immunofluorescence, staining Arp2/3 subunits or, which is often easier, cortactin.

2.3.3. Force transmission to the substrate

In an amoeboid migration, no traction forces are exerted as cells do not form focal adhesions. Friction forces are rather supposed to promote migration (Bergert et al., 2015).

Similarly, when confined in PEG-coated microchannels, HT29-MTX cell clusters do not form focal adhesions, nor do they induce traction forces on PEG-coated PDMS substrates (**Figure 73**, **Figure 74**). Increasing passive friction forces through the addition of BSA in microchannels coatings (Bergert et al., 2015) increased clusters migration as in single cells. These results indicate that CAM is not traction-based, as proposed in other models of collective cell migration, and would rather rely on friction forces like what has been proposed in single cell amoeboid migration (Bodor et al., 2020; Reversat et al., 2020). However, it is very challenging to measure such low friction forces and very few groups have tried to measure them. Indeed, the current systems used to quantify traction forces for mesenchymal migration do not allow for measurement of friction forces of such a low amplitude, and modelling is still required to estimate the stresses exerted by amoeboid single cells (Bergert et al., 2015)

We investigated the role of integrins in CAM, given that the role of these transmembrane proteins, coupled to the cytoskeleton, was proposed in single cell amoeboid migration (Reversat et al., 2020). The inhibition of α V integrins with cilengitide (cRGD peptide) in HT29-MTX clusters led to their relocalisation to endosomal compartments and lower migration speed in PEG-coated microchannels. Thus, these experiments suggest that α V integrins could play a role in force transmission to the substrate through generation of active propulsive friction forces at the membrane.

Of note, α V integrins are also present at cell-cell contacts, as well as β 1 integrins, thus, we cannot exclude their contribution in cell coordination or intercellular force transmission. Interestingly, to date, while integrins have been often observed at intercellular contacts, this role has hardly been described (Zajac et al., 2018; Zuidema et al., 2020). Integrins could be implicated in the regulation of membrane tension in tetraspanin-enriched microdomains (TEMs), or in interactions with the RGD domains of cadherins (Zuidema et al., 2020). Integrins being predominantly known for their interaction with ECM, we could also investigate a role in cluster coordination through interaction with intercellular ECM secreted by cells.

As CAM has been often observed on mucin-secreting cell types at this point, either from PDXs (MUC CRC), patient samples (pseudomyxoma, CRC) and cell lines (HT29-MTX), another hypothesis for the generation of friction forces could be non-specific interactions through secreted mucins, or glycocalyx (Friedl and Bröcker, 2000). In cancer, these proteins have been shown to regulate the activity of membrane receptors such as integrins by regulating their clustering and the accessibility to ligands (Paszek et al., 2014). Their role in cell migration has not been described yet.

We observed a thick layer of mucin produced at the apical pole of TSIPs. This mucin secretion could prevent focal adhesion formation *in vivo* by creating an isolating layer surrounding clusters.

A role for glycocalyx in CAM could also explain why clusters from HT29-MTX cell line, which are mucin-secreting, migrates better than HT29 clusters (Lesuffleur et al., 1993).

All in all, the nature and amplitude of the forces exerted on the substrate during amoeboid cell migration is still elusive and understanding how it works in single amoeboid cells would greatly help understanding how it could be mediated in CAM.

2.3.4. Complementary mechanisms inspired by the knowledge of single cell amoeboid migration

As stated above, we observed that the underlying mechanism is fundamentally different from the main amoeboid mode of migration we know for single cells, based on persistent myosin retrograde flows. Based on our observations and biophysical modelling, we thus proposed the “polarised jiggling” as driving CAM. This mechanism could be complemented by others, that could vary among cell types and explain in part the residual motion after actomyosin contractility inhibition.

We have investigated another mechanism described for single cells: the osmotic engine described by Stroka and colleagues (Stroka et al., 2014). It relies on the activity of Na⁺/H⁺ pumps. Of note, it does not rely on actomyosin contractility which we demonstrated plays an important role in CAM (**Figure 77**, **Figure 78**). Thus, this mechanism could only be complementary and not the major mechanism.

Their inhibition in HT29-MTX clusters did not lead to a decrease of CAM, indicating that this mechanism is apparently not at stake (**Figure 77**). However, other observations suggested that external medium influx/efflux could be at play in some clusters that display CAM. Indeed, HT29-MTX often display vacuoles, and TSIPs and PDX#3 display a striking pulsatile activity. It could also be related to mucin production and release. The questions as to whether this pulsatile activity could contribute to cluster migration is still open, and it is possible that there are differences between cell types. We cannot exclude a contribution of other water or ion channels than Na⁺/H⁺ pumps mentioned above (aquaporins, NaK-ATPases, ...). They could be investigated either with inhibitors (such as ouabain to inhibit NaK-ATPases pumps) or immunofluorescence, with special attention given on their distribution between the front and back. We indeed already observed by immunofluorescence that aquaporins are present at cell-cell contacts in TSIPs. Of note, a hypertonic culture medium, induced by the addition of sucrose, results in the loss of the pulsatile activity of TSIPs. However, such treatments can be detrimental for cell clusters viability, which would obviously result in low migration. These questions can be further explored, while answering these sub-questions: which cell types could be affected by liquid transport, and how it would be regulated at a cluster scale.

Another complementary mechanism to the “polarised jiggling” could be what is called “chimneying”. Similar to the movements of climbers, pushing walls to move up, it consists in cells exerting normal forces on the substrate, hence increased friction anchoring to allow for forward movement. This mechanism has been proposed theoretically for focal adhesion-independent migration of leukocytes under confinement. The normal forces could be exerted by actin polymerisation against the channels walls, and several quantitative models have been proposed (Hawkins et al., 2009). It also predicts a gradient of normal forces to the rear of the cell. While this model has not been reported *in vitro* per se yet, several observations in different cell types are consistent with cells exerting pressure on the walls, either from intracellular pressure or from actin polymerisation (Paluch et al., 2016).

During CAM, branched actin polymerisation inhibition (Arp2/3 inhibitor CK666) significantly decreased CAM for PDX#3, HT29 and HT29-MTX (not shown). This suggests a role for branched actin polymerisation, which could be either in cluster polarisation or intercellular communication as mentioned in a previous section, but could therefore also play a role in a chimneying mechanism. Formin inhibition (e.g. SMIFH2 inhibitor) can be also investigated, as this chimneying mechanism could rather rely on linear actin elongation.

Interference reflection microscopy can provide complementary information about the distance between cell and the substrate, its distribution in cell clusters, and thus the pressure exerted on channel wall. It can

be combined with actin polymerisation and contractility inhibitory experiments. Direct observations of dark areas indicate close contacts, and quantitative analysis can be provided to quantify the distance (Barr and Bunnell, 2009; Lämmermann et al., 2008; Limozin and Sengupta, 2009; Verschueren, 1985).

2.4. Polarised jiggling

After our hypotheses based on collective and single cell amoeboid migration had been discarded, we requested the collaboration of biophysicists. We needed innovative models. Indeed, in cell biology, interactions between physicists and biologists are growing and models based on active matter theory are of great help to understand complex biological phenomena such as cell migration and morphogenesis (Alert and Trepat, 2020; Callan-Jones and Voituriez, 2016; Julicher et al., 2007; Maiuri et al., 2015; Marchetti et al., 2013; Prost et al., 2015).

Based on our biological experimental results, they were able to propose a model to understand the force-generation mechanism in our system, highlighting the key minimal ingredients. “Polarised jiggling” is applicable for clusters behaving as elastic solids with friction forces on the substrate. It relies on fluctuating movements of cells and myosin and is steered by myosin polarisation.

It was inspired by synthetic crawling robots and had only been proposed theoretically to date : it can be seen as a micron scale, continuous, stochastic version of vibrating crawling robots whose motion is based on cycling asymmetric friction forces on a substrate (Deblais et al., 2018; Giomi et al., 2013; Wu et al., 2019). Experimentally, a research group created recently several functional bioengineered organoids based on artificial intelligence modelling (Kriegman et al., 2020). Among them, one caught our attention as sharing similarities with CAM “polarised jiggling”: this type of organoids composed of ectoderm cells and cardiac cell progenitors, had migratory abilities. The contractile cardiac cell progenitors are in contact with the substrate and more abundant at the rear, and there is low (if any) cell rearrangement. As in our model of “polarised jiggling”, these cell clusters seem to move as elastic solids and contractile stresses are expected to be higher at the rear. The group did not propose theoretical insights on how movement is produced, nevertheless it has to be noted that it occurs on planar surfaces and may also rely on the organoid adherence to the substrate.

The source of this internal jiggling has not been fully identified at this point. Yet, myosin activity is likely to be translated into the fluctuating myosin displacements observed at the cortex. Cellular jiggling is observed in the whole thickness of the clusters: it can be expected to originate from this cortical contractility and transmitted to more internal layers. It could also rather rise from individual stochastic movements in the whole cluster, potentially relying on individual cell contractile activity.

The first hypothesis can be questioned, as we did not observe higher fluctuations of nuclei or myosin jiggling at the rear of the cluster, where myosin is more concentrated (not shown). In this hypothesis of a jiggling originating from the cortical cell layer, we could also expect a dissipation between cell layers. However, this is complicated to address by only measuring nuclei speeds, as their degrees of liberty vary from the outer layer and the cluster core.

Of note, the typical spatial scale of these stochastic movements has not been evaluated at this point but could give insights on cell coordination in the cluster. In addition, it could allow us to understand whether this mode of migration is specific to cell cohorts or could also be displayed by single cells. This could be suggested by a subcellular typical scale of the fluctuations of myosin flow speeds. Nevertheless, the gradient of contractile stress could be too low to allow for cell displacement at a single cell level, making CAM “polarised jiggling” one of the mechanisms specific to collective migration (Clark et al., 2020; Sunyer et al., 2016).

3. OUTLOOKS ON COLLECTIVE AMOEBOID MIGRATION

Apart from the force-generating mechanism, the understanding of collective cell migration in non-adhesive environments raises some key questions: e.g. how is polarity established at the onset of migration? Can we envision that CAM integrates the cell migration plasticity landscape? How does CAM truly occur *in vivo*?

3.1. Investigating polarity establishment in CAM

Cells are polarised during migration, either as single cells or collectives, which can be induced by external cues or generated spontaneously. During CAM, we showed that at the cortex, actin and myosin are polarised at the rear of the cluster while no external cue is provided in our system, either mechanical or chemical.

3.1.1. Increased actomyosin contractility inducing spontaneous polarisation

An increased cell contractility can lead to spontaneous polarisation in single cells (Hawkins et al., 2011; Salbreux et al., 2012). This mechanism could be at play at a supracellular scale in cell clusters, with some adaptations: as myosin cannot flow from one cell to the other, it could occur at a cell level and be propagated in the cluster through intercellular mechanical or chemical communication. This increase of contractility is often induced by confinement in single cells but can also be intrinsic.

As we observed that the nuclei of the outer layer were thinner and more elongated, and even more in migrating clusters, we interrogated the cPLA2 pathway related to nucleus stretching and cell contractility highlighted by the Piel lab (Lomakin et al., 2020). When cells are confined enough to compress their nucleus, the nuclear envelope unfolds and releases calcium. Calcium would activate cPLA2 at the nuclear envelope, triggering the release of arachidonic acid that activates actomyosin contractility. However, activation or inhibition of this pathway did not show a significant effect on cell migration: cPLA2 inhibition by two different drugs did not lead to a significant decrease in cell migration nor did it induce a major decrease of myosin recruitment at the cortex (**Figure 79**). Thus, it may not play an important role in cluster polarisation and CAM. This could be explained by the fact that under confinement, cells rather reorganise relative to each other in the cluster, preventing them to undergo a confinement high enough to induce cPLA2 pathway (**Figure 70**).

The hypothesis of an increased contractility can be further studied by direct activation of slow or non-migrating clusters, or of whole populations (particularly those that migrate less, such as TSIPs). Chemical compounds can trigger actomyosin contractility, for example lysophosphatidic acid, a small phospholipid that regulates calcium levels (Cremers et al., 2003; Inoue et al., 1995; Toews et al., 1997) or calyculin A, which increases the level of phosphorylation of MLC (Chabaud et al., 2015; Liu et al., 2015).

A global optogenetic activation can also be envisioned, which would allow to follow a same cluster before and after contractility enhancement. This should be performed together with the expression of myosin coupled to a fluorophore to monitor cluster polarisation. However, we already noted that increasing contractility by RhoA activation on one side of the clusters did not induce cluster migration (**Figure 78**). Yet, increasing on one side only can be not sufficient, or the level of activation may have been sufficient to induce cluster change of direction but too low to induce polarisation. Of note, while it would thus be interesting to increase the level of illumination while activation RhoA in the whole cluster, we could be limited by the toxicity related to blue light illumination.

To increase cell contractility through mechanical confinement, an interesting tool is the dynamic cell confiner: it allows to follow a cell during its confinement while monitoring the actomyosin ring (Le Berre et al., 2012; Liu et al., 2015). This could be adapted to monitoring cluster confinement, with the issue of cluster

thickness: a similar section has to be followed over time to compare myosin recruitment at the membrane, and its z position will vary with cluster confinement.

These experiments inducing an overall increase of contractility could also lead, rather than polarisation, to single cell detachment. Indeed, reduced contractility has to be maintained to allow for the maintenance of cell-cell junctions (Charrasse et al., 2006). In addition, we already observed that nocodazole treatment increases the detachment of round single cells: it induces microtubule depolymerisation, which can indeed trigger actomyosin contractility by the release of the Rho GEF GEF-H1 (Kopf et al., 2020; Seetharaman et al., 2021).

Other experiments can be designed to investigate more generally the intrinsic properties of cell clusters that allow for their migration, and thus, among others, their polarisation. In particular, after sorting migrating and non-migrating cell clusters, molecular profiling can be performed, either in whole exome or RNA sequencing. Special attention can be given to pathways related to actomyosin contractility. The sorting between migrating and non-migrating clusters can be performed for a same cell type, by photoconverting fluorescent probes in fast clusters, fixing cells clusters in the channels and subsequent cell sorting (Konen et al., 2017). Specific microfluidic channels can also be designed to collect fast clusters on the opposite end of their injection.

3.1.2. Induction of polarisation by supracellular cluster organisation or at a single cell level

If a front-rear leader-follower organisation is identified, polarisation could emerge from its impact on actomyosin distribution, but also from self-generated cues. Indeed, I presented in introduction different collective models that generate either a local chemical gradient or internal polarisation at cell-cell junctions (Dalle Nogare et al., 2014; Hayer et al., 2016). Thus, we can hypothesise that an asymmetrical front rear organisation of the cell cohort would be able to spontaneously generate a polarisation at the cluster scale, which can occur through various pathways. This should thus be investigated by comparing the molecular profiles of front and rear cells, or spatial distribution of these molecular pathways' activation (receptors to chemoattractants, cell-cell junctions' composition or shape, actin-related pathways, ...).

In addition, we can wonder whether cells are also polarised at the single cell level, which can be observed in cell sheets through the orientation of the centrosome-nuclei axis (Etienne-Manneville and Hall, 2003; Yamada and Sixt, 2019). We can expect polarisation of either some cells, all cells, or only cells of the outer layer. RhoGTPases FRET biosensors can also be used to measure the activities of RhoA and Rac1 at a subcellular and supracellular scale (Beco et al., 2018).

All in all, these questions regarding cluster polarisation can be investigated in simpler systems, such as clusters of a few cells (<5), as collective migration can emerge from two cells (Zhang et al., 2021) . Indeed, the Coppey lab has recently observed that HT29-MTX cell clusters of a few cells are able to perform CAM in PEG-coated microchannels (unpublished results). These small clusters even display an actomyosin cortex, whose polarisation has not been assessed for yet.

3.2. CAM integrates the cell migration plasticity landscape

Collective amoeboid migration is displayed by 3D cell cohorts under external constraints such as non-adhesive but confining environments, or because of intrinsic properties, which happens for TSIPs that segregate integrins inside clusters.

3.2.1. Observations of switches in cluster phenotypes

Interestingly, some observations suggest that cell clusters of diverse types are able to switch from a protrusive adhesive phenotype to a round non-adhesive phenotype able to display CAM, and conversely. In collagen-coated channels or in collagen gels, different cell clusters (from HT29 and HT29-MTX cell lines and PDX#3) display a wetting morphology, associated to a protrusive phenotype, while they maintain a round dewetting morphology in PEG-coated microchannels (**Figure 72**). Similarly, I observed that the inhibition of actomyosin contractility (Y27632, blebbistatin) induces a protrusive phenotype (**Figure 77**). The inhibition of focal adhesion formation was even able to rescue migration for HT29-MTX clusters in collagen-I-coated microchannels (**Figure 73k**). This indicates their ability to switch from the conventional traction-based migration to CAM following inhibition of focal adhesion formation. These results are similar to what was observed in single cells, that change their mode of migration depending on cell contractility and adhesiveness to the substrate (Liu et al., 2015).

To study this plasticity in collective cell migration, it would be interesting to assess whether some cell clusters are able to migrate in both adhesive and non-adhesive phenotypes, or whether they can either perform one or the other mode. Indeed, the protrusive morphology in collagen-coated microchannels is associated to a dramatic decrease of migration speed for HT29 and HT29-MTX cell clusters. It is consistent with the lower migration speed of adherent single cells compared to amoeboid ones but in addition, clusters harbouring a protrusive phenotype display low polarisation which may explain this very low motility. This absence of polarisation can be related to the absence of guidance cue in the microchannels. Therefore, a directed migration for adhesive clusters in collagen-coated microchannels could be activated by a chemotactic gradient. Molecular gradient generation can be, in principle, performed in microchannels or chambers, by combining them with microfluidics to maintain the gradient over hours.

Overall, these results suggest a plasticity in collective migration between a protrusive focal adhesion-based and a rounded focal adhesion-independent motility.

3.2.2. Transitions between mesenchymal and amoeboid collective modes, and single cell and collective amoeboid modes

This plasticity seems to occur under similar determinants as in single cell migration: cell adhesion and cell contractility (Liu et al., 2015; Sanz-Moreno et al., 2008). Further studies must be conducted to investigate the determinants of what we could call collective amoeboid-to-mesenchymal transition (CAMT) and conversely CMAT, starting by those found in single cell transitions: cell confinement, level of adhesion and contractility. Similar tools as those used for MAT/AMT in single cell migration can be used, and microchannels can be of great help to vary confinement and level of attachment in a controlled manner (Liu et al., 2015). Optogenetic tools such as those we used would also allow for investigating the impact of the level of contractility and protrusive activity on cell migration plasticity.

In addition, while a transition between conventional traction-based migration to single cell amoeboid migration has been shown, we can wonder whether a collective amoeboid-to-single cell amoeboid transition (CAT) occurs as well (Hegerfeldt et al., 2002). Determinants that should be investigated primarily include cell-cell adhesion levels, proteolytic activity and 3D confinement. Of note, embedding TSIPs in Matrigel-agarose matrices did not lead to a CAT (not shown) contrary to what Ulrich and colleagues reported for glioma cells (Ulrich et al., 2010).

Therefore, CAM completes what was a missing piece to the current puzzle of cell migration modes (**Figure 85**). It could easily be integrated in the transitions between the migration modalities known to date, based on various degrees of cell-cell and cell-substrate adhesions, cell contractility and proteolytic activity.

3.3. *In vivo* relevance of CAM

In the course of their metastatic dissemination, tumour cells hijack all modes of single or collective migration described to date (**Figure 85**) (Friedl and Alexander, 2011). By adding CAM to the modes of migration they can display, this increased plasticity could be an advantage in tumour dissemination by allowing cells to adapt to any environment they encounter during their journey towards secondary sites.

3.3.1. CAM in physiological contexts

Of note, while CAM was mainly observed in cancer cell cohorts, I reported that it can be performed by healthy colon tissue from two different patients as well (**Figure 68**). Thus, CAM may not be a cancer-specific feature, and could rather be a physiological feature that tumour cells can activate when released in small groups. Indeed, cancer cells are known to reactivate processes inherited from embryonic development, such as cell proliferation and migration, participating in their abnormal tumoral development.

An interesting physiological situation where CAM could be enabled is during embryonic development, when the blastocyst invades the endometrium. This process is poorly understood, but we know that blastocysts display their apical pole outwards as TSIPs do (Aplin and Ruane, 2017; Louvet et al., 1996; Maître, 2017). To investigate whether blastocysts can also display CAM, murine blastocysts can be retrieved 2-4 days after fertilization to challenge their migration *in vitro*. They can be either embedded in Matrigel or injected in PEG-coated microchannels of $80 \times 80 \mu\text{m}^2$, as they are a little bigger than TSIPs. Murine endometrium can also be cultured to allow for invasion tests (Tan et al., 2005; Ye et al., 2012).

3.3.2. *In vivo* environments deprived of ECM would favour CAM

Here, I showed that cancer primary specimens and cell lines can adopt collective amoeboid migration. This can result from intrinsic oncogenic features, such as in TSIPs, where the inverted apico-basal polarity prevents cluster adhesion to ECM-rich tissues (Zajac et al., 2018). CAM can also occur as a non-cell autonomous process, when cancer cell clusters are confined into environments to which they are unable to adhere, such as PEG-coated microchannels.

I investigated CAM in simplified systems, microchannels, to prevent focal adhesion formation, control confinement, and allow powerful imaging. These 1D-confining systems mimic *in vivo* environments such as perineural or perimuscular tracks and lymphatics (Wolf and Friedl, 2011).

Indeed, lymphatic capillaries form a non-adhesive conduit as endothelial cells expose their apical pole to the lumen in which tumour cells can transit. In addition, lymphatic and blood vessels can display diameters in the order of magnitude of the microchannels in which we performed our study, 10 to $100 \mu\text{m}$ wide (Fischer et al., 1996; Ivanov et al., 1981; Jafarnejad et al., 2015).

Overall, CAM could be in principle displayed in any major dissemination routes and metastatic sites that are deprived of conventional ECM and provide cell confinement. These encompass perimuscular tracks, the lumen of lymphatic vessels, lymph nodes and between the mesothelial sheets of peritoneal and pleural cavities, which are important metastatic sites and where the presence of tumour cell clusters has been reported (**Figure 15-Figure 18**) (Barresi et al., 2012; Brown et al., 2018; Friedl and Alexander, 2011; Lämmermann et al., 2008; Law and Martin, 2020; Lim et al., 2010; Paul et al., 2017; Ruitter et al., 2001; Zajac et al., 2018).

To confirm it *in vitro*, cluster collective migration could be monitored between pieces of mice or patients' peritoneal membranes, collected during surgery. Nevertheless, CAM contribution *in vivo* in lymphatic transport can be questioned as flow speeds much higher than CAM velocities measured *in vitro* have been

reported in such capillaries: between 500 to 1000 $\mu\text{m}/\text{min}$, and even higher in blood capillaries (Fischer et al., 1996; Ivanov et al., 1981; Jafarnejad et al., 2015). Even at the end of capillaries where this flow is significantly reduced, it can reach 200 $\mu\text{m}/\text{min}$ (Jackson, 2019). Thus, cells can be expected to be transported by the flow rather than active migration. Live *in vivo* imaging combined with control versus inhibition of CAM can help elucidate this question.

In addition, CAM could also certainly be displayed in hyaluronic acid-rich environments such as in brain, that have been shown to promote single cell amoeboid migration (Cui et al., 2020).

All in all, these results also strengthen the contribution of epithelial collective cell migration in cancer dissemination, in accordance with recent findings (Cheung and Ewald, 2016; Liotta et al., 1976; Ruitter et al., 2001; Zajac et al., 2018).

3.3.3. CAM in dense ECM-rich environments

Our results show that clusters from diverse cell types can display collective amoeboid migration when confined in non-adhesive environments. However, at this point, in adhesive environments such as collagen-I-coated microchannels and 3D collagen gels, we only observed TSIPs as able to perform CAM (**Figure 65**) (Zajac et al., 2018). Indeed, other cell clusters switch to a protrusive morphology, while TSIPs intrinsic properties prevent them from being plastic and changing to a protrusive phenotype.

The characteristics of TSIPs migration in 3D environments can now be further analysed based on CAM polarised jiggling mechanism. The polarised jiggling features should also be assessed in presence of extracellular matrix to confirm that CAM as I presented it here, occurs in 3D ECM-rich structures.

In these complex environments, we can also expect a contribution of other molecular mechanisms to CAM.

For clusters that do not produce a thick layer of mucins around them, they could take advantage of matrix topology like single cells, to migrate by pushing on the fibres thanks to their cortical blebs (**Figure 76**) (Tozluoğlu et al., 2013).

The blebbing activity could also create space in the matrix, similar to the “mechanical worrying” observed by Welf and colleagues in melanoma single cells (Welf et al., 2020). While the mechanism they report relies on short-lived focal adhesions on collagen fibres, we could imagine that the blebbing activity during CAM would only push the matrix around the clusters to create space. For TSIPs and PDX#3 clusters that display a pulsatile activity, these pulses could also deform the matrix to create space all around clusters. This mechanism would certainly not be extremely efficient and could explain the very slow migration observed in 3D collagen-I gels (**Figure 65**) (Zajac et al., 2018). Investigating this pathway would require timelapse imaging of the myosin cortex and collagen fibres at short timescales and during hours to monitor cluster migration.

Otherwise, given the size of cell clusters and their low deformability, a certain level of cluster-matrix interactions and proteolysis may be required to pass through the pore sizes of $40\mu\text{m}^2$ found *in vivo* (Wolf et al., 2009). This would lead to an intermediate mechanism recapitulating single cell amoeboid and conventional collective migration features.

In line with this hypothesis, preliminary results in microchannels filled (as opposed to coated) with polymerised collagen-I matrix revealed that TSIPs could exert traction on these loose fibres (**Figure 73**). They remodel collagen fibres and pull on it while keeping their rounded shape. This leads to very fast migration when it occurs to only one side of the cluster.

This simple 1D setting could be used to precisely investigate the interaction between cell clusters and collagen fibres, as it provides better conditions for imaging than 3D collagen gels. Another intermediate before 3D collagen gels can be chambers filled with collagen matrix: they create more 3D-like conditions

by surrounding cell clusters with collagen while keeping good imaging conditions. The role of matrix metalloproteinases (MMPs) could be investigated in these settings, for example by first incubating clusters with the broad MMP inhibitor GM6001. It could reveal that cell clusters displaying CAM express high levels of MMP to migrate, as round amoeboid melanoma single cells do (Orgaz et al., 2014). The nature of cluster-matrix interaction, in particular the role of integrins and other focal adhesion components, should also be investigated. Of note, as we already reported that FAK, Src and integrin $\alpha 2$ are non-contributory, it suggests that if this interaction relies on focal adhesion pathways, it may not play a crucial role in CAM in 3D conditions (**Figure 65**). As I already observed that, in 1D microchannels, clusters stall if they pull on both sides on collagen fibres, we can indeed imagine that in 3D, simultaneous small interactions and pulling forces could occur all around clusters, resulting in almost no migration.

Overall, CAM could endow the migration of cell clusters across a wide spectrum of tissues for which they may not express the correct repertoire of receptors, reminiscent of leukocytes navigating all kinds of environments using an integrin-independent mode of migration.

4. TARGETING CELL MIGRATION IN TUMOUR DISSEMINATION

To conclude on the clinical implication of my work, these results highlighted the plasticity of cells either in migration (**Chapter IV**) or topology (**Chapter V**). They result respectively in migration in various environments and lower response to chemotherapies in the apical-out conformation. Both mechanisms were identified primarily in colorectal cancer, but are likely to be broadened to other solid tumours. Indeed, I already identified several types of cancer that form cell clusters displaying CAM (**Figure 68**) and our team also identified TSIPs in other cancer types (unpublished data).

These findings also highlight the challenges of targeting tumour cell dissemination. Indeed, tumour treatment today mainly relies on targeting cell cycle or immune response. Yet, the example of TSIPs reveals that slowly proliferating tumours may be less responsive to chemotherapies while still disseminating actively (Xue et al., 2006). Their response to immunotherapies remains to be determined but could also be decreased due to their topology.

Given that metastasis accounts today for most deaths from cancer, there is growing interest in targeting cell migration directly. ROCK inhibition of TSIPs *in vitro* led to a significant decrease in cell migration (**Figure 65, Figure 77**). Despite the plasticity of migration that we could expect, preliminary experiments in mice showed that inhibition of ROCK (Dupont et al., 2011; Dyberg et al., 2019; Hinsenkamp et al., 2016; Whatcott et al., 2017) or integrins signalling (Kren et al., 2007) lead to decreased dissemination. Rho/ROCK inhibitors could reasonably be used in clinic as one of them, Fasudil, is already validated in Japan to treat vasospasms and a clinical trial is ongoing to extend its use against amyotrophic lateral sclerosis in Europe (Koch et al., 2020).

The results in mice also suggest that inhibition of these pathways could inhibit any mode of cell migration (which is plausible as actomyosin contractility plays an important role whatever the mechanism). It can also suggest the existence of an intrinsic preferential mechanism for certain cell types, that was inhibited by these inhibitors. Last, it can reveal that cells need plasticity to perform an efficient migration in all environments, which was prevented by blocking one or the other mode of migration by these pathways. Understanding the underlying mechanisms of collective and single cell migration will help finding the appropriate targets in cell migration.

Another interesting target in TSIP-producing cancer could be the production itself of these tumour intermediates. Preliminary results from our lab suggest that this “collective apical budding” occurs also in

a contractility-dependent fashion, which may suggest a chance to target both mechanisms at the same time.

Conclusion

During my PhD, we were able to show that a focal adhesion-independent mode of migration occurs. It is displayed in various cancer and non-cancer cell types, and its extent remains to be explored. To investigate this new mode of collective migration, I developed new experimental and analytical tools: patient explants in microchannels, nuclei and cluster tracking, ...

Experiments revealed that this new mode of collective migration is indeed strikingly different from the focal-adhesion and traction-based mechanisms of collective motion known to date. It does not rely on focal-adhesion formation, and rather on cell contractility and myosin polarisation. These features are similar to amoeboid single cell migration, hence the name "collective amoeboid migration" (CAM). However, the force generation mechanism is different: rather than myosin or cellular persistent retrograde flows, it relies on "polarised jiggling", i.e. fluctuating deformations measured by cellular or myosin displacements. We proposed an analytical model to confirm the following ingredients are sufficient to induce collective amoeboid migration: a cluster behaving as an elastic solid, friction forces, myosin polarisation and fluctuating deformations.

In addition, I showed that TSIPs, which display CAM because of their intrinsic inverted apico-basal polarity, are less sensitive to chemotherapies in their apical-out topology than in an apical-in conventional topology. Together with their increased invasive properties, this is in line with lower prognostic of patients that display TSIPs.

These results indicate that the cellular mechanisms underlying cell cluster dissemination and response to treatments, can be investigated *in vitro*. They revealed new migration features and additional effects of an inverted apico-basal polarisation. As being not specific to colorectal cancer, they also raised important questions in a more general way: how are cell clusters polarised to allow for CAM? Is CAM really occurring *in vivo*? What type(s) of cell migration plasticity can occur implying CAM? Which other cancer-related features do TSIPs display?

Annexes

**Cell clusters adopt a collective amoeboid mode of migration
in confined non-adhesive environments.**

Short title: Collective amoeboid migration of cell clusters

Authors: Diane-Laure Pagès^{1,2#}, Emmanuel Dornier^{1#}, Jean De Seze³, Li Wang⁴, Rui Luan¹, Jérôme Cartry¹, Charlotte Canet-Jourdan^{1,2}, Joel Raingeaud¹, Raphael Voituriez^{5,6}, Mathieu Coppey³, Matthieu Piel⁴ and Fanny Jaulin^{1*}.

Affiliations :

¹ INSERM U-1279, Gustave Roussy, Villejuif, F-94805, France.

² Université Paris Saclay, 114 rue Edouard Vaillant, Villejuif, F-94805, France

³ Laboratoire Physico Chimie Curie, Institut Curie, PSL Research University, Sorbonne Université, CNRS, Paris 75005, France.

⁴ Institut Curie and Institut Pierre Gilles de Gennes, PSL Research University, CNRS, UMR 144, Paris, France

⁵ Laboratoire de Physique Théorique de la Matière Condensée, UMR 7600 CNRS/Sorbonne Université, 4 Place Jussieu, 75255 Paris Cedex, France.

⁶Laboratoire Jean Perrin, UMR 8237 CNRS/Sorbonne Université, 4 Place Jussieu, 75255 Paris Cedex, France.

Equal contribution

*Correspondence to: Fanny Jaulin: fanny.jaulin@gustaveroussy.fr

One Sentence Summary:

Clusters organise as polarised and contractile super-cells to migrate without adhesion.

Abstract:

Cell migration is essential to most living organisms. Single cell migration involves two distinct mechanisms, either a focal adhesion- and traction-dependent mesenchymal motility or an adhesion-independent but contractility-driven propulsive amoeboid locomotion. Cohesive migration of a group of cells, also called collective cell migration, has been only described as an adhesion- and traction-dependent mode of locomotion where the driving forces are mostly exerted at the front by leader cells. Here, by studying primary cancer specimens and cell lines from colorectal cancer, we demonstrate the existence of a second mode of collective migration which does not require adhesion to the surroundings and relies on a polarised supracellular contractility. Cell clusters confined into non-adhesive microchannels migrate in a rounded morphology, independently of the formation of focal adhesions or protruding leader cells, and lacking internal flow of cells, ruling-out classical traction-driven collective migration. Like single cells migrating in an amoeboid fashion, the clusters display a supracellular actin cortex with myosin II enriched at the rear. Using pharmacological inhibitors and optogenetics, we show that this polarised actomyosin activity powers migration and propels the clusters. This new mode of migration, that we named collective amoeboid, could be enabled by intrinsic or extrinsic neoplastic features to enable the metastatic spread of cancers.

Main Text:

Migration is a fundamental property of cells. Emerging in early eukaryotes, migration supports individual cell displacement as well as metazoan development and homeostasis (1). It is also deregulated in pathological conditions, such as cancer, where it fuels their metastatic spread (2). Two distinct mechanisms are used by single cells to generate the migration forces (3). They result from the cells' ability to adhere, or not, to the surrounding extracellular matrix (ECM) and their level of contractility. In traction-based mesenchymal migration, integrin interaction with the ECM and focal adhesion formation convert branched-actin polymerisation into large protrusions and forward forces (3, 4). In contrast, amoeboid single cells use a propulsive locomotion that does not require specific adhesion and is driven by acto-myosin contractility of the rear (5, 6). Cells can also move in a cohesive manner as a group (7–9). At the front of the cluster, leader cells form prominent protrusions where the combined action of actin polymerization and integrin engagement triggers lamellipodia and focal adhesion formation. Using the substrate as an anchor, leaders pull on follower cells, instructing directionality and generating important traction forces (10, 11). The contribution of follower cells is more elusive, but it has recently been shown that their increased contractility produces a treadmill of lateral cells to support the migration of neural crest clusters (12). To date, our knowledge on collective cell movement suggests it only takes the form of an adhesion-dependent traction-based mode of locomotion and whether it could also occur through an alternative mechanism has not been investigated.

Through the analysis of primary tumour explants retrieved from patients with metastatic colorectal cancer (CRC), we identified TSIPs (Tumour Spheres with Inverted Polarity) as tumour cell clusters with an inverted apico-basolateral polarity (13). The atypical topology of the clusters exposes carcinoma cells' apical membranes to the microenvironment and precludes adhesion receptors, such as integrins, to interact with the surrounding ECM in the peritumoral stroma (Fig. 1A). Yet, TSIPs efficiently invade tissues and are associated with high metastatic burden and poor patient prognosis (13). This suggests that the motility of TSIPs does not require integrin function and raises the possibility of an adhesion-independent mode of collective cell migration. To test this hypothesis, we engineered micro-devices (channels and chambers) deprived of any physiological substrates and chemotactic cues by coating them with the anti-adhesive polymer polyethylene glycol (PEG, Fig. 1B). Time-lapse imaging proved that TSIPs obtained from two independent patients migrated into the non-adhesive microchannels (Fig. 1C(a), fig. S1A and movie S1). To determine whether this type of migration is specific to TSIPs or could be used by other collectives, we assessed the migration of clusters assembled from colorectal carcinoma cell lines in PEG-coated microchannels. Indeed, clusters from HT29, HT29-MTX and three lines of circulating tumour cells (CTC31,44, 45, (14)) were able to collectively migrate under these conditions (Fig. 1, C(b) to E, and movie S2). To characterise this new mode of collective migration, considering the durations of consecutive migration and pauses (fig. S1, B and C), we monitored trajectories of individual clusters every hour over one day (Fig. 1D). Some clusters did not move in the course of the experiment while some reached up to 2 mm/d. Average speeds ranged from $150 \pm 21 \mu\text{m}/\text{d}$ to $77 \pm 4 \mu\text{m}/\text{d}$ for TSIPs and HT29s which are the fastest. The migration of CTCs was slower, varying from $37 \pm 2 \mu\text{m}/\text{d}$ to $27 \pm 2 \mu\text{m}/\text{d}$ (Fig. 1E) (values are expressed as speed \pm standard error of the mean). Clusters displayed a very persistent migration over time (from 0.65 ± 0.03 to 0.75 ± 0.03 in average) and could reach a maximum instantaneous speed of $28 \pm 3 \mu\text{m}/\text{h}$ in average (Fig. 1D and F, and fig. S1D). Although quite slow when compared with single cell migration in experimental settings, this is in the order of magnitude of collective migration speeds reported in vivo (15, 16).

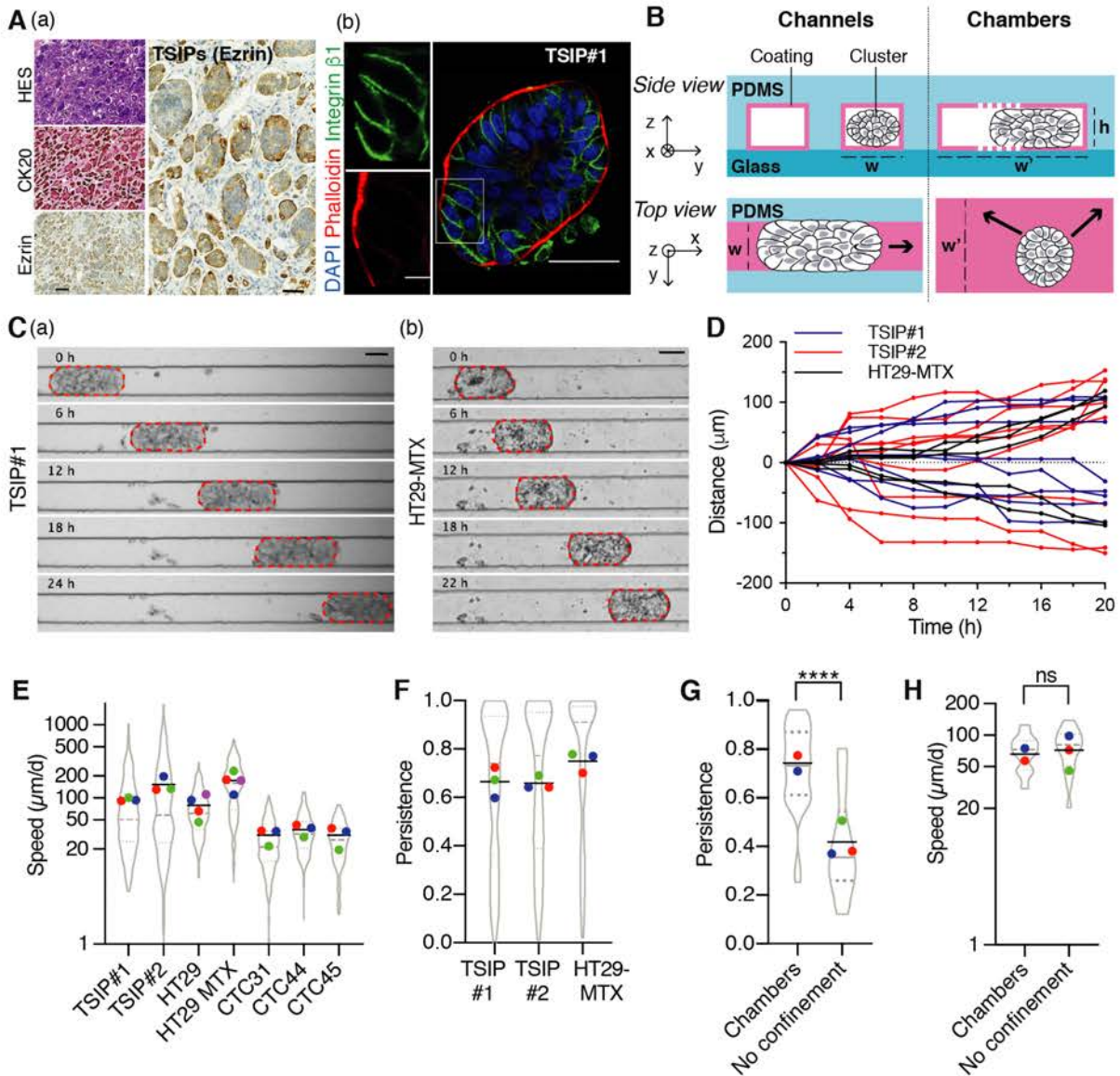


Fig. 1. Cell clusters migrate into non-adhesive microchannels. (A) Representative tumour specimen of CRC (micropapillary subtype) stained with Hematoxylin/Eosin/Saffron (HES), anti-Cytokeratin 20 (CK20) and anti-Ezrin at low (left) and high (right) magnification (a) and immunofluorescence of a transverse section of TSIP#1 embedded in collagen-1 for 24h (b). The boxed region is shown at high magnification. (B) Schematic representation, not to scale, of the channels (width: $w=60\mu\text{m}$; height: $h=30\mu\text{m}$) (left) and chambers (width: $w'=500\mu\text{m}$) (right). (C) Time-lapse sequences of migration of TSIP#1 (a) and HT29-MTX (b) in PEG-coated microchannels. (D) Representative tracks of clusters migrating in one direction (positive numbers) or the other (negative numbers) in PEG-coated microchannels. $n=5$ to 9 representative clusters of each cell type. (E and F) Clusters' migration speed (E, log2-scale, $n=118$ to 208 clusters per cell type) and persistence (F, $n=107$ to 124 clusters per cell type) in PEG-coated microchannels over one day. (G and H) Speed (G, log2-scale, unpaired Student's t-test) and persistence (H, Mann-Whitney test) for HT29-MTX migration over a day, depending on their confinement. Designs are coated with PEG+F127. $n=30$ clusters (chambers), $n=18$ clusters (no confinement). ns, not significant, **** $P<0.0001$ (Kruskal-Wallis test). Violin plots display the whole population of clusters, median (dashed grey line) and quartiles (dotted grey lines). The coloured dots represent the mean of each independent experiments and the black line the mean of all experiments for each condition. All data represented as violin plots are from $N=3$ independent experiments, except HT29 and HT29-MTX in (E, $N=4$) and chambers in (G) and (H) ($N=2$). Scale bars: $200\mu\text{m}$ (A,a, low magnification), $50\mu\text{m}$ [(A,a, high magnification), (A,b, low magnification), (C)] and $10\mu\text{m}$ (A,b, high magnification).

We next assessed the role of confinement by comparing migration of clusters confined in one dimension (microchambers, Fig. 1B and fig. S2A) or not confined (loading chambers, fig. S2B). Confinement did not increase clusters' speed but favoured persistence, as described for single cells (Fig. 1, G and H) (6, 17, 18).

Once confined into microchannels, small clusters migrate as fast as the largest ones, showing no correlation between speed and size (fig. S2, C to E). In all instances, the collective migration is associated with a compact rounded morphology into non-adhesive microchannels that contrasts with the loose and spread shape clusters can adopt when the microchannels are coated with collagen-1 (Fig. 2A). Measuring the contact angles between the cluster boundary and the microchannel walls highlights the “dewetting” morphology of the clusters and the absence of protrusion for HT29, HT29-MTX and TSIPs migrating in PEG-coated microchannels (Fig. 2, A and B). Collagen-1 coating reduces HT29 and HT29-MTX migration speed while, as expected, TSIPs remain unaffected due to their inverted polarity (Fig. 2C and 1A). Together, these experiments suggest that confined cell clusters can display a persistent motility in non-adhesive environments.

To directly study the contribution of focal adhesion to cluster migration, we expressed turquoise-tagged paxillin in HT29-MTX. While fluorescent paxillin revealed numerous foci at collagen-1 interface, they were nearly absent in PEG-coated microchannels (Fig. 2, D and E, and movie S3). To functionally assess the participation of focal adhesions, we silenced talin-1, an essential component of integrin-mediated functions (19). This had no effect on HT29-MTX cluster migration (Fig. 2, F and G). Hence, interfering with intrinsic and extrinsic components of cell adhesion to their substrate demonstrates that clusters can migrate without the conventional molecular machinery powering traction-based collective migration (20–22).

We next tested whether a coordinated retrograde flow of cells, or cell treadmilling, could participate in this non-adhesive cluster migration, as was proposed before in a developmental context (12). To this end, we expressed cherry-tagged histone 2B (H2B) in HT29 clusters to monitor individual cell movements during migration in PEG-coated channels. Confocal fluorescence imaging showed that individual cell tracks follow the trajectory of the centre of mass of the cluster (Fig. 2H, fig. S3A and movie S4). To precisely test the hypothesis of flows of cells generating migration (Fig. S3, B to G), three areas were defined on a middle cross section of the cluster and cell trajectories were examined (Fig. 2I(a)). In each area, the measurement of the instantaneous speed of cells in the cluster’s reference frame directly confirmed the absence of significant fluxes of cells (Fig. 2J and fig. S3, C and F). As a consequence, the relative velocity of cells in contact with the microchannel walls was positive, in the direction of the motion of the cluster (Fig. 2K). In the hypothesis of a propulsion mechanism based on flows of cells, this would indicate the presence of resistive friction forces only and the absence of propulsion forces, excluding a mechanism based on an internal treadmilling of cells (fig. S3 D and G). Thus, clusters translate, with all cells remaining at the same relative position in the group during migration (Fig. 2I(b) and fig.S3A).

The classical mechanisms of traction-driven collective migration being ruled-out, we reasoned that the acto-myosin cytoskeleton could power focal adhesion-independent cluster migration, as it does in amoeboid single cells (5, 6, 23, 24). Expressing the fluorescent probes F-tractin and myosin light chain (MLC) in HT29-MTX revealed a robust peripheral supracellular acto-myosin cortex as reported at the boundaries of other migrating collectives (Fig. 3A) (25). This peripheral cortex is evenly distributed in static

clusters, however, during migration, it exhibits

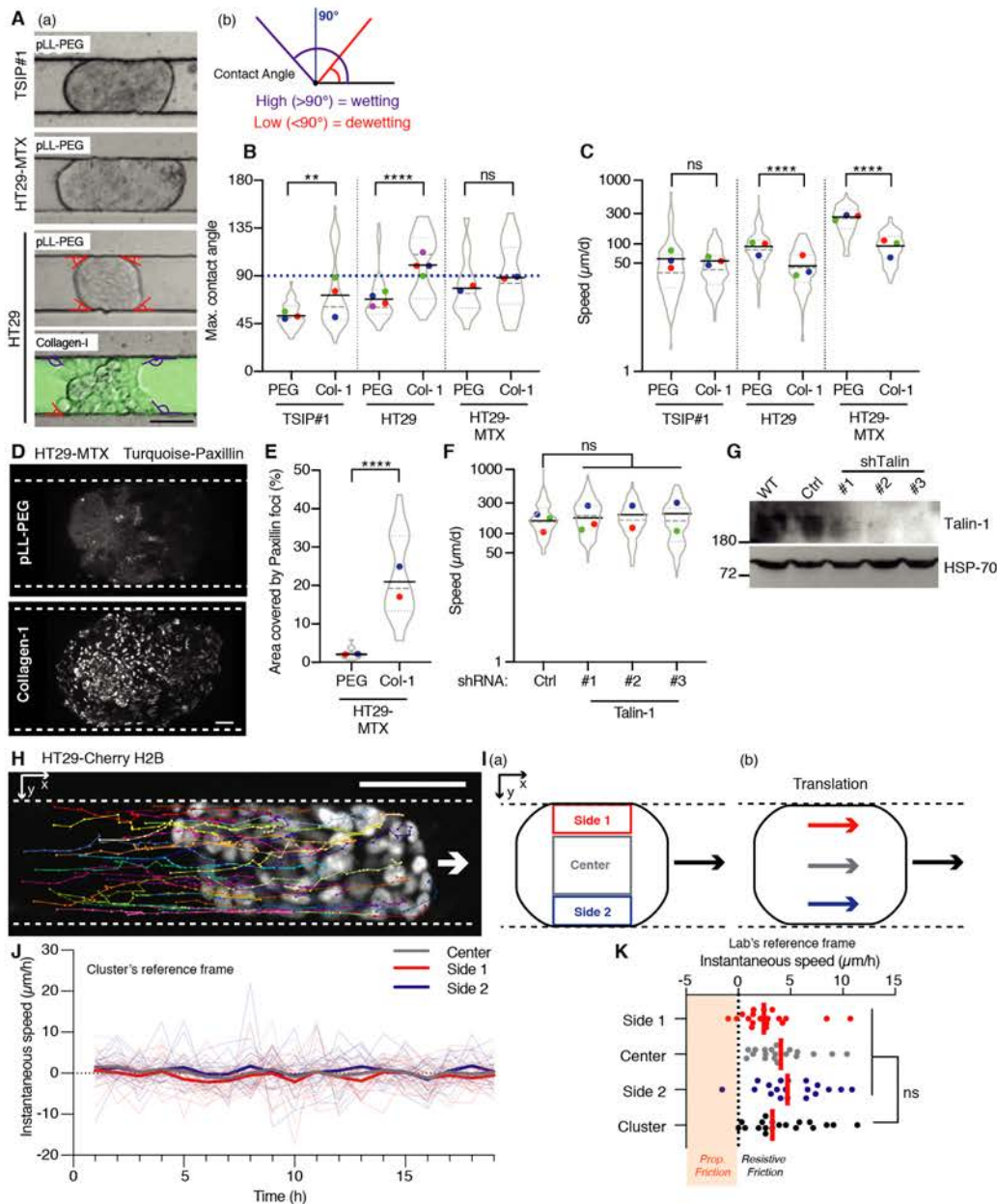


Fig. 2. Collective migration occurs without focal-adhesions nor cell flows. (A to C) Representative images (A), maximum contact angles (B) and speeds (C) of clusters migrating in PEG- or Cy5-collagen-1(Col-1)-coated microchannels. Wetting or dewetting contact angles are represented on the cluster (A,a) and as a schematic representation (A,b); $n=39$ to 59 clusters were used to quantify the maximum contact angle (B, Mann-Whitney test). $n=90$ to 166 clusters were analysed to calculate migration speeds (C, two-tailed Student's t test). (D and E) Representative images of the bottom plan of the cluster (D) and area covered by paxillin foci (E) for HT29-MTX stably expressing mTurquoise-Paxillin in PEG- or Col-1-coated microchannels. $n=19$ to 28 clusters (E, Mann-Whitney test). (F and G) Speed of clusters in PEG-coated microchannels (F) and corresponding western blot (G) for HT29-MTX stably expressing 3 different shRNA targeting Talin-1 or a control shRNA. $n=62$ to 154 clusters (F, one-way ANOVA). (H) Representative nuclei tracks of the middle cross-section of an HT-29 cluster stably expressing mCherry-H2B, migrating one day in a PEG-coated microchannel. (I) Definition of areas in the cluster (a), to scale, and schematic representation of cluster's global translation (b). Side 1: cluster's side going most rearward/less forward in average. (J) Instantaneous speed of cells in each area, in the reference frame of the clusters. Bold lines: average of individuals tracks calculated from regions of $n=16$ clusters from 3 independent experiments. (K) For one representative cluster, instantaneous speed of cells in each area and cluster speed, lab's reference frame. Orange: cells could generate propulsive (Prop.) friction. $n=19$ timepoints (paired Friedman test). Experiments were performed independently for each cell lines. Violin plots are described in Fig. 1 legend and coloured dots refer to the same experiment. All data represented as violin plots are from $N=3$ independent experiments, except HT29-MTX in (B) and (E), and sRNA#2 and #3 in (F) that were performed twice. ns, not significant, $**P<0.01$, $****P<0.0001$. Scale bars: $50\mu\text{m}$ [(A) and (H)], $10\mu\text{m}$ (D).

a front/rear polarisation, with a 1.5- and 1.8-fold enrichment toward the back of the cluster for F-

tractin and MLC respectively (Fig. 3, A and B, and movie S5). To assess whether this supracellular acto-myosin cortex contributes to cluster migration, we first used pharmacological inhibitors. Interfering with Myosin-II or ROCK activities using blebbistatin and Y27632 reduced TSIP#1 migration speed from $80 \pm 7 \mu\text{m/d}$ to $50 \pm 6 \mu\text{m/d}$ and $43 \pm 3 \mu\text{m/d}$, respectively (Fig. 3, C and D, and fig. S4A). Similarly, using these inhibitors on HT29-MTX decreased their migration by 3- and 2.9-fold, respectively (Fig. 3, C and D, and fig. S4B). Then, we tested whether increasing contractility at the rear was sufficient to power cluster migration. To this end, we used optogenetics to manipulate acto-myosin contractility via its upstream regulator RhoA. We infected HT29-MTX cells with the optoRhoA system, which enables an acute spatiotemporal recruitment of RhoA activator ARHGEF11 to the membrane using the CRY2/CIBN light gated optogenetic dimerization system (fig. S5, A and B) (26). We illuminated one side of the clusters, either at the front of already moving clusters or randomly for static ones. We monitored their trajectories for up to 20 hours by using an automated stage and activation routine maintaining a constant illumination region despite the movement of the cluster (Fig. 3E). Control clusters expressing the optogenetic dimeriser without RhoA activator pursued their migration in their initial direction with their speed sometimes reduced by mild phototoxicity or large local protein recruitment at the membrane (27). In contrast, illuminating clusters expressing optoRhoA impacted their migratory behaviours. Light stimulation initiated the migration of static clusters and was even able to revert the direction of migrating ones (Fig. 3, F to H, and fig. S5C, and movie S6). This demonstrates that increasing acto-myosin activity in a subset of cells is both sufficient to induce migration and dictate directionality taken by the entire cluster (Fig. 3, F to H, and fig. S5C). Altogether, these experiments show that a supracellular polarised acto-myosin contractility contributes to the driving force that propels clusters of cells into non-adhesive environments.

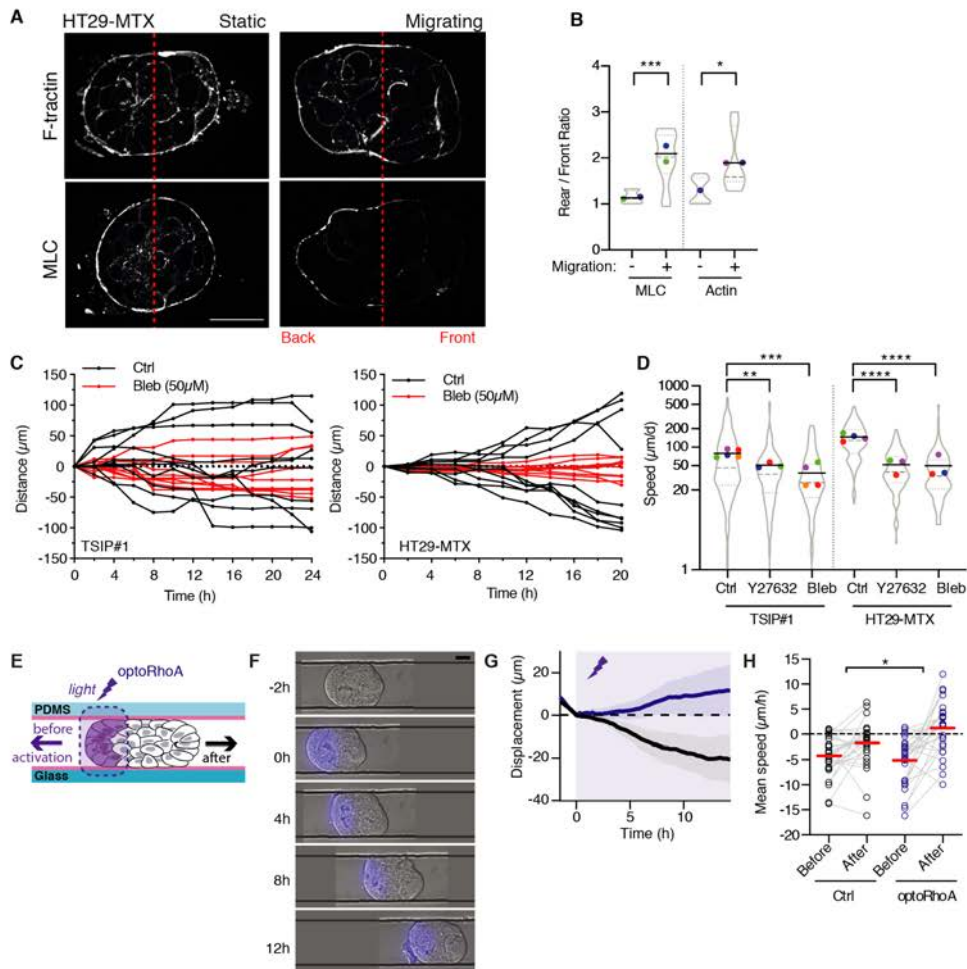


Fig. 3. A supracellular contractile actin cortex powers focal adhesion-independent collective migration. (A) Median section of HT29-MTX stably expressing F-tractin-mRuby3 (top) and mTurquoise-MLC (bottom), in PEG+F127-coated channels. (B) Quantification of the F-tractin (Actin) and MLC (Myosin Light Chain) ratios between rear and front of the clusters, as indicated in Methods. $n=7$ to 13 clusters (Mann-Whitney test). (C) Representative tracks of clusters treated with Blebbistatin. $n=10$ clusters each. (D) Speed of clusters treated with Y27632, Blebbistatin, or DMSO (Ctrl), log₂-scale. $n=106$ to 205 clusters (Mann-Whitney test). (E to H) Optogenetic manipulations: Experimental setup (E), representative time-lapse sequences (F, dark grey lines are microchannel walls), migration profiles (G, means \pm sem) and mean speeds before ($-2h < t < 0h$) and after ($4h < t < 10h$) optogenetic activation (H). In G and H, the control (CRY2PHR-mCherryN1/CIBN-eGFP-CaaX) is represented as black line or dots and optoRhoA as purple line or dots. The purple zones represent the optogenetic activation period. $n=27$ clusters from 3 independent experiments (two-tailed Student's t test on the after-before speed differences between control and optogenetic constructs). Experiments were performed independently for each cell types. Violin plots are described in Fig. 1 legend and coloured dots refer to the same experiment. All data represented as violin plots are from $N=3$ independent experiments, except in (B, $N=2$, and $N=1$ for Actin in non-migrating clusters), and TSIP#1 in Blebbistatin (E) ($N=4$). ns, not significant, * $P < 0.05$, ** $P < 0.01$, *** $P < 0.001$, **** $P < 0.0001$. Scale bars, $30 \mu\text{m}$.

Here, we report a second mode of collective migration that shares striking features with amoeboid single cell motility (Fig. 4). Cell clusters collectively migrate within non-adhesive microchannels in the absence of protruding leader cells, focal adhesions or cell flows. Similar to amoeboid cells, clusters mobilise the contractility of a supracellular acto-myosin cortex at the rear and adopt a propulsive mode of migration. By analogy, we named this new mode of cell locomotion "collective amoeboid migration". Tumour cells have the capacity to hijack the 3 modes of cell migration described to date (28). Here, we show that colorectal cancer primary specimens and cell lines can also adopt collective amoeboid migration. This results from intrinsic oncogenic features, such as in TSIPs, where the inverted apico-basolateral polarity prevents cluster adhesion to ECM-rich tissues (13). This propulsion-based mode of collective migration could also be enabled as a non-cell autonomous process, when cancer cell clusters are exposed to environments deprived of conventional ECM. These encompass major dissemination routes such as the lumen of lymphatic vessels or the peritoneal and pleural cavities (29–33). Collective amoeboid migration could thus foster cancer metastatic spread.

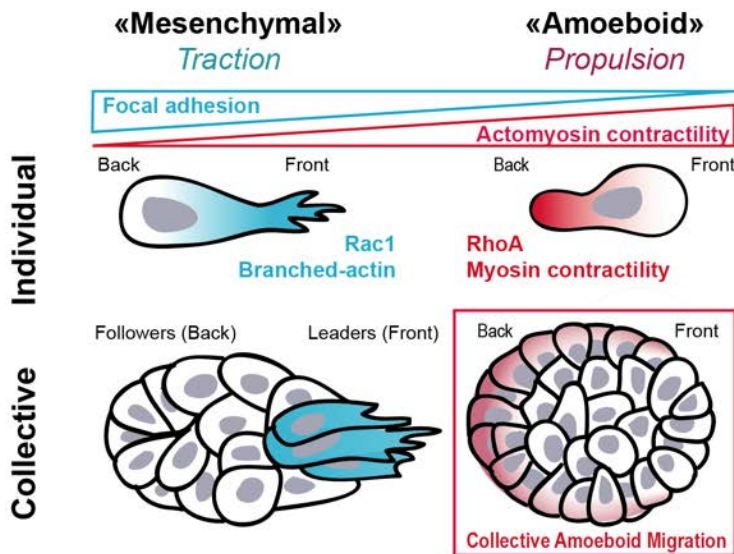


Fig. 4. Model of cell migration modes. Schematic representation of the different modes of cell migration based on the ability of the cells to adhere to each other (individual versus collective migration) and to their environment (mesenchymal versus amoeboid). This results in traction- or propulsion-based locomotion, where the force is respectively generated by Rac1-dependent actin polymerization or RhoA-dependent actomyosin contractility. The second mode of collective migration we report here occurs without the formation of focal adhesion and relies on acto-myosin contractility at the rear. By analogy with single cells, it has been named «collective amoeboid migration» and represents a fourth mode of cell migration.

References and Notes:

1. K. M. Yamada, M. Sixt, Mechanisms of 3D cell migration. *Nat Rev Mol Cell Biol.* **20**, 738–752 (2019).
2. A. W. Lambert, D. R. Pattabiraman, R. A. Weinberg, Emerging Biological Principles of Metastasis. *Cell.* **168**, 670–691 (2017).
3. D. L. Bodor, W. Pönisch, R. G. Endres, E. K. Paluch, Of Cell Shapes and Motion: The Physical Basis of Animal Cell Migration. *Dev. Cell.* **52**, 550–562 (2020).
4. M. Innocenti, New insights into the formation and the function of lamellipodia and ruffles in mesenchymal cell migration. *Cell Adh Migr.* **12**, 401–416 (2018).
5. E. K. Paluch, I. M. Aspalter, M. Sixt, Focal Adhesion-Independent Cell Migration. *Annu. Rev. Cell Dev. Biol.* **32**, 469–490 (2016).
6. Y.-J. Liu, M. Le Berre, F. Lautenschlaeger, P. Maiuri, A. Callan-Jones, M. Heuzé, T. Takaki, R. Voituriez, M. Piel, Confinement and low adhesion induce fast amoeboid migration of slow mesenchymal cells. *Cell.* **160**, 659–672 (2015).
7. P. Friedl, J. Locker, E. Sahai, J. E. Segall, Classifying collective cancer cell invasion. *Nat. Cell Biol.* **14**, 777–783 (2012).
8. P. Friedl, D. Gilmour, Collective cell migration in morphogenesis, regeneration and cancer. *Nat. Rev. Mol. Cell Biol.* **10**, 445–457 (2009).
9. K. J. Cheung, A. J. Ewald, A collective route to metastasis: Seeding by tumor cell clusters. *Science.* **352**, 167–169 (2016).
10. R. Mayor, S. Etienne-Manneville, The front and rear of collective cell migration. *Nat. Rev. Mol. Cell Biol.* **17**, 97–109 (2016).

11. E. Theveneau, C. Linker, Leaders in collective migration: are front cells really endowed with a particular set of skills? *F1000Res.* **6**, 1899 (2017).
12. A. Shellard, A. Szabó, X. Trepas, R. Mayor, Supracellular contraction at the rear of neural crest cell groups drives collective chemotaxis. *Science.* **362**, 339–343 (2018).
13. O. Zajac, J. Raingeaud, F. Libanje, C. Lefebvre, D. Sabino, I. Martins, P. Roy, C. Benatar, C. Canet-Jourdan, P. Azorin, M. Polrot, P. Gonin, S. Benbarche, S. Souquere, G. Pierron, D. Nowak, L. Bigot, M. Ducreux, D. Malka, C. Lobry, J.-Y. Scoazec, C. Eveno, M. Pocard, J.-L. Perfettini, D. Elias, P. Dartigues, D. Goéré, F. Jaulin, Tumour spheres with inverted polarity drive the formation of peritoneal metastases in patients with hypermethylated colorectal carcinomas. *Nature Cell Biology*, 1 (2018).
14. F. Grillet, E. Bayet, O. Villeronce, L. Zappia, E. L. Lagerqvist, S. Lunke, E. Charafe-Jauffret, K. Pham, C. Molck, N. Rolland, J. F. Bourgaux, M. Prudhomme, C. Philippe, S. Bravo, J. C. Boyer, L. Canterel-Thouennon, G. R. Taylor, A. Hsu, J. M. Pascussi, F. Hollande, J. Pannequin, Circulating tumour cells from patients with colorectal cancer have cancer stem cell hallmarks in ex vivo culture. *Gut.* **66**, 1802–1810 (2017).
15. D. Krndija, F. El Marjou, B. Guirao, S. Richon, O. Leroy, Y. Bellaiche, E. Hannezo, D. Matic Vignjevic, Active cell migration is critical for steady-state epithelial turnover in the gut. *Science.* **365**, 705–710 (2019).
16. B. Weigelin, G.-J. Bakker, P. Friedl, Intravital third harmonic generation microscopy of collective melanoma cell invasion: Principles of interface guidance and microvesicle dynamics. *Intravital.* **1**, 32–43 (2012).
17. B. Winkler, I. S. Aranson, F. Ziebert, Confinement and substrate topography control cell migration in a 3D computational model. *Commun Phys.* **2**, 1–11 (2019).
18. J. A. Mosier, A. Rahman-Zaman, M. R. Zanutelli, J. A. Vanderburgh, F. Bordeleau, B. D. Hoffman, C. A. Reinhart-King, Extent of Cell Confinement in Microtracks Affects Speed and Results in Differential Matrix Strains. *Biophys. J.* **117**, 1692–1701 (2019).
19. Z. Sun, M. Costell, R. Fässler, Integrin activation by talin, kindlin and mechanical forces. *Nat. Cell Biol.* **21**, 25–31 (2019).
20. F. Gunawan, A. Gentile, R. Fukuda, A. T. Tsedeke, V. Jiménez-Amilburu, R. Ramadass, A. Iida, A. Sehara-Fujisawa, D. Y. R. Stainier, Focal adhesions are essential to drive zebrafish heart valve morphogenesis. *J Cell Biol.* **218**, 1039–1054 (2019).
21. E. H. Barriga, K. Franze, G. Charras, R. Mayor, Tissue stiffening coordinates morphogenesis by triggering collective cell migration in vivo. *Nature.* **554**, 523–527 (2018).
22. Y. Hegerfeldt, M. Tusch, E.-B. Bröcker, P. Friedl, Collective cell movement in primary melanoma explants: plasticity of cell-cell interaction, beta1-integrin function, and migration strategies. *Cancer Res.* **62**, 2125–2130 (2002).
23. T. Lämmermann, B. L. Bader, S. J. Monkley, T. Worbs, R. Wedlich-Söldner, K. Hirsch, M. Keller, R. Förster, D. R. Critchley, R. Fässler, M. Sixt, Rapid leukocyte migration by integrin-independent flowing and squeezing. *Nature.* **453**, 51–55 (2008).

24. M. Bergert, A. Erzberger, R. A. Desai, I. M. Aspalter, A. C. Oates, G. Charras, G. Salbreux, E. K. Paluch, Force transmission during adhesion-independent migration. *Nat. Cell Biol.* **17**, 524–529 (2015).
25. A. Shellard, R. Mayor, Supracellular migration - beyond collective cell migration. *J. Cell. Sci.* **132** (2019), doi:10.1242/jcs.226142.
26. L. Valon, A. Marín-Llauradó, T. Wyatt, G. Charras, X. Trepát, Optogenetic control of cellular forces and mechanotransduction. *Nat Commun.* **8**, 14396 (2017).
27. X. Meshik, P. R. O’Neill, N. Gautam, Physical Plasma Membrane Perturbation Using Subcellular Optogenetics Drives Integrin-Activated Cell Migration. *ACS Synth Biol.* **8**, 498–510 (2019).
28. P. Friedl, S. Alexander, Cancer invasion and the microenvironment: plasticity and reciprocity. *Cell.* **147**, 992–1009 (2011).
29. D. J. Ruiter, J. H. van Krieken, G. N. van Muijen, R. M. de Waal, Tumour metastasis: is tissue an issue? *Lancet Oncol.* **2**, 109–112 (2001).
30. S.-B. Lim, C. S. Yu, S. J. Jang, T. W. Kim, J. H. Kim, J. C. Kim, Prognostic significance of lymphovascular invasion in sporadic colorectal cancer. *Dis. Colon Rectum.* **53**, 377–384 (2010).
31. V. Barresi, L. Reggiani Bonetti, E. Vitarelli, C. Di Gregorio, M. Ponz de Leon, G. Barresi, Immunohistochemical assessment of lymphovascular invasion in stage I colorectal carcinoma: prognostic relevance and correlation with nodal micrometastases. *Am. J. Surg. Pathol.* **36**, 66–72 (2012).
32. M. Brown, F. P. Assen, A. Leithner, J. Abe, H. Schachner, G. Asfour, Z. Bago-Horvath, J. V. Stein, P. Uhrin, M. Sixt, D. Kerjaschki, Lymph node blood vessels provide exit routes for metastatic tumor cell dissemination in mice. *Science.* **359**, 1408–1411 (2018).
33. J. Law, E. Martin, “*Transcoelomic Spread*”, in *Concise Medical Dictionary* (Oxford University Press, ed. 10, 2020).
34. S. Julien, A. Merino-Trigo, L. Lacroix, M. Pocard, D. Goéré, P. Mariani, S. Landron, L. Bigot, F. Nemati, P. Dartigues, L. B. Weiswald, D. Lantuas, L. Morgand, E. Pham, P. Gonin, V. Dangles-Marie, B. Job, P. Dessen, A. Bruno, A. Pierré, H. De Thé, H. Soliman, M. Nunes, G. Lardier, L. Calvet, B. Demers, G. Prévost, P. Vrignaud, S. Roman-Roman, O. Duchamp, C. Berthet, Characterization of a large panel of patient-derived tumor xenografts representing the clinical heterogeneity of human colorectal cancer. *Clin. Cancer Res.* **18**, 5314–5328 (2012).
35. M. J. Kennedy, R. M. Hughes, L. A. Peteya, J. W. Schwartz, M. D. Ehlers, C. L. Tucker, Rapid blue-light-mediated induction of protein interactions in living cells. *Nat Methods.* **7**, 973–975 (2010).
36. K. E. Rothenberg, D. W. Scott, N. Christoforou, B. D. Hoffman. Vinculin force-sensitive dynamics at focal adhesions enable effective directed cell migration. *Biophys J.* **114**, 1680–1694 (2018).
37. A. Hayer, L. Shao, M. Chung, L.-M. Joubert, H. W. Yang, F. C. Tsai, A. Bisaria, E. Betzig, T. Meyer. Engulfed cadherin fingers are polarized junctional structures between collectively migrating endothelial cells. *Nat Cell Biol.* **18**, 1311–1323 (2016).
38. C. M. Kenific, S. J. Stehbens, J. Goldsmith, A. M. Leidal, N. Faure, J. Ye, T. Wittmann, J. Debnath. NBR1 enables autophagy-dependent focal adhesion turnover. *J. Cell Biol.* **212**, 577–590 (2012).
39. J. Schindelin, I. Arganda-Carreras, E. Frise, V. Kaynig, M. Longair, T. Pietzsch, S. Preibisch, C. Rueden, S. Saalfeld, B. Schmid, J.-Y. Tinevez, D. J. White, V. Hartenstein, K. Eliceiri, P. Tomancak, A. Cardona. Fiji: an open-source platform for biological-image analysis. *Nat. Methods* **9**, 676–682 (2012).

40. J.-Y. Tinevez, N. Perry, J. Schindelin, G. M. Hoopes, G. D. Reynolds, E. Laplantine, S. Y. Bednarek, S. L. Shorte, K. W. Eliceiri. TrackMate: An open and extensible platform for single-particle tracking. *Methods* **115**, 80-90 (2017).
41. S. J. Lord, K. B. Velle, R. D. Mullins, L. K. Fritz-Laylin. SuperPlots: Communicating reproducibility and variability in cell biology. *J. Cell Biol.* **219**, e202001064 (2020).

Acknowledgements: We thank the members of the Jaulin, Piel and Montagnac laboratories for helpful discussions. We thank T. Manoliu and C. Laplace from the PFIC facility for their technical help. We thank M. Polrot from the PFEP facility for assistance with the animal work. We thank the C. Robert lab for the plasma cleaner. We thank J. Pannequin for the CTC cell lines. We thank W. Beng and K. Vaidziulyte for the automated tracking algorithm used in optogenetics. **Funding:** This work was supported by grants from INCA-PLBIO (2018-1-PLBIO-04-IGR-1), ARC (PAJ20181208275) and LNCC-IDF (R19102LL) to F.J. as well as fund raising against colorectal cancer from the Gustave Roussy foundation. M.C. thanks the Labex CelTisPhyBio (ANR-10-LBX-0038) and the Institut Convergences Q-life ANR-17-CONV-0005. We thank the Philantropia fellowship to D.-L.P., the FRM fellowship to E.D., the AMX fellowship to J.D.S. and the Taxe d'Apprentissage 2019 (to D.-L.P., Univ. Paris-Saclay, France). **Author contributions:**

All authors provided intellectual input. D.-L.P., E.D., and R.L. designed the research, performed the experiments and analysed the data. J.D.S. and M.C. conceived, performed and analysed the optogenetics experiments. L.W. and M.P. designed and validated the microfabricated devices. J.C. prepared the organoids and helped for the animal work. C.C.-J. performed immunostainings on TSIPs. J.R. analysed the contractility of cell clusters. C.M.C, R.V. and M.P. provided scientific input. F.J. conceptualised the project, designed the research and wrote the manuscript. **Competing interests:** Authors declare no competing interests. **Data and materials availability:** All data is available in the main text or the supplementary materials.

Materials and Methods

Biological material and cell culture

Human primary specimens. The human study protocols followed all relevant ethical regulations in accordance with the declaration of Helsinki principles. The study was approved by the ethic committee at Gustave Roussy hospital and written informed consent was obtained from all patients.

Tumoroids generated from Patient-Derived Xenografts. Two human colorectal tumours (TSIP#1 corresponding to LRB-0009C and TSIP#2 corresponding to IGR-0014P) from the CReMEC tumour collection (34) were maintained in immunocompromised mice. Animal experiments were compliant with French legislation and EU Directive 2010/63. The project received a favourable evaluation from Animal Care and Use Committee n°26 and granted French government authorization under number 517-2015042114005883 and 8867-2017020914112908. Mice were obtained from Charles River and Gustave Roussy facility, housed and bred at the Gustave Roussy animal core facility (accreditation D94-076-11) and euthanized following endpoints validated by the Ethical Committee and the French government (Ministère de l'Enseignement Supérieur, de la Recherche et de l'Innovation). Tumoroids (TSIPs) formation from PDXs was adapted from the protocol described in (13). Tumours between 1000-1500 mm³ are minced and incubated in 5 to 10ml of DMEM medium containing GlutaMAX (31966-021, Gibco) supplemented with 2 mg/ml collagenase-VIII (Sigma, C2139) for 1h15 at 37°C under agitation. Tumour fragments are resuspended in 50ml of DMEM and filtered through 100µm cell strainers (EASYstrainer, 542000). Filtered tumour cells and clusters are pelleted at 800g for 10min. Pellets are further washed 4 times by adding 10ml of DMEM medium and pulse-centrifugated at 800g and 300g to collect clusters only. Clusters are cultured in suspension in DMEM medium supplemented with 10% foetal bovine serum (FBS, 10270-106, Gibco) (called "full DMEM"). They form tumoroid in 6-well ultralow attachment plates (Corning, CLS3471-24EA) after 3 days of culture. All media are supplemented with 1% penicillin and streptomycin (P/S, Gibco, 15140-122).

Cell lines. HT29 (ATCC® HTB-38) are grown in full DMEM. HT29-MTX (HT29-MTX-E12, 12040401, ECACC) culture medium requires the addition of 1% non-essential amino acids (NEAA, Gibco, 11140050). Cell lines are dissociated with 0.05% trypsin-EDTA. All media are supplemented with 1% penicillin and streptomycin (P/S, Gibco, 15140-122). To produce clusters from HT29 and HT29-MTX cell lines, 1.5 million cells were plated in a Petri dish, with 10ml of culture medium. Cluster formation requires 3-5 days.

Circulating Tumour Cell lines (CTC31, CTC44, CTC45) are a gift from Julie Pannequin and cultivated as previously described (14). In brief, they are maintained in suspension as clusters in advanced DMEM-F12 (Gibco, 12634-010) supplemented with 1% GlutaMax (Invitrogen, 35050-061), 1% N2 supplement (Invitrogen, 17502-048), 20ng/ml of human EGF and 10ng/ml of human FGF-2. They are split once a week, by pelleting at 300g for 5min and incubated with Accumax for 45min at 37°C. 5ml of PBS containing 2% FBS is then added to inactivate Accumax. Clusters are filtered through a 40µm strainer, pelleted and resuspended in M12 medium.

All cell lines and clusters are cultured in a humidified incubator at 37°C under a 5% CO₂ atmosphere.

Microchannels, drug incubation and cluster loading.

Dimensions of the channels. Three types of microchannels were designed, with different width (w), height (h), length (l). The microchannels that were used for most migration studies have the following dimensions: h=30µm, w=60µm, l=7mm (confinement in two dimensions, one degree of freedom along X axis). The microchambers are h=30µm, w=500µm, l=7mm (providing confinement in one dimension, two degrees of freedom for migration along X and Y axes). The loading chamber's height (h=180µm) allows for quantification of clusters' displacement without confinement.

Microchannels preparation and drug incubation. Chips are made of a polydimethylsiloxane mixture (PDMS, Neyco, Sylgard-184 Dow Corning) 10:1 w:w with crosslinker, polymerised for at least 48h. Loading holes are made with a 1mm hole puncher. Chips are sterilized with 70% ethanol for a few minutes, dried and activated for 1min in a plasma chamber (Diener, Zepto V2, 30W) together with a glass substrate (12-well-glass-bottom plate (CellVis, P12-1.5H-N), 6-well-glass-bottom plate (MatTek, P06G-1.5-20-F) or 25-mm glass coverslip for optogenetic experiments). Channels are stuck to the activated glass before being coated for at least 30 min with an anti-adhesive reagent (0.1mg/ml pLL-g-PEG (pLL(20)-G[3.5]-PEG(2) from SuSoS) or pLL-g-PEG + 1% Pluronic F-127) or 20µg/ml rat-tail collagen-I (Corning, 354236). Channels are washed once in full DMEM and then submerged with medium for 1h to overnight. When adding drugs (Y27632, 25µM (Sigma, Y0503-5MG); Blebbistatin, 50µM (Calbiochem, 203391)), or DMSO for the control, to the medium, chips are incubated with the medium and drugs at least 3h prior to cluster loading.

Cluster loading. Clusters are filtered on a 70µm strainer (EASYStrainer, 542070), pelleted by a 400g pulse centrifugation and resuspended at 250 clusters/µl in full DMEM. Clusters are loaded using a 25 or 50µl syringe (Hamilton, 702SNR 22/51mm/pst3).

Plasmids, virus production and infection

Plasmids. The ARHGEF11 domain was amplified and cloned into CRY2PHR-mCherry. pCIBN(deltaNLS)-pmGFP (Addgene plasmid # 26867; <http://n2t.net/addgene:26867>; RRID:Addgene_26867) (35) and pCRY2PHR-mCherryN1 (Addgene plasmid # 26866; <http://n2t.net/addgene:26866>; RRID:Addgene_26866) (35) were a gift from Chandra Tucker. H2B-RFP and LifeAct-mCherry were gifts from the Hall lab. pRRL-Vinculin-Venus was a gift from B. Hoffman (36) (Addgene plasmid #111833; <http://n2t.net/addgene:111833>; RRID:Addgene_111833), pLV-Ftractin-mRuby3-p2A-mTurquoise-MLC-IRES-Blast was a gift from T. Meyer (37) (Addgene plasmid # 85146; <http://n2t.net/addgene:85146>; RRID:Addgene_85146) and pLentiblast-Paxillin-mTurquoise was a gift from J. Debnath (38) (Addgene plasmid #74206; <http://n2t.net/addgene:74206>; RRID:Addgene_74206). A GIPZ lentiviral shRNA transduction starter kit containing control shRNA and Talin constructs was purchased from Horizon Discovery (clone IDs (catalog number): V2LHS_56643 (RHS4430-200185645); V3LHS_366591 (RHS4430-200290073); V3LHS_366592 (RHS4430-200294817)).

Virus production and infection. Ectopic expression of fluorescent probes and shRNA was achieved using lentiviruses. Lentiviruses are obtained by co-transfection with the packaging vectors pMD2G (Addgene plasmid #12259; <http://n2t.net/addgene:12259>; RRID:Addgene_12259) and pCMVdr8,74 (Addgene plasmid #8455; <http://n2t.net/addgene:8455>; RRID:Addgene_8455) into HEK293T cells with the transfection reagent JetPrime (Polyplus, 114-15). Lentiviruses-containing supernatants were collected on days 2 and 3 following transfection, concentrated by ultracentrifugation (24000g, 2h) and stored at -80°C .

Infection was performed as described previously (13). Briefly, HT29-MTX (1×10^6 cells) are exposed to lentiviruses in 500 μl full DMEM containing 16 $\mu\text{g/ml}$ protamin overnight before being sorted by FACS to establish stable cell lines. Cell lines were then chosen for experiments as specified in the legends. Moreover, Vinculin-Venus-expressing HT29-MTX were used in Fig. 2, (B) and (C) (2 experiments out of 3); F-tractin-mRuby3/mTurquoise-MLC/Vinculin-Venus-expressing HT29-MTX were used in Fig. 3, (B) and (C); and for Fig. 3, (F) to (I), and fig. S5, optoRhoA HT29-MTX expressed ARHGEF11-CRY2PHR-mCherry and CIBN-GFP, and controls express CRY2PHR-mCherryN1 and CIBN-eGFP-CaaX.

Live Imaging, microscope acquisition and optogenetic experiments.

Time-lapse imaging. Timelapse bright-field imaging was done using an Olympus inverted X83 microscope with a Hamamatsu camera or a Spinning Disk CSU-W1 (Yokogawa) with a Prime 95B sCMOC camera. The latter one was also used for live fluorescence imaging.

Optogenetics. Clusters are incubated in the chips for at least 1 hour before imaging. Experiments were performed at 37°C in 5% CO_2 in a heating chamber (Pecon, Meyer Instruments, Houston, TX) placed on an inverted microscope model No. IX71 equipped with a 60 \times objective with NA 1.45 (Olympus, Melville, NY) and a camera ORCA-Flash4 (Hamamatsu, Japan). The microscope was controlled with the software Metamorph (Molecular Devices, Eugene, OR). Differential interference contrast (DIC) imaging was performed with a far-red filter in the illumination path to avoid CRY2 activation. Optogenetic stimulations were performed every 2-2,5 or 5min with a DMD in epi-mode (DLP Light Crafter, Texas Instruments) illuminated with a SPECTRA Light Engine (Lumencor, Beaverton, OR USA) at 440 ± 10 nm. Total Internal Reflection Fluorescence (TIRF) images were acquired using an azimuthal TIRF module (iLas2; Roper Scientific, Tucson, AZ). An automated tracking algorithm was designed in MATLAB coupled to a feedback-loop routine for the optogenetic activation.

Immunofluorescence, antibodies, histology and immunohistochemistry

Immunofluorescence of TSIP#1 in collagen. Immunofluorescence was performed on samples fixed after 3 days of incubation in collagen-1, as described previously (13). Images were acquired with a SpinningDisk CSU-W1 (Yokogawa) with a Zyla sCMOC camera driven by an Olympus X83.

Antibodies and dyes. Primary antibodies: P5D2 (anti-integrin $\beta 1$, 1:500) was purchased from DSHB (deposited by Wayner, E.A. (DSHB Hybridoma Product P5D2)). Secondary antibodies: anti-Mouse-FITC (1:250, Jackson Immuno Research, 711-545-152). Dyes: Alexa Fluor Phalloidin 488 (1:1000, Life technology,

A12379), DAPI, Alexa647-collagen-1 (coupling of the collagen was done in-house, using Invitrogen labelling kit #A20006).

Histology and immunohistochemistry. CRC (micropapillary histotype) obtained after surgical resection was formalin-fixed and paraffin embedded (FFPE) according to routine protocols. 3mm sections of FFPE samples were deparaffinised, unmasked (Ph8) and rehydrated prior Hematoxylin Eosin Saffron (HES) or immunohistochemistry.

Immunohistochemistry. Sections were immunostained with Ezrin (1:100, BD Biosciences, 610603) or CK20 specific mouse monoclonal antibody, (clone Ks20.8, Dako, Glostrup, Denmark). Stainings were performed with Ventana BenchMark XT immunostainer (Ventana Medical Systems, Tucson, AZ) utilizing UltraView DABv3 kit (Ventana). The chromogene was 3,3'-diaminobenzidine (DAB) in all the stainings.

Image analysis

Analysis of clusters' displacements from bright-field time-lapse sequences. For bright-field movies, displacement of clusters' centroid was tracked every hour using the Manual Tracking plugin in ImageJ. Clusters that were too small to be confined or dissociating during the experiment were ignored. Speed ($\mu\text{m}/\text{day}$) corresponds to the accumulated distance over 1 day (20 to 24h, and 17h for Fig.1 G and H). For observations during $\leq 20\text{h}$, speed was extrapolated to 24h.

Cell segmentation for cell tracking in optogenetic experiments. Movies were analysed using custom-built routines in Fiji (39) and MATLAB (The MathWorks, Natick, MA). ARHGEF11-CRY2-mCherry signal was used to segment clusters by applying a gaussian filter and a threshold. Trajectories were then analysed in MATLAB, taking the displacement of the center of each segmented cluster along the microchannel.

Persistence is calculated as the ratio of the total displacement of the cluster monitored every 1h for 1 day, over the Euclidean distance. *Maximum instantaneous speed* is calculated as the maximum speed reached in one hour by a cluster. *Maximum migration period duration* is the longest period of continuous migration over 1px (1.07 μm to 1.369 μm) per hour. *Pause duration* is the length of time where a cluster stays immobile (i.e. migrates less than 1px (1.07 μm to 1.369 μm) per hour) between the migratory phases. Hence, one cluster can display several pauses over the imaging period. *Aspect ratio* is calculated as the clusters' length over the width of the channel (60 μm).

Analysis of Paxillin foci. Images are treated with the Subtract background plugin, using a 2-pixels rolling ball. Threshold is then set to highlight and best separate all the foci. Characteristics of each structures is then collected using the Analyse Particles ImageJ plugin, considering particles of 10-infinite sizes.

Analysis of nuclei movements. Nuclei from the middle plane were imaged every 15min, manually tracked every hour and displayed using TrackMate (40) ImageJ plug-in. A custom-made R code was designed to

subtract cluster centroid's displacement to nuclei's movement, classify the nuclei by location within the cluster (center, side 1, side 2), and represent the tracks in the cluster reference frame (Fig. S3A). As a rotation of clusters could happen in one or the other direction and could be hidden by averaging the lateral movements on several clusters, we defined Side 1 for each cluster as the cluster's side going most rearward (or less forward) in average, while the other side was called side 2.

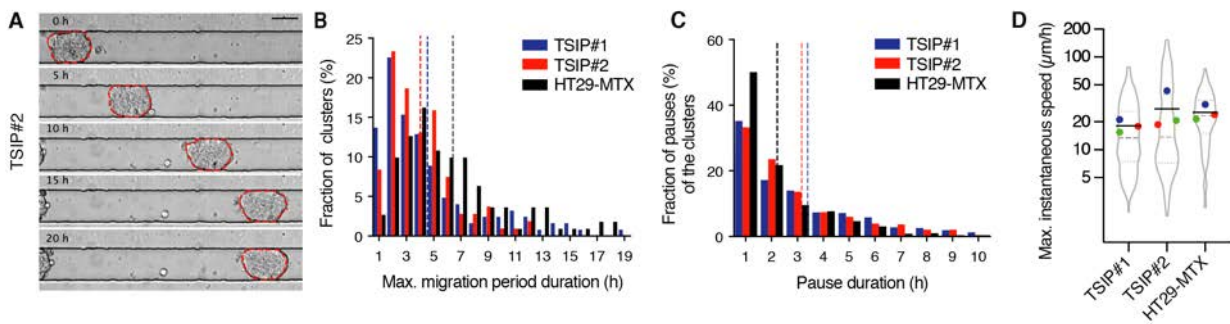
Analysis of MLC and actin polarization. Direction of migration for each cluster is determined by tracking its movement for at least 2h prior to fluorescence imaging. Myosin and actin localisation are determined in the middle section of the sphere using a spinning disk fluorescence microscope. 20-pixel Subtract background is performed before using a 15 pixels wide line scan of the cortex to measure the intensity of myosin and actin signal in each half of the cluster. The intensity in each half is normalised to the perimeter of the line scan to calculate the rear to front ratio.

Western blot.

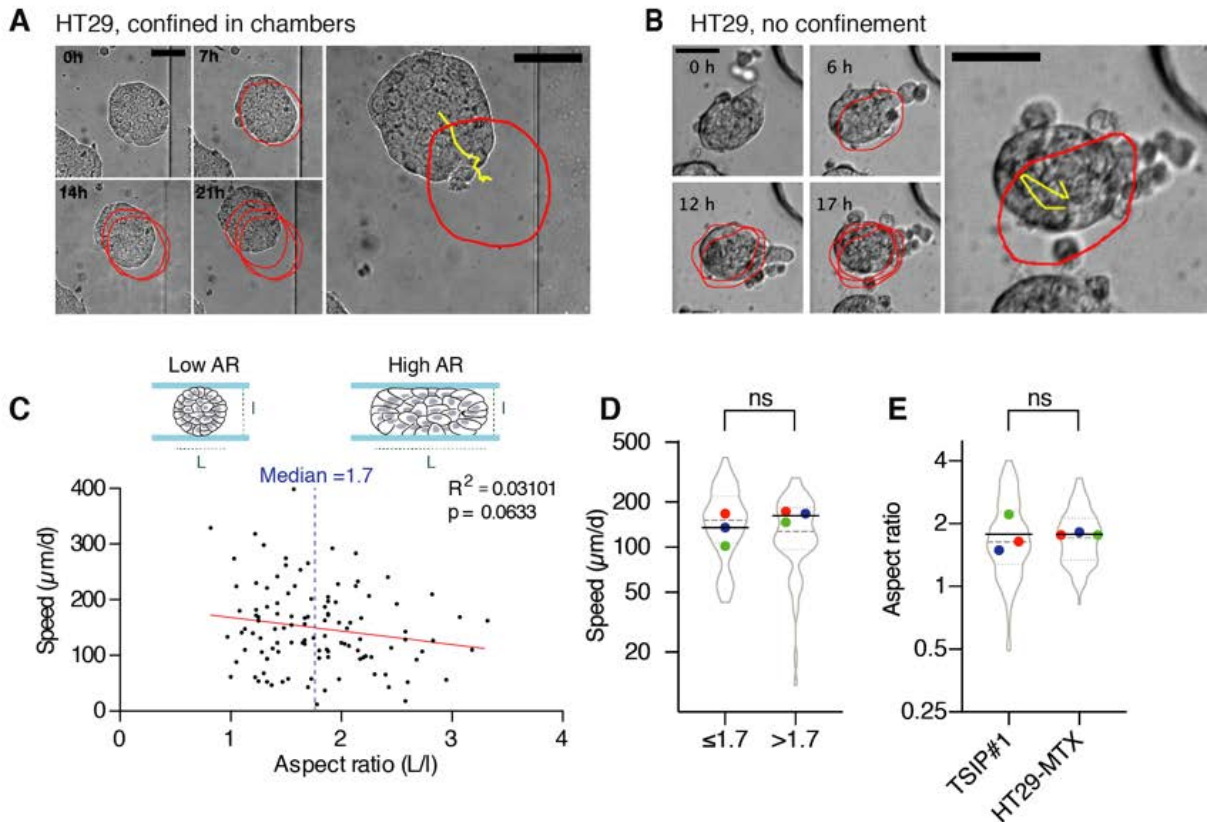
Western blots were conducted as described previously (13), with PVDF membranes (GE Healthcare). Primary antibody was anti-Talin 1 antibody (ab71333, Abcam) and secondary antibody was anti-rabbit, HRP-linked (7074, Cell Signaling).

Statistics and reproducibility

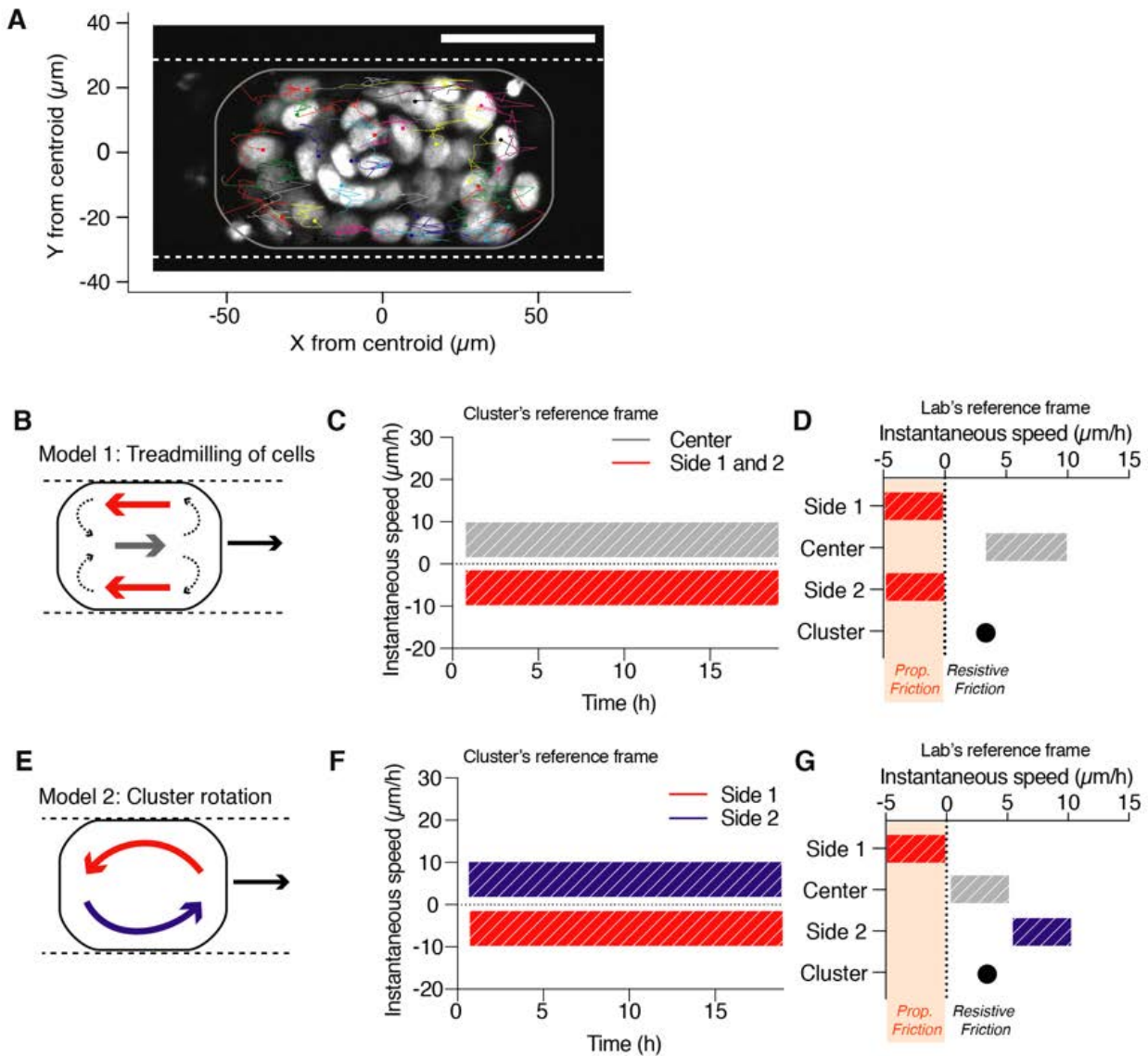
Normality or lognormality of all data distribution was tested using the Kolmogorov-Smirnov, d'Agostino-Pearson or Shapiro-Wilk test in Prism 8 (GraphPad). When distributions are best fitted by a lognormal distribution, statistical tests were performed on log-transformed data. Significance for datasets displaying normal distributions were calculated in Prism with unpaired two-tailed Student's t test or one-way analysis of variance (ANOVA) and Holm-Sidak's multiple comparison test when comparing more than two conditions. Significance for non-normal distributed datasets were calculated in Prism using a Mann-Whitney test or a Kruskal-Wallis test and Dunn's multiple comparison test when comparing more than two conditions. Significance for non-normal distributed paired datasets (Fig. 2K) were calculated in Prism using Friedman test and Dunn's multiple comparison test when comparing more than two conditions. P values of statistical significance are represented as ****P <0.0001, ***P <0.001, **P <0.01, *P <0.05, ns, not significant. The exact value is indicated when possible. n numbers are indicated in the figure legends as well as the N number of independent experiments. Violin plots display the whole population of clusters, median (dashed grey line) and quartiles (dotted grey lines) (41). The coloured dots represent the mean of each independent experiments and the black line is the mean of all experiments for each condition. Experiments were performed independently for each cell lines and for each individual graph, coloured dots for the same cell line refer to the same experiment.

**Fig. S1.**

Characterisation of clusters' migration. (A) Time-lapse sequences of TSIP#2 migration every 5h migrating in a PEG-coated microchannel. Scale bar, 50 μm . (B) Histogram of the longer period of consecutive migration achieved by each cluster (maximum (Max.) migration period duration) migrating one day in PEG-coated microchannels. (C) Histogram of the duration of pauses occurring during clusters' migration during one day in PEG-coated microchannels. For (B) and (C), dashed lines: mean. (D) Maximum instantaneous speed of clusters migrating one day in PEG-coated microchannels, log₂-scale. For (B) to (D), n=107 to 124 clusters from 3 independent experiments. Violin plot is described in Fig. 1 legend.

**Fig. S2.**

Confinement increases the persistence of cluster migration in non-adhesive microchannels, independently of their size. (A and B) Representative time-lapse sequences of HT29 displacement, confined in microchambers (A) and in loading chambers (B, no confinement), coated with PEG+F127. Red circles: consecutive positions (every 6 or 7h); yellow: track of the cluster's centroid monitored every hour for one day. Scale bars, $50\mu\text{m}$. (C) Speed and aspect ratio (AR) of HT29-MTX clusters migrating one day in PEG-coated microchannels. $n=112$ clusters from 3 independent experiments. Line: linear regression. (D) Comparison of the speed of HT29-MTX clusters migrating one day in PEG-coated microchannels, depending on their aspect ratio (relative to median $AR=1.7$, illustrated in (C)), log₂-scale. $n=112$ clusters from 3 independent experiments (Mann-Whitney test). (E) Aspect ratio of clusters migrating one day in PEG-coated microchannels, log₂-scale. $n=112$ or 162 clusters from 3 independent experiments (two-tailed Student's *t* test). ns, not significant. Violin plots are described in Fig. 1 legend and in (D), coloured dots refer to the same experiment. All data represented as violin plots are from $N=3$ independent experiments.

**Fig. S3.**

Adhesion-independent collective migration is not mediated by a cell flow. (A) Representative tracks of nuclei in the cluster's reference frame, migrating in a PEG-coated microchannel over one day (same cluster as in Fig. 2H). (B to G) Hypothetical models, corresponding to Fig. 2, (I) to (K). Schematic representation of cell treadmilling (Model 1, B) or rotation of the whole cluster (Model 2, E) generating propulsive friction with microchannel walls. (C and F) Expected range (hatched rectangles) of instantaneous speed of the cells present in each zone, in the cluster's reference frame. (D and G) Expected range (hatched rectangles) of mean instantaneous speed of cells in contact with the microchannel walls, considering the same mean instantaneous speed of the cluster as in Fig. 2K, lab's reference frame. Orange zone corresponds to cell speeds ≤ 0 capable of generating a propulsive (Prop.) friction against the microchannel walls

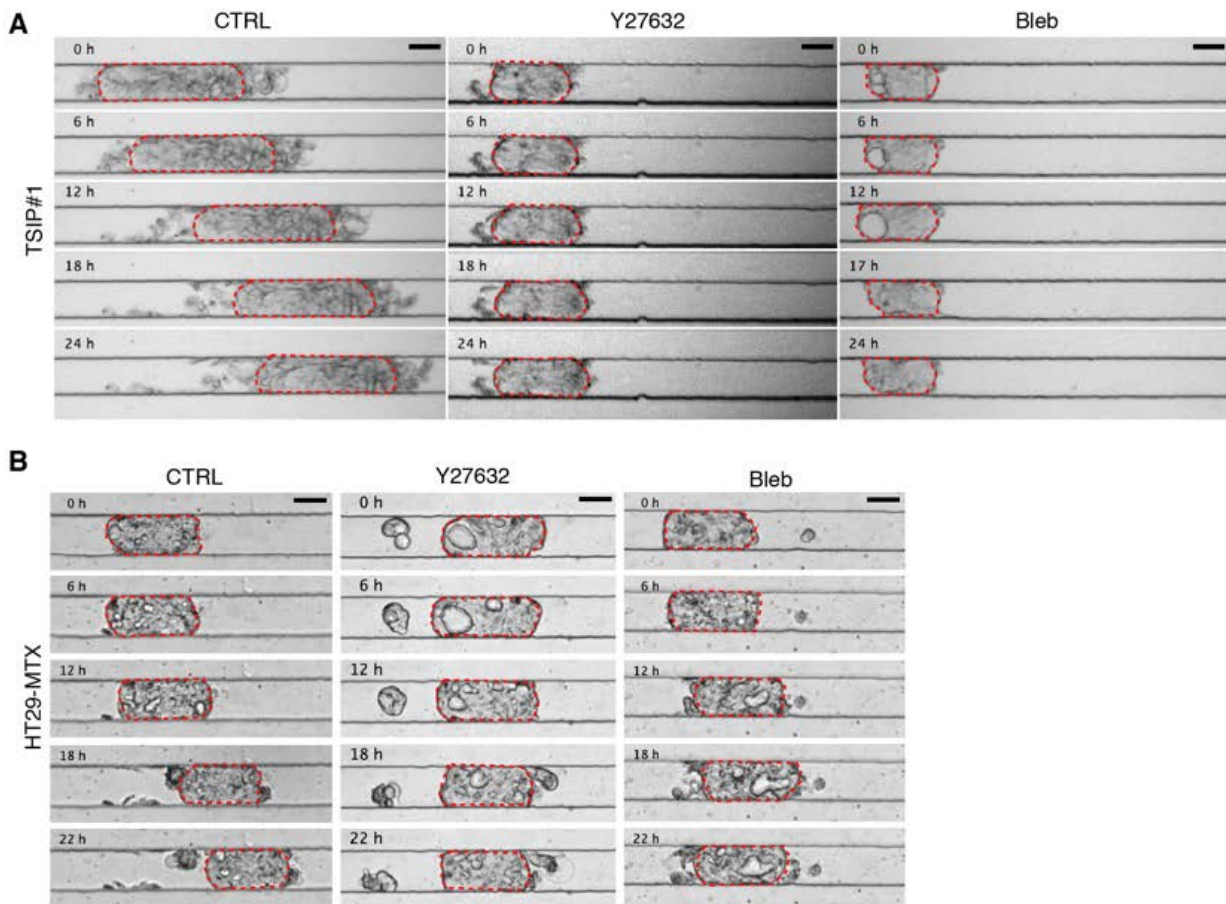
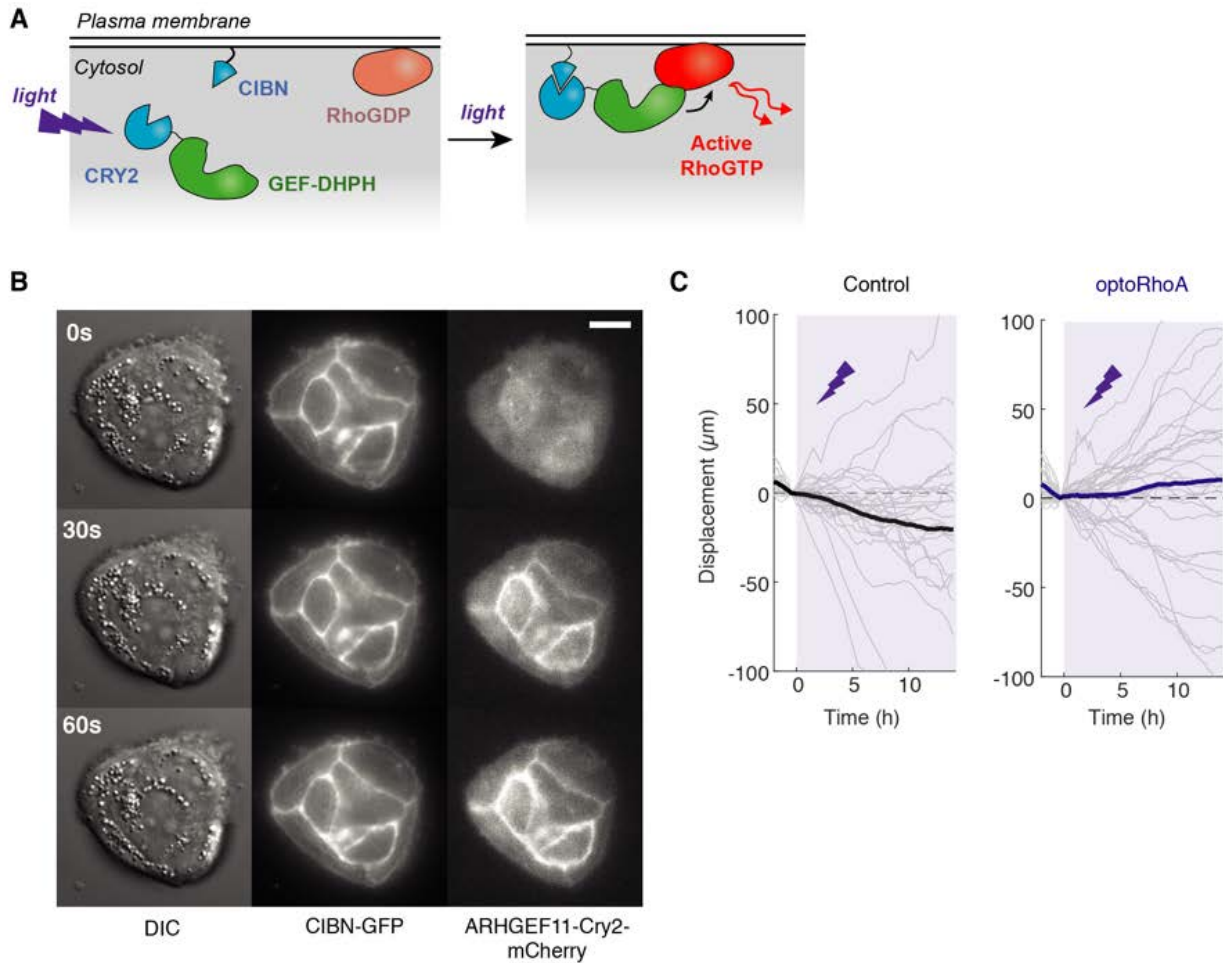


Fig. S4.

Inhibition of acto-myosin contractility prevents focal adhesion-independent collective migration.

Time-lapse sequences of TSIP#1 (**A**) and HT29-MTX (**B**) displacement in PEG-coated microchannels over a day. (Left) control condition, (middle) after Y27632 (25 μ M) treatment, (right) after Blebbistatin (50mM) treatment. Scale bar, 50 μ m.

**Fig. S5.**

Activation of RhoA induces cluster migration and dictates directionality. (A) Schematic of the molecular effect of light activation in optoRhoA cells. (B) Global activation of optoRhoA cell lines. ARHGEF11-Cry2-mCherry and CIBN-GFP are observed in Total Internal Reflection Fluorescence (TIRF). Activation every 30s with 488nm-laser. Scale bar, 10 μ m. (C) Displacement of clusters (grey) before ($-2\text{h} < t < 0\text{h}$) and after ($0\text{h} < t < 15\text{h}$) optogenetic activation of optoRhoA stably expressing cells and control cells. Means are represented in bold. Purple zone: optogenetic activation. $n=27$ for optoRhoA from 3 independent experiments.

Movie S1.

TSIP#1 (top) and TSIP#2 (bottom) clusters migrate collectively in PEG-coated microchannels. Movie was recorded every hour over 24 hours. Scale bars, 50µm.

Movie S2.

HT29-MTX clusters migrate in PEG-coated microchannels. Movie was recorded every hour over 20 hours. Scale bar, 50µm.

Movie S3.

HT29-MTX clusters stably expressing Paxillin-mTurquoise in a collagen-I-coated microchannel (left) or in a PEG-coated microchannel (right). Movie was recorded every 3 min over 2.5 hours. Scale bar, 30µm.

Movie S4.

HT29 cluster stably expressing mCherry-H2B migrating in a PEG-coated microchannel. Movie was recorded every 15min over 24 hours. Scale bar, 50µm.

Movie S5.

HT29-MTX clusters stably expressing mTurquoise-MLC static (left) or migrating (right) in PEG+F127-coated microchannels. Movie was recorded every 5 min over 3 hours. Scale bar, 30µm.

Movie S6.

OptoRhoA HT29-MTX cluster migrating in a PEG-coated microchannel before and after optogenetic activation. Optogenetic activation, represented in blue, starts at 0min. Movie was recorded every 10min over 14h hours. Dark grey lines represent microchannel walls. Scale bar, 20µm.

Movie S7.

CRY2PHR-mCherryN1/CIBN-eGFP-CaaX-expressing HT29-MTX cluster (control for optoRhoA clusters) migrating in a PEG-coated microchannel before and after optogenetic activation. Optogenetic activation, represented in blue, starts at 0min. Movie was recorded every 10min over 15h hours. Dark grey lines represent microchannel walls. Scale bar, 20µm.

ANNEX 2. SUPPLEMENTARY TEXT ON « POLARISED JIGGLING » MODEL

This supplementary text has been submitted together with the manuscript Pagès et al.

The following correspondences have to be taken into account between this version of the [Supplementary Text](#) (associated with the submitted version of the manuscript) and this **PhD manuscript**:

- [Fig. 3a-c](#) corresponds to **Figure 77a-c**
- [Fig. 5l](#) corresponds to **Figure 82c**
- [Fig. 6c](#) corresponds to **Figure 83e**
- [Ref. 24](#) corresponds to (Baule et al., 2008)

Supplementary model for “Polarised contractile jiggling drives the collective amoeboid migration of cell clusters”

In this supplementary section, we demonstrate the mechanism via which a cluster may migrate even when no *persistent* intracluster cellular flow or intracellular actin flow is present. In the experiments, nuclear tracking demonstrates that cell exchanges are rare implying that the cluster moves essentially as a solid medium. This implies that the motion of the cluster is not driven by a flow of cells as this would require cell rearrangements at long times. Instead, both the direction and the speed of the cluster is dictated by a gradient in the myosin concentration which is clearly observed in migrating clusters (see Fig. 3a-c of the main text), but is absent in non-migrating one. Investigating further, fluctuations of both myosin flow speeds and cell nuclei speeds positively correlated with cluster migration speed (Fig. 5l, 6c). The action of myosin in the experiments leads to a contractile active stress in the cluster. Since the average myosin concentration displays a clear gradient in motile clusters, this implies a gradient of contractile active stresses which we conjecture drives the cluster motility. A minimal stochastic description of myosin concentration, with either formation or destruction of myosin molecules or simple diffusion, leads to a Poisson distribution for the concentration. Therefore, the amplitude of myosin fluctuations is proportional to the time-averaged concentration and therefore, should display the same gradient. The proportionality of the active contractile stress with the myosin concentration implies that it too has both an inhomogeneous time-averaged part and a fluctuating part whose strength displays the same in-homogeneity. By symmetry, the time-averaged part of the inhomogeneous active stress can only make the effective elastic moduli of the cluster inhomogeneous and this cannot lead to motion. In contrast, a *gradient* in the strength of the fluctuating part of the contractile stress leads to cluster motility, as we demonstrate in this appendix.

We construct a minimal model of the cluster as a solid with a gradient of active contractile stress fluctuations to understand the origin of the motility. The fluctuations observed in the experiment have a much shorter timescale compared to the timescale of cluster motion. Therefore, in our proof-of-principle model, we consider the stress fluctuations to be uncorrelated in space and time. First we consider a simple dimer model for the cluster, which is essentially equivalent to the model of^{24,53} to illustrate the emergence of motility due to an asymmetry of the active fluctuation strength in Sec. A. Then we demonstrate that this simple model describes the essential mechanism of asymmetric fluctuation-driven motility of a solid in B. We do this by starting with the general equations of motion of a three-dimensional solid driven by an asymmetric contractile fluctuating stress and systematically deriving an equivalent one-dimensional model. While we cannot obtain an exact expression for the motility in this continuum model, we demonstrate numerically that its discretised version is motile. Together with the experiments, this establishes a new mechanism for motility of a cell cluster modelled as a solid medium endowed with a polarised fluctuating contractile stress.

A. Dimer model

We first start with a minimal dimer model (Fig. ST 1), developed by^{24,53} and then generalise this and demonstrate that the cell cluster can self-propel via an active noise-driven mechanism. In this section, we divide the cluster into two parts, back and front, which are connected by an elastic

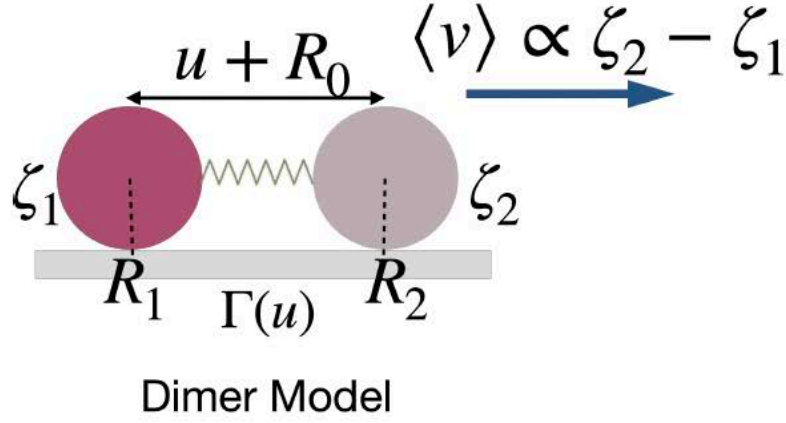


Fig. ST 1. Dimer model. Model of a dimer with two distinct active noise strengths ζ_1 and ζ_2 on the two beads and a strain u -dependent friction with the substrate. The positions of the two beads are R_1 and R_2 and the equilibrium separation between them is R_0 .

element (spring). We model the two parts of the cell cluster as two beads with mass m and positions R_1 and R_2 , with an equilibrium distance R_0 . The extension of the elastic element or the strain is $u = R_2 - R_1 - R_0$. The equation of motion for the two units of the dimer are $\dot{R}_1 = v_1$, $\dot{R}_2 = v_2$,

$$m\dot{v}_1 = -\Gamma(u)v_1 - \partial_{R_1}F_R + \xi_1 \quad (1)$$

and

$$m\dot{v}_2 = -\Gamma(u)v_2 - \partial_{R_2}F_R + \xi_2, \quad (2)$$

where F_R is the spring potential of the elastic element and we have assumed, for simplicity, that the friction coefficient $\Gamma(u)$ for both the beads are the same, but it depends on the strain^{24,53} and where the stochastic noises ξ_1 and ξ_2 have the correlations

$$\langle \xi_1(t)\xi_1(t') \rangle = 2(T + \zeta_1)\Gamma(u)\delta(t - t'), \quad (3)$$

$$\langle \xi_2(t)\xi_2(t') \rangle = 2(T + \zeta_2)\Gamma(u)\delta(t - t'), \quad (4)$$

with T being a passive noise strength and ζ_1 and ζ_2 being the active noise strength due to contractility on beads 1 and 2 respectively, and $\langle \xi_1(t)\xi_2(t') \rangle = 0$. The only effect of activity in this model is stochastic (as argued earlier, a non-stochastic active force in a solid only leads to a modification of the elasticity, here the spring potential) and enters through the active noise strength which is assumed to have a gradient i.e., $\zeta_1 \neq \zeta_2$. Essentially this model was first proposed by^{24,53} as a general model of active motility. The only, minor, difference between the model presented here and the one in^{24,53} is that while (1) and (2) describe an equilibrium system in the limit $\zeta_1 = \zeta_2$ even in the presence of a strain-dependent friction, it does not in^{24,53}. We include this extra constraint in our model to highlight the *minimal* conditions required for noise-driven motility. However, the active noise correlators need not be proportional to $\Gamma(u)$ in a generic active system or even a typical one. Relaxing this constraint makes the system *more* active, in a sense, and the conclusion that gradients in the strength of random fluctuations can drive motion remains unchanged. Note further that here active noise is not conserved. However, we show how this model can be obtained by starting from the equations of motion of a momentum conserved gel in a confined geometry, with appropriate boundary conditions on the walls, in section B.

We now eliminate the inertial terms in (1) and (2), as is appropriate for the highly overdamped system being considered here, by taking the standard zero-mass limit^{57,60} yielding two stochastic equations for R_1 and R_2 :

$$\Gamma(u)\dot{R}_1 = -\partial_{R_1}F_R + \sqrt{2(T + \zeta_1)\Gamma(u)}\xi_1 - \frac{(T + \zeta_1)}{2}\partial_{R_1}\ln\Gamma(u) \quad (5)$$

and

$$\Gamma(u)\dot{R}_2 = -\partial_{R_2}F_R + \sqrt{2(T + \zeta_2)\Gamma(u)}\xi_2 - \frac{(T + \zeta_2)}{2}\partial_{R_2}\ln\Gamma(u). \quad (6)$$

when the now multiplicative noises are interpreted in the Stratonovich convention. The final terms in (5) and (6) are noise-induced drifts^{61,62}. When the noise is interpreted in other conventions, the numerical factor in front of the final terms in (5) and (6) changes. It is 1 instead of 1/2 when the noises are interpreted in the Ito sense and, for a general α interpretation⁵⁴⁻⁵⁶, it is $(1 - \alpha)$ with $\alpha = 0$ for Ito, 1/2 for Stratonovich and 1 for Hanggi-Klementovich interpretations⁵⁴. The interpretation of the active noises along with the noise-induced drift can be fixed, in general, by demanding that the noise-induced forces must vanish, on average. This implies that there is no external force on the system as a whole on average and that the total friction force on the dimer vanishes on average. We explicitly show that this is the case. The total friction force, averaged over the noise, is

$$\begin{aligned} \langle \Gamma(u)\dot{R}_1 \rangle + \langle \Gamma(u)\dot{R}_2 \rangle = \\ \langle \sqrt{2(T + \zeta_1)\Gamma(u)}\xi_1 \rangle + \frac{(T + \zeta_1)}{2}\langle \partial_u \ln\Gamma(u) \rangle + \langle \sqrt{2(T + \zeta_2)\Gamma(u)}\xi_2 \rangle - \frac{(T + \zeta_2)}{2}\langle \partial_u \ln\Gamma(u) \rangle \end{aligned} \quad (7)$$

where the averages over the Gaussian noise can be performed using the Novikov theorem⁵⁹ and⁵⁸, yielding

$$\begin{aligned} \langle \sqrt{2(T + \zeta_1)\Gamma(u)}\xi_1 \rangle &= \left\langle \partial_{R_1}[\sqrt{2(T + \zeta_1)\Gamma(u)}] \frac{\delta R_1}{\delta \xi_1} \right\rangle \\ &= - \left\langle \partial_u[\sqrt{2(T + \zeta_1)\Gamma(u)}] \frac{1}{2} \frac{\sqrt{2(T + \zeta_1)\Gamma}}{\Gamma} \right\rangle = -\frac{T + \zeta_1}{2}\langle \partial_u \ln\Gamma \rangle \end{aligned} \quad (8)$$

and

$$\begin{aligned} \langle \sqrt{2(T + \zeta_2)\Gamma(u)}\xi_2 \rangle &= \left\langle \partial_{R_2}[\sqrt{2(T + \zeta_2)\Gamma(u)}] \frac{\delta R_2}{\delta \xi_2} \right\rangle \\ &= \left\langle \partial_u[\sqrt{2(T + \zeta_2)\Gamma(u)}] \frac{1}{2} \frac{\sqrt{2(T + \zeta_2)\Gamma}}{\Gamma} \right\rangle = \frac{T + \zeta_2}{2}\langle \partial_u \ln\Gamma \rangle. \end{aligned} \quad (9)$$

This immediately implies that

$$\langle \Gamma(u)\dot{R}_1 \rangle + \langle \Gamma(u)\dot{R}_2 \rangle = 0. \quad (10)$$

This also implies that for $\langle v_1 \rangle = \langle v_2 \rangle \neq 0$, Γ must be a function of u (if it is a constant, it can be taken out of the average and (10) would then imply that the average velocities must be 0^{24,53}). We now write (5) and (6) in terms of the mobility $M = 1/\Gamma$:

$$\dot{R}_1 = -M(u)\partial_{R_1}F_R + \sqrt{2(T + \zeta_1)M}\xi_1 + \frac{T + \zeta_1}{2}\partial_{R_1}M \quad (11)$$

$$\dot{R}_2 = -M(u)\partial_{R_2}F_R + \sqrt{2(T + \zeta_2)M}\xi_2 + \frac{T + \zeta_2}{2}\partial_{R_2}M, \quad (12)$$

Since the average strain $\langle u \rangle$ should go to a constant value at the steady state, the steady-state centre-of-mass velocity of the bead-spring system must be

$$\langle v \rangle = \langle \dot{R}_1 \rangle = \langle \dot{R}_2 \rangle \quad (13)$$

where the angular brackets denote averages over the noise. That is,

$$\begin{aligned} -\langle M(u)\partial_{R_1}F_R \rangle + \left\langle \sqrt{2(T + \zeta_1)M}\xi_1 \right\rangle + \frac{T + \zeta_1}{2}\langle \partial_{R_1}M \rangle \\ = -\langle M(u)\partial_{R_2}F_R \rangle + \left\langle \sqrt{2(T + \zeta_2)M}\xi_2 \right\rangle + \frac{T + \zeta_2}{2}\langle \partial_{R_2}M \rangle. \end{aligned} \quad (14)$$

Again computing the noise averages using the Novikov theorem

$$\left\langle \sqrt{2(T + \zeta_1)M}\xi_1 \right\rangle = \frac{T + \zeta_1}{2}\langle \partial_{R_1}M \rangle \quad (15)$$

and

$$\left\langle \sqrt{2(T + \zeta_2)M}\xi_2 \right\rangle = \frac{T + \zeta_2}{2}\langle \partial_{R_2}M \rangle, \quad (16)$$

we get the steady-state velocity

$$\langle v \rangle = -\langle M\partial_{R_1}F_R \rangle + (T + \zeta_1)\langle \partial_{R_1}M \rangle = -\langle M\partial_{R_2}F_R \rangle + (T + \zeta_2)\langle \partial_{R_2}M \rangle = \frac{\zeta_2 - \zeta_1}{2}\langle \partial_u M \rangle \quad (17)$$

The condition $\langle \dot{u} \rangle = 0$ implies

$$-2\langle M(u)\partial_u F_R \rangle + 2\bar{T}\langle \partial_u M \rangle = 0 \quad (18)$$

where $2\bar{T} = 2T + \zeta_1 + \zeta_2$. The average is over the noise, i.e., over the distribution of u , $P(u)$ and hence,

$$\int du P(u)[-M(u)\partial_u F_R + \bar{T}\partial_u M] = 0. \quad (19)$$

This will be the case if $P\partial_u F_R = -\bar{T}\partial_u P$, in which case, the integrand in (19) becomes a total derivative. This implies

$$P = S e^{-F_R/\bar{T}} \quad (20)$$

where S is a normalisation constant such that $\int_{-\infty}^{\infty} du P(u) = 1$. This implies

$$\langle v \rangle = S \frac{\zeta_2 - \zeta_1}{2} \int_{-\infty}^{\infty} du [\partial_u M(u)] e^{-F_R/\bar{T}}. \quad (21)$$

Assuming F_R is harmonic, $M(u)$ has to be odd in u for the integral to be non-vanishing. In particular, if $M(u) = \alpha_0 + \alpha_1 u$, the $\partial_u M(u) = \alpha_1$ and using the normalisation of $P(u)$, we get

$$\langle v \rangle = \frac{\zeta_2 - \zeta_1}{2} \alpha_1. \quad (22)$$

This clearly shows that the steady state velocity of the dimer is proportional to the gradient of the active noise.

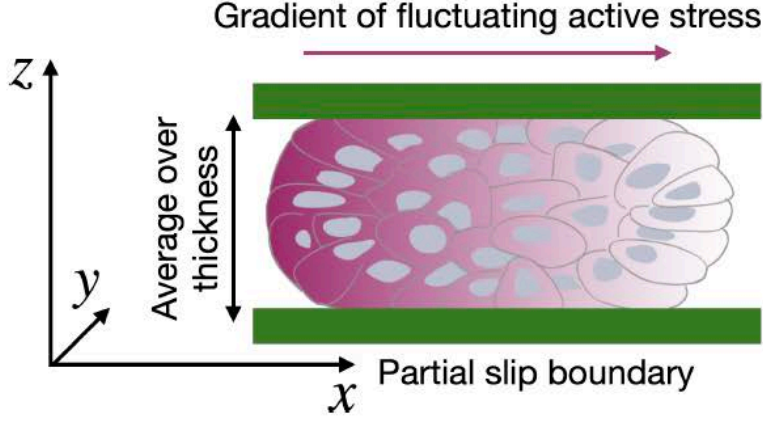


Fig. ST 2. Model of a confined cell cluster. A confined cell cluster modelled as an elastic solid with a gradient of a fluctuating active stress. We average the cluster over the z direction, assuming partial slip boundary condition to obtain an effectively two-dimensional description. We then assume that the gradient is only along \hat{x} and that the strain fields are also purely along \hat{x} to obtain an effective one-dimensional description.

B. Continuum version

In this section, we demonstrate that the mechanism described above holds for a more realistic description of the cell cluster as well. We model the cell cluster as a three-dimensional solid (see Fig. ST 2) and average over the thickness of the cell cluster to show how motility can arise without either cell exchange or persistent intracellular actin flows.

The hydrodynamic variables describing the solid are $\bar{\mathbf{R}}$, the displacement field and $\bar{\mathbf{v}}$, the velocity field. We assume that the concentration ρ is a constant ρ_0 . The hydrodynamic equations of motion are $d\bar{\mathbf{R}}/dt = \bar{\mathbf{v}}$ and

$$\rho_0 \frac{d\bar{\mathbf{v}}}{dt} = \bar{\nabla} \cdot [\boldsymbol{\eta}[\bar{\mathbf{U}}] : \{\bar{\nabla}\bar{\mathbf{v}} + (\bar{\nabla}\bar{\mathbf{v}})^T\}] - (\mathbf{I} - \bar{\nabla}\bar{\mathbf{R}}) \cdot \frac{\delta F_{\bar{\mathbf{R}}}}{\delta \bar{\mathbf{R}}} + \bar{\boldsymbol{\xi}} \quad (23)$$

where the $d/dt \equiv \partial_t + \bar{\mathbf{v}} \cdot \bar{\nabla}$ represents the convected derivative, $\bar{\mathbf{U}} = (1/2)[\bar{\nabla}\bar{\mathbf{R}} + (\bar{\nabla}\bar{\mathbf{R}})^T]$ is the strain tensor, $\boldsymbol{\eta}$ is the general, rank-four viscosity tensor, $F_{\bar{\mathbf{R}}}$ is the elastic free energy and $\bar{\boldsymbol{\xi}}$ is the noise with the correlator

$$\langle \bar{\xi}_i(\mathbf{r}, t) \bar{\xi}_j(\mathbf{r}', t') \rangle = -2\bar{\nabla}^2 [T + \zeta(\mathbf{x})] \eta_{ij}[\bar{\mathbf{U}}] \delta(\mathbf{r} - \mathbf{r}') \delta(t - t'). \quad (24)$$

Apart from the presence of a position-dependent active fluctuating stress parametrised by the position-dependent contractility $\zeta(\mathbf{x})$, these equations describe the dynamics of a *passive* solid, albeit one with a strain-dependent damping coefficient $\boldsymbol{\eta}[\bar{\mathbf{U}}]$. The form of the equations of motion⁶³ are dictated by the requirement that in the limit $\zeta(\mathbf{x}) \rightarrow \text{const.}$, the distribution for $\bar{\mathbf{R}}$ and $\bar{\mathbf{v}}$ reduces to the equilibrium one. Note that an inhomogeneous but time-independent active stress in this system has to be $\propto \zeta(\mathbf{x})\bar{\mathbf{U}}$, from symmetry, leading to a force density $\bar{\nabla} \cdot (\zeta(\mathbf{x})\bar{\mathbf{U}})$. However, this force density would simply modify the coefficients of the terms arising from the free energy, in effect leading to a solid with an inhomogeneous elastic coefficient. This alone would be insufficient for motility.

In the experiments, the solid is strongly confined at least in one direction, which we take to be along \hat{z} . Therefore, we average (23) along the \hat{z} direction taking strain-free boundary conditions for

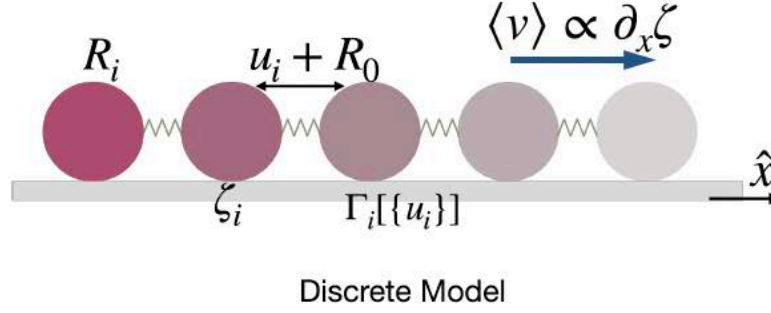


Fig. ST 3. Discretised model. The continuous elastic medium is discretised to yield a discrete model with bead positions R_i , acted on by active fluctuating forces ζ_i , which have a friction with the substrate Γ_i that depends on the local strain u_i .

the displacement field and partial-slip boundary condition for the velocity field i.e., $\bar{v}_\perp = \beta \partial_z \bar{v}_\perp$, $\bar{v}_z = 0$ at both boundaries, where β is a slip length. This averaging, to the lowest order in gradients, generically yields $d\mathbf{R}/dt = \mathbf{v}$ and

$$\rho_0 \frac{d\mathbf{v}}{dt} = -\mathbf{\Gamma}[\mathbf{U}] \cdot \mathbf{v} - (\mathbf{I} - \nabla \mathbf{R}) \cdot \frac{\delta F_R}{\delta \mathbf{R}} + \boldsymbol{\xi} \quad (25)$$

where $\mathbf{\Gamma}$ is an effective friction coefficient which depends on the slip length and becomes proportional to the thickness of the system H along the z direction for $\beta = 0$, ∇ is the in-plane gradient, \mathbf{v} and \mathbf{R} are the thickness-averaged planar velocity and the displacement fields $\mathbf{v} = (1/H) \int dz \mathbf{V}_\perp$ and $\mathbf{R} = (1/H) \int dz \bar{\mathbf{R}}_\perp$, \mathbf{U} is the thickness-averaged strain tensor $\mathbf{U} = (1/2)[\nabla \mathbf{R} + (\nabla \mathbf{R})^T]$, and $\boldsymbol{\xi}$ is the averaged noise. For thermodynamic consistency, the noise must have the form

$$\langle \xi_i(\mathbf{x}, t) \xi_j(\mathbf{x}', t') \rangle = 2[T + \zeta(\mathbf{x})] \Gamma_{ij}[\mathbf{U}] \delta(\mathbf{x} - \mathbf{x}') \delta(t - t') \quad (26)$$

with $\mathbf{x} \equiv (x, y)$.

The position-dependent active contractile cap is assumed to be symmetric in the $y-z$ plane i.e., in the thickness averaged model, it is assumed to be symmetric along the y axis. We also assume that any asymmetry in $\mathbf{\Gamma}$ is also coaxial with the contractile asymmetry i.e., it is only along \hat{x} . Therefore, the displacement field in the \hat{y} direction, R_y is uniform i.e., $\partial_x R_y = \partial_y R_y = 0$. Similarly, the displacement field along \hat{x} , R_x is uniform along \hat{y} , i.e. $\partial_y R_x = 0$. This allows us construct a simplified one-dimensional model retaining only the x -component of the velocity and the displacement field $R_x \equiv R$, $v_x \equiv v$ and $u \equiv U_{xx}$, which, upon ignoring the advective nonlinearity in both the displacement field and the velocity field equations and the elastic force nonlinearity in the velocity equation, read $\partial_t R = v$ and

$$\rho_0 \partial_t v = -\Gamma[u]v - \frac{\delta F_R}{\delta R} + \xi \quad (27)$$

or, in terms of the strain field, $\partial_t u = \partial_x v$ and

$$\rho_0 \partial_t v = -\Gamma[u]v + \partial_x \frac{\delta F_u}{\delta u} + \xi \quad (28)$$

with the noise correlator

$$\langle \xi(x, t) \xi(x', t') \rangle = 2[T + \zeta(x)] \Gamma[u] \delta(x - x') \delta(t - t'). \quad (29)$$

Since the system we consider is highly overdamped, we now eliminate the inertia which technically involves taking the zero-mass limit. However, due to the noise and the damping depending on u and x , this is somewhat involved and is most clearly performed in a discretised version of (27) or (28). We therefore now consider a discrete version of the continuum model with N particles (see Fig. ST 3). Without loss of generality, we take all particles to have the same mass m leading to the discretised equation of motion $\dot{R}_i = v_i$ and

$$m\dot{v}_i = -\Gamma_i[\{u_i\}]v_i - \partial_{R_i}F_R + \xi_i \quad (30)$$

where the overdot represents partial derivative and

$$\langle \xi_i(t)\xi_j(t') \rangle = 2\Gamma_i[\{u_i\}]\delta_{ij}(T + \zeta_i)\delta(t - t'), \quad (31)$$

and $u_i = R_{i+1} - R_i - R_0$ is the discretised version of the strain variable with R_0 being the microscopic, equilibrium separation between the i -th and $i + 1$ -th elements (equivalent to a lattice spacing). We now eliminate the inertial term in (30) by taking the standard zero-mass limit^{24,57,60} which yields a set of stochastic equations for R_i which in the Stratonovich interpretation reads

$$\Gamma_i[\{u_i\}]\dot{R}_i = -\partial_{R_i}F_R + \sqrt{2(T + \zeta_i)\Gamma_i[\{u_i\}]} \xi_i - \frac{(T + \zeta_i)}{2} \partial_{R_i} \ln \Gamma_i[\{u_i\}]. \quad (32)$$

Considering only two particles i.e., $i = 1, 2$, now leads to the dimer model described earlier. As a consistency check for this equation of motion, we demonstrate that the average external force on the system as a whole is 0, as in the dimer:

$$\sum_i \Gamma_i[\{u_i\}]\dot{R}_i = \sum_i \sqrt{2(T + \zeta_i)\Gamma_i[\{u_i\}]} \xi_i - \sum_i \frac{(T + \zeta_i)}{2} \partial_{R_i} \ln \Gamma_i[\{u_i\}]. \quad (33)$$

Averaging over the noise, using Novikov theorem,

$$\langle \sqrt{2(T + \zeta_i)\Gamma_i[\{u_i\}]} \xi_i \rangle = \left\langle \sqrt{2(T + \zeta_i)} \partial_{R_i} \sqrt{\Gamma_i[\{u_i\}]} \frac{\delta R_i}{\delta \xi_i} \right\rangle = \left\langle \frac{T + \zeta_i}{2} \partial_{R_i} \ln \Gamma_i[\{u_i\}] \right\rangle \quad (34)$$

we find that

$$\sum_i \langle \Gamma_i[\{u_i\}]\dot{R}_i \rangle = \sum_i \left\langle \frac{T + \zeta_i}{2} \partial_{R_i} \ln \Gamma_i[\{u_i\}] \right\rangle - \sum_i \left\langle \frac{(T + \zeta_i)}{2} \partial_{R_i} \ln \Gamma_i[\{u_i\}] \right\rangle = 0. \quad (35)$$

This implies that the total friction force on the solid is 0 on average and the total active force on the solid is also 0 on average. This also implies that for the solid to be motile on average, i.e., for $\langle \dot{R}_i \rangle \neq 0$, the friction coefficient *must* depend on the local strain u_i . Writing (32) in terms of the motility $M_i = \Gamma_i^{-1}$, we have

$$\dot{R}_i = -M_i[\{u_i\}]\partial_{R_i}F_R + \sqrt{2(T + \zeta_i)M_i[\{u_i\}]} \xi_i + \frac{(T + \zeta_i)}{2} \partial_{R_i}M_i[\{u_i\}], \quad (36)$$

or writing this as an equation in terms of the strain variable $R_{i+1} - R_i - R_0 = u_i$ which should have a steady state even when $\langle \dot{R}_i \rangle \neq 0$ and noting that for any variable A ,

$$\partial_{R_i}A = \partial_{u_{i-1}}A - \partial_{u_i}A, \quad (37)$$

$$\begin{aligned} \dot{u}_i = & M_{i+1}(\partial_{u_{i+1}} - \partial_{u_i})F_u - M_i(\partial_{u_i} - \partial_{u_{i-1}})F_u + \sqrt{2(T + \zeta_{i+1})M_{i+1}}\xi_{i+1} - \sqrt{2(T + \zeta_i)M_i}\xi_i \\ & - \frac{(T + \zeta_{i+1})}{2}(\partial_{u_{i+1}} - \partial_{u_i})M_{i+1} + \frac{(T + \zeta_i)}{2}(\partial_{u_i} - \partial_{u_{i-1}})M_i. \end{aligned} \quad (38)$$

The equation for the centre-of-mass velocity of the cluster $v = (1/N)\sum_i \dot{R}_i$ is

$$Nv = \sum_i M_i(\partial_{u_i} - \partial_{u_{i-1}})F_u + \sum_i \sqrt{2(T + \zeta_i)M_i}\xi_i - \sum_i \frac{(T + \zeta_i)}{2}(\partial_{u_i} - \partial_{u_{i-1}})M_i. \quad (39)$$

Taking the average over the noise again using the Novikov theorem, this simplifies to

$$N\langle v \rangle = \left\langle \sum_i M_i(\partial_{u_i} - \partial_{u_{i-1}})F_u \right\rangle - \left\langle \sum_i (T + \zeta_i)(\partial_{u_i} - \partial_{u_{i-1}})M_i \right\rangle \quad (40)$$

where the average has to be taken with respect to the steady state distribution of u_i , $P[\{u_i\}]$. We therefore write the Fokker-Planck equation for $P[\{u_i\}]$ implied by (38):

$$\begin{aligned} \partial_t P[\{u_i\}] = & \sum_i \partial_{u_i} [M_i \{ (T + \zeta_i)(\partial_{u_i} - \partial_{u_{i-1}})P + P(\partial_{u_i} - \partial_{u_{i-1}})F_u \} \\ & - M(u_{i+1}) \{ (T + \zeta_{i+1})(\partial_{u_{i+1}} - \partial_{u_i})P + P(\partial_{u_{i+1}} - \partial_{u_i})F_u \}]. \end{aligned} \quad (41)$$

From these discretised equations, we can write the continuum forms of (38), (40) and (41) recognising the operator $\partial_{u_{i+1}} - \partial_{u_i} \equiv \partial_x \delta / \delta u$ where the derivative applies to the field with respect to which the functional derivative is taken and not to the argument of the functional derivative. This yields

$$\dot{u}(x) = \partial_x \left[M[u] \partial_x \frac{\delta F_u}{\delta u} \right] + \partial_x \sqrt{2[T + \zeta(x)]M[u]} \xi(x, t) - \partial_x \left[\frac{T + \zeta(x)}{2} \partial_x \frac{\delta M[u]}{\delta u} \right], \quad (42)$$

where x is a coordinate that is, by definition, fixed to the solid,

$$\langle v \rangle = \frac{1}{L} \int dx \left\langle M[u] \partial_x \frac{\delta F_u}{\delta u} \right\rangle - \frac{1}{L} \int dx \left\langle \{T + \zeta(x)\} \partial_x \frac{\delta M[u]}{\delta u} \right\rangle, \quad (43)$$

where L is the length of the cluster, and

$$\partial_t P[u(x)] = - \int dx \frac{\delta}{\delta u} \partial_x \left[M[u] \left\{ (T + \zeta(x)) \partial_x \frac{\delta P}{\delta u} + \partial_x \frac{\delta F_u}{\delta u} P \right\} \right]. \quad (44)$$

It is also worth writing the continuum version of (32)

$$\Gamma[u(x)]v = \partial_x \frac{\delta F_u}{\delta u} + \sqrt{2[T + \zeta(x)]\Gamma[u(x)]}\xi(x, t) + \frac{T + \zeta(x)}{2} \partial_x \frac{\delta \ln \Gamma[u(x)]}{\delta u} \quad (45)$$

to explicitly demonstrate, as a consistency check, that the total, average friction force is 0. Using

$$\langle \sqrt{2[T + \zeta(x)]\Gamma[u(x)]}\xi(x, t) \rangle = - \left\langle \frac{T + \zeta(x)}{2} \partial_x \frac{\delta \ln \Gamma[u(x)]}{\delta u} \right\rangle \quad (46)$$

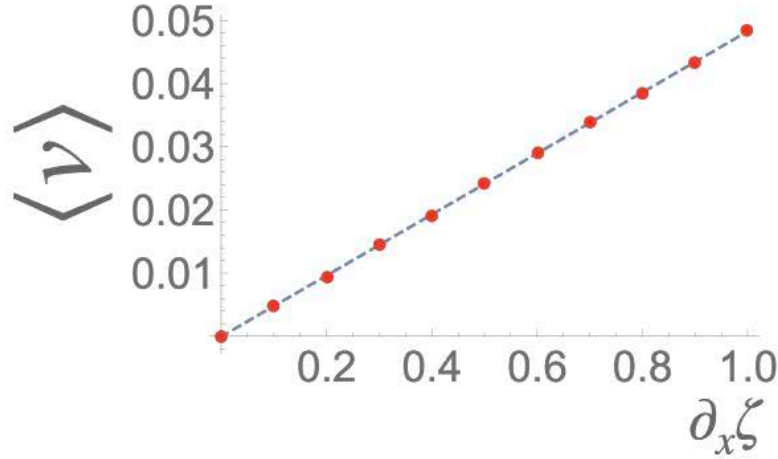


Fig. ST 4. Cluster velocity as a function of gradient of the strength of active fluctuations. The plot of velocity vs $\partial_x \zeta$ from a numerical simulation of the discrete elastic model with 5 beads. The mobility is taken to be $M = M_0 + M_1 u$ (with the constraint that it can't be negative) with $M_1/M_0 = 0.1$. The potential is taken to be harmonic with a spring constant k and a lattice spacing R_0 . The time is non-dimensionalised by $1/M_0 k$ and the length by R_0 . The time-step in the numerical simulation, performed using an Euler-Maruyama scheme, is 0.01, and the numerics were averaged over 5×10^7 time-steps. Each point is additionally an average over 10 independent runs performed by reinitialising the random number generator.

and noting that $\int dx \partial_x \delta W / \delta u = 0$, we see that

$$\int dx \langle \Gamma[u(x)] v \rangle = 0. \quad (47)$$

Equations (42), (43) and (44) or equivalently (38), (40) and (41) completely specifies our model of a solid that is driven by a fluctuating active noise.

That the position-dependence of $\zeta(x)$ is necessary for $\langle v \rangle \neq 0$ can be seen from the following argument. If $\zeta(x)$ doesn't depend on position, then it merely enhances the fluctuation strength T uniformly. Therefore, if a position-independent activity could lead to the motility of a cluster, then a solid at a uniform temperature T should also be motile. As expected, that is not the case; the steady state condition from (44) in this case is

$$T \partial_x \frac{\delta P}{\delta u} = - \left(\partial_x \frac{\delta F_u}{\delta u} \right) P. \quad (48)$$

which leads to the steady-state distribution

$$P[u] = S e^{-F_u/T} \quad (49)$$

where S is a normalisation. In this case, the average velocity is

$$L \langle v \rangle = S \int \mathcal{D}u \int dx e^{-F_u/T} \left[M[u] \partial_x \frac{\delta F_u}{\delta u} - T \partial_x \frac{\delta M[u]}{\delta u} \right] \quad (50)$$

Then, using

$$-T \frac{\delta e^{-F_u/T}}{\delta u} = e^{-F_u/T} \frac{\delta F_u}{\delta u} \quad (51)$$

and

$$\int dx e^{-F_u/T} T \partial_x \frac{\delta M[u]}{\delta u} = - \int dx T M[u] \partial_x \frac{\delta e^{-F_u/T}}{\delta u}, \quad (52)$$

one can see that the term in the square brackets in (50) is 0. This implies that $\langle v \rangle = 0$ in the absence of a position-dependent active noise as expected from physical considerations is consistent with the fact that the experiment cluster does not move in the absence of myosin gradient. Thus we have established that a strain-dependent damping coefficient and a position-dependent active noise are both necessary for the solid to be motile. We have not established that they are sufficient. To demonstrate the latter explicitly requires finding the steady state distribution for u which is, in general, impossible in this nonequilibrium system. Defining $W[u] = -\ln P[u]$ as the effective potential, we see that the potential condition

$$\partial_x \frac{\delta W}{\delta u} = \frac{1}{[T + \zeta(x)]} \left(\partial_x \frac{\delta F_u}{\delta u} \right) \quad (53)$$

cannot be satisfied in general.

Since we cannot obtain the velocity of the active solid analytically in the continuum model (though we do demonstrate necessary conditions for it), we resort to numerical simulations. We integrate (36) using an Euler-Maruyama scheme, using a harmonic free-energy and a mobility that depends linearly on the strain, for a small system with $i \in [1, 5]$. As shown in the main text and in Fig. ST 4, this yields a non-zero average velocity for the cluster $\langle v \rangle \propto \partial_x \zeta$. We have also checked numerically that using a harmonic free energy with a *gradient* of spring constants in (36) does not lead to motility in the absence of a gradient of fluctuations, i.e., when $\partial_x \zeta = 0$. This models a solid with an inhomogeneous but constant in time active contractile stress which, as expected, is not motile. Thus, within our simple model, a gradient of the fluctuating part of the active stress, which is implied by the observed gradient of myosin concentration, is the only requirement for the motility of the cluster (see Fig 3a). Note further, that if the strength of the fluctuations are enhanced uniformly everywhere in the cluster such that $\zeta \rightarrow \kappa \zeta$, then $\langle v \rangle \propto \partial_x \zeta \rightarrow \kappa \partial_x \zeta$. That is, the speed of the cluster is expected to increase proportionately with a uniform enhancement of fluctuation strength. This is consistent with the experimental observation that both the nuclear fluctuations and the fluctuations of the myosin flow speed are proportional to the cluster speed (see Fig. 5l and 6c) as both are related to the fluctuations of the contractile stress.

We present a *minimal* model to demonstrate that a solid can become motile purely due to active fluctuations whose strength varies along the solid. For this, we imposed conditions on our model that make it *more* equilibrium-like; for instance, we assumed that the correlator of the active noise is proportional to the mobility and that the active fluctuations are spatiotemporally uncorrelated. Liberating the model from either of these constraints makes it even more nonequilibrium (in the sense that there are more sources of entropy production) and makes it *more* likely to be motile. We have checked both analytically and numerically that liberating the strain-dependence of the active noise from the mobility, and even not having a strain-dependence doesn't change the necessary conditions for motion described earlier. However, when the noise correlator is liberated from the constraint of being proportional to mobility, a gradient of stress fluctuations is no longer required for motility. While a gradient of effective elastic moduli, for instance due to an inhomogeneous but time-independent contractile stress, is still not sufficient for motility in the absence of a gradient in the fluctuation-strength, a gradient of the effective *friction* coefficient is, as shown in^{24,53}. As in this model, the effective temperature, defined as the ratio of the noise correlation and friction then becomes inhomogeneous leading to motion. However, based on our observation of a myosin

concentration gradient, which directly implies an inhomogeneous contractile stress, which generically has both an average and a time-dependent, fluctuating part, but does not necessarily affect the viscosity or the friction, we believe that our model is the more parsimonious one.

-
- [53] K. Vijay Kumar, S. Ramaswamy, M. Rao, *Phys. Rev. E* 77, 020102 (2008)
 - [54] A. W. C. Lau, T. C. Lubensky, *Phys. Rev. E* 76, 011123 (2007)
 - [55] L. F. Cugliandolo, V. Lecomte, F. Van Wijland, *J. Phys. A* 52, 50LT01 (2019)
 - [56] V. Lecomte, F. Van Wijland, *J. Phys. A* 50, 345001 (2017)
 - [57] J. M. Sancho, M. S. Miguel, and D. Dürr, *J. Stat. Phys.* 28, 291 (1982)
 - [58] R. F. Fox, *Phys. Rev. A* 33, 467 (1986)
 - [59] E. A. Novikov, *Sov. Phys. — JETP* 20, 1290 (1965)
 - [60] D. Ryter, *Z. Phys. B* 41, 39 (1981)
 - [61] D. Ryter, U. Dekker, *J. Math. Phys.* 21, 2662 (1980)
 - [62] U. Dekker, D. Ryter, *J. Math. Phys.* 21, 2666 (1980)
 - [63] S. P. Das, R. Schilling, *Phys. Rev. E* 50, 1265 (1994)

ANNEX 3. CANET-JOURDAN ET AL., UNDER REVISION

NB: Here, PDX#1 = TSIPs.

Patient-derived organoids identify an apico-basolateral polarity switch associated with survival in colorectal cancer.

Authors: Charlotte Canet-Jourdan¹, Diane-Laure Pagès^{1#}, Clémence Nguyen-Vigouroux^{1#}, Jérôme Cartry^{1#}, Olivier Zajac^{2#}, Christophe Desterke³, Jean-Baptiste Lopez¹, Emie Gutierrez-Mateyron⁴, Nicolas Signolle⁵, Julien Adam⁵, Joel Raingeaud¹, Mélanie Polrot⁶, Patrick Gonin⁶, Jacques R.R. Mathieu¹, Sylvie Souquere⁷, Gerard Pierron⁷, Maximiliano Gelli⁸, Peggy Dartigues⁹, Michel Ducreux^{8,10}, Valeria Barresi¹¹ and Fanny Jaulin^{1*}.

Affiliations:

¹ INSERM U-1279, Gustave Roussy, Villejuif, F-94805, France.

² Institut Curie, PSL Research University, CNRS UMR 144, F-75005 Paris, France.

³ INSERM UMR-S-MD A9, Hôpital Paul Brousse, Villejuif, F-94805, France

⁴ INSERM U-1030, Gustave Roussy, Villejuif, F-94805, France.

⁵ INSERM Unit U981, Experimental Pathology, Gustave Roussy, 94805 Villejuif, France

⁶ Plateforme d'Evaluation Préclinique, AMMICA UMS 3655/ US 23, Gustave Roussy, Villejuif, F-94805, France.

⁷ UMR-9196, Gustave Roussy, Villejuif, F-94805, France.

⁸ Department of Medical Oncology, Gustave Roussy, Villejuif, F-94805.

⁹ Pathology Department, Gustave Roussy, Villejuif, F-94805, France.

¹⁰ Paris-Saclay University, Saint-Aubin, F-91190, France.

¹¹ Department of Diagnostics and Public Health, University of Verona, Verona 37129, Italia.

Equal contribution

*Correspondence to: Fanny Jaulin: fanny.jaulin@gustaveroussy.fr

The authors declare no competing financial interests.

Abstract

The metastatic progression of cancer remains a major issue in patient treatment. Yet, the molecular and cellular mechanisms underlying this process remains unclear. Here, we use primary explants and organoids from patients harboring mucinous colorectal carcinoma (MUC CRC), a poor prognosis histological form of digestive cancers, to study the architecture, invasive behavior and chemoresistance of tumor cell intermediates. We report that these tumors maintain a robust apico-basolateral polarity as they spread in the peritumoral stroma or organotypic collagen-I gels. We identified two distinct topologies: MUC CRCs either display a conventional “apical-in” polarity or, more frequently, harbor an inverted “apical-out” topology. Transcriptomic analyses combined with interference experiments on organoids showed that TGF β and focal adhesion signaling pathways are the main drivers of polarity orientation. Finally, this apical-out topology is associated with increased resistance to chemotherapeutic treatments in organoids and decreased patient survival in the clinic. Thus, patient-derived organoids have the potential to bridge histological, cellular and molecular analyses to decrypt onco-morphogenic programs and stratify cancer patients.

Introduction

With one million new cases worldwide every year, colorectal carcinoma (CRC) is the second leading cause of cancer-related death (W.H.O., 2020). Metastases, seeded by invasive cells, are responsible for almost all deaths from CRC. Despite the heterogeneity of CRCs, invasion and dissemination have principally been studied in the context of the epithelial-to-mesenchymal transition (EMT). This model proposes that carcinoma progression and invasion are associated with the partial or complete loss of epithelial architecture as the EMT transcriptional program is activated to endow cells with migratory and proteolytic activities. Numerous correlative evidence between CRC progression and EMT activation have been found (Brabletz, 2005; Wellner et al., 2009). Yet, it is still unclear whether this transcriptional program is causative to invasion and metastases formation or enabling other cell properties such as stemness or resistance to chemotherapies (Nieto et al., 2016). 3D reconstruction of CRC histological specimens demonstrated the absence of individual single cells at the tumor margins and point to tumor “buds” or “clusters” as the tumor intermediates conquering the invasive front (Barresi et al., 2015; Spaderna et al., 2006; Tsai et al., 2019). Across cancer types, functional studies have proven the predominant participation of collective cancer cell behaviors in the metastatic seeding of secondary lesions (Cheung et al., 2013; Commander et al., 2020; Friedl and Gilmour, 2009; Friedl et al., 2012; Ilina and Friedl, 2009; Ilina et al., 2020). Tumor cell clusters harbor increased migratory fitness and survival capabilities, allowing them to navigate in the peritumoral stroma but also circulate into the lymphatic and hematogenous systems to reach secondary organs (Aceto et al., 2014; Cheung et al., 2016). Yet, the mechanisms that fuel the metastatic spread of digestive cancers are under-investigated and understanding the oncogenic pathways and cellular components underlying CRC dissemination remains a major unmet medical need.

The organization of the invading tumor cell clusters varies a lot with cancer types. Histological specimens of cancer patients revealed that tumors mostly retain architectural features of the tissue they are originating from at any stage of their metastatic progression. This assessment allows pathologists to identify the type of cancer, independently of the primary or secondary organ location, and points to tissue architecture as a dominant trait of cancers. Yet, scientific investigations based on the genetic manipulations of animal models have suggested that epithelial apico-basolateral polarity was a tumor-suppressor feature lost during carcinoma formation and progression (Bilder, 2004; Bilder et al., 2000). This concept has recently been challenged by the *ex vivo* culture of patient-derived cancer specimens. The analysis of live primary tumor explants from large cohorts of CRC patients monitored *ex vivo* by

microscopy provided unexpected findings on cell cluster organization during invasion. These studies revealed a strong collective behavior, an intense epithelial addiction and two distinct topologies and morphologies in disseminating CRCs depending on their genomic profile (Okuyama et al., 2016). Chromosomal instable cancers, associated with the conventional Lieberkuhnian histological types of CRC, invade while maintaining the apico-basolateral polarity with an inward apical pole (“apical-in”) delineating large luminal cavities in the migrating cell cohort (Libanje et al., 2019). In contrast, CRC evolving along the chromosomal stable and hypermethylated pathways spread as spherical clusters of hundred cells that display an inverted “apical-out” topology with the apical pole surrounding the periphery, in contact with patient fluids and tissues. These tumor intermediates, named “Tumor Spheres with Inverted Polarity” (TSIPs), form in the primary tumor and retain their inverted topology as they invade tissues to initiate metastases in the peritoneum (Zajac et al., 2018). The hypermethylated CRCs arise from serrated precursors lesions and give rise to several histological forms of CRC that are associated with poor patient prognosis. These include mucinous CRC (MUC CRC), the second most frequent type of CRC, associated with an increased secretion of mucins (Jass, 2007).

Here, we combined histological, cellular and molecular approaches from live primary cancer explants and patient-derived organoids to investigate the organization and polarity of MUC CRCs. This study revealed that organoids are relevant tools to study tumor invasive behaviors and sensitivity to therapies. This uncovered two subtypes of MUC CRCs, based on a switch in their apico-basolateral polarity orientation, that are associated with distinct patient outcome.

Results

Primary tumor organoids revealed an apico-basolateral polarity switch in the metastatic dissemination of mucinous CRCs to the peritoneum.

We collected TSIPs from patients with metastatic colorectal carcinoma, and investigated their phenotypes either in suspension or in contact with extracellular matrix. TSIPs were retrieved from the peritoneal effusions at the time of cytoreductive surgery. They were immediately embedded in collagen-I gels, a surrogate of the peritumoral stroma (Wolf and Friedl, 2011). As reported previously, 66% of the TSIPs retained the same inverted apico-basolateral polarity they displayed in suspension (Zajac et al., 2018). The remaining 34% of TSIPs lost their peripheral apical staining in collagen-I. Instead, basolateral proteins, such as EpCam and E-cadherin, localized at the extracellular matrix

(ECM) abutting membrane (Fig. 1A, 1B and 1C). Concomitantly, a large central cavity formed within the cell cluster (stars, Fig. 1A and 1C). The enrichment of the actin staining at the membrane outlining the cavity suggested that an apical pole had formed there, which was confirmed using the apical marker ezrin (Fig. 1C). Together, the staining revealed that, while all TSIPs have an inverted apical-out topology in suspension in patient peritoneal effusions, a subset of them reverted their polarity to a conventional apical-in polarity when embedded in collagen-I. To assess whether this could also happen during tissue invasion, we monitored TSIPs invading into peritoneum explants (Zajac et al., 2018). In this assay, we detected TSIPs forming a central lumen outlined with a robust actin staining, reminiscent of the observation made in collagen-I gels (Fig. 1D). To exclude any experimental artefact, we explored the histology of Formalin Fixed Paraffin Embedded (FFPE) specimens from our patient cohort. Hematoxylin Eosin Saffron (HES) staining identified two distinct histological architectures, which were very homogenous in some patients and consistent with the TSIP phenotype *ex vivo* in collagen-I (Fig. 1E and 1F). As an example, Patient#6, who had all TSIPs retaining their apical-out topology in collagen-I, presented solid cell masses with an outward ezrin staining, revealing the inverted topology in the metastatic tissue (Fig. 1E and 1F top panel). In contrast, Patient#1, who had 79% of TSIPs reverting to an apical-in phenotype in collagen-I, had metastases with a glandular organization, where the apical pole of cancer cell faces large internal luminal cavities (Fig. 1E and 1F bottom panel). Together, these results show that the unique inverted topology of patients' TSIPs in suspension (peritoneal effusions) is maintained in ECM-rich tissues in most cases (apical-out phenotype) (Fig. 1G). Yet, for a third of the patients, the TSIPs switch to a normal polarity orientation with an inward apical pole surrounding a central lumen (apical-in phenotype).

Apico-basolateral polarity orientation is a cell-autonomous features of mucinous CRCs

The observations made from patient explants suggested differential polarity orientation in the course of MUC CRC dissemination. Moreover, since tumor architecture correlated with TSIP topology *ex vivo*, both in peritoneum and collagen-I invasion assays, we reasoned that the polarity orientation was a cell-autonomous feature. To validate this hypothesis, we selected three patient-derived xenograft (PDX) mice models from an independent collection of CRCs (Julien et al., 2012). We selected histotype (MUC CRC) and analyzed the architecture of the human tumor in patients and into the mice subcutaneous stroma. The histological assessment based on HES staining revealed two distinct architectures, PDX#1 and PDX#2 displayed tumor cell masses surrounded by mucin while PDX#3 organized as sheets forming glandular structures delineating mucin areas (Fig. 2A, top panels and supplementary Fig. 1A). Of note, the phenotypes were more homogenous in the mice xenografts than in patients. We then assessed the apico-basolateral polarization of these tumors. PDX#3 harbored a

conventional epithelial organization, with the apical membranes of cancer cells facing inward and delimiting a central lumen (apical-in phenotype). In contrast, the tumor cell clusters in PDX#1 and PDX#2 displayed an outward ezrin staining facing the mucin aureole, corresponding to the apical-out phenotype (Fig. 2A, bottom panels). Organoids have recently emerged as relevant experimental models to study oncogenesis (Dekkers et al., 2021). We generated tumors organoids from the three PDXs and embedded them in collagen-I gels as a surrogate of the peritumoral stroma (Ricard-Blum, 2011) to assess their organization and polarity. Strikingly, all organoids remained highly cohesive, and we never observed dissociation or single cell detachment followed by invasion. We then assessed their polarity, either apical-in, apical-out, or as partial phenotypes, following their morphology (lumen, protrusions) and ezrin localization (Supplementary Fig. 2). Like patients TSIPs, while all organoids had an inverted apico-basolateral polarity in suspension (Supplementary Fig. 1B and 1C), they adopted different topologies in collagen-I depending on the tumor they were originating from. Respectively 84% and 98% of organoids produced from PDX#1 and PDX#2 displayed an apical-out topology in collagen-I (Fig. 2B and 2C). To the contrary, organoids from PDX#3 harbored an apical-in phenotype and formed lumens in collagen-I (Fig. 2B and 2C). Electron microscopy confirmed the two polarity phenotypes observed by immunofluorescence, showing microvilli at internal (apical-in) or external (apical-out) membranes (Fig. 2D). Thus, the PDXs and the organoids recapitulated the observations made from the patients and attested that MUC CRCs represent a heterogenous group of cancers with different polarity orientation. The distinct topologies appeared in vivo in the murine stroma and in vitro in simple collagen-I gels, showing this feature is mostly cell autonomous.

Apical-out and apical-in organoids harbor different expression profiles

We used the organoids to compare the expression profiles of the two topologies and determine the mechanism of polarity orientation in MUC CRCs. PDX#1, PDX#2 and PDX#3 organoids were maintained in suspension or embedded into collagen-I for 3 days, then, their RNA was extracted and analyzed (Fig. 3A, triplicates). Whole transcriptome experiments were performed in each experimental condition for each PDX. Human Clarius S chip were done for each specimen, and, after RMA (Robust Multichip Average) normalization, a supervised analysis was investigated by Analysis of Variance. The response of the PDX organoids to collagen-I embedding was measured by Significance Analysis for Microarray algorithm in transcriptome. These analyses revealed that collagen-I regulated more genes in organoids from PDX#3 (156 specific genes, supplementary table 1) as compared to organoids from PDX#1 and PDX#2 (34 specific genes, supplementary table 2), among which only 2 are in common (Fig. 3B). In line with these results, the global gene signature of collagen-I response allowed to drastically discriminate collagen-I embedded PDX#3 organoids from all other transcriptomic

profiles (Euclidean distances, Fig. 3C). This is confirmed to be significant by unsupervised principal component analysis (p-value = 2.84e-11, Fig. 3D and supplementary Fig 3). In order to identify the pathways differentially activated by collagen-I in organoids made from PDX#3 *versus* PDX#1 and PDX#2, we performed Gene Set Enrichment Analysis (GSEA). This revealed a repression of cell cycle progression and an activation of the Sonic Hedgehog (SHH), Transforming Growth Factor beta (TGF β), Hypoxia and Focal adhesion pathways with respective NES of +2.07, +2.33, +2.67 and +1.47 (Fig. 3E and 3F). Overall, these analyses identified the signaling pathways activated by collagen-I in apical-in organoids (PDX#3) and revealed that they are not induced in apical-out CRC organoids (PDX#1 and #2) after embedding in ECM.

Downregulated TGF β signaling prevents normal apico-basolateral polarity orientation in MUC CRC

To assess which one(s) of these signaling event(s) control(s) polarity orientation, we performed interference experiments using the organoids in collagen-I gels. No major component of the SHH pathway were differentially regulated between apical-in and apical-out tumors, neither this pathway was reported in the literature to regulate apico-basolateral polarity, thus, we did not investigate this pathway as a polarity regulator. To mimic hypoxia *ex vivo*, we incubated organoids from PDX#1 and PDX#2 with desferrioxamine (DFO), an inhibitor of HIF1 α degradation. This treatment did not impact the polarity orientation relative to controls (Supplementary Fig. 4A-C). Therefore, the hypoxic status of the cells is correlated to polarity but is not causative to its orientation.

We next investigated the participation of TGF β signaling to polarity orientation. We first stimulated apical-out organoids made from PDX#1 and PDX#2 with TGF β . We did not observe the induction of EMT and the dissociation of migratory single cells and therefore could assess clusters' polarity. We observed a clear response of organoids from PDX#1 to TGF β stimulation associated with an important decrease from 82% to 26% of inverted apical-out polarity, (Fig. 4A and 4B). In contrast, the organoids from PDX#2 treated with TGF β were indistinguishable from the controls, keeping their apical-out topology (Fig. 4A and 4B). Exome sequencing of TGF β receptors and effectors identified that all harbor the TGFBR2 K153fs frame-shift mutation reported to decrease TGF β signaling (de Miranda et al., 2015) while only PDX#2 displays a Smad4 W268* mutation, truncating half of the protein (Fig. 4C). This likely explains why this tumor is insensitive to TGF β stimulation. Conversely, we inhibited TGF β signaling in apical-in organoids generated from PDX#3 using two independent inhibitors of TGF β receptor I (TGFBR1), SB431542 and A83-01. The drugs were either added to the collagen-I gels (treatment) or preceding their embedding in the matrix (pre-treatment). Both inhibitors altered

polarity orientation in PDX#3 embedded into collagen-I (Fig. 4D and data not shown). While the proportion of apical-in organoids dropped, the apical-out phenotype increased significantly, from 0% to up to 26% and 88% after treatment showed that TGF β signaling controls the apico-basolateral polarity orientation of MUC CRC organoids (Fig. 4E).

The balance between integrin-mediated adhesion and contractility controls polarity orientation in MUC CRCs

The GSEA analysis also revealed that the focal adhesion pathway is activated in PDX#3 embedded in collagen-I, but not in the PDX#1 and PDX#2 which retain their apical-out topology in the matrix. Interestingly, integrin β 1 (ITGB1), the main component of focal adhesions, controls the orientation of apico-basolateral polarity in normal renal cell lines through the downregulation of the serine/threonine kinase ROCK (Bryant et al., 2010; Bryant et al., 2014; Ferrari et al., 2008; Liu et al., 2007). Thus, we tested whether ITGB1 and ROCK could regulate polarity orientation in MUC CRC. Organoids from PDX#1 and PDX#2 were incubated with Y27632, a pharmacological inhibitor of ROCK. This treatment reduced the number of organoids with inverted polarity by 28 and 6-fold, respectively (Fig. 5A and 5B). Strikingly, this was associated with the appearance of internal apical membranes surrounding one or several luminal cavities, reminiscent of the apical-in topology (Fig. 5A and 5B). Conversely, inhibiting ITGB1 with the function blocking antibody AIIB2 and shRNA (shITGB1) strongly repressed the apical-in phenotype in organoids from PDX#3, with the vast majority harboring an apical-out topology in collagen-I (87% and 52% respectively Fig. 5C and 5D). Using calyculin-A, an inhibitor of the phosphatase antagonizing ROCK-mediated myosin-II phosphorylation, we observed a similar phenotype, with 90% of the organoids preserving their inverted apico-basolateral polarity (Fig. 5C and 5D). Thus, the topology of MUC CRCs is determined by the same core machinery as in non-transformed cells.

We then investigated whether the balance between adhesion and contractility could relate to defective TGF β signaling. We hypothesized that decreased activation of non-canonical TGF β signaling could increase the levels of RhoA, ROCK and therefore contractility. However, western blot experiments showed that the amount of phosphorylated myosin-II, a read-out for ROCK activity (Yu et al., 2005), is similar in the 3 PDXs (Supplementary Fig. 5A). Thus, we reasoned that TGF β inactivation could rather impair integrin function in apical-out organoids. We first observed that ITGB1 activity controls the apical-in orientation of organoids from PDX#1 and PDX#2 treated with Y27632 (Supplementary Fig. 5B and 5C), indicating that β 1 integrins are functional and do not harbor loss-of-function mutation

in apical-out organoids. Yet, TGF β is a known regulator of ITGB1 transcription and the microarray analysis revealed that PDX#1 and PDX#2 harbored lower levels of ITGB1 mRNA (Fig. 5E). In line with this, we found that the levels of ITGB1 protein detected by immunofluorescence in PDX#1 and PDX#2 are lower than in PDX#3 and increased during polarity reversion in collagen-I gel (Supplementary Fig. 5D and 5E). Finally, preventing ITGB1 activation using function blocking antibodies circumvented the apico-basolateral polarity reversion induced by TGF β in PDX#1 (Fig. 5F and 5G). Together, these results show that the unbalanced levels of ITGB1-mediated adhesion and actomyosin contractility are involved in the inverted apical-out topology detected in MUC CRCs downstream of TGF β -signaling.

Apico-basolateral polarity orientation influences response to chemotherapies

In order to determine the physio-pathological relevance of MUC CRC apico-basolateral polarity orientation, we tested whether organoid topology could influence response to chemotherapeutic agents. We compared the survival of PDX#1 and PDX#3 organoids, in their native or inverted topologies, after treatment with cytotoxic agents widely used in CRC: Oxaliplatin, 5-Fluorouracil (5-FU) and Irinotecan (SN-38). We used the IC70 concentrations based on the dose-response curve obtained from a collection of 25 organoids derived from CRC patients (Supplementary Fig. 6A). PDX#1 in its native topology (apical-out) and treated with Y27632 (apical-in, Supplementary Fig. 6B) were incubated with the drugs for 2-5 days and the number of viable cells was assessed using ATP-bioluminescence (Fig. 6A). The viability of the organoids in response to the three drug treatments was increased in the apical-out topology, as shown by the apical-out/apical-in viability ratio which is over 1 (Fig. 6A and supplementary Fig. 6C). Using a similar strategy, we added cytotoxic agents to PDX#3 in their native (apical-in) and inverted topologies (apical-out induced by AIIB2 function blocking antibody, Supplementary Fig. 6B) topologies. Likewise, cell survival to the three drug treatments was enhanced in the apical-out as to compared with the apical-in topology (Fig. 6B and Supplementary Fig. 6D). Together these experiments on both PDX models ruled-out off-target effect from AIIB2 or Y27632. They pointed to the inverted apico-basolateral polarity as a protective topology against chemotherapeutics-induced cell death. This could be explained by the lower proliferation rate detected in the apical-out polarity (Fig 6C and 6D). Furthermore, and independently of the genetic make-up of the tumor, we also observed lower mitotic indexes and proliferation rates in the live primary specimens harboring an apical-out topology as to compare with apical-in (Fig. 6E and 6F presenting patient specimens included in Fig. 1).

Apico-basolateral polarity orientation correlates with patients' survival

Finally, to determine whether polarity orientation could impact the clinical outcome of patient with MUC CRCs, we performed a histological analysis using an independent published annotated cohort of MUC CRC patients⁷. The apico-basolateral polarity orientation of CRC clusters was automatically assessed using an algorithm created in Definiens Developer XD (Definiens, Munich, Germany) software and applied to 36 patient specimens. Tumor specimens were stained for CRC cell types (identified by Cytokeratin 20 staining), stroma (Nuclear Red, Pink) and the mucus (Alcian Blue; Fig. 7A, left panel). The polarity orientation was determined based on CRC clusters shape and their relative localization to the stroma and the mucus. CRC clusters were classified into apical-in (red) or apical-out categories (yellow/green, Fig. 7A, right panels). The results obtained through this morphometry analysis showed that a third of patients (9/36) harbored mostly an apical-out organization and two thirds (27/36) displayed a glandular apical-in architecture (Fig 7B). We also calculated a polarity score, based on the ratio between apical-in and apical-out components. For the prediction of death from mucinous CRC, we used Receiver under Operating Characteristics (ROC) analyses to calculate the most accurate cut-off values of the number of apical-out clusters and the polarity score. Log rank test with Kaplan-Meier curves showed that patients harboring a CRC with a high number of apical-out clusters (> 92) had a significantly shorter cancer-specific survival (CSS) than patients having a CRC with a low count of apical-out clusters (≤ 92) ($P = 0.04$; H.R.: 2.5; C.I.: 1-6.3) (Fig. 7C). Similarly, the patients having a CRC with a low polarity score (ratio apical-in/apical-out < 2.75) had significantly shorter CSS than those harboring a CRC with a high score (≥ 2.75) ($P = 0.02$; H.R.: 3.1; C.I.: 1.1-8.4) (Fig. 7D). Together, these data point to two subgroups of MUC CRC patients based on the architecture of their tumor and the topology of the apico-basolateral polarity. The clinical outcome of the patients is correlated to polarity orientation, the apical-out MUC CRCs being associated with shorter cancer-specific survival.

Discussion

Thus, the live and fixed primary cancer specimens retrieved from MUC CRC patients prove that apico-basolateral polarity is maintained in the course of their dissemination. Yet, apical-in and apical-out topologies exist, resulting from the cell-autonomous properties of the cancer and from the micro-environment, tissue or fluid, that the clusters encounter in their journey to secondary sites. This study, together with several recent articles, clearly challenge the assumption that epithelial differentiation and polarity act as tumor suppressors (Negri et al., 2005; Saito et al., 2018). Here, we identified that MUC CRCs constitute a heterogenous histological group of cancers based on the apico-basolateral polarity

orientation of the tumor. Most MUC CRCs originate from serrated precursor lesions, and as such they use a *bona fide* TSIP-based metastatic cascade where the apical-out phenotype is sustained at all stages, in tissues and fluids (Jass, 2007). In this study, we identified that about a third of the patients with MUC CRC produced TSIPs with inverted topology, only transiently in peritoneal effusions, while most of the tumor is organized with a conventional apical-in glandular architecture in tissues. In this subset of patients, depending on the activation of integrins by ECM, the apico-basolateral polarity of the cancer clusters is switched “in” and “out” in the course of their dissemination.

The two distinct subgroups of MUC CRCs, based on their ability to switch polarity or to maintain a *bona fide* apical-out topology from the primary tumor to the metastatic site (TSIPs), could result from divergent onco-morphogenetic pathways downstream of the serrated precursor lesion. Alternatively, this heterogeneity among MUC CRCs may result from the phenotypic convergence of distinct genetic groups of CRCs. Indeed, we previously identified an apical-in phenotype in conventional Lieberkuhnian CRCs (Libanje et al., 2019). Interestingly, pathologists have reported that radio-chemo therapies induce a mucin-secretory response in some of these cancers evolving toward MUC CRC in the course of the disease (Heino and Massagué, 1989; Thorpe et al., 2013).

Using transcriptomic analyses and interference experiments in organoids, we investigated the pathways regulating polarity orientation in MUC CRCs and identified integrin signaling as a crucial player in apico-basolateral polarity orientation. By interfering with ITGB1 signaling, we could switch the normal polarity of organoids from PDX#3 to an apical-out phenotype, demonstrating they are causative in this mechanism. This is in line with previous studies demonstrating that polarity orientation is dependent on integrins activation by their engagement with components of the ECM such as laminin-1, collagen-IV and fibronectin (Gudjonsson et al., 2002; Okuyama et al., 2016). This also likely explains why in apical-in MUC CRCs, the cancer cell clusters display an apical-out topology in suspension in peritoneal effusions where their integrins cannot be engaged and activated by ECM. Interestingly, this work revealed that a conserved intracellular core machinery controls the positioning of the apical pole away from the ECM in normal and transformed epithelial cells. This involves the balance between the adhesion and contractility, regulated by the GTPases Rac1 and RhoA through their effectors such as ROCK (Bryant et al., 2010; Bryant et al., 2014; Datta et al., 2017; Margaron et al., 2019).

We also showed that ITGB1 acts downstream of the TGF β signaling: function blocking antibodies against ITGB1 prevented the apical-in phenotype induced by TGF β stimulation and low TGF β signaling is associated with decreased ITGB1 mRNA levels. The canonical TGF β signaling is known to regulate many cellular functions, including integrin-mediated adhesion, through the control

of their dimerization, exposure at the cell surface or expression (Dongre and Weinberg, 2019; Gandalovičová et al., 2016; Sheppard et al., 1992; Zambruno et al., 1995). These results are also in line with our previous findings showing that TGF β is an important regulator of polarity orientation (Zajac et al., 2018). Our experiments demonstrate that a downregulation in TGF β prevents the organoids from correctly polarizing when embedded in matrix. In these MUC CRCs, this is dominated by the canonical effectors, as a truncation of Smad4 prevents polarity reversion in response to TGF β stimulation. While this pathway is mostly described to control apico-basolateral polarity establishment and maintenance (de Miranda et al., 2015; Gracia et al., 2019; Huang et al., 2020; Jung et al., 2019), we show that TGF β also controls polarity orientation. This confirms our previous findings (Zajac et al., 2018) and observations made from 3D culture and micropatterned breast and kidney cell lines (Burute and Thery, 2012). Based on these studies, we envision MUC CRC carcinogenesis as, at least, a two-step process. First, early downregulation of TGF β signaling promotes the budding of TSIPs from the serrated precursor lesion. While this alteration is necessary for the polarity inversion, it is not sufficient. There is/are second alteration(s) that trigger(s) the robust apical-out phenotype observed in tissues for about 2/3 of the patients. These alterations can either be within the TGF β pathway itself (like Smad 4 loss of function mutation) or pathways that crosstalk with TGF β , integrins and/or contractility.

Interestingly, while TGF β pathway is one of the main inducers of EMT, it is downregulated in MUC CRCs and other TSIP-producing tumors through a mutation in TGFBR2 that reduces the activation of its cytosolic effectors (Cheung et al., 2016; Zajac et al., 2018). This could likely explain why we never observe the dissociation of individual mesenchymal cell from patients explants or the 3 MUC CRC PDXs/organoids used in this study. This contrasts with single cell dissociation and mesenchymal features associated with the invasion of a subset of organoids made from pancreatic cancer (Ashley et al., 2019). Yet, TSIP-based dissemination is associated with poor patient prognosis. This is in line with several studies on other EMT-independent mode of collective invasion, demonstrating that the interaction between cohesive tumor cells provides important signal for cancer cells survival in the peritumoral stroma or the hematogenous circulation (Aceto et al., 2014; Al Habyan et al., 2018; Padmanaban et al., 2019).

To test whether polarity orientation could be associated with different patient outcomes, we developed an automated morphometric tool and applied it to MUC CRCs histological specimens to quantify a polarity score. Applied to the analysis of tumor specimens retrieved from a published cohort of patients with MUC CRC (Barresi et al., 2015), this revealed that the apical-out topology is associated with

shorter patient survival. Functional investigation in patient-derived organoids showed that polarity orientation influences response to chemotherapeutic treatment, the apical-out topology being associated with increased drug resistance (Ashley et al., 2019). This could result from the low proliferative activity we detect in this subset of tumors, but alternative mechanisms may also be at play. Indeed, the apical and basolateral membranes are structurally and functionally very different (Gassama-Diagne et al., 2006; Kroepfl and Gardinier, 2001). Thus, the inverted topology, positioning the apical pole at the interface between cancer cells and their surrounding micro-environment, could also interfere with additional cellular functions and processes such as invasion, immune surveillance or drugs in-take/out-take (Kroepfl and Gardinier, 2001; Wosen et al., 2018). Intriguingly, inverted apico-basolateral polarity of tumor cell clusters has been described in micropapillary histotypes of CRC, breast, bladder, lung carcinomas and is also associated with poor patient prognosis (Ahmed et al., 2012; Cserni, 2014; Kryvenko et al., 2013), showing this is a general feature of carcinomas. Thus, the polarity score could be used to stratify patients harboring a variety of cancers.

In this study, we developed innovative approaches and used organoids to bridge knowledge gained from histological and molecular profiling in order to decipher the mechanism of MUC CRCs organization and polarity. In the past decade, organoids have proven to be crucial tools to decrypt the biology of cancers and they are currently evaluated for their utility in the treatment of patients (Vlachogiannis et al., 2018; Yao et al., 2020). These cancer avatars have mainly been used to unlock the key mutational events associated with cell transformation or cancer progression and study the response and resistance to therapeutic agents (Drost and Clevers, 2018; Sato and Clevers, 2013; Tuveson and Clevers, 2019; Zanoni et al., 2020). Here, rather than cultivating organoids into Matrigel (components of the basal lamina) as usually done, we embedded them into collagen-I tridimensional hydrogels, an established surrogate of the peritumoral stroma (Doyle et al., 2015; Wolf and Friedl, 2011). This revealed that organoids recapitulate the main features of tumor architecture observed from patient histological specimens or primary explants, including the apico-basolateral polarity and its orientation. This is in agreement with parallel studies from our lab on NOS CRC and TSIPs (Libanje et al., 2019; Roy et al., 2017) as well as recent published work on pancreatic, breast cancer and glioblastomas (Goranci-Buzhala et al., 2020; Han et al., 2020; Koga et al., 2020; Padmanaban et al., 2020). Thus, organoids stand as tridimensional living tools that complement the inert histological 2D specimens, providing unique and relevant morpho-dynamic information on tumor cell behaviors.

Acknowledgements

We thank all the patients who participated in this study and the medical staff for their assistance with the acquisition of primary human specimens. We thank the members of the Jaulin Lab and the Digestive Cancer Unit for discussion, technical services provided by PFIC and PETRA core facilities (especially O. Bawa, and V. Marty). We thank DSHB (University of Iowa) for antibodies. This work was supported by the INCA-PLBIO program (2018-1-PL BIO-04-1, 2020-1-PL BIO-04), Agence Nationale de la Recherche (ANR-20-CE13-0031-01), INSERM programme 3R (20CR046-00), La ligue contre le cancer (comité 94), subvention foundation ARC (PAJ20181208275), the Gustave Roussy Foundation (“Mars Bleu” and parrainage), doctoral scholarship from Paris-Saclay University and the French Ministry of Superior Education, La Fondation pour la recherche médicale (FDT201904007976) and Research and the “taxe d’apprentissage” Gustave Roussy (2016 to C.C.J.).

Authors contribution

CCJ, DLP, CNV, JC, OZ, JBL, EG and JR designed research, performed experiments and analysed the data. MP and PG carried mice experiments. CD performed the bioinformatic analysis, GP and SS the electron microscopy. MG and MD provided clinical samples. VB, PD, JA and NS performed the histological analyses. FJ conceived the project, designed research and wrote the manuscript. All provided intellectual input.

Material and Methods

Recovery and characterization of peritoneal effusions from CRC patients

The human study protocols followed all relevant ethical regulations in accordance with the declaration of Helsinki principles. The study was approved by the ethics committee (CPP IDF 10), under protocol NI-2015-06-03, at Gustave Roussy and Lariboisière Hospitals. Written informed consent was obtained from all patients. Peritoneal effusions from a total of 59 patients with CRC were collected (as described in Zajac et al.). In brief, the peritoneal effusions were collected immediately after laparotomy and before cytoreductive surgery. The fluid was collected by addition and reabsorption of 500 ml of saline solution and processed in the laboratory within 2 h after collection for characterization of polarity orientation.

Organoid preparation from Patient-Derived Xenografts

Animal experiments were compliant with French legislation and EU Directive 2010/63. The project was validated by the Ethical Committee (CEEA) n°26 and was then granted French government authorizations under number 517-2015042114005883 and 2734-2015111711418501. Mice were obtained from Charles River, housed and bred at the Gustave Roussy animal core facility (accreditation number E-94-076-11). Animals were humanely euthanized according to endpoints that were validated by the Ethical Committee and the French government (Ministère de l'Enseignement Supérieur, de la Recherche et de l'Innovation).

Three human colorectal tumors (PDX#1 corresponding to LRB-0009C, PDX#2 corresponding to IGR-0012P and PDX#3 corresponding to IGR-014P) from the CReMEC tumor collection were maintained in NSG mice (NOD-scid IL2Rgamma^{null}, from Charles River, France) as previously described by Julien et al. Briefly, small tumor fragments were subcutaneously engrafted on the flank of anesthetized mice (2.5% isoflurane).

Tumor growth was measured at least once a week. When the volume reach 1500 mm³, mice were sacrificed and tumors were used for ex vivo experiments and 50 mm³ fragments engrafted on the flank of new mice. Organoids were prepared according to Sato et al. and adapted for muco-secreting tumors as follows: The PDX#1, PDX#2 or PDX#3 tumors between 1000-1500 mm³ were retrieved from the mice, minced into small fragments using a sterile scalpel and were incubated for 1h at 37°C in a final volume of 5 to 10 ml of culture medium (DMEM) without FBS and with 2 mg/ml collagenase (Sigma, C2139). The samples were then mixed with 20 ml of DMEM and filtered on 100 µm mesh size cell strainers (EASYstrainer, 542000). Digested tumor clusters were pelleted in by 4 pulse-centrifugations at 1500 rpm. The tumor fragments, free of single cells, were maintained 3 days in ultra-low attachment

plates (Corning, CLS3471) in culture medium. Then, organoids were pelleted at 1500 rpm and characterized (staining with apico-basolateral polarity markers demonstrated the organoids display the characteristics of TSIPs as show in Zajac et al). Organoids were used for survival and invasion experiments as well as for mice intraperitoneal injection.

Western blot:

Cells were lysed with SDS sample buffer [62.5 mM Tris-HCl (pH 6.8), 10% glycerol, 0.002% bromophenol blue, 2% SDS, and 5% β -mercaptoethanol] and lysates were boiled for 10 min. The samples were subjected to SDS-PAGE and proteins were transferred to nitrocellulose membranes (GE healthcare). Membranes were incubated for 30 min in Blocking Solution [Tris-buffered saline (TBS) containing 0.1% Tween-20, 3% BSA] and further incubated with the appropriate primary antibody overnight at 4°C. The following primary antibodies were used at the indicated dilutions: Phospho-T18/S19-MLC (1:1000, Cell Signalling Technology, 3674S), MLC2 (1:1000, Cell Signalling Technology, 3672S) and HSC70 (1:4000, Santa Cruz, sc-7298). The membranes were then washed three times with 0.1% Tween-20/TBS and incubated for 45 min with secondary antibody conjugated to horseradish peroxidase (GE Healthcare). Bound antibodies were detected with enhanced chemoluminescence.

ITGB1 silencing using shRNA

10⁴ clusters from PDXs obtained right after tumor dissociation (see method above) were placed in 1mL of DMEM in a low attachment 6 well plate and were infected using the lentiviral vectors shITGB1 (VB200629-1112fft, Vector Builder) based on the MOI given by the manufacturer or shRNA Renilla for control condition. The following day, 2mL of media were added. After 3 days, the organoids were placed in collagen-I gels (see method below) and the infection rate was observed using GFP. An organoid was considered properly infected and expressing the shRNA if at least 80% of the cells were GFP-positive.

Organoid polarity assessment

Collagen-I (Corning, 354236) was neutralized with 1.0 M NaOH and 10x MEM (Life Technologies, 21430-02) according to the ratio: 1.0:0.032:0.1 (vol/vol/vol). The concentration was then adjusted to 2 mg/ml with DMEM 1X and the collagen-I was incubated on ice for 1-1h15. The organoids embedded in neutralized Collagen-I were added on top of the pre-coated well at a concentration of 30-50 Organoids/5 μ l (ibidi 8-well chamber). The gel was allowed to polymerize for 45 min at 37°C.

Organoids were then cultured in culture medium supplemented with FBS 10 % for up to 6 days (3 days for PDX#3). The drugs were diluted in the media as followed: AIIB2 (DSHB, AB528306), A83-01 (Sigma Aldrich, 909910-43-6, 100 μ M), Blebbistatin (Calbiochem, 203391, 10 μ M), Calyculin-A (Clinisciences, sc-24000A, 1 nM), SB431542 (Sellekchem, S1067, 10 μ M), TGF β (R&D System, P01137, 20 ng/ml), Y27632 (Calbiochem, 688000, 25 μ M).

After incubation for 3 to 6 days in low adherence culture plates, the apico-basolateral polarity of organoids was quantified after immunostaining using anti-Ezrin or anti-P-ERM. Organoids are considered with an inverted polarity when at least 75% of the total peripheral cells displayed an outward apical pole in one confocal Z-section and displays protrusions (see Supp. Fig. 2 for phenotypes).

For organoids stained in suspension, they were fixed 10 min in PFA 4% after 3 days in low adherence culture plates in complete medium then embedded in collagen-I gels for immunofluorescent staining.

Immunofluorescence, antibodies, histology and immunohistochemistry

Immunofluorescence: Samples were washed twice in PBS supplemented with Ca²⁺ (0.1 mM) and Mg²⁺ (1 mM) and fixed in 4% PFA for 45 min (TSIPs and peritoneum. Permeabilization was performed in PBS supplemented with 0.5% Triton X-100 for 45 min. Primary antibodies were incubated overnight at 4 °C at the dilutions listed below in antibody diluent, PBS with 10% serum supplemented by 0.1% Triton X-100. Secondary antibodies used at 1/500 (Jackson ImmunoResearch, AffiniPure goat anti-mouse AlexaFluor, 488 715-545-150, AffiniPure goat anti-rabbit Cy3, 711-165-152 or LifeTechnologies goat anti-mouse 647, A21241, donkey anti-rabbit 488, A21206), phalloidin 1/1000 (Life Technologies) and DAPI (1 μ g/mL) were incubated overnight at 4°C or 2h at room temperature.

Primary antibodies: CK20 1/200 (Abcam, ab76126), E-cadherin 1/200 (Abcam, ab1416), EpCam 1/200 (MA5-12436), Ezrin 1/100 (DSHB, AB_210031), GM130 1/200 (NovusBio, NBP1-89757), Vimentin 1/500 (ThermoFisher Scientific, PA1-16759).

Histology: CRC and peritoneum specimens obtained after surgical resection were formalin fixed and paraffin embedded according to routine protocols. Peritoneal effusions were concentrated by centrifugation and fixed in formalin, then embedded for cytoblock. Sections (3 μ m) of formalin-fixed and paraffin- embedded samples were deparaffinized, unmasked (pH 8) and rehydrated before hematoxylin–eosin–safron or alcian blue staining, immunohistochemistry or immunofluorescence.

Immunohistochemistry: Sections were immunostained with ezrin (1:100; 610603, BD Biosciences) or anti-CK20 mouse monoclonal antibody (clone Ks20.8, Dako). Stainings were performed with Ventana BenchMark XT immunostainer (Ventana Medical Systems) using the UltraView DABv3 kit (Ventana). The chromogene was 3,3'-diaminobenzidine (DAB) in all the stainings. Histochemical staining with Alcian Blue (pH 2.5) was performed with Ventana BenchMark Special Stains (Ventana Medical Systems) utilizing the V1.00.0010 process. Peritoneal effusion smears were stained using May–Grünwald–Giemsa.

Automated morphometry analysis

Image analysis was performed after manual selection of the regions of interest by the senior pathologist. As these regions were too large to be assessed in totality, they were divided into blocks of pixels that were processed individually and finally stitched. Images show four different classes: background, DAB stained CK, Alcian Blue colored mucus areas and nuclear red (pink) colored areas of stroma. All these classes were first segmented. Background areas are pixels whose brightness is higher than 215. CK clusters are pixels whose value is lower than 165 on blue component image. Mucin areas are pixels whose red component on blue component ratio is lower than 1, whereas stroma areas are pixels whose red on blue ratio is higher than 1, but that are not CK. Connected components are then computed for each class and small areas are discarded. To find the apical status of each CK cluster, the program looks if it is surrounded by mucus (apical-out) or if it touches or is enclosed by a stroma area (apical-in). CK clusters surrounded by mucus that enclose a mucus area are discarded.

Microscopy, images treatment and analyses

Confocal imaging: Images were acquired using a SpinningDisk CSU-W1 (Yokogawa) with a ZylasCMOC camera piloted with an Olympus X83. Images were processed using ImageJ or Metamorph softwares.

Electron microscopy: Isolated TSIPs were fixed in 2 % glutaraldehyde in 0.1 M phosphate buffer pH 7.3 and deposited in drops of neutralized collagen-I (2 mg/ml) allowed to polymerize for 10 min at room temperature laid on a glass coverslip. TSIPs were washed 30 min in phosphate buffer, post-fixed with 2% osmic acid at room temperature and rinsed in water. Samples were dehydrated in ethanol and embedded in Epon. Polymerization was complete after 48 hours at 60°C. Ultrathin sections were collected on 100-mesh grids coated with Formvar and carbon, stained with uranyl acetate and lead citrate and observed with a FEI Technai Spirit transmission electron microscope at 80 Kv. Digital images were taken with a SIS MegaviewIII CCD camera.

Microarray

Samples preparation: RNA was extracted using the RNeasy minikit (Qiagen, Cat. No. 74104) from organoids either after three days in suspension (wash one time in PBS supplemented with calcium and magnesium as mentioned above) or after three days in collagen-I gels (2 mg/mL, see Organoids polarity assessment).

Transcriptome experiments: Whole transcriptome experiments have been processed on each PDX line: 009C (#1), 012P (#2) and 014P (#3) and two experimental conditions: culture in suspension and culture on collagen. Each biological condition was tested in triplicate inside the transcriptome experimental map which represents 18 transcriptome experiments. Starting from 100 ng of total RNA microarray, probes were synthesized and labeled with WT Plus Affymetrix chemistry in order to hybridized Clarius S Human microarray chip in Affymetrix microarray station.

Transcriptome analysis: Transcriptome analysis was performed with RMA normalization algorithm from Transcriptome Analysis Console (TAC, Applied Biosystems) software version 4.0. Two Analysis Of Variance (ANOVA) was performed with MEV standalone software (version 4.9.0) with implementation of 500 permutations and decomposition on supervised factors: collagen-I effect, PDX phenotype IN & OUT. During this supervised analysis interaction factor was subtract from the results. Downstream bioinformatics analyses were performed with the open-source R software environment version 3.5.3 under Bioconductor dependencies (Huber et al., 2015). Supervised differential expressed gene signature to see collagen-I effect on PDX was performed with Significance Analysis for Microarray (SAM) algorithm (Tusher et al., 2001) with a fold change threshold of 2 and a false discovery rate (FDR) less than 5 percent. Expression heatmaps were drawn with pheatmap R-package with transcriptome normalized data. Unsupervised principal component analysis representation used FactoMineR library. Geneset enrichment analysis was done with Java standalone software GSEA version 4.0.3 (Subramanian et al., 2005). The microarray datas are available on GEO with the access number GSE152299.

Assessment of polarity-related chemosensitivity

Organoids were prepared as described above (see Organoid preparation from PDXs). After 3 days in suspension, they were filtered on a 70µm cell strainer and placed in a collagen-I mix (see Organoid polarity assessment) and evenly distributed in a 48-wells NUNC plate (ThermoFisher, #150687) using

the Integra Assist Plus. Polarity reversion was obtained by incubating with Y27632 or AIIB2 on PDX#1 and PDX#3 respectively (see Organoid polarity assessment).

After polarity reversion was achieved, the medium was withdrawn and drugs were added using the Tecan D300e (software: D300e control version3.4.1) as follows: 5-Fluorouracil, Oxaliplatin and Irinotecan at the IC70 determined on CRC organoids. Control conditions were obtained using DMSO. After 2 days, ATP levels were assessed using CellTiter-Glo 3D according to the manufacturer's instructions and bioluminescence was measured with the BioTek Synergy LK (software: Gen5™ version 3.10) in white-bottom 96-well plates.

The ATP bioluminescence signal was averaged over the 3 wells of the same condition in the apical-in or apical-out topology. This provided ATP (Chemo A-in) or ATP (Chemo A-out) values when organoids were treated with a chemotherapeutic agent, and ATP (Ctrl A-in) or ATP(Ctrl A-out) in control condition.

Viability in apical-in and apical-out topologies were then calculated as follows:

$$\text{Viability A - in} = \frac{\text{ATP(Chemo A - in)}}{\text{ATP(Ctrl A - in)}} \quad \text{and} \quad \text{Viability A - out} = \frac{\text{ATP(Chemo A - out)}}{\text{ATP(Ctrl A - out)}}$$

Finally, the ratio between apical-in and apical-out topologies was calculated as:

$$\text{Viability Ratio} = \frac{\text{Viability A - out}}{\text{Viability A - in}}$$

References :

- Aceto, N., Bardia, A., Miyamoto, D. T., Donaldson, M. C., Wittner, B. S., Spencer, J. A., Yu, M., Pely, A., Engstrom, A., Zhu, H., et al. (2014). Circulating tumor cell clusters are oligoclonal precursors of breast cancer metastasis. *Cell* 158, 1110–1122.
- Ahmed, A. R. H., Griffiths, A. B., Tilby, M. T., Westley, B. R. and May, F. E. B. (2012). TFF3 Is a Normal Breast Epithelial Protein and Is Associated with Differentiated Phenotype in Early Breast Cancer but Predisposes to Invasion and Metastasis in Advanced Disease. *The American Journal of Pathology* 180, 904–916.
- Al Habyan, S., Kalos, C., Szyzborski, J. and McCaffrey, L. (2018). Multicellular detachment generates metastatic spheroids during intra-abdominal dissemination in epithelial ovarian cancer. *Oncogene* 37, 5127–5135.
- Ashley, N., Ouaret, D. and Bodmer, W. F. (2019). Cellular polarity modulates drug resistance in primary colorectal cancers via orientation of the multidrug resistance protein ABCB1. *J Pathol* 247, 293–304.
- Barresi, V., Reggiani Bonetti, L., Ieni, A., Domati, F. and Tuccari, G. (2015). Prognostic significance of grading based on the counting of poorly differentiated clusters in colorectal mucinous adenocarcinoma. *Human Pathology* 46, 1722–1729.
- Bilder, D. (2004). Epithelial polarity and proliferation control: links from the *Drosophila* neoplastic tumor suppressors. *Genes Dev* 18, 1909–1925.
- Bilder, D., Li, M. and Perrimon, N. (2000). Cooperative Regulation of Cell Polarity and Growth by *Drosophila* Tumor Suppressors. *Science* 289, 113–116.
- Brabletz, T. (2005). Invasion and metastasis in colorectal cancer: Epithelial-mesenchymal transition, mesenchymal-epithelial transition, stem cells and β -catenin. *Cells Tissues Organs*.
- Bryant, D. M., Datta, A., Rodríguez-Fraticelli, A. E., Peränen, J., Martín-Belmonte, F. and Mostov, K. E. (2010). A molecular network for de novo generation of the apical surface and lumen. *Nat Cell Biol* 12, 1035–1045.
- Bryant, D. M., Rognot, J., Datta, A., Overeem, A. W., Kim, M., Yu, W., Peng, X., Eastburn, D. J., Ewald, A. J., Werb, Z., et al. (2014). A Molecular Switch for the Orientation of Epithelial Cell Polarization. *Developmental Cell* 31, 171–187.
- Burute, M. and Thery, M. (2012). Spatial segregation between cell–cell and cell–matrix adhesions. *Current Opinion in Cell Biology* 24, 628–636.
- Cheung, K. J., Gabrielson, E., Werb, Z. and Ewald, A. J. (2013). Collective Invasion in Breast Cancer Requires a Conserved Basal Epithelial Program. *Cell* 155, 1639–1651.
- Cheung, K. J., Padmanaban, V., Silvestri, V., Schipper, K., Cohen, J. D., Fairchild, A. N., Gorin, M. A., Verdone, J. E., Pienta, K. J., Bader, J. S., et al. (2016). Polyclonal breast cancer metastases arise from collective dissemination of keratin 14-expressing tumor cell clusters. *Proc. Natl. Acad. Sci. U.S.A.* 113,.
- Commander, R., Wei, C., Sharma, A., Mouw, J. K., Burton, L. J., Summerbell, E., Mahboubi, D., Peterson, R. J., Konen, J., Zhou, W., et al. (2020). Subpopulation targeting of pyruvate dehydrogenase and GLUT1 decouples metabolic heterogeneity during collective cancer cell invasion. *Nat Commun* 11, 1533.
- Cserni, G. (2014). Reversed polarity of the glandular epithelial cells in micropapillary carcinoma of the large intestine and the EMA/MUC1 immunostain. *Pathology* 46, 527–532.
- Datta, A., Sandilands, E., Mostov, K. E. and Bryant, D. M. (2017). Fibroblast-derived HGF drives acinar lung cancer cell polarization through integrin-dependent RhoA-ROCK1 inhibition. *Cell Signal* 40, 91–98.
- de Miranda, N. F. C. C., van Dinther, M., van den Akker, B. E. W. M., van Wezel, T., ten Dijke, P. and Morreau, H. (2015). Transforming Growth Factor β Signaling in Colorectal Cancer Cells With Microsatellite Instability Despite Biallelic Mutations in TGFBR2. *Gastroenterology* 148, 1427-1437.e8.

- Dekkers, J. F., van Vliet, E. J., Sachs, N., Rosenbluth, J. M., Kopper, O., Rebel, H. G., Wehrens, E. J., Piani, C., Visvader, J. E., Verissimo, C. S., et al. (2021). Long-term culture, genetic manipulation and xenotransplantation of human normal and breast cancer organoids. *Nat Protoc* 16, 1936–1965.
- Dongre, A. and Weinberg, R. A. (2019). New insights into the mechanisms of epithelial-mesenchymal transition and implications for cancer. *Nat Rev Mol Cell Biol* 20, 69–84.
- Doyle, A. D., Carvajal, N., Jin, A., Matsumoto, K. and Yamada, K. M. (2015). Local 3D matrix microenvironment regulates cell migration through spatiotemporal dynamics of contractility-dependent adhesions. *Nat Commun* 6, 8720.
- Drost, J. and Clevers, H. (2018). Organoids in cancer research. *Nat Rev Cancer* 18, 407–418.
- Ferrari, A., Veligodskiy, A., Berge, U., Lucas, M. S. and Kroschewski, R. (2008). ROCK-mediated contractility, tight junctions and channels contribute to the conversion of a preapical patch into apical surface during isochoric lumen initiation. *J Cell Sci* 121, 3649–3663.
- Friedl, P. and Gilmour, D. (2009). Collective cell migration in morphogenesis, regeneration and cancer. *Nat Rev Mol Cell Biol* 10, 445–457.
- Friedl, P., Locker, J., Sahai, E. and Segall, J. E. (2012). Classifying collective cancer cell invasion. *Nat Cell Biol* 14, 777–783.
- Gandalovičová, A., Vomastek, T., Rosel, D. and Brábek, J. (2016). Cell polarity signaling in the plasticity of cancer cell invasiveness. *Oncotarget* 7, 25022–25049.
- Gassama-Diagne, A., Yu, W., ter Beest, M., Martin-Belmonte, F., Kierbel, A., Engel, J. and Mostov, K. (2006). Phosphatidylinositol-3,4,5-trisphosphate regulates the formation of the basolateral plasma membrane in epithelial cells. *Nat Cell Biol* 8, 963–970.
- Goranci-Buzhala, G., Mariappan, A., Gabriel, E., Ramani, A., Ricci-Vitiani, L., Buccarelli, M., D’Alessandris, Q. G., Pallini, R. and Gopalakrishnan, J. (2020). Rapid and Efficient Invasion Assay of Glioblastoma in Human Brain Organoids. *Cell Reports* 31, 107738.
- Gracia, M., Theis, S., Proag, A., Gay, G., Benassayag, C. and Suzanne, M. (2019). Mechanical impact of epithelial-mesenchymal transition on epithelial morphogenesis in *Drosophila*. *Nat Commun* 10, 2951.
- Gudjonsson, T., Rønnov-Jessen, L., Villadsen, R., Rank, F., Bissell, M. J. and Petersen, O. W. (2002). Normal and tumor-derived myoepithelial cells differ in their ability to interact with luminal breast epithelial cells for polarity and basement membrane deposition. *J Cell Sci* 115, 39–50.
- Han, Y. L., Pegoraro, A. F., Li, H., Li, K., Yuan, Y., Xu, G., Gu, Z., Sun, J., Hao, Y., Gupta, S. K., et al. (2020). Cell swelling, softening and invasion in a three-dimensional breast cancer model. *Nat. Phys.* 16, 101–108.
- Heino, J. and Massagué, J. (1989). Transforming growth factor- β switches the pattern of integrins expressed in MG-63 human osteosarcoma cells and causes a selective loss of cell adhesion to laminin. *Journal of Biological Chemistry* 264, 21806–21811.
- Huang, W., Navarro-Serer, B., Jeong, Y. J., Chianchiano, P., Xia, L., Luchini, C., Veronese, N., Dowiak, C., Ng, T., Trujillo, M. A., et al. (2020). Pattern of Invasion in Human Pancreatic Cancer Organoids Is Associated with Loss of SMAD4 and Clinical Outcome. *Cancer Res* 80, 2804–2817.
- Huber, W., Carey, V. J., Gentleman, R., Anders, S., Carlson, M., Carvalho, B. S., Bravo, H. C., Davis, S., Gatto, L., Girke, T., et al. (2015). Orchestrating high-throughput genomic analysis with Bioconductor. *Nat Methods* 12, 115–121.
- Iliina, O. and Friedl, P. (2009). Mechanisms of collective cell migration at a glance. *J Cell Sci* 122, 3203–3208.
- Iliina, O., Gritsenko, P. G., Syga, S., Lippoldt, J., La Porta, C. A. M., Chepizhko, O., Grosser, S., Vullings, M., Bakker, G.-J., Starruß, J., et al. (2020). Cell-cell adhesion and 3D matrix confinement determine jamming transitions in breast cancer invasion. *Nat Cell Biol* 22, 1103–1115.

- Jass, J. R. (2007). Classification of colorectal cancer based on correlation of clinical, morphological and molecular features. *Histopathology* 50, 113–130.
- Julien, S., Merino-Trigo, A., Lacroix, L., Pocard, M., Goéré, D., Mariani, P., Landron, S., Bigot, L., Nemati, F., Dartigues, P., et al. (2012). Characterization of a large panel of patient-derived tumor xenografts representing the clinical heterogeneity of human colorectal cancer. *Clin Cancer Res* 18, 5314–5328.
- Jung, H.-Y., Fattet, L., Tsai, J. H., Kajimoto, T., Chang, Q., Newton, A. C. and Yang, J. (2019). Apical-basal polarity inhibits epithelial-mesenchymal transition and tumour metastasis by PAR-complex-mediated SNAIL degradation. *Nat Cell Biol* 21, 359–371.
- Koga, Y., Song, H., Chalmers, Z. R., Newberg, J., Kim, E., Carrot-Zhang, J., Piou, D., Polak, P., Abdulkadir, S. A., Ziv, E., et al. (2020). Genomic Profiling of Prostate Cancers from Men with African and European Ancestry. *Clin Cancer Res* 26, 4651–4660.
- Kroepfl, J. F. and Gardinier, M. V. (2001). Mutually exclusive apicobasolateral sorting of two oligodendroglial membrane proteins, proteolipid protein and myelin/oligodendrocyte glycoprotein, in Madin-Darby canine kidney cells. *J. Neurosci. Res.* 66, 1140–1148.
- Kryvenko, O. N., Chitale, D. A., Yoon, J., Arias-Stella, J., Meier, F. A. and Lee, M. W. (2013). Precursor Lesions of Mucinous Carcinoma of the Breast: Analysis of 130 Cases. *American Journal of Surgical Pathology* 37, 1076–1084.
- Libanje, F., Raingeaud, J., Luan, R., Thomas, Z., Zajac, O., Veiga, J., Marisa, L., Adam, J., Boige, V., Malka, D., et al. (2019). ROCK2 inhibition triggers the collective invasion of colorectal adenocarcinomas. *EMBO J* 38, e99299.
- Liu, K. D., Datta, A., Yu, W., Brakeman, P. R., Jou, T.-S., Matthay, M. A. and Mostov, K. E. (2007). Rac1 is required for reorientation of polarity and lumen formation through a PI 3-kinase-dependent pathway. *Am J Physiol Renal Physiol* 293, F1633-1640.
- Margaron, Y., Nagai, T., Guyon, L., Kurzawa, L., Morel, A.-P., Pinheiro, A., Blanchoin, L., Reyat, F., Puisieux, A. and Théry, M. (2019). Biophysical properties of intermediate states of EMT outperform both epithelial and mesenchymal states. *bioRxiv* 797654.
- Negri, F. V., Wotherspoon, A., Cunningham, D., Norman, A. R., Chong, G. and Ross, P. J. (2005). Mucinous histology predicts for reduced fluorouracil responsiveness and survival in advanced colorectal cancer. *Ann Oncol* 16, 1305–1310.
- Nieto, M. A., Huang, R. Y.-J., Jackson, R. A. and Thiery, J. P. (2016). EMT: 2016. *Cell* 166, 21–45.
- Okuyama, H., Kondo, J., Sato, Y., Endo, H., Nakajima, A., Piulats, J. M., Tomita, Y., Fujiwara, T., Itoh, Y., Mizoguchi, A., et al. (2016). Dynamic Change of Polarity in Primary Cultured Spheroids of Human Colorectal Adenocarcinoma and Its Role in Metastasis. *Am J Pathol* 186, 899–911.
- Padmanaban, V., Krol, I., Suhail, Y., Szczerba, B. M., Aceto, N., Bader, J. S. and Ewald, A. J. (2019). E-cadherin is required for metastasis in multiple models of breast cancer. *Nature* 573, 439–444.
- Padmanaban, V., Grasset, E. M., Neumann, N. M., Fraser, A. K., Henriot, E., Matsui, W., Tran, P. T., Cheung, K. J., Georgess, D. and Ewald, A. J. (2020). Organotypic culture assays for murine and human primary and metastatic-site tumors. *Nat Protoc* 15, 2413–2442.
- Ricard-Blum, S. (2011). The collagen family. *Cold Spring Harb Perspect Biol* 3, a004978.
- Roy, P., Canet-Jourdan, C., Annereau, M., Zajac, O., Gelli, M., Broutin, S., Mercier, L., Paci, A., Lemare, F., Ducreux, M., et al. (2017). Organoids as preclinical models to improve intraperitoneal chemotherapy effectiveness for colorectal cancer patients with peritoneal metastases: Preclinical models to improve HIPEC. *Int J Pharm* 531, 143–152.
- Saito, Y., Desai, R. R. and Muthuswamy, S. K. (2018). Reinterpreting polarity and cancer: The changing landscape from tumor suppression to tumor promotion. *Biochimica et Biophysica Acta (BBA) - Reviews on Cancer* 1869, 103–116.

- Sato, T. and Clevers, H. (2013). Growing self-organizing mini-guts from a single intestinal stem cell: mechanism and applications. *Science* 340, 1190–1194.
- Sheppard, D., Cohen, D. S., Wang, A. and Busk, M. (1992). Transforming growth factor beta differentially regulates expression of integrin subunits in guinea pig airway epithelial cells. *Journal of Biological Chemistry* 267, 17409–17414.
- Spaderna, S., Schmalhofer, O., Hlubek, F., Berx, G., Eger, A., Merkel, S., Jung, A., Kirchner, T. and Brabletz, T. (2006). A Transient, EMT-Linked Loss of Basement Membranes Indicates Metastasis and Poor Survival in Colorectal Cancer. *Gastroenterology* 131, 830–840.
- Subramanian, A., Tamayo, P., Mootha, V. K., Mukherjee, S., Ebert, B. L., Gillette, M. A., Paulovich, A., Pomeroy, S. L., Golub, T. R., Lander, E. S., et al. (2005). Gene set enrichment analysis: A knowledge-based approach for interpreting genome-wide expression profiles. *Proc. Natl. Acad. Sci. U.S.A.* 102, 15545–15550.
- Thorpe, D., Stringer, A. and Butler, R. (2013). Chemotherapy-induced mucositis: the role of mucin secretion and regulation, and the enteric nervous system. *Neurotoxicology* 38, 101–105.
- Tsai, J.-H., Jeng, Y.-M., Yuan, C.-T., Lin, Y.-L., Cheng, M.-L. and Liau, J.-Y. (2019). Traditional Serrated Pathway-associated Colorectal Carcinoma: Morphologic Reappraisal of Serrated Morphology, Tumor Budding, and Identification of Frequent PTEN Alterations. *American Journal of Surgical Pathology* 43, 1042–1051.
- Tusher, V. G., Tibshirani, R. and Chu, G. (2001). Significance analysis of microarrays applied to the ionizing radiation response. *Proc. Natl. Acad. Sci. U.S.A.* 98, 5116–5121.
- Tuveson, D. and Clevers, H. (2019). Cancer modeling meets human organoid technology. *Science* 364, 952–955.
- Vlachogiannis, G., Hedayat, S., Vatsiou, A., Jamin, Y., Fernández-Mateos, J., Khan, K., Lampis, A., Eason, K., Huntingford, I., Burke, R., et al. (2018). Patient-derived organoids model treatment response of metastatic gastrointestinal cancers. *Science* 359, 920–926.
- Wellner, U., Schubert, J., Burk, U. C., Schmalhofer, O., Zhu, F., Sonntag, A., Waldvogel, B., Vannier, C., Darling, D., zur Hausen, A., et al. (2009). The EMT-activator ZEB1 promotes tumorigenicity by repressing stemness-inhibiting microRNAs. *Nat Cell Biol* 11, 1487–1495.
- W.H.O. (2020). Source: Globocan 2020. *Globocan*.
- Wolf, K. and Friedl, P. (2011). Extracellular matrix determinants of proteolytic and non-proteolytic cell migration. *Trends in Cell Biology* 21, 736–744.
- Wosen, J. E., Mukhopadhyay, D., Macaubas, C. and Mellins, E. D. (2018). Epithelial MHC Class II Expression and Its Role in Antigen Presentation in the Gastrointestinal and Respiratory Tracts. *Front. Immunol.* 9, 2144.
- Yao, Y., Xu, X., Yang, L., Zhu, J., Wan, J., Shen, L., Xia, F., Fu, G., Deng, Y., Pan, M., et al. (2020). Patient-Derived Organoids Predict Chemoradiation Responses of Locally Advanced Rectal Cancer. *Cell Stem Cell* 26, 17-26.e6.
- Yu, W., Datta, A., Leroy, P., O'Brien, L. E., Mak, G., Jou, T.-S., Matlin, K. S., Mostov, K. E. and Zegers, M. M. P. (2005). β 1-Integrin Orients Epithelial Polarity via Rac1 and Laminin. *MBoC* 16, 433–445.
- Zajac, O., Raingeaud, J., Libanje, F., Lefebvre, C., Sabino, D., Martins, I., Roy, P., Benatar, C., Canet-Jourdan, C., Azorin, P., et al. (2018). Tumour spheres with inverted polarity drive the formation of peritoneal metastases in patients with hypermethylated colorectal carcinomas. *Nat Cell Biol* 20, 296–306.
- Zambruno, G., Marchisio, P. C., Marconi, A., Vaschieri, C., Melchiori, A., Giannetti, A. and De Luca, M. (1995). Transforming growth factor-beta 1 modulates beta 1 and beta 5 integrin receptors and induces the de novo expression of the alpha v beta 6 heterodimer in normal human keratinocytes: implications for wound healing. *Journal of Cell Biology* 129, 853–865.
- Zanoni, M., Cortesi, M., Zamagni, A., Arienti, C., Pignatta, S. and Tesei, A. (2020). Modeling neoplastic disease with spheroids and organoids. *J Hematol Oncol* 13, 97.

Figures

Figure 1

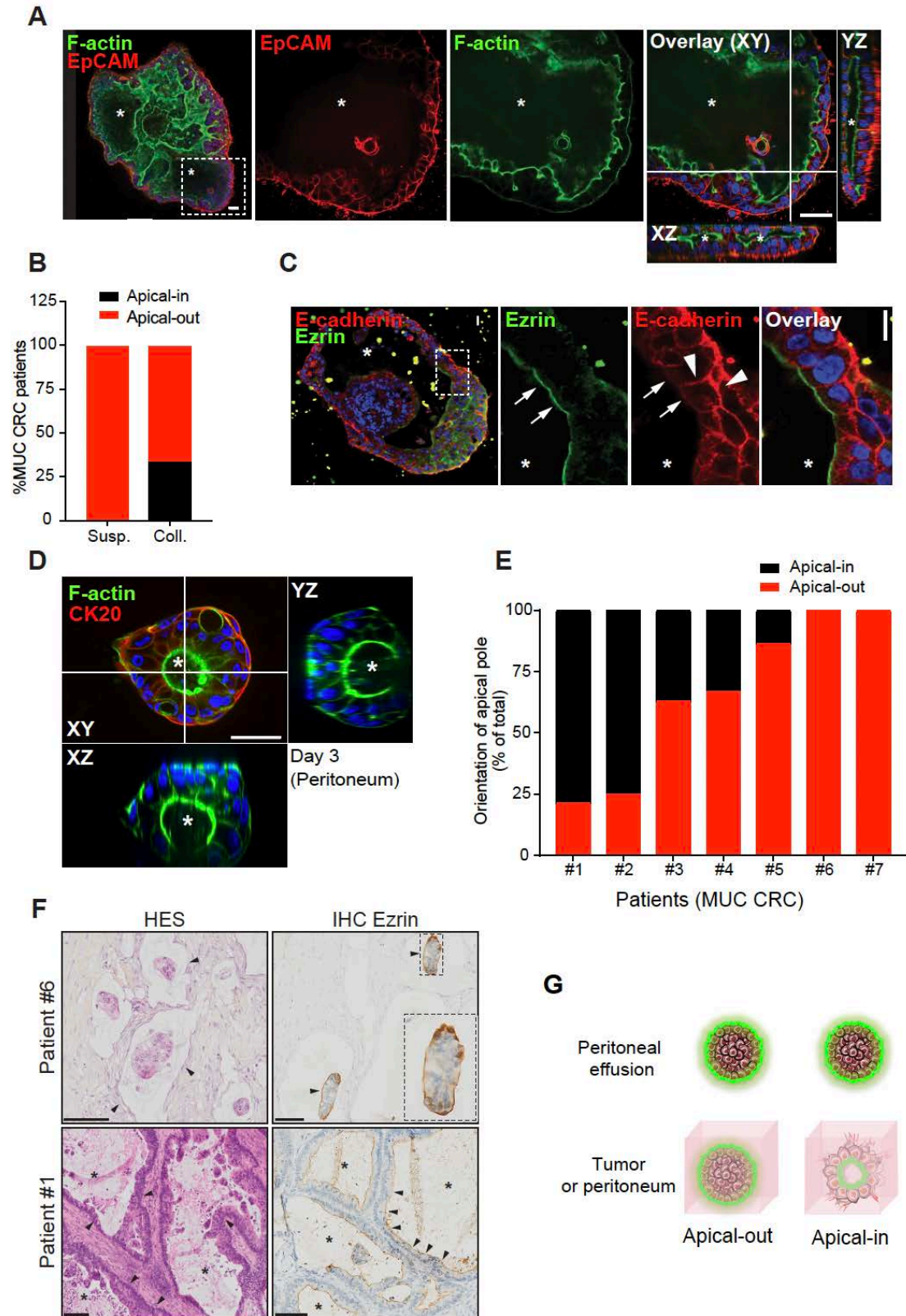


Fig.1: MUC CRC patients display two distinct histological architectures and TSIP behaviors.

(A) Representative images of a patient MUC CRC TSIP forming a luminal cavity after 6 days in a 3D collagen-I gel, immunostained for EpCAM, F-actin and DAPI (blue). *=luminal cavity, scale bar=50 μ m.

(B) Quantification of TSIPs polarity in suspension (from peritoneal effusions) and after 3 to 6 days in collagen-I gels. The graph shows the percentage of patients displaying apical-out vs. apical-in organoids based on the outward or luminal localization of ezrin respectively, in one confocal-Z-section (30 TSIPs/patient for 7 patients).

(C) Representative image of a MUC CRC patient's TSIP displaying an apical-in topology after spending 6 days in a collagen-I gel, immunostained for ezrin, E-cadherin and DAPI (blue). *=lumen, scale bar=20 μ m.

(D) Representative images of a TSIP adhering to a peritoneal explant from the matching patient and forming a central cavity after 3 days, immunostained for CK20, F-actin and DAPI. *=luminal cavity, scale bar= 50 μ m.

(E) Quantification of TSIPs polarity gathered from peritoneal effusions after 6 days in collagen-I gels. The graph shows the percentage of apical-out vs. apical-in TSIPs based on the outward or luminal localization of ezrin respectively, in one confocal-Z-section (30 TSIPs/patient for 7 patients).

(F) HES staining and IHC for Ezrin of peritoneal metastases collected during cytoreductive surgery of MUC CRC patients #1 and #6. *=lumen, scale bar=100 μ m.

(G) Schematic representation of TSIPs' polarity in suspension, in the primary tumor, the peritoneum or after embedding in matrix.

Data are represented as mean \pm s.e.m.

Figure 2

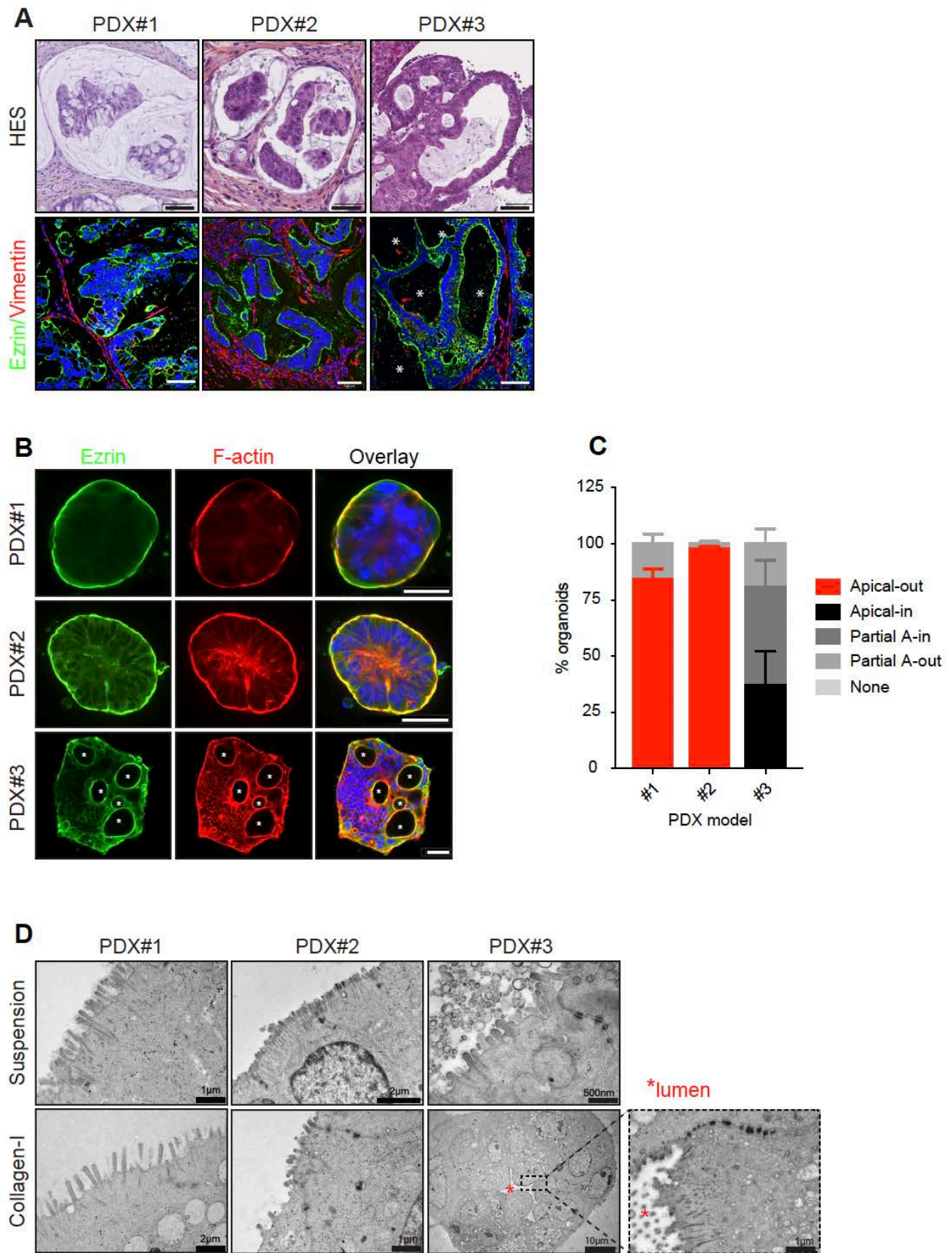


Fig.2: Polarity orientation is a cell autonomous feature of MUC CRCs.

(A) HES staining (top panel) and ezrin, vimentin (for stromal cells) and DAPI (blue) immunostaining (bottom panel) of MUC CRC PDX tumors: Apical-out (PDX#1 and #2) and Apical-in (PDX#3). *=lumen, scale bar=50 μ m (top panel) and 100 μ m (bottom panel).

(B) Organoids from PDXs after 3 days in collagen-I gels, immunostained for ezrin, F-actin and DAPI (blue). *=lumen, scale bar=50 μ m.

(C) Quantification of PDX' organoids apico-basolateral polarity orientation based on Supplementary Fig. 2 criteria in one confocal-Z-section (n=3 independent experiments, with 85, 90 and 69 organoids counted for PDX#1, PDX#2 and PDX#3 respectively).

(D) Electron microscopy of organoids in suspension or after 3 days in 3D collagen-I gels showing microvilli at the periphery for PDX#1 and PDX#2 and at the lumen for PDX#3.

Data are represented as mean \pm s.e.m.

Figure 3

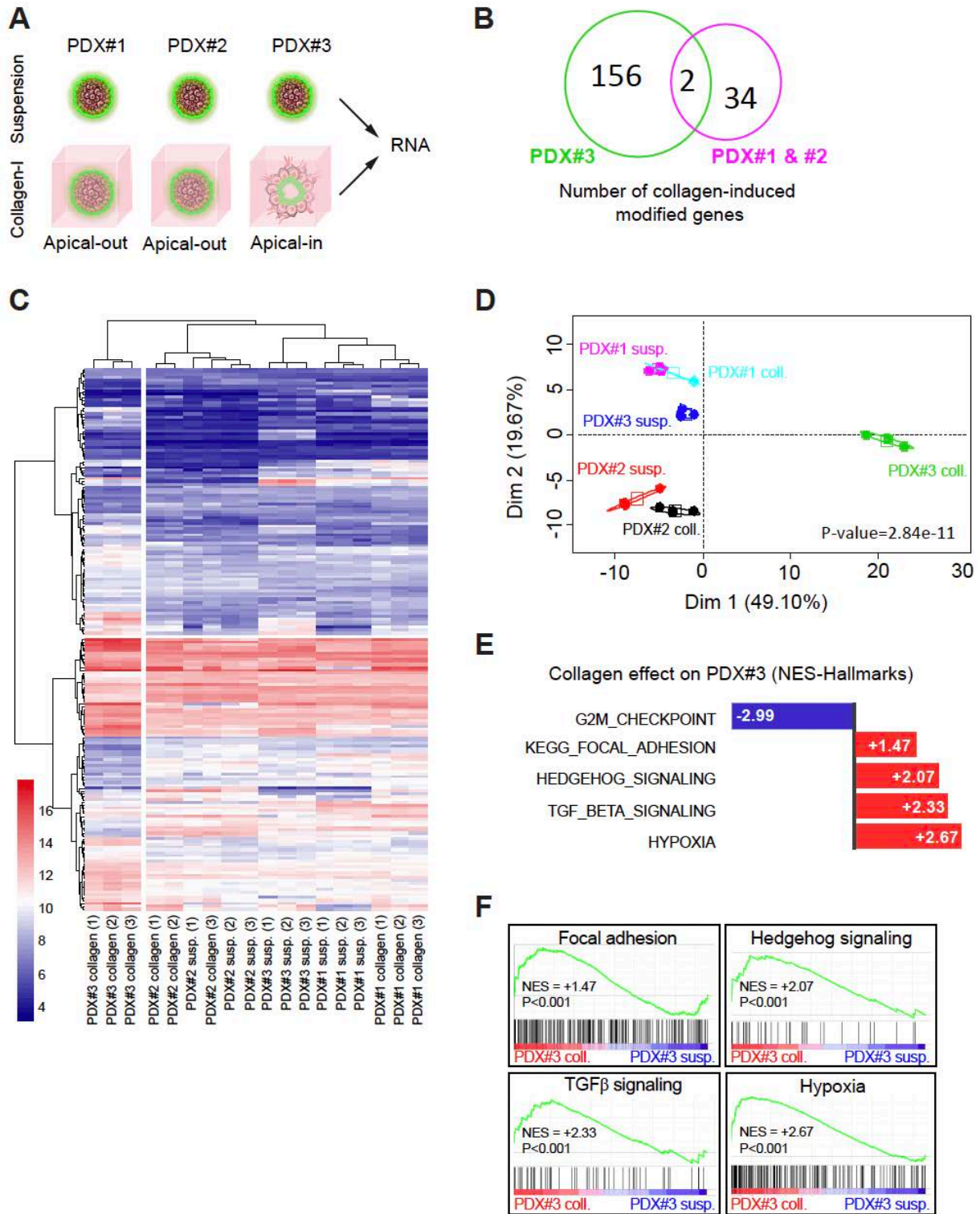


Fig.3: Apical-in and apical-out organoids harbor different expression profiles when embedded into 3D collagen-I gels.

(A) Schematic representation of the protocol used to generate mRNA for the microarray. Organoids' RNA was extracted either after 3 days in suspension or after 3 days in 3D collagen-I gels.

(B) Venn diagram representing the number of genes regulated by collagen-I embedding.

(C) Discrimination of PDX#3 organoids in response to collagen-I stimulation. Corresponding to supplementary table #1.

(D) Results from (B) and (C) are confirmed by an unsupervised principal component analysis.

(E, F) The Gene set enrichment analysis revealed that PDX#3 organoids in collagen-I specifically repress the cell cycle progression (G2M checkpoint) and activate four pathways: Focal adhesion, Sonic Hedgehog, TGF β and hypoxia signaling.

Data are represented as mean \pm s.e.m.

Figure 4

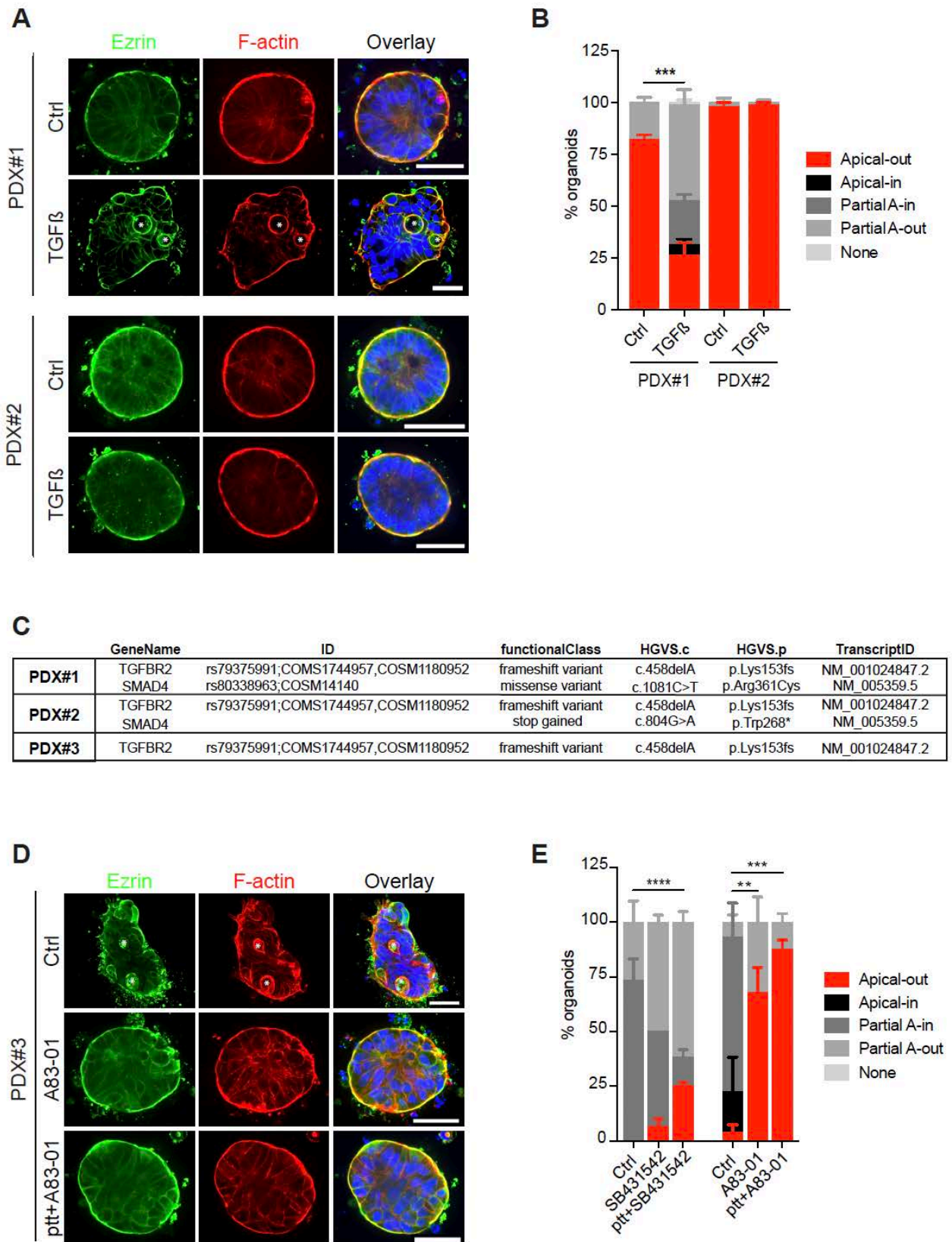


Fig.4: TGF β is involved in the orientation of apico-basolateral polarity.

(A) Immunostainings for ezrin, F-actin and DAPI (blue) after 3 days in collagen, in control condition or under treatment of TGF β (20ng/mL) for PDX#1 and #2. *=lumen, scale bar=50 μ m

(B) Quantifications of PDX#1 and PDX#2 organoids' phenotypes in collagen after TGF β treatment (n=3 experiments for each PDX with 79 and 81 organoids counted for control and TGF β conditions respectively for PDX#1, and 90 organoids counted for PDX#2 in both conditions).

(C) Summary table recapitulating TGF β signaling pathways mutations in PDXs, obtained by whole exome sequencing.

(D) Immunostainings for ezrin, F-actin and DAPI (blue) in control condition, of PDX#3 pre-treated (ptt) in suspension for 3 days or not, and then treated in collagen-I gels for 3 days with A83-01 (10mM). *=lumen, scale bar=50 μ m.

(E) Quantification of PDX#3 organoids' phenotypes treated and pre-treated with SB431542 (10 μ M) or A83-01 (10mM) (n=3 experiments with 82, 90 and 90 organoids counted for control, SB431542 and ptt+431542 conditions respectively, and 61, 90 and 90 organoids counted for control, A83-01 and ptt+A83-01 conditions respectively).

Statistics: unpaired two-tailed t-tests were performed for panel B, one-way ANOVA for panel E with ****P<0.0001, ***P<0.001, **P<0.01.

Data are represented as mean \pm s.e.m.

Figure 5

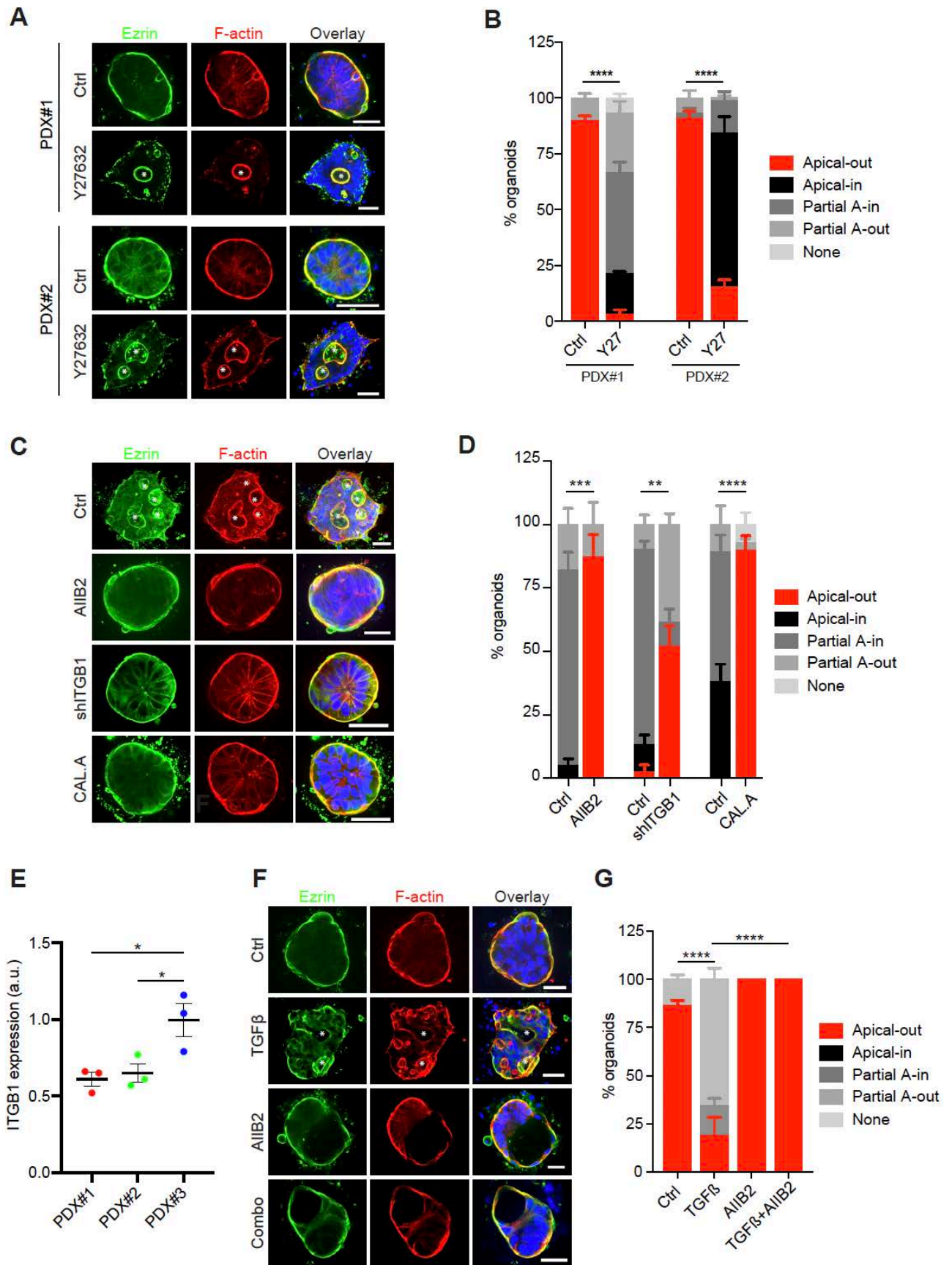


Fig.5: The balance between adhesion and contractility drives organoids apico-basolateral polarity.

(A) Organoids from PDX#1 (top panel) and PDX#2 (bottom panel) immunostained for ezrin, F-actin and DAPI (blue) after 6 days in collagen, in control condition or after treatment with Y27632 (25 μ M).

(B) Quantifications of PDX#1 and PDX#2 organoids' phenotypes in collagen after Y27632 (Y27) treatment (n=3 experiments with 90 and 88 PDX1# organoids counted for control and Y27632 conditions respectively, and 91 and 92 for PDX#2).

(C) Organoids from PDX#3 after 3 days in collagen, in control condition or after treatment with AIIB2 (1 μ g/mL), shITGB1 or Calyculin-A (CAL.A, 1nM) and immunostained for ezrin, F-actin and DAPI (blue).

(D) Quantifications of PDX#3 organoids' phenotypes in collagen after AIIB2, Calyculin-A treatment or shITGB1 (n=3 experiments with 67 and 80 organoids counted for control and AIIB2 conditions respectively, 74 and 88 for control and shITGB1 conditions respectively, and 75 and 69 for control and CAL.A respectively).

(E) ITGB1 mRNA expression (from microarray analysis) of PDX#1, #2 and #3 after 3 days in collagen-I gels.

(F) Organoids from PDX#1 immunostained for ezrin, F-actin and DAPI in control condition and after treatment with TGF β (20ng/mL), AIIB2 (1 μ g/mL) or the two combined, in collagen-I gels.

(G) Quantification of PDX#1 organoids' phenotypes in collagen after TGF β , AIIB2 or TGF β and AIIB2 treatments (n=4 experiments with 120, 90, 116 and 120 organoids counted for control, TGF β , AIIB2 and TGF β +AIIB2 conditions respectively).

*=lumen, scale bars=50 μ m.

Statistics: unpaired two-tailed t-tests were performed for panel B, D and E, one-way ANOVA for panel G with ****P<0.0001, ***P<0.001, **P<0.01, *P<0.05.

Data are represented as mean \pm s.e.m.

Figure 6

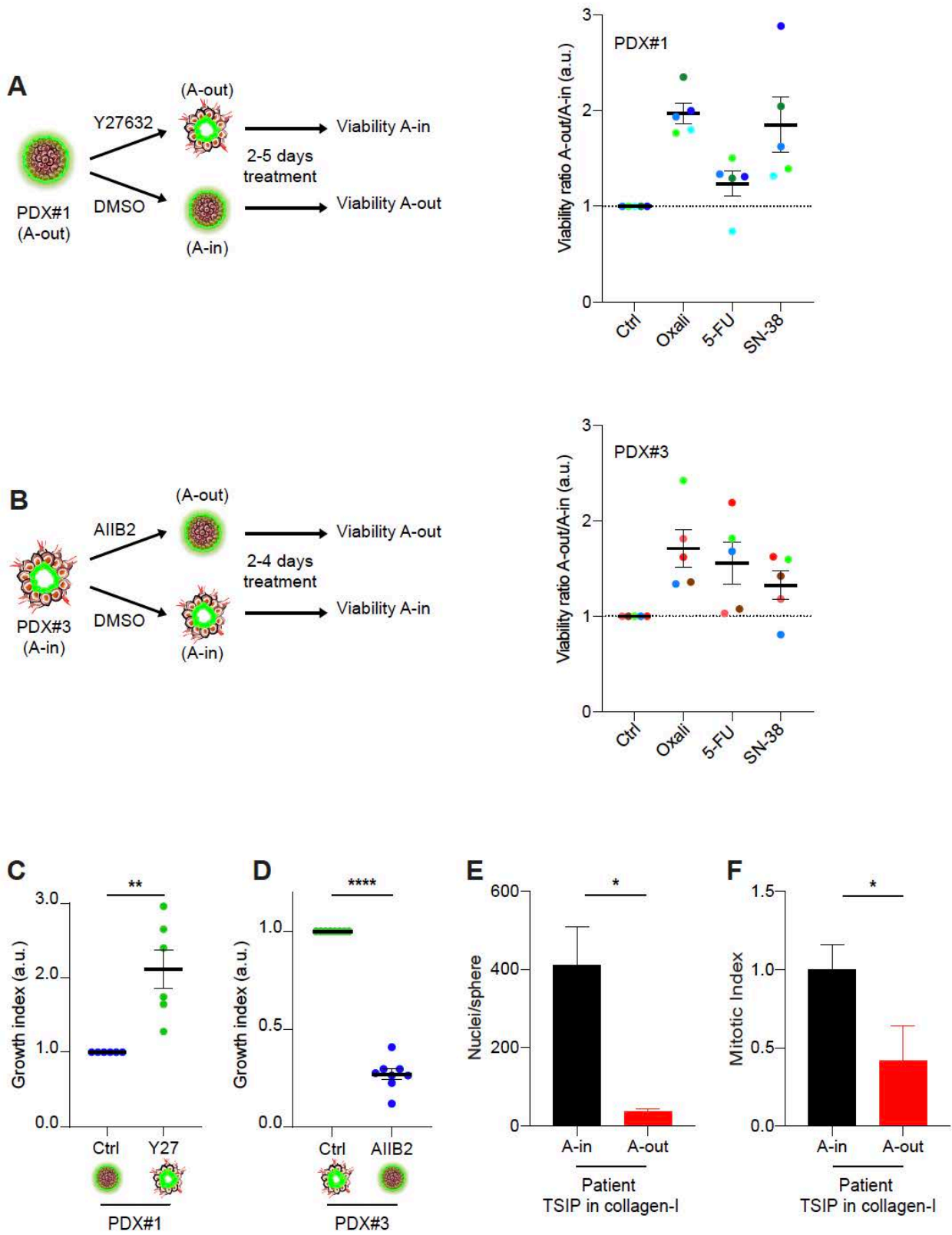


Fig.6: Organoids apico-basolateral polarity could predict response to chemotherapy.

(A) Left: schematic representation of the protocol for assessment of polarity-related chemosensitivity for PDX#1. Right: viability ratio A-out/A-in of PDX#1 organoids in control condition or after treatment for 2 to 5 days with Oxaliplatin (Oxali, 10 μ M), 5-Fluorouracil (5-FU, 1.8 μ M) or Irinotecan (SN-38, 6.10⁻³ μ M).

(B) Left: schematic representation of the protocol for assessment of polarity-related chemosensitivity for PDX#3. Right: viability ratio A-out/A-in of PDX#3 organoids in control condition or after treatment for 2 to 4 days with Oxaliplatin (Oxali, 10 μ M), 5-Fluorouracil (5-FU, 1.8 μ M) or Irinotecan (SN-38, 6.10⁻³ μ M).

Chemotherapeutics agents were used at the IC70 (see Supplementary Fig. 5A). Each color point represents a separated experiment. Viability ratio calculation is detailed in Material and Methods.

(C) Growth index using ATP-bioluminescence for PDX#1 organoids in control condition (Ctrl) or after polarity reversion (Y27632), normalized to control condition.

(D) Growth index using ATP-bioluminescence for PDX#3 organoids in control condition (Ctrl) or after polarity reversion (AIB2), normalized to control condition.

(E) Number of nuclei per TSIP, associated with apical-in and apical-out morphologies, counted using DAPI staining, respectively from n=19 TSIPs and 7792 nuclei and n=10 TSIPs and 364 nuclei from 3 patients.

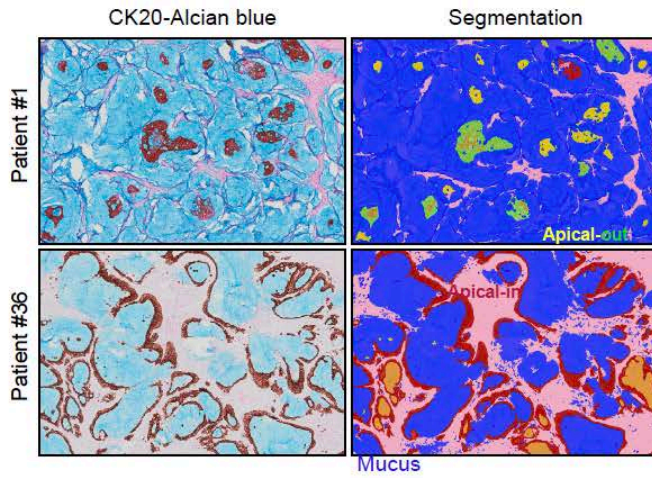
(F) Mitotic index, associated with apical-in and apical-out topologies, respectively from n=19 TSIPs and 7792 nuclei and n=10 TSIPs and 364 nuclei from 3 patients.

Statistics: unpaired two-tailed t-tests were performed for panel C, D, E and F with ****P<0.0001, **P<0.01, *P<0.05.

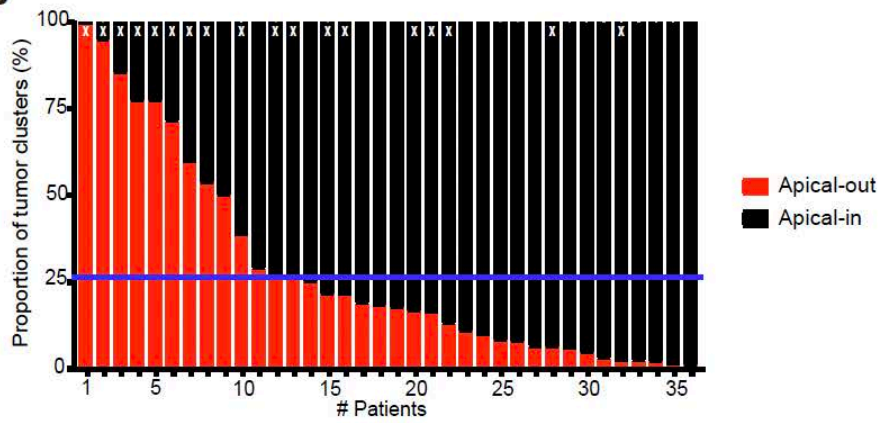
Data are represented as mean \pm s.e.m.

Figure 7

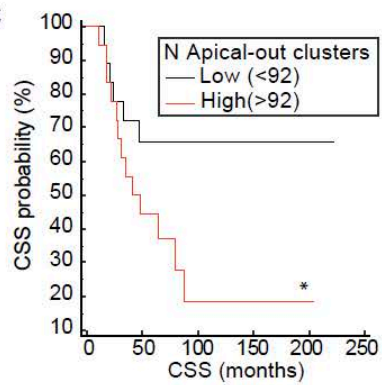
A



B



C



D

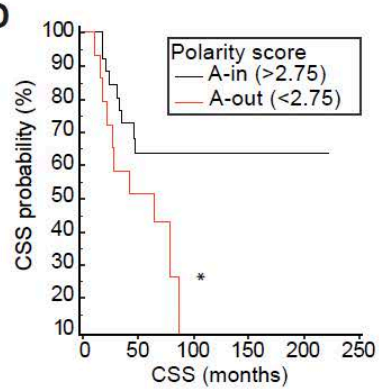


Fig.7: Apico-basolateral polarity correlates with patients' survival.

(A) Staining for CK20 and Alcian blue of two MUC CRC patients and the corresponding segmentation from the morphometry analysis. The top panels show a region that is mostly represented by apical-out tumoral component (yellow and green) while tumor in the bottom panels harbors an apical-in (red) architecture.

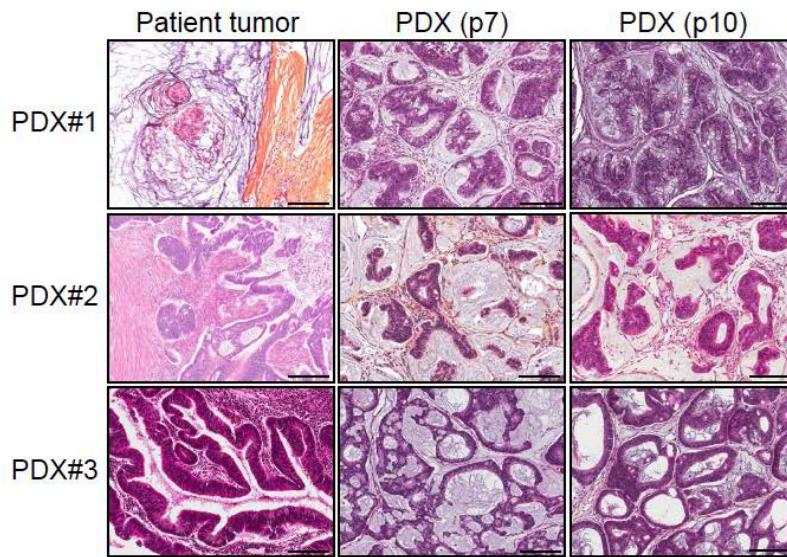
(B) Quantitative representation of the apical-in (black) and apical-out (red) components for each MUC CRC patient (the white X represent patients with a number of apical-out clusters >92 used to generate the graph C, the blue line indicates the polarity score to 2.75 used in the graph D).

(C,D) Kaplan-Meier curves displaying cancer-specific survival depending on the number of apical-out clusters (C) and polarity score (D).

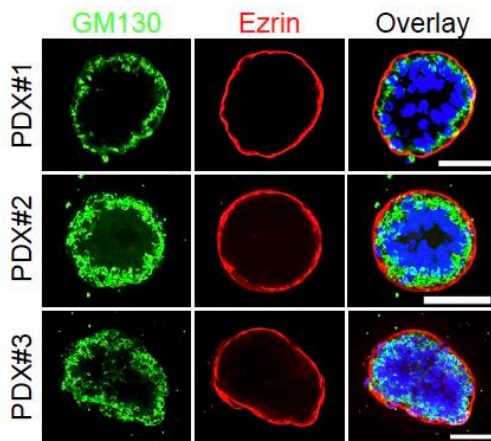
Statistics: log-rank tests for panels C and D with *P<0.05.

Supplementary Figures

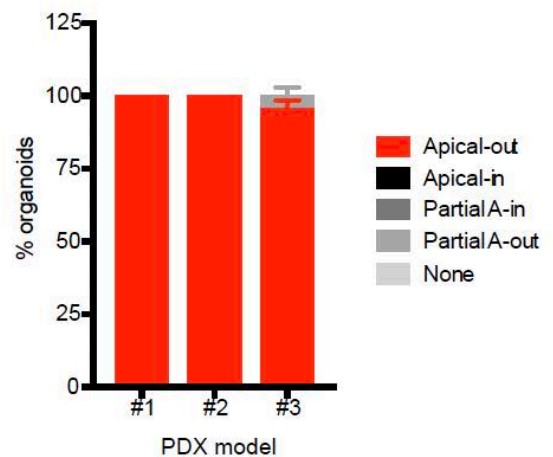
A



B



C



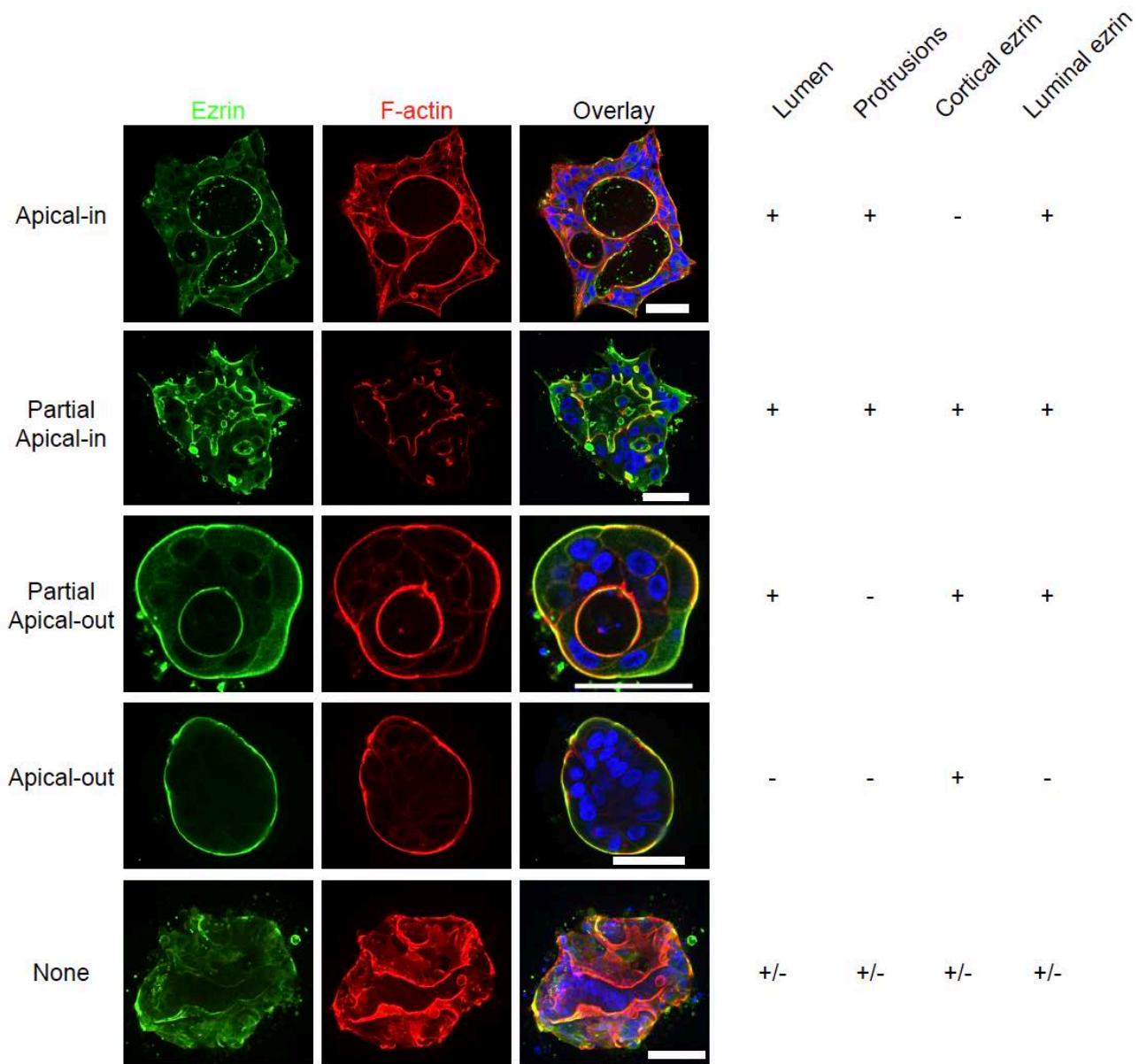
Supplementary Figure 1:

(A) HES staining of patient tumors that were used to make PDX and HES staining of 2 different passages of PDX (p7 and p10). Scale bar=250 μ m.

(B) Organoids from PDX#1, #2 and #3 fixed after 3 days in suspension and stained with GM130 (Golgi apparatus), ezrin and DAPI (blue). Scale bar=50 μ m.

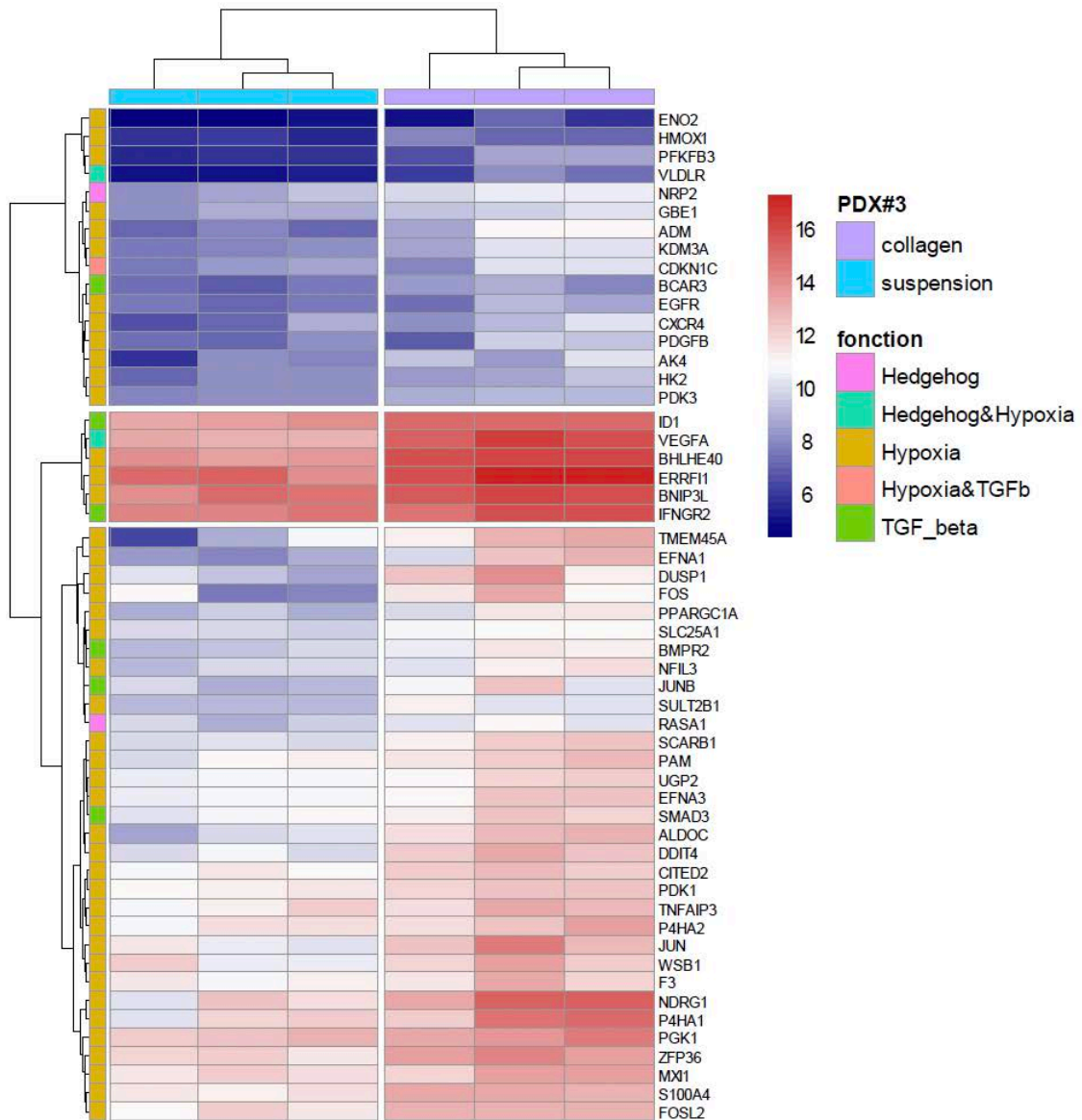
(C) Quantifications of PDX#1, #2 and #3 organoids' polarity after 3 days in in suspension for n=3 independent experiments.

Data are represented as mean \pm s.e.m.



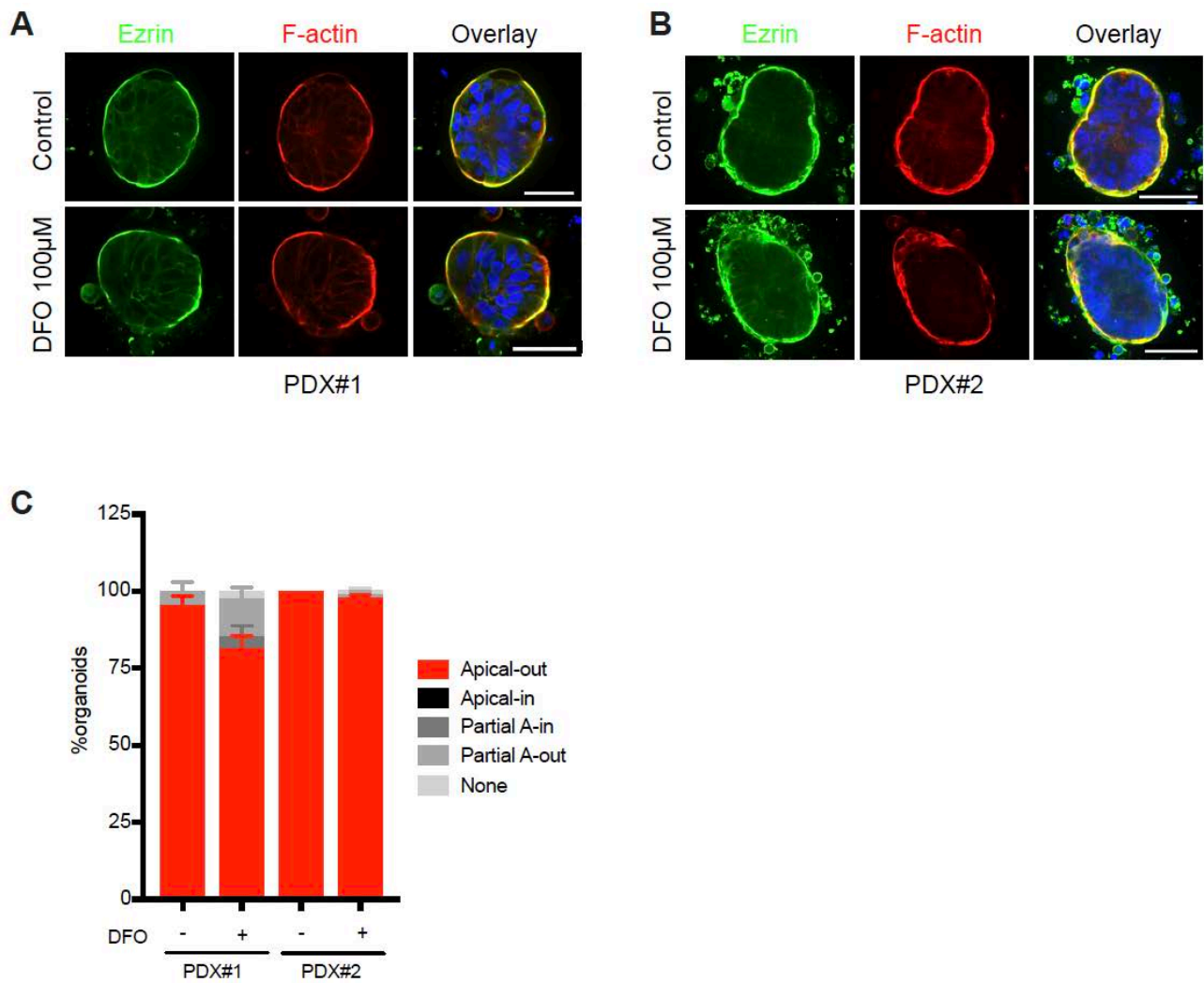
Supplementary Figure 2:

Representative images of organoids polarity after 3 to 6 days in collagen-I gels and immunostained for ezrin, F-actin and DAPI (blue). Various topologies are observed and quantified based on morphological characteristics and localization of ezrin. Scale bar=50µm.



Supplementary Figure 3 (corresponding to supplementary table 1):

In GSEA collagen-1 PDX#3 specific signature, 54 genes were found up regulated with a fold change over 2 and reclassified experimental groups.

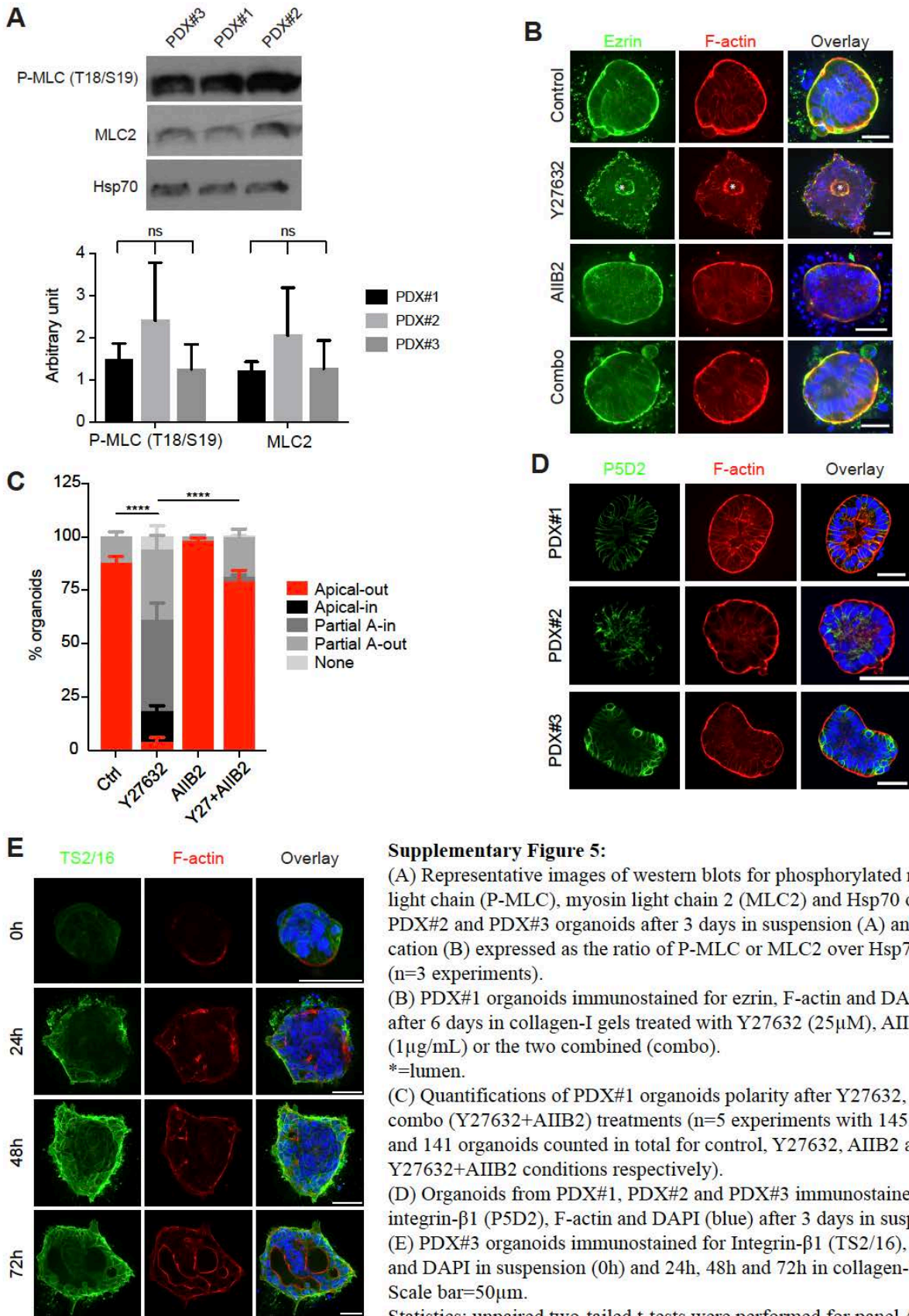


Supplementary Figure 4:

(A,B) Organoids from PDX#1 (A) and #2 (B) treated with DFO (100µM for 3 days) in collagen-I gels and immunostained for ezrin, F-actin and DAPI (blue). Scale bar=50µm.

(C) Quantifications of PDX#1 and PDX#2 organoids' phenotypes after DFO treatment (n=3 experiments with 88 and 73 PDX#1 organoids counted for control and DFO conditions respectively, and 90 PDX#2 organoids for each condition).

Data are represented as mean±s.e.m.



Supplementary Figure 5:

(A) Representative images of western blots for phosphorylated myosin light chain (P-MLC), myosin light chain 2 (MLC2) and Hsp70 of PDX#1, PDX#2 and PDX#3 organoids after 3 days in suspension (A) and quantification (B) expressed as the ratio of P-MLC or MLC2 over Hsp70 signal (n=3 experiments).

(B) PDX#1 organoids immunostained for ezrin, F-actin and DAPI (blue) after 6 days in collagen-I gels treated with Y27632 (25 μ M), AIIB2 (1 μ g/mL) or the two combined (combo).

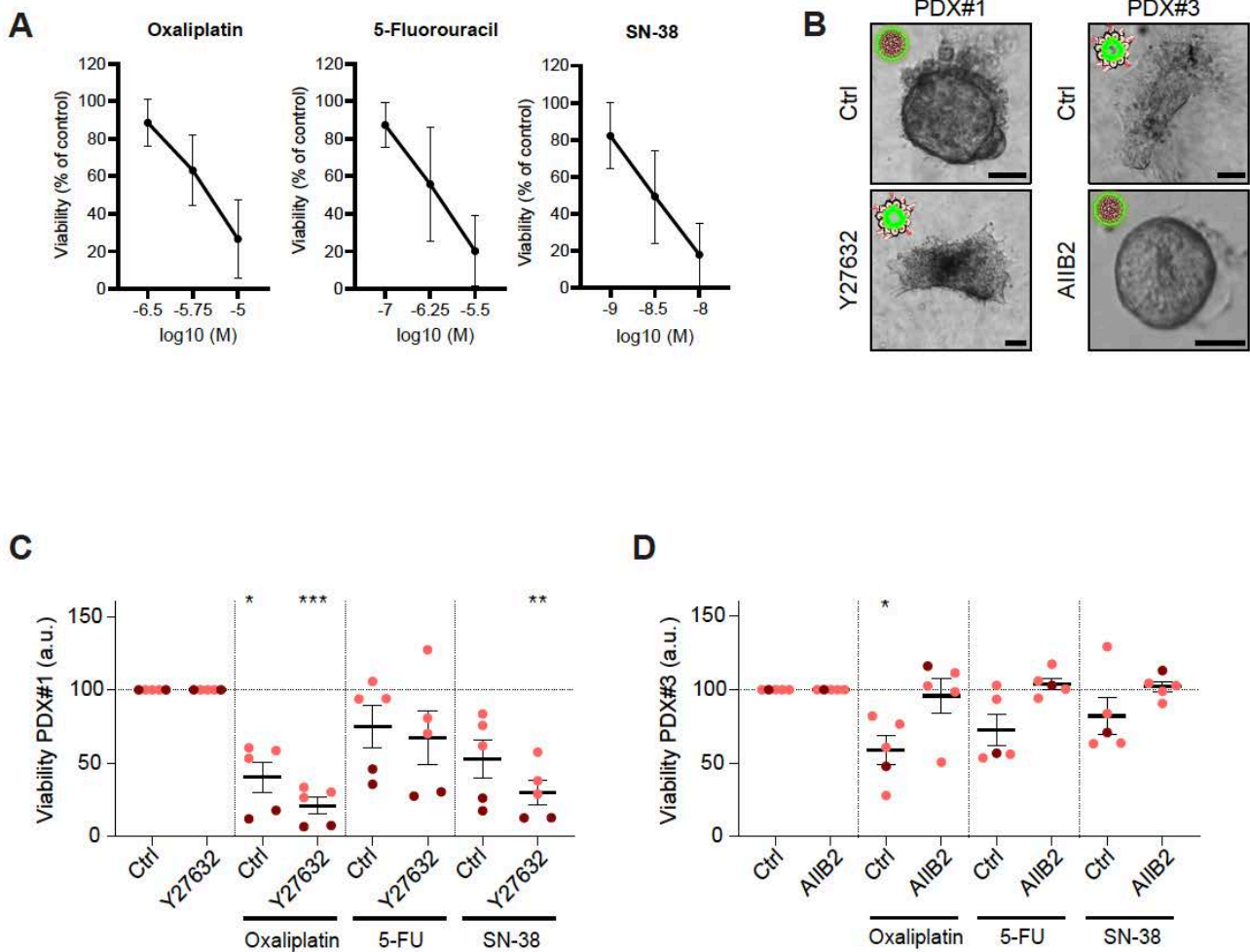
*=lumen.

(C) Quantifications of PDX#1 organoids polarity after Y27632, AIIB2 or combo (Y27632+AIIB2) treatments (n=5 experiments with 145, 141, 146 and 141 organoids counted in total for control, Y27632, AIIB2 and Y27632+AIIB2 conditions respectively).

(D) Organoids from PDX#1, PDX#2 and PDX#3 immunostained for integrin- β 1 (P5D2), F-actin and DAPI (blue) after 3 days in suspension. (E) PDX#3 organoids immunostained for Integrin- β 1 (TS2/16), F-actin and DAPI in suspension (0h) and 24h, 48h and 72h in collagen-I gel. Scale bar=50 μ m.

Statistics: unpaired two-tailed t-tests were performed for panel A, one-way ANOVA for panel C with ****P<0.0001.

Data are represented as mean \pm s.e.m.

**Supplementary Figure 6:**

(A) Average viability (measured as ATP levels quantification) as a function of chemotherapy concentration for a cohort of 25 patients CRC organoids treated with Oxaliplatin, 5-Fluorouracil and Irinotecan (SN-38), used to determine the IC₇₀. Error bars are SD.

(B) Representative bright field images of PDX#1 in control condition (Ctrl) or treated with Y27632 (25 μM) (left panel) and PDX#3 in control condition or treated with AIIB2 (1 μg/mL) (right panel). Scale bar=50 μm.

(C,D) Viability of PDX#1 (C) and PDX#3 (D) organoids in wild-type (Ctrl) or treated with Y27632 (25 μM), then incubated for 2 days (orange dots) or 4-5 days (red dots) with Oxaliplatin (10 μM), 5-Fluorouracil (5-FU, 1.8 μM) or Irinotecan (SN-38, 6.10⁻³ μM). Viability is quantified as the average ATP levels in triplicates, normalized by ATP levels of the control condition (either Ctrl, AIIB2 or Y27632) (see Material and Methods).

Statistics: one-way ANOVA for C and D with ***P<0.001, **P<0.01, *P<0.05.

Data are represented as mean±s.e.m.

Supplementary table 1

Genes regulated by collagen-I in PDX#3.

gene	PDX#3 ratio Coll/Susp	gene	PDX#3 ratio Coll/Susp	gene	PDX#3 ratio Coll/Susp
C3	45,89	BAZ2A	2,70	RGS2	-2,18
KCTD11	14,89	HIST1H2AC	2,69	NT5DC2	-2,24
CLIC3	12,91	PARP14	2,68	OGFOD1	-2,26
GPER1	11,85	CIDEB	2,66	FAM109B	-2,31
LRP1	10,43	FOXN3	2,65	SLC37A3	-2,32
ALOX15B	9,51	DOCK4	2,60	C16orf62	-2,32
CA9	8,36	MTRNR2L9	2,56	KLHL18	-2,37
SORL1	8,09	KAT2B	2,56	MRRF	-2,37
SCD	7,80	EYA4	2,55	IPO9	-2,38
CEMIP	7,34	UGT2A3	2,52	ZAK	-2,39
VEGFA	6,79	MTRNR2L6	2,51	MFSD1	-2,42
AHNAK	6,74	TLK1	2,50	ITGAE	-2,42
HSD3B1	6,13	ELMSAN1	2,50	L3MBTL2	-2,46
FLNB	5,94	TANC1	2,48	HSPA14	-2,49
DDIT4	5,87	ANO6	2,46	NUBPL	-2,51
SERPINA1	5,79	PER2	2,45	SUPT16H	-2,58
GAL3ST1	5,74	SLC41A2	2,45	SLC39A8	-2,61
SLC22A18	5,58	SPG11	2,43	CHID1	-2,64
MYO7B	5,44	PITX2	2,39	REEP4	-2,68
SYNPO	5,33	VPS13C	2,38	PADI2	-2,74
NPY4R	4,89	PRPF8	2,35	HACD3	-2,78
PRKAA2	4,87	ARL4A	2,30	CMSS1	-2,82
C6orf223	4,82	PTK6	2,29	SLC25A32	-2,91
BHLHE40	4,76	NBAS	2,27	NMU	-2,95
PRAP1	4,69	PTGR1	2,22	STEAP4	-3,05
CA2	4,47	CCL14	2,21	CLPB	-3,08
PRKCDP	4,27	MAN2A1	2,20	RTKN2	-3,10
NOXO1	4,21	SEC24A	2,19	MTHFD1	-3,27
ATP2B4	4,16	CST3	2,19	DDIAS	-3,47
CDC42BPB	3,89	SLC25A1	2,13	CACNB4	-3,49
AGRN	3,88	FZD5	2,13	TRMT1	-3,59
ACSS2	3,85	NAT8	2,12	ELOVL7	-3,66
FAM213A	3,43	PAK2	2,12	RCC1	-3,81
DYNC1H1	3,43	KDM5B	2,11	APOBEC3B	-3,84
QSER1	3,43	SECISBP2L	2,11	FANCI	-4,09
S100A4	3,35	PSD4	2,08	REP15	-4,47
TRIB3	3,23	ACSL3	2,07	CORO1A	-4,82
PTPRF	3,22	PDK3	2,07	TACC1	-4,85
TRIB2	3,07	MIA3	2,04	CDCA7L	-5,00
MSL1	3,06	PGAM1	2,03	COCH	-5,40
HMOX1	3,06	EPAS1	2,02	CGB1	-6,28
DUSP6	3,01	RPL29	2,00	TMEM173	-6,45
PRSS12	2,99	PSMD1	-2,01	CGB	-6,76
TFF3	2,98	C20orf196	-2,03	CGB8	-7,91
AMOT	2,95	COL3A1	-2,05	SLC43A1	-9,08
PIK3C2B	2,95	RRP7A	-2,05	REG1B	-11,66
PLA2R1	2,95	MED24	-2,08	HEPACAM2	-20,39
ITGB4	2,93	SETD7	-2,08	REG1A	-29,72
NBEAL1	2,93	TTC13	-2,10		
TMEM135	2,87	GLE1	-2,10		
ID1	2,82	MBTPS2	-2,12		
IGF2R	2,82	DHDDS	-2,12		
GTF2IRD2B	2,73	TFSM	-2,13		
LAMA5	2,73	SLC20A2	-2,16		
ZFAND3	2,71	CASP2	-2,17		

Supplementary table 2**Genes regulated by collagen-I in PDX#1 and PDX#2.**

gene	PDX#1 and PDX#2 ratio Coll/Susp
CCL20	34,74
UBD	23,45
CXCL8	12,68
MMP7	8,85
PI3	7,25
TNFAIP3	5,68
GLIPR1	5,65
TNFRSF9	5,24
BIRC3	4,88
PLAU	4,84
NDUFA4L2	4,41
CXCL1	4,30
SPRR2A	4,12
CXCL11	4,00
IL1B	3,91
IL32	3,46
IL1A	3,41
ARRDC3	3,08
KRT6A	3,03
S100A3	2,78
SERPINB9	2,73
DCBLD2	2,70
MAOB	2,69
VNN1	2,60
IFI6	2,56
CLIC3	2,33
LAMC2	2,22
SDC4	2,20
GUCA2A	2,20
B3GALT5	2,15
TGM2	2,13
BHLHE40	2,09
ADGRF1	2,08
SULT1B1	2,08
CD83	1,96
IFNGR2	1,96

List of figures

Figure 1. Cell migration in physiology and cancer across scales and typical associated speed.....	18
Figure 2. Main modes of cancer cell migration.	18
Figure 3. Epithelial architecture.....	21
Figure 4. Early gastrulation movements: emboly and epiboly, and specific associated cell behaviours. ...	22
Figure 5. Epithelial-to-mesenchymal transition (EMT) drives single cell motility in development.....	23
Figure 6. Molecular and structural changes associated with EMT, driven by EMT transcription factors (TFs).	24
Figure 7. <i>In vivo</i> migration of cell clusters.	25
Figure 8. Formation of branched tubular networks.	26
Figure 9. Cell migration involved in wound healing.	27
Figure 10. Gut renewal is mediated by active migration from the crypt to the tip of the villus.	29
Figure 11. Elongation of mammary ducts through proliferation, migration, and radial intercalation.....	29
Figure 12. Histological subtypes of colorectal cancer.....	31
Figure 13. Consensus molecular subtypes in colorectal cancer.	32
Figure 14. Hallmarks of cancer: 10 key features promoting tumour development.....	33
Figure 15. Tumour cells can spread through hematogenous and lymphatic circulation.....	34
Figure 16. Perineural invasion of pancreatic cancer cells.	35
Figure 17. Transcoelomic spread through peritoneum.	36
Figure 18. The environment provides paths of least resistance favouring cancer cell invasion.....	37
Figure 19. Tumour spheres with inverted polarity (TSIPs) are the main intermediates of CRC dissemination in patients.	40
Figure 20. Schematic representation of TSIPs forming by collective apical budding.....	40
Figure 21. Collective dissemination in cancer.	41
Figure 22. PDX models used to study TSIP polarity reversion.....	42
Figure 23. Techniques for studying cancer cell motility.....	43
Figure 24. Guidance of cell migration by external cues.	47
Figure 25. Types of protrusions in migrating cells and corresponding actin network (red).....	50
Figure 26. Polymerisation of actin filaments through ATP hydrolysis cycles and with different attachment constants at both ends (bold arrows).	51
Figure 27. Cellular structures (top) and corresponding actin architecture (bottom).....	52
Figure 28. Branched actin nucleation and actin polymerisation at the leading edge drive lamellipodia extension.	53
Figure 29. Putative pathways leading to upregulation of cell motility depending on the RAS (KRAS, HRAS) and BRAF activating mutations in colon cancer progression.	54
Figure 30. Myosin II drives cell contractility.....	55
Figure 31. Myosin contractility promotes blebbing and generation of polarised flows.	56
Figure 32. Activation and inactivation of small Rho GTPases by GEFs and GAPs.	56
Figure 33. Small Rho GTPases drive cell polarisation and protrusion formation through subtle regulation of actin dynamics.	57
Figure 34. Scheme of the migration modes known to date.....	58
Figure 35. Front of migrating fibroblasts in 2D and 3D environments, stained for cortactin and F-actin.	59
Figure 36. Steps of single cell mesenchymal migration.	59
Figure 37. Scheme depicting cell mesenchymal mode of migration.....	60
Figure 38. Integrin α and β dimers can form 24 combinations with different specificities to ECM components.	60
Figure 39. The maturation of focal adhesions allows cells to undergo increasing tension forces.....	61

Figure 40. Actin filament elongation and force transmission.....	62
Figure 41. The velocity of PtK1 epithelial cells (from rat kangaroo kidney) displays an optimum velocity at intermediate concentration of fibronectin (FN).....	63
Figure 42. Morphology of collective cell migration.....	64
Figure 43. Common features between collective cell migration and single cell mesenchymal migration	65
Figure 44. Position of steering cells during collective cell migration in three representative models.	66
Figure 45. Polarisation at the single cell level during epithelial collective migration of <i>Drosophila</i> follicle cells.....	67
Figure 46. Cadherin fingers in a migrating HUVEC endothelial cell sheet.....	67
Figure 47. Self-generation of directional cues during collective cell migration.....	68
Figure 48. Cell flows sustaining collective cell migration.....	69
Figure 49. Tug-of-war model.....	70
Figure 50. Main characteristics of amoeboid mode of migration.....	71
Figure 51. Schematic comparison of stresses exerted by cells during mesenchymal versus amoeboid cell migration.....	72
Figure 52. Actomyosin retrograde flow-mediated amoeboid migration.....	73
Figure 53. Amoeboid cells can use the environmental topology.....	74
Figure 54. Osmotic engine model.....	74
Figure 55. Extracellular and intracellular parameters drive determination of the mode of migration.	75
Figure 56. Cell migration plasticity.....	76
Figure 57. Mesenchymal-to-amoeboid transition (MAT).....	77
Figure 58. Switch between amoeboid and mesenchymal modes of migration upon small Rho GTPase Rac regulation.....	78
Figure 59. Mesenchymal to amoeboid transition under confinement and low adhesion.....	78
Figure 60. Deregulation of extracellular matrix in cancer progression.....	79
Figure 61. Changes in substrate stiffness drive different patterns of single cell migration.....	80
Figure 62. Cell-cell adhesion modulation during migration through partial or full EMT.....	82
Figure 63. Jamming and unjamming in epithelial monolayers.....	83
Figure 64. Changes in substrate stiffness drive different modes of collective cell migration.....	84
Figure 65. TSIPs can invade in collagen matrices in an integrin-independent but contractility-dependent fashion.....	85
Figure 66. Main known cell migration modes and determinants of their plasticity.....	86
Figure 67. Non-adhesive environments to study collective migration.....	106
Figure 68. Cell clusters from a variety of transformed and non-transformed cell types migrate collectively in non-adhesive microchannels.....	107
Figure 69. Cell clusters migration in other geometries.....	108
Figure 70. Clusters confinement is not related with migration speed.....	109
Figure 71. Characteristics of collective migration in PEG-coated microchannels.....	110
Figure 72. Clusters display no protrusive activity when migrating in PEG-coated microchannels.....	111
Figure 73. Collective migration in PEG-coated microchannels does not depend on focal adhesion formation.....	113
Figure 74. Clusters do not form focal contacts on PEG substrates, nor do they exert traction forces.....	115
Figure 75. In non-adhesive conditions, cluster migration relies on friction, which could be mediated by integrins.....	116
Figure 76. Cell clusters maintain epithelial cell-cell junctions and a supracellular actomyosin cortex when confined in non-adhesive microchannels.....	118
Figure 77. The contractility of the polarised acto-myosin cortex drives focal-adhesion independent collective migration.....	119
Figure 78. Polarised RhoA and Rac1 activity dictate cluster direction of migration.....	122

Figure 79. Nuclei of the outer cell layer are more deformed, but this does not lead to cluster increased contractility and polarisation through cPLA2 pathway.	123
Figure 80. Clusters translate as solids with no persistent cell flows.	124
Figure 81. Cell clusters do not display persistent retrograde myosin flows during migration in non-adhesive microchannels.	125
Figure 82. Myosin jiggling promotes cluster instantaneous displacement and, with myosin polarisation, directed motion.	127
Figure 83. Cellular jiggling promotes cluster migration over long timescales.	128
Figure 84. Model of collective amoeboid migration, driven by polarised jiggling.	130
Figure 85. Scheme of cell migration modes.	131
Figure 86. Automated image segmentation and cluster tracking.	133
Figure 87. Organoid reversion and determination of drug concentration.	138
Figure 88. TSIPs and PDX#3 clusters are less sensitive to chemotherapies in their apical-out conformation.	139
Figure 89. Apical-out spheres display lower proliferation rate and their presence correlates with lower patients survival.	141

References

- Abercrombie, M. (1980). The Croonian Lecture, 1978 - The crawling movement of metazoan cells. *Proc. R. Soc. Lond. B* 207, 129–147. <https://doi.org/10.1098/rspb.1980.0017>.
- Aceto, N., Bardia, A., Miyamoto, D.T., Donaldson, M.C., Wittner, B.S., Spencer, J.A., Yu, M., Pely, A., Engstrom, A., Zhu, H., et al. (2014). Circulating Tumor Cell Clusters Are Oligoclonal Precursors of Breast Cancer Metastasis. *Cell* 158, 1110–1122. <https://doi.org/10.1016/j.cell.2014.07.013>.
- Alberts, B., Johnson, A., Lewis, J., Raff, M., Roberts, K., and Walter, P. (2002). *The Extracellular Matrix of Animals. Molecular Biology of the Cell*. 4th Edition.
- Alberts, B., Bray, D., Hopkin, K., Johnson, A., Lewis, J., Raff, M., Roberts, K., and Walter, P. (2010). *Essential Cell Biology* (Garland Science).
- Alert, R., and Trepast, X. (2020). Physical Models of Collective Cell Migration. *Annu. Rev. Condens. Matter Phys.* 11, 77–101. <https://doi.org/10.1146/annurev-conmatphys-031218-013516>.
- Alitalo, A., and Detmar, M. (2012). Interaction of tumor cells and lymphatic vessels in cancer progression. *Oncogene* 31, 4499–4508. <https://doi.org/10.1038/onc.2011.602>.
- Amit, M., Na'ara, S., and Gil, Z. (2016). Mechanisms of cancer dissemination along nerves. *Nat Rev Cancer* 16, 399–408. <https://doi.org/10.1038/nrc.2016.38>.
- Andrew, N., and Insall, R.H. (2007). Chemotaxis in shallow gradients is mediated independently of PtdIns 3-kinase by biased choices between random protrusions. *Nat Cell Biol* 9, 193–200. <https://doi.org/10.1038/ncb1536>.
- Aoyagi, T., Terracina, K.P., Raza, A., and Takabe, K. (2014). Current treatment options for colon cancer peritoneal carcinomatosis. *World Journal of Gastroenterology* 20, 12493–12500. <https://doi.org/10.3748/wjg.v20.i35.12493>.
- Aplin, J.D., and Ruane, P.T. (2017). Embryo–epithelium interactions during implantation at a glance. *J Cell Sci* 130, 15–22. <https://doi.org/10.1242/jcs.175943>.
- Ashley, N., Ouaret, D., and Bodmer, W.F. (2019). Cellular polarity modulates drug resistance in primary colorectal cancers via orientation of the multidrug resistance protein ABCB1. *The Journal of Pathology* 247, 293–304. <https://doi.org/10.1002/path.5179>.
- Bapat, A.A., Hostetter, G., Von Hoff, D.D., and Han, H. (2011). Perineural invasion and associated pain in pancreatic cancer. *Nat Rev Cancer* 11, 695–707. <https://doi.org/10.1038/nrc3131>.
- Barker, N., Ridgway, R.A., van Es, J.H., van de Wetering, M., Begthel, H., van den Born, M., Danenberg, E., Clarke, A.R., Sansom, O.J., and Clevers, H. (2009). Crypt stem cells as the cells-of-origin of intestinal cancer. *Nature* 457, 608–611. <https://doi.org/10.1038/nature07602>.
- Barr, V.A., and Bunnell, S.C. (2009). Interference Reflectance Microscopy. *Curr Protoc Cell Biol* CHAPTER, Unit-4.23. <https://doi.org/10.1002/0471143030.cb0423s45>.
- Barresi, V., Reggiani Bonetti, L., Vitarelli, E., Di Gregorio, C., Ponz de Leon, M., and Barresi, G. (2012). Immunohistochemical assessment of lymphovascular invasion in stage I colorectal carcinoma: prognostic relevance and correlation with nodal micrometastases. *Am. J. Surg. Pathol.* 36, 66–72. <https://doi.org/10.1097/PAS.0b013e31822d3008>.
- Barresi, V., Reggiani Bonetti, L., Ieni, A., Domati, F., and Tuccari, G. (2015). Prognostic significance of grading based on the counting of poorly differentiated clusters in colorectal mucinous adenocarcinoma. *Hum Pathol* 46, 1722–1729. <https://doi.org/10.1016/j.humphath.2015.07.013>.

- Barriga, E.H., Franze, K., Charras, G., and Mayor, R. (2018). Tissue stiffening coordinates morphogenesis by triggering collective cell migration in vivo. *Nature* 554, 523–527. <https://doi.org/10.1038/nature25742>.
- Baule, A., Kumar, K.V., and Ramaswamy, S. (2008). Exact solution of a Brownian inchworm model for self-propulsion. *J. Stat. Mech.* 2008, P11008. <https://doi.org/10.1088/1742-5468/2008/11/P11008>.
- Bear, J.E., and Haugh, J.M. (2014). Directed migration of mesenchymal cells: where signaling and the cytoskeleton meet. *Current Opinion in Cell Biology* 30, 74–82. <https://doi.org/10.1016/j.ceb.2014.06.005>.
- Beaune, G., Blanch-Mercader, C., Douezan, S., Dumond, J., Gonzalez-Rodriguez, D., Cuvelier, D., Ondarçuhu, T., Sens, P., Dufour, S., Murrell, M.P., et al. (2018). Spontaneous migration of cellular aggregates from giant keratocytes to running spheroids. *Proc Natl Acad Sci USA* 115, 12926–12931. <https://doi.org/10.1073/pnas.1811348115>.
- Beco, S. de, Vaidžiulytė, K., Manzi, J., Dalier, F., Federico, F. di, Cornilleau, G., Dahan, M., and Coppey, M. (2018). Optogenetic dissection of Rac1 and Cdc42 gradient shaping. *Nat Commun* 9, 1–13. <https://doi.org/10.1038/s41467-018-07286-8>.
- Beerling, E., Ritsma, L., Vriskoop, N., Derksen, P.W.B., and van Rheenen, J. (2011). Intravital microscopy: new insights into metastasis of tumors. *Journal of Cell Science* 124, 299–310. <https://doi.org/10.1242/jcs.072728>.
- Bergert, M., Erzberger, A., Desai, R.A., Aspalter, I.M., Oates, A.C., Charras, G., Salbreux, G., and Paluch, E.K. (2015). Force transmission during adhesion-independent migration. *Nat. Cell Biol.* 17, 524–529. <https://doi.org/10.1038/ncb3134>.
- Betapudi, V. (2014). Life without double-headed non-muscle myosin II motor proteins. *Frontiers in Chemistry* 2, 45. <https://doi.org/10.3389/fchem.2014.00045>.
- Binamé, F., Bidaud-Meynard, A., Magnan, L., Piquet, L., Montibus, B., Chabadel, A., Saltel, F., Lagrée, V., and Moreau, V. (2016). Cancer-associated mutations in the protrusion-targeting region of p190RhoGAP impact tumor cell migration. *Journal of Cell Biology* 214, 859–873. <https://doi.org/10.1083/jcb.201601063>.
- Bodor, D.L., Pönisch, W., Endres, R.G., and Paluch, E.K. (2020). Of Cell Shapes and Motion: The Physical Basis of Animal Cell Migration. *Dev. Cell* 52, 550–562. <https://doi.org/10.1016/j.devcel.2020.02.013>.
- te Boekhorst, V., and Friedl, P. (2016). Chapter Seven - Plasticity of Cancer Cell Invasion—Mechanisms and Implications for Therapy. In *Advances in Cancer Research*, D.R. Welch, and P.B. Fisher, eds. (Academic Press), pp. 209–264.
- Boutillon, A., Giger, F.A., and David, N.B. (2018). Analysis of In Vivo Cell Migration in Mosaic Zebrafish Embryos. In *Cell Migration*, A. Gautreau, ed. (New York, NY: Springer New York), pp. 213–226.
- Boyer, B., Tucker, G.C., Vallés, A.M., Franke, W.W., and Thiery, J.P. (1989). Rearrangements of desmosomal and cytoskeletal proteins during the transition from epithelial to fibroblastoid organization in cultured rat bladder carcinoma cells. *Journal of Cell Biology* 109, 1495–1509. <https://doi.org/10.1083/jcb.109.4.1495>.
- Bray, F., Ferlay, J., Soerjomataram, I., Siegel, R.L., Torre, L.A., and Jemal, A. (2018). Global cancer statistics 2018: GLOBOCAN estimates of incidence and mortality worldwide for 36 cancers in 185 countries. *CA: A Cancer Journal for Clinicians* 68, 394–424. <https://doi.org/10.3322/caac.21492>.
- Brenner, H., Kloor, M., and Pox, C.P. (2014). Colorectal cancer. *The Lancet* 383, 1490–1502. [https://doi.org/10.1016/S0140-6736\(13\)61649-9](https://doi.org/10.1016/S0140-6736(13)61649-9).
- Bronsert, P., Enderle-Ammour, K., Bader, M., Timme, S., Kuehs, M., Csanadi, A., Kayser, G., Kohler, I., Bausch, D., Hoepfner, J., et al. (2014). Cancer cell invasion and EMT marker expression: a three-dimensional study of the human cancer–host interface. *The Journal of Pathology* 234, 410–422. <https://doi.org/10.1002/path.4416>.
- Brown, M., Assen, F.P., Leithner, A., Abe, J., Schachner, H., Asfour, G., Bago-Horvath, Z., Stein, J.V., Uhrin, P.,

- Sixt, M., et al. (2018). Lymph node blood vessels provide exit routes for metastatic tumor cell dissemination in mice. *Science* 359, 1408–1411. <https://doi.org/10.1126/science.aal3662>.
- Burute, M., Prioux, M., Blin, G., Truchet, S., Letort, G., Tseng, Q., Bessy, T., Lowell, S., Young, J., Filhol, O., et al. (2017). Polarity Reversal by Centrosome Repositioning Primes Cell Scattering during Epithelial-to-Mesenchymal Transition. *Developmental Cell* 40, 168–184. <https://doi.org/10.1016/j.devcel.2016.12.004>.
- Cai, D., Chen, S.-C., Prasad, M., He, L., Wang, X., Choemmel-Cadamuro, V., Sawyer, J.K., Danuser, G., and Montell, D.J. (2014). Mechanical Feedback through E-Cadherin Promotes Direction Sensing during Collective Cell Migration. *Cell* 157, 1146–1159. <https://doi.org/10.1016/j.cell.2014.03.045>.
- Callan-Jones, A.C., and Voituriez, R. (2016). Actin flows in cell migration: from locomotion and polarity to trajectories. *Current Opinion in Cell Biology* 38, 12–17. <https://doi.org/10.1016/j.ceb.2016.01.003>.
- Calon, A., Lonardo, E., Berenguer-Llergo, A., Espinet, E., Hernando-Momblona, X., Iglesias, M., Sevillano, M., Palomo-Ponce, S., Tauriello, D.V.F., Byrom, D., et al. (2015). Stromal gene expression defines poor-prognosis subtypes in colorectal cancer. *Nat Genet* 47, 320–329. <https://doi.org/10.1038/ng.3225>.
- Cano, A., Pérez-Moreno, M.A., Rodrigo, I., Locascio, A., Blanco, M.J., del Barrio, M.G., Portillo, F., and Nieto, M.A. (2000). The transcription factor Snail controls epithelial–mesenchymal transitions by repressing E-cadherin expression. *Nat Cell Biol* 2, 76–83. <https://doi.org/10.1038/35000025>.
- Cardoso Dos Santos, M., Déturche, R., Vézy, C., and Jaffiol, R. (2016). Topography of Cells Revealed by Variable-Angle Total Internal Reflection Fluorescence Microscopy. *Biophysical Journal* 111, 1316–1327. <https://doi.org/10.1016/j.bpj.2016.06.043>.
- Case, L.B., and Waterman, C.M. (2015). Integration of actin dynamics and cell adhesion by a three-dimensional, mechanosensitive molecular clutch. *Nat. Cell Biol.* 17, 955–963. <https://doi.org/10.1038/ncb3191>.
- Chabaud, M., Heuzé, M.L., Bretou, M., Vargas, P., Maiuri, P., Solanes, P., Maurin, M., Terriac, E., Le Berre, M., Lankar, D., et al. (2015). Cell migration and antigen capture are antagonistic processes coupled by myosin II in dendritic cells. *Nat Commun* 6, 7526. <https://doi.org/10.1038/ncomms8526>.
- Chamier, L. von, Laine, R.F., Jukkala, J., Spahn, C., Krentzel, D., Nehme, E., Lerche, M., Hernández-Pérez, S., Mattila, P.K., Karinou, E., et al. (2020). ZeroCostDL4Mic: an open platform to use Deep-Learning in Microscopy (Bioinformatics).
- Charras, G., and Paluch, E. (2008). Blebs lead the way: how to migrate without lamellipodia. *Nat Rev Mol Cell Biol* 9, 730–736. <https://doi.org/10.1038/nrm2453>.
- Charrasse, S., Comunale, F., Grumbach, Y., Poulat, F., Blangy, A., and Gauthier-Rouvière, C. (2006). RhoA GTPase Regulates M-Cadherin Activity and Myoblast Fusion. *MBoC* 17, 749–759. <https://doi.org/10.1091/mbc.e05-04-0284>.
- Chen, Y., Kotian, N., Aranjuez, G., Chen, L., Messer, C.L., Burtscher, A., Sawant, K., Ramel, D., Wang, X., and McDonald, J.A. (2020). Protein phosphatase 1 activity controls a balance between collective and single cell modes of migration. *ELife* 9. <https://doi.org/10.7554/eLife.52979>.
- Cheung, K.J., and Ewald, A.J. (2016). A collective route to metastasis: Seeding by tumor cell clusters. *Science* 352, 167–169. <https://doi.org/10.1126/science.aaf6546>.
- Cheung, K.J., Gabrielson, E., Werb, Z., and Ewald, A.J. (2013). Collective Invasion in Breast Cancer Requires a Conserved Basal Epithelial Program. *Cell* 155, 1639–1651. <https://doi.org/10.1016/j.cell.2013.11.029>.
- Cheung, K.J., Padmanaban, V., Silvestri, V., Schipper, K., Cohen, J.D., Fairchild, A.N., Gorin, M.A., Verdone, J.E., Pienta, K.J., Bader, J.S., et al. (2016). Polyclonal breast cancer metastases arise from collective dissemination of keratin 14-expressing tumor cell clusters. *Proc. Natl. Acad. Sci. U.S.A.* 113, E854–863.

<https://doi.org/10.1073/pnas.1508541113>.

Christiansen, J.J., and Rajasekaran, A.K. (2006). Reassessing Epithelial to Mesenchymal Transition as a Prerequisite for Carcinoma Invasion and Metastasis. *Cancer Res* 66, 8319–8326. <https://doi.org/10.1158/0008-5472.CAN-06-0410>.

Chuai, M., Hughes, D., and Weijer, C.J. (2012). Collective Epithelial and Mesenchymal Cell Migration During Gastrulation. *Curr Genomics* 13, 267–277. <https://doi.org/10.2174/138920212800793357>.

Ciobanasiu, C., Faivre, B., and Le Clainche, C. (2014). Actomyosin-dependent formation of the mechanosensitive talin–vinculin complex reinforces actin anchoring. *Nature Communications* 5, 3095. <https://doi.org/10.1038/ncomms4095>.

Clark, A.G., and Vignjevic, D.M. (2015). Modes of cancer cell invasion and the role of the microenvironment. *Current Opinion in Cell Biology* 36, 13–22. <https://doi.org/10.1016/j.ceb.2015.06.004>.

Clark, A.G., Maitra, A., Jacques, C., Simon, A., Pérez-González, C., Trepap, X., Voituriez, R., and Vignjevic, D.M. (2020). Viscoelastic relaxation of collagen networks provides a self-generated directional cue during collective migration. *BioRxiv* 2020.07.11.198739. <https://doi.org/10.1101/2020.07.11.198739>.

Clevers, H. (2016). Modeling Development and Disease with Organoids. *Cell* 165, 1586–1597. <https://doi.org/10.1016/j.cell.2016.05.082>.

Coles, C.H., and Bradke, F. (2015). Coordinating neuronal actin-microtubule dynamics. *Current Biology: CB* 25, R677–691. <https://doi.org/10.1016/j.cub.2015.06.020>.

Combedazou, A., Choismel-Cadamuro, V., Gay, G., Liu, J., Dupré, L., Ramel, D., and Wang, X. (2017). Myosin II governs collective cell migration behaviour downstream of guidance receptor signalling. *J Cell Sci* 130, 97–103. <https://doi.org/10.1242/jcs.179952>.

Condeelis, J. (1990). Molecular Analysis of Amoeboid Chemotaxis. *Cancer Investigation* 8, 659–660. <https://doi.org/10.3109/07357909009018939>.

Consalvo, K.M., Rijal, R., Tang, Y., Kirolos, S.A., Smith, M.R., and Gomer, R.H. (2019). Extracellular signaling in Dictyostelium. *Int. J. Dev. Biol.* 63, 395–405. <https://doi.org/10.1387/ijdb.190259rg>.

Cornillon, S., Gebbie, L., Benghezal, M., Nair, P., Keller, S., Wehrle-Haller, B., Charette, S.J., Brückert, F., Letourneur, F., and Cosson, P. (2006). An adhesion molecule in free-living Dictyostelium amoebae with integrin β features. *EMBO Rep* 7, 617–621. <https://doi.org/10.1038/sj.embor.7400701>.

Cortés-Guiral, D., Hübner, M., Alyami, M., Bhatt, A., Ceelen, W., Glehen, O., Lordick, F., Ramsay, R., Sgarbura, O., Van Der Speeten, K., et al. (2021). Primary and metastatic peritoneal surface malignancies. *Nat Rev Dis Primers* 7, 1–23. <https://doi.org/10.1038/s41572-021-00326-6>.

Cremers, B., Flesch, M., Kostenis, E., Maack, C., Niedernberg, A., Stoff, A., Südkamp, M., Wendler, O., and Böhm, M. (2003). Modulation of myocardial contractility by lysophosphatidic acid (LPA). *J Mol Cell Cardiol* 35, 71–80. [https://doi.org/10.1016/s0022-2828\(02\)00279-1](https://doi.org/10.1016/s0022-2828(02)00279-1).

Crosas-Molist, E., Samain, R., Kohlhammer, L., Orgaz, J.L., George, S.L., Maiques, O., Barcelo, J., and Sanz-Moreno, V. (2022). Rho GTPase signaling in cancer progression and dissemination. *Physiological Reviews* 102, 455–510. <https://doi.org/10.1152/physrev.00045.2020>.

Cui, Y., Cole, S., Pepper, J., Otero, J.J., and Winter, J.O. (2020). Hyaluronic acid induces ROCK-dependent amoeboid migration in glioblastoma cells. *Biomater Sci* <https://doi.org/10.1039/d0bm00505c>.

Dalle Nogare, D., Somers, K., Rao, S., Matsuda, M., Reichman-Fried, M., Raz, E., and Chitnis, A.B. (2014). Leading and trailing cells cooperate in collective migration of the zebrafish posterior lateral line primordium. *Development*

141, 3188–3196. <https://doi.org/10.1242/dev.106690>.

David, N.B., Sapède, D., Saint-Etienne, L., Thisse, C., Thisse, B., Dambly-Chaudière, C., Rosa, F.M., and Ghysen, A. (2002). Molecular basis of cell migration in the fish lateral line: Role of the chemokine receptor CXCR4 and of its ligand, SDF1. *PNAS* *99*, 16297–16302. <https://doi.org/10.1073/pnas.252339399>.

Davis, J.R., Luchici, A., Mosis, F., Thackery, J., Salazar, J.A., Mao, Y., Dunn, G.A., Betz, T., Miodownik, M., and Stramer, B.M. (2015). Inter-cellular forces orchestrate contact inhibition of locomotion. *Cell* *161*, 361–373. <https://doi.org/10.1016/j.cell.2015.02.015>.

Deblais, A., Barois, T., Guerin, T., Delville, P.H., Vaudaine, R., Lintuvuori, J.S., Boudet, J.F., Baret, J.C., and Kellay, H. (2018). Boundaries Control Collective Dynamics of Inertial Self-Propelled Robots. *Phys Rev Lett* *120*, 188002. <https://doi.org/10.1103/PhysRevLett.120.188002>.

Dekker, E., Tanis, P.J., Vleugels, J.L.A., Kasi, P.M., and Wallace, M.B. (2019). Colorectal cancer. *The Lancet* *394*, 1467–1480. [https://doi.org/10.1016/S0140-6736\(19\)32319-0](https://doi.org/10.1016/S0140-6736(19)32319-0).

Dillekås, H., Rogers, M.S., and Straume, O. (2019). Are 90% of deaths from cancer caused by metastases? *Cancer Medicine* *8*, 5574–5576. <https://doi.org/10.1002/cam4.2474>.

Dogterom, M., and Koenderink, G.H. (2019). Actin–microtubule crosstalk in cell biology. *Nature Reviews Molecular Cell Biology* *20*, 38–54. <https://doi.org/10.1038/s41580-018-0067-1>.

Doyle, A.D., Sykora, D.J., Pacheco, G.G., Kutys, M.L., and Yamada, K.M. (2021). 3D mesenchymal cell migration is driven by anterior cellular contraction that generates an extracellular matrix prestrain. *Developmental Cell* *56*, 826–841.e4. <https://doi.org/10.1016/j.devcel.2021.02.017>.

Drost, J., Karthaus, W.R., Gao, D., Driehuis, E., Sawyers, C.L., Chen, Y., and Clevers, H. (2016). Organoid culture systems for prostate epithelial and cancer tissue. *Nat Protoc* *11*, 347–358. <https://doi.org/10.1038/nprot.2016.006>.

DuChez, B.J., Doyle, A.D., Dimitriadis, E.K., and Yamada, K.M. (2019). Durotaxis by Human Cancer Cells. *Biophysical Journal* *116*, 670–683. <https://doi.org/10.1016/j.bpj.2019.01.009>.

Dumortier, J.G., Martin, S., Meyer, D., Rosa, F.M., and David, N.B. (2012). Collective mesendoderm migration relies on an intrinsic directionality signal transmitted through cell contacts. *PNAS* *109*, 16945–16950. <https://doi.org/10.1073/pnas.1205870109>.

Dupont, S., Morsut, L., Aragona, M., Enzo, E., Giulitti, S., Cordenonsi, M., Zanconato, F., Le Digabel, J., Forcato, M., Bicciato, S., et al. (2011). Role of YAP/TAZ in mechanotransduction. *Nature* *474*, 179–183. <https://doi.org/10.1038/nature10137>.

Dyberg, C., Andonova, T., Olsen, T.K., Brodin, B., Kool, M., Kogner, P., Johnsen, J.I., and Wickström, M. (2019). Inhibition of Rho-Associated Kinase Suppresses Medulloblastoma Growth. *Cancers* *12*. <https://doi.org/10.3390/cancers12010073>.

Epstein, J.A., and Parmacek, M.S. (2005). Recent Advances in Cardiac Development With Therapeutic Implications for Adult Cardiovascular Disease. *Circulation* *112*, 592–597. <https://doi.org/10.1161/CIRCULATIONAHA.104.479857>.

Etienne-Manneville, S., and Hall, A. (2002). Rho GTPases in cell biology. *Nature* *420*, 629–635. <https://doi.org/10.1038/nature01148>.

Etienne-Manneville, S., and Hall, A. (2003). Cdc42 regulates GSK-3 β and adenomatous polyposis coli to control cell polarity. *Nature* *421*, 753–756. <https://doi.org/10.1038/nature01423>.

Evers, E.E., Zondag, G.C.M., Malliri, A., Price, L.S., ten Klooster, J.-P., van der Kammen, R.A., and Collard, J.G. (2000). Rho family proteins in cell adhesion and cell migration. *European Journal of Cancer* *36*, 1269–1274.

[https://doi.org/10.1016/S0959-8049\(00\)00091-5](https://doi.org/10.1016/S0959-8049(00)00091-5).

Ewald, A.J., Brenot, A., Duong, M., Chan, B.S., and Werb, Z. (2008). Collective Epithelial Migration and Cell Rearrangements Drive Mammary Branching Morphogenesis. *Developmental Cell* 14, 570–581. <https://doi.org/10.1016/j.devcel.2008.03.003>.

Ewald, A.J., Huebner, R.J., Palsdottir, H., Lee, J.K., Perez, M.J., Jorgens, D.M., Tauscher, A.N., Cheung, K.J., Werb, Z., and Auer, M. (2012). Mammary collective cell migration involves transient loss of epithelial features and individual cell migration within the epithelium. *Journal of Cell Science* 125, 2638–2654. <https://doi.org/10.1242/jcs.096875>.

Fan, F., Samuel, S., Evans, K.W., Lu, J., Xia, L., Zhou, Y., Sceusi, E., Tozzi, F., Ye, X.-C., Mani, S.A., et al. (2012). Overexpression of Snail induces epithelial–mesenchymal transition and a cancer stem cell–like phenotype in human colorectal cancer cells. *Cancer Medicine* 1, 5–16. <https://doi.org/10.1002/cam4.4>.

Fessler, E., and Medema, J.P. (2016). Colorectal Cancer Subtypes: Developmental Origin and Microenvironmental Regulation. *Trends Cancer* 2, 505–518. <https://doi.org/10.1016/j.trecan.2016.07.008>.

Fischer, K.R., Durrans, A., Lee, S., Sheng, J., Li, F., Wong, S.T.C., Choi, H., El Rayes, T., Ryu, S., Troeger, J., et al. (2015). Epithelial-to-mesenchymal transition is not required for lung metastasis but contributes to chemoresistance. *Nature* 527, 472–476. <https://doi.org/10.1038/nature15748>.

Fischer, M., Franzeck, U.K., Herrig, I., Costanzo, U., Wen, S., Schiesser, M., Hoffmann, U., and Bollinger, A. (1996). Flow velocity of single lymphatic capillaries in human skin. *Am J Physiol* 270, H358–363. <https://doi.org/10.1152/ajpheart.1996.270.1.H358>.

Fletcher, D.A., and Mullins, R.D. (2010). Cell mechanics and the cytoskeleton. *Nature* 463, 485–492. <https://doi.org/10.1038/nature08908>.

van der Flier, L.G., and Clevers, H. (2009). Stem cells, self-renewal, and differentiation in the intestinal epithelium. *Annu Rev Physiol* 71, 241–260. <https://doi.org/10.1146/annurev.physiol.010908.163145>.

Friedl, P., and Alexander, S. (2011). Cancer invasion and the microenvironment: plasticity and reciprocity. *Cell* 147, 992–1009. <https://doi.org/10.1016/j.cell.2011.11.016>.

Friedl, P., and Bröcker, E.-B. (2000). The biology of cell locomotion within three-dimensional extracellular matrix. *CMLS, Cell. Mol. Life Sci.* 57, 41–64. <https://doi.org/10.1007/s000180050498>.

Friedl, P., and Gilmour, D. (2009). Collective cell migration in morphogenesis, regeneration and cancer. *Nat. Rev. Mol. Cell Biol.* 10, 445–457. <https://doi.org/10.1038/nrm2720>.

Friedl, P., and Mayor, R. (2017). Tuning Collective Cell Migration by Cell–Cell Junction Regulation. *Cold Spring Harb Perspect Biol* 9, a029199. <https://doi.org/10.1101/cshperspect.a029199>.

Friedl, P., and Wolf, K. (2003). Tumour-cell invasion and migration: diversity and escape mechanisms. *Nat Rev Cancer* 3, 362–374. <https://doi.org/10.1038/nrc1075>.

Friedl, P., and Wolf, K. (2010). Plasticity of cell migration: a multiscale tuning model. *The Journal of Cell Biology* 188, 11–19. <https://doi.org/10.1083/jcb.200909003>.

Friedl, P., Noble, P.B., Walton, P.A., Laird, D.W., Chauvin, P.J., Tabah, R.J., Black, M., and Zänker, K.S. (1995). Migration of coordinated cell clusters in mesenchymal and epithelial cancer explants in vitro. *Cancer Res.* 55, 4557–4560. .

Friedl, P., Borgmann, S., and Bröcker, E.-B. (2001). Amoeboid leukocyte crawling through extracellular matrix: lessons from the Dictyostelium paradigm of cell movement. *Journal of Leukocyte Biology* 70, 491–509. <https://doi.org/10.1189/jlb.70.4.491>.

- Friedl, P., Locker, J., Sahai, E., and Segall, J.E. (2012). Classifying collective cancer cell invasion. *Nat. Cell Biol.* *14*, 777–783. <https://doi.org/10.1038/ncb2548>.
- Fritz-Laylin, L.K., Lord, S.J., and Mullins, R.D. (2017a). WASP and SCAR are evolutionarily conserved in actin-filled pseudopod-based motility. *Journal of Cell Biology* *216*, 1673–1688. <https://doi.org/10.1083/jcb.201701074>.
- Fritz-Laylin, L.K., Riel-Mehan, M., Chen, B.-C., Lord, S.J., Goddard, T.D., Ferrin, T.E., Nicholson-Dykstra, S.M., Higgs, H., Johnson, G.T., Betzig, E., et al. (2017b). Actin-based protrusions of migrating neutrophils are intrinsically lamellar and facilitate direction changes. *ELife* *6*, e26990. <https://doi.org/10.7554/eLife.26990>.
- Fujimori, T., Nakajima, A., Shimada, N., and Sawai, S. (2019). Tissue self-organization based on collective cell migration by contact activation of locomotion and chemotaxis. *Proc Natl Acad Sci USA* *116*, 4291–4296. <https://doi.org/10.1073/pnas.1815063116>.
- Gaggioli, C., Hooper, S., Hidalgo-Carcedo, C., Grosse, R., Marshall, J.F., Harrington, K., and Sahai, E. (2007). Fibroblast-led collective invasion of carcinoma cells with differing roles for RhoGTPases in leading and following cells. *Nat Cell Biol* *9*, 1392–1400. <https://doi.org/10.1038/ncb1658>.
- Gardel, M.L., Schneider, I.C., Aratyn-Schaus, Y., and Waterman, C.M. (2010). Mechanical integration of actin and adhesion dynamics in cell migration. *Annu Rev Cell Dev Biol* *26*, 315–333. <https://doi.org/10.1146/annurev.cellbio.011209.122036>.
- Gerhardt, H., Golding, M., Fruttiger, M., Ruhrberg, C., Lundkvist, A., Abramsson, A., Jeltsch, M., Mitchell, C., Alitalo, K., Shima, D., et al. (2003). VEGF guides angiogenic sprouting utilizing endothelial tip cell filopodia. *Journal of Cell Biology* *161*, 1163–1177. <https://doi.org/10.1083/jcb.200302047>.
- Ghabrial, A., Luschnig, S., Metzstein, M.M., and Krasnow, M.A. (2003). Branching morphogenesis of the *Drosophila* tracheal system. *Annu Rev Cell Dev Biol* *19*, 623–647. <https://doi.org/10.1146/annurev.cellbio.19.031403.160043>.
- Ghysen, A., and Dambly-Chaudière, C. (2007). The lateral line microcosmos. *Genes Dev.* *21*, 2118–2130. <https://doi.org/10.1101/gad.1568407>.
- Giampieri, S., Manning, C., Hooper, S., Jones, L., Hill, C.S., and Sahai, E. (2009). Localized and reversible TGFbeta signalling switches breast cancer cells from cohesive to single cell motility. *Nat. Cell Biol.* *11*, 1287–1296. <https://doi.org/10.1038/ncb1973>.
- Giavazzi, F., Paoluzzi, M., Macchi, M., Bi, D., Scita, G., Manning, M.L., Cerbino, R., and Marchetti, M.C. (2018). Flocking transitions in confluent tissues. *Soft Matter* *14*, 3471–3477. <https://doi.org/10.1039/c8sm00126j>.
- Giomi, L., Hawley-Weld, N., and Mahadevan, L. (2013). Swarming, swirling and stasis in sequestered bristle-bots. *Proceedings of the Royal Society A: Mathematical, Physical and Engineering Sciences* *469*, 20120637. <https://doi.org/10.1098/rspa.2012.0637>.
- Golovkine, G., Reboud, E., and Huber, P. (2018). *Pseudomonas aeruginosa* Takes a Multi-Target Approach to Achieve Junction Breach. *Front Cell Infect Microbiol* *7*, 532. <https://doi.org/10.3389/fcimb.2017.00532>.
- Grasset, E.M., Bertero, T., Bozec, A., Friard, J., Bourget, I., Pisano, S., Lecacheur, M., Maiel, M., Bailleux, C., Emelyanov, A., et al. (2018). Matrix Stiffening and EGFR Cooperate to Promote the Collective Invasion of Cancer Cells. *Cancer Res* *78*, 5229–5242. <https://doi.org/10.1158/0008-5472.CAN-18-0601>.
- Greenburg, G., and Hay, E.D. (1982). Epithelia suspended in collagen gels can lose polarity and express characteristics of migrating mesenchymal cells. *Journal of Cell Biology* *95*, 333–339. <https://doi.org/10.1083/jcb.95.1.333>.
- Grillet, F., Bayet, E., Villeronce, O., Zappia, L., Lagerqvist, E.L., Lunke, S., Charafe-Jauffret, E., Pham, K., Molck, C., Rolland, N., et al. (2017). Circulating tumour cells from patients with colorectal cancer have cancer stem cell

- hallmarks in ex vivo culture. *Gut* 66, 1802–1810. <https://doi.org/10.1136/gutjnl-2016-311447>.
- Gritsenko, P.G., Ilina, O., and Friedl, P. (2012). Interstitial guidance of cancer invasion. *J. Pathol.* 226, 185–199. <https://doi.org/10.1002/path.3031>.
- Guinney, J., Dienstmann, R., Wang, X., de Reyniès, A., Schlicker, A., Soneson, C., Marisa, L., Roepman, P., Nyamundanda, G., Angelino, P., et al. (2015). The consensus molecular subtypes of colorectal cancer. *Nat Med* 21, 1350–1356. <https://doi.org/10.1038/nm.3967>.
- Gunawan, F., Gentile, A., Fukuda, R., Tsedeke, A.T., Jiménez-Amilburu, V., Ramadass, R., Iida, A., Sehara-Fujisawa, A., and Stainier, D.Y.R. (2019). Focal adhesions are essential to drive zebrafish heart valve morphogenesis. *J Cell Biol* 218, 1039–1054. <https://doi.org/10.1083/jcb.201807175>.
- Gudem, G., Van Loo, P., Kremeyer, B., Alexandrov, L.B., Tubio, J.M.C., Papaemmanuil, E., Brewer, D.S., Kallio, H.M.L., Högnäs, G., Annala, M., et al. (2015). The evolutionary history of lethal metastatic prostate cancer. *Nature* 520, 353–357. <https://doi.org/10.1038/nature14347>.
- Gupton, S.L., and Waterman-Storer, C.M. (2006). Spatiotemporal Feedback between Actomyosin and Focal-Adhesion Systems Optimizes Rapid Cell Migration. *Cell* 125, 1361–1374. <https://doi.org/10.1016/j.cell.2006.05.029>.
- Hanahan, D., and Weinberg, R.A. (2000). The hallmarks of cancer. *Cell* 100, 57–70. .
- Hanahan, D., and Weinberg, R.A. (2011). Hallmarks of Cancer: The Next Generation. *Cell* 144, 646–674. <https://doi.org/10.1016/j.cell.2011.02.013>.
- Haslam, A., Kim, M.S., and Prasad, V. (2021). Updated estimates of eligibility for and response to genome-targeted oncology drugs among US cancer patients, 2006-2020. *Annals of Oncology* 32, 926–932. <https://doi.org/10.1016/j.annonc.2021.04.003>.
- Hawkins, R.J., Piel, M., Faure-Andre, G., Lennon-Dumenil, A.M., Joanny, J.F., Prost, J., and Voituriez, R. (2009). Pushing off the Walls: A Mechanism of Cell Motility in Confinement. *Phys. Rev. Lett.* 102, 058103. <https://doi.org/10.1103/PhysRevLett.102.058103>.
- Hawkins, R.J., Poincloux, R., Bénichou, O., Piel, M., Chavrier, P., and Voituriez, R. (2011). Spontaneous Contractility-Mediated Cortical Flow Generates Cell Migration in Three-Dimensional Environments. *Biophysical Journal* 101, 1041–1045. <https://doi.org/10.1016/j.bpj.2011.07.038>.
- Hayer, A., Shao, L., Chung, M., Joubert, L.-M., Yang, H.W., Tsai, F.-C., Bisaria, A., Betzig, E., and Meyer, T. (2016). Engulfed cadherin fingers are polarized junctional structures between collectively migrating endothelial cells. *Nat. Cell Biol.* 18, 1311–1323. <https://doi.org/10.1038/ncb3438>.
- Heanue, T.A., and Pachnis, V. (2007). Enteric nervous system development and Hirschsprung’s disease: advances in genetic and stem cell studies. *Nat Rev Neurosci* 8, 466–479. <https://doi.org/10.1038/nrn2137>.
- Hegerfeldt, Y., Tusch, M., Bröcker, E.-B., and Friedl, P. (2002). Collective cell movement in primary melanoma explants: plasticity of cell-cell interaction, beta1-integrin function, and migration strategies. *Cancer Res.* 62, 2125–2130. .
- van Helvert, S., and Friedl, P. (2016). Strain Stiffening of Fibrillar Collagen during Individual and Collective Cell Migration Identified by AFM Nanoindentation. *ACS Appl. Mater. Interfaces* 8, 21946–21955. <https://doi.org/10.1021/acsami.6b01755>.
- Herman, C.M., Wilcox, G.E., Kattan, M.W., Scardino, P.T., and Wheeler, T.M. (2000). Lymphovascular Invasion as a Predictor of Disease Progression in Prostate Cancer. *The American Journal of Surgical Pathology* 24, 859–863. .
- Hidalgo-Carcedo, C., Hooper, S., Chaudhry, S.I., Williamson, P., Harrington, K., Leitinger, B., and Sahai, E. (2011). Collective cell migration requires suppression of actomyosin at cell–cell contacts mediated by DDR1 and the cell

- polarity regulators Par3 and Par6. *Nat Cell Biol* 13, 49–59. <https://doi.org/10.1038/ncb2133>.
- Hino, N., Rossetti, L., Marín-Llauradó, A., Aoki, K., Trepát, X., Matsuda, M., and Hirashima, T. (2020). ERK-Mediated Mechanochemical Waves Direct Collective Cell Polarization. *Developmental Cell* 53, 646–660.e8. <https://doi.org/10.1016/j.devcel.2020.05.011>.
- Hinsenkamp, I., Schulz, S., Roscher, M., Suhr, A.-M., Meyer, B., Munteanu, B., Fuchser, J., Schoenberg, S.O., Ebert, M.P.A., Wängler, B., et al. (2016). Inhibition of Rho-Associated Kinase 1/2 Attenuates Tumor Growth in Murine Gastric Cancer. *Neoplasia* 18, 500–511. <https://doi.org/10.1016/j.neo.2016.07.002>.
- Hirata, E., Ichikawa, T., Horike, S., and Kiyokawa, E. (2018). Active K-RAS induces the coherent rotation of epithelial cells: A model for collective cell invasion in vitro. *Cancer Sci* 109, 4045–4055. <https://doi.org/10.1111/cas.13816>.
- Hood, J.D., and Cheresch, D.A. (2002). Role of integrins in cell invasion and migration. *Nat Rev Cancer* 2, 91–100. <https://doi.org/10.1038/nrc727>.
- Huang, Y., Tong, L., Yi, L., Zhang, C., Hai, L., Li, T., Yu, S., Wang, W., Tao, Z., Ma, H., et al. (2018). Three-dimensional hydrogel is suitable for targeted investigation of amoeboid migration of glioma cells. *Molecular Medicine Reports* 17, 250–256. <https://doi.org/10.3892/mmr.2017.7888>.
- Ilina, O., Gritsenko, P.G., Syga, S., Lippoldt, J., La Porta, C.A.M., Chepizhko, O., Grosser, S., Vullings, M., Bakker, G.-J., Starruß, J., et al. (2020). Cell–cell adhesion and 3D matrix confinement determine jamming transitions in breast cancer invasion. *Nature Cell Biology* 22, 1103–1115. <https://doi.org/10.1038/s41556-020-0552-6>.
- Innocenti, M. (2018). New insights into the formation and the function of lamellipodia and ruffles in mesenchymal cell migration. *Cell Adh Migr* 12, 401–416. <https://doi.org/10.1080/19336918.2018.1448352>.
- Inoue, C.N., Forster, H.G., and Epstein, M. (1995). Effects of Lysophosphatidic Acid, a Novel Lipid Mediator, on Cytosolic Ca²⁺ and Contractility in Cultured Rat Mesangial Cells. *Circulation Research* 77, 888–896. <https://doi.org/10.1161/01.RES.77.5.888>.
- Isella, C., Terrasi, A., Bellomo, S.E., Petti, C., Galatola, G., Muratore, A., Mellano, A., Senetta, R., Cassenti, A., Sonetto, C., et al. (2015). Stromal contribution to the colorectal cancer transcriptome. *Nat Genet* 47, 312–319. <https://doi.org/10.1038/ng.3224>.
- Ivanov, K.P., Kalinina, M.K., and Levkovich YuI, null (1981). Blood flow velocity in capillaries of brain and muscles and its physiological significance. *Microvasc Res* 22, 143–155. [https://doi.org/10.1016/0026-2862\(81\)90084-4](https://doi.org/10.1016/0026-2862(81)90084-4).
- Jackson, D.G. (2019). Leucocyte Trafficking via the Lymphatic Vasculature— Mechanisms and Consequences. *Frontiers in Immunology* 10. .
- Jacobelli, J., Bennett, F.C., Pandurangi, P., Tooley, A.J., and Krummel, M.F. (2009). Myosin-IIA and ICAM-1 Regulate the Interchange between Two Distinct Modes of T Cell Migration. *The Journal of Immunology* 182, 2041–2050. <https://doi.org/10.4049/jimmunol.0803267>.
- Jafarnejad, M., Woodruff, M.C., Zawieja, D.C., Carroll, M.C., and Moore, J.E. (2015). Modeling Lymph Flow and Fluid Exchange with Blood Vessels in Lymph Nodes. *Lymphat Res Biol* 13, 234–247. <https://doi.org/10.1089/lrb.2015.0028>.
- Jain, S., Cachoux, V.M.L., Narayana, G.H.N.S., de Beco, S., D’Alessandro, J., Cellerin, V., Chen, T., Heuzé, M.L., Marcq, P., Mège, R.-M., et al. (2020). The role of single-cell mechanical behaviour and polarity in driving collective cell migration. *Nat. Phys.* <https://doi.org/10.1038/s41567-020-0875-z>.
- Jain, S., Ladoux, B., and Mège, R.-M. (2021). Mechanical plasticity in collective cell migration. *Current Opinion in Cell Biology* 72, 54–62. <https://doi.org/10.1016/j.ceb.2021.04.006>.

- Julicher, F., Kruse, K., Prost, J., and Joanny, J. (2007). Active behavior of the Cytoskeleton. *Physics Reports* 449, 3–28. <https://doi.org/10.1016/j.physrep.2007.02.018>.
- Julien, S., Merino-Trigo, A., Lacroix, L., Pocard, M., Goéré, D., Mariani, P., Landron, S., Bigot, L., Nemati, F., Dartigues, P., et al. (2012). Characterization of a large panel of patient-derived tumor xenografts representing the clinical heterogeneity of human colorectal cancer. *Clin. Cancer Res.* 18, 5314–5328. <https://doi.org/10.1158/1078-0432.CCR-12-0372>.
- Justus, C.R., Leffler, N., Ruiz-Echevarria, M., and Yang, L.V. (2014). In vitro Cell Migration and Invasion Assays. *J Vis Exp* <https://doi.org/10.3791/51046>.
- Kawauchi, T. (2012). Cell Adhesion and Its Endocytic Regulation in Cell Migration during Neural Development and Cancer Metastasis. *Int J Mol Sci* 13, 4564–4590. <https://doi.org/10.3390/ijms13044564>.
- Kenific, C.M., Stehbens, S.J., Goldsmith, J., Leidal, A.M., Faure, N., Ye, J., Wittmann, T., and Debnath, J. (2016). NBR1 enables autophagy-dependent focal adhesion turnover. *J Cell Biol* 212, 577–590. <https://doi.org/10.1083/jcb.201503075>.
- Kennedy, M.J., Hughes, R.M., Peteya, L.A., Schwartz, J.W., Ehlers, M.D., and Tucker, C.L. (2010). Rapid blue-light-mediated induction of protein interactions in living cells. *Nat Methods* 7, 973–975. <https://doi.org/10.1038/nmeth.1524>.
- Kenry, Leong, M.C., Nai, M.H., Cheong, F.C., and Lim, C.T. (2015). Viscoelastic effects of silicone gels at the micro- and nanoscale. *Procedia IUTAM* 20–30. <https://doi.org/10.1016/j.piutam.2014.12.004>.
- Khalil, A.A., and Friedl, P. (2010). Determinants of leader cells in collective cell migration. *Int Bio (Cam)* 2, 568–574. <https://doi.org/10.1039/c0ib00052c>.
- Kleinman, H.K., and Martin, G.R. (2005). Matrigel: basement membrane matrix with biological activity. *Semin. Cancer Biol.* 15, 378–386. <https://doi.org/10.1016/j.semcancer.2005.05.004>.
- Koch, J.C., Kuttler, J., Maass, F., Lengenfeld, T., Zielke, E., Bähr, M., and Lingor, P. (2020). Compassionate Use of the ROCK Inhibitor Fasudil in Three Patients With Amyotrophic Lateral Sclerosis. *Frontiers in Neurology* 11. .
- Kojima, M., Sugimoto, K., Kobayashi, M., Ichikawa-Tomikawa, N., Kashiwagi, K., Watanabe, T., Soeda, S., Fujimori, K., and Chiba, H. (2021). Aberrant Claudin-6–Adhesion Signaling Promotes Endometrial Cancer Progression via Estrogen Receptor α . *Mol Cancer Res* 19, 1208–1220. <https://doi.org/10.1158/1541-7786.MCR-20-0835>.
- Konen, J., Summerbell, E., Dwivedi, B., Galior, K., Hou, Y., Rusnak, L., Chen, A., Saltz, J., Zhou, W., Boise, L.H., et al. (2017). Image-guided genomics of phenotypically heterogeneous populations reveals vascular signalling during symbiotic collective cancer invasion. *Nat Commun* 8, 15078. <https://doi.org/10.1038/ncomms15078>.
- Kopf, A., Renkawitz, J., Hauschild, R., Girkontaite, I., Tedford, K., Merrin, J., Thorn-Seshold, O., Trauner, D., Häcker, H., Fischer, K.-D., et al. (2020). Microtubules control cellular shape and coherence in amoeboid migrating cells. *J Cell Biol* 219, e201907154. <https://doi.org/10.1083/jcb.201907154>.
- Krebs, A.M., Mitschke, J., Lasierra Losada, M., Schmalhofer, O., Boerries, M., Busch, H., Boettcher, M., Mougiakakos, D., Reichardt, W., Bronsert, P., et al. (2017). The EMT-activator Zeb1 is a key factor for cell plasticity and promotes metastasis in pancreatic cancer. *Nat Cell Biol* 19, 518–529. <https://doi.org/10.1038/ncb3513>.
- Kren, A., Baeriswyl, V., Lehembre, F., Wunderlin, C., Strittmatter, K., Antoniadis, H., Fässler, R., Cavallaro, U., and Christofori, G. (2007). Increased tumor cell dissemination and cellular senescence in the absence of β 1-integrin function. *EMBO J* 26, 2832–2842. <https://doi.org/10.1038/sj.emboj.7601738>.
- Kriebel, P.W., Barr, V.A., and Parent, C.A. (2003). Adenylyl Cyclase Localization Regulates Streaming during Chemotaxis. *Cell* 112, 549–560. [https://doi.org/10.1016/S0092-8674\(03\)00081-3](https://doi.org/10.1016/S0092-8674(03)00081-3).

- Kriegman, S., Blackiston, D., Levin, M., and Bongard, J. (2020). A scalable pipeline for designing reconfigurable organisms. *PNAS* *117*, 1853–1859. <https://doi.org/10.1073/pnas.1910837117>.
- Krndija, D., El Marjou, F., Guirao, B., Richon, S., Leroy, O., Bellaiche, Y., Hannezo, E., and Matic Vignjevic, D. (2019). Active cell migration is critical for steady-state epithelial turnover in the gut. *Science* *365*, 705–710. <https://doi.org/10.1126/science.aau3429>.
- Kurusu, S., Suetsugu, S., Yamazaki, D., Yamaguchi, H., and Takenawa, T. (2005). Rac-WAVE2 signaling is involved in the invasive and metastatic phenotypes of murine melanoma cells. *Oncogene* *24*, 1309–1319. <https://doi.org/10.1038/sj.onc.1208177>.
- Kurosaka, S., and Kashina, A. (2008). Cell biology of embryonic migration. *Birth Defects Research Part C: Embryo Today: Reviews* *84*, 102–122. <https://doi.org/10.1002/bdrc.20125>.
- Lachowski, D., Cortes, E., Pink, D., Chronopoulos, A., Karim, S.A., P. Morton, J., and del Río Hernández, A.E. (2017). Substrate Rigidity Controls Activation and Durotaxis in Pancreatic Stellate Cells. *Sci Rep* *7*, 2506. <https://doi.org/10.1038/s41598-017-02689-x>.
- Lam, P., and Huttenlocher, A. (2013). Interstitial leukocyte migration in vivo. *Current Opinion in Cell Biology* *25*, 650–658. <https://doi.org/10.1016/j.ceb.2013.05.007>.
- Lambert, A.W., Pattabiraman, D.R., and Weinberg, R.A. (2017). Emerging Biological Principles of Metastasis. *Cell* *168*, 670–691. <https://doi.org/10.1016/j.cell.2016.11.037>.
- Lämmermann, T., Bader, B.L., Monkley, S.J., Worbs, T., Wedlich-Söldner, R., Hirsch, K., Keller, M., Förster, R., Critchley, D.R., Fässler, R., et al. (2008). Rapid leukocyte migration by integrin-independent flowing and squeezing. *Nature* *453*, 51–55. <https://doi.org/10.1038/nature06887>.
- Lamouille, S., Xu, J., and Derynck, R. (2014). Molecular mechanisms of epithelial–mesenchymal transition. *Nat Rev Mol Cell Biol* *15*, 178–196. <https://doi.org/10.1038/nrm3758>.
- Law, J., and Martin, E. (2020). transcoelomic spread. In *Concise Medical Dictionary*, (Oxford University Press), p.
- Le Berre, M., Aubertin, J., and Piel, M. (2012). Fine control of nuclear confinement identifies a threshold deformation leading to lamina rupture and induction of specific genes. *Integr Biol (Camb)* *4*, 1406–1414. <https://doi.org/10.1039/c2ib20056b>.
- Lennon-Duménil, A.-M., and Moreau, H.D. (2021). Barotaxis: How cells live and move under pressure. *Curr Opin Cell Biol* *72*, 131–136. <https://doi.org/10.1016/j.ceb.2021.07.006>.
- Lesuffleur, T., Porchet, N., Aubert, J.P., Swallow, D., Gum, J.R., Kim, Y.S., Real, F.X., and Zweibaum, A. (1993). Differential expression of the human mucin genes MUC1 to MUC5 in relation to growth and differentiation of different mucus-secreting HT-29 cell subpopulations. *J Cell Sci* *106* (Pt 3), 771–783. <https://doi.org/10.1242/jcs.106.3.771>.
- Libanje, F., Raingeaud, J., Luan, R., Thomas, Z., Zajac, O., Veiga, J., Marisa, L., Adam, J., Boige, V., Malka, D., et al. (2019). ROCK2 inhibition triggers the collective invasion of colorectal adenocarcinomas. *The EMBO Journal* *38*, e99299. <https://doi.org/10.15252/embj.201899299>.
- Lim, S.-B., Yu, C.S., Jang, S.J., Kim, T.W., Kim, J.H., and Kim, J.C. (2010). Prognostic significance of lymphovascular invasion in sporadic colorectal cancer. *Dis. Colon Rectum* *53*, 377–384. <https://doi.org/10.1007/DCR.0b013e3181cf8ae5>.
- Limozin, L., and Sengupta, K. (2009). Quantitative Reflection Interference Contrast Microscopy (RICM) in Soft Matter and Cell Adhesion. *ChemPhysChem* *10*, 2752–2768. <https://doi.org/10.1002/cphc.200900601>.
- Liotta, L.A., Kleinerman, J., and Saldel, G.M. (1976). The Significance of Hematogenous Tumor Cell Clumps in the

Metastatic Process. *Cancer Res* 36, 889–894. .

Liu, Y.-J., Le Berre, M., Lautenschlaeger, F., Maiuri, P., Callan-Jones, A., Heuzé, M., Takaki, T., Voituriez, R., and Piel, M. (2015). Confinement and low adhesion induce fast amoeboid migration of slow mesenchymal cells. *Cell* 160, 659–672. <https://doi.org/10.1016/j.cell.2015.01.007>.

Lo, C.-M., Wang, H.-B., Dembo, M., and Wang, Y. (2000). Cell Movement Is Guided by the Rigidity of the Substrate. *Biophysical Journal* 79, 144–152. [https://doi.org/10.1016/S0006-3495\(00\)76279-5](https://doi.org/10.1016/S0006-3495(00)76279-5).

Lodish, H.F., Berk, A., Kaiser, C., Krieger, M., Scott, M.P., Bretscher, A., Ploegh, H.L., and Matsudaira, P.T. (2008). *Molecular cell biology* (New York: W.H. Freeman).

Lomakin, A.J., Cattin, C.J., Cuvelier, D., Alraies, Z., Molina, M., Nader, G.P.F., Srivastava, N., Sáez, P.J., Garcia-Arcos, J.M., Zhitnyak, I.Y., et al. (2020). The nucleus acts as a ruler tailoring cell responses to spatial constraints. *Science* 370. <https://doi.org/10.1126/science.aba2894>.

Loomis, W.F., Fuller, D., Gutierrez, E., Groisman, A., and Rappel, W.-J. (2012). Innate Non-Specific Cell Substratum Adhesion. *PLOS ONE* 7, e42033. <https://doi.org/10.1371/journal.pone.0042033>.

Lord, S.J., Velle, K.B., Mullins, R.D., and Fritz-Laylin, L.K. (2020). SuperPlots: Communicating reproducibility and variability in cell biology. *J Cell Biol* 219. <https://doi.org/10.1083/jcb.202001064>.

Louvet, S., Aghion, J., Santa-Maria, A., Mangeat, P., and Maro, B. (1996). Ezrin Becomes Restricted to Outer Cells Following Asymmetrical Division in the Preimplantation Mouse Embryo. *Developmental Biology* 177, 568–579. <https://doi.org/10.1006/dbio.1996.0186>.

Lowe, D.G. (2004). Distinctive Image Features from Scale-Invariant Keypoints. *International Journal of Computer Vision* 60, 91–110. <https://doi.org/10.1023/B:VISI.0000029664.99615.94>.

Loza, A.J., Koride, S., Schimizzi, G.V., Li, B., Sun, S.X., and Longmore, G.D. (2016). Cell density and actomyosin contractility control the organization of migrating collectives within an epithelium. *MBoC* 27, 3459–3470. <https://doi.org/10.1091/mbc.e16-05-0329>.

Lu, P., Takai, K., Weaver, V.M., and Werb, Z. (2011). Extracellular Matrix Degradation and Remodeling in Development and Disease. *Cold Spring Harbor Perspectives in Biology* 3, a005058–a005058. <https://doi.org/10.1101/cshperspect.a005058>.

Maître, J.-L. (2017). Mechanics of blastocyst morphogenesis. *Biology of the Cell* 109, 323–338. <https://doi.org/10.1111/boc.201700029>.

Maître, J.-L., Turlier, H., Illukkumbura, R., Eismann, B., Niwayama, R., Nédélec, F., and Hiiragi, T. (2016). Asymmetric division of contractile domains couples cell positioning and fate specification. *Nature* 536, 344–348. <https://doi.org/10.1038/nature18958>.

Maiuri, P., Terriac, E., Paul-Gilloteaux, P., Vignaud, T., McNally, K., Onuffer, J., Thorn, K., Nguyen, P.A., Georgoulia, N., Soong, D., et al. (2012). The first World Cell Race. *Current Biology* 22, R673–R675. <https://doi.org/10.1016/j.cub.2012.07.052>.

Maiuri, P., Rupprecht, J.-F., Wieser, S., Rupprecht, V., Bénichou, O., Carpi, N., Coppey, M., De Beco, S., Gov, N., Heisenberg, C.-P., et al. (2015). Actin flows mediate a universal coupling between cell speed and cell persistence. *Cell* 161, 374–386. <https://doi.org/10.1016/j.cell.2015.01.056>.

Mak, M., Reinhart-King, C.A., and Erickson, D. (2011). Microfabricated Physical Spatial Gradients for Investigating Cell Migration and Invasion Dynamics. *PLOS ONE* 6, e20825. <https://doi.org/10.1371/journal.pone.0020825>.

Makrodouli, E., Oikonomou, E., Koc, M., Andera, L., Sasazuki, T., Shirasawa, S., and Pintzas, A. (2011). BRAF and RAS oncogenes regulate Rho GTPase pathways to mediate migration and invasion properties in human colon cancer

cells: a comparative study. *Molecular Cancer* 10, 118. <https://doi.org/10.1186/1476-4598-10-118>.

Malinverno, C., Corallino, S., Giavazzi, F., Bergert, M., Li, Q., Leoni, M., Disanza, A., Frittoli, E., Oldani, A., Martini, E., et al. (2017). Endocytic reawakening of motility in jammed epithelia. *Nature Mater* 16, 587–596. <https://doi.org/10.1038/nmat4848>.

Marchetti, M.C., Joanny, J.F., Ramaswamy, S., Liverpool, T.B., Prost, J., Rao, M., and Simha, R.A. (2013). Hydrodynamics of soft active matter. *Rev. Mod. Phys.* 85, 1143–1189. <https://doi.org/10.1103/RevModPhys.85.1143>.

Martin, P. (1997). Wound Healing--Aiming for Perfect Skin Regeneration. *Science* 276, 75–81. <https://doi.org/10.1126/science.276.5309.75>.

Matsumoto, K., Nakayama, Y., Inoue, Y., Minagawa, N., Katsuki, T., Shibao, K., Tsurudome, Y., Hirata, K., Nagata, N., and Itoh, H. (2007). Lymphatic Microvessel Density is an Independent Prognostic Factor in Colorectal Cancer: *Diseases of the Colon & Rectum* 50, 308–314. <https://doi.org/10.1007/s10350-006-0792-y>.

Matthews, J., Schuster, B., Kashaf, S.S., Liu, P., Bilgic, M., Rzhetsky, A., and Tay, S. (2022). OrganoID: a versatile deep learning platform for organoid image analysis (Bioengineering).

Mattila, P.K., and Lappalainen, P. (2008). Filopodia: molecular architecture and cellular functions. *Nat Rev Mol Cell Biol* 9, 446–454. <https://doi.org/10.1038/nrm2406>.

Mayor, R., and Etienne-Manneville, S. (2016). The front and rear of collective cell migration. *Nat Rev Mol Cell Biol* 17, 97–109. <https://doi.org/10.1038/nrm.2015.14>.

MBInfo MBInfo | Defining Mechanobiology.

McCann, C.P., Rericha, E.C., Wang, C., Losert, W., and Parent, C.A. (2014). Dictyostelium Cells Migrate Similarly on Surfaces of Varying Chemical Composition. *PLOS ONE* 9, e87981. <https://doi.org/10.1371/journal.pone.0087981>.

McKenzie, A.J., Hicks, S.R., Svec, K.V., Naughton, H., Edmunds, Z.L., and Howe, A.K. (2018). The mechanical microenvironment regulates ovarian cancer cell morphology, migration, and spheroid disaggregation. *Sci Rep* 8, 7228. <https://doi.org/10.1038/s41598-018-25589-0>.

van Meer, B.J., de Vries, H., Firth, K.S.A., van Weerd, J., Tertoolen, L.G.J., Karperien, H.B.J., Jonkheijm, P., Denning, C., IJzerman, A.P., and Mummery, C.L. (2017). Small molecule absorption by PDMS in the context of drug response bioassays. *Biochemical and Biophysical Research Communications* 482, 323–328. <https://doi.org/10.1016/j.bbrc.2016.11.062>.

Meijering, E., Dzyubachyk, O., and Smal, I. (2012). Methods for cell and particle tracking. *Methods Enzymol* 504, 183–200. <https://doi.org/10.1016/B978-0-12-391857-4.00009-4>.

Merz, A.J., and Higgs, H.N. (2003). Listeria Motility: Biophysics Pushes Things Forward. *Current Biology* 13, R302–R304. [https://doi.org/10.1016/S0960-9822\(03\)00231-8](https://doi.org/10.1016/S0960-9822(03)00231-8).

Meshik, X., O'Neill, P.R., and Gautam, N. (2019). Physical Plasma Membrane Perturbation Using Subcellular Optogenetics Drives Integrin-Activated Cell Migration. *ACS Synth Biol* 8, 498–510. <https://doi.org/10.1021/acssynbio.8b00356>.

Miller, K.G. (2002). Extending the Arp2/3 complex and its regulation beyond the leading edge. *Journal of Cell Biology* 156, 591–593. <https://doi.org/10.1083/jcb.200201107>.

Minsky, B., and Mies, C. (1989). The clinical significance of vascular invasion in colorectal cancer. *Dis. Colon Rectum* 32, 794–803. <https://doi.org/10.1007/BF02562132>.

- Mishra, A.K., Mondo, J.A., Campanale, J.P., and Montell, D.J. (2019). Coordination of protrusion dynamics within and between collectively migrating border cells by myosin II. *MBoC* 30, 2490–2502. <https://doi.org/10.1091/mbc.E19-02-0124>.
- Mizejewski, G.J. (1999). Role of integrins in cancer: survey of expression patterns. *Proc Soc Exp Biol Med* 222, 124–138. <https://doi.org/10.1046/j.1525-1373.1999.d01-122.x>.
- Molinie, N., and Gautreau, A. (2018). The Arp2/3 Regulatory System and Its Deregulation in Cancer. *Physiological Reviews* 98, 215–238. <https://doi.org/10.1152/physrev.00006.2017>.
- Montell, D.J. (2003). Border-cell migration: the race is on. *Nat Rev Mol Cell Biol* 4, 13–24. <https://doi.org/10.1038/nrm1006>.
- Montell, D.J., Yoon, W.H., and Starz-Gaiano, M. (2012). Group choreography: mechanisms orchestrating the collective movement of border cells. *Nat. Rev. Mol. Cell Biol.* 13, 631–645. <https://doi.org/10.1038/nrm3433>.
- Montero, J.-A., and Heisenberg, C.-P. (2004). Gastrulation dynamics: cells move into focus. *Trends in Cell Biology* 14, 620–627. <https://doi.org/10.1016/j.tcb.2004.09.008>.
- Mosier, J.A., Rahman-Zaman, A., Zanotelli, M.R., VanderBurgh, J.A., Bordeleau, F., Hoffman, B.D., and Reinhart-King, C.A. (2019a). Extent of Cell Confinement in Microtracks Affects Speed and Results in Differential Matrix Strains. *Biophysical Journal* 117, 1692–1701. <https://doi.org/10.1016/j.bpj.2019.09.024>.
- Mosier, J.A., Rahman-Zaman, A., Zanotelli, M.R., VanderBurgh, J.A., Bordeleau, F., Hoffman, B.D., and Reinhart-King, C.A. (2019b). Extent of Cell Confinement in Microtracks Affects Speed and Results in Differential Matrix Strains. *Biophys. J.* 117, 1692–1701. <https://doi.org/10.1016/j.bpj.2019.09.024>.
- Nagtegaal, I.D., and Hugen, N. (2015). The Increasing Relevance of Tumour Histology in Determining Oncological Outcomes in Colorectal Cancer. *Curr Colorectal Cancer Rep* 11, 259–266. <https://doi.org/10.1007/s11888-015-0280-7>.
- Najafi, A., and Golestanian, R. (2004). Simple swimmer at low Reynolds number: three linked spheres. *Phys Rev E Stat Nonlin Soft Matter Phys* 69, 062901. <https://doi.org/10.1103/PhysRevE.69.062901>.
- Nelson, W.J. (2003). Adaptation of core mechanisms to generate cell polarity. *Nature* 422, 766–774. <https://doi.org/10.1038/nature01602>.
- Nelson, R.D., Quie, P.G., and Simmons, R.L. (1975). Chemotaxis under agarose: a new and simple method for measuring chemotaxis and spontaneous migration of human polymorphonuclear leukocytes and monocytes. *J. Immunol.* 115, 1650–1656. .
- Neumann, N.M., Perrone, M.C., Veldhuis, J.H., Huebner, R.J., Zhan, H., Devreotes, P.N., Brodland, G.W., and Ewald, A.J. (2018). Coordination of Receptor Tyrosine Kinase Signaling and Interfacial Tension Dynamics Drives Radial Intercalation and Tube Elongation. *Developmental Cell* 45, 67-82.e6. <https://doi.org/10.1016/j.devcel.2018.03.011>.
- Niggemann, B., Drell, T.L., Joseph, J., Weidt, C., Lang, K., Zaenker, K.S., and Entschladen, F. (2004). Tumor cell locomotion: differential dynamics of spontaneous and induced migration in a 3D collagen matrix. *Exp. Cell Res.* 298, 178–187. <https://doi.org/10.1016/j.yexcr.2004.04.001>.
- O'Brien, L.E., Jou, T.S., Pollack, A.L., Zhang, Q., Hansen, S.H., Yurchenco, P., and Mostov, K.E. (2001). Rac1 orientates epithelial apical polarity through effects on basolateral laminin assembly. *Nat. Cell Biol.* 3, 831–838. <https://doi.org/10.1038/ncb0901-831>.
- Orgaz, J.L., Pandya, P., Dalmeida, R., Karagiannis, P., Sanchez-Laorden, B., Viros, A., Albregues, J., Nestle, F.O., Ridley, A.J., Gaggioli, C., et al. (2014). Diverse matrix metalloproteinase functions regulate cancer amoeboid migration. *Nat Commun* 5, 1–13. <https://doi.org/10.1038/ncomms5255>.

- Pagès, D.-L., Dornier, E., Seze, J.D., Wang, L., Luan, R., Cartry, J., Canet-Jourdan, C., Raingeaud, J., Voituriez, R., Coppey, M., et al. (2020). Cell clusters adopt a collective amoeboid mode of migration in confined non-adhesive environments. *BioRxiv* 2020.05.28.106203. <https://doi.org/10.1101/2020.05.28.106203>.
- Palamidessi, A., Malinverno, C., Frittoli, E., Corallino, S., Barbieri, E., Sigismund, S., Beznoussenko, G.V., Martini, E., Garre, M., Ferrara, I., et al. (2019). Unjamming overcomes kinetic and proliferation arrest in terminally differentiated cells and promotes collective motility of carcinoma. *Nat. Mater.* *18*, 1252–1263. <https://doi.org/10.1038/s41563-019-0425-1>.
- Paluch, E.K., Aspalter, I.M., and Sixt, M. (2016). Focal Adhesion-Independent Cell Migration. *Annu. Rev. Cell Dev. Biol.* *32*, 469–490. <https://doi.org/10.1146/annurev-cellbio-111315-125341>.
- Paszek, M.J., DuFort, C.C., Rossier, O., Bainer, R., Mouw, J.K., Godula, K., Hudak, J.E., Lakins, J.N., Wijekoon, A.C., Cassereau, L., et al. (2014). The cancer glycocalyx mechanically primes integrin-mediated growth and survival. *Nature* *511*, 319–325. <https://doi.org/10.1038/nature13535>.
- Pathak, A., and Kumar, S. (2012). Independent regulation of tumor cell migration by matrix stiffness and confinement. *PNAS* *109*, 10334–10339. <https://doi.org/10.1073/pnas.1118073109>.
- Paul, C.D., Mistriotis, P., and Konstantopoulos, K. (2017). Cancer cell motility: lessons from migration in confined spaces. *Nat. Rev. Cancer* *17*, 131–140. <https://doi.org/10.1038/nrc.2016.123>.
- Péron, G., Mourrain, P., Courty, S., Ghislain, J., Becker, T.S., Rosa, F.M., and David, N.B. (2008). Live Analysis of Endodermal Layer Formation Identifies Random Walk as a Novel Gastrulation Movement. *Current Biology* *18*, 276–281. <https://doi.org/10.1016/j.cub.2008.01.028>.
- Poincloux, R., Collin, O., Lizárraga, F., Romao, M., Debray, M., Piel, M., and Chavrier, P. (2011). Contractility of the cell rear drives invasion of breast tumor cells in 3D Matrigel. *PNAS* *108*, 1943–1948. <https://doi.org/10.1073/pnas.1010396108>.
- Poujade, M., Grasland-Mongrain, E., Hertzog, A., Jouanneau, J., Chavrier, P., Ladoux, B., Buguin, A., and Silberzan, P. (2007). Collective migration of an epithelial monolayer in response to a model wound. *PNAS* *104*, 15988–15993. <https://doi.org/10.1073/pnas.0705062104>.
- Prost, J., Jülicher, F., and Joanny, J.-F. (2015). Active gel physics. *Nature Phys* *11*, 111–117. <https://doi.org/10.1038/nphys3224>.
- Purcell, E.M. (1977). Life at low Reynolds number. *American Journal of Physics* *45*, 3–11. <https://doi.org/10.1119/1.10903>.
- Repo, H., Kostiala, A.A., and Kosunen, T.U. (1978). Use of leucocyte migration under agarose to study spontaneous and directed locomotion of leucocytes. *Immunology* *35*, 539–548. .
- Reversat, A., Gaertner, F., Merrin, J., Stopp, J., Tasciyan, S., Aguilera, J., Vries, I. de, Hauschild, R., Hons, M., Piel, M., et al. (2020). Cellular locomotion using environmental topography. *Nature* 1–4. <https://doi.org/10.1038/s41586-020-2283-z>.
- Richardson, J., Gauert, A., Briones Montecinos, L., Fanlo, L., Alhashem, Z.M., Assar, R., Marti, E., Kabla, A., Härtel, S., and Linker, C. (2016). Leader Cells Define Directionality of Trunk, but Not Cranial, Neural Crest Cell Migration. *Cell Reports* *15*, 2076–2088. <https://doi.org/10.1016/j.celrep.2016.04.067>.
- Ridley, A.J., Schwartz, M.A., Burridge, K., Firtel, R.A., Ginsberg, M.H., Borisy, G., Parsons, J.T., and Horwitz, A.R. (2003). Cell Migration: Integrating Signals from Front to Back. *Science* *302*, 1704–1709. <https://doi.org/10.1126/science.1092053>.
- Roca-Cusachs, P., Conte, V., and Trepat, X. (2017). Quantifying forces in cell biology. *Nat Cell Biol* *19*, 742–751. <https://doi.org/10.1038/ncb3564>.

- Román-Fernández, Á., Roignot, J., Sandilands, E., Nacke, M., Mansour, M.A., McGarry, L., Shanks, E., Mostov, K.E., and Bryant, D.M. (2018). The phospholipid PI(3,4)P₂ is an apical identity determinant. *Nature Communications* 9, 5041. <https://doi.org/10.1038/s41467-018-07464-8>.
- Romero, S., Le Clainche, C., and Gautreau, A.M. (2020). Actin polymerization downstream of integrins: signaling pathways and mechanotransduction. *Biochemical Journal* 477, 1–21. <https://doi.org/10.1042/BCJ20170719>.
- Ronteix, G., Jain, S., Angely, C., Cazaux, M., Khazen, R., Bousso, P., and Baroud, C.N. (2021). A Multiscale Immuno-Oncology on-Chip System (MIOCS) establishes that collective T cell behaviors govern tumor regression. 2021.03.23.435334. <https://doi.org/10.1101/2021.03.23.435334>.
- Rottner, K., and Schaks, M. (2019). Assembling actin filaments for protrusion. *Current Opinion in Cell Biology* 56, 53–63. <https://doi.org/10.1016/j.ceb.2018.09.004>.
- Roure, O. du, Saez, A., Buguin, A., Austin, R.H., Chavrier, P., Siberzan, P., and Ladoux, B. (2005). Force mapping in epithelial cell migration. *PNAS* 102, 2390–2395. <https://doi.org/10.1073/pnas.0408482102>.
- Roussos, E.T., Balsamo, M., Alford, S.K., Wyckoff, J.B., Gligorijevic, B., Wang, Y., Pozzuto, M., Stobezki, R., Goswami, S., Segall, J.E., et al. (2011). Mena invasive (MenaINV) promotes multicellular streaming motility and transendothelial migration in a mouse model of breast cancer. *Journal of Cell Science* 124, 2120–2131. <https://doi.org/10.1242/jcs.086231>.
- Ruiter, D.J., van Krieken, J.H., van Muijen, G.N., and de Waal, R.M. (2001). Tumour metastasis: is tissue an issue? *Lancet Oncol.* 2, 109–112. [https://doi.org/10.1016/S1470-2045\(00\)00229-1](https://doi.org/10.1016/S1470-2045(00)00229-1).
- Ruprecht, V., Wieser, S., Callan-Jones, A., Smutny, M., Morita, H., Sako, K., Barone, V., Ritsch-Marte, M., Sixt, M., Voituriez, R., et al. (2015). Cortical Contractility Triggers a Stochastic Switch to Fast Amoeboid Cell Motility. *Cell* 160, 673–685. <https://doi.org/10.1016/j.cell.2015.01.008>.
- Sadati, M., Taheri Qazvini, N., Krishnan, R., Park, C.Y., and Fredberg, J.J. (2013). Collective migration and cell jamming. *Differentiation* 86, 121–125. <https://doi.org/10.1016/j.diff.2013.02.005>.
- Sadok, A., McCarthy, A., Caldwell, J., Collins, I., Garrett, M.D., Yeo, M., Hooper, S., Sahai, E., Kuemper, S., Mardakheh, F.K., et al. (2015). Rho Kinase Inhibitors Block Melanoma Cell Migration and Inhibit Metastasis. *Cancer Res* 75, 2272–2284. <https://doi.org/10.1158/0008-5472.CAN-14-2156>.
- Sahai, E. (2005). Mechanisms of cancer cell invasion. *Current Opinion in Genetics & Development* 15, 87–96. <https://doi.org/10.1016/j.gde.2004.12.002>.
- Sahai, E. (2007). Illuminating the metastatic process. *Nat Rev Cancer* 7, 737–749. <https://doi.org/10.1038/nrc2229>.
- Sahai, E., and Marshall, C.J. (2003). Differing modes of tumour cell invasion have distinct requirements for Rho/ROCK signalling and extracellular proteolysis. *Nat Cell Biol* 5, 711–719. <https://doi.org/10.1038/ncb1019>.
- Salbreux, G., Charras, G., and Paluch, E. (2012). Actin cortex mechanics and cellular morphogenesis. *Trends in Cell Biology* 22, 536–545. <https://doi.org/10.1016/j.tcb.2012.07.001>.
- Sanz-Moreno, V., Gadea, G., Ahn, J., Paterson, H., Marra, P., Pinner, S., Sahai, E., and Marshall, C.J. (2008). Rac Activation and Inactivation Control Plasticity of Tumor Cell Movement. *Cell* 135, 510–523. <https://doi.org/10.1016/j.cell.2008.09.043>.
- Sanz-Moreno, V., Gaggioli, C., Yeo, M., Albrengues, J., Wallberg, F., Viros, A., Hooper, S., Mitter, R., Féral, C.C., Cook, M., et al. (2011). ROCK and JAK1 Signaling Cooperate to Control Actomyosin Contractility in Tumor Cells and Stroma. *Cancer Cell* 20, 229–245. <https://doi.org/10.1016/j.ccr.2011.06.018>.
- Sawant, K., Chen, Y., Kotian, N., Preuss, K.M., and McDonald, J.A. (2018). Rap1 GTPase promotes coordinated collective cell migration in vivo. *Mol. Biol. Cell* 29, 2656–2673. <https://doi.org/10.1091/mbc.E17-12-0752>.

- Schindelin, J., Arganda-Carreras, I., Frise, E., Kaynig, V., Longair, M., Pietzsch, T., Preibisch, S., Rueden, C., Saalfeld, S., Schmid, B., et al. (2012). Fiji: an open-source platform for biological-image analysis. *Nature Methods* 9, 676–682. <https://doi.org/10.1038/nmeth.2019>.
- Schwitalla, S., Fingerle, A.A., Cammareri, P., Nebelsiek, T., Göktuna, S.I., Ziegler, P.K., Canli, O., Heijmans, J., Huels, D.J., Moreaux, G., et al. (2013). Intestinal tumorigenesis initiated by dedifferentiation and acquisition of stem-cell-like properties. *Cell* 152, 25–38. <https://doi.org/10.1016/j.cell.2012.12.012>.
- SEER Training Modules Cancer Classification.
- Seetharaman, S., and Etienne-Manneville, S. (2020). Cytoskeletal Crosstalk in Cell Migration. *Trends in Cell Biology* 30, 720–735. <https://doi.org/10.1016/j.tcb.2020.06.004>.
- Seetharaman, S., Vianay, B., Roca, V., Farrugia, A.J., De Pascalis, C., Boëda, B., Dingli, F., Loew, D., Vassilopoulos, S., Bershadsky, A., et al. (2021). Microtubules tune mechanosensitive cell responses. *Nat. Mater.* 1–12. <https://doi.org/10.1038/s41563-021-01108-x>.
- SenGupta, S., Parent, C.A., and Bear, J.E. (2021). The principles of directed cell migration. *Nat Rev Mol Cell Biol* <https://doi.org/10.1038/s41580-021-00366-6>.
- Shellard, A., and Mayor, R. (2019). Supracellular migration - beyond collective cell migration. *J. Cell. Sci.* 132. <https://doi.org/10.1242/jcs.226142>.
- Shellard, A., and Mayor, R. (2021a). Collective durotaxis along a self-generated stiffness gradient in vivo. *Nature* 1–5. <https://doi.org/10.1038/s41586-021-04210-x>.
- Shellard, A., and Mayor, R. (2021b). Durotaxis: The Hard Path from In Vitro to In Vivo. *Developmental Cell* 56, 227–239. <https://doi.org/10.1016/j.devcel.2020.11.019>.
- Shellard, A., Szabó, A., Trepát, X., and Mayor, R. (2018). Supracellular contraction at the rear of neural crest cell groups drives collective chemotaxis. *Science* 362, 339–343. <https://doi.org/10.1126/science.aau3301>.
- Shin, H., Kim, D., and Helfman, D.M. (2017). Tropomyosin isoform Tpm2.1 regulates collective and amoeboid cell migration and cell aggregation in breast epithelial cells. *Oncotarget* 8, 95192–95205. <https://doi.org/10.18632/oncotarget.19182>.
- Shirure, V.S., and George, S.C. (2017). Design considerations to minimize the impact of drug absorption in polymer-based organ-on-a-chip platforms. *Lab Chip* 17, 681–690. <https://doi.org/10.1039/C6LC01401A>.
- Simpson, P. (1983). MATERNAL-ZYGOTIC GENE INTERACTIONS DURING FORMATION OF THE DORSOVENTRAL PATTERN IN DROSOPHILA EMBRYOS. *Genetics* 105, 615–632. <https://doi.org/10.1093/genetics/105.3.615>.
- Solnica-Krezel, L., and Sepich, D.S. (2012). Gastrulation: Making and Shaping Germ Layers. *Annu. Rev. Cell Dev. Biol.* 28, 687–717. <https://doi.org/10.1146/annurev-cellbio-092910-154043>.
- Stacker, S.A., Williams, S.P., Karnezis, T., Shayan, R., Fox, S.B., and Achen, M.G. (2014). Lymphangiogenesis and lymphatic vessel remodelling in cancer. *Nat Rev Cancer* 14, 159–172. <https://doi.org/10.1038/nrc3677>.
- Staneva, R., El Marjou, F., Barbazan, J., Krndija, D., Richon, S., Clark, A.G., and Vignjevic, D.M. (2019). Cancer cells in the tumor core exhibit spatially coordinated migration patterns. *J Cell Sci* 132, jcs220277. <https://doi.org/10.1242/jcs.220277>.
- Stevenson, R.P., Veltman, D., and Machesky, L.M. (2012). Actin-bundling proteins in cancer progression at a glance. *J Cell Sci* 125, 1073–1079. <https://doi.org/10.1242/jcs.093799>.
- Stoker, M., and Perryman, M. (1985). An epithelial scatter factor released by embryo fibroblasts. *J Cell Sci* 77, 209–

223. .

- Stringer, C., Michaelos, M., and Pachitariu, M. (2020). Cellpose: a generalist algorithm for cellular segmentation. 2020.02.02.931238. <https://doi.org/10.1101/2020.02.02.931238>.
- Stroka, K.M., Jiang, H., Chen, S.-H., Tong, Z., Wirtz, D., Sun, S.X., and Konstantopoulos, K. (2014). Water Permeation Drives Tumor Cell Migration in Confined Microenvironments. *Cell* 157, 611–623. <https://doi.org/10.1016/j.cell.2014.02.052>.
- Sun, Z., Costell, M., and Fässler, R. (2019). Integrin activation by talin, kindlin and mechanical forces. *Nat. Cell Biol.* 21, 25–31. <https://doi.org/10.1038/s41556-018-0234-9>.
- Sung, H., Ferlay, J., Siegel, R.L., Laversanne, M., Soerjomataram, I., Jemal, A., and Bray, F. (2021). Global Cancer Statistics 2020: GLOBOCAN Estimates of Incidence and Mortality Worldwide for 36 Cancers in 185 Countries. *CA: A Cancer Journal for Clinicians* 71, 209–249. <https://doi.org/10.3322/caac.21660>.
- Sunyer, R., Conte, V., Escribano, J., Elosegui-Artola, A., Labernadie, A., Valon, L., Navajas, D., García-Aznar, J.M., Muñoz, J.J., Roca-Cusachs, P., et al. (2016). Collective cell durotaxis emerges from long-range intercellular force transmission. *Science* 353, 1157–1161. <https://doi.org/10.1126/science.aaf7119>.
- Tan, D.S., Agarwal, R., and Kaye, S.B. (2006). Mechanisms of transcoelomic metastasis in ovarian cancer. *The Lancet Oncology* 7, 925–934. [https://doi.org/10.1016/S1470-2045\(06\)70939-1](https://doi.org/10.1016/S1470-2045(06)70939-1).
- Tan, Y., Tan, D., He, M., Gu, M., Wang, Z., Zeng, G., and Duan, E. (2005). A Model for Implantation: Coculture of Blastocysts and Uterine Endometrium in Mice. *Biol Reprod* 72, 556–561. <https://doi.org/10.1095/biolreprod.104.032821>.
- Teo, J.L., Gomez, G.A., Weeratunga, S., Davies, E.M., Noordstra, I., Budnar, S., Katsuno-Kambe, H., McGrath, M.J., Verma, S., Tomatis, V., et al. (2020). Caveolae Control Contractile Tension for Epithelia to Eliminate Tumor Cells. *Developmental Cell* 0. <https://doi.org/10.1016/j.devcel.2020.05.002>.
- Theveneau, É., and David, N. (2014). Migrations cellulaires collectives. *Med Sci (Paris)* 30, 751–757. <https://doi.org/10.1051/medsci/20143008012>.
- Theveneau, E., and Linker, C. (2017). Leaders in collective migration: are front cells really endowed with a particular set of skills? *F1000Res* 6, 1899. <https://doi.org/10.12688/f1000research.11889.1>.
- Theveneau, E., and Mayor, R. (2012). Neural crest delamination and migration: From epithelium-to-mesenchyme transition to collective cell migration. *Developmental Biology* 366, 34–54. <https://doi.org/10.1016/j.ydbio.2011.12.041>.
- Thiery, J.P., Acloque, H., Huang, R.Y.J., and Nieto, M.A. (2009). Epithelial-Mesenchymal Transitions in Development and Disease. *Cell* 139, 871–890. <https://doi.org/10.1016/j.cell.2009.11.007>.
- Toews, M.L., Ustinova, E.E., and Schultz, H.D. (1997). Lysophosphatidic acid enhances contractility of isolated airway smooth muscle. *Journal of Applied Physiology* 83, 1216–1222. <https://doi.org/10.1152/jappl.1997.83.4.1216>.
- Tozluoğlu, M., Tournier, A.L., Jenkins, R.P., Hooper, S., Bates, P.A., and Sahai, E. (2013). Matrix geometry determines optimal cancer cell migration strategy and modulates response to interventions. *Nat. Cell Biol.* 15, 751–762. <https://doi.org/10.1038/ncb2775>.
- Travis, J. (2011). *Mysteries of the Cell*. Science <https://doi.org/10.1126/science.334.6059.1046-a>.
- Treat, X., Wasserman, M.R., Angelini, T.E., Millet, E., Weitz, D.A., Butler, J.P., and Fredberg, J.J. (2009). Physical forces during collective cell migration. *Nature Phys* 5, 426–430. <https://doi.org/10.1038/nphys1269>.
- Tseng, Q. (2011). Etude d'architecture multicellulaire avec le microenvironnement contrôlé. phdthesis. Université

de Grenoble.

- Tseng, Q., Duchemin-Pelletier, E., Deshiere, A., Balland, M., Guillou, H., Filhol, O., and Théry, M. (2012). Spatial organization of the extracellular matrix regulates cell-cell junction positioning. *Proc Natl Acad Sci U S A* *109*, 1506–1511. <https://doi.org/10.1073/pnas.1106377109>.
- Uechi, H., and Kuranaga, E. (2018). Mechanisms of unusual collective cell movement lacking a free front edge in *Drosophila*. *Current Opinion in Genetics & Development* *51*, 46–51. <https://doi.org/10.1016/j.gde.2018.06.012>.
- Ulrich, T.A., Jain, A., Tanner, K., MacKay, J.L., and Kumar, S. (2010). Probing cellular mechanobiology in three-dimensional culture with collagen-agarose matrices. *Biomaterials* *31*, 1875–1884. <https://doi.org/10.1016/j.biomaterials.2009.10.047>.
- Valon, L., Marín-Llauradó, A., Wyatt, T., Charras, G., and Trepât, X. (2017). Optogenetic control of cellular forces and mechanotransduction. *Nat Commun* *8*, 14396. <https://doi.org/10.1038/ncomms14396>.
- Venturini, V., Pezzano, F., Català Castro, F., Häkkinen, H.-M., Jiménez-Delgado, S., Colomer-Rosell, M., Marro, M., Tolosa-Ramon, Q., Paz-López, S., Valverde, M.A., et al. (2020). The nucleus measures shape changes for cellular proprioception to control dynamic cell behavior. *Science* *370*. <https://doi.org/10.1126/science.aba2644>.
- Verschueren, H. (1985). Interference reflection microscopy in cell biology: methodology and applications. *Journal of Cell Science* *75*, 279–301. .
- Vicente-Manzanares, M., Ma, X., Adelstein, R.S., and Horwitz, A.R. (2009). Non-muscle myosin II takes centre stage in cell adhesion and migration. *Nat Rev Mol Cell Biol* *10*, 778–790. <https://doi.org/10.1038/nrm2786>.
- Wang, H., and Unternaehrer, J.J. (2019). Epithelial-mesenchymal Transition and Cancer Stem Cells: At the Crossroads of Differentiation and Dedifferentiation. *Dev Dyn* *248*, 10–20. <https://doi.org/10.1002/dvdy.24678>.
- Wang, H., Lacoche, S., Huang, L., Xue, B., and Muthuswamy, S.K. (2013). Rotational motion during three-dimensional morphogenesis of mammary epithelial acini relates to laminin matrix assembly. *Proc. Natl. Acad. Sci. U.S.A.* *110*, 163–168. <https://doi.org/10.1073/pnas.1201141110>.
- Wang, H., Guo, X., Wang, X., Wang, X., and Chen, J. (2020). Supracellular Actomyosin Mediates Cell-Cell Communication and Shapes Collective Migratory Morphology. *IScience* *23*, 101204. <https://doi.org/10.1016/j.isci.2020.101204>.
- Wang, W., Mouneimne, G., Sidani, M., Wyckoff, J., Chen, X., Makris, A., Goswami, S., Bresnick, A.R., and Condeelis, J.S. (2006). The activity status of cofilin is directly related to invasion, intravasation, and metastasis of mammary tumors. *Journal of Cell Biology* *173*, 395–404. <https://doi.org/10.1083/jcb.200510115>.
- Wang, X., He, L., Wu, Y.I., Hahn, K.M., and Montell, D.J. (2010). Light-mediated activation reveals a key role for Rac in collective guidance of cell movement in vivo. *Nat Cell Biol* *12*, 591–597. <https://doi.org/10.1038/ncb2061>.
- Webb, D.J., Parsons, J.T., and Horwitz, A.F. (2002). Adhesion assembly, disassembly and turnover in migrating cells – over and over and over again. *Nat Cell Biol* *4*, E97–E100. <https://doi.org/10.1038/ncb0402-e97>.
- Weber, G.F., Bjerke, M.A., and DeSimone, D.W. (2012). A Mechanoresponsive Cadherin-Keratin Complex Directs Polarized Protrusive Behavior and Collective Cell Migration. *Developmental Cell* *22*, 104–115. <https://doi.org/10.1016/j.devcel.2011.10.013>.
- Weigel, B., Bakker, G.-J., and Friedl, P. (2012). Intravital third harmonic generation microscopy of collective melanoma cell invasion: Principles of interface guidance and microvesicle dynamics. *Intravital* *1*, 32–43. <https://doi.org/10.4161/intv.21223>.
- Weigel, B., Bakker, G.-J., and Friedl, P. (2016). Third harmonic generation microscopy of cells and tissue organization. *J. Cell. Sci.* *129*, 245–255. <https://doi.org/10.1242/jcs.152272>.

- Welf, E.S., Driscoll, M.K., Sapoznik, E., Murali, V.S., Weems, A., Roh-Johnson, M., Dean, K.M., Fiolka, R., and Danuser, G. (2020). Worrying drives cell migration in mechanically unrestrained environments. *BioRxiv* 2020.11.09.372912. <https://doi.org/10.1101/2020.11.09.372912>.
- Wensink, G.E., Elias, S.G., Mullenders, J., Koopman, M., Boj, S.F., Kranenburg, O.W., and Roodhart, J.M.L. (2021). Patient-derived organoids as a predictive biomarker for treatment response in cancer patients. *Npj Precis. Onc.* 5, 30. <https://doi.org/10.1038/s41698-021-00168-1>.
- Whatcott, C.J., Ng, S., Barrett, M.T., Hostetter, G., Von Hoff, D.D., and Han, H. (2017). Inhibition of ROCK1 kinase modulates both tumor cells and stromal fibroblasts in pancreatic cancer. *PLoS One* 12. <https://doi.org/10.1371/journal.pone.0183871>.
- Wicki, A., Lehembre, F., Wick, N., Hantusch, B., Kerjaschki, D., and Christofori, G. (2006). Tumor invasion in the absence of epithelial-mesenchymal transition: podoplanin-mediated remodeling of the actin cytoskeleton. *Cancer Cell* 9, 261–272. <https://doi.org/10.1016/j.ccr.2006.03.010>.
- Winkler, B., Aranson, I.S., and Ziebert, F. (2019). Confinement and substrate topography control cell migration in a 3D computational model. *Commun Phys* 2, 1–11. <https://doi.org/10.1038/s42005-019-0185-x>.
- Wolf, K., and Friedl, P. (2011). Extracellular matrix determinants of proteolytic and non-proteolytic cell migration. *Trends in Cell Biology* 21, 736–744. <https://doi.org/10.1016/j.tcb.2011.09.006>.
- Wolf, K., Müller, R., Borgmann, S., Bröcker, E.-B., and Friedl, P. (2003a). Amoeboid shape change and contact guidance: T-lymphocyte crawling through fibrillar collagen is independent of matrix remodeling by MMPs and other proteases. *Blood* 102, 3262–3269. <https://doi.org/10.1182/blood-2002-12-3791>.
- Wolf, K., Mazo, I., Leung, H., Engelke, K., von Andrian, U.H., Deryugina, E.I., Strongin, A.Y., Bröcker, E.-B., and Friedl, P. (2003b). Compensation mechanism in tumor cell migration: mesenchymal–amoeboid transition after blocking of pericellular proteolysis. *Journal of Cell Biology* 160, 267–277. <https://doi.org/10.1083/jcb.200209006>.
- Wolf, K., Alexander, S., Schacht, V., Coussens, L.M., von Andrian, U.H., van Rheenen, J., Deryugina, E., and Friedl, P. (2009). Collagen-based cell migration models in vitro and in vivo. *Seminars in Cell & Developmental Biology* 20, 931–941. <https://doi.org/10.1016/j.semcdb.2009.08.005>.
- Wu, Y., Yim, J.K., Liang, J., Shao, Z., Qi, M., Zhong, J., Luo, Z., Yan, X., Zhang, M., Wang, X., et al. (2019). Insect-scale fast moving and ultrarobust soft robot. *Science Robotics* 4. <https://doi.org/10.1126/scirobotics.aax1594>.
- Xue, C., Wyckoff, J., Liang, F., Sidani, M., Violini, S., Tsai, K.-L., Zhang, Z.-Y., Sahai, E., Condeelis, J., and Segall, J.E. (2006). Epidermal Growth Factor Receptor Overexpression Results in Increased Tumor Cell Motility In vivo Coordinately with Enhanced Intravasation and Metastasis. *Cancer Res* 66, 192–197. <https://doi.org/10.1158/0008-5472.CAN-05-1242>.
- Yamada, K.M., and Sixt, M. (2019). Mechanisms of 3D cell migration. *Nat Rev Mol Cell Biol* 20, 738–752. <https://doi.org/10.1038/s41580-019-0172-9>.
- Yamaguchi, N., Mizutani, T., Kawabata, K., and Haga, H. (2015). Leader cells regulate collective cell migration via Rac activation in the downstream signaling of integrin β 1 and PI3K. *Scientific Reports* 5, 7656. <https://doi.org/10.1038/srep07656>.
- Ye, T.-M., Pang, R.T.K., Leung, C.O.N., Liu, W., and Yeung, W.S.B. (2012). Development and characterization of an endometrial tissue culture model for study of early implantation events. *Fertility and Sterility* 98, 1581–1589. <https://doi.org/10.1016/j.fertnstert.2012.08.013>.
- Yip, A.K., Chiam, K.-H., and Matsudaira, P. (2015). Traction stress analysis and modeling reveal that amoeboid migration in confined spaces is accompanied by expansive forces and requires the structural integrity of the membrane–cortex interactions. *Integr. Biol.* 7, 1196–1211. <https://doi.org/10.1039/C4IB00245H>.

- Yolland, L., Burki, M., Marcotti, S., Luchici, A., Kenny, F.N., Davis, J.R., Serna-Morales, E., Müller, J., Sixt, M., Davidson, A., et al. (2019). Persistent and polarized global actin flow is essential for directionality during cell migration. *Nat. Cell Biol.* *21*, 1370–1381. <https://doi.org/10.1038/s41556-019-0411-5>.
- Zajac, O., Raingeaud, J., Libanje, F., Lefebvre, C., Sabino, D., Martins, I., Roy, P., Benatar, C., Canet-Jourdan, C., Azorin, P., et al. (2018). Tumour spheres with inverted polarity drive the formation of peritoneal metastases in patients with hypermethylated colorectal carcinomas. *Nature Cell Biology* *1*. <https://doi.org/10.1038/s41556-017-0027-6>.
- Zamir, E.A., Rongish, B.J., and Little, C.D. (2008). The ECM Moves during Primitive Streak Formation—Computation of ECM Versus Cellular Motion. *PLOS Biology* *6*, e247. <https://doi.org/10.1371/journal.pbio.0060247>.
- Zeidman, I., and Buss, J.M. (1952). Transpulmonary Passage of Tumor Cell Emboli. *Cancer Res* *12*, 731–733. .
- Zeng, Q., Michael, I.P., Zhang, P., Saghafinia, S., Knott, G., Jiao, W., McCabe, B.D., Galván, J.A., Robinson, H.P.C., Zlobec, I., et al. (2019). Synaptic proximity enables NMDAR signalling to promote brain metastasis. *Nature* *573*, 526–531. <https://doi.org/10.1038/s41586-019-1576-6>.
- Zhang, C., Zhang, L., Xu, T., Xue, R., Yu, L., Zhu, Y., Wu, Y., Zhang, Q., Li, D., Shen, S., et al. (2020). Mapping the spreading routes of lymphatic metastases in human colorectal cancer. *Nat Commun* *11*, 1993. <https://doi.org/10.1038/s41467-020-15886-6>.
- Zhang, J., Goliwas, K.F., Wang, W., Taufalele, P.V., Bordeleau, F., and Reinhart-King, C.A. (2019). Energetic regulation of coordinated leader–follower dynamics during collective invasion of breast cancer cells. *Proc Natl Acad Sci USA* *116*, 7867–7872. <https://doi.org/10.1073/pnas.1809964116>.
- Zhang, X., Chan, T., and Mak, M. (2021). Morphodynamic signatures of MDA-MB-231 single cells and cell doublets undergoing invasion in confined microenvironments. *Sci Rep* *11*, 6529. <https://doi.org/10.1038/s41598-021-85640-5>.
- Zheng, X., Carstens, J.L., Kim, J., Scheible, M., Kaye, J., Sugimoto, H., Wu, C.-C., LeBleu, V.S., and Kalluri, R. (2015). Epithelial-to-mesenchymal transition is dispensable for metastasis but induces chemoresistance in pancreatic cancer. *Nature* *527*, 525–530. <https://doi.org/10.1038/nature16064>.
- Zuidema, A., Wang, W., and Sonnenberg, A. (2020). Crosstalk between Cell Adhesion Complexes in Regulation of Mechanotransduction. *BioEssays* *42*, 2000119. <https://doi.org/10.1002/bies.202000119>.

Titre : Mécanismes cellulaires de l'invasion collective des cancers et de leur réponse aux traitements

Mots clés : migration collective, cancer, migration amiboïde, organoïdes, micro-canaux.

Résumé : Les métastases sont responsables de la majorité des décès liés au cancer et malgré les avancées importantes de ces dernières décennies, des thérapies efficaces peinent à être identifiées pour chaque patient. A la source de ces difficultés se trouvent des processus cellulaires complexes dont le décryptage est donc d'importance capitale.

La migration cellulaire joue un rôle clé dans la dissémination tumorale ainsi que dans de nombreux processus physiologiques. Ce travail de thèse caractérise un nouveau mode de migration collective identifié chez des intermédiaires tumoraux de patients. Grâce à l'utilisation de micro-canaux et de microscopie, nous avons montré que ces cellules tumorales sont capables de migrer collectivement sans former d'adhésions focales avec leur substrat. Comme les cellules uniques amiboïdes (lymphocytes,

amibes), leur mode de migration repose plutôt sur la contractilité des cellules et la polarisation d'un cortex supracellulaire d'actomyosine. Nous l'avons appelé « migration collective amiboïde ». Indépendante de flux rétrogrades de myosine ou de cellules, cette migration est permise par des mouvements contractiles aléatoires et est orientée par la polarisation du cortex.

Cette migration collective peut être induite par un environnement non-adhérent ou par les propriétés cellulaires. En particulier, les TSIPs sont des intermédiaires tumoraux qui présentent spontanément ce mode de migration à cause de leur polarité épithéliale inversée. Cette thèse présente en outre la relation entre l'inversion de polarité et la moindre réponse aux chimiothérapies, étudiée *in vitro* sur des organoïdes.

Title : Cellular mechanisms of cancer collective invasion and response to treatments

Keywords : collective invasion, cancer, amoeboid migration, organoids, microchannels.

Abstract : Metastases cause most cancer deaths and despite the great advances of the last decades, finding an efficient therapy for each patient remains a challenge. Therefore, deciphering the complex cellular processes underlying cancer biology is a current major issue.

Cell invasion plays a key role in cancer dissemination as well as in crucial physiological processes. This PhD work aimed at deciphering the mechanisms underlying a new mode of collective cell migration identified in patients' tumour intermediates. Using microchannels and microscopy, we showed that collective cell migration can occur independently from the formation of focal adhesions with the substrate. Like amoeboid single cells (lymphocytes, amoebas), their mode of migration rather relies on

cell contractility and the polarization of a supracellular actomyosin cortex. We called it "collective amoeboid migration". Independent from retrograde myosin or cellular flows, it emerges from stochastic contractile stress and is oriented by cortex polarization.

This collective migration mode can be induced by anti-adhesive properties of the environment or by intrinsic cellular properties. We highlight here the example of TSIPs, tumour intermediates displaying spontaneously this mode of migration because of their inverted polarity. This PhD work also presents the relationship between TSIP polarity inversion and their lower response to chemotherapies. It was investigated *in vitro* on organoids from patient-derived xenografts.